2004

Data analysis and anode materials for lithium ion batteries

Matthew John Lindsay
University of Wollongong

Data Analysis and Anode Materials for Lithium Ion Batteries

A thesis submitted in fulfilment of the
requirements for the award of the degree

Doctor of Philosophy

from

UNIVERSITY OF WOLLONGONG

by

Matthew John Lindsay, B Eng (Materials Honours: Class I)

Institute for Superconducting and Electronic Materials
Department of Materials Engineering
Faculty of Engineering

2004

Thesis Certification

CERTIFICATION

I, Matthew J. Lindsay, declare that this thesis, submitted in fulfilment of the requirements for the award of Doctor of Philosophy, in the Institute for Superconducting and Electronic Materials, University of Wollongong, is wholly my own work unless otherwise referenced or acknowledged. The document has not been submitted for qualifications at any other academic institution.

Matthew J. Lindsay

18th October 2004

Contents

List of Tables

List of Figures

List of Equations

List of Abbreviations and Symbols

β	Peak width in radians due to material
η	Overpotential
θ	Incident angle of X-ray beam to the planes of atoms
λ	Wavelength of X-ray
ρ	Density
$\omega_{\max}$	Maximum phase
A	Particle surface area
A	Minimum potential in cyclic voltammetry data set
a	Particle dimension
A_{CS}	Cross sectional area of adsorbate molecule
ATCO	Advanced tin composite oxide
BET	Brunauer – Emmet – Teller
Bi-2212	$Bi_2Sr_2Ca_{1-x}Y_xCu_2O_{8+\delta}$
BPR	Ball to powder ratio
BTS	Battery testing system
B	Observed peak width in radians
B	Maximum potential in cyclic voltammetry data set
b	Peak width in radians due to instrumental broadening
C	BET constant
C	Potential between cycling endpoints used in the sorting of data
C_{dl}	Capacitor
CV	Cyclic voltammetry
DEC	Diethyl carbonate
d_{hkl}	Distance between two adjacent parallel planes
DMC	Dimethyl carbonate
DME	Dimethoxyethane
E	Electromotive force
E	Potential perturbation in impedance spectroscopy
EC	Ethylene carbonate
E_{dc}	Constant direct current potential
EIS	Electrochemical impedance spectroscopy
EMC	Ethyl methyl carbonate
emf	Electromotive Force
EPDM	Ethylene propylene diene terpolymer
E_r	Reversible Potential
F	Faraday's constant
f	Frequency (Hz)
FWHM	Full width at half maxima
g	grams
GBL	γ – butyrolactone
i	BET plot intercept
INCO	International Nickel Company
JCPDS	Joint Committee of Powder Diffraction Standards
K	Scherrer equation shape constant
M	Molar mass of lithium host

M	Molecular weight of adsorbate
MA	Mechanical alloying
MCMB	Mesocarbon microbeads
MM	Mechanical milling
N	Avogadros constant
n	Number of moles of lithium in the reaction product
n	Order of X-ray reflection and is any integer such that $\sin\theta \leq 1$
$\frac{P}{P_0}$	Relative pressure
PC	Propylene carbonate
PCAs	Process control additives
PDF	Powder diffraction file
psi	Pounds per square inch
PVDF	Polyvinyldiene fluoride
R	Particle dimension
r	Particle dimension
R_{ct}	Resistor
R_e	Resistor
rpm	Revolutions per minute
S	Specific surface area
s	BET plot slope
SEI	Solid electrolyte interphase
SEM	Scanning electron microscope
S_t	Total surface area
t	Particle dimension in Scherrer equation
TCO	Tin composite oxide
TEM	Transmission electron microscope
THF	Tetrahydrofuran
V	Particle volume
VBA	Visual basic for applications
W	Warburg Element
W	Weight of adsorbed gas at a relative pressure $\frac{P}{P_0}$
w	Sample weight
W_m	Weight of adsorbed gas in monolayer
wt. %	Weight percent
X	Any number such that $1 \leq \mathbf{X} \leq 99$
x	Constant particle volume
XRD	X-ray diffraction
y	Constant particle surface area

Abstract

In order to improve the capacity of lithium ion batteries higher capacity anode materials are required to replace the existing carbonaceous materials. The higher capacity materials must however also have a good cycle life. Many materials have been investigated to try and find a material offering such a desirable combination of properties. A number of materials are investigated as possible anode materials for lithium ion batteries including intermetallics with compositions based on $FeAl_3$, $Al_{47}Fe_{15}Si_{38}$, $Al_{20}Fe_5Si_2$, Al_9FeSi_3, FeSi and $FeSi_2$ along with other materials such as $Bi_2Sr_2CaCu_2O_8$, $Bi_2Sr_2Ca_{0.3}Y_{0.7}Cu_2O_8$, and nanometre SiC.

The intermetallic materials for the investigation were prepared through the arc melting of the constituent elements together followed by ball milling. The $Bi_2Sr_2CaCu_2O_8$ and $Bi_2Sr_2Ca_{0.3}Y_{0.7}Cu_2O_8$ materials were also ball milled but were initially prepared through the spray drying of nitrate solutions with subsequent sintering operations. The SiC materials were obtained through commercial suppliers.

Although many of the materials offered a high initial discharge capacity the capacity was not maintained over the following cycles. All the materials did however demonstrate the dramatic influence that the microstructure can have on the electrochemical properties of the material. Given the variability of the electrochemical performance with the alteration of the microstructure, improvement of the cycle life through exploration of microstructural variation may be possible.

Although a range of intermetallic compositions were examined and there were differences in the experimental methods used to examine them the results do suggest that for intermetallic materials compositions with under 60 weight percent of active material and a specific surface area less than 180 m^2/g should be examined.

Acknowledgments

I wish to acknowledge the support of:

My supervisor Professor H. K. Liu, for her support and encouragement throughout my PhD candidature.

The financial support of ISEM and DEETYA during my candidature.

Babs Allen without whom ISEM would be lost and I may have lost my sanity.

My parents Doug and Heather for giving me a love of learning and their continual support throughout my education.

Chapter 1 Introduction

Lithium ion batteries have found widespread and growing usage throughout the world particularly for portable consumer electronics. The existing materials in lithium batteries create limits on the enabling of technology through for example the size, capacity and cycle life of cells. Despite the popularity of the notebook computer, powerful enough to replace a desktop computer, it is not possible to achieve a full working day of run time without a second fully charged battery. Electric vehicles are an application that lithium batteries are being explored for and in order for it to be realised higher capacity cells with a long cycle life are necessary. Portable consumer electronics also benefit from the same properties that allow longer run times or smaller batteries for the same run time.

In order to achieve higher capacities however existing materials in commercial cells need to be replaced with higher capacity alternatives. One of the materials being targeted for replacement is the existing carbon anode material found in the majority of commercial cells. A diverse range of materials has been explored as possible replacements to carbon and although many offer much higher initial capacity it tends to decline rapidly in subsequent cycles.

Prior to presenting details on the search for new anode materials for lithium ion batteries background information is presented on a number of topics including batteries and ball milling (Chapter 2). Background material on batteries includes an introduction to batteries themselves, a brief history of the battery and a review of lithium battery components including an examination of the variety of materials considered as anode materials. As ball milling is frequently used to produce many of the materials for investigation including here a history of ball milling and an examination of the effect of milling variables is also presented.

A variety of experimental procedures are required to examine anode materials for lithium ion batteries including those for the preparation of the anode materials themselves, structural and microstructural characterisation, and fabrication for electrochemical testing and the testing itself (Chapter 3). The materials themselves were prepared using a variety of techniques including arc melting, ball milling and spray drying. Characterisation of the materials themselves includes the use of techniques such as SEM, XRD and BET. Details of the fabrication of the electrodes themselves and assembly into cells along with the electrochemical testing procedures are also presented.

In order to effectively analyse raw data originating from electrochemical testing analysis software was developed and an examination of the methodology employed is presented in Chapter 4. The software is capable of analysing data from both cyclic voltammetry and charge/discharge experiments from a variety of test equipment. The algorithms employed to achieve this are presented and examined.

In the continuing search for new anode materials a number of materials will be explored as possible replacements for existing carbon materials. Intermetallics and oxides are just two of the classes of materials that are being explored as alternative anode materials. Nanomaterials in a number of classes of materials are also receiving significant attention.

Two binary aluminium – iron based intermetallic materials are examined as possible anode materials based on the $FeAl_3$ composition (Chapter 5). The materials themselves were characterised using SEM, BET and XRD whilst the electrochemical properties were examined with techniques such as constant current charge/discharge and cyclic voltammetry.

Three ternary aluminium – iron – silicon intermetallic materials with compositions corresponding to $Al_{47}Fe_{15}Si_{38}$, $Al_{20}Fe_5Si_2$ and Al_9FeSi_3 are examined as possible anode materials (Chapter 6). The materials themselves were characterised using SEM, BET and XRD whilst the electrochemical properties were examined with techniques such as constant current charge/discharge and impedance spectroscopy.

Four binary iron – silicon based intermetallic materials based on compositions of FeSi (Chapter 7) and $FeSi_2$ (Chapter 8) are examined as possible anode materials for lithium ion batteries. The materials themselves were characterised using SEM, BET and XRD whilst the electrochemical properties were examined with techniques such as constant current charge/discharge and cyclic voltammetry.

Other than the intermetallic materials examined four other materials were also examined. Two oxide materials based on compositions of $Bi_2Sr_2CaCu_2O_8$ and $Bi_2Sr_2Ca_{0.3}Y_{0.7}Cu_2O_8$ were also examined as anode materials for lithium ion batteries (Chapter 9). The materials themselves were characterised with SEM, BET and XRD whilst the electrochemical properties were examined with techniques such as constant current charge/discharge. A variety of nanomaterials that have been examined as hydrogen storage materials have also been explored for use in lithium ion batteries and two nanometre SiC samples from commercial suppliers are examined as anode materials for lithium ion batteries (Chapter 10). The materials themselves were

characterised using SEM, TEM, BET and XRD whilst the electrochemical properties were examined with techniques such as constant current charge/discharge and cyclic voltammetry.

Following the presentation of the experimental results a discussion of the results follows (Chapter 11) and conclusions are drawn from the experimental results (Chapter 12). Supplemental information then follows in the four appendices covering details on the effect of variables on specific surface area (Appendix A), manuals for the software developed (Appendix B & Appendix C), BET analysis (Appendix D) and list of publications (Appendix E).

Chapter 2 Literature Survey

2.1 Cells and Batteries

A cell is a "Device which uses energy from a chemical action to produce electrical energy, usually consisting of a container with two electrodes immersed in an electrolyte" [1]. By definition a battery is a number of these devices connected together but the term is also commonly used to refer to a single cell [2]. Individual cells can be connected in numerous configurations depending on the desired characteristics of the assembled battery. These main characteristics are the electromotive force (emf) and capacity. The emf is a measure of the "driving force for the completion of an electrochemical reaction" [3] and is measured in volts (V). Where one volt (V) is the emf required to impart one joule (J) of energy to a charge of one coulomb (C) [3]. Whilst the capacity is a measure of the current output capability for a period of time, measured in mAh or Ah.

A single cell might have a potential of 1.2 V and a capacity of 1400 mAh (Figure 2-1a) but by arranging six identical cells in different configurations a battery with higher capacity and/or potential can be created. By connecting six of these cells in series (Figure 2-1b) a battery with a higher potential of 7.2 V is created but the capacity is still 1400 mAh. If the six cells were instead connected in parallel (Figure 2-1c) the potential would remain 1.2 V but the capacity would be increased to 8400 mAh. Both the capacity and potential can be increased simultaneously by combining series and parallel elements. By connecting a pair of three cells connected in series in parallel the potential (Figure 2-1d) can be increased to 3.6 V and simultaneously the capacity increased to 4200 mAh.

2.2 Oxidation and Reduction

The chemical actions from which cells produce electrical energy are oxidation – reduction or redox reactions. A simple definition of redox reactions is a chemical reaction in which one or more of the reactive species such as an atom, ion or molecule changes its oxidation state [3]. When a reactive species loses electrons and thus is more positively charged it has been oxidised (higher oxidation state) [3]. Whilst when a reactive species gains an electron and thus is more negatively charged it has been

reduced (lower oxidation state) [3]. From such definitions it is apparent that oxidation and reduction are complementary reactions as if one occurs so must the other.

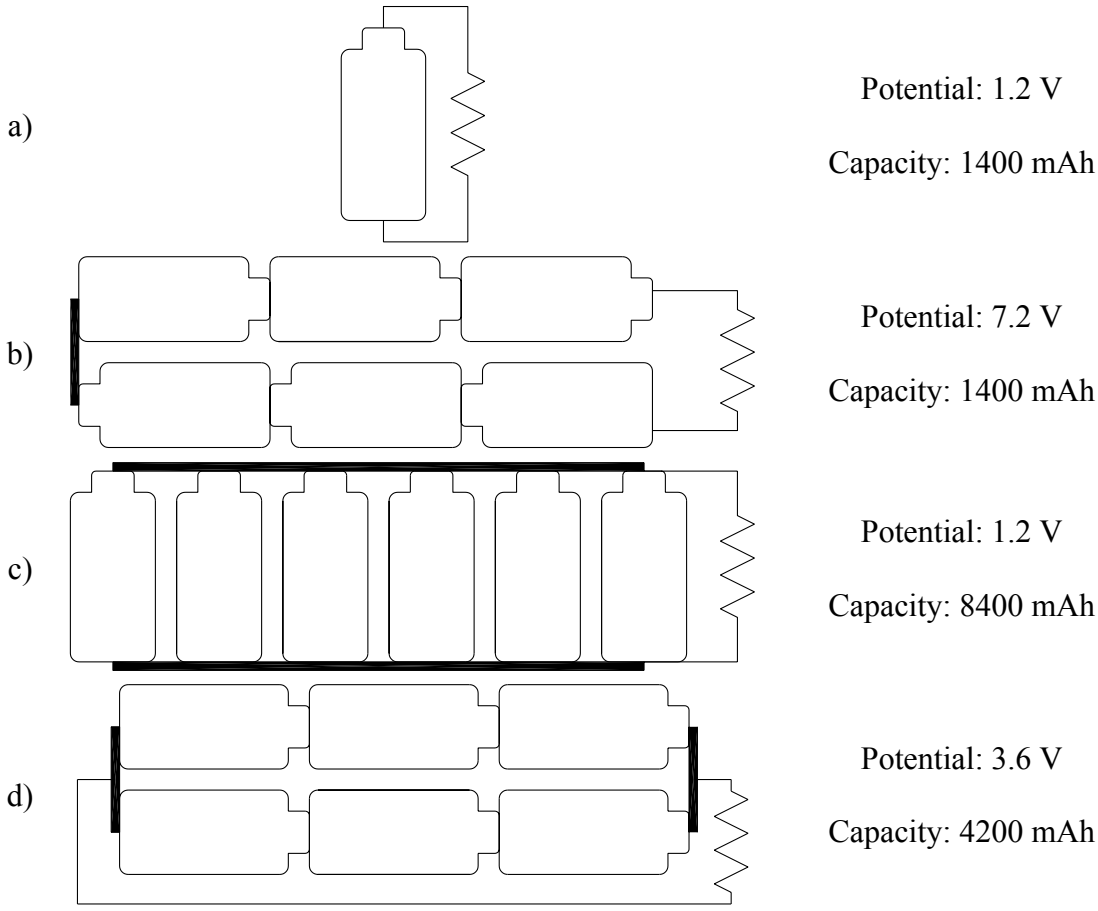

Figure 2-1: Assorted arrangements of cells into batteries and effect on potential and capacity.

A reduction reaction for instance in which a reactive species gains electrons needs a source of electrons, this source is the complementary oxidation reaction. The species that is reduced is called the oxidising agent or oxidant whilst the species that is oxidised is called the reducing agent or reductant. An example of a simple redox reaction involving metal and ions of zinc and silver is shown in 2-1. In this example zinc metal is oxidised by silver ions to zinc ions whilst silver ions are reduced to silver metal by zinc metal.

$$Zn + 2Ag^{+} \rightarrow \quad Zn^{2+} + 2Ag \qquad \textbf{2-1}$$

Although oxidation and reduction must occur simultaneously for convenience the reactions are frequently written as half reactions, which are the individual oxidation and reduction reactions. For the silver – zinc example (2-1) the oxidation half reaction of zinc metal to zinc ions is shown in 2-2 whilst the reduction half reaction of silver ions to silver metal is shown in 2-3.

$$Zn \rightarrow \quad Zn^{2+} + 2e^{-} \qquad \textbf{2-2}$$

$$2Ag^{+} + 2e^{-} \rightarrow \quad 2Ag \qquad \textbf{2-3}$$

The transfer of electrons in redox reactions is not always as obvious as it is for the zinc – silver example. The combustion of hydrogen in oxygen to form water is one such example (2-4). In this case hydrogen has been oxidised and oxygen reduced.

$$2H_2 + O_2 \rightarrow \quad 2H_2O \qquad \textbf{2-4}$$

2.3 Bonding and Atomic Order

Solid materials are composed of atoms bonded to each other by different bond types and in a variety of arrangements with respect to each other. Materials can be classified according to both their bonds and the regularity of the arrangement of atoms [4].

2.3.1 Bonding

There are three different types of chemical or primary bonding found between atoms in solid materials. These are ionic, covalent and metallic bonding and in each case the bonding involves the outer valence electrons of the atom. Generally the bonding is a result of the tendency of atoms to reach a stable electron structure through complete filling of the outer electron shell [4].

2.3.1.1 Ionic Bonding

Ionic bonding forms between metals and non-metals and is a result of coulombic bonding forces [4]. Metallic elements tend to give up their outer valence electrons and hence become positively charged whilst the non-metallic elements will tend to accept the additional electrons and become negatively charged to assume a stable electron configuration. The bonding is then a result of the attraction between the two ions as a result of their net charge. As a result of the bonding ionic materials are hard and brittle and electrical and thermal insulators [4].

2.3.1.2 Covalent Bonding

Covalent bonds result in stable electron configurations in the bonded atoms through the sharing of valence electrons between adjacent atoms [4]. A variety of materials exhibit covalent bonding including non-metallic molecules such as H_2, other

molecules such as H_2O and some elemental solids such as diamond [4]. Very few compounds however show pure covalent or ionic bonding, as bonding is typically a mixture of the two [4].

2.3.1.3 Metallic Bonding

Metallic bonding is found in metals and their alloys and a simple model is used to approximate the bonding [4]. This model considers a metallic bonded material as consisting of positive charged metallic ions located in a sea of delocalised valence electrons. As a result of the free valence electrons metallically bonded materials are good thermal and electrical conductors [4].

2.3.2 Atomic Order

Crystalline materials have atoms arranged in a periodic array over large atomic distances and are described as having long range order [4]. Whilst nanocrystalline materials have only limited long range order with a grain size typically in the range of 5 – 20 nm [5]. A material with short range order has a structural correlation length of the order of atomic distances [5] and is described as amorphous. Amorphous metallic materials are also referred to as metallic glasses.

2.4 Components of a Cell

There are three basic components to a cell, two electrodes (anode and cathode) and an electrolyte (Figure 2-2). The electrode that is oxidised is called the anode or negative electrode whilst the electrode that is reduced is called the cathode or positive electrode. The anode and cathode of a cell are labelled according to this definition for the discharge of the cell. The electrolyte is an ionic conductor that allows transfer of ions between the electrodes. When the two electrodes are connected through an external circuit (such as the resistor depicted in Figure 2-2) electrons flow from the anode to the cathode as a result of the redox reaction. At the same time anions (negative ions) flow through the electrolyte to the anode and cations (positive ions) to the cathode.

2.5 Classification of Batteries

Batteries fall into two broad categories based on their ability to be recharged electrically. Primary batteries cannot be recharged whilst secondary batteries can. In addition to this further classifications are based on the chemistry of the redox reactions.

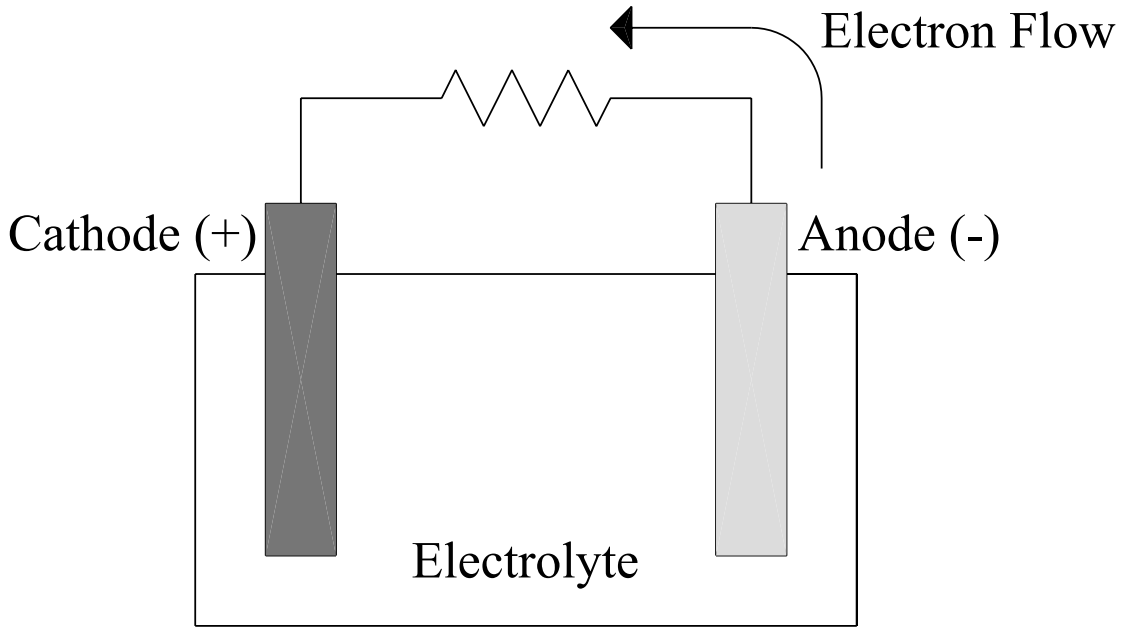

Figure 2-2: Basic components of an electrochemical cell.

2.5.1 Dry Cell

The dry cell is a primary battery widely used for flashlights and other small portable devices and is based on redox reactions between zinc and manganese dioxide (MnO_2). The general reactions occurring in such a cell are the oxidation of zinc at the anode (2-5) and reduction of manganese dioxide (2-6) [3].

$$Zn \rightarrow \quad Zn^{2+} + 2e^{-} \qquad \textbf{2-5}$$

$$2NH_4^{+} + 2MnO_2 + 2e^{-} \rightarrow \quad Mn_2O_3 + 2NH_3 + H_2O \qquad \textbf{2-6}$$

2.5.2 Lead Acid Battery

The lead acid battery is a secondary battery and is widely used in automobiles as a starter battery along with other applications as storage batteries. The oxidation reaction (2-7) and the reduction reaction (2-8) both produce lead sulphate during discharge at their respective electrodes [6]. The emf for this reaction from standard reduction potentials is 2.04 V [6].

$$Pb + HSO_4^{-} \rightarrow \quad PbSO_4 + 2e^{-} + H^{+} \qquad \textbf{2-7}$$

$$PbO_2 + 3H^{+} + HSO_4^{-} + 2e^{-} \rightarrow \quad PbSO_4 + 2H_2O \qquad \textbf{2-8}$$

2.5.3 Nickel – Cadmium Battery

The nickel – cadmium battery is a secondary battery that has been widely used to power portable consumer electronics. This is however declining in favour of more environmentally friendly systems. The oxidation reaction (2-9) and reduction reaction (2-10) for the nickel cadmium battery has an emf of 1.30 V from standard reduction potentials [6].

$$Cd + 2OH^- \rightarrow \quad Cd(OH)_2 + 2e^- \qquad \textbf{2-9}$$

$$2NiOOH + 2H_2O + 2e^- \rightarrow \quad 2Ni(OH)_2 + 2OH^- \qquad \textbf{2-10}$$

2.5.4 Nickel – Metal Hydride Battery

The nickel – metal hydride battery is a development of the nickel – cadmium battery with the cadmium being replaced by a metal hydride. The oxidation reaction (2-11) and the reduction reaction (2-12) for the discharge of a nickel – metal hydride battery is similar to that of the nickel – cadmium systems [6]. The emf is however slightly higher than that of nickel – cadmium batteries at 1.35 V.

$$MH + OH^- \rightarrow \quad M + H_2O + e^- \qquad \textbf{2-11}$$

$$NiOOH + H_2O + e^- \rightarrow \quad Ni(OH)_2 + OH^- \qquad \textbf{2-12}$$

2.5.5 Lithium Ion Battery

The basic components of a lithium ion battery (Figure 2-3) are the anode, cathode, separator and electrolyte. Both the anode and cathode are comprised of electrode materials attached to a substrate called a current collector. The current collector for the cathode is aluminium whilst that for the anode is copper. The separator provides physical separation of the anode and cathode and is micro porous allowing lithium ions to pass through it. During discharge lithium ions are transported from the anode to the cathode with the reverse happening during charging. Commercial lithium ion batteries frequently have a carbon based anode material and an oxide based cathode material such as $LiCoO_2$. The oxidation and reduction reactions for the discharge of such a configuration are shown in 2-13 and 2-14 respectively [7].

$$LiCoO_2 \rightarrow \quad Li_{1-x}CoO_2 + xLi^+ + xe^- \qquad \textbf{2-13}$$

$$C + xLi^+ + xe^- \rightarrow \quad Li_xC \qquad \textbf{2-14}$$

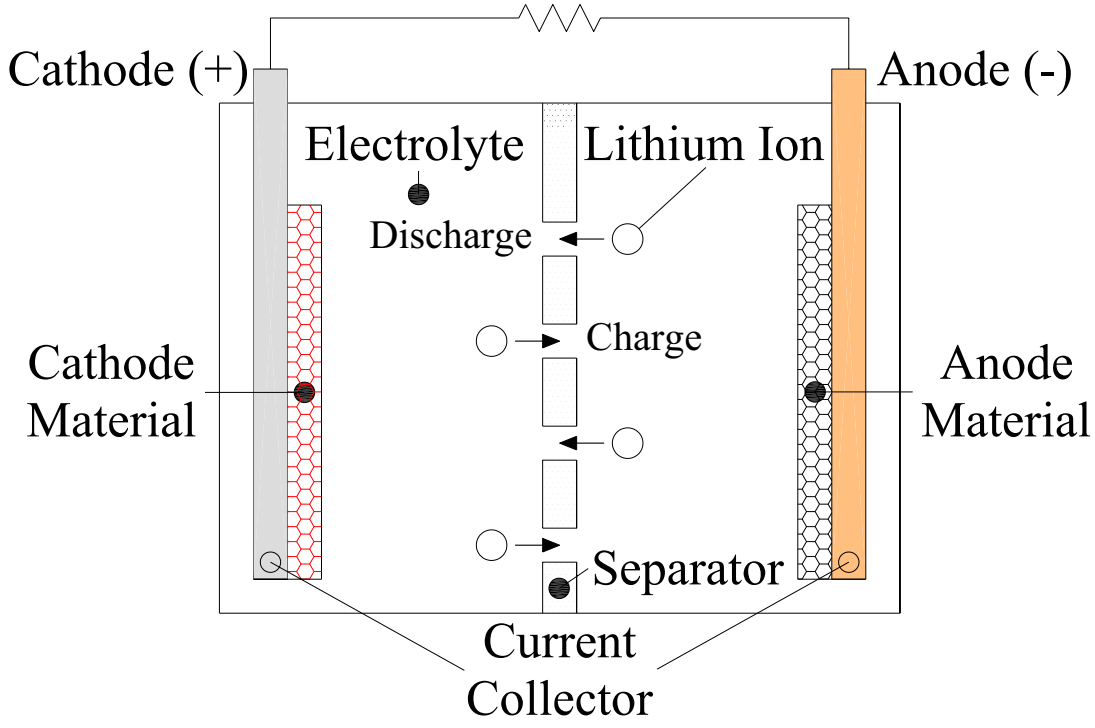

Figure 2-3: Basic components of lithium ion battery.

2.6 Historical Development of Batteries

Batteries may have been used up to 4300 years ago by the Egyptians to electroplate antimony onto copper and by the Parthians (ca. 250 bc) to electroplate silver [8]. The start of the development of modern batteries is however traced to the work of Luigi Galvani working at Bologna University (Italy) in 1791. In his work Galvani observed the contraction of the muscles of a frog when touched by a metallic object and called the phenomenon “animal electricity” [8]. Prompted by the claims of Galvani, Alessandro Volta (Italy) began a series of experiments utilising combinations of different materials with zinc, lead, tin and iron used as positive plates whilst copper, silver, gold and graphite were used as the negative plates [8]. By 1800 Volta had developed a battery that was to become known as a “voltaic pile”. The voltaic pile consisted of alternating zinc and silver discs separated by cloth or paper soaked in a solution of either sodium hydroxide or brine [2]. By 1834 Faraday had derived a number of quantitative laws based on experiments conducted with the voltaic pile [2].

By 1802 William Cruickshank (England) had developed the first battery capable of being mass produced [8]. This consisted of a series of zinc and copper plates in a wooden box filled with electrolyte (brine or watered down acid) and had the advantage of not drying out and providing more energy than the voltaic pile [8]. Grooves in the

wooden box held the plates in place and the cell was sealed with cement [8]. The first rechargeable battery couple was also demonstrated in 1802 by Johann Ritter [6].

Development of various battery systems continued and in 1836 John Frederic Daniell (England) developed the "Daniell Cell" which was based on copper and zinc in sulphuric acid and delivered a steadier current than the voltaic pile [8]. In 1859 another cell was developed using sulphuric acid called the lead – acid cell by Gaston Planté (France). The lead – acid cell was able to deliver large currents and was rechargeable [2] but the only way the cell could be charged at the time was through the use of primary cells [9] and it remained a laboratory curiosity for nearly two decades [2].

In 1866 Georges Leclanché (France) developed the Leclanché cell, a wet cell based on a zinc anode and cathode of manganese dioxide mixed with carbon [9]. The Lechlanché cell has undergone a number of refinements with the first occurring in 1888 by Gassner (USA) creating a dry cell utilising a moistened cathode and a swollen starch or plaster of paris separator [9].

In 1899 Wlademar Junger (Sweden) developed the nickel cadmium battery which was soon followed in 1901 by an alternate design by Thomas Edison (USA) featuring the replacement of cadmium with iron [8]. As the materials costs of both systems were high in comparison to dry cells and lead acid batteries, practical applications were limited [8]. In 1932 Shlecht and Ackermann's (Germany) development of the sintered pole plate allowed higher load currents and improved the longevity of nickel cadmium cells [8]. Development of the nickel cadmium battery continued and in 1947 it reached its basic state of today with the complete sealing of the cell by Neumann (France) [8]. Development and refinements have however continued and during the 1980s the batteries improved significantly [10].

The zinc – manganese dioxide cell was developed further during the 1950s by Union Carbide (USA) with the use of an alkaline electrolyte offering higher capacity than the previous versions of the cell [2]. The alkaline cell consisted of a cathode composed of a mixture of high purity manganese dioxide and carbon, an electrolyte of potassium hydroxide and a powdered zinc alloy anode contained in a steel can.

The nickel – hydrogen system was developed as a replacement for the nickel cadmium system for space applications [11]. The nickel metal hydride system was developed for terrestrial application from the work on nickel – hydrogen cells [11]. It is very similar to the nickel – cadmium system with the cadmium electrode of that system being replaced with an alloy capable of adsorbing hydrogen on charge and releasing it

on discharge [12]. Early work on the system was conducted during the 1970s [11] but the desire for longer running times saw development accelerated during the 1980s [10] and commercialised in 1990 [8].

Although zinc/manganese oxide cells have traditionally been primary batteries in 1992 a rechargeable alkaline manganese (RAM) battery was commercialised by Kordesch (Canada) [8]. A rechargeable version had been developed in the 1960s though its cycle life was poor compared to nickel cadmium cells and was unable to recover from deep discharge [12]. For an AA sized cell these have a capacity of 2 – 3 Ah compared to 0.5 – 1.0 Ah for nickel cadmium and 1 – 1.5 Ah for nickel metal hydride [11]. The life of the cells is dependent on the degree to which they are discharged in use. If fully discharged and then charged only ten cycles may be possible but at lower degrees of discharge up to 80 cycles are possible [11].

Initial work on lithium based batteries commenced during the 1960s with exploration of the chemistry and electrochemistry of lithium systems [13]. A number of primary lithium cells were marketed during the 1970s after overcoming early difficulties with the production of commercial cells [13]. During the 1980s large scale production of primary cells was in progress having overcome the difficulties with manufacturing and design [13]. The dominant systems were couples of lithium with sulphur dioxide (SO_2), thionyl chloride ($SOCl_2$), carbon monofluoride ($(CF)_n$) and manganese dioxide (MnO_2) [13].

The development of secondary based lithium systems was also underway and the first demonstration of reversible insertion of lithium into carbon in 1983 was key to it [14]. Following this development Sony introduced the first commercial cells using carbon – based anodes around 1990. Greater versatility in cell packaging became available with the commercial use of polymer electrolytes in 1999 [8].

2.7 Secondary Lithium Ion Batteries

Lithium was an attractive anode material with a number of favourable properties including its high theoretical capacity of 3860 mAh/g. When lithium metal anodes were used in rechargeable batteries part of the lithium was deposited as a “lithium sludge” limiting the cycle life to a maximum of 200 cycles [10]. The lithium sludge also presented a severe safety problem as its high surface area made it highly reactive [10]. Due to severe safety problems and rapid loss of capacity with cycling metallic lithium electrodes have seen little further use in commercial secondary cells. By using materials

other than metallic lithium as the anode the cell voltage, capacity, and rate capability are reduced [15].

As a result of the problems with metallic lithium anodes an alternative anode material was needed and carbon materials were found to be suitable for this role. The theoretical capacity of carbon is however only 372 mAh/g and as a result there is considerable interest in replacing it with something else that offers higher capacities to increase the final capacity and cycle life of the complete cell. Numerous materials have been investigated as possible replacements for these carbon based materials with increased interest following the 1996 announcement of Fuji Photo Film of an amorphous tin – based composite oxide (TCO or ATCO) as anode materials [16].

Materials investigated include chalcogenides [17], silicides [18], transition metal oxides [19], lithium alloys [20-22] as well as a number of composite microstructures [21, 23, 24]. None of these have been investigated fully and it is not clear which has the best potential to replace current carbon materials [25]. Despite the diverse range of materials examined electrochemical results typically show rapid decline in discharge capacity with cycling (capacity fade). One of the major causes of the rapid decline in capacity is thought to be the mechanical degradation of the electrode.

In many cases the accommodation of lithium within the structure results in significant expansion of the host material and the continuous volume changes during cycling results in the cracking and crumbling of the electrode (decrepitation). If metallic tin for instance is used as an anode material full reaction with lithium to form $Li_{22}Sn_5$ results in a 676 % increase in volume [26]. As a result of the cracking pieces of the electrode become electrically isolated from it and can no longer contribute to its capacity. The situation is not helped by the fact that many lithium – metal phases are relatively brittle and the mechanical stresses generated during cycling can easily induce decay in the mechanical and hence electrochemical properties [15]. The dimensional stability of electrode materials is thus an important parameter to maintaining electrochemical performance with cycling. A range of parameters including the grain size, shape, texture and orientation also have a strong influence on the dimensional stability of a material [15].

A small particle and grain size has been shown in a number of studies to improve electrochemical performance through reduced degradation of the electrode [27-30]. Reduction in grain and particle size alone can not fully solve the problems of

mechanical degradation as modelling of the behaviour has shown the critical grain size to prevent such failure is below the unit cell size of most single phase materials [31]. The results of the model were also confirmed through experimental work [32]. Nevertheless the use of materials with a small particle and grain size is a key requirement in the reduction of electrode degradation.

Cracking of electrodes has also been shown to occur on a larger scale than the individual particles as a result of in situ investigations carried out using atomic force and optical microscopy [33]. In this case SiSn sputter deposited films were examined and following the first discharge contraction of the film in directions both parallel and perpendicular to the substrate resulted in crack patterns similar to dried mud. The 1 – 8 μm film then consisted of a series of 30 μm flakes that were able to expand and contract without further cracking being evident.

The use of dimensionally stable structures for lithium ion electrode materials has been suggested and many examples of such structures exist in nature including diamonds and sapphires [34]. Thackeray suggested that highly symmetric structures such as cubic structures may provide enhanced cycle life through increased stability of both the lithiated and delithiated structures [34]. Benedek and Thackeray have investigated materials on the basis of structural compatibility of the lithiated and delithiated structures and found that other factors also influence electrochemical performance [35].

2.7.1 Electrolytes

All electrolytes have been shown to be thermodynamically unstable towards lithium with kinetic stability dependent on the formation of a passivating layer on the lithium [36]. This layer is called the solid electrolyte interphase (SEI) and is important for all electrodes in lithium ion batteries though it has been more widely examined in relation to anode materials [15]. Many other battery systems use aqueous electrolytes but lithium ion batteries do not as the operating potential is limited by the decomposition of water [37]. The use of aqueous electrolytes can also be limited by their reactivity with the electrode components though this can be overcome by appropriately formulating an electrolyte [38]. Nonaqueous electrolytes are more stable in the lithium ion environment but their ionic conductivities are about two orders of magnitude lower than aqueous electrolytes [37]. The lower ionic conductivities also necessitates lithium ion battery designs incorporating thin electrodes (0.1 mm) [38].

Liquid electrolytes are typically composed of at least two solvents and a lithium salt. One of the solvents is typically a cyclic ester or lactone, which have a high dielectric constant and high viscosity. Whilst the other solvent is an aliphatic ester or ether, which have a low dielectric constant and low viscosity [37]. The high dielectric constant solvent promotes the dissociation of lithium salts [37] and controls the formation of the SEI [39]. The low viscosity solvent enhances the movement of lithium ions between the electrodes [37] and hence its conductivity [39]. Selected examples of solvents utilised in lithium batteries are presented in Table 2-1. Some solvents have been found to be detrimental to the electrochemical performance of the batteries in which they were used. Propylene carbonate (PC) based solutions degrade highly graphitised carbons on charging which has seen ethylene carbonate (EC) used almost exclusively when graphite anodes are used in lithium ion batteries [37]. A number of different lithium salts have been used in such solvents and the highest ionic conductivity is observed with lithium hexafluoro phosphate ($LiPF_6$) and is the most widely used in commercial batteries [37]. Other common lithium salts used in electrolytes include $LiClO_4$, $LiAsF_6$ and $LiBF_4$ [39]. A number of novel lithium salts that have superior stability and high ionic conductivity have been reported and include salts such as $LiN(SO_2CF_3)_2$, $LiN(SO_2C_2F_5)_2$, $LiN(SO_2CF_3)(SO_2C_4F_9)$, $LiPF_{6-n}(CF_3)_n$ and $LiPF_{6-n}(C_2F_5)_n$ [37].

Other types of electrolytes such as polymer gels have also been investigated for a number of reasons. The demand for portable devices have seen demands for smaller batteries grow but producing cells under 4 mm thick with a metal case is not possible [37]. Using a polymer based electrolyte a battery with a case composed of an aluminium/resin – laminate film overcame this limitation in 1999 [37] with its use possible as a result the lower levels of evaporation of solvents from polymer electrolytes [37]. Inaba *et. al* [37] described polymer gel electrolytes as "composed of an electrochemically inactive polymer matrix swollen by a lithium salt solution in a compatible solvent". Suitable combination of polymer matrix, lithium salt and solvents have ionic conductivities comparable to liquid electrolytes [37]. In addition to polymer gel electrolytes another polymer electrolyte described as dry polymer is another alternative to liquid electrolytes. This type of electrolyte however only consists of a polymer and a lithium salt [37].

Table 2-1: Typical lithium ion battery solvents.

Cyclic Esters and Lactones *	Aliphatic Esters and Ether *
Ethylene Carbonate (EC)	Dimethyl Carbonate (DMC)
Propylene Carbonate (PC)	Diethyl Carbonate (DEC)
γ – butyrolactone (GBL)	Ethyl Methyl Carbonate (EMC)
	Dimethoxyethane (DME)
	Tetrahydrofuran (THF)

* – Based on materials listed by Inaba *et. al.* [37].

2.7.2 Anode Materials

A number of different materials have been investigated as possible anode materials for lithium ion batteries. This includes the carbon materials that still dominate in commercial cells as well as a number of materials that have been suggested as possible replacements. Such materials include a range of oxides, nitrides, intermetallics and other forms of carbons. Increasingly composite materials are also being examined in an effort to find suitable electrode materials by combining desirable properties of a number of materials.

2.7.2.1 Carbons

The capacity and reversibility of carbon materials vary according to its source and heat treatment history [40]. Both of these parameters effect the microstructure of the material including crystallite size, interplanar spacing, surface area, and composition [40]. As a result a large number of carbon materials have been and continue to be investigated as anode materials for lithium ion batteries. It is not however just different types of carbons such as graphites [41, 42], hard carbons and nanotubes [43-47] being investigated, as surface modification and composites are also increasingly being examined. Examples of modification include milling of graphite materials [48, 49] and coating with various materials such as metals including tin and nickel [50-52] and zirconia [53]. Composites with carbons have also been explored including a graphite – tin oxide composite [54] and carbon nanotube – Sn_2Sb composite [55].

The theoretical capacity of graphitic carbons is 372 mAh/g but other carbon materials do exhibit higher capacity [15]. For graphitic carbons the higher the crystallinity the higher the resulting capacity of the material with natural graphite

possessing a perfectly crystalline structure [56]. Crystallinity affects not only the capacity but also the shape of the charge and discharge profiles. Low crystallinity graphites exhibiting a sloped charge and discharge characteristics but as the crystallinity is increased the profiles flatten out [56]. Graphitic carbons are still common in commercial lithium ion batteries and in such applications a particle size of 10 μm is typical [15]. Like lithium, carbon materials are also thermodynamically unstable in all known electrolytes though unlike lithium SEI formation is not spontaneous but occurs during the first few discharge cycles [15].

The insertion of lithium into graphitic carbons occurs in a number of stages and is theoretically completely reversible [15]. In practice however this is not realised with the first discharge greater than the theoretical capacity as a result of SEI formation and the subsequent charge is only 80 – 95 % [15]. In subsequent cycles however the charge capacity is nearly 100 % of the discharge capacity [15].

2.7.2.2 Oxides

A wide range of oxide materials has been investigated as anode materials for lithium ion batteries. Most of the investigations into oxide materials have been carried out following Fuji Photo Films announcement of tin based composite oxides (TCO). Oxides such as WO_2, MoO_2, and Nb_2O_5 had been investigated as anode materials long before the announcement of TCO [19]. Other than tin oxide and TCO a number of other oxides have also been investigated in recent years and examples are presented in Table 2-2. TCO are not a simple oxide material like many of the other materials that have been subsequently investigated but are a composite of a number of oxide materials including SnO, B_2O_3, $Sn_2P_2O_7$, Al_2O_3 [15]. It is however only the tin (II) components of the TCO that contribute to the electrochemical capacity with the other oxides of boron, aluminium and phosphorous forming a dimensionally stable glassy network [15]. During the first discharge of such a material the SnO reacts with Li to from Li_2O and metallic Sn [15]. The formation of Li_2O is irreversible and is responsible for a large irreversible capacity [15] and on subsequent discharges the lithium alloys with the metallic tin [15]. As for other materials the particle size has an influence on the electrochemical properties of the material [57].

Table 2-2: Metal oxide materials examined in recent years.

Metal Oxide	Reference
CoO	[57-60]
Co_3O_4	[57, 59-63]
CuO	[19, 57, 58, 64]
Cu_2O	[57, 58, 64]
FeO	[57, 58]
Fe_2O_3	[19, 65, 66]
In_2O_3	[19]
NiO	[57, 58, 67]
PbO	[19]
Sb_2O_3	[19]
SiO_x	[68]
Ta_2O_5	[69, 70]
TiO_2	[71, 72]
ZnO	[19, 69, 73-75]

A number of different compositions of tin based amorphous oxides have been investigated other than the original $Sn_{1.0}B_{0.56}P_{0.40}Al_{0.42}O_{0.36}$ from Fuji's patent [76]. The first discharge capacities of both TCO and SnO_2 are typically over 1000 mAh/g but have been reported as high as 1900 mAh/g [77]. Following the first discharge a capacity of around 500 mAh/g is common though the cycle life varies [16, 46, 73, 76-87]. The best cycle life was demonstrated by SnO_2 synthesised using template synthesis with capacities of 700 mAh/g for up to 800 cycles [80, 81] and also demonstrated high rate capability.

2.7.2.3 Nitrides

A number of nitride materials have been investigated based on Li_3N a compound that has been investigated thoroughly as a solid electrolyte at room temperature because of its high lithium conductivity [88]. These materials have the same structure as Li_3N and a composition of $Li_{3-x}M_xN$ where x is Co, Ni or Cu [89]. A number of investigations have been carried out with differing results on cycle life [88-97]. Shodai *et. al.* reported that after a decline in capacity during the first few cycles stable

capacities were reached for $Li_{2.6}Co_{0.4}N$ (760 mAh/g), $Li_{2.6}Cu_{0.4}N$ (650 mAh/g) and $Li_{2.6}Ni_{0.4}N$ (180 mAh/g) [93]. Wang *et. al.* also examined $Li_{2.6}Co_{0.4}N$ but a stable capacity was not reached with a gradual decline in capacity to around 600 mAh/g after 45 cycles but the $Li_{2.6}Co_{0.20}Cu_{0.20}N$ material they examined was more stable with 91 % of the initial capacity of 609 mAh/g maintained after 45 cycles [96]. Whilst Kang *et. al.* also reported a high initial capacity of over 1000 mAh/g for $Li_{2.6}Co_{0.4}N$ materials the capacity declined to under 35 % of the initial capacity in 50 cycles [90]. The cycle life was improved slightly by iron doping ($Li_{2.6}Co_{0.35}Fe_{0.05}N$) which reduced the initial capacity to 900 mAh/g but after 50 cycles the capacity was still 60 % of the original [90].

A number of other nitride materials not based on the Li_3N structure have also been investigated including boron – carbon – nitrides [98, 99], Ge_3N_4 [100], Cu_3N [101], Sn_3N_4 [102] as well as other lithium metal nitrides such as Li_3FeN_2 and Li_7MnN_4 [100].

2.7.2.4 Intermetallics

Intermetallic materials are one class of materials that have been investigated to try and limit the electrode degradation from decrepitation and are stoichiometric compounds formed by metallic elements. Examination of binary phase diagrams for the constituent elements of binary intermetallics show most intermetallics are line compounds though some do have compositional width. The bonding in intermetallics is still metallic in nature but the structure is distinct from those of the constituent elements.

Not all intermetallic materials are suitable for investigation as anode materials. For lithium battery anode applications metallic elements are classified into two groups based on the ability of the metal to form intermetallic phases with lithium itself. This determination is typically made through reference to the metal – lithium binary phase diagram. The first group are considered as “active” materials and are able to form intermetallic phases with lithium. The second group are considered as “inactive” materials and are not able to form an intermetallic phase with lithium. In this case the phase diagram shows no phases formed between the metal and lithium and the only phase regions being lithium, the metal and a mixture of the two (solid solution). Following such a classification examples of active materials include tin, silicon, aluminium, and bismuth whilst inactive materials include iron, nickel, and copper.

The active and inactive components have specific roles in this application. The active material through its reaction with lithium generates the capacity of the material whilst the inactive material provides a matrix to buffer the volume expansion of the active materials reaction with lithium and being a metal it also contributes electrical conductivity. Through buffering the volume expansion the integrity of the electrode and hence its electrochemical performance can be maintained. It is this combination of properties that has seen intermetallics targeted as anode materials for lithium ion batteries. The need for such inactive components is readily seen when the size of the volume increase for various active materials are considered. Examples of the volume increases and theoretical discharge capacities for a number of active materials are presented in Table 2-3. For the materials presented with a theoretical capacity greater than that of carbon (372 mAh/g) the minimum volume increase is 70.64 % for zinc and LiZn formation ranging to 676.31 % for tin and $Li_{22}Sn_5$ formation. Even with the use of the inactive matrix deterioration of the electrode as a result of the volume expansion can still result. When the active metals particle size is less than 100 nm there is a tendency for the particles to agglomerate into micrometer scale particles during repeated cycling [103, 104]. The larger particle size will lead to a large volume change increasing the stress levels around the particle and disintegration of the electrode as a result [105].

Most of the investigations of intermetallics for lithium ion batteries have been carried out on combinations of one active and one inactive component though others are possible and have been investigated. Other combinations include the use of two active components as well as three component systems utilising either two active or inactive components.

2.7.2.4.1 Reactions with Lithium

Three different general reaction types are possible for the reaction of lithium with intermetallic materials for lithium ion batteries. These have been described as reconstitution or addition, displacement and mixed [35]. General examples of these are presented using the theoretical intermetallic AB_y in which B is more active towards lithium than A. The examples represent the initial insertion reaction only since as the insertion continues the reaction type can change.

Table 2-3: Theoretical discharge capacities and volume increase for selected active metals.

Discharged Species	Charged Species	Volume Increase (%) *	Capacity (mAh/g)
Al	LiAl	96.78	993
Bi	LiBi	75.88	128
Bi	Li_3Bi	176.51	385
C	LiC_6	9.35	372
Cd	$LiCd_3$	17.60	79
Cd	Li_3Cd	267.71	715
Pb	LiPb	44.70	129
Pb	$Li_{22}Pb$	233.66	569
Sb	Li_3Sb	147.14	660
Si	Li_2Si	175.12	1908
Si	Li_4Si	322.57	3817
Sn	$Li_{22}Sn_5$	676.31	994
Zn	$LiZn_4$	11.33	102
Zn	LiZn	70.64	410

* Based on data compiled by Besenhard *et al.* [106]

2.7.2.4.1.1 Reconstitution or Addition Reaction

In addition reactions (2-15) lithium reacts with an intermetallic (AB_y) to form a new lithiated compound (Li_xAB_y) [35].

$$xLi + AB_y \rightarrow \quad Li_xAB_y \qquad \textbf{2-15}$$

2.7.2.4.1.2 Displacement Reaction

In a displacement reaction (2-16) lithium reacts with an intermetallic (AB_y) and forms a lithiated compound (Li_xB_y) with one of the constituents of the intermetallic (B) whilst the other intermetallic constituent (A) is displaced [35].

$$xLi + AB_y \rightarrow \quad Li_xB_y + A \qquad \textbf{2-16}$$

2.7.2.4.1.3 Mixed Reaction

The mixed reaction (2-17) involves elements of both the addition and displacement reactions [35]. In this case only part of the intermetallic constituent A is displaced whilst a new ternary lithium compound is formed as well ($Li_xA_{1-z}B_y$).

$$xLi + AB_y \rightarrow \quad Li_x A_{1-z} B_y + A_z \qquad \textbf{2-17}$$

2.7.2.4.2 Aluminium Based

Only a few aluminium based intermetallic materials have been investigated as anode materials for lithium ion batteries and include Al_2Cu, Al_6Mn and Al_4Mn [107]. These three intermetallics were however reported as inactive with the small capacities observed attributed to the carbon content of the electrode. The electrochemical reactivity of aluminium with lithium is however well known and anodes based on LiAl have been widely used including commercially. Depending on the cycling conditions LiAl anodes can be cycled up to 1000 times [108]. Aluminium [109, 110] and a number of binary aluminium alloys [108, 111-113] have also been examined as anode materials. The second metal utilised in such alloys affects both the mechanical properties and electrochemical behaviour [108]. When Yang *et. al.* examined aluminium (spherical particles typical size 0.1 – 0.5 μm) electrodes lithium could hardly be extracted from the structure making further cycling impossible [110]. An aluminium – silicon carbide composite was also examined with the addition of the inactive SiC resulting in better cycling performance of the aluminium electrode [114].

2.7.2.4.3 Tin Based

As most of the intermetallic materials examined for application as anode materials for lithium ion batteries have been based on tin as an active material a large number of different tin based materials have been investigated. Some intermetallic combinations with tin have been investigated more than others such as those with copper, nickel and iron. Other tin based intermetallics to be investigated include Ag – Sn [115], Ca – Sn [116], Ce – Sn [117], Mg – Sn [118, 119], Mn – Sn [120], Si – Sn [121], Sb – Cu – Sn [122], and Zr – Sn [123]. Amongst the many tin based materials investigated two materials were also found to react with lithium in a different manner. In this case lithium was found to react only with the tin atoms in the grain boundaries of nanostructured $SnMn_3C$ and $SnFe_3C$ whilst the remaining tin in the grain was unreactive [120, 124].

2.7.2.4.3.1 Copper – Tin

Unlike most other intermetallic materials the insertion reaction of lithium into the intermetallic Cu_6Sn_5 has been found to correspond to an insertion reaction with the

formation of $Li_xCu_6Sn_5$ ($0 < x < 13$) [125]. On further incorporation of lithium however this phase breaks down with the formation of copper and various lithium – tin phases [126]. The initial investigation of the material by Kepler *et. al* [125, 127, 128] also included a composition with excess tin (Cu_6Sn_6) and excess copper (Cu_6Sn_4) from either side of the Cu_6Sn_5 composition. The electrochemical properties varied with the composition with improved cycle life observed by limiting the discharge to 0.2 V (Table 2-4).

Table 2-4: Selected discharge capacities of copper – tin intermetallics investigated by Kepler *et. al.*

Composition	Discharge Voltage limit	1st Discharge Capacity (mAh/g)*	10th Discharge Capacity (mAh/g)*
Cu_6Sn_6	0 V	350	180
Cu_6Sn_6	0.2 V	215	150
Cu_6Sn_5	0 V	340	175
Cu_6Sn_5	0.2 V	210	175
Cu_6Sn_4	0 V	440	280
Cu_6Sn_4	0.2 V	165	190

* Kepler et. al [125, 127, 128]

A number of subsequent investigations of the alloy have reported both higher capacities and improved cycle life [126, 129-133]. Capacities greater than 500 mAh/g were common though the cycle life of the materials varied dramatically based on the production technique and processing conditions. Techniques used to produce the alloys included electro-deposition, mechanical alloying, melt spinning and gas atomisation.

2.7.2.4.3.2 Nickel – Tin

A number of investigations have been carried out into nickel – tin based anode materials from powders produced using mechanical alloying [134-139] and as deposited thin films [139, 140]. These investigations covered a range of materials including Ni_3Sn_2 and Ni_3Sn_4 and produced a variety of electrochemical results. The first discharge capacities alone varied from 30 – 1550 mAh/g (Table 2-5).

2.7.2.4.3.3 Iron – Tin

Mao *et. al.* have conducted a number of detailed investigations on iron tin based materials including composites with carbon [20, 21, 141-143]. There are four binary iron – tin intermetallics and those with higher iron content exhibited a better cycle life at

the expense of capacity. The first discharge and reversible capacities of annealed and ball milled binary iron – tin intermetallics from one of Mao *et. al.* investigations [143] are presented in Table 2-6.

Another of Mao *et. al.* investigations [20] saw Sn_2Fe investigated through mechanical alloying with various carbon additions. Despite the addition of carbon the powder produced was a mixture of Sn_2Fe and carbon. In this case although the addition of carbon resulted in a small reduction in capacity it had the benefit of reducing the irreversible capacity.

Table 2-5: First discharge capacities of various nickel – tin anode materials.

Material	1st Discharge Capacity	Reference
NiSn +Al_2O_3	429 mAh/g	[136]
NiSn +Al_2O_3	250 mAh/g	[136]
Ni_3Sn_2	≈ 1500 mAh/cm^3	[139]
Ni_3Sn_2	30 mAh/g	[139]
56 wt. % Sn	65 mAh/g	[138]
57 wt. % Sn	59 mAh/g	[138]
58 wt. % Sn	550 mAh/g	[138]
70.4 wt. % Sn	290 mAh/g	[140]
Ni_3Sn_4	300 mAh/g	[137]
Ni_3Sn_4	380 mAh/g	[137]
Ni_3Sn_4	200 mAh/g	[137]
Ni_3Sn_4	225 mAh/g	[137]
Ni_3Sn_4	1550 mAh/g	[134, 135]
Ni_3Sn_4	590 mAh/g	[134, 135]
76.7 wt. % Sn	600 mAh/g	[140]
91.4 wt. % Sn	850 mAh/g	[140]
95.9 wt. % Sn	890 mAh/g	[140]

In another of Mao *et. al.* investigations stable cycle life was achieved by the combination of Sn_2Fe with an inactive phase $SnFe_3C$. A combination of about 25 wt. % Sn_2Fe and 75 wt. % $SnFe_3C$ had an initial discharge capacity of 300 mAh/g and after 40 cycles still had a discharge capacity of around 200 mAh/g.

Table 2-6: Discharge and reversible capacities of binary iron – tin intermetallics.

Material	1st Discharge (mAh/g)		Reversible (mAh/g)	
	Annealed	Ball milled	Annealed	Ball milled
Sn_2Fe	650	680	600	650
SnFe	60	400	50	320
Sn_2Fe_3	47	280	20	200
Sn_3Fe_5	77	220	60	150

2.7.2.4.4 Silicon Based

A number of investigations have been carried out into the electrochemical properties of silicon – based materials. The high theoretical capacity of silicon makes it of interest as an anode material for lithium ion batteries. Unlike other active materials silicon reacts with lithium to form amorphous rather than crystalline materials [144]. The cycling behaviour of silicon powder based electrodes is however poor and a number of investigations have been carried out utilizing different matrix materials to improve the performance.

By combining silicon with graphite materials [145, 146] the cycle life of silicon materials was improved while still maintaining a high capacity (Table 2-7). The materials with 50 wt. % silicon still had a capacity over 1700 mAh/g after 10 cycles [146] whilst that with 19.2 wt. % silicon had a capacity of 1000 mAh/g at the same stage [145]. The best cyclability was however exhibited by the material with the lowest silicon content (4.6 wt. % Si). Stable discharge capacity of 300 mAh/g has been shown for a silicon – titanium nitride composite over 20 cycles but this is under half of the theoretical capacity based on the silicon content of 776 mAh/g [24].

There have also been a number of studies examining the properties of silicon thin film materials. These have all reported high initial capacities but the cycle life has varied. Bourderau *et. al.* reported an initial discharge capacity of 1000 mAh/g but following the first 3 cycles faded rapidly to 30 mAh/g after 20 cycles [147]. Measurements of stress during cycling suggested that by limiting the discharge voltage to 0.1 V electrochemical performance should be enhanced as a result of the lower stress levels from reduced incorporation of lithium [148]. Graetz *et. al* also investigated silicon thin film materials prepared using two different methods resulting in a nanocrystalline and an amorphous film [149]. The nanocrystalline films had an initial

discharge capacity of 1000 mAh/g and declined to 500 mAh/g after 50 cycles. The amorphous film on the other hand had an initial discharge capacity of 3500 mAh/g and maintained a stable capacity of 2000 mAh/g over 50 cycles. An amorphous film 250 nm thick investigated by Maranchi *et. al.* showed a first discharge capacity of 4100 mAh/g and stable capacity of 3500 mAh/g for 30 cycles [150]. The best demonstration of cycle life was however that shown by Ohara *et. al.* also with an amorphous film with a capacity over 1500 mAh/g maintained over 700 cycles [151]

Table 2-7: Selected capacities of graphite – silicon composites.

Material (wt. % Si)	1st Discharge Capacity (mAh/g)	1st Charge Capacity (mAh/g)	Reference
4.6	403	359	[145]
9.8	545	444	[145]
19.2	1034	832	[145]
30.3	1443	1104	[145]
38.6	1833	1353	[145]
50	2775	2097	[146]

A number of silicon based intermetallic materials have also been investigated for their suitability as anode materials for lithium ion batteries. Materials investigated include $CaSi_2$, $CoSi_2$, $FeSi_2$, $NiSi_2$ and Mg_2Si with the electrochemical performance varying but the discharge profiles were very similar [152-154].

2.7.2.4.4.1 Iron – Silicon

A number of studies have evaluated the properties of various iron – silicon based materials with intermetallic [135, 153] and other compositions investigated [155]. The investigation of Ahn *et. al* [135] and Wang *et. al.* [153] reported a maximum discharge capacity of approximately 1100 mAh/g for a nanocrystalline material with a composition of $FeSi_2$ though composed of a mixture of FeSi and Si. In the case of Wang's investigation the maximum capacity was reached on the third cycle after an initial discharge capacity of 620 mAh/g and declining to a capacity of 320 mAh/g after 25 cycles. A microcrystalline sample examined by Ahn produced by the annealing of the nanocrystalline sample resulting in a mixture of FeSi and $FeSi_2$ with a reduced initial discharge capacity of 762 mAh/g. The cycle life of the nanocrystalline material

was also better with a discharge capacity of 170 mAh/g after 15 cycles compared to 80 mAh/g for the microcrystalline sample.

An investigation by Lee *et. al* [155] examined a number of different iron – silicon compositions and composites with carbon. The initial discharge capacity and behaviour on cycling varied with composition and processing conditions with selected results presented in Table 2-8. The cycling performance could be improved slightly by reducing the upper cutoff voltage from 2.0 V to 1.2 V.

Table 2-8: Discharge capacities of selected iron – silicon based materials investigated by Lee *et. al.*

Material	1st Discharge (mAh/g)	10th Discharge (mAh/g)
Graphite – $Fe_{20}Si_{80}$ (50:50 wt. %)*		
Ball milled 30 minutes	790	500
Ball milled 60 minutes	850	500
Ball milled 120 minutes	1150	500
$Fe_{27}Si_{73}$		
Ball milled 10 hours	310	160
Ball milled 20 hours	275	150
$Fe_{33}Si_{67}$	240	100
$Fe_{20}Si_{80}$		
Ball milled 10 hours	1350	300
Ball milled 15 hours	1200	500
Ball milled 25 hours	990	380
Ball milled 35 hours	525	290

* $Fe_{20}Si_{80}$ was pre-milled for 15 hours before subsequent milling with graphite.

2.7.2.4.4.2 Magnesium – Silicon

A number of investigations have been carried out on the electrochemical properties of Mg_2Si intermetallics prepared as both thin films [156, 157] and powders [18, 40, 158]. The first discharge capacities varied between 700 mAh/g [40] and 1370 mAh/g [18] for electrodes fabricated from powders. Whilst for a nanocrystalline thin film electrode the first discharge capacity was 790 mAh/g whilst that of an amorphous thin film was 2241 mAh/g [156]. There is however some disagreement over the reaction mechanism with lithium, with the formation of a ternary lithium phase and the formation of various lithium tin and magnesium phases suggested.

2.7.2.4.5 Antimony Based

A number of antimony based materials have been investigated particularly based on structural considerations with the majority focusing on SnSb and InSb. Though a number of other antimony based compounds have also been investigated including Zn_4Sb [105], Zn_4Sb_3 [159], $CoSb_3$ [105, 160], $CoFe_3Sb_{12}$ [105], MnSb [161], Mn_2Sb [161], Ag_3Sb [162], AlSb [163, 164], GaSb [164] and $MgSb_3$ [165] with the formation of Li_3Sb typical.

Amongst these antimonides InSb, GaSb, and AlSb have a zinc blende (diamond cubic) structure which provides interstitial sites that lithium can occupy [166] and a favourable three dimensional framework for the diffusion of lithium [166].

2.7.2.4.5.1 Tin – Antimony

A number of tin – antimony based materials have been investigated including various tin – antimony compositions, composites and coatings. The electrochemical performance of the tin – antimony materials was better than that of tin and antimony alone [167]. The most widely investigated tin – antimony composition was $SnSb_{0.14}$ with an initial and second discharge capacity of around 800 mAh/g and 600 mAh/g respectively before declining to around 400 mAh/g after 30 cycles being typical [110, 168-171]. A range of other compositions have however been examined including $SnSb_{0.23}$, $SnSb_{0.42}$, SnSb, $SnSb_{1.2}$, and $SnSb_2$, [167, 171-173]. A number of composite materials have been examined including $Li_{2.6}Co_{0.4}N$ [171, 174], coated on mesocarbon microbeads (MCMB) [104, 173] and coated with Li_3PO_4 and $ROCO_2Li$ [173].

2.7.2.4.5.2 Indium – Antimony

InSb has a zinc blende structure and the capacity and cycle life vary dramatically with the voltage endpoints. An initial discharge capacity of 740 mAh/g has been reported for discharge to 0 V but when cycled between 0 – 1.3 V the capacity decayed rapidly to under 200 mAh/g in the first 10 cycles [175]. In InSb both indium and antimony can react with lithium and if the lower voltage limit is raised to 0.5 V or above the reaction with indium is prevented and the capacity fade is less pronounced [175]. When cycled above 0.5 V initial capacities up to 450 mAh/g [164, 166, 175] have been reported and greater than 250 mAh/g retained over 12 cycles [175].

2.7.2.5 Others

In addition to the carbon, oxide, nitride and intermetallic materials already mentioned a wide variety of other materials have also been investigated. Many of these materials have a layered structure and include:

- Chalcogenides such as $(PbS)_{1.14}(TaS_2)_2$, and Ta_2Te_3 [17, 176]
- Vanadates such as $Mn(VO_3)_2$, and $Co(VO_3)_2$ [177-184]
- Borates such as $FeBO_3$, VBO_3, and SnB_2O_4 [185-187]
- Spinel structures such as $Li[CrTi]O_4$, $Li[Li_{1/3}Ti_{5/3}]O_4$, and $Li_4Ti_5O_{12}$ [188-199]
- A variety of materials based on metal oxides such as $Li_3CuFe_3O_7$, $Li_2Ti_3O_7$, $LiFeO_2$, and Li_5FeO_4 [200-204]

Other materials to be examined include $SnSO_4$ [205], lead tin fluorides [206], $Sn_2P_2O_7$ [207], $Pb_3(PO_4)_2$ [208], SnS_2 [209], $CoFe_3Sb_{12}$ [210], CoP_3 [211], and SiB_3 [152].

2.7.3 Cathode Materials

Like anode materials a wide variety of materials have been investigated as cathodes though common materials include $LiMn_2O_4$, $LiNiO_2$, $LiCoO_2$ [15] with $LiCoO_2$ based materials the dominant cathode material in lithium ion batteries [212]. Of these materials $LiNiO_2$ has the highest discharge capacity whilst that of $LiCoO_2$ is slightly lower and $LiMn_2O_4$ even lower again. Both $LiNiO_2$ and $LiMn_2O_4$ however have poor cyclability [212]. Partial substitutions are frequently used on these materials and as a result the electrochemical properties are influenced. The cyclability of $LiNiO_2$ for instance can be improved through the partial substitution for nickel of cobalt and/or manganese [212].

2.8 Mechanical Alloying and Mechanical Milling

Ball milling is a technique frequently used for the preparation of intermetallic materials for a wide range of applications including for investigation as anode materials in lithium ion batteries. The two main ball-milling techniques are mechanical alloying (MA) and mechanical milling (MM). For mechanical alloying a mixture of starting materials are milled together whilst in mechanical milling the starting material is a single material.

Mechanical alloying was developed around 1966 by John Benjamin and his co-workers at the Paul D. Merica Research Laboratory as part of the International Nickel Company's (INCO) efforts to develop a nickel based superalloy for gas turbine applications [213]. Initially the process was referred to as "milling/mixing" until termed "mechanical alloying" by Ewan C. McQueen, a patent attorney for INCO [214].

In the 1980s new possibilities for the application of MA and MM were discovered with announcements of successful production of amorphous materials using both processes. In 1981 a Russian group led by Yermakov demonstrated amorphisation of intermetallic powders by MM [214]. The announcement by Koch however of the formation of an amorphous phase from the MA of an elemental blend of nickel and niobium was what sparked such interest to establish MA as a field of research all over the world [214]. The mechanical milling process operated only on alloys that have already been formed using other techniques, whilst mechanical alloying allowed formation in the process. This process then allows the synthesis of materials that may have been difficult to synthesize using other techniques as a result of limitations such as high melting points and low vapour pressure.

Through the use of MA and MM a variety of different structures can be produced and as a result a range of properties can be observed for the same material composition. A large number of parameters influence the MA and MM process and such parameters are not completely independent. The milling parameters can influence both the product phase and/or the microstructure [213]. The starting materials for both MA and MM are typically high purity commercial powders with a particle size in the range 1 – 200 μm [213].

2.8.1 Milling Parameters

Some of the variables that can influence the properties of materials that are mechanically milled or alloyed include:

- Type of mill
- Milling container
- Milling speed
- Milling time
- Milling atmosphere
- Ball to powder ratio

- Size of balls
- Process control additives

2.8.1.1 Type of Mill

Two of the most common ball mills used for mechanical alloying/milling in the laboratory are the Fritsch Pulverisette planetary ball mill and SPEX shaker mills. Both mills are considered as high energy and although the linear ball velocity is higher in the planetary mill the SPEX mill is considered as more energetic due to the frequency of impacts being much greater [214].

2.8.1.1.1 Planetary Ball Mill

The Fritsch planetary ball mill consists of a horizontal rotating plate on which a number of milling containers (1, 2 or 4) can be mounted and each rotates about its own axis in the opposite direction to that of the plate (Figure 2-4). In basic models of the mill the vial and disc rotation speed can't be independently varied though this is possible in modified versions [214].

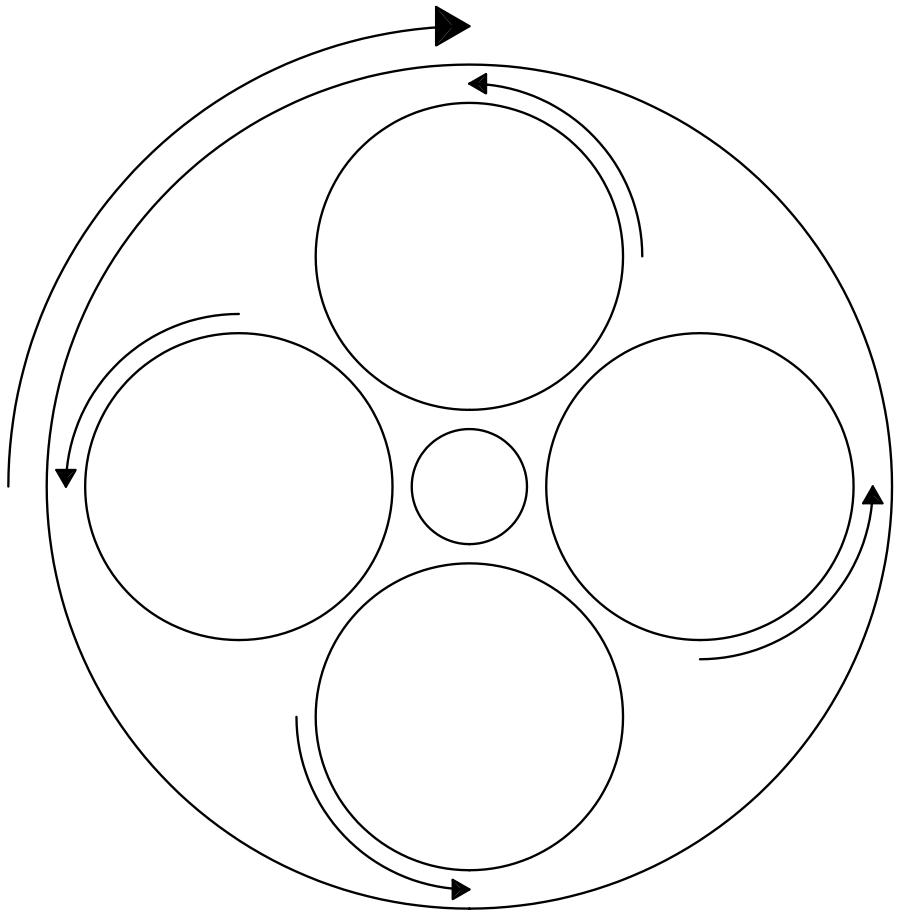

Figure 2-4: Schematic of planetary ball mill.

2.8.1.1.2 Spex Shaker Mill

The Spex shaker mill can contain either one or two milling containers and the shaking motion appears to trace a figure eight in the horizontal plane. The motion is not confined to the horizontal plane however as oscillations are occurring in all three directions. The oscillations are around 5 cm and occur at speeds up to around 1200 rpm [213].

2.8.1.2 Milling Containers and Balls

Milling containers and balls are readily available in a range of materials to suit a range of milling purposes. Common materials include various steels (stainless, tool, hardened chromium, tempered, bearing steel and tungsten carbide lined), tungsten carbide, zirconia, agate, alumina and silicon nitride. The composition of the powder being milled can be influenced by contamination with impurities from the milling container and balls being composed of a different material or alteration of the chemistry when composed of the same material [213]. As a result the choice of milling container can be an important consideration. The synthesis of NiAl from a nickel – aluminium elemental blend using stainless steel containers and balls resulted in iron contamination around 18 atomic % whilst when using hard chrome steel the level was around only 5 atomic % [214]. The effect of such additions from the milling material is not necessarily harmful. In milling a copper – nickel elemental blend in stainless steel and hard chrome steel complete alloying and the formation of a solid solution was observed compared to no alloying observed when tungsten carbide media were used [214].

The internal shape of the milling container also has an influence on the milling. When comparing the X-ray diffraction patterns of silicon – germanium mixtures in differently shaped vials in a Spex mill the milling time to reach the same state was nine hours for flat ended vials and fifteen hours in round ended vials [213].

The influence of the milling container and balls are not limited to affecting the chemistry of the powder either as the density and size also influences the powder properties. The density of the balls for instance needs to be high enough to create enough impact force on the powders [213]. In general larger and higher density balls will generate higher impact energies than smaller or less dense balls [213]. In blending a mixture of aluminium and titanium with 15 mm diameter balls a solid solution of

aluminium in titanium was formed whilst when 20 and 25 mm diameter balls were used only a mixture of titanium and aluminium resulted [213].

2.8.1.3 Milling Speed

The milling speed can have an important influence but this varies with the type of mill. Above a certain critical speed for instance the balls will remain pinned to the walls of the milling container and not exert any impact force on the powder [213]. Below this critical speed however the higher the milling speed the higher the milling intensity will be.

For the higher milling intensities higher temperatures may also be reached and the effects of this can vary. Where diffusion is required to aid the homogenisation or alloying of the powders this can be beneficial whilst it may be a disadvantage through increased rate of transformation process and subsequent decomposition of metastable phases [213]. An increase in crystal size and decrease in internal strain has also been reported for higher milling intensities through dynamic recyrstallisation processes [213].

2.8.1.4 Milling Time

According to Suryanarayana the milling time is the most important milling parameter [213]. The level of contamination will increase with milling time and some undesirable phases may form if a powder is milled to long [213]. Substantial reduction in particle size usually occurs with milling time and typically takes the format of exponential decay.

2.8.1.5 Milling Atmosphere

The milling atmosphere can contaminate the powder and as a result milling is frequently carried out in evacuated, or argon, or helium charged milling vessels [213]. Other atmospheres can be used if particular affects are desired. Nitrogen and ammonia atmospheres have been used to produce nitrides and hydrogen atmospheres to produce hydrides [213]. The presence of air in the milling vessel can result in the formation of oxides and nitrides [213]. Even when formation of such phases does not result the atmosphere can still affect the properties of the resultant material. Milling of chromium – iron mixtures in various atmospheres demonstrated different constitution. When the milling was carried out in argon no amorphous phase was formed and chromium peaks

were still present in X-ray diffraction patterns [213]. However when milled in either an air/argon mixture or nitrogen the material formed was completely amorphous [213].

2.8.1.6 Ball to Powder Ratio

The ball to powder (BPR) or charge ratio is another important milling parameter and represents the weight ratio of the milling balls to the powder charge. A wide range of BPR have been used in a variety of investigations from values as low as 1:1 to as high as 220:1 [213]. BPR ratios in the range 5:1 – 10:1 are widely used [214].

2.8.1.7 Process Control Additives

Process control additives (PCAs) are also called surfactants or lubricants and can be solid, liquids or gases [213]. The main effect of PCAs is in reducing the effect of cold welding [213]. Making them particularly useful when milling ductile materials such as aluminium and tin [214] where excessive cold welding presents a large problem. A large range of PCAs are utilised and the most important are stearic acid, methanol, ethanol, and hexane [213]. The use of and amount of PCAs used has been shown to contribute to a reduction in particle size [213] and the level of contamination from the milling media [214]. The use of both organic and inorganic fluids when milling metals however leaves small amounts of fluid dispersed throughout each particle [215].

2.9 Conclusions

A large number of battery chemistries have been developed since the first were investigated at least 1200 years ago. Amongst these lithium ion batteries are one of the most recent and offer high capacity and high operating voltage per cell. Many different materials have been investigated for the electrodes and electrolytes of lithium ion batteries. Despite the diverse range of materials investigated as anode materials carbon based anodes still dominate in commercial cells. Intermetallics are just one class of materials being investigated as replacements for the existing carbon based materials. Although the initial discharge capacities are high stable cycling at such capacities are yet to be realised. Intermetallics are frequently prepared by ball milling which offers a large number of variables to alter the microstructure of the milled material. Although the exact role of microstructure on electrochemical properties is unknown it does influence the electrochemical properties.

Chapter 3 Experimental Techniques

A number of techniques are required to investigate anode materials for lithium ion batteries. These include techniques to produce the materials, examine their physical and electrochemical properties and the analysis of the results from them.

3.1 Materials Production

3.1.1 Intermetallics

Constituent elements were weighed out in the correct proportions before being melted together using an arc melting system. This system melts the components together using an electrical arc that is formed in a partial argon atmosphere between a tungsten electrode and a water-cooled copper plate. The copper plate contains a series of depressions that hold materials that are to be melted. Prior to the desired intermetallic materials being melted some titanium was melted in order to capture any residual oxygen in the system. An alloy slug results from the process that must be crushed to provide a suitable feed material for ball milling. The crushing process entails placing the slug between two sheets of paper and steel plates that are then pressed together using a hydraulic press (Enerpac 10 tonne). The crushed material is then sieved using a 150 μm sieve with the retained portion being recrushed until it passes through the sieve.

3.1.2 Bi-2212

Two Bi-2212 ($Bi_2Sr_2Ca_{1-x}Y_xCu_2O_{8+\delta}$) samples were examined with nominal compositions corresponding to x = 0 and 0.7. These were produced from nitrate precursor materials through a spray drying process followed by calcining and sintering operations. The nitrate precursors (Table 3-1) were weighed out in the required proportions and dissolved in distilled water with the aid of stirring, nitric acid additions, and a hot water bath. The solution was then retained in the hot water bath whilst it was spray dried using a Yumato Pulvis GB22 unit. The spray drying process involves the atomisation of the solution into a hot gas carrier stream removing most of the water content. The powder is then carried into a cyclone where the powder is collected at the bottom of it in a collection vessel. The basic features of spray drying apparatus are presented in Figure 3-1.

Table 3-1: Nitrate precursors used in the fabrication of Bi-2212.

Nitrate Chemical Formula	Molecular Weight	Purity
$Bi(NO_3)_3 \cdot 5H_2O$	485.07	98 %
$Sr(NO_3)_2$	211.63	99 %
$Ca(NO_3)_2 \cdot 4H_2O$	236.15	99 %
$Cu(NO_3)_2 \cdot 3H_2O$	241.60	99.5 %
$Y(NO_3)_3 \cdot 6H_2O$	383.01	99.9 %

The powder material from the spray drying process was then decomposed in a calcining operation of six hours duration at 550°C in a Eurotherm controlled Ceramic Engineering muffle furnace. The calcined material was then ground by hand in a mortar and pestle before being placed into 25 mm diameter dies for pellet formation. The pellets were formed by compressing the powders in the metal dies using a hydraulic press with the pressure set on 4000 psi and delivered at this level for 8 seconds.

The pellets were then sintered in a 1300°C Laboratory muffle furnace featuring a Eurotherm 903P controller with a thermal program consisting of a five hour ramp to 850°C, a five hour dwell at 850°C followed by a five hour ramp down to 120°C. The pellets were then reground and pressed in preparation for a second sintering operation. The second sintering operation was carried out at 860°C for the undoped sample (x = 0) and 890°C for the doped sample (x = 0.7) with a thermal program consisting of a two hour ramp to temperature followed by twenty-four hours at temperature and furnace cooling to room temperature. To allow ball milling to be carried out the pellets were once again broken down into powder through hand grinding in a mortar and pestle.

3.2 Ball Milling

Ball milling operations were carried out using a Fritsch Pulverisette-5 planetary ball mill. All milling operations were carried out in steel milling jars with 5 mm diameter stainless steel balls and an air atmosphere. There was however differences in the other milling parameters utilised between the various materials examined. Two different milling vessels were used with one having an internal diameter of 80 mm and volume of 200 cm^3 whilst the other had an internal diameter of 85 mm and volume of 140 cm^3. A ball:powder ratio of 20:1 was used for most milling operations though a

higher ratio of 60:1 was used on a few occasions. Milling was typically carried out at 160 rpm though a slower speed of 90 rpm was also utilised. Ethanol was also commonly added as a process control additive up to a level of the top of the milling balls.

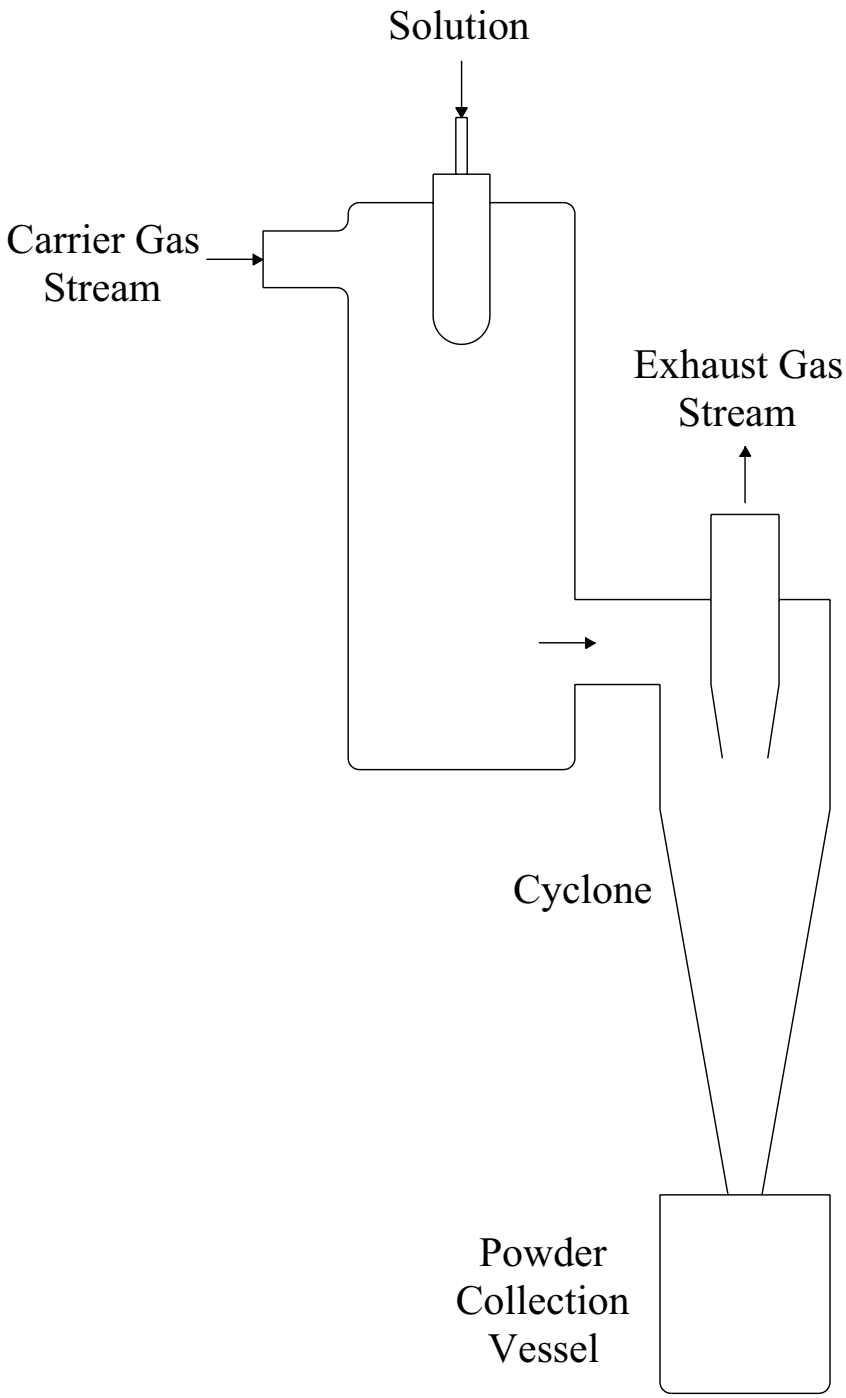

Figure 3-1: General components of spray drying apparatus.

3.3 Electrode Fabrication

In general electrode materials were mixed with a conductive additive (Vulcan XC-72) in a 10:1 ratio by weight before being made into slurry through the addition of a 5 wt. % solution of polyvinylidene fluoride (PVDF) binder in dimethyl phthalate. In some cases particularly with very fine materials the addition of extra solution was required to obtain the desired viscosity of the slurry for electrode pasting.

The slurry was then coated in a thin layer onto copper foil substrates of approximately 1 cm diameter using a metallic spatula. The electrodes were then dried overnight in a furnace at 120°C before being pressed with a hydraulic press. The hydraulic pressure on the press was set at 4,000 psi and the electrodes were subjected to the pressure delivered by the ram at this level for eight seconds. Finished electrodes typically consisted of 85 wt. % electrode material, 10 wt. % conductivity additive and 5 wt. % PVDF.

3.4 Cell Construction and Assembly

Following fabrication of electrodes they were placed into an argon filled glove box (Mbraun Unilab) ready for assembly into custom Teflon test cells. Test cells consist of a Teflon case with a threaded hole to accept two stainless steel bolts as the terminals of the cell and a small stainless steel spring. A schematic of a two electrode Teflon test cell is presented in Figure 3-2. Atmospheric sealing of the cell is achieved through wrapping the threads of the bolts with Teflon tape and the melting of dental wax around the bolt heads. Three electrode test cells were also utilised with the same construction as two electrode cells with the addition of a small stainless steel bolt treaded into an additional hole in the Teflon case. In order to act as a reference electrode the end of the bolt is covered in lithium.

Test cells were assembled by placing the electrode to be tested into the bottom of the cell followed by a microporous polypropylene separator (Celgard). Metallic lithium was then pressed onto a 1 cm diameter circle of woven stainless steel mesh (250 grade) before being placed in the test cell mesh side up. Electrolyte was then added to the cell which was Merck LP30 – 1 M $LiPF_6$ in a 1:1 mixture by volume of ethylene carbonate (EC) and dimethyl carbonate (DMC).

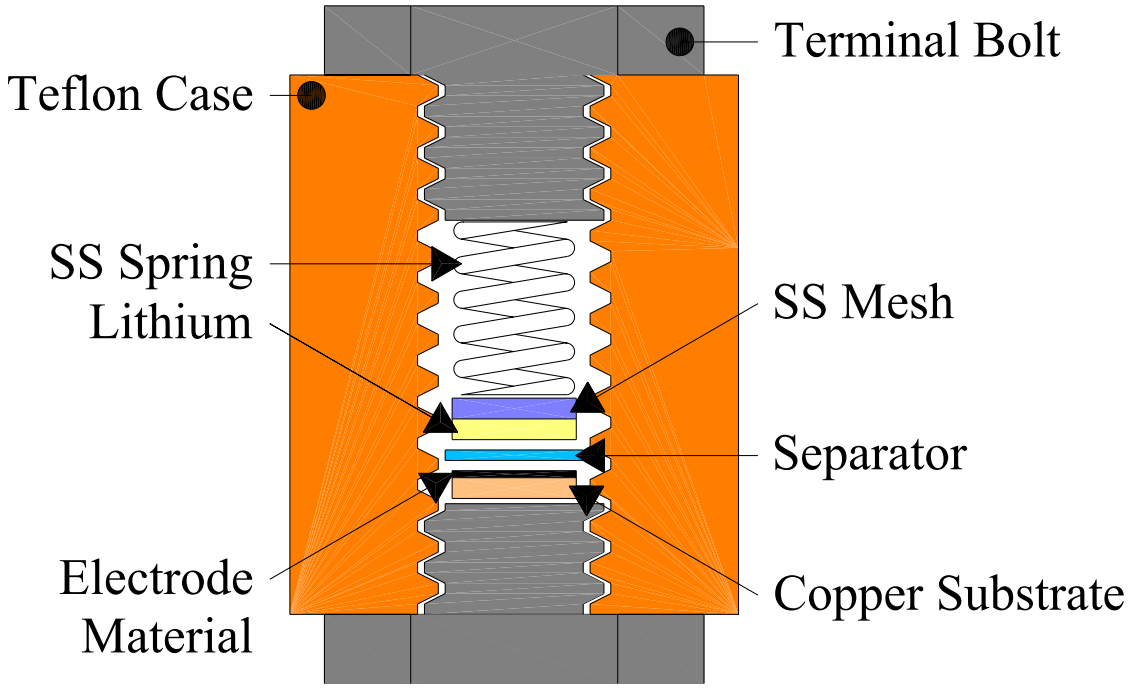

Figure 3-2: Schematic of Teflon test cell construction and cell assembly.

3.5 Characterisation

In order to effectively study electrode materials for lithium batteries it is necessary to study not just the electrochemical properties but also to examine the microstructure.

3.5.1 Electrochemical Characterisation

A number of techniques such as constant current charge/discharge, cyclic voltammetry and impedance spectroscopy are useful for observing a variety of electrochemical properties. In some cases theoretical values can be calculated and compared to the values measured.

3.5.1.1 Variables Effecting Electrochemical Properties

A wide variety of variables can affect the electrochemical properties of materials including those associated with the materials themselves, the makeup and fabrication of the electrode and the electrochemical testing procedure itself. Properties of the materials that can influence the electrochemical properties include its composition, particle size and its distribution as well as its morphology. A number of variables from the fabrication of the electrode influence the properties as well, such as the use and amount of conductive additives, binder choice and proportion as well as the film thickness and

density. Whilst the electrochemical properties are also influenced by the electrochemical test procedure itself through choice of such parameters as the testing current and the potential window in which cells are cycled. Selected examples of the influence such parameters can have on the electrochemical properties in lithium ion batteries follow.

When nanostructured materials (crystallite size less than 10 nm) are utilised a number of important materials properties change [6] which will ultimately affect the electrochemical performance of such materials. In nanocrystalline metallic materials the electrical resistivity is increased compared to materials with a larger crystalline size whilst it decreases for ceramic materials [6]. The strength and hardness are also higher in nanocrystalline intermetallic materials [6]. Whilst the decrease in conductivity may be a disadvantage for intermetallic materials the increase in strength may be advantageous in reducing the deterioration of the electrode through cracking and crumbling. The influence of nano-materials on the electrochemical properties has been observed in a number of instances. Experimentally nanostructured electrodes [80, 216-218] and those composed of nanocrystalline particles [219] have demonstrated better rate capability than those with larger crystal sizes. Shao-Horn *et. al.* however observed that while nanocrystalline FeS_2 (Average particle size 0.5 μm and crystal size of 50 nm) offered better rate capability than FeS_2 with 10 μm particles it did not offer an improvement over 1 μm particles [219].

It is not however just the particle and crystalline size that can influence the properties as Sato *et. al* found that the distribution itself also has an influence after examining the effect of packing particles of different average size using carbon [220]. Three different powders were used, each with a different average diameter and in all combinations examined the optimum performance was observed when the electrode consisted of 70 wt. % of the larger average particle size and 30 wt. % of the smaller average particle size. The densities of the electrodes were also compared and this composition also corresponded to the maximum density observed.

Mass transport often limits the electrochemical performance of lithium ion batteries and as a result the fabrication of electrodes as thin films (60 – 90 μm) consisting of small particles (5 – 30 μm) [15] on substrates 20 μm thick [15] is common. The thickness of the film and its density are important parameters and Shim *et. al* investigated the effect of electrode thickness and density on the electrochemical properties of natural graphite electrodes [221]. Different densities were achieved by

pressing the electrodes with a variety of forces including an unpressed sample. Pressing resulted in a decrease in both the reversible capacity and irreversible capacity loss during the formation cycles. The cycling performance of pressed electrodes was also more stable than those of unpressed samples.

Takamura *et. al.* examined the influence of conductive additive loading on electrochemical properties and found that homogeneity of the electrode was more important [222]. The addition of conductive additives did improve electrochemical performance however a homogenous slurry was found to be necessary for high performance regardless of the presence of conductive additives. Dominko *et. al.* made a similar observation in concluding that the distribution of carbon black around active particles is critical, with even an electrode consisting of only 2 wt. % carbon black uniformly distributed offering better kinetics than one with 10 wt. % carbon black distributed non-uniformly [223]. The homogeneity of the electrodes was also recognised as a key factor by Nanjundaswamy *et. al* in their examination of the coating techniques themselves [224].

Frannson *et. al* examined the effect of carbon black and binder on electrochemical properties [225]. In the voltage range 0.01 – 1.5 V no difference in cycling performance was observed between the binders polyvinylidene fluoride (PVDF) and ethylene propylene diene terpolymer (EPDM) though irreversible capacity increased with increasing amounts of carbon black. Cyclic voltammetry in the same voltage range however showed an additional peak during the first discharge at 0.35 V that was associated with the PVdF binder.

In many of these cases however the differences on a percentage basis are very small and the results observed might in fact be within the normal error limits of the experiment or the result of a combination of differences rather than the single difference it was attributed to.

3.5.1.2 Constant Current (Galvanostatic) Charge – Discharge

A number of properties can be determined from charge/discharge experiments in addition to the capacity of the material itself. The properties can however be influenced by the choice of current as a result of rate capabilities of various materials. Constant current charge – discharge testing was carried out on 5 V – 5 mA Neware Battery Testers (BTS) utilizing a current of 50 μA. Charging and discharging of cells was

carried out between the voltage end points of 0.01 V and 3.0 V for all materials except Bi-2212 based materials which were over the range 0.70 – 3.00 V.

3.5.1.2.1 Charging Currents

When carrying out constant current charging to determine the capacity two different criteria are frequently used to determine the appropriate current to use. These are based on either the electrode surface area or its mass. The current density criterion is based on the electrodes surface area, where the current density is simply the current divided by the electrodes surface area. The C rate is the other method and in this case is based on the discharge of the theoretical capacity of carbon (372 mAh/g) over a period of time. A discharge current of 74.4 mA/g over five hours is referred to as the C/5 rate ($5 \times 74.4 = 372$) whilst 37.2 mA/g over ten hours is referred to as the C/10 rate. If the current is fixed at 50 mA both criteria vary significantly with the surface area for current density and mass for C rate. This variation can be seen in Figure 3-3 where surface area is considered using the diameter of circular electrodes and mass in Figure 3-4. Such variation is an important consideration as the measured capacity does vary with current density and C rate with the capacity declining for both higher C rates and current densities.

3.5.1.2.2 Capacity

Although capacity is often seen expressed in mAh or Ah on commercial cells the specific and volumetric capacities are of greater relevance in the search for new electrode materials. The specific capacity (mAh/g) is the capacity (mAh) divided by the mass (g) of the electrode material whilst the volumetric capacity (mAh/cm^3) is the capacity divided by the volume the electrode material occupies. Unless stated otherwise where capacity is mentioned henceforth it is the specific capacity being referred to.

The theoretical capacity can be calculated using a relationship between the number of moles of lithium in the reaction product and the molar mass of the lithium host (3-1). The theoretical capacities of a number of anode materials for lithium ion batteries are presented in Table 3-2.

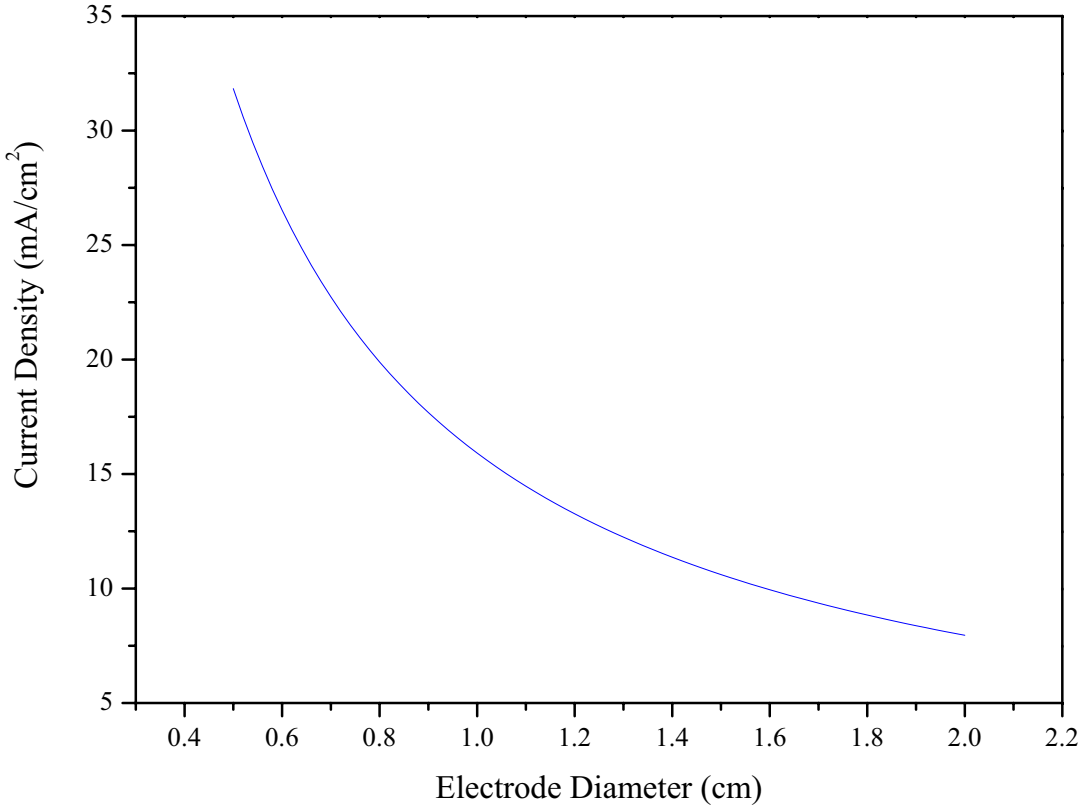

Figure 3-3: Variation of current density with electrode diameter for a fixed current of 50 µA.

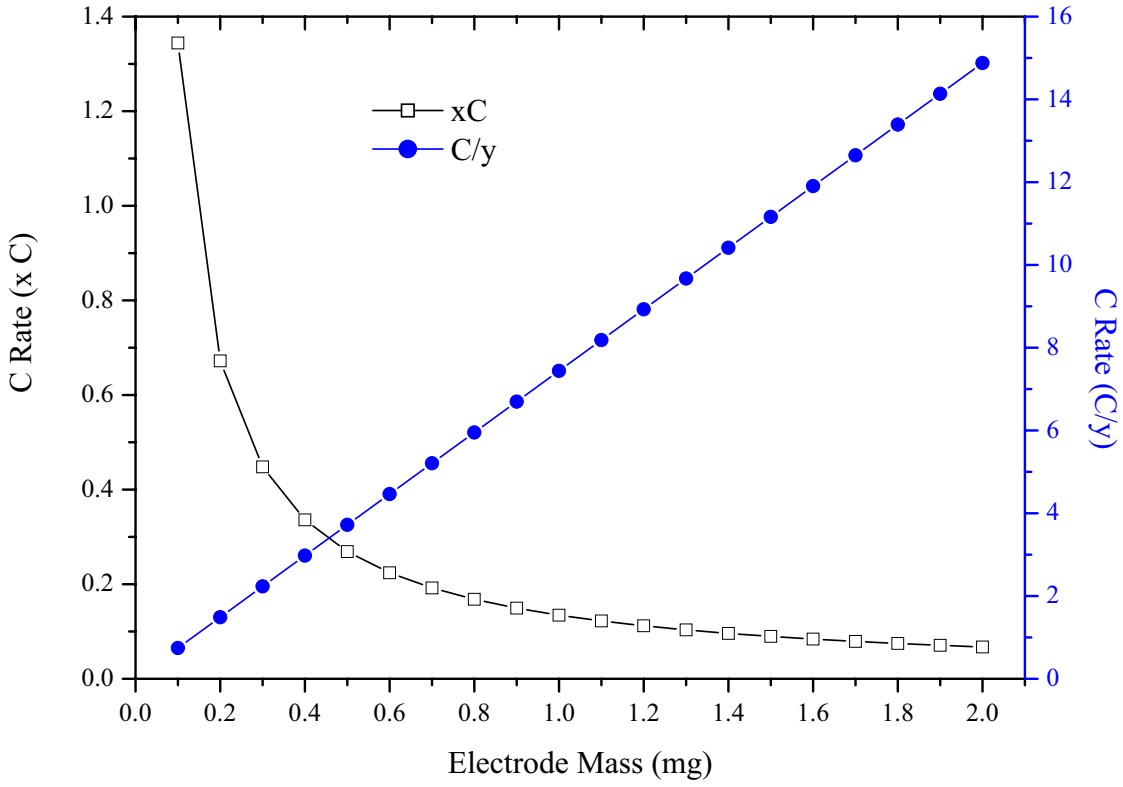

Figure 3-4: Variation of C rate with electrode mass for a fixed current of 50 µA.

$$\text{Capacity}\left(\frac{mAh}{g}\right) = \frac{Fn}{3.6M} \qquad \textbf{3-1}$$

Where F is Faraday's constant 96487 $\frac{C}{mole}$

n is the number of moles of lithium in the reaction product

M is the molar mass in grams of the lithium host

Table 3-2: Theoretical capacities of selected lithium ion battery anode materials.

Host Material	Reaction Product	Capacity (mAh/g)
Al	LiAl	993
Bi	Li_3Bi	385
C	LiC_6	372
Ca	Li_2Ca	1337
Cd	Li_3Cd	715
Pb	$Li_{10}Pb_3$	431
Sb	Li_3Sb	660
Si	$Li_{22}Si_5$	4199
Sn	$Li_{22}Sn_5$	994
Zn	LiZn	410

Although the theoretical capacity can be calculated it is rarely maintained and a difference between discharge capacity is typical particularly in the first cycle. A given discharge capacity can be represented as a reversible and irreversible capacity (Figure 3-5). The reversible capacity represents the portion of the capacity that was reversible on charge and is the charge capacity. The irreversible capacity on the other hand is the portion of capacity that wasn't recovered on charge and is the difference between the discharge and charge capacities.

3.5.1.2.3 Cycle Life

Cycle life and variation of capacity with cycle number are also examined from charge/discharge data. Cycle life is typically considered as the number of cycles it takes for the discharge capacity to fall to 80 % of the initial discharge capacity. The features of the charge and discharge profiles also provide details on the reaction mechanisms.

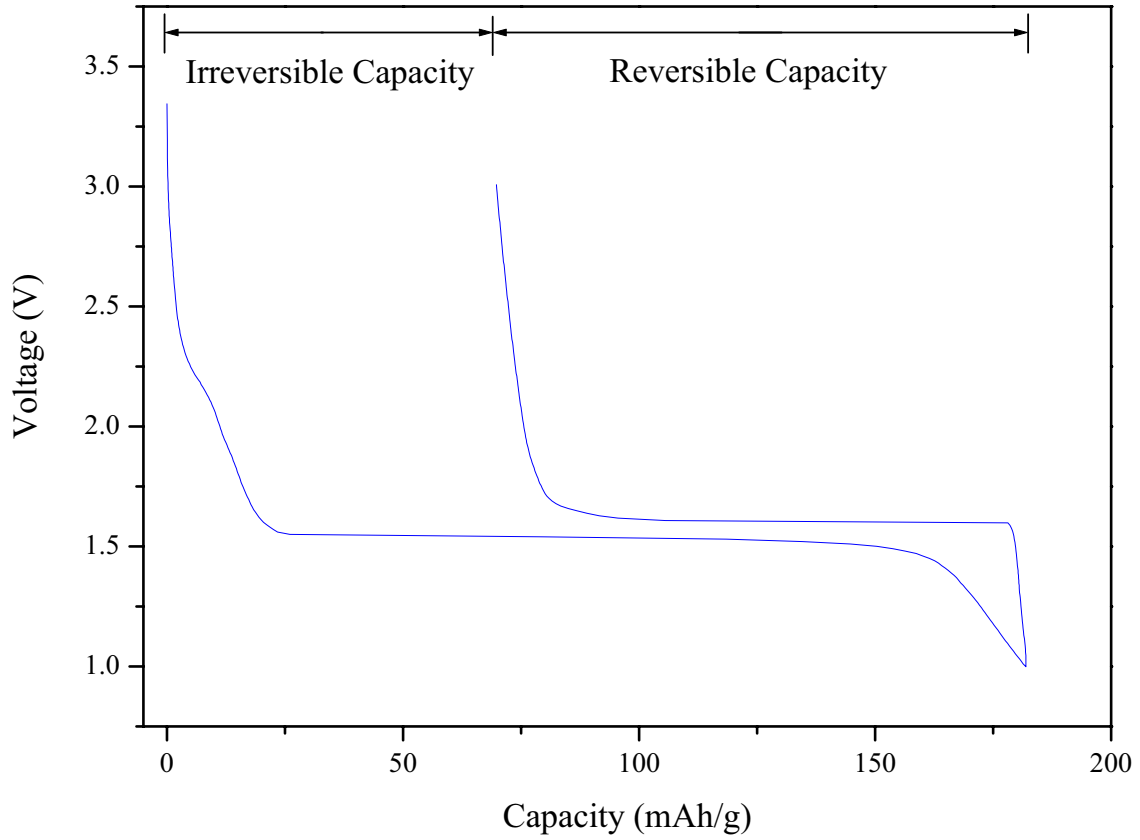

Figure 3-5: Schematic illustrating reversible and irreversible capacity.

3.5.1.2.4 Coulombic Efficiency

By examining the ratio between the discharge and subsequent charge capacity the coulombic efficiency is calculated (3-2). This can be considered as a measure of a number of properties including the ease with which lithium ions can be extracted from the structure (occurs during charging). A higher coulombic efficiency indicates that lithium ions are more difficult to extract from the structure and hence the reversibility of the reaction is reduced.

$$\text{Coulombic Efficiency}\,(\%) = \frac{\text{Discharge Capacity}}{\text{Charge Capacity}} \times 100 \qquad \textbf{3-2}$$

3.5.1.2.5 Differential Capacity

Voltage plateaus in the profile typically have a reaction associated with them, such as formation of one of the Li – Sn alloys. The differentiation of charge and discharge profiles (capacity with respect to voltage) can be used to further assess the reaction mechanisms and where the changes in mechanisms occur (Figure 3-6). The example shown is for the charge and discharge cycle indicated in Figure 3-5. The lower

portion of the differential capacity plot corresponds to the discharge whilst the upper to the charge. The peaks in the differential capacity plot reflect the plateau during discharge occurring at a lower voltage than that on charge.

Where corresponding peaks in the charge and discharge can be clearly identified the reversible potential (E_r) and overpotential (η) can be calculated using 3-3 and 3-4 respectively [122]. For the example illustrated the reversible potential is calculated as 1.5742 V whilst the overpotential as 0.0340 V. Sharp peaks in differential capacity plots are typical of large crystalline materials where the reaction plateaus are well defined whilst broad peaks are typical of nanocrystalline materials where reaction plateaus are less defined.

$$E_r = \frac{V_{deinsertion} + V_{insertion}}{2} \qquad \textbf{3-3}$$

$$\eta = \frac{V_{deinsertion} - V_{insertion}}{2} \qquad \textbf{3-4}$$

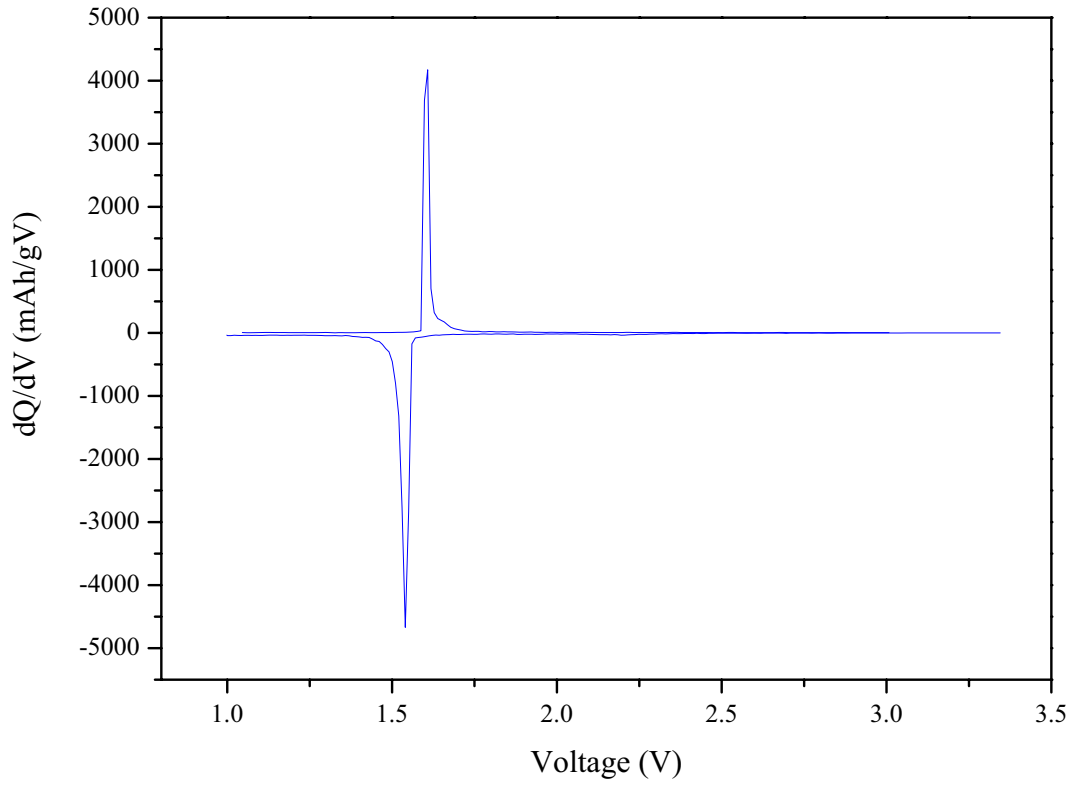

Figure 3-6: Example of differential capacity plot.

3.5.1.3 Cyclic Voltammetry

Cyclic voltammetry or linear sweep voltammetry basically applies a voltage to the electrode that is varied linearly whilst the current response is measured. Further details on the differences in chemical reactions are provided by cyclic voltammetry (CV). Cyclic voltammetry specifically concerns the oxidation and reduction reactions that occur during charge and discharge procedures. The position (potential) of peaks in CV can be used to determine the reaction occurring at the given potential whilst the current describes the intensity of the reaction. The separation of respective oxidation and reduction peaks for a given reaction also provides an indication of the stability and reversibility of the reaction. Cyclic voltammetry was carried out on three electrode cells using EG&G 362 potentiostats over the voltage range 0.01 V to 3.00 V at a scan rate of 1 mV per second. Experimental data for CV was acquired using Maclabs and Chart software.

3.5.1.4 Electrochemical Impedance Spectroscopy (EIS)

The ac impedance spectroscopy technique (Figure 3-7) involves the application of a small potential perturbation (E) at various frequencies (f) at a given dc potential (E_{dc}). The current response is monitored and as a result the variation of resistance with frequency for the material can be examined. Following ac impedance analysis models of the behaviour can be generated in a format similar to electrical circuits. These models can contain familiar electrical components such as resistors, capacitors and inductors but also other unfamiliar elements such as constant phase and Warburg elements.

A common impedance spectra consists of a low frequency semicircle and a high frequency tail (Figure 3-8). The semicircle is the result of the interaction between the resistor (R_{ct}) and capacitor (C_{dl}) and is the result of kinetic processes. The tail on the other hand is a result of diffusion processes and is represented in the model by a Warburg element.

Impedance measurements were carried out on three electrode cells on an EG&G 6310 impedance analyser controlled by M398 software with an ac perturbation of 5 mV over the frequency range 5 mHz to 100 kHz. Prior to impedance measurements being carried out cells were first discharged to 0.01 V under a constant current discharge of 50 μA and then potentiostatically conditioned at 0.01 V for 1 hour.

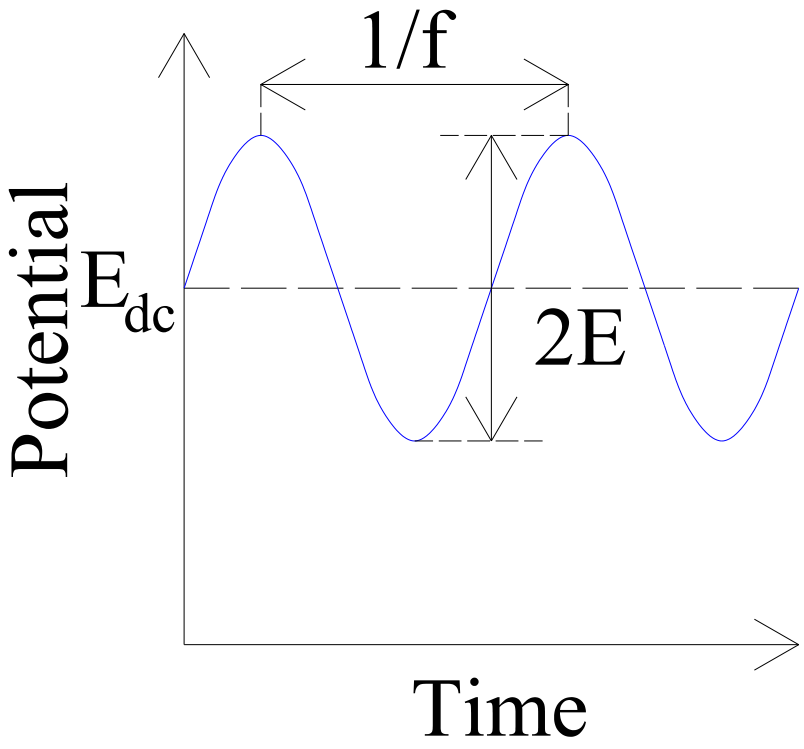

Figure 3-7: Basics of ac impedance technique.

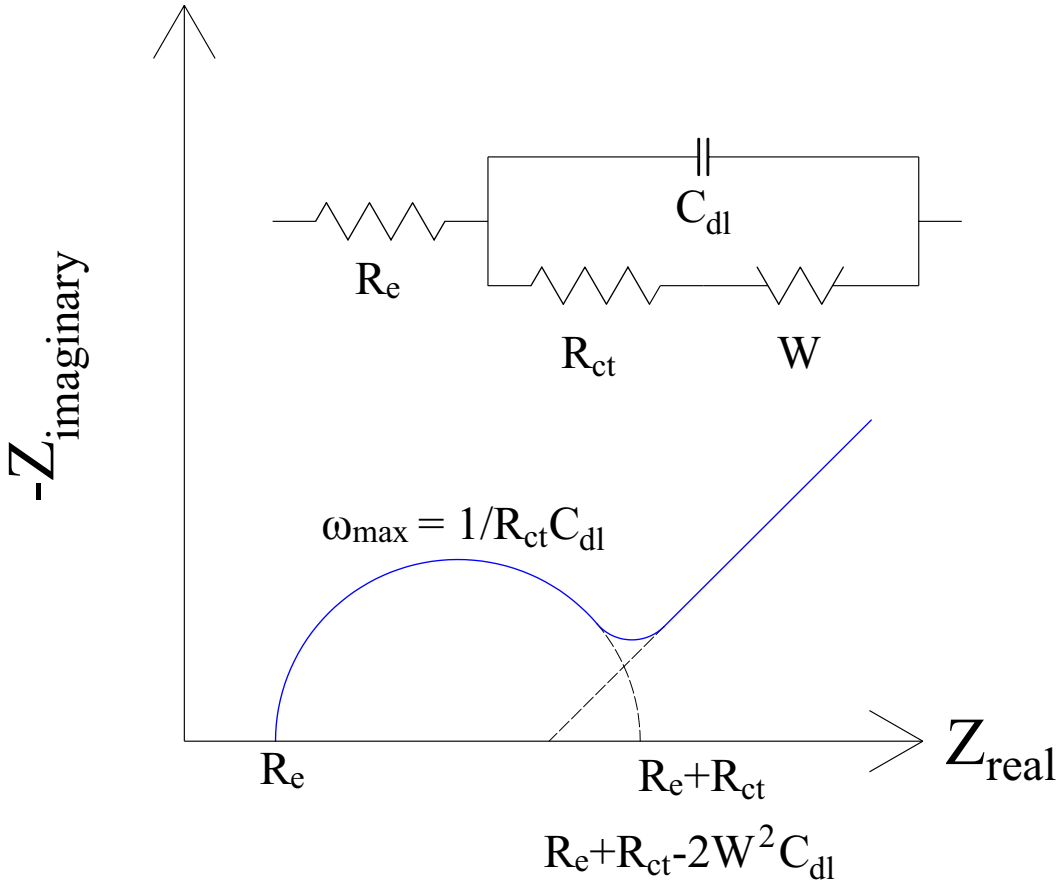

Figure 3-8: Common impedance spectra and equivalent circuit for such spectra.

3.5.2 Microstructural Characterisation

The microstructure of the electrode materials is also important to the electrochemical properties of materials and a variety of techniques can be used to investigate it.

3.5.2.1 X-Ray Diffraction (XRD)

Based on the interaction of X-rays with periodic arrangements of atoms such as those found in crystalline materials details on the structure of the material can be gathered. The interactions which make this analysis possible are found to satisfy Braggs Law (3-5) [4].

$$n\lambda = \quad 2d_{hkl}\sin\theta \qquad \textbf{3-5}$$

Where n is the order of reflection and is any integer such that $\sin\theta \leq 1$

λ is the wavelength of X-ray

d_{hkl} is the distance between two adjacent parallel planes

θ is the incident angle of the X-ray beam to the planes of atoms

By subjecting materials to incident X-rays at a variety of angles an X-ray diffraction pattern can be produced. An XRD pattern typically consists of a number of peaks of various intensities over a range of angles. Analysis of the angular positions, peak intensities and shapes can then be used to give information on the crystal structure and physical state of the material being investigated [226].

Information that can be gained from application of XRD includes identification and quantitative analysis of crystalline compounds, crystal structure determination and analysis of residual stress and crystallite size [226]. Accurate determination of the interplanar distance (d_{hkl}) and relative intensities is necessary for phase identification [226]. Routine identification can however be carried out by comparison to the data published in the X-ray powder diffraction file (PDF) by the Joint Committee on Powder Diffraction Standards (JCPDS) [226]. Residual stress can affect peak width as a result of microstress whilst their position can be influenced by macrostresses [226]. The peak width is however also influenced by crystallite size with finer crystalline size materials exhibiting broader peaks.

Crystallite size can be estimated from XRD patterns using the Scherrer equation (3-6) [226] but this does not however consider the effect that microstresses have on peak width. The effect of microstresses can also be calculated and is found to be proportional to $\tan\theta$ [226]. It is possible to determine the contribution of both crystalline size and stress to peak broadening by a variety of approaches including that of Williamson and Hall [227].

$$\beta = \frac{K\lambda}{t\cos\theta} \qquad \textbf{3-6}$$

Where K is a constant which is frequently taken as 0.9

t is the particle dimension

β is the peak width in radians

The XRD instrument however also contributes to the total broadening observed and to determine the effect of other parameters it must first be taken into account. The peak width observed (B) can be considered a result of the contributions of both the sample (β) and the instrument (b). Scherrer proposed that the peak width due to the sample alone could be determined using the simple relationship (3-7) [228]. It has however been found that a correction used first by Warren and Briscoe has greater general validity (3-8) [228].

$$\beta = B - b \qquad \textbf{3-7}$$

$$\beta = \sqrt{B^2 - b^2} \qquad \textbf{3-8}$$

XRD was carried out on a Phillips PW1730 diffractometer using Cu Kα radiation with an accelerating voltage of 40 kV and current of 20 mA. Scans were typically acquired using a scanning rate of one degree per minute. Powder smears were prepared on slides using ethanol to allow XRD to be carried out.

3.5.2.2 Gas Adsorption – Surface Area Analysis

The specific surface area (m^2/kg or cm^2/g) is determined using the Brunauer – Emmet – Teller (BET) method by measuring the amount of nitrogen gas adsorbed by a monomolecular coverage of the powder [215]. The method does not measure just the exterior surface area but also the surface area of any pores at the surface in which the

nitrogen can be adsorbed. Before any measurements can be made the sample must be degassed to remove any gas currently adsorbed on the surface of the powder. This is accomplished in a desorption process under vacuum with simultaneous heating of the sample.

From an adsorption isotherm – a series of measurements of the volume of gas adsorbed as a function of pressure, the volume can be calculated using the relationship derived by Brunauer, Emmet, and Teller (3-9) [229].

$$\frac{1}{W\left(\frac{P_0}{P}-1\right)} = \frac{1}{W_m C}+\frac{C-1}{W_m C}\left(\frac{P}{P_0}\right) \qquad \textbf{3-9}$$

Where W is the weight of adsorbed gas at a relative pressure $\frac{P}{P_0}$

W_m is the weight of adsorbed gas in the monolayer

C is the BET constant

To determine the surface area using the BET equation a plot of $\frac{1}{W\left(\frac{P_0}{P}-1\right)}$ vs $\frac{P}{P_0}$ which usually results in a straight line for the range $0.05 \le \frac{P}{P_0} \le 0.35$ is utilised [229]. The slope (s) and intercept (i) can then be used to determine W_m by solving the slope (3-10) and intercept (3-11) equations for W_m (3-12) [229]. Using 3-11 and 3-12 the BET constant can then be solved (3-13) [229].

$$s = \frac{C-1}{W_m C} \qquad \textbf{3-10}$$

$$i = \frac{1}{W_m C} \qquad \textbf{3-11}$$

$$W_m = \frac{1}{s+i} \qquad \textbf{3-12}$$

$$C = \frac{s}{i}+1 \qquad \textbf{3-13}$$

The total surface area (S_t) can be calculated using 3-14 [229] and specific surface area (S) can then be calculated (3-15) by dividing it by the sample weight (w).

$$S_t = \frac{W_m N A_{CS}}{M} \qquad \textbf{3-14}$$

Where W_m is the weight of adsorbed gas in the monolayer

N is Avogadro's constant (6.02252×10^{23} molecules/mole)

A_{CS} is the cross sectional area of the adsorbate molecule

M is the molecular weight of the adsorbate

The cross sectional area of a nitrogen gas molecule is 16.2×10^{-20} m^2 at its boiling point of –195.16ºC (77.55ºK) [229].

$$S = \frac{S_t}{w} \qquad \textbf{3-15}$$

From a theoretical viewpoint the specific surface area (S) can be considered as the particles surface area (A) divided by the product of the particles volume (V) and its density (ρ) (3-16).

$$S = \frac{A}{V\rho} \qquad \textbf{3-16}$$

The specific surface area is inversely proportional to both density of the material and particle size, and differences in specific surface area can be substantial as a result of variation of them. The particle shape is also an important parameter with a sphere possessing the minimum area to volume ratio and hence specific surface area whilst a chain of atoms bonded along the axis only the maximum [229]. By considering theoretical spherical particles with different densities and particles sizes these effects can be examined (Figure 3-9). For particle radii in the range 0.1 – 1 μm and densities between 1 and 5 g/cm^3 the specific surface area varies between 0.6 and 30 m^2/g.

The specific surface areas of a number of theoretical particles (Figure 3-10a) have been compared to that of a sphere of a radius r (Figure 3-10b). A sphere with twice the volume of the sphere with a radius r has the smallest specific surface area

whilst a cylinder with a radius of r and height of $r/10$ has the largest of those examined. If the particles are considered on the basis of equal volume (Figure 3-10c) or mass the situation is a little different (Figure 3-10d). Here all the specific surface areas are very close to that of the sphere with only the cylinder with a radius R and height of $R/10$ being much greater than that of the sphere (approximately 3.09 times). The situation is the same when the particles (Figure 3-10e) are considered on the basis of equal surface area. In this case (Figure 3-10f) the specific surface areas are again close to that of the sphere with the cylinder with a radius R and height or $R/10$ having a much greater specific surface area (approximately 5.44 times).

Degassing and BET were carried out on a Quantachrome Nova 1000 tester with analysis of the results performed with Nova enhanced data reduction software. All samples were vacuum degassed for a minimum of three hours at 200°C prior to BET being carried out. Adsorption and desorption isotherms were measured over the P/P_0 range of 0.27 to 0.36. The adsorption isotherm contained 15 points whilst the desorption isotherm consisted of 14 points.

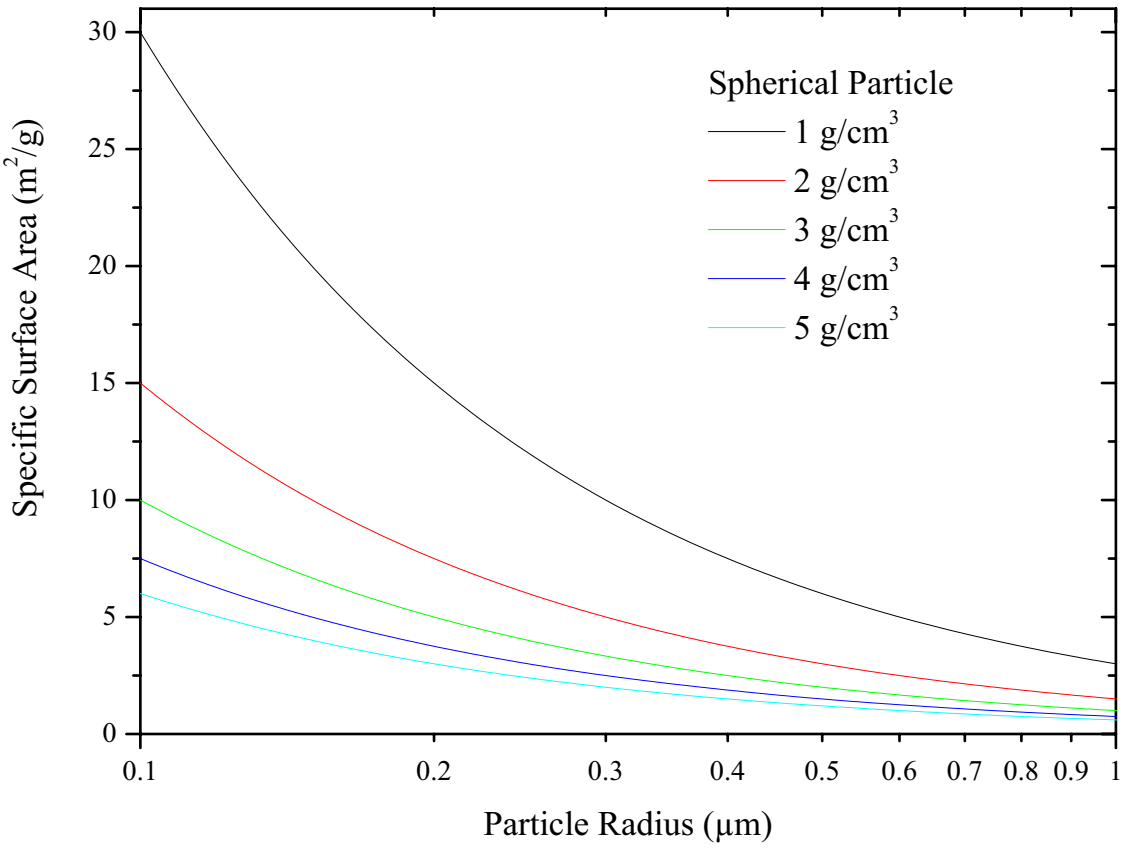

Figure 3-9: Effect of particle density and dimensions on the specific surface area for spherical particles.

3.5.2.3 Scanning Electron Microscope (SEM)

The scanning electron microscope is a powerful technique for investigating the microstructure of a variety of materials. The SEM is similar in many ways to a reflected light microscope but it makes use of a beam of electrons rather than light. The working distance in the SEM is the distance between the sample and the final objective lens and is an important parameter for the SEM. A short working distance provides higher resolutions but at the expense of depth of field whilst a long working distance provides a high depth of field at the expense of resolution. The working distance is not the only parameter that influences the image however as a smaller beam size and higher accelerating voltage also can improve the resolution.

Prior to examination samples were mounted on aluminium stubs with carbon conductive tape and sputter coated with gold using a Dynovac Minicoater. SEM was carried out on a Leica Stereoscan 440.

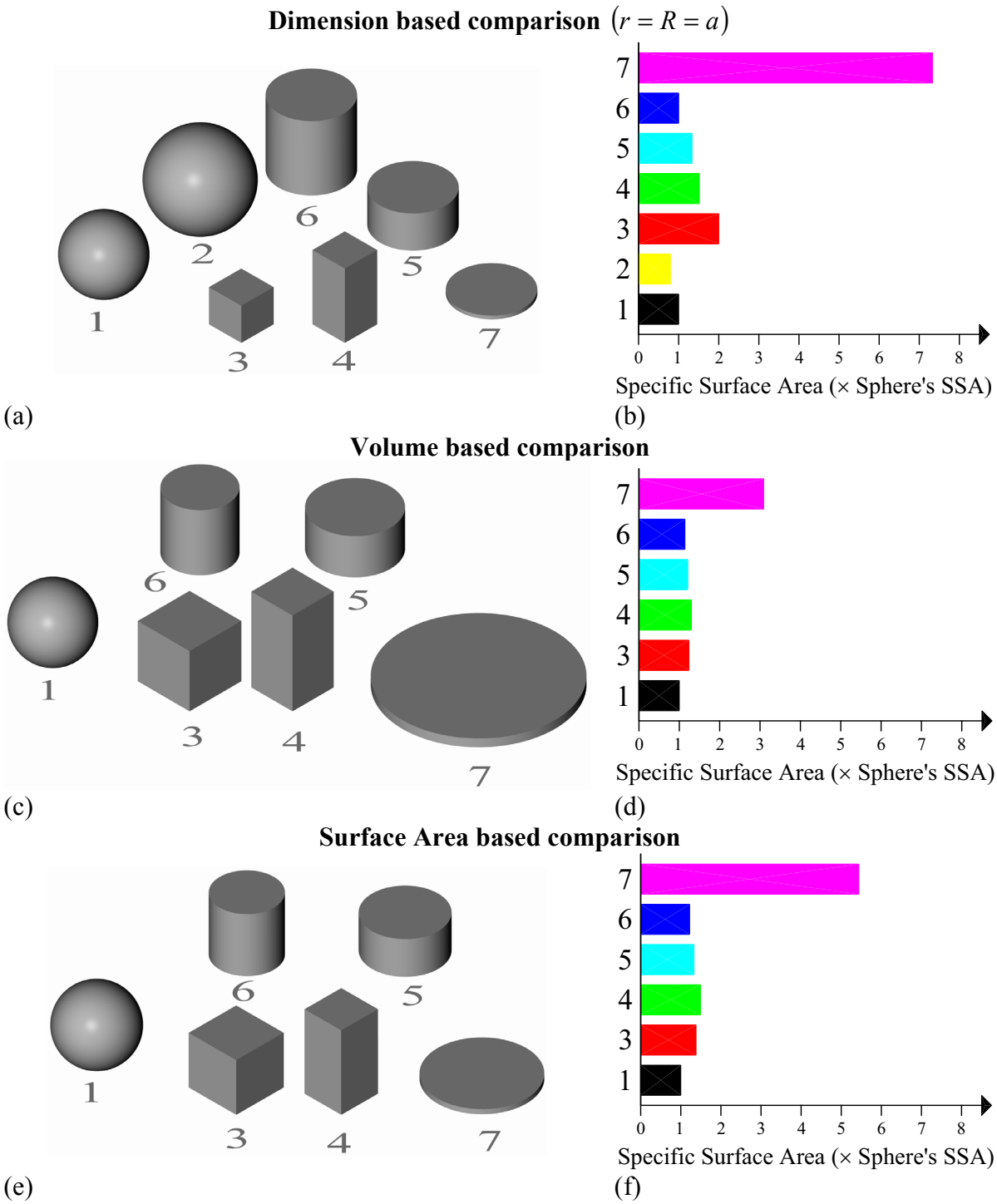

Figure 3-10: Comparisons of specific surface area and particle size for comparisons based on dimension, volume and surface area[a].

[a] Refer to Appendix A for full details of derivation of results

Chapter 4 Data Analysis

When electrochemical testing of cells was commenced a limitation of the battery testing devices immediately became apparent. The data from the devices could only be output to a plain text format comprising the recorded data only. With no method to convert the raw data to relevant parameters a tremendous amount of time would have been spent doing this conversion. The situation could however be rectified by developing software to carry out this function.

The choice of the development platform in this case was Microsoft Excel with utilisation of its macro language of Visual Basic for Applications (VBA). This platform allowed a rapid solution to be developed that could carry out the required functions using only basic spreadsheet functions. Yet could then be expanded to provide a polished solution with the utilisation of VBA.

The key part to the development of such a solution is the development of appropriate algorithms to sort the data in the required manner. Algorithms were required for three different processes based on two different types of equipment. These included results from charge/discharge testing and cyclic voltammetry testing conducted on EG&G potentiostat/galvanostat and charge/discharge testing carried out on Neware battery testing systems (BTS). A guide to using the spreadsheet and extended details on the sorting algorithms can be found in its manual presented in Appendix B. Brief details on selected algorithms are presented in this chapter along with a discussion on the application of Microsoft Excel for data analysis purposes.

4.1 Sorting Algorithms

The particularities of the testing procedures carried out on the devices required the development of three main algorithms. Two of the algorithms were required for testing conducted on the EG&G potentiostat and one for the Neware BTS.

4.1.1 Potentiostat – Charge/Discharge Algorithm

Simple constant current charge/discharge testing carried out on the EG&G instrument has a data set comprising time, voltage and current data. Through the use of an appropriate algorithm a table of charge and discharge capacities can be generated and the profiles of individual charge/discharge steps can be extracted. To accomplish this an algorithm based on comparison of current is utilized.

The sorting algorithm is comprised of two statements and if either of the statements is true a new step is identified (schematic Figure 4-1). The two statements are:

- If the previous points current is negative (< 0) and the current points current is greater than or equal to zero (≥ 0) then the current point represents a new step
- If the previous points current is positive (> 0) and the current points current is less than or equal to zero (≤ 0) then the current point represents a new step

4.1.2 Potentiostat – Cyclic Voltammetry Algorithm

Cyclic voltammetry (CV) testing carried out on the EG potentiostat also has a data set comprised of time, voltage and current data. Through the use of an appropriate algorithm the individual CV cycles can be separated out. The algorithm in this case is a little different due to the difficulty in identifying individual CV cycles. In order to sort CV data it is initially treated as two separate segments with the separation occurring at a point **C** (Figure 4-2).

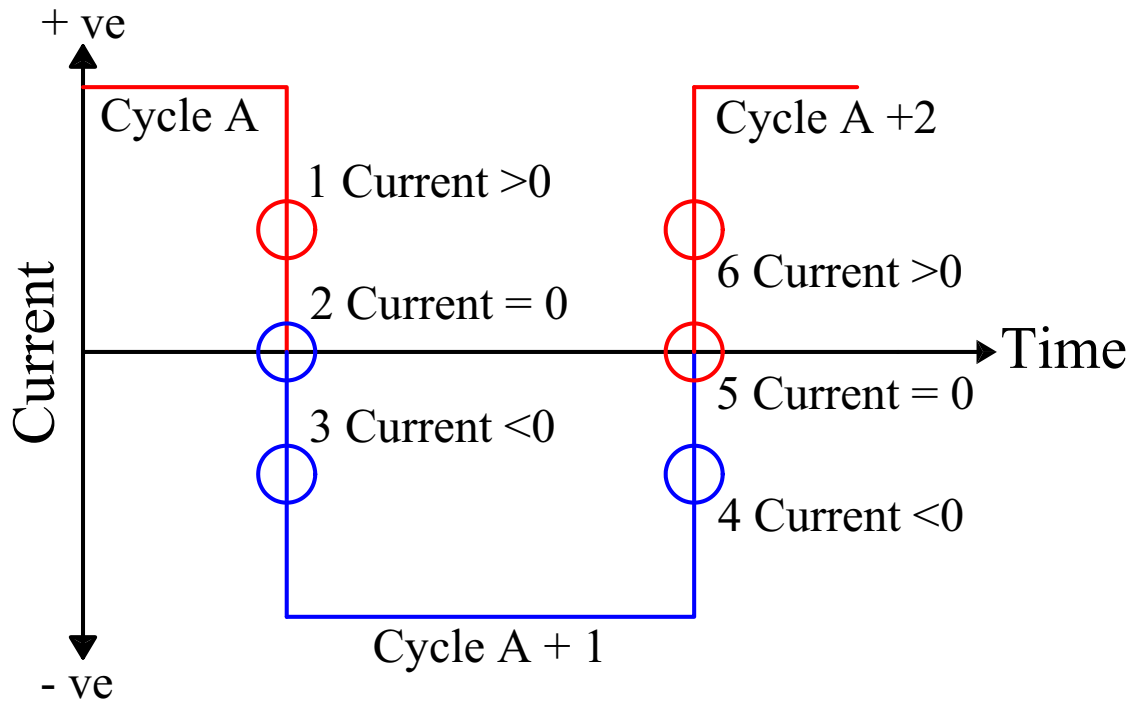

Figure 4-1: Schematic of sorting algorithm for potentiostat charge discharge.

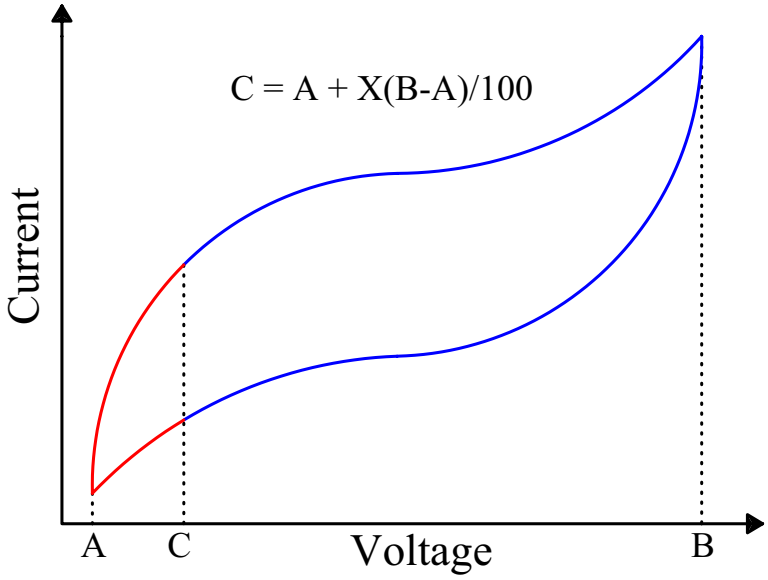

Figure 4-2: Basis of sorting algorithm for cyclic voltammetry data.

The two segments are then:

- Voltage region greater than or equal to **C** (Blue region in Figure 4-2)
- Voltage region less than **C** (Red region in Figure 4-2)

The value of **C** needs to be selected so that it is as close as possible to either the upper or lower cycling endpoints of the voltammogram. Through the choice of **C** the cycle will be composed of either discharge and subsequent charge or charge and subsequent discharge. In use the value of **C** is determined according to another variable **X** where;

$$\mathbf{C} = \mathbf{A} + \mathbf{X}\,(\mathbf{B} - \mathbf{A})/100$$

and $\mathbf{X}$ is such that $1 \leq \mathbf{X} \leq 99$

A is the minimum voltage in the data

B is the maximum voltage in the data

Through consideration of a number of parameters CV data can be sorted in the desired manner. The value of **X** is manipulated so that **C** is as close as possible to the cycling endpoints of the voltammetry whilst still identifying the correct number of cycles. If **X** is chosen so that **C** is identified near the cycling maximum (high cutoff) the sorted data will consist of discharge and the subsequent charge. Whilst choosing **X** so that **C** is identified near the cycling minimum (low cutoff) the sorted data will consist of charge and the subsequent discharge. For complete cycles to be identified the initial voltage in the file is also an important variable. The effects of such parameters on the sorting of a theoretical CV test are considered in Figure 4-3 (high cutoff) and Figure 4-4 (low cutoff).

4.1.2.1 High Cutoff

< Cutoff

- Given a hypothetical CV experiment where the first point in the data set is less than the cutoff value.
- The voltage – time relationship for the first few cycles of this experiment are shown in Figure 4-3a demonstrating which cycle the data will belong to.
- The hypothetical voltammograms for the first and subsequent cycles are shown in Figure 4-3b and Figure 4-3e respectively.

> Cutoff

- Given a hypothetical CV experiment where the first point in the data set is greater than the cutoff value.
- The voltage – time relationship for the first few cycles of this experiment are shown in Figure 4-3c demonstrating which cycle the data will belong to.
- The hypothetical voltammograms for the first and subsequent cycles are shown in Figure 4-3d and Figure 4-3e respectively.

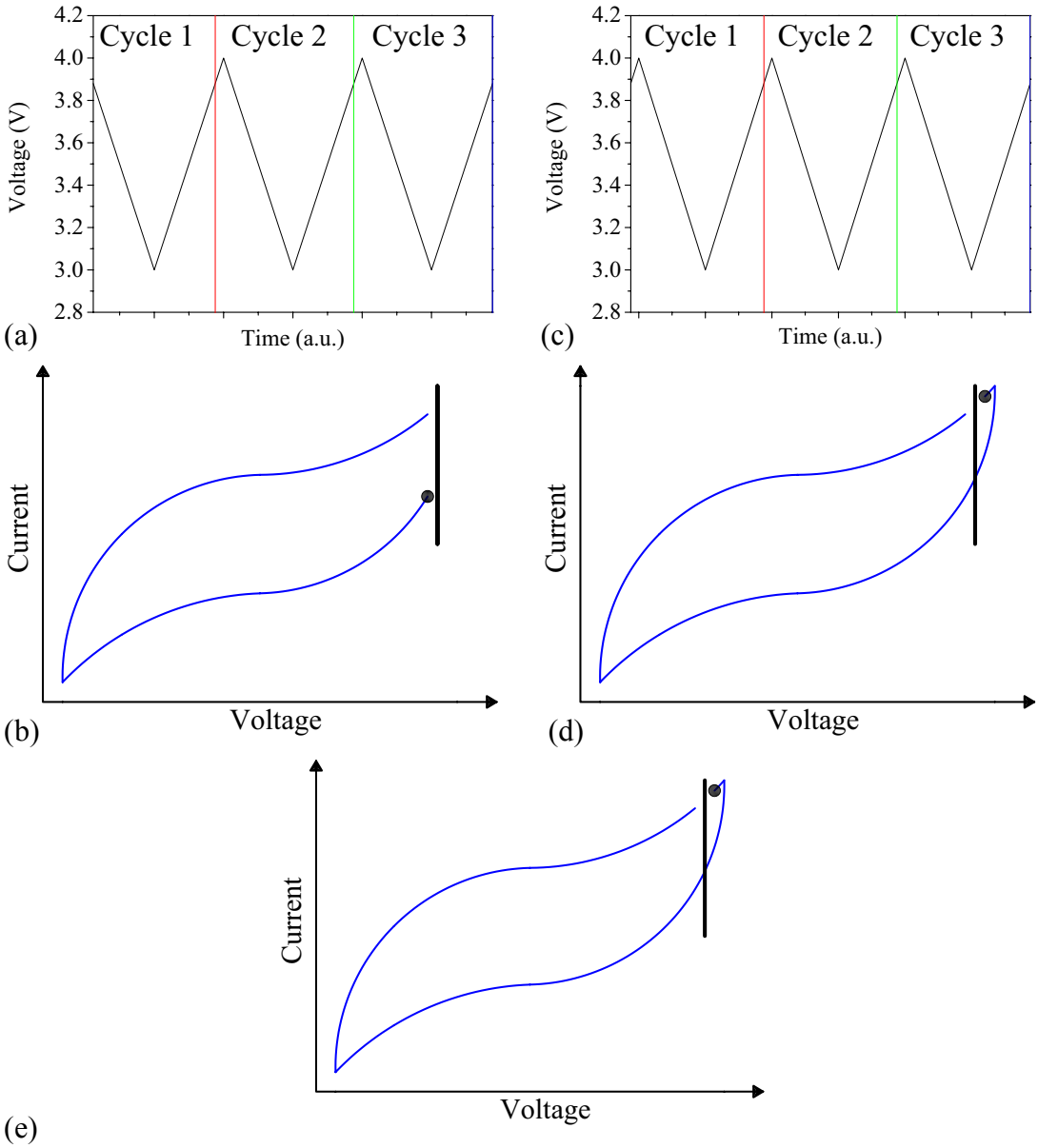

The solid black dot in these figures indicates the starting point of the voltammogram.

Figure 4-3: Effect of parameters in sorting CV data for high cutoff value.

4.1.2.2 Low Cutoff

< Cutoff

- Given a hypothetical CV experiment where the first point in the data set is less than the cutoff value.
- The voltage – time relationship for the first few cycles of this experiment are shown in Figure 4-4a demonstrating which cycle the data will belong to.
- The hypothetical voltammograms for the first and subsequent cycles are shown in Figure 4-4b and Figure 4-4e respectively.

> Cutoff

- Given a hypothetical CV experiment where the first point in the data set is greater than the cutoff value.
- The voltage – time relationship for the first few cycles of this experiment are shown in Figure 4-4c demonstrating which cycle the data will belong to.
- The hypothetical voltammograms for the first and subsequent cycles are shown in Figure 4-4d and Figure 4-4e respectively.

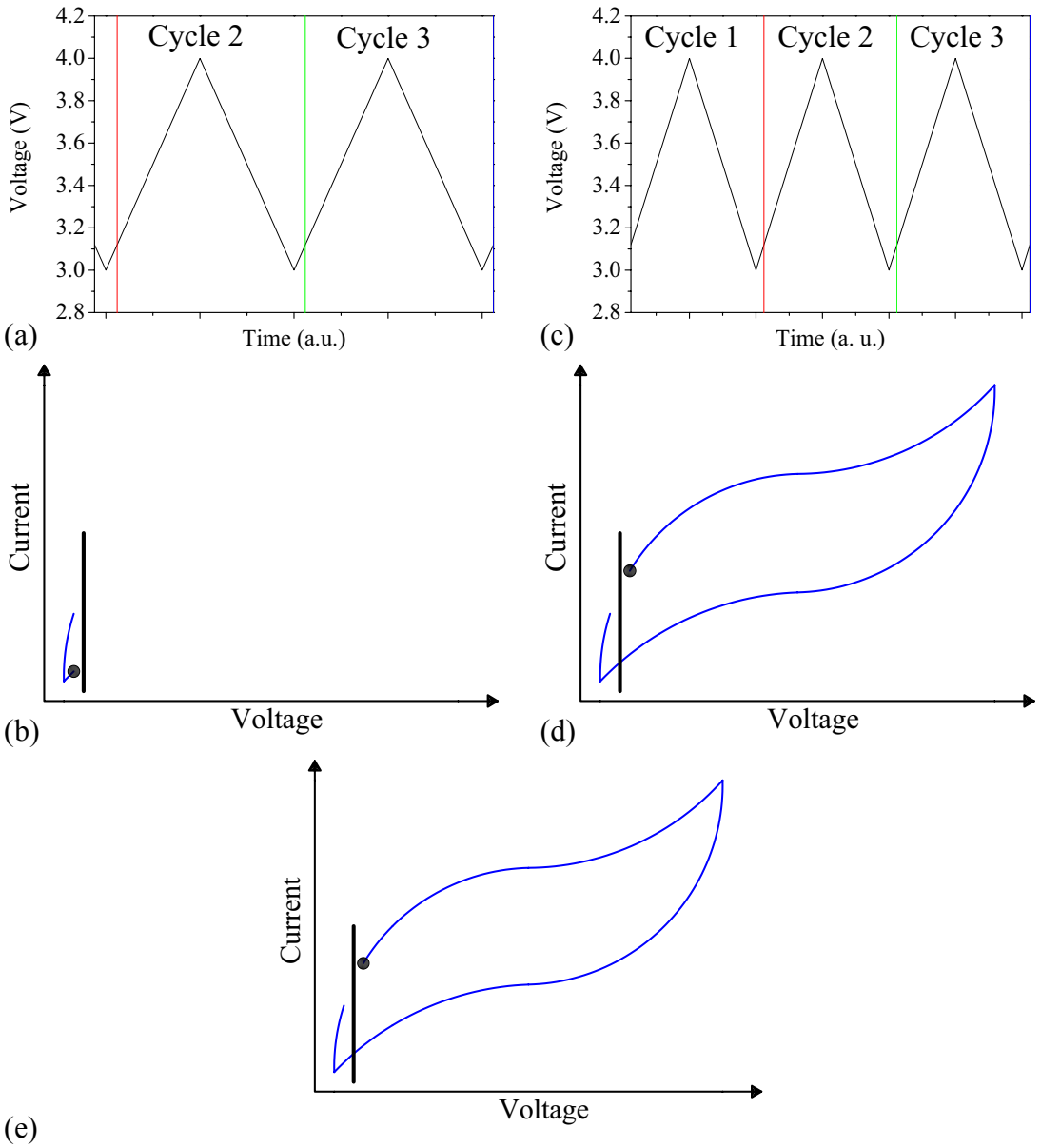

The solid black dot in these figures indicates the starting point of the voltammogram.

Figure 4-4: Effect of parameters in sorting CV data for low cutoff value.

4.1.3 Neware BTS – Charge/Discharge Algorithm

The charge/discharge testing carried out on the Neware BTS has a data set comprised of time, voltage, current and capacity data. Through the use of an appropriate algorithm the profiles of individual charge discharge steps can be extracted. A table of capacity values is also compiled but makes use of an alternate file containing only part of the entire data set. The testing procedure is not limited to constant current charge and discharge steps necessitating a more complex algorithm than that for charge/discharge conducted on the EG&G potentiostat. Other steps that can occur in the test process include rest periods and constant voltage charging. The algorithm is able to work for all these possibilities and makes use of the time and current data contained within the file. This particular algorithm identifies a rest period following a charge or discharge process as belonging to that step.

The algorithm is composed of two statements and both must be true for a point to be identified as the start of a new cycle step (schematic Figure 4-5). The statements are:

- The current points Time = 0
- One of the following must be true:
    1. The previous points current $\geq$ -0.01 and the current points current < 0
    2. The previous points current $\leq$ 0.01 and the current points current > 0

4.2 Microsoft Excel and VBA

Following the design of the algorithms they were incorporated into an Excel spreadsheet. Initially the spreadsheet required a large degree of manual manipulation such as copy and paste operations but this was quickly reduced through the use of recorded macros alone. With the basic functionality of the spreadsheet created it was then refined through the use of VBA to automate the entire procedure.

Through utilisation of VBA a range of functions could be performed to create a polished software solution. A key part of such a solution is the ability to use both built-in and custom dialog boxes. These allowed a processing method to be selected, a file to be selected for processing, and other relevant processing parameters to be gathered. Following this the processing could be carried out and where appropriate the output saved automatically.

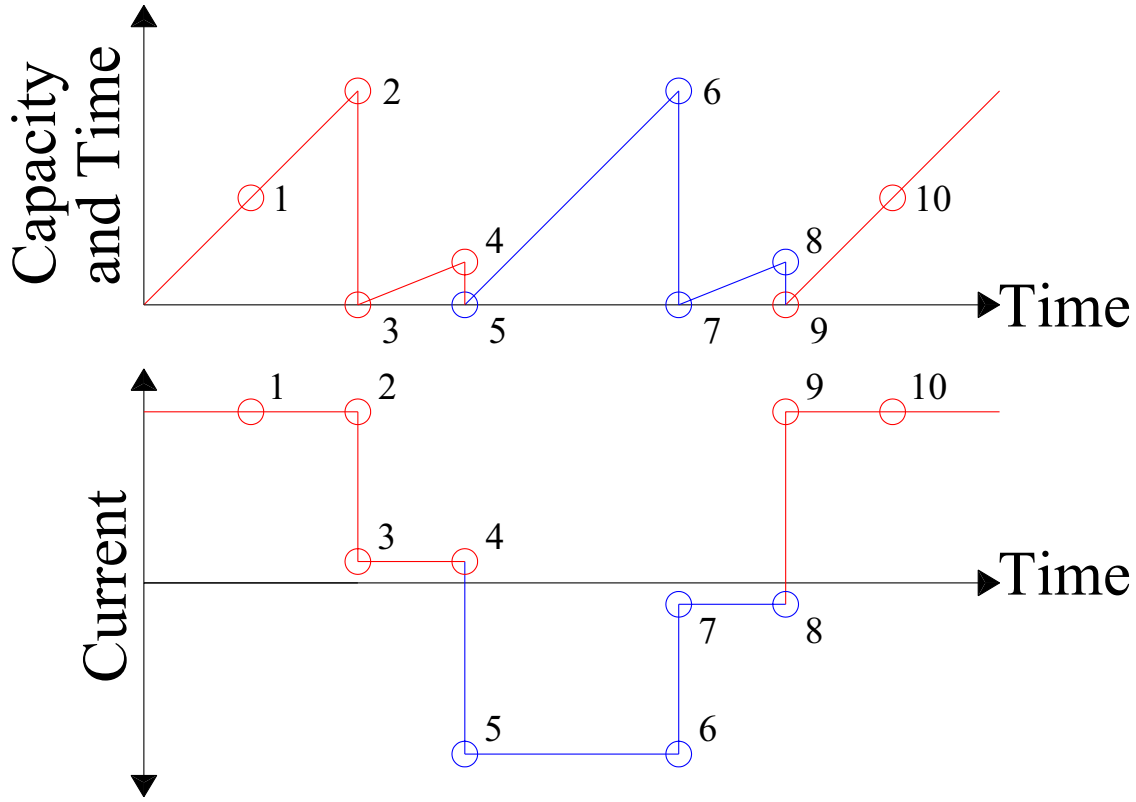

Figure 4-5: Schematic of sorting algorithm for Neware BTS.

4.3 Graphing the Outputted Data

Although Excel has graphical capabilities these were not utilised to produce graphs from the processed output due to the large number of variables for the process. These include the purpose of the graphs and personal preferences for graphs. Given that the data was now in a standard format graphing could however easily be carried out in any number of software packages including Excel using templates. In this way individuals can generate their own graph templates that suit the individual preferences and requirements for the presentation of their own data. Such an approach also allowed additional parameters such as differential capacity and coulombic efficiency to be calculated if they were desired.

4.3.1 Additional Data Manipulation

Although individual charge/discharge steps can be separated out using the algorithms provided in the BatteryTestDataProcessing spreadsheet different representations of this data may sometimes be desired. In order to fulfil this role a second spreadsheet was created to manipulate the data of separated cycles from BatteryTestDataProcessing spreadsheet. Additional details of which are presented in its

manual available in Appendix C. The spreadsheet does not create the graphs but outputs a text file containing the data from which they can be directly created.

Four alternative graphical formats were identified as potentially useful and were based on three primary formats described as:

A – Continuous

B – Cyclic

C – Pairs

The fourth format is an alternate representation of the standard pair format.

4.3.1.1 A – Continuous

The continuous method produces a format in which the maximum capacity of the previous cycle step becomes the minimum for the following cycle step, which is repeated for all the data within the original file (Figure 4-6).

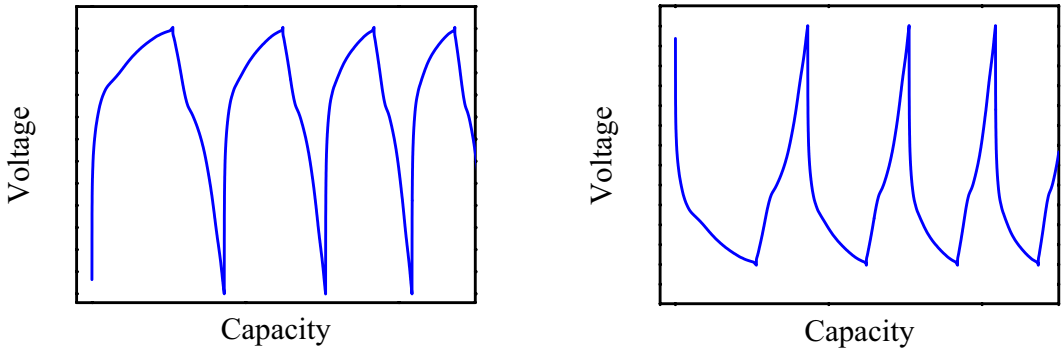

Figure 4-6: Examples of graphical output for A – Continuous method.

4.3.1.2 B – Cyclic

The cyclic method produces a format in which the maximum capacity of an odd cycle becomes the starting point for subtracting the capacity of the following even cycle step. The minimum capacity of the even cycle step then becomes the starting point for the addition of capacity of the following odd cycle step (Figure 4-7).

4.3.1.3 C – Pairs

The standard pairs method takes cycle steps in pairs from the start of the file and the maximum capacity of the first cycle step is added to the capacity of the second cycle step of the pair (Figure 4-8). The pairs separate first cycle method is basically the same but instead of taking pairs from the start of the file the first cycle step remains on its own and the remaining cycle steps are taken in pairs.

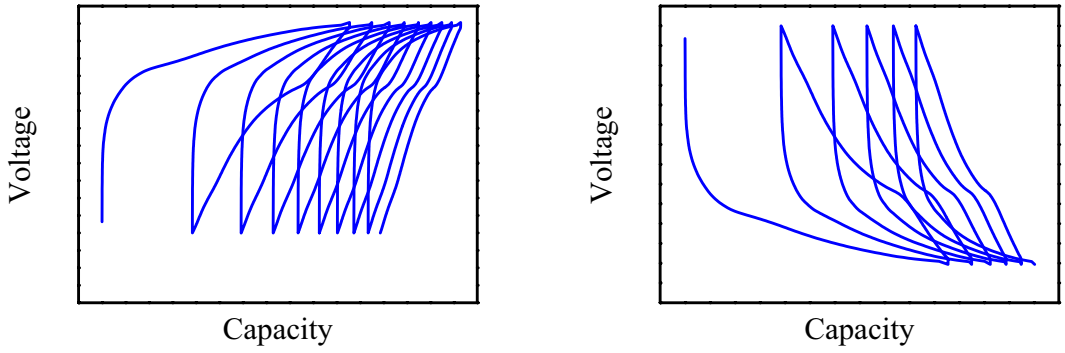

Figure 4-7: Examples of graphical output for B – Cyclic method.

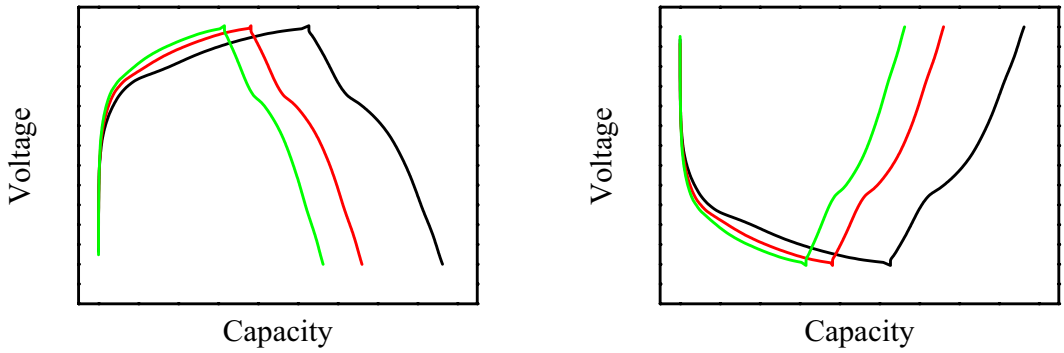

Figure 4-8: Examples of graphical output for C – Pairs method.

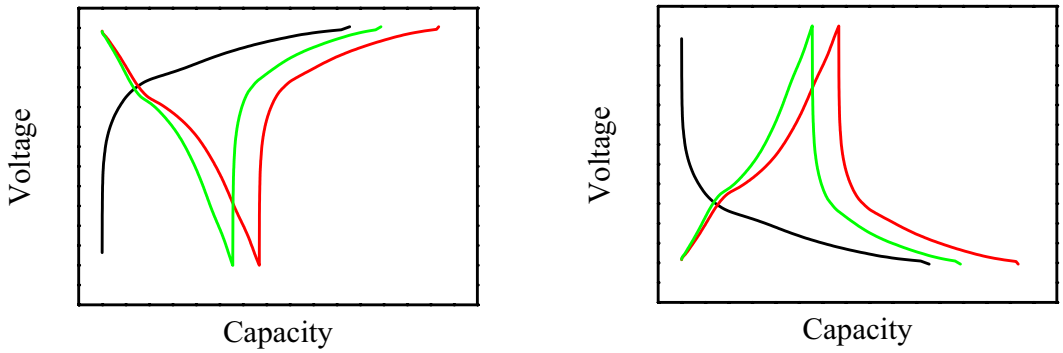

Figure 4-9: Examples of graphical output for C – Pairs Separate First Cycle method.

4.4 Conclusions

Through the development of an Excel spreadsheet featuring VBA code the rapid processing of a variety of electrochemical test data has been enabled. The development of a second spreadsheet also enabled the results of charge discharge data to be presented in a variety of formats other than the standard output from the original spreadsheet. By enabling the rapid processing of electrochemical test data more time can be spent conducting other experiments.

Chapter 5 Aluminium Based Binary Intermetallics

A range of intermetallic materials has been investigated as anode materials for lithium ion batteries particularly based on tin and silicon as active materials. The few aluminium based intermetallic materials that have been considered have been reported as inactive (Al_2Cu, Al_6Mn, Al_4Mn) with the small reversible capacities observed attributed to the carbon content of the electrode [107]. If however a number of issues such as theoretical capacity and volume expansion on lithiation are considered there is merit in considering the use of aluminium based intermetallics.

If the aluminium – lithium binary phase diagram is examined three Al – Li phases are indicated as forming (AlLi, Al_2Li_3, Al_4Li_9) [230]. The theoretical capacity of a pure aluminium electrode is typically given as 993 mAh/g corresponding to the formation of LiAl phase. This is despite the fact that Al – Li phases exist with higher lithium content and the formation of them during electrochemical insertion of lithium has been reported (Al_4Li_9) [231]. The theoretical capacities of the higher lithium content alloys Al_2Li_3 and Al_4Li_9 are 1490 mAh/g and 2235 mAh/g respectively. The theoretical capacity of AlLi at 993 mAh/g even though lower than the other Al – Li phases is still as high as that of the lithium richest Li – Sn phase ($Li_{22}Sn_5$).

Aluminium also offers a potential benefit over tin due to its lower volume expansion on lithium insertion. Whilst full reaction of lithium with metallic tin to form $Li_{22}Sn_5$ results in a 676 % increase in volume the corresponding increase for lithium's reaction with metallic aluminium to form LiAl is only 97 % [106].

Following examination of a number of binary phase diagrams of aluminium and metals inactive to lithium the iron – aluminium phase $FeAl_3$ was chosen for investigation. This phase consisting of a high weight percentage of aluminium (59 wt. %) offered a high theoretical capacity and also offered some compositional width. The theoretical discharge capacity of $FeAl_3$ given full reaction of aluminium with lithium to form LiAl equates to 588 mAh/g whilst for complete formation of Al_4Li_9 it equates to 1323 mAh/g.

5.1 Fe_2Al_5 Based Anode Materials

High purity iron (chip 99.98 % Aldrich) and aluminium (shot 99.9 % Aldrich) were weighed out in the proportions corresponding to stoichiometric $FeAl_3$. The iron and aluminium were then combined to form an alloy slug with the use of an arc melter.

The alloy slug was then crushed a number of times until the resultant fines passed through a 150 μm sieve. The crushing process was completed relatively quickly given the brittle nature of the resultant alloy.

The material that passed through the 150 μm sieve was then milled in a Pulverisette-5 planetary ball mill at a speed of 90 rpm in a steel milling vessel. The milling vessel had an internal diameter of 80 mm and volume of approximately 200 cm^3. The milling media were 5 mm diameter stainless steel balls utilised with a ball to powder ratio of approximately 20:1 (173g balls: 8.852g powder). Ethanol was also added as a process control additive to the level of the top of the balls. Powder was removed at a number of intervals in small quantities up to a total milling time of 10,000 minutes. Powder was removed at total milling times of 100, 500, 2,000 and the final milling time of 10,000 minutes. Where milling continued after powder was removed ethanol was added to the milling jar if required to bring it back up to its initial level. The various powders and other results derived from their use will be referred to using a prefix of BM followed by the milling time of the powder in minutes. Whilst the unmilled material that passed through the 150 μm sieve is referred to as BM0.

The fabrication of electrodes resulted in loadings of approximately 14 mg for BM0, 5 mg for BM100 and 1 mg for the remaining samples. The differences between the electrodes were not however limited to the materials loading as there were also differences in the use of Vulcan XC-72 conductivity additive. Electrodes of the first three materials (BM0, BM100 and BM500) contained no conductive additive whilst the final two samples (BM2,000 and BM10,000) contained a loading of approximately 10 weight percent conductivity additive. The final composition of the electrodes corresponded to 85 – 95 wt. % powder, 10 – 0 wt. % conductivity additive and 5 wt. % PVDF.

5.1.1 Results

5.1.1.1 Structural and Microstructural Characterisation

The XRD pattern of the unmilled material (BM0 in Figure 5-1) did not correspond to the cubic structure of $FeAl_3$ but rather the orthorhombic structure of Fe_2Al_5 (JCPDS card 47-1435). Also evident from the diffraction patterns is that the diffraction peaks are well defined up to a milling time of 500 minutes and significant

broadening of peaks occurs with increasing milling time. The diffraction patterns of the 2,000 and 10,000 minute samples can however be described as X-ray amorphous.

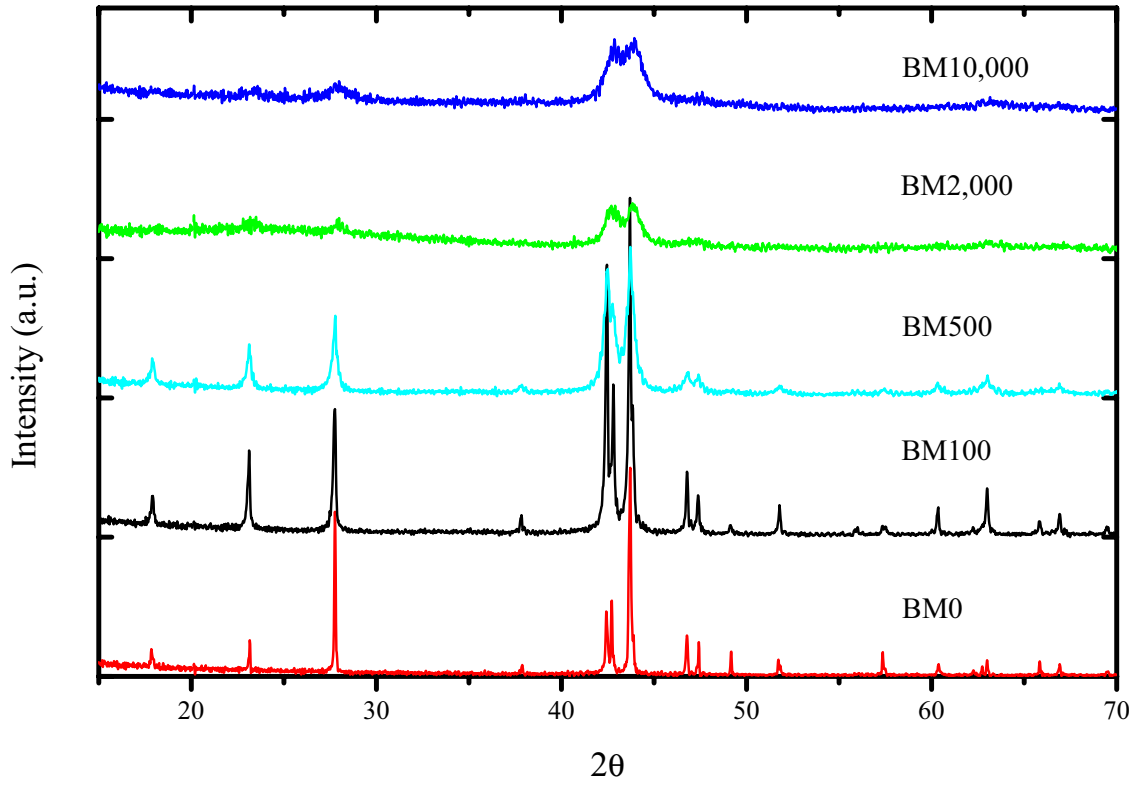

Figure 5-1: XRD patterns of ball milled Fe_2Al_5.

Full width at half maxima (FWHM) were determined using the Traces program for the (111) (020) peak and the crystalline size was estimated using the Scherrer equation (3-6) using a value of 0.9 for the K constant. The broadening due to the sample itself was determined by subtraction of the instrumental error according to 3-8. From such an approach the crystallite size was estimated as over 100 nm for BM0, 72 nm for BM100 and 41 nm for BM500.

In order to examine the effect of milling on the particle size of the Fe_2Al_5 powders SEM was used to examine the particle size (Figure 5-3). Examination of the micrographs showed a continuous decrease in the maximum particle size observed from 100 μm for BM0 to 0.5 μm for BM10,000 (Figure 5-2).

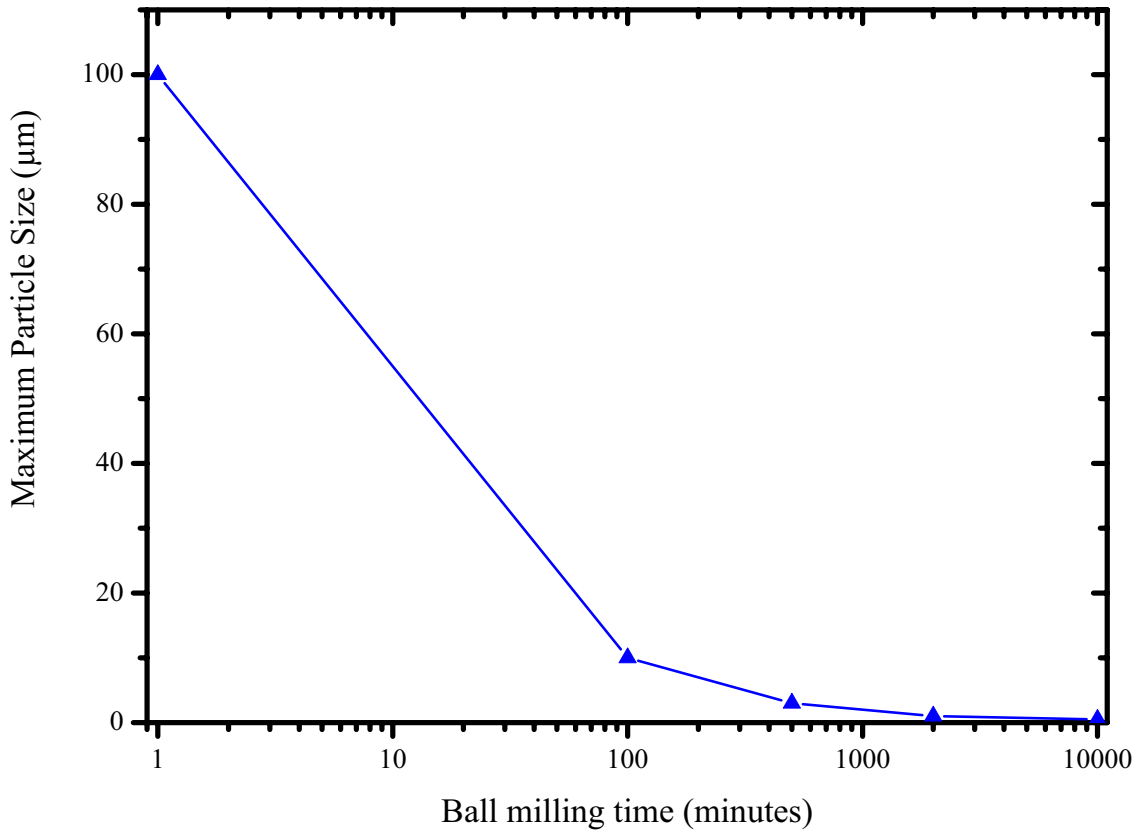

Figure 5-2: Variation of maximum particle size with ball milling time for Fe_2Al_5 materials.

5.1.1.2 Electrochemical Characterisation

The electrochemical properties of Fe_2Al_5 were evaluated with the use of the prepared alloy electrodes as working electrodes and metallic lithium foils as the counter electrode. From constant current charge/discharge (50 µA, 0.01 – 3.00 V) of Fe_2Al_5 electrodes an increase in the first discharge capacity with an increase in milling time is seen (Figure 5-4). The first charge capacity also increases with an increase in milling time (Figure 5-5) but is substantially lower than the first discharge.

The difficulty in extracting lithium from the Fe_2Al_5 structure is evident in the low first charge capacities in comparison to the first discharge. The subsequent discharges are also significantly lower (Figure 5-6) with the second discharge capacity of BM10,000 approximately 30 % of the first discharge and 40 % for the other materials. The variation in capacity with milling time is particularly evident for milling times of greater than 100 minutes and for the first discharge capacity (Figure 5-7).

(a)

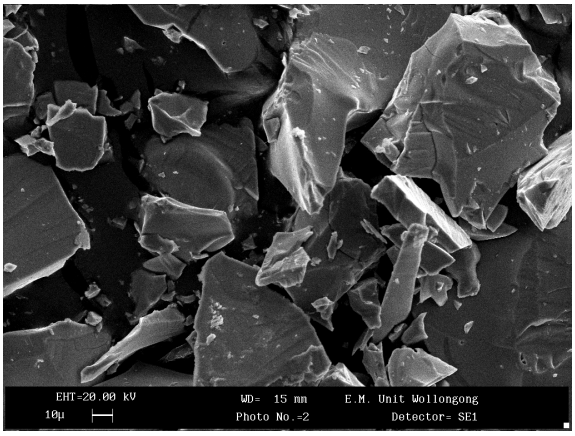

(b)

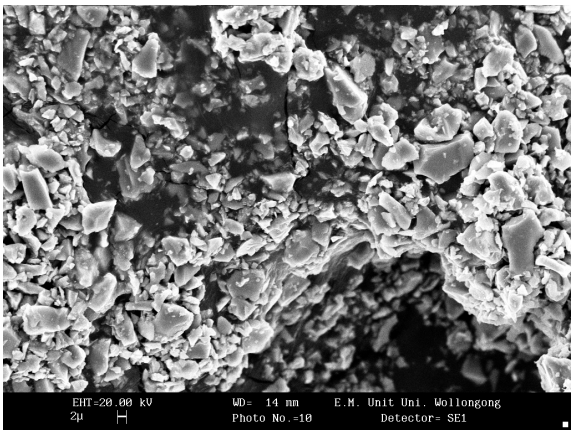

(c)

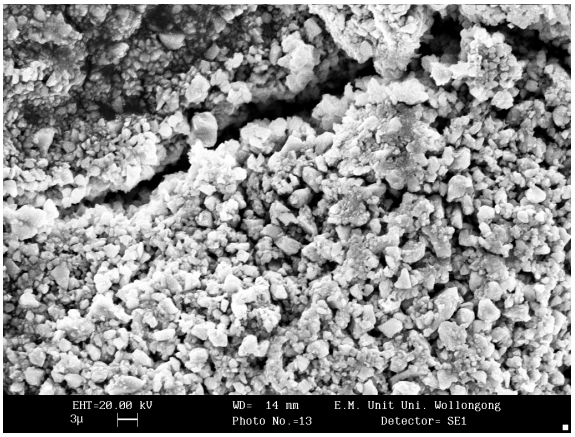

(d)

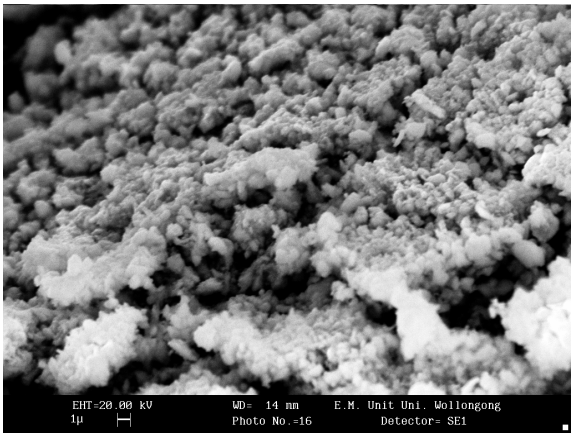

Figure 5-3: SEM micrographs of selected Fe_2Al_5 ball milled powder samples: (a) <150 µm, (b) 100 minutes, (c) 500 minutes, (d) 2,000 minutes.

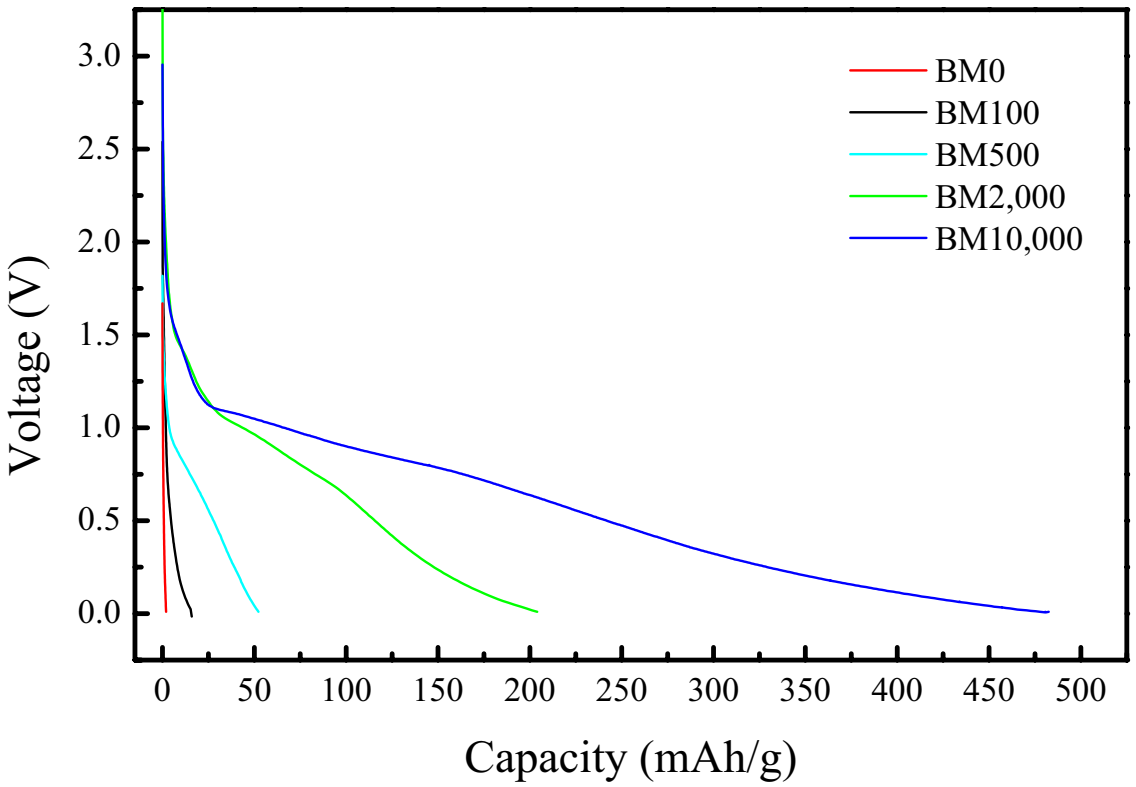

Figure 5-4: First discharge of various ball milled Fe_2Al_5 materials.

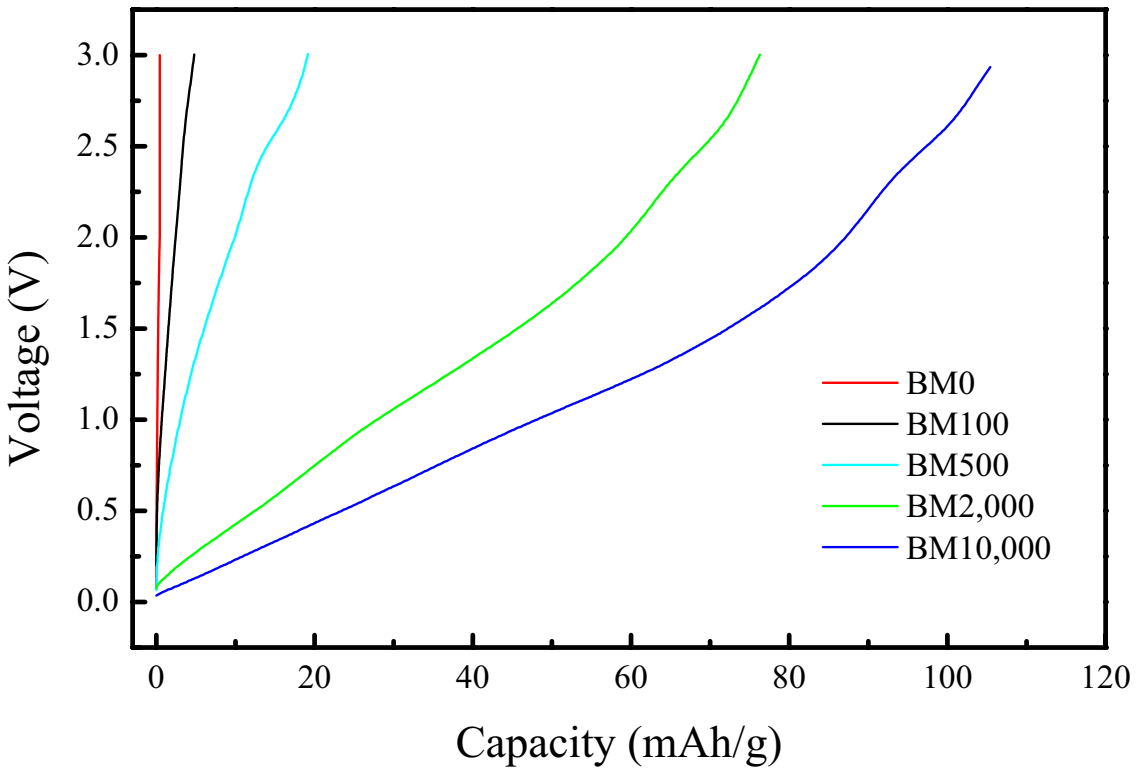

Figure 5-5: First charge of various ball milled Fe_2Al_5 materials.

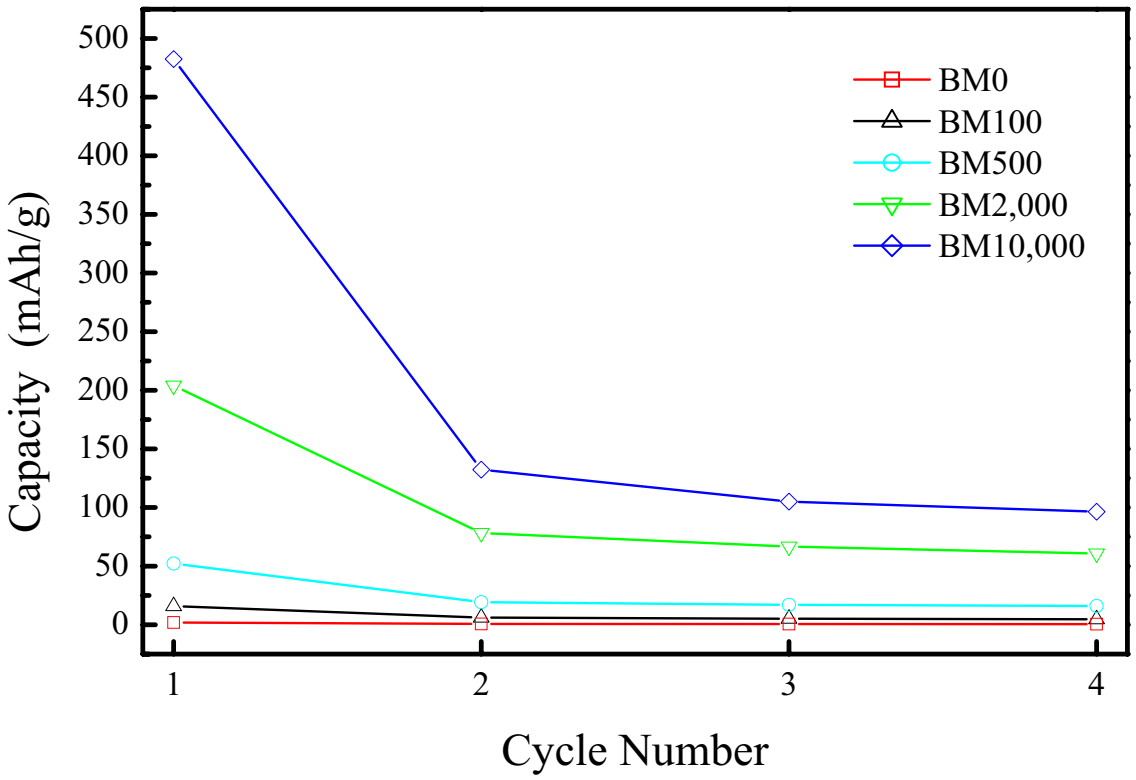

Figure 5-6: Variation of discharge capacity of Fe_2Al_5 electrodes with ball milling time.

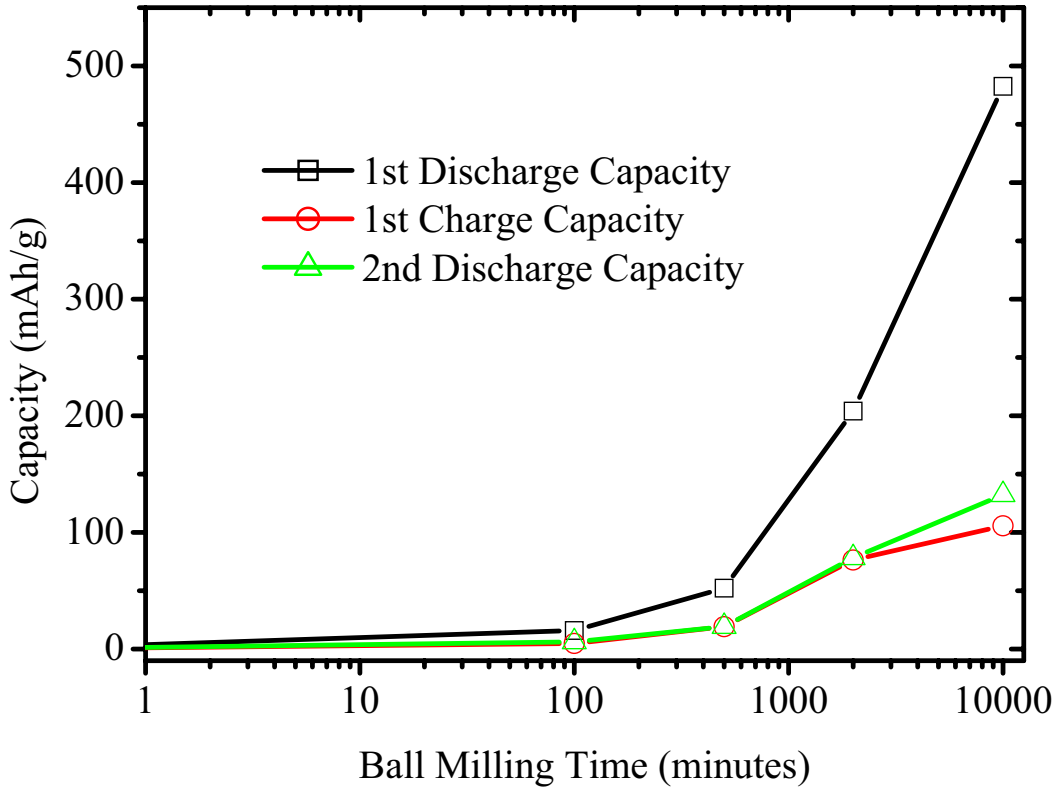

Figure 5-7: Variation of capacity of Fe_2Al_5 with ball milling time.

A number of broad peaks are evident in both differential capacity (Figure 5-8) and cyclic voltammetry (Figure 5-9) plots suggesting a number of reactions are occurring during the charge discharge process.

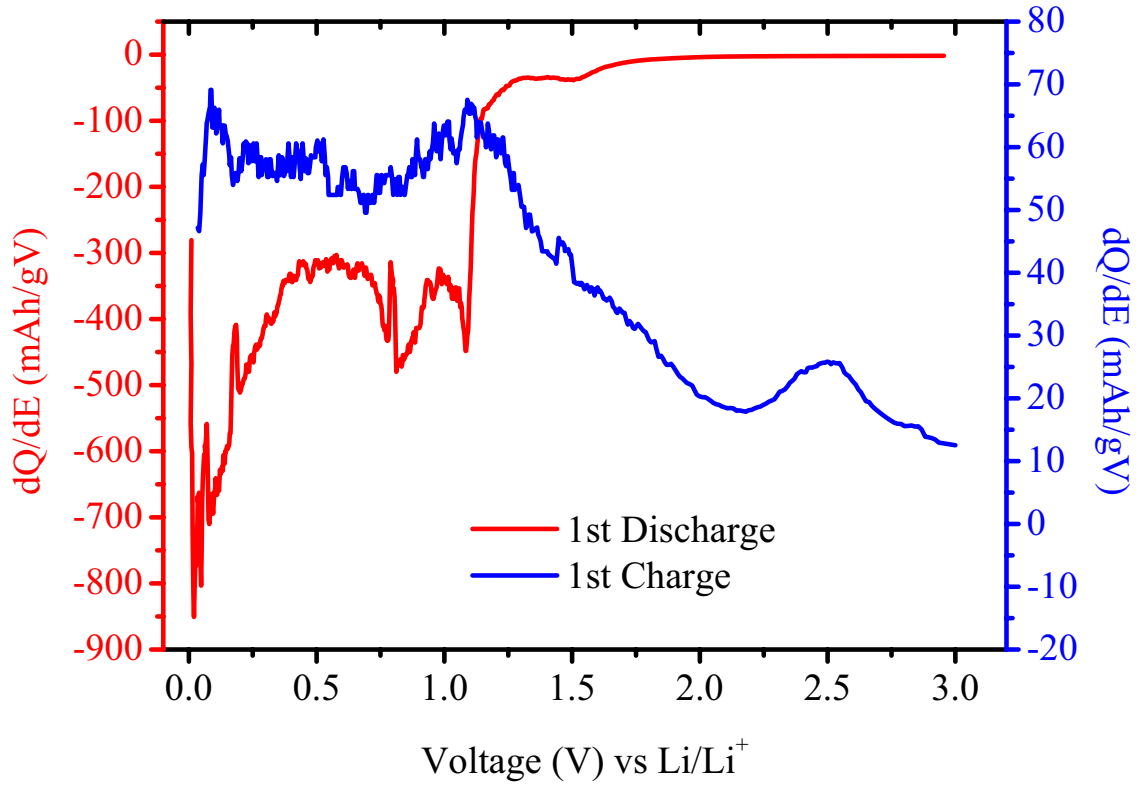

Figure 5-8: Differential capacity plots for first charge and discharge of BM10,000 electrode.

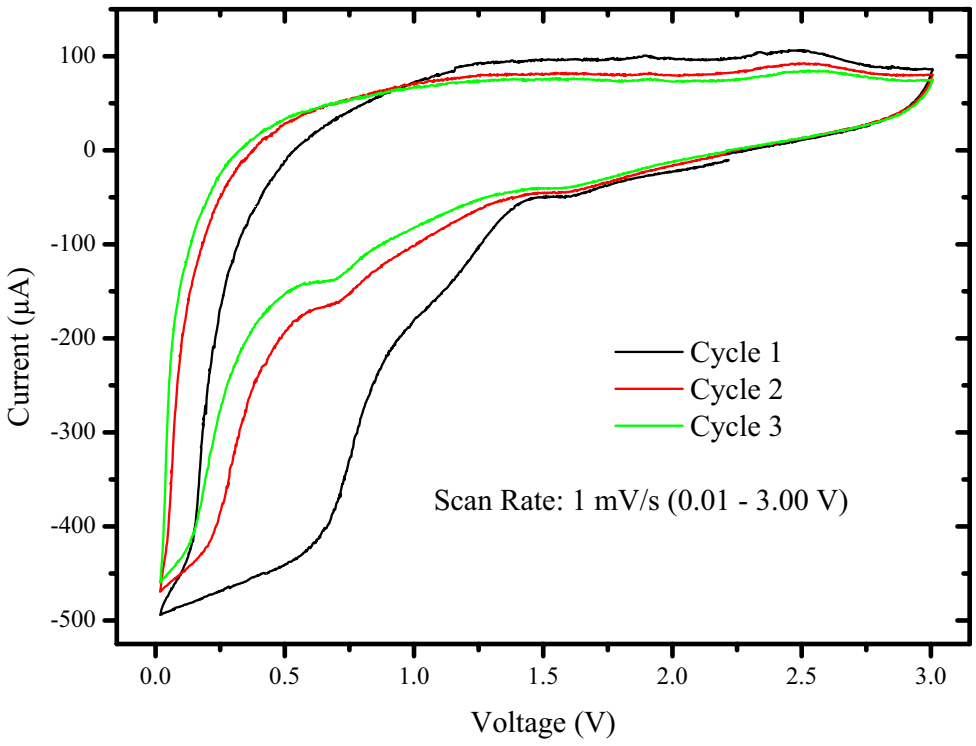

Figure 5-9: Cyclic voltammetry of BM10,000 electrode.

5.1.2 Discussion

As the melting point of aluminium is much lower than that of iron if any material was to have been lost during the melting process it would be expected to be aluminium. The iron content would also be expected to increase slightly during the milling process as a result of pickup from the steel milling vessel and grinding media. Revision of the theoretical capacity to reflect the Fe_2Al_5 phase that XRD showed the alloy to be is reasonable. Fe_2Al_5 has a theoretical discharge capacity of 543 mAh/g for the formation of AlLi and 1223 mAh/g for the formation of Al_4Li. These theoretical capacities are 45 mAh/g and 100 mAh/g lower than for formation of AlLi and Al_4Li_9 respectively for the $FeAl_3$ phase.

The crystallite sizes estimated with the Scherrer equation will not represent the true crystallite size of the material as the effect of stress on peak broadening has not been taken into account. The broadening due to stress would be expected to have contributed to the total broadening given the ball milling process employed. The estimates of crystallite size are not however unrealistic as they are well above the minimum crystallite sizes for the mechanical milling of aluminium (20 – 24 nm) and iron (8 nm) reported in a compilation by Koch [232]. The crystallite sizes are also much larger than the 10 nm reported for a number of aluminium based intermetallics (Al_2Cu, Al_6Mn, and Al_4Mn) that were evaluated as anode materials for lithium ion batteries [107]. The particle sizes of all the ball milled materials are also similar to the 1 – 10 μm range reported in the same investigation [107].

However unlike previous aluminium intermetallics investigated [107] activity towards lithium was observed. In the previous case the small reversible capacity of 20 mAh/g was attributed to the carbon content of the electrode. In this case however the BM500 electrode contained no carbon and after the first discharge of 52 mAh/g the initial reversible capacity was 20 mAh/g. The low charge capacities and steep charge profile do however indicate that lithium is not easily extracted from the Fe_2Al_5 structure.

Whilst the first discharge capacity of BM10,000 is consistent with the theoretical capacity of Fe_2Al_5 for the formation of LiAl (543 mAh/g) differential capacity and cyclic voltammetry indicate that other reactions are occurring. Cyclic voltammetry of Al thin films has shown the reaction $Al + Li \leftrightarrow AlLi$ occurs at approximately 0.2 V on discharge and 0.45 V on charge [109]. Given these values the formation of AlLi may be

occurring on discharge though it is not evident as a standalone peak whilst there is little evidence of the reverse reaction occurring on charging.

Further modification of the microstructure through for instance further milling and/or annealing operations may be able to improve the capacity retention. Even though the cycle performance was poor the activity of aluminium-based intermetallics has been demonstrated in contract to previous reports of inactivity.

5.1.3 Conclusions

In contrast to previous investigations of aluminium based intermetallic materials Fe_2Al_5 demonstrated clear interaction with lithium with a comparable particle size and larger crystallite size. With electrodes based on crystalline Fe_2Al_5 that had been milled for 500 minutes and containing no conductivity additive having a reversible capacity of 20 mAh/g. Though ball milling improves the electrochemical performance of Fe_2Al_5 it is not to a degree sufficient to be considered as a viable alternative to existing anode materials. Overcoming the difficulty in removing lithium from the structure is necessary for better electrochemical performance of Fe_2Al_5 materials to be demonstrated. Further modification of the microstructure may provide the key to achieving this and additional milling and/or annealing operations are two means by which this may be achieved.

Uncertainty does however exist over the reaction mechanism responsible for the capacity of Fe_2Al_5. Whilst the initial discharge capacity of the BM10,000 electrodes is consistent with the theoretical capacity for AlLi formation, differential capacity and cyclic voltammetry suggest that other reactions are also occurring. The lack of distinct peaks in cyclic voltammetry, in particular, corresponding to formation and consumption of LiAl does not offer conclusive evidence of the $Al + Li \leftrightarrow AlLi$ reaction occurring.

5.2 $Al_{13}Fe_4$ Based Anode Materials

Iron and aluminium powder were weighed out in the proportions corresponding to stoichiometric $FeAl_3$. In this case the iron and aluminium powder were mixed together and the powder mixture placed in a 25 mm diameter die ready for compaction using an Enerpac 10 tonne hydraulic press. The hydraulic pressure on the press was set at 6,000 psi and the samples were subjected to the pressure delivered by the ram at this level for six seconds. The resulting pellet was then melted into an alloy slug using an arc melter. The alloy slug was then crushed a number of times until the resultant fines passed through a 150 μm sieve.

The material that passed through the 150 μm sieve was then milled in a Pulverisette-5 planetary ball mill at a speed of 160 rpm in a steel-milling vessel. The milling vessel had an internal diameter of 80 mm and volume of approximately 200 cm^3. The milling media were 5 mm diameter stainless steel balls utilised with a ball to powder ratio of approximately 20:1 (64.0661g balls: 3.3030g powder). In this case the powder charge did not consist of the alloy alone but of alloy powder with a 9.7 weight percent addition of Vulcan XC-72. Ethanol was also added as a process control additive to the level of the top of the balls. Powder was removed at a number of intervals in small quantities up to a total milling time of 260 hours. Powder was removed at total milling times of 50, 120, 190 and the final milling time of 260 hours. Where milling continued after powder was removed ethanol was added to the milling jar if required to bring it back up to its initial level. The various powders and other results derived from their use will be referred to using a prefix of BM followed by the milling time of the powder in hours. Whilst the unmilled material that passed through the 150 μm sieve is referred to as BM0.

The fabrication of electrodes resulted in loadings of approximately 14 mg for BM0 and 1 mg for the remaining samples. The carbon content of the electrodes also varied as a result of the carbon addition to the milled material. The unmilled electrode contained only the carbon that was added during electrode fabrication whilst the milled electrodes also contained the carbon that was added at the start of the milling process. The final composition of the electrodes corresponded to 79 – 86 wt. % alloy powder, 16 – 9 wt. % conductivity additive (Vulcan XC-72) and 5 wt. % PVDF.

5.2.1 Results

5.2.1.1 Structural and Microstructural Characterisation

The XRD pattern of the unmilled material (BM0 in Figure 5-10) did not correspond to the cubic structure of $FeAl_3$ but rather the monoclinic structure of $Al_{13}Fe_4$ (JCPDS card 29-42). The diffraction patterns of the other ball-milled materials do not exhibit any well-defined peaks and are described as X-ray amorphous.

In order to examine the effect of milling on the particle size of the $Al_{13}Fe_4$ powders SEM was used to examine the particle size (Figure 5-11). Examination of the micrographs showed a continuous decrease in the maximum particle size observed from

130 μm for BM0 to 1 μm for BM260 (Figure 5-12). Multipoint BET revealed a specific surface area for the BM260 material of 55 m^2/g.

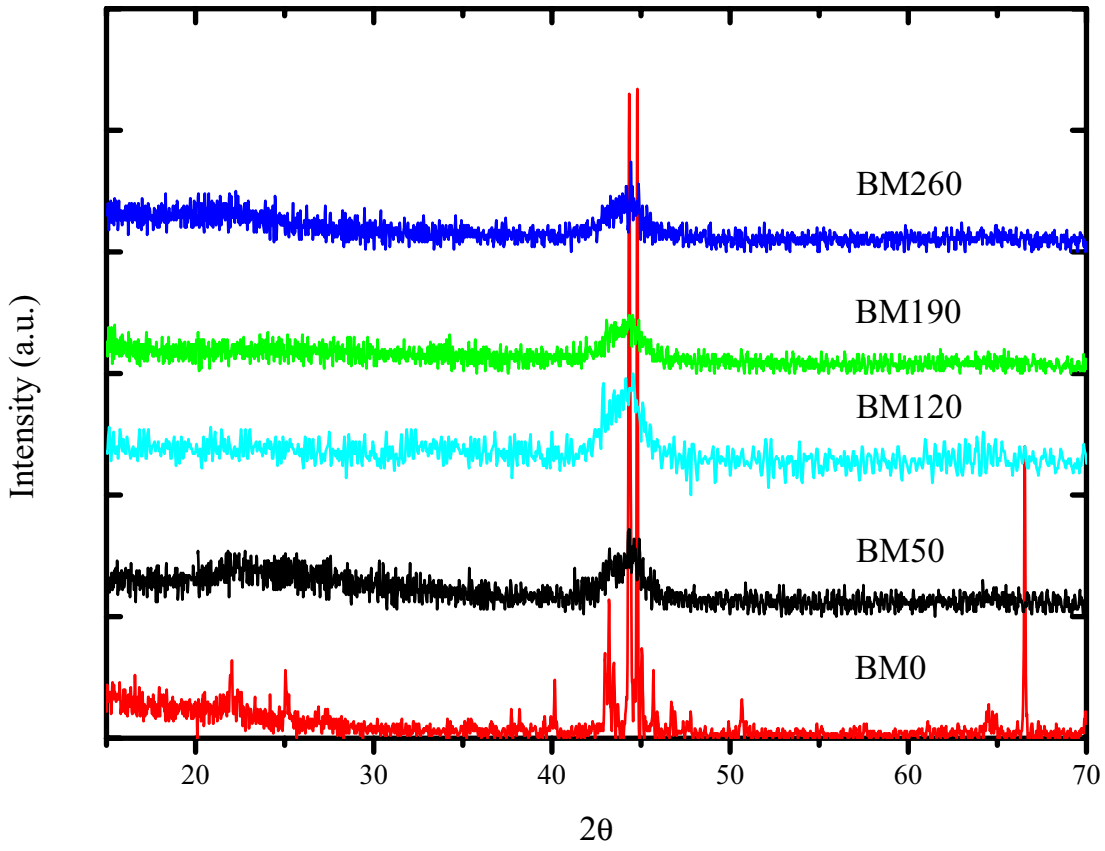

Figure 5-10: XRD patterns of milled $Al_{13}Fe_4$ materials.

5.2.1.2 Electrochemical Characterisation

The electrochemical properties of $Al_{13}Fe_4$ were evaluated with the use of the prepared alloy electrodes as working electrodes and metallic lithium foils as the counter electrode. The constant current charge/discharging (50 μA, 0.01 – 3.00 V) of $Al_{13}Fe_4$ electrodes demonstrated an increase in the first discharge (Figure 5-13) and charge capacity (Figure 5-14) with an increase in milling time. The increase in charge (Figure 5-16) and discharge (Figure 5-15) capacity with milling time was also evident in subsequent cycles.

Lithium is not easily extracted from the $Al_{13}Fe_4$ structure as indicated by the low charge capacities in comparison to the first discharge. The first charge capacity as a proportion of the first discharge reaches a maximum of 33 % for BM50 and BM120 and 40 % for BM50 for the second discharge (Figure 5-17). The increase in capacity with milling time is particularly evident for milling times of greater than 120 hours and for the first discharge capacity (Figure 5-18).

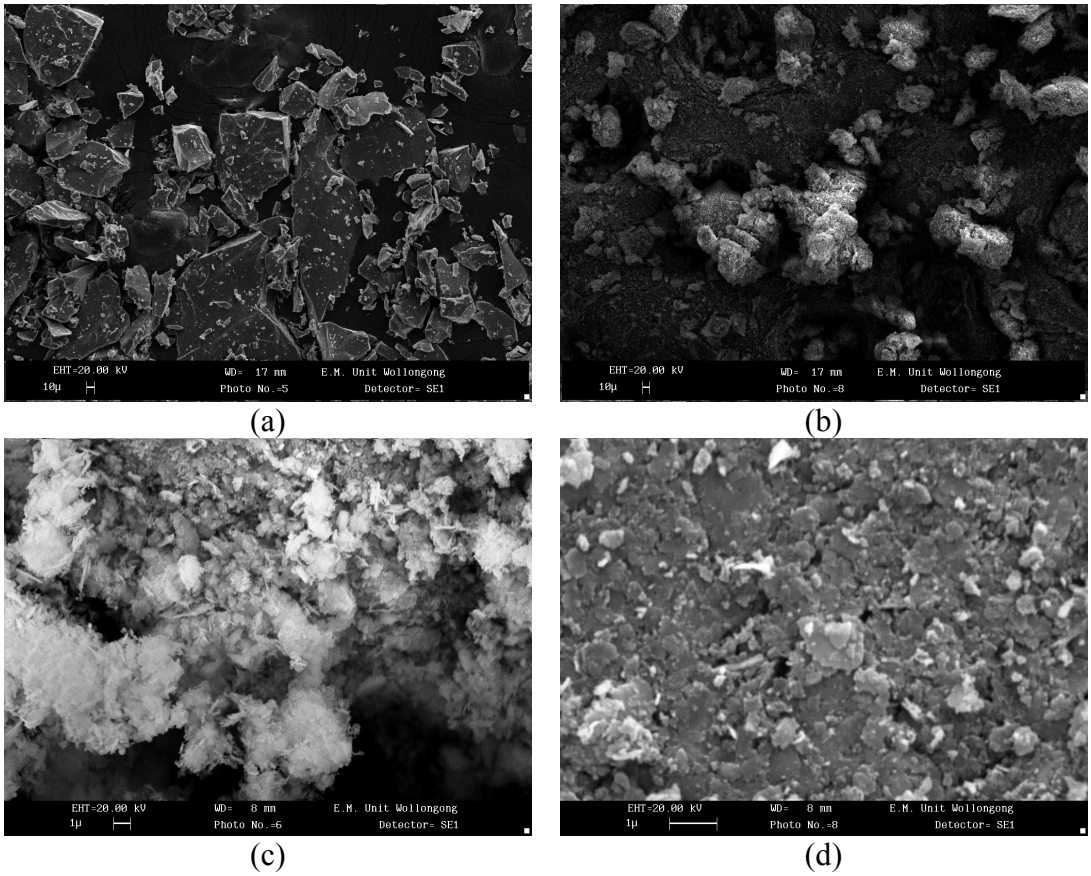

Figure 5-11: Selected SEM micrographs of ball milled $Al_{13}Fe_4$ materials: (a) 150 µm, (b) 50 hours, (c) 190 hours, (d) 260 hours.

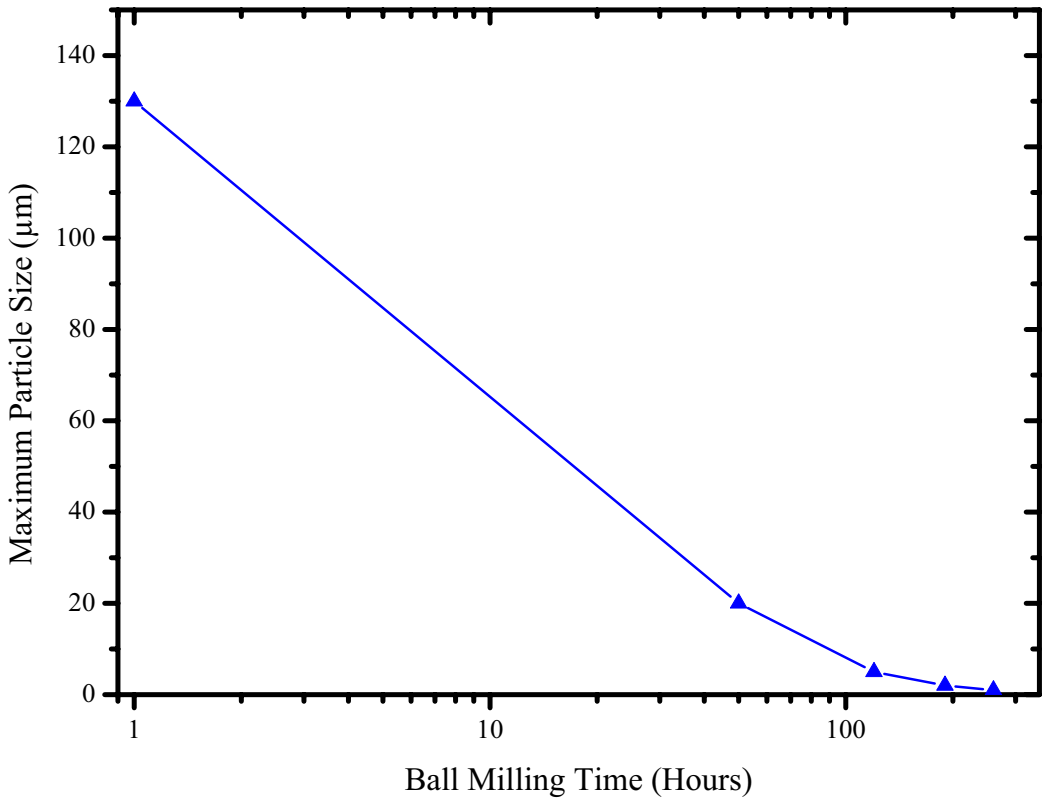

Figure 5-12: Variation of maximum particle size of $Al_{13}Fe_4$ with ball milling time.

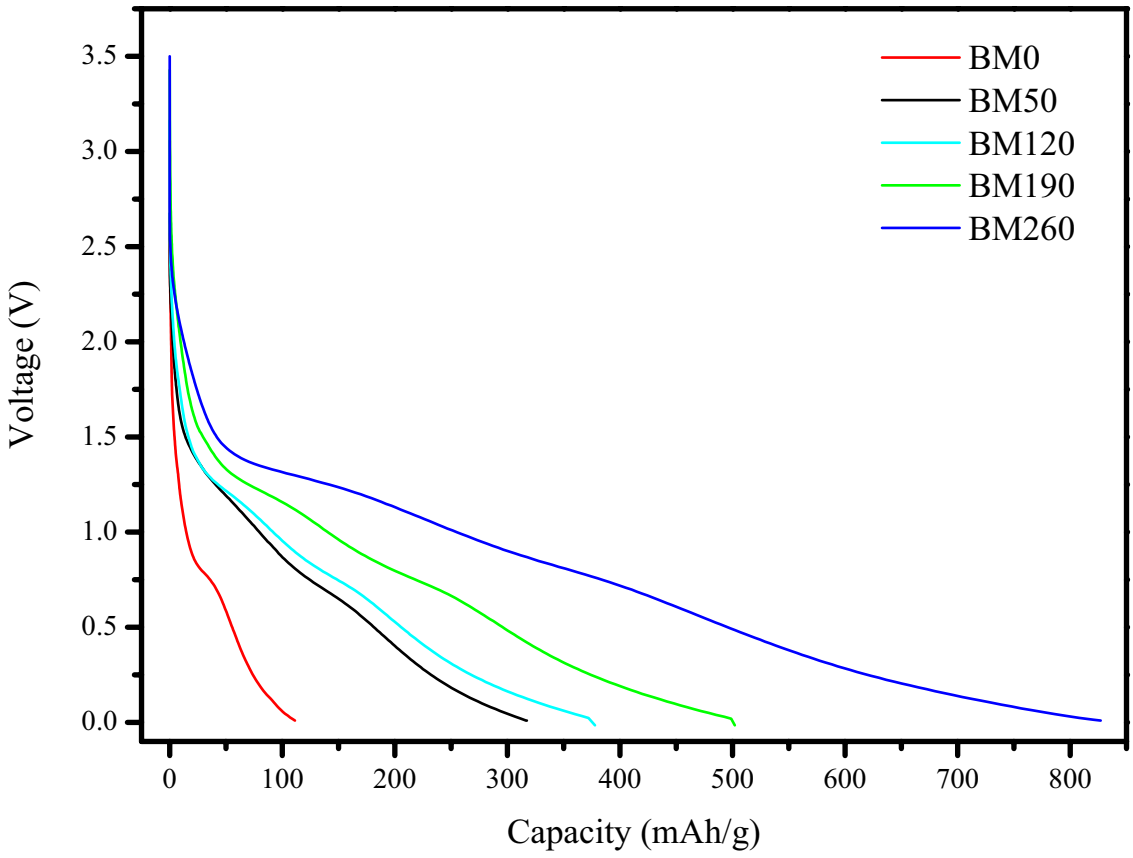

Figure 5-13: First discharge of various ball milled $Al_{13}Fe_4$ materials.

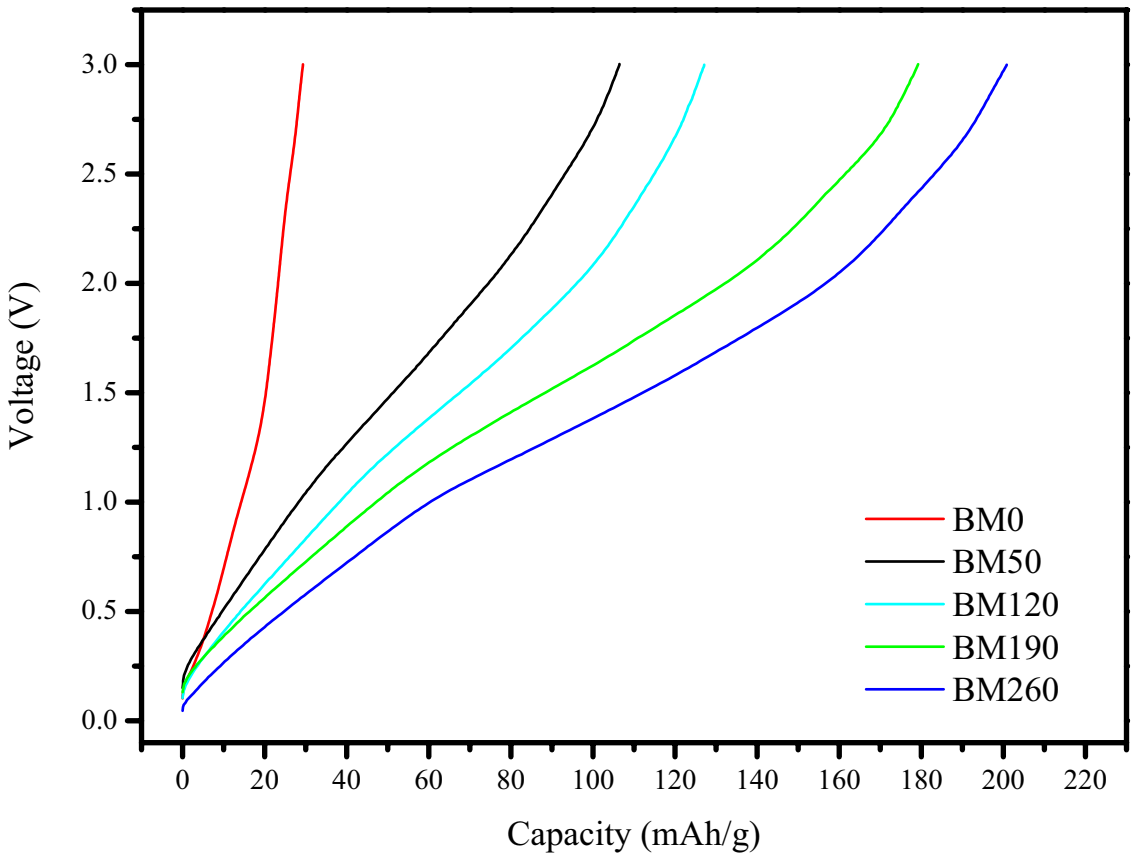

Figure 5-14: First charge of various ball milled $Al_{13}Fe_4$ materials.

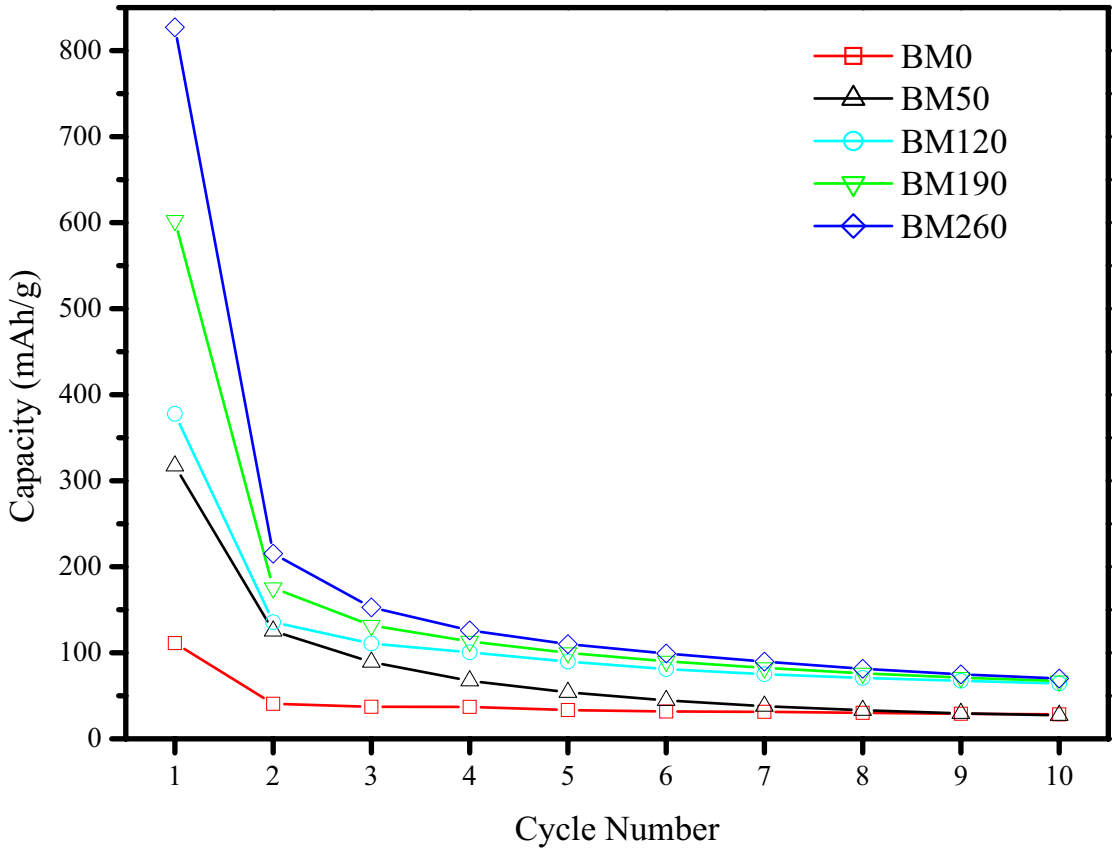

Figure 5-15: Variation of discharge capacity of $Al_{13}Fe_4$ with milling time.

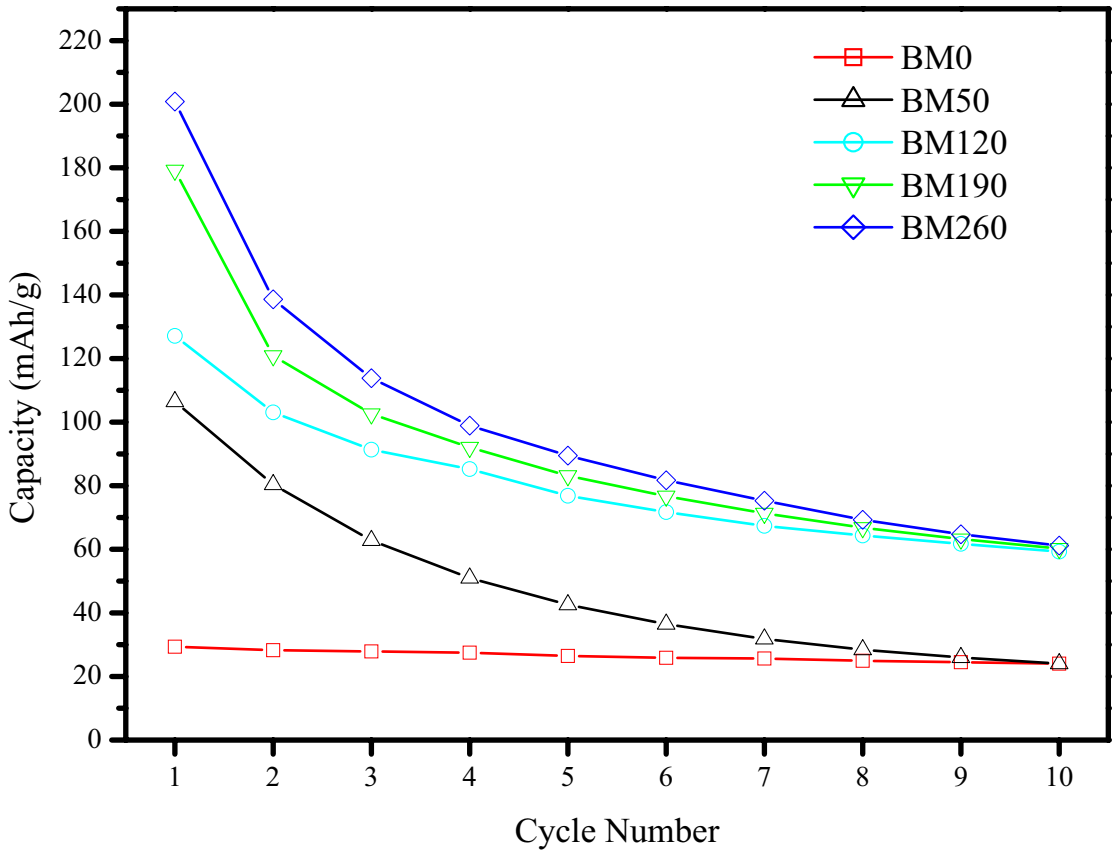

Figure 5-16: Variation of charge capacity of $Al_{13}Fe_4$ with milling time.

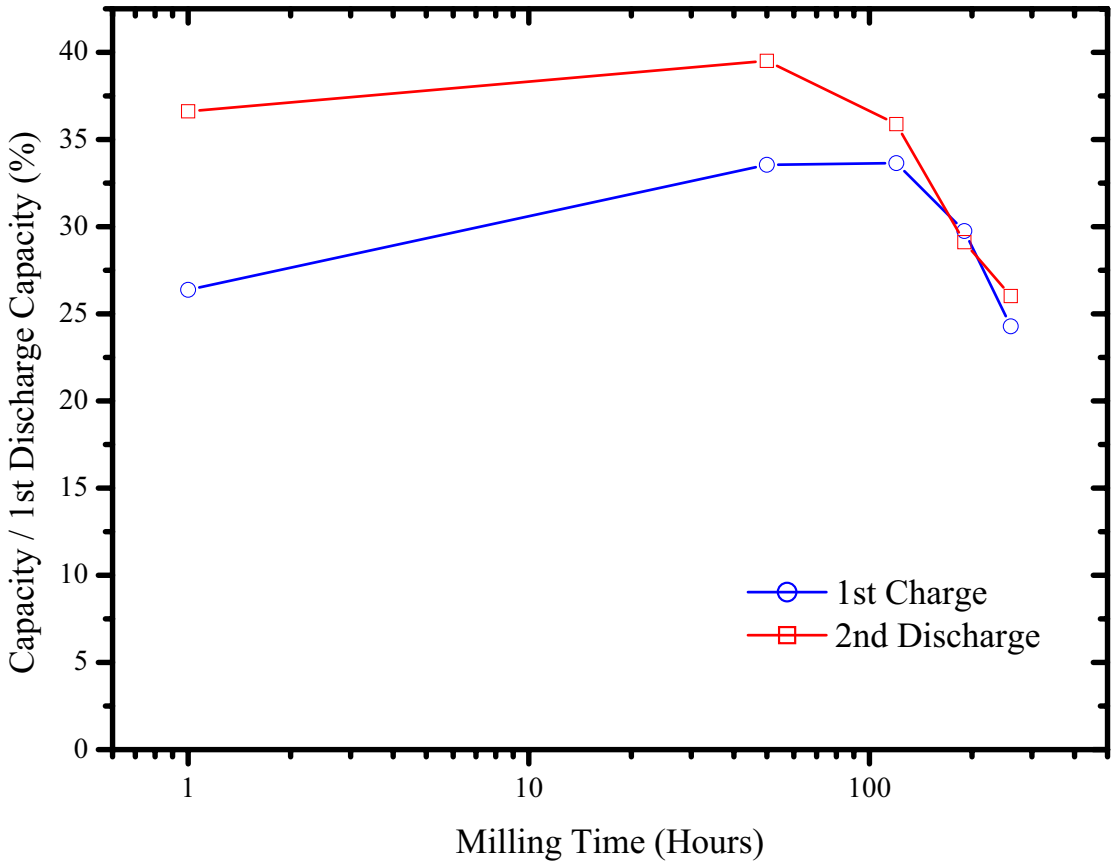

Figure 5-17: Variation of capacity relative to the first discharge for various milling times.

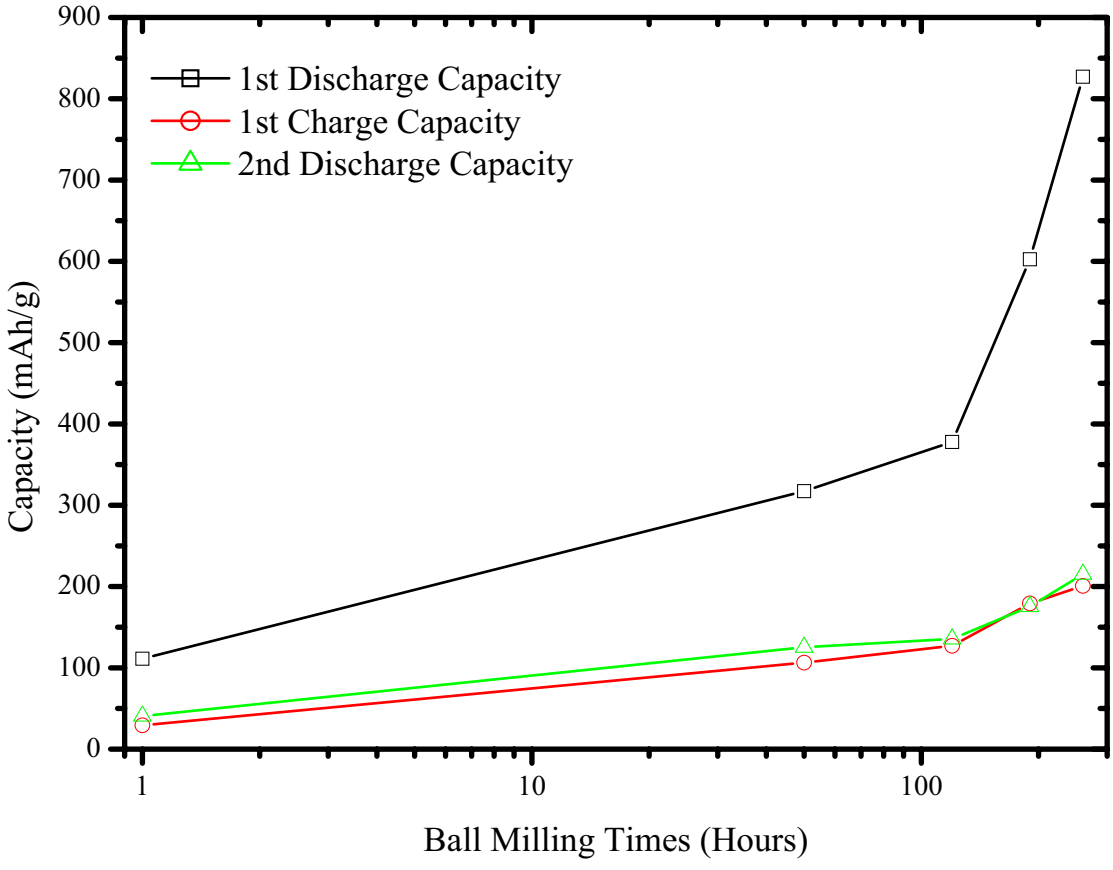

Figure 5-18: Variation of capacity with milling time for $Al_{13}Fe_4$ materials.

For all the milled material two broad peaks are evident in differential capacity plots of the first discharge whilst the unmilled material only one is evident. The two peaks are located at approximately 0.75 V and 1.25 V with only the 0.75 V peak evident in the unmilled results. The position of the 1.25 V shifts to slightly higher voltages with an increase in milling time whilst the position of the 0.75 V is relatively constant. Distinct peaks are not however evident for the differential capacity plots of the first charge.

Cyclic voltammetry of the BM260 material (Figure 5-20) does not indicate any well-defined peaks such as were evident in the differential capacity plots. The shape of the voltammogram for the first cycle is different to those of subsequent cycles not just for the discharge but also for the charge.

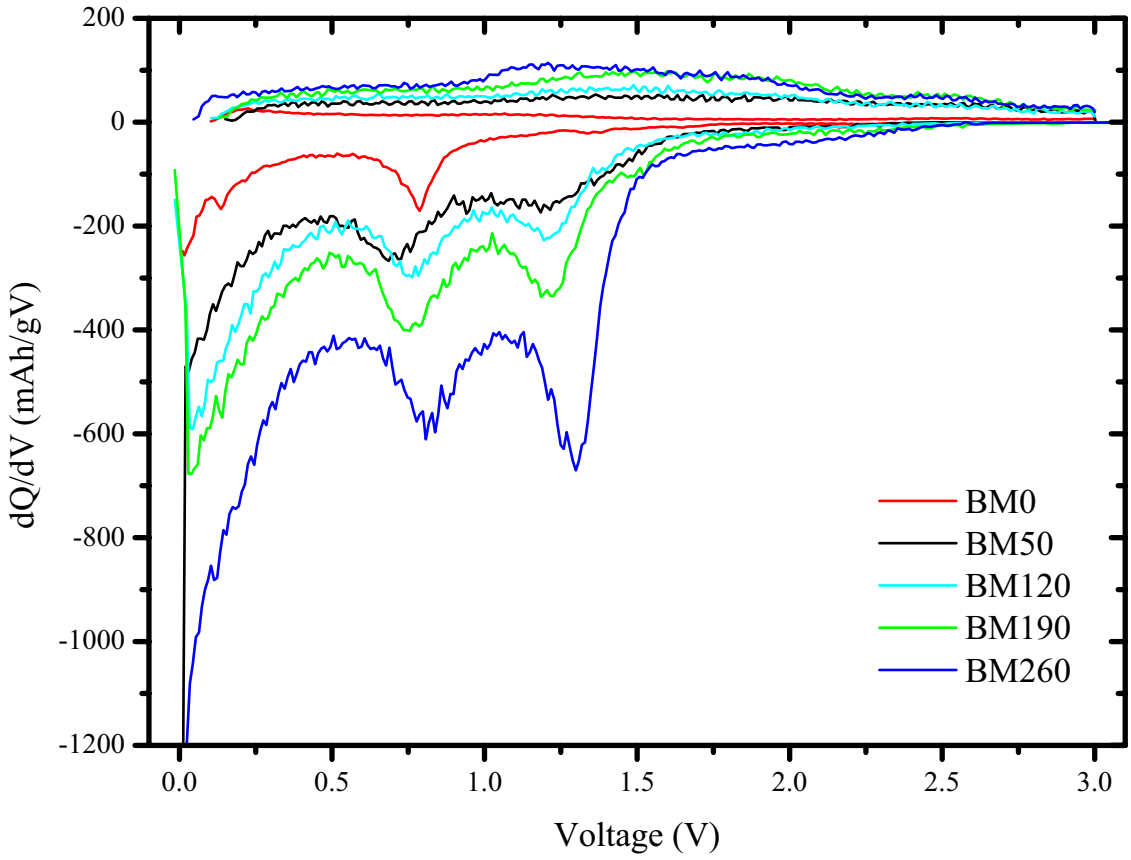

Figure 5-19: Differential capacity plots for the first charge and discharge of $Al_{13}Fe_4$ materials.

5.2.2 Discussion

The intimate mixture of aluminium and iron powders in the compressed pellet has led to the production of an intermetallic with a composition very close to that of the original composition. The first discharge capacity of the BM260 material of 827 mAh/g is much greater than that of the $FeAl_3$ composition for the formation of AlLi. The

$Al_{13}Fe_4$ material has again demonstrated the activity of aluminium based intermetallic materials towards lithium unlike the inactivity observed by Dahn et. al. of a number of aluminium based intermetallic materials [107].

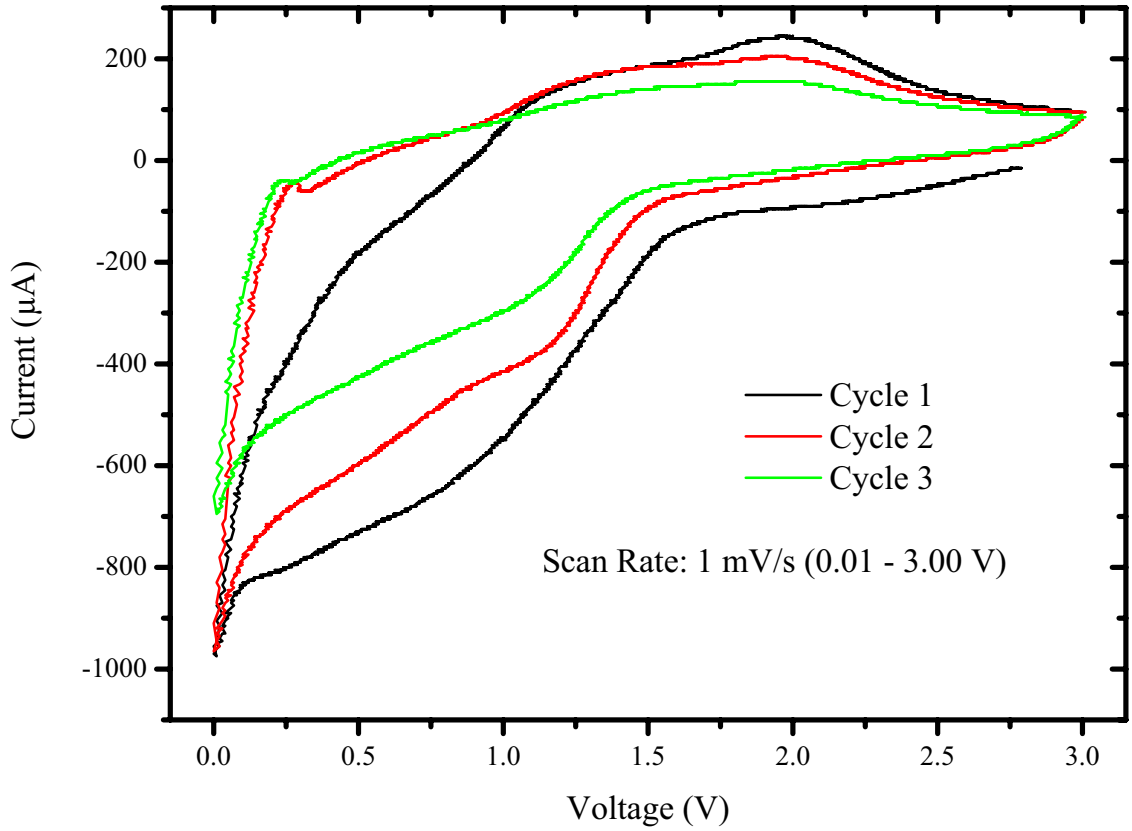

Figure 5-20: Cyclic voltammetry of $Al_{13}Fe_4$ ball milled 260 hours electrode.

Differential capacity plots indicate at least two reactions occurring during discharge with no prominent reactions occurring during charge. The location of these two discharge peaks remains constant for all the samples noting that the 1.25 V peak is not evident in the unmilled material. This suggests that the reaction mechanism itself has not changed dramatically as a result of the ball milling process but the capacity of the reaction has increased. Cyclic voltammetry on the other hand does not indicate any distinct peaks, though the shape of the voltammogram does not preclude the reactions observed in differential capacity plots.

Both charge and discharge capacities increased with increasing milling time though in both cases the capacity declined rapidly with increasing number of cycles. Further modification of the microstructure may be able to improve the retention of capacity further. Even with the poor cycle life of this aluminium based intermetallic material the activity towards lithium of a binary aluminium based intermetallic has been demonstrated. There is however uncertainty over the reaction mechanism responsible

for the observed capacity with no distinct peaks observed in either cyclic voltammetry or differential capacity plots at 0.2 V during discharge which has been attributed to the formation of LiAl [109].

5.2.3 Conclusions

The activity of another aluminium based intermetallic material has been observed in contrast to the inactivity of a number of materials examined by Dahn *et. al*. Even though ball milling resulted in improved charge and discharge capacities this was not to a sufficient degree to be considered as an alternative to current commercial anode materials. Removing inserted lithium from the structure is required to achieve better electrochemical performance from $Al_{13}Fe_4$ materials. This may be possible to achieve by further modification of the microstructure and the use of additional milling and/or annealing operations are likely methods to accomplish this.

The electrochemical results did not however confirm the reaction mechanism responsible for the observed capacity. Although differential capacity and cyclic voltammetry results do not preclude the formation of AlLi during discharge the reverse reaction of Al and Li formation during charge is doubtful.

5.3 Conclusions

The activity of Fe_2Al_5 and $Al_{13}Fe_4$ towards lithium has been demonstrated in contrast to the earlier investigation of a number of aluminium based intermetallic materials by Dahn et. al. [107] which were reported as inactive. Although the first discharge capacity of Fe_2Al_5 BM10,000 (482 mAh/g) was consistent with the capacity expected for LiAl formation that of $Al_{13}Fe_4$ BM260 (827 mAh/g) was nearly 300 mAh/g greater and thus inconsistent with that as the sole reaction mechanism. In both cases however conclusive proof is not offered in either differential capacity plots or cyclic voltammetry for the formation of LiAl.

For either of these materials to be considered as viable replacements for existing commercial materials the difficulty in extracting lithium from the structure needs to be overcome. Modification of the microstructure through further ball milling and/or annealing operations may provide the means to accomplish this.

Chapter 6 Aluminium Based Ternary Intermetallics

Having demonstrated that aluminium based binary intermetallics show some activity towards lithium the investigation was continued with the introduction of a third component to form a ternary intermetallic. In this case ternary intermetallics featuring two active materials (aluminium and silicon) and one inactive material in iron were the subject of the investigation. A number of Al – Fe – Si ternary phases have been claimed by a number of researchers and have been reviewed by Raynor *et. al.* [233]. Raynor *et. al.* also commented that the characterisation of these phases is hindered for a number of reasons including [233];

- Existence of several phases over a small compositional range (Particularly in the Al corner)
- Order-disorder reactions in the Fe corner
- Numerous invariant reactions
- Complex crystal structures

Based on the Raynor *et. al.* review two phases identified as τ_4 and τ_5 were chosen for investigation and the compositions utilised were $Al_{47}Fe_{15}Si_{38}$ (τ_4) and $Al_{20}Fe_5Si_2$ (τ_5). A third ternary composition of Al_9FeSi_3 was identified from the JCPDS X-ray database (JCPDS card 20-33). The cell parameters given in the JCPDS card for this phase compare favourably to that of the τ_4 phase.

6.1 $Al_{47}Fe_{15}Si_{38}$

Aluminium, iron and silicon powder were weighed out in the proportions corresponding to stoichiometric $Al_{47}Fe_{15}Si_{38}$. The metal powders were mixed together and placed in a 25 mm diameter die ready for compaction using an Enerpac 10 tonne hydraulic press. The hydraulic pressure on the press was set at 6,000 psi and the samples were subjected to the pressure delivered by the ram at this level for six seconds. The resulting pellet was then melted into an alloy slug using an arc melter. The alloy slug was then crushed a number of times until the resultant fines passed through a 150 μm sieve.

The material that passed through the 150 μm sieve was then milled in a Pulverisette-5 planetary ball mill at a speed of 160 rpm in a steel-milling vessel. The milling vessel had an internal diameter of 80 mm and volume of approximately 200

cm^3. The milling media were 5 mm diameter stainless steel balls utilised with a ball to powder ratio of approximately 20:1 (160g balls: 8.032 g powder). Ethanol was added as a process control additive to the level of the top of the balls. Powder was removed at a number of intervals in small quantities up to a total milling time of 285 hours. Powder was removed at total milling times of 50, 120, 190 and the final milling time of 285 hours. Where milling continued after powder was removed ethanol was added to the milling jar if required to bring it back up to its initial level. The various powders and other results derived from their use will be referred to using a prefix of BM followed by the milling time of the powder in hours. Whilst the unmilled material that passed through the 150 μm sieve is referred to as BM0.

The fabrication of electrodes resulted in loadings of approximately 2 mg for BM0 and 1 mg for the remaining samples. The final composition of the electrodes corresponded to 85 wt. % powder, 10 wt. % conductivity additive and 5 wt. % PVDF.

The theoretical discharge capacity of $Al_{47}Fe_{15}Si_{38}$ given full reaction of aluminium and silicon with lithium to form LiAl and $Li_{22}Si_5$ respectively equates to 1810 mAh/g whilst if complete formation of Al_4Li_9 occurs it equates to 2306 mAh/g.

6.1.1 Results

6.1.1.1 Structural and Microstructural Characterisation

The XRD pattern of the unmilled material (BM0 in Figure 6-1) corresponded to the orthorhombic structure of Al_3FeSi_2 (JCPDS card 83-614) rather than the tetragonal structure of the τ_4 phase. The material was not however pure with SiO_2 (JCPDS card 76-933) matched in the pattern along with a number of other weak unmatched peaks. The diffraction patterns of the materials following ball milling do not exhibit any well defined peaks and are described as X-ray amorphous.

In order to examine the effect of milling on the particle size of the Al_3FeSi_2 powders SEM was used to examine the particle size (Figure 6-2). The particle size decreased from a maximum of 120 μm for BM0 to 1 μm and under for all the ball milled materials. BET was utilised to examine the specific surface area of the BM285 material, which was determined as 206 m^2/g.

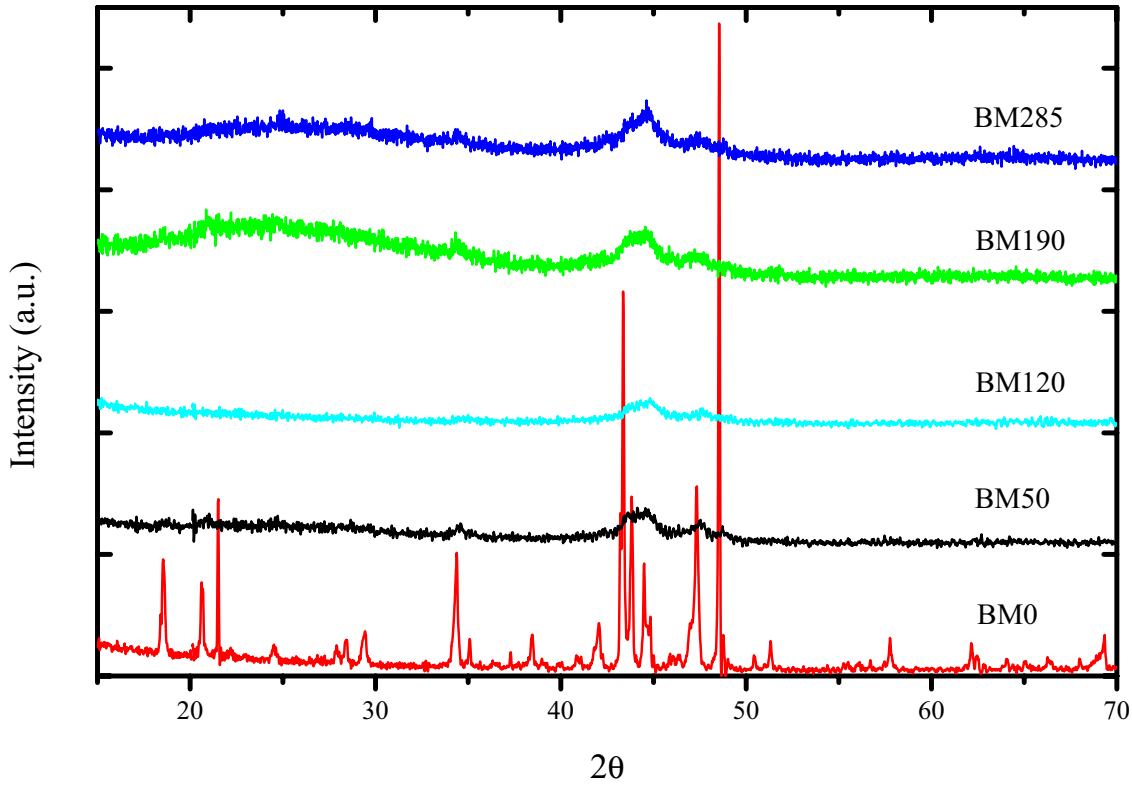

Figure 6-1: XRD patterns of ball milled Al_3FeSi_2 materials.

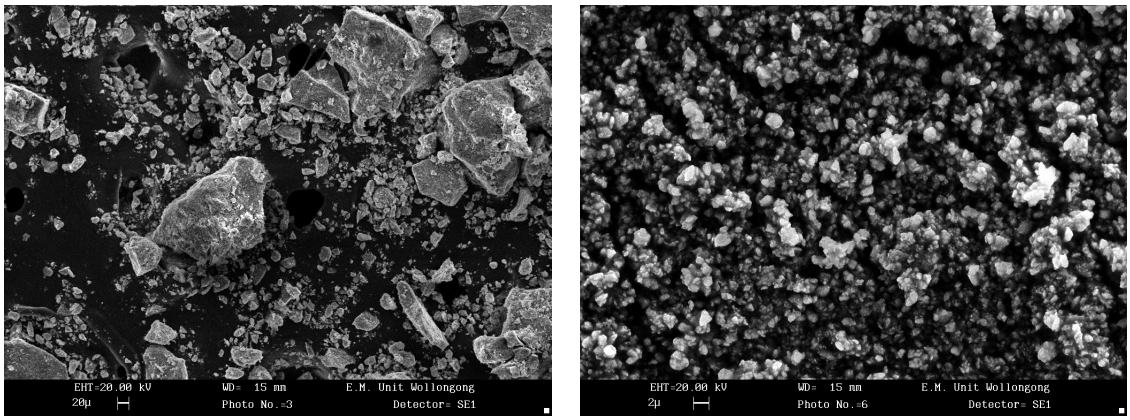

(a) (b)

Figure 6-2: Selected SEM micrographs of ball milled Al_3FeSi_2 materials: (a) 150 µm, (b) 50 hours.

6.1.1.2 Electrochemical Characterisation

The electrochemical properties of Al_3FeSi_2 were evaluated with the use of the prepared alloy electrodes as working electrodes and metallic lithium foils as the counter electrode. The constant current charge/discharging (50 µA, 0.01 – 3.00 V) of Al_3FeSi_2 electrodes demonstrated varying electrochemical properties with milling time. The first discharge capacity (Figure 6-3) increases with milling time up to a capacity of 494 mAh/g (BM120) before declining to 276 mAh/g (BM285). The first charge capacities

(Figure 6-4) on the other hand varied between 25 and 34 mAh/g for milling times up to 190 hours and increased to 71 mAh/g for BM285. The first charge and discharge profiles also showed differences between the various milled materials.

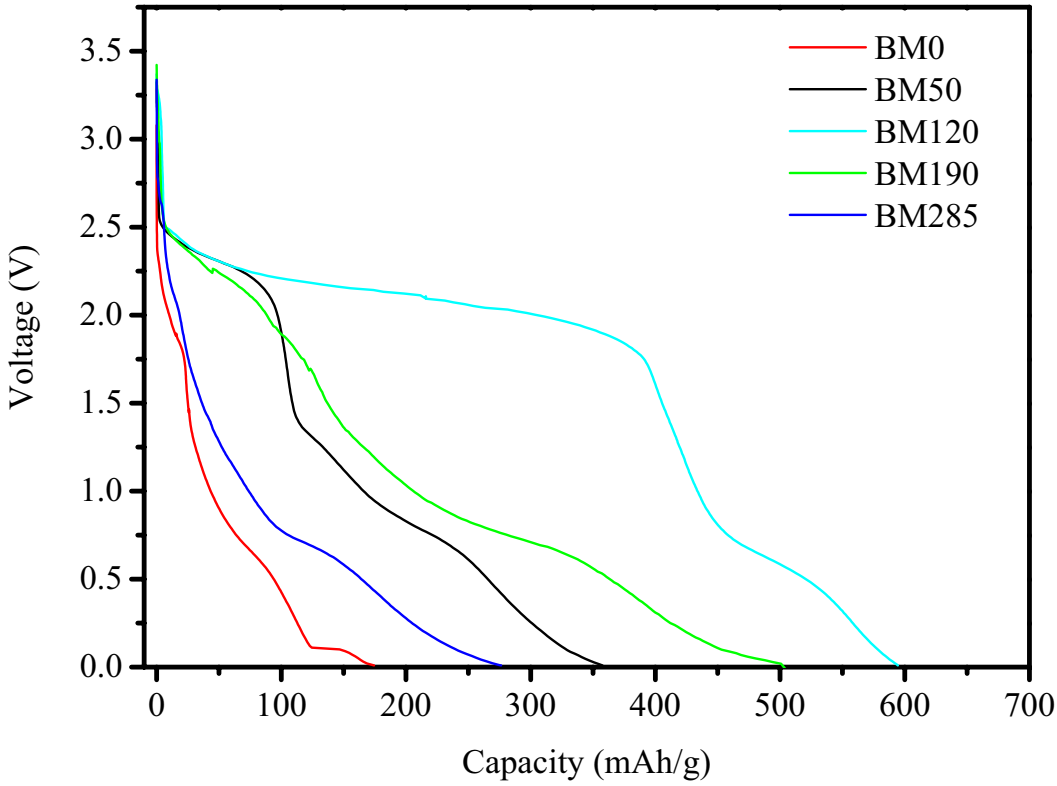

Figure 6-3: First discharge of various ball milled Al_3FeSi_2 materials.

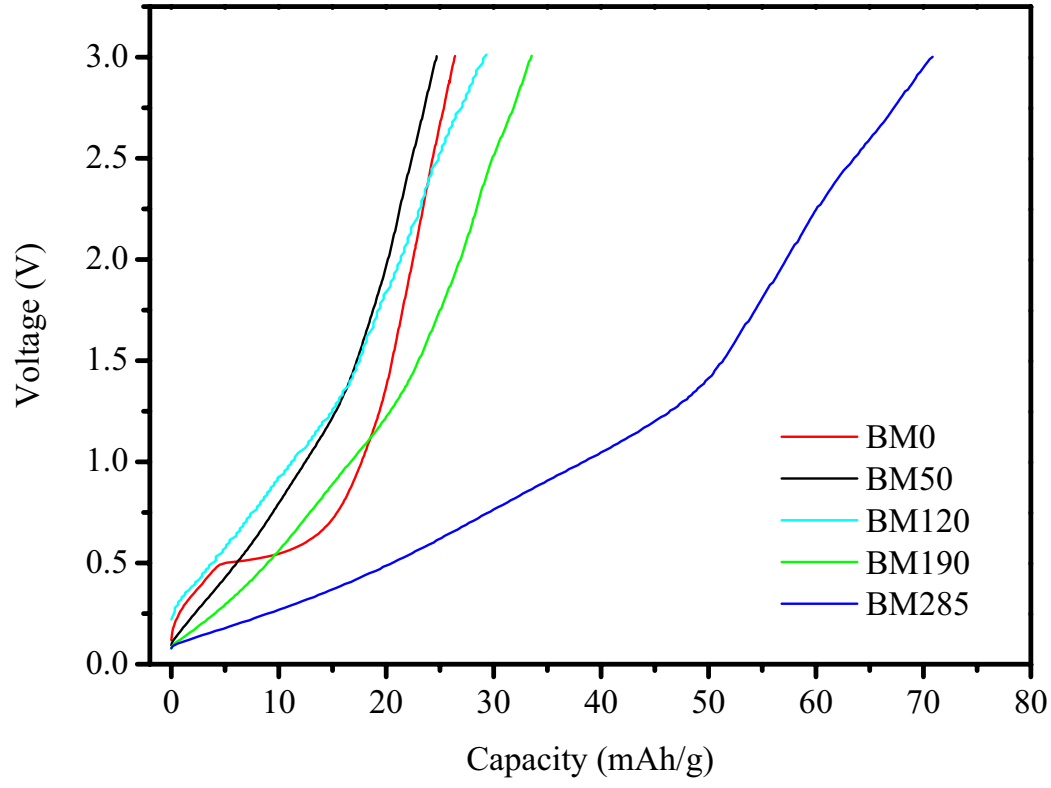

Figure 6-4: First charge of various ball milled Al_3FeSi_2 materials.

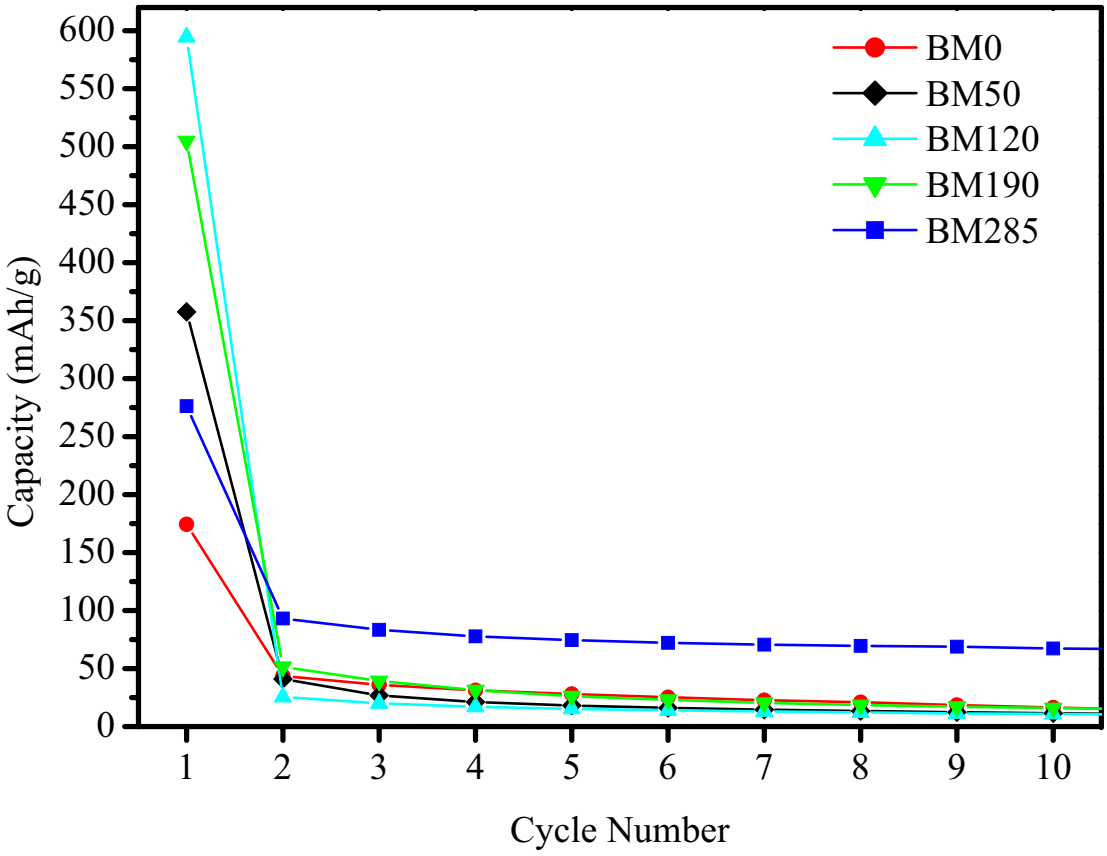

Figure 6-5: Variation of discharge capacity of Al_3FeSi_2 with milling time.

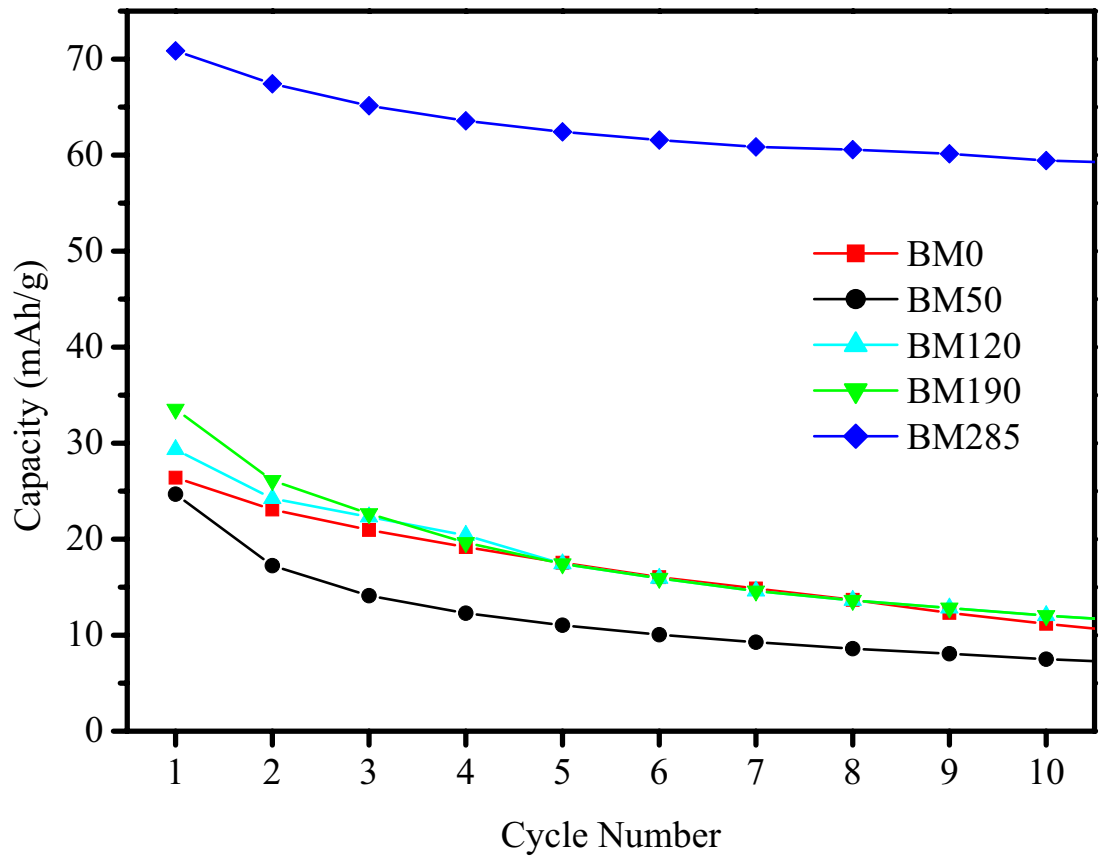

Figure 6-6: Variation of charge capacity of Al_3FeSi_2 with milling time.

Extraction of lithium from the Al_3FeSi_2 structure is difficult as demonstrated by the low charge capacities in comparison to the discharge capacities. The cycling performance of all the materials was particularly poor. The discharge capacities for the materials milled up to and including 190 hours fell to under 51 mAh/g on the second discharge and to under 16 mAh/g within 10 cycles (Figure 6-5). The performance of the BM285 material was better with a second discharge capacity of 93 mAh/g and a capacity over 50 mAh/g maintained over 50 cycles. The behaviour of charge capacity on cycling (Figure 6-6) was similar to that of the discharge with the materials up to and including the 190 hours sample demonstrating similar capacities from the first cycle and only that of the BM285 material much larger (approximately two times).

Differential capacity plots of the first charge and discharge of BM285 (Figure 6-7) shows a large peak at 0.72 V during discharge whilst that of the charge is featureless. Impedance spectroscopy was also carried out on BM285 following the first discharge to 0.01 V (Figure 6-8) and exhibited a depressed semicircle at low frequency and a high frequency tail.

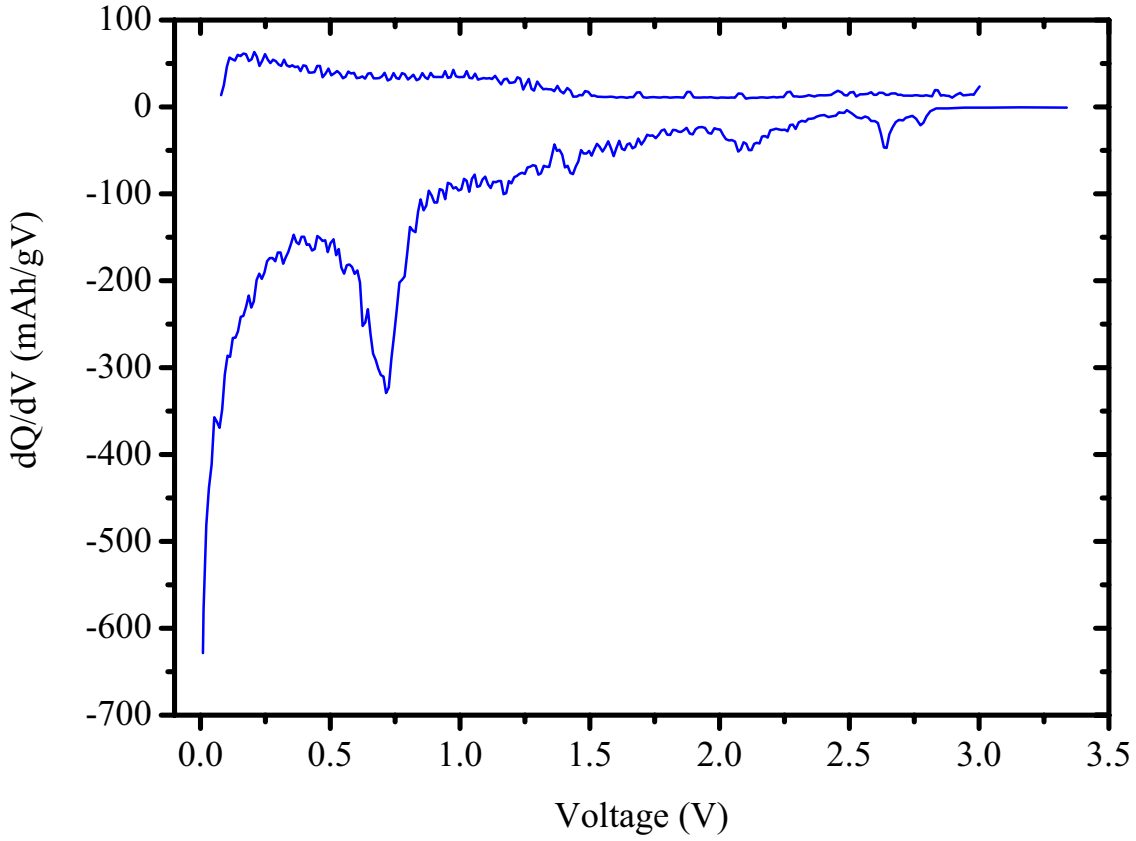

Figure 6-7: Differential capacity plot for the first charge and discharge of BM285 Al_3FeSi_2.

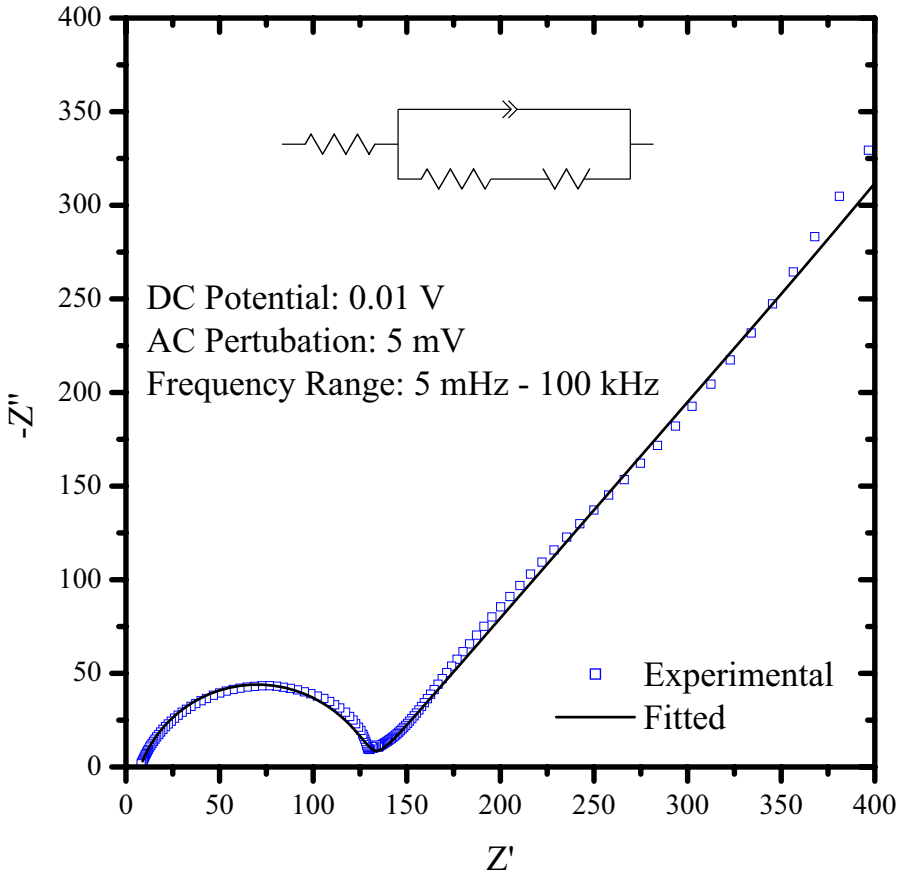

Figure 6-8: Nyquist plot of ac impedance spectroscopy of Al_3FeSi_2 after the first discharge.

6.1.2 Discussion

The intimate mixture of aluminium, iron and silicon powders in the compressed pellet has led to the production of an intermetallic with a composition very close to that of the original composition. The variation of the first charge and discharge capacity with milling time suggests that the microstructure has a significant influence on the electrochemical properties. Even the highest discharge capacity of 594 mAh/g (BM120) is well below the theoretical capacity for full reaction with lithium to form LiAl and $Li_{22}Si_5$ (1810 mAh/g). This suggests that even on the first discharge a large portion of the alloy has not been lithiated to reach these compositions. Thus the lithiation of aluminium and/or silicon is at least being retarded in these materials. Microstructural modification may however be able to improve the discharge capacities in line with the theoretical capacities and improve the cycle life of the material. The highest discharge capacity is however greater than the theoretical capacity for complete reaction to form LiAl alone (397 mAh/g) though lower than for complete formation of $Li_{22}Si_5$ alone (1412 mAh/g). Even though the cycle life is poor the activity of a ternary aluminium based intermetallic has been demonstrated.

Differential capacity plot of BM285 indicates only one reaction occurring during discharge (0.72 V) and none of note occurring during charge. Uncertainty over the reaction mechanism responsible for the observed discharge capacities still remains. A simple electric circuit composed of two resistors, a constant phase element and a Warburg element was found to model the observed impedance spectra of the BM285 material as presented in Figure 6-8.

6.1.3 Conclusions

The activity of a ternary aluminium based intermetallic material has been observed with the electrochemical properties varying with milling time. The discharge capacities were however well under the theoretical capacity of the material suggesting the lithiation reaction is being retarded in these materials. It is not just the lithiation reaction being impeded however as the low charge capacities also demonstrate that extraction of lithium from the structure is also difficult. Further modification of the microstructure may be able to improve both and as a result improve both the capacity and cycle life of the material. The electrochemical results did not confirm the reaction mechanism responsible for the observed capacity.

6.2 $Al_{20}Fe_5Si_2$

Aluminium, iron and silicon powder were weighed out in the proportions corresponding to stoichiometric $Al_{20}Fe_5Si_2$. The metal powders were mixed together and placed in a 25 mm diameter die ready for compaction using an Enerpac 10 tonne hydraulic press. The hydraulic pressure on the press was set at 6,000 psi and the samples were subjected to the pressure delivered by the ram at this level for six seconds. The resulting pellet was then melted into an alloy slug using an arc melter. The alloy slug was then crushed a number of times until the resultant fines passed through a 150 μm sieve.

The material that passed through the 150 μm sieve was then milled in a Pulverisette-5 planetary ball mill at a speed of 160 rpm in a steel-milling vessel. The milling vessel had an internal diameter of 80 mm and volume of approximately 200 cm^3. The milling media were 5 mm diameter stainless steel balls utilised with a ball to powder ratio of approximately 20:1 (100.27g balls: 5.030 g powder). Ethanol was added as a process control additive to the level of the top of the balls. Powder was removed at a number of intervals in small quantities up to a total milling time of 285 hours. Powder

was removed at total milling times of 45, 119, 215 and the final milling time of 285 hours. Where milling continued after powder was removed ethanol was added to the milling jar if required to bring it back up to its initial level. The various powders and other results derived from their use will be referred to using a prefix of BM followed by the milling time of the powder in hours. Whilst the unmilled material that passed through the 150 μm sieve is referred to as BM0.

The fabrication of electrodes resulted in loadings of approximately 2 mg for BM0 and 1 mg for the remaining samples. The final composition of the electrodes corresponded to 85 wt. % powder, 10 wt. % conductivity additive and 5 wt. % PVDF.

The theoretical discharge capacity of $Al_{20}Fe_5Si_2$ given full reaction of aluminium and silicon with lithium to form LiAl and $Li_{22}Si_5$ respectively equates to 882 mAh/g whilst if complete formation of Al_4Li_9 occurs it equates to 1648 mAh/g.

6.2.1 Results

6.2.1.1 Structural and Microstructural Characterisation

The XRD pattern of the unmilled material (BM0 in Figure 6-9) corresponded to the hexagonal structure of Al_8Fe_2Si (JCPDS card 41-894) with aluminium also present. The structure of this phase (Al_8Fe_2Si) corresponds to the τ_5 phase ($Al_{20}Fe_5Si_2$) identified in the summary of Raynor *et. al.* [233]. The diffraction patterns of the materials after milling do not however exhibit any well defined peaks and are described as X-ray amorphous.

In order to examine the effect of milling on the particle size of the Al_8Fe_2Si powders SEM was used to examine the particle size (Figure 6-10). The particle size decreased from a maximum of 100 μm for BM0 to 1 μm and under for all the ball milled materials. Through BET analysis the specific surface area of the BM285 material was determined as 145 m^2/g.

6.2.1.2 Electrochemical Characterisation

The electrochemical properties of Al_8Fe_2Si were evaluated with the use of the prepared alloy electrodes as working electrodes and metallic lithium foils as the counter electrode. The electrochemical properties from constant current charge/discharging (50 μA, 0.01 – 3.00 V) of Al_8Fe_2Si electrodes varied with milling time. The first discharge capacity (Figure 6-11) increased continuously with milling time up to a capacity of 320

mAh/g though the profiles did vary somewhat. The first charge capacities (Figure 6-12) on the other hand increased to a maximum of 103 mAh/g for BM45 before decreasing to 46 mAh/g for BM285. In this case only the charge profile of the unmilled material was different to those of the other materials. After the first cycle however the discharge (Figure 6-13) and charge (Figure 6-14) capacities were highest for BM45 and lowest for the BM285. The capacities of the other milled materials were found between the two and decreased inline with the increase in milling time.

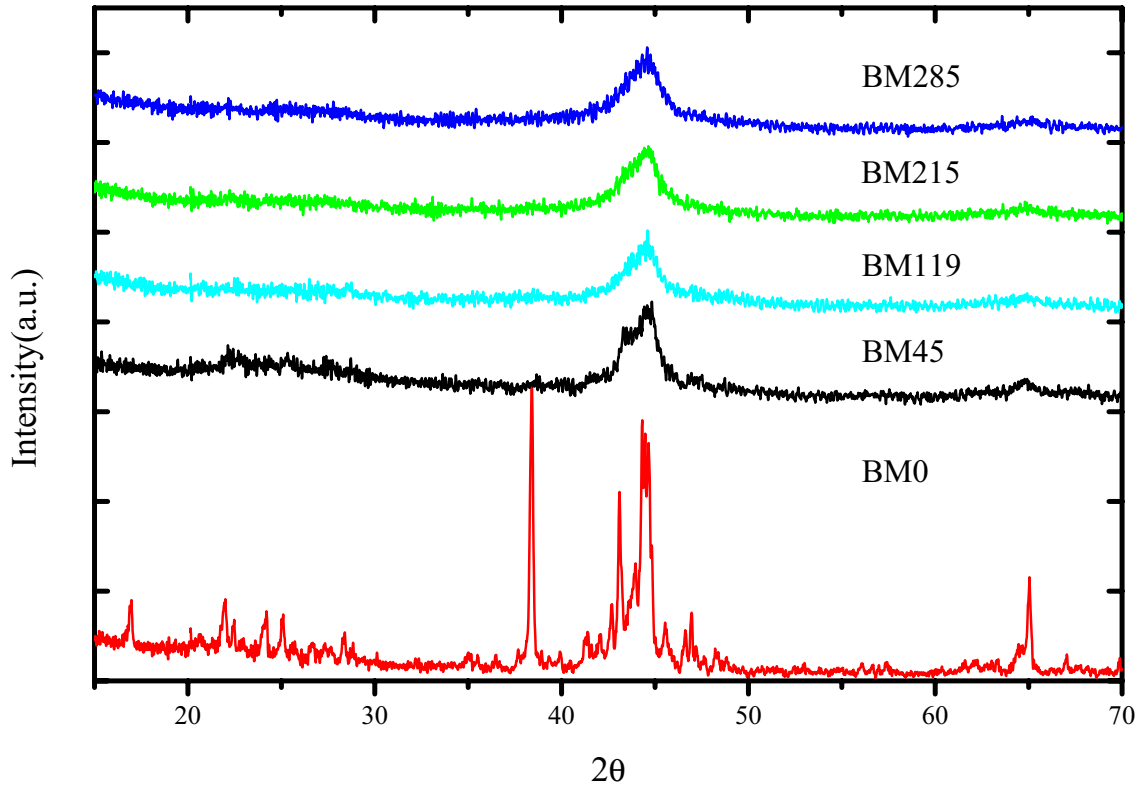

Figure 6-9: XRD patterns of ball milled Al_8Fe_2Si materials.

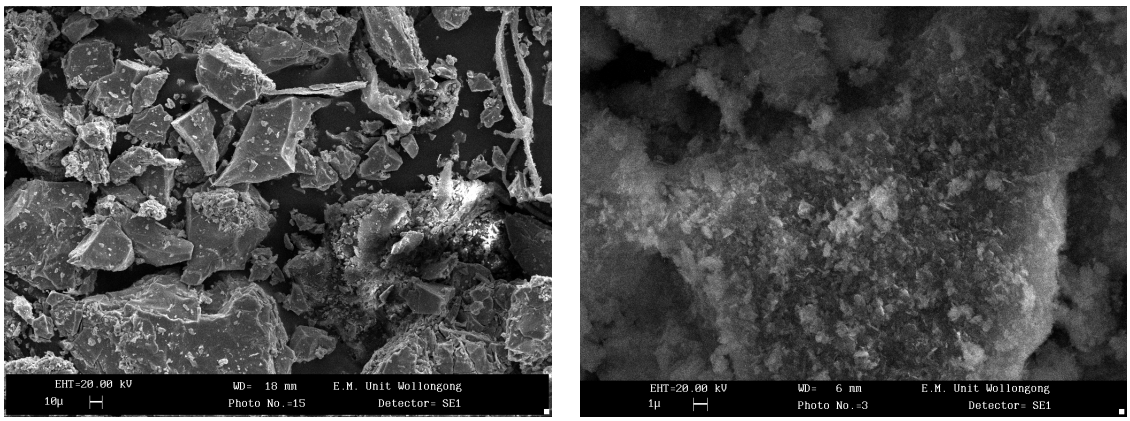

(a) (b)

Figure 6-10: Selected SEM micrographs of ball milled Al_8Fe_2Si materials: (a) 150 µm, (b) 215 hours.

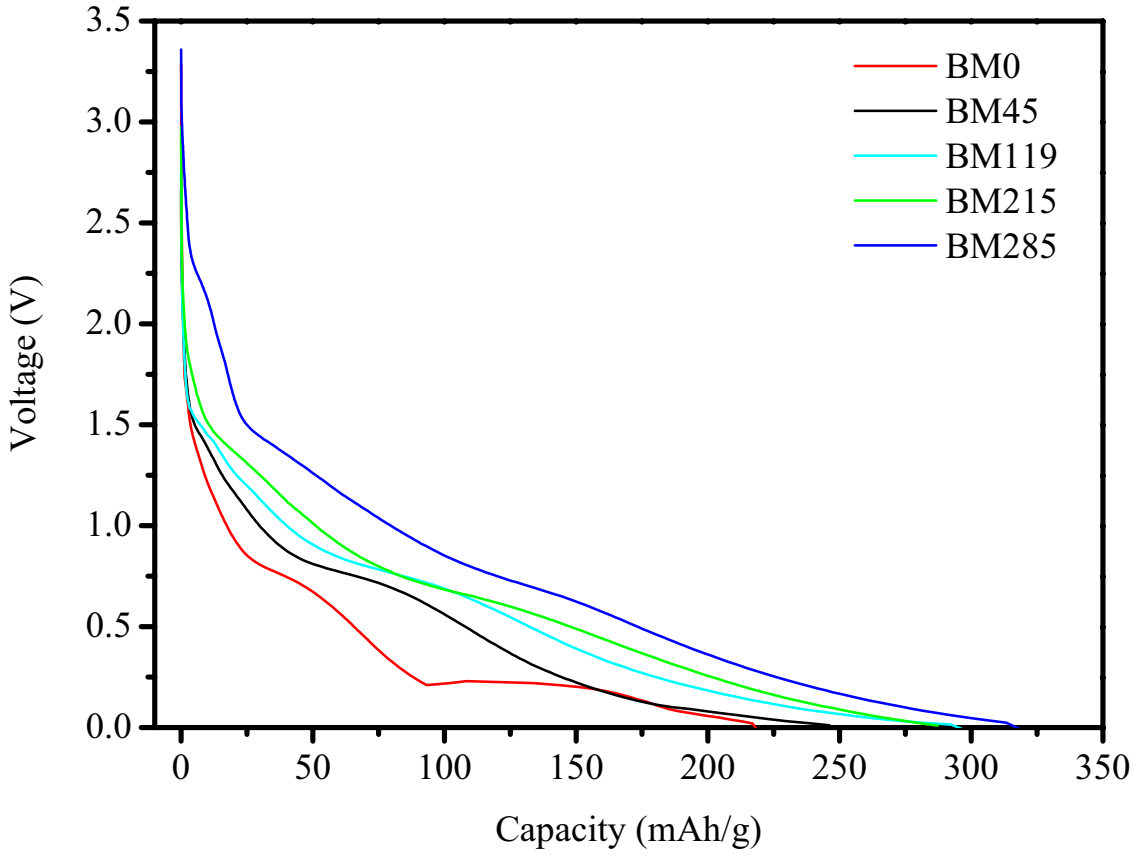

Figure 6-11: First discharge of various ball milled Al_8Fe_2Si materials.

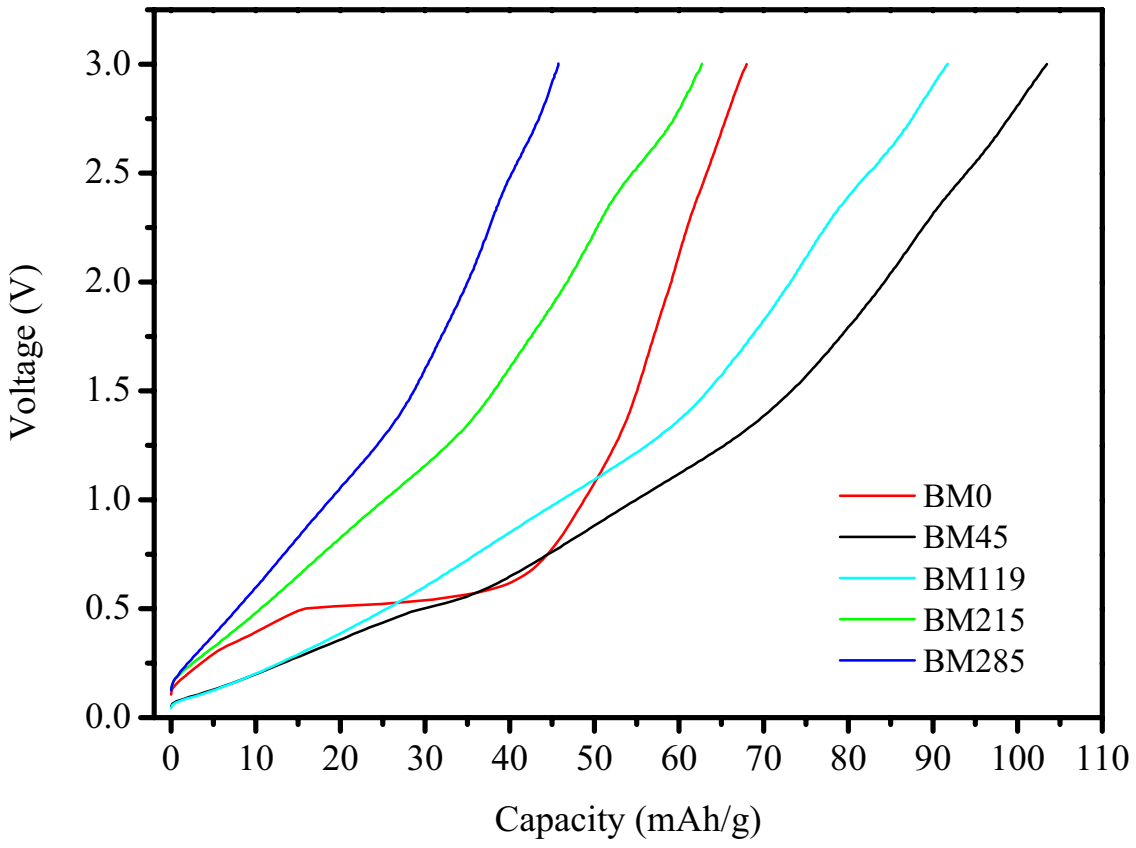

Figure 6-12: First charge of various ball milled Al_8Fe_2Si materials.

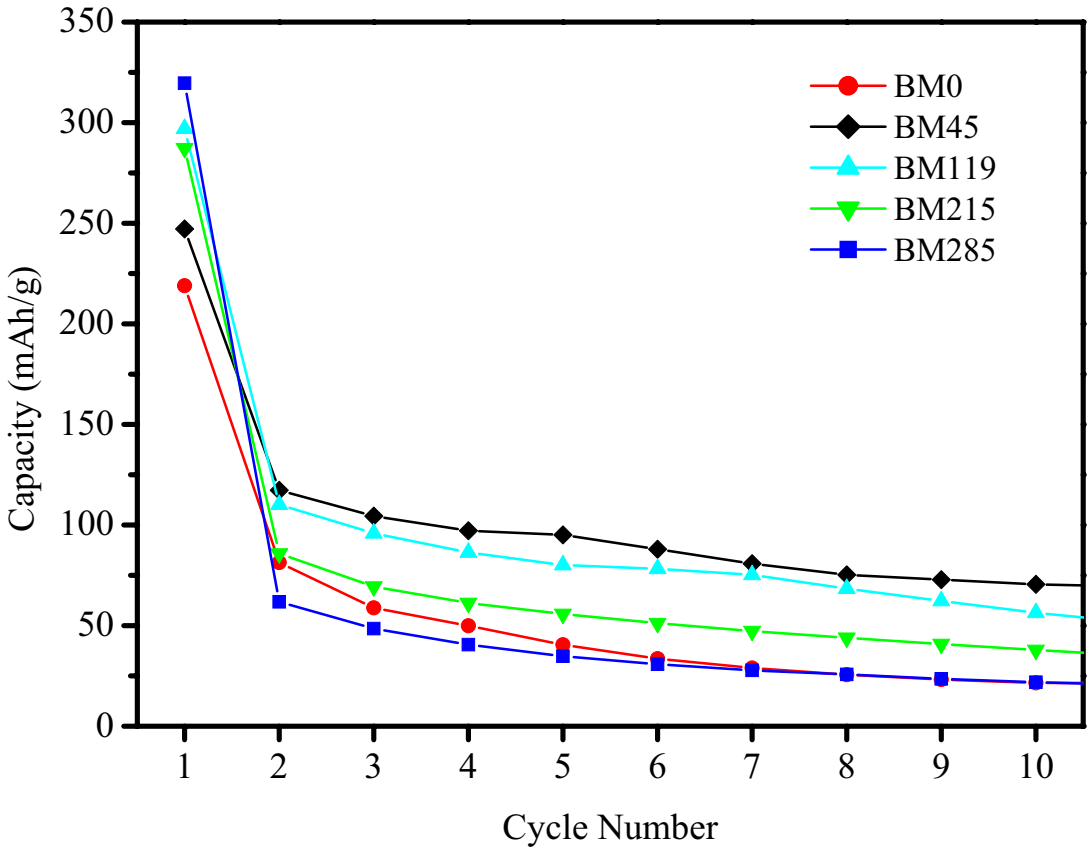

Figure 6-13: Variation of discharge capacity of Al_8Fe_2Si with milling time.

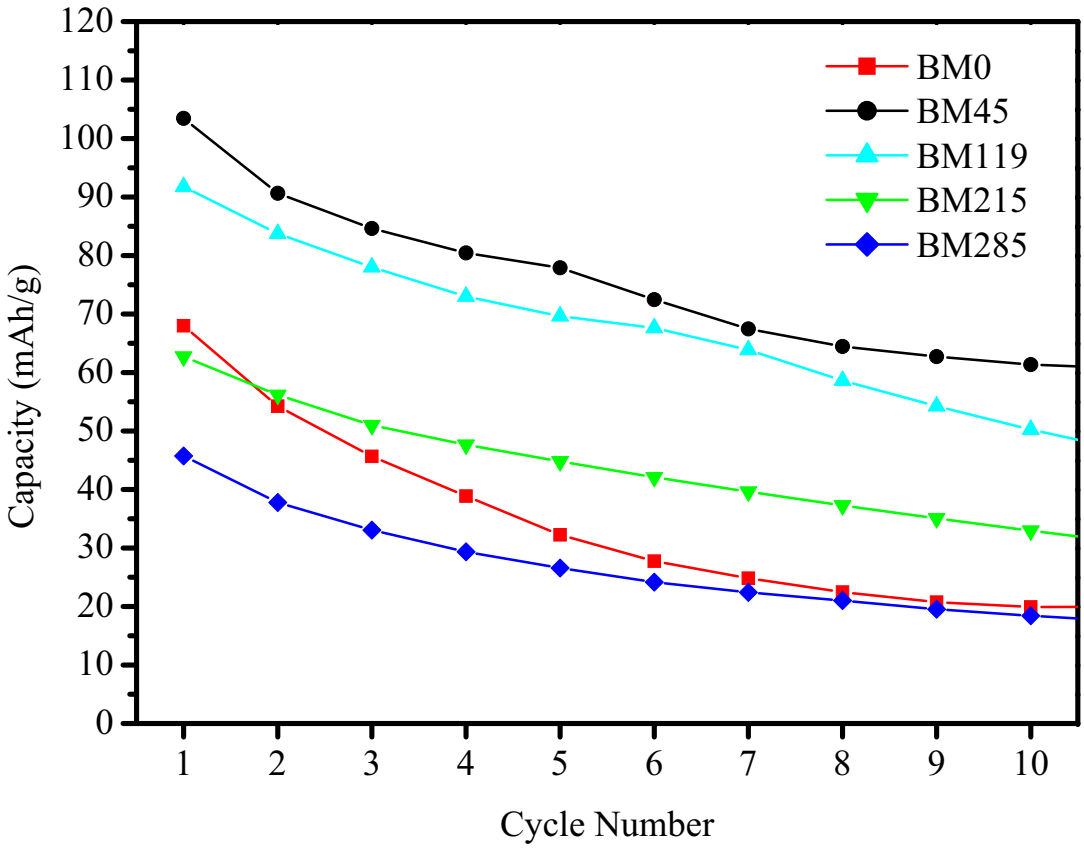

Figure 6-14: Variation of charge capacity of Al_8Fe_2Si with milling time.

The extraction of lithium from the Al_8Fe_2Si structure is difficult as demonstrated by the low charge capacities in comparison to the discharge capacities particularly as the milling time is increased. Within ten cycles the discharge capacities were in the range of 22 – 71 mAh/g and the charge capacities in a lower range of 18 – 61 mAh/g.

Differential capacity plots of the first charge and discharge of BM45 and BM285 (Figure 6-15) are very similar with the notable exception that peaks are visible in the charge of the BM45 material. Whilst differential capacity plots of BM0 also show a second peak on discharge and the same peak during the charge. Impedance spectroscopy was also carried out on BM285 following the first discharge to 0.01 V (Figure 6-16) and exhibited a depressed semicircle at low frequency and a high frequency tail.

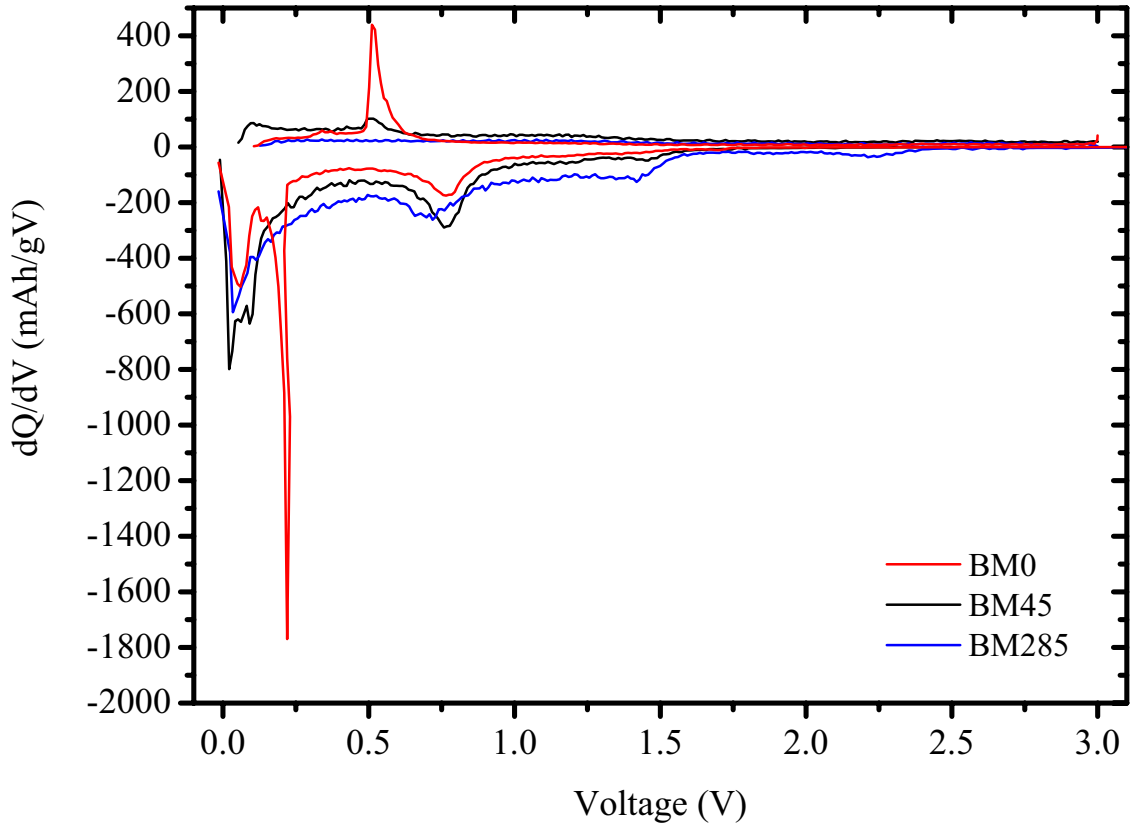

Figure 6-15: Differential capacity plot for the first cycle of BM0, BM45 and BM285 Al_8Fe_2Si.

6.2.2 Discussion

The intimate mixture of aluminium, iron and silicon powders in the compressed pellet has led to the production of an intermetallic with a structure the same as the target phase ($Al_{20}Fe_5Si_2$) though the composition is a little different (Al_8Fe_2Si). Variation of the first charge and discharge capacity with milling time suggests that the microstructure has a significant influence on the electrochemical properties. Even the

highest discharge capacity of 320 mAh/g (BM285) is well below the theoretical capacity for full reaction with lithium to form LiAl and $Li_{22}Si_5$ (882 mAh/g). This suggests that even on the first discharge a significant amount of active material is not alloying with lithium to reach completely lithiated compositions. Thus the lithiation is at least being retarded in these materials. Microstructural modification may however be able to improve the discharge capacities in line with the theoretical capacities and improve the cycle life of the material. The highest discharge capacity of 320 mAh/g is however between the theoretical capacities for complete lithiation of silicon to from $Li_{22}Si$ (270 mAh/g) and that for aluminium to form LiAl (613 mAh/g).

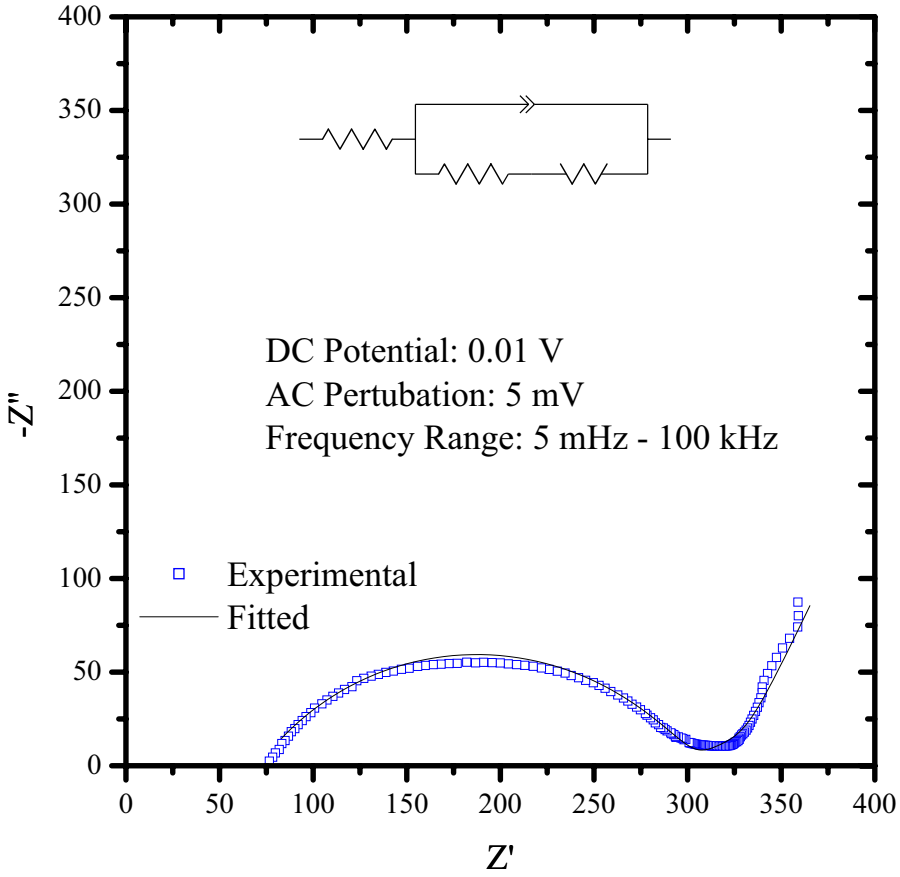

Figure 6-16: Nyquist plot of ac impedance spectroscopy of Al_8Fe_2Si after the first discharge.

Differential capacity plots of BM0, BM45 and BM285 indicate a distinct peak around 0.75 V during discharge and in the case of BM0 and BM45 a distinct peak at 0.51 V during the first charge. A second peak is also evident in the discharge of BM0 at 0.22 V. This peak may correspond to the lithiation reaction $(Li + Al \rightarrow LiAl)$ and that observed during charge in BM0 and BM45 to the delithiation reaction $(LiAl \rightarrow Li + Al)$ which have been observed in cyclic voltammetry of aluminium thin films at 0.2 V and 0.45 V respectively [109]. If this is the case the peaks may not be observed in materials

milled for longer times as a result of the reduction in intensity and increase in peak breadth as a result of the reduction in crystallite size. This is already evident in the BM45 material with no peak evident at 0.22 V on discharge and the intensity of the 0.51 V reduced considerably.

A simple electric circuit composed of two resistors, a constant phase element and a Warburg element was found to model the observed impedance spectra of the BM285 material as presented in Figure 6-16.

6.2.3 Conclusions

The activity of a ternary aluminium based intermetallic material has been observed with the electrochemical properties varying with milling time. The discharge capacities were however well under the theoretical capacity of the material suggesting the lithiation reaction is being retarded in these materials. The delithiation reaction is also influenced with the charge capacities also low. Further modification of the microstructure may be able to improve both and as a result improve both the capacity and cycle life of the material. Differential capacity plots for the BM0 and BM45 material do however suggest that lithiation and delithiation of aluminium is occurring.

6.3 Al_9FeSi_3

High purity iron (chip 99.98 % Aldrich) and aluminium (shot 99.9 % Aldrich) and silicon powder were weighed out in the proportions corresponding to stoichiometric Al_9FeSi_3. The silicon powder was placed beneath the other components to avoid vaporisation. The metals were combined to form an alloy slug with the use of an arc melter. Crushing of the alloy to a fine particle size proved to be difficult and as a result it was reduced to a particle size of approximately 1 mm only prior to milling.

The coarse material was then milled in a Pulverisette-5 planetary ball mill in a steel-milling vessel with an internal diameter of 80 mm and volume of approximately 200 cm^3. The milling media were 5 mm diameter stainless steel balls utilised with a ball to powder ratio of approximately 20:1 (102.75 g balls: 5.098 g powder). Ethanol was added as a process control additive to the level of the top of the balls. Milling was initially carried out at 90 rpm up to a milling time of 135 hours before being increased to 125 rpm to the total milling time of 251 hours. Powder was removed during the initial milling period at total milling times of 70, 135 and 251 hours. Where milling continued after powder was removed ethanol was added to the milling jar if required to bring it

back up to its initial level. Powders and other results derived from their use will be referred to using a prefix of BM followed by the milling time of the powder in hours.

Coarse particles still remained after this time however and the material was then passed through a 150 μm sieve and milling continued. In this case the milling was continued in a milling jar with a volume of 140 cm^3 and a ball to powder ratio of approximately 60:1 (93.2442 g balls: 1.5026 g powder). Powder was then removed at a number of intervals in small quantities up to a further milling time of 260 hours. Powder was removed at milling times of 50, 120, 190 and the final milling time of 260 hours. The various remilled powders and other results derived from their use will be referred to using a prefix of RM followed by the remilling time of the powder in hours.

The fabrication of electrodes resulted in loadings of approximately 1 mg for all the samples. The final composition of the electrodes corresponded to 85 wt. % powder, 10 wt. % conductivity additive and 5 wt. % PVDF.

The theoretical discharge capacity of Al_9FeSi_3 given full reaction of aluminium and silicon with lithium to form LiAl and $Li_{22}Si_5$ respectively equates to 1554 mAh/g whilst if complete formation of Al_4Li_9 occurs it equates to 2341 mAh/g.

6.3.1 Results

6.3.1.1 Structural and Microstructural Characterisation

The XRD pattern of the BM251 material (Figure 6-17) corresponded to the monoclinic structure of Al_5FeSi (JCPDS card 49-1499) with aluminium and silicon also present. The structure of this phase (Al_5FeSi) does not correspond to the tetragonal phase of Al_9FeSi_3 (JCPDS card 20-33) material on which its composition was based. The diffraction patterns of the materials after remilling do not however exhibit any defined peaks and are described as X-ray amorphous.

In order to examine the effect of milling on the particle size of the Al_5FeSi powders SEM was used to examine the particle size (Figure 6-18). The particle size decreased from a maximum of 100 μm for BM70, BM135 and BM251, decreasing to 0.5 μm following 260 hours of remilling (Figure 6-19). Through BET analysis the specific surface area of the RM260 material was determined as 341 m^2/g.

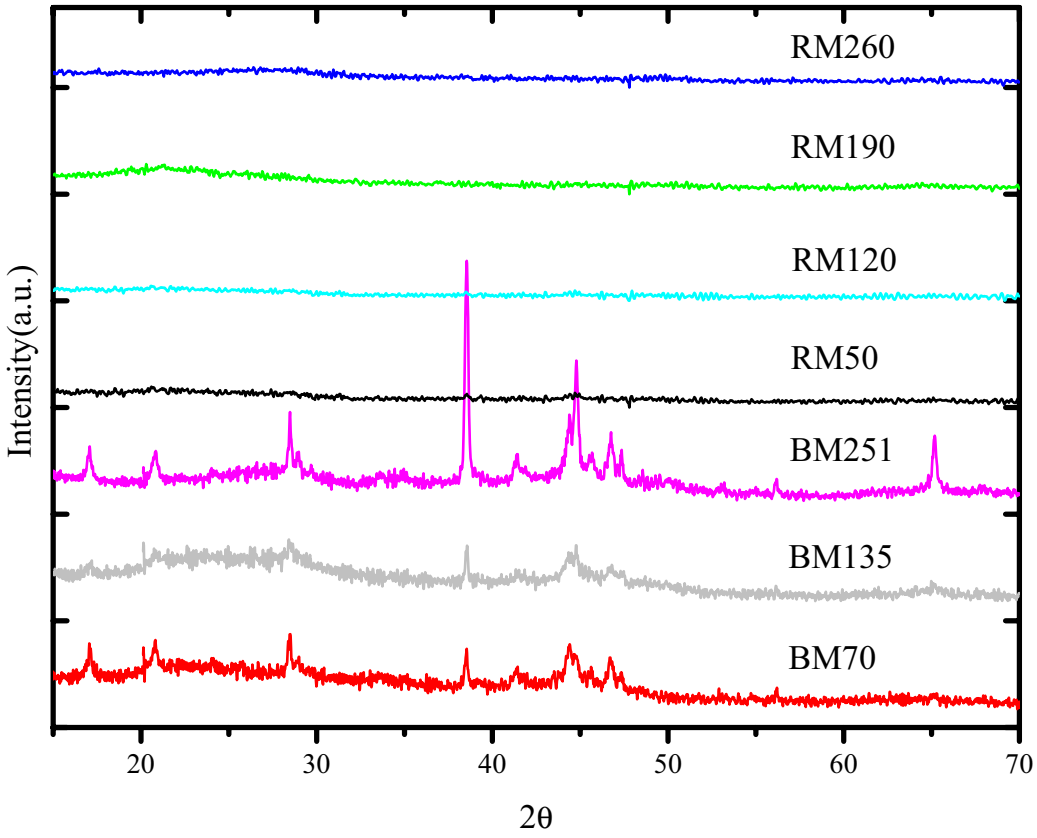

Figure 6-17: XRD patterns of ball milled Al_5FeSi materials.

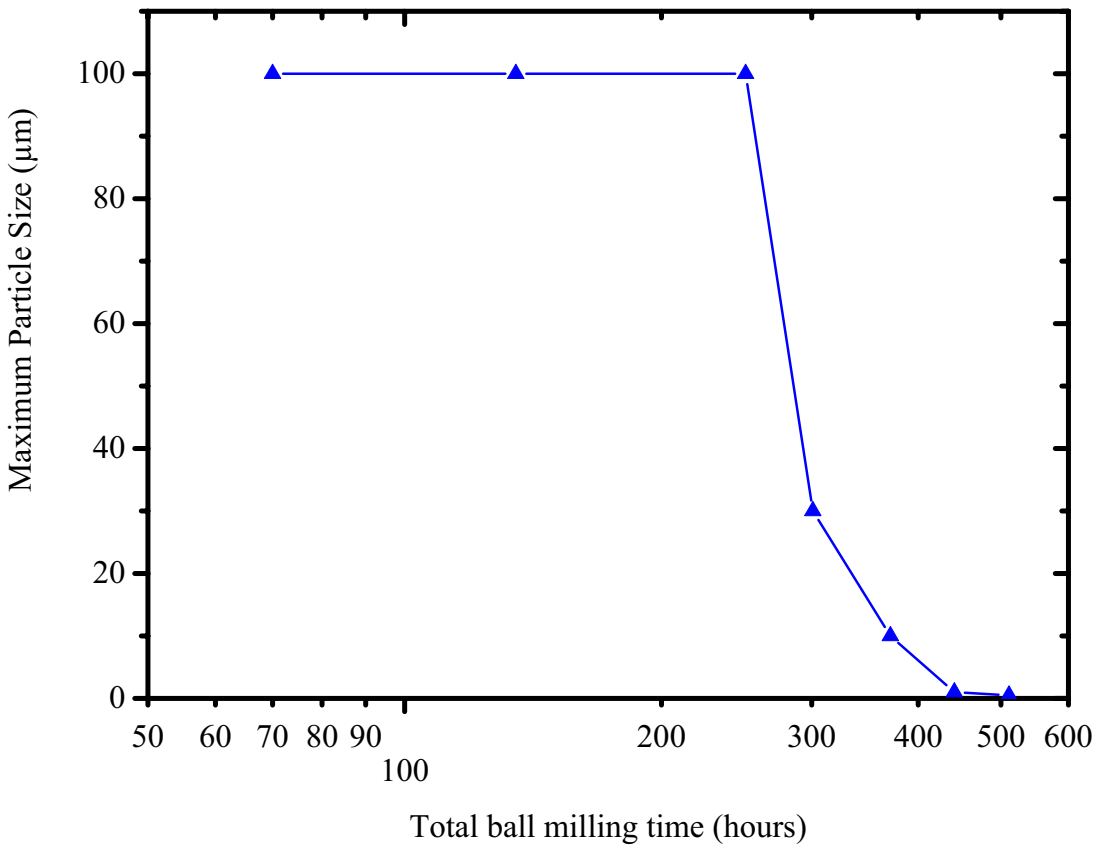

Figure 6-18: Variation of maximum particle size with total ball milling time for Al_5FeSi materials,

(a)

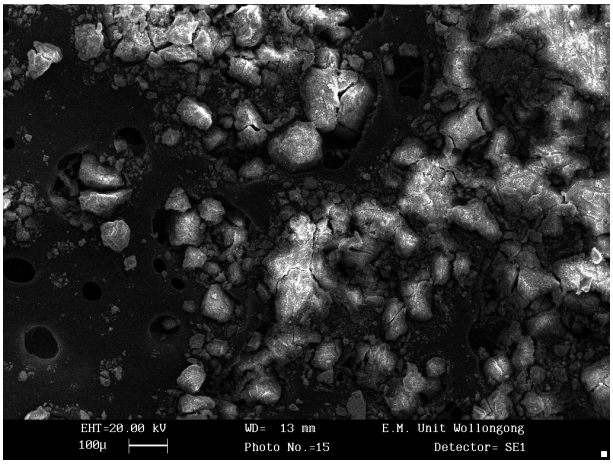

(b)

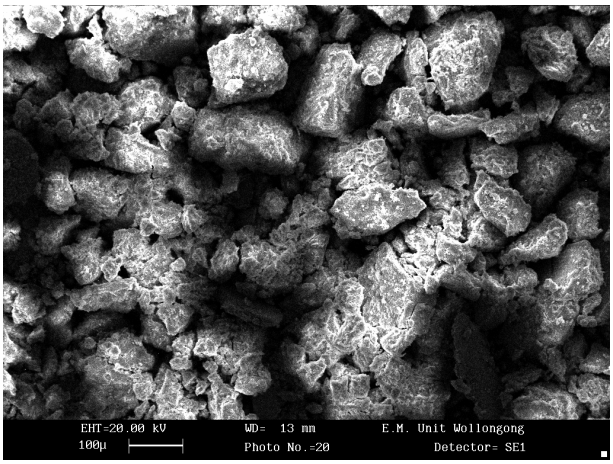

(c)

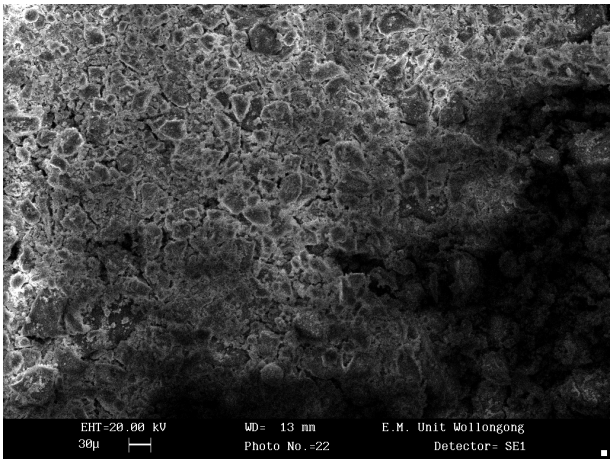

Figure 6-19: SEM micrographs of selected Al_5FeSi ball milled powder samples: (a) 70 hours, (b) 251 hours, (c) remilled 55 hours.

6.3.1.2 Electrochemical Characterisation

The electrochemical properties of Al_5FeSi were evaluated with the use of the prepared alloy electrodes as working electrodes and metallic lithium foils as the counter electrode. The electrochemical properties from constant current charge/discharging (50

μA, 0.01 – 3.00 V) of Al_5FeSi electrodes varied with milling time particularly between the milled (BM) and remilled (RM) materials. The first discharge capacity increased continuously amongst the milled materials (BM70, BM135, BM251) but then decreased with increasing remilling time (Figure 6-20). Although the first discharge capacity of RM260 is slightly higher than RM190 the capacities are very similar. The discharge profiles for all the remilled materials are essentially the same though there are some differences to those of the milled materials. The BM251 material exhibited the highest discharge capacity of 375 mAh/g. The first charge capacities (Figure 6-21) varied during the initial milling period increasing from the BM70 material (11 mAh/g) to approximately the same value for the BM135 (64 mAh/g) and BM251 (63 mAh/g) materials though the charge profile for each varied. The charge capacities of the remilled materials then decreased to values between 24 and 28 mAh/g with the highest capacity exhibited by RM260.

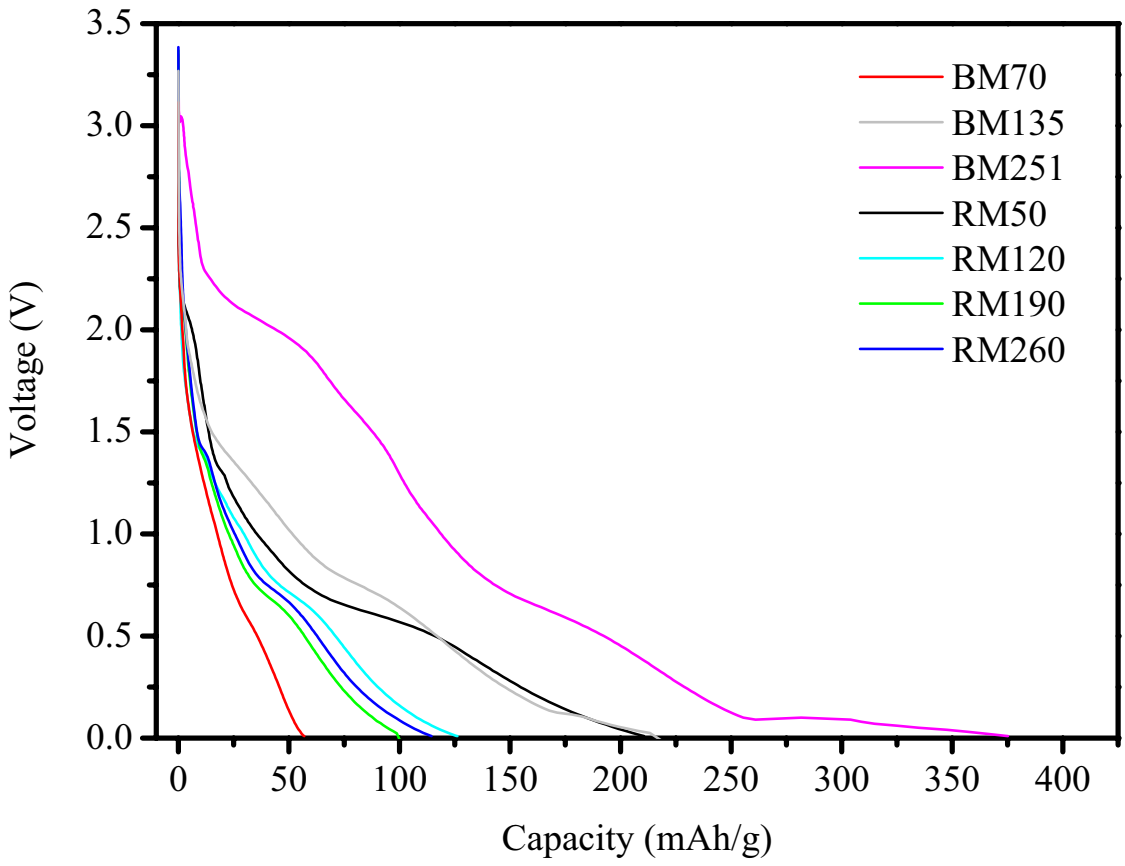

Figure 6-20: First discharge of various ball milled Al_5FeSi materials.

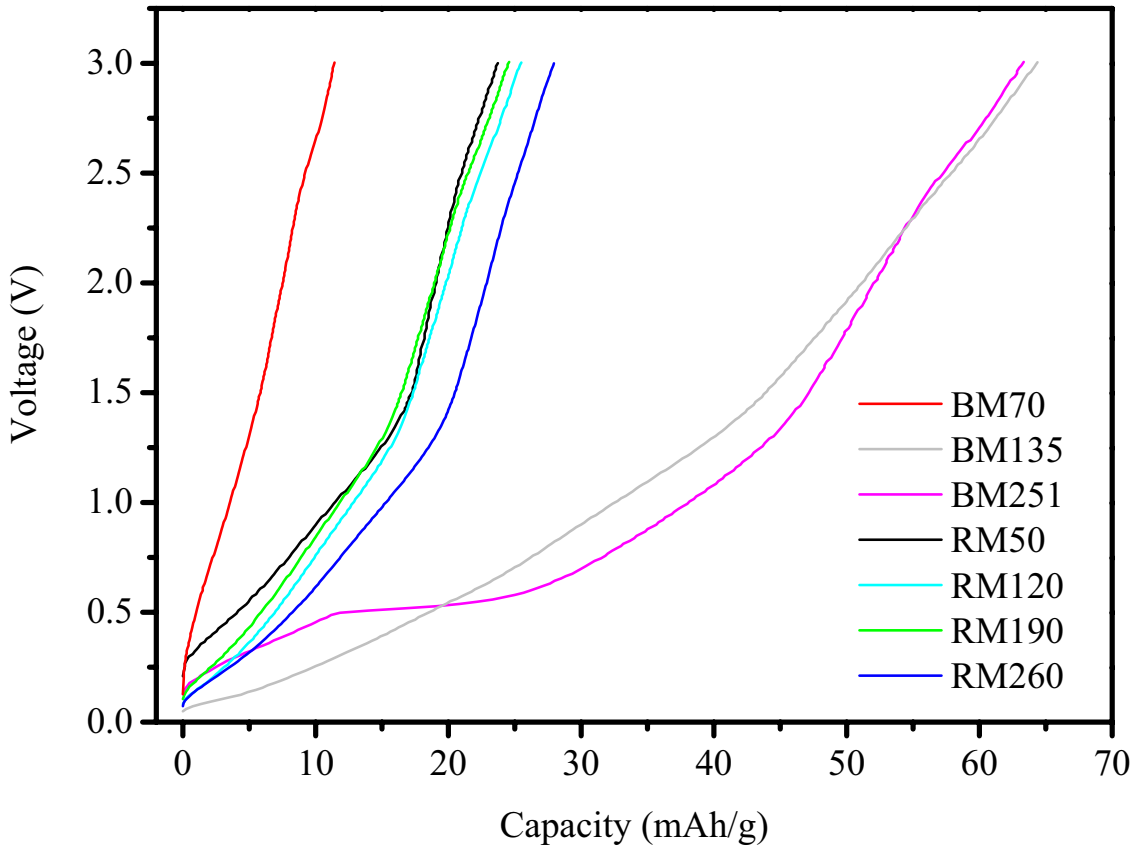

Figure 6-21: First charge of various ball milled Al_5FeSi materials.

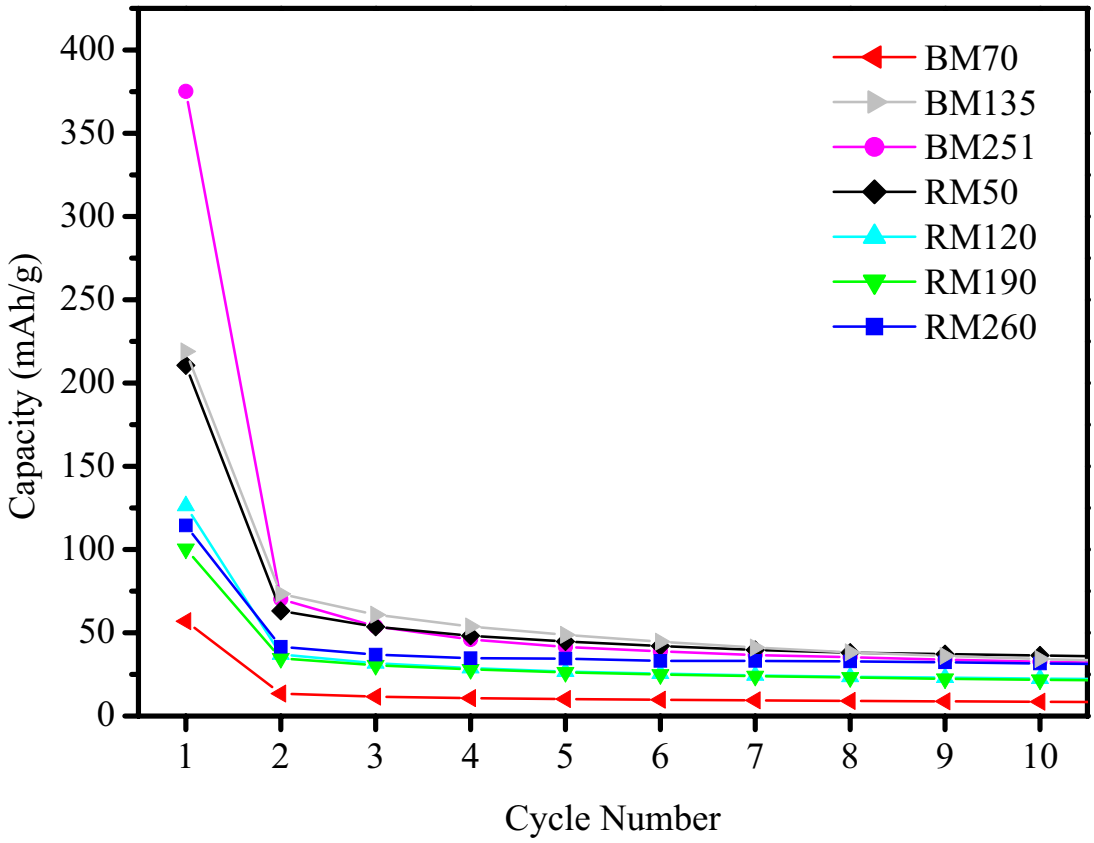

Figure 6-22: Variation of discharge capacity of Al_5FeSi with milling time.

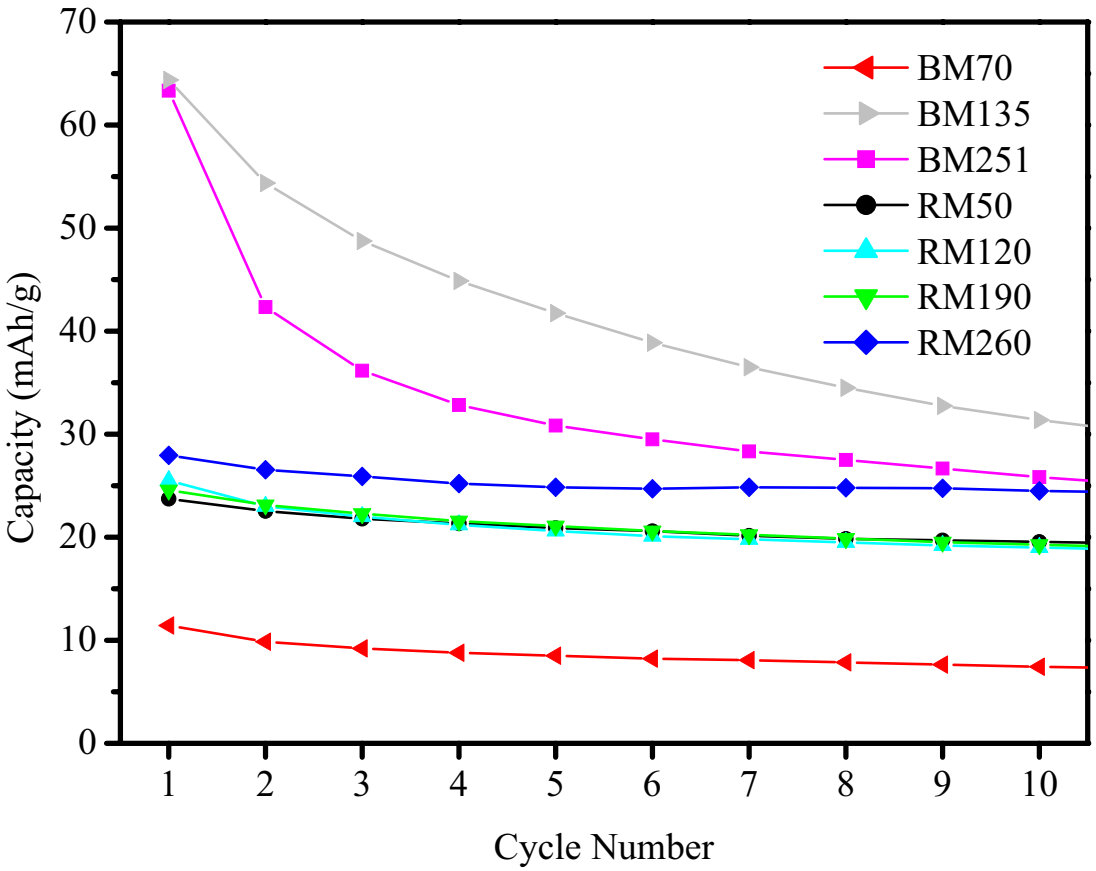

Figure 6-23: Variation of charge capacity of Al_5FeSi with milling time.

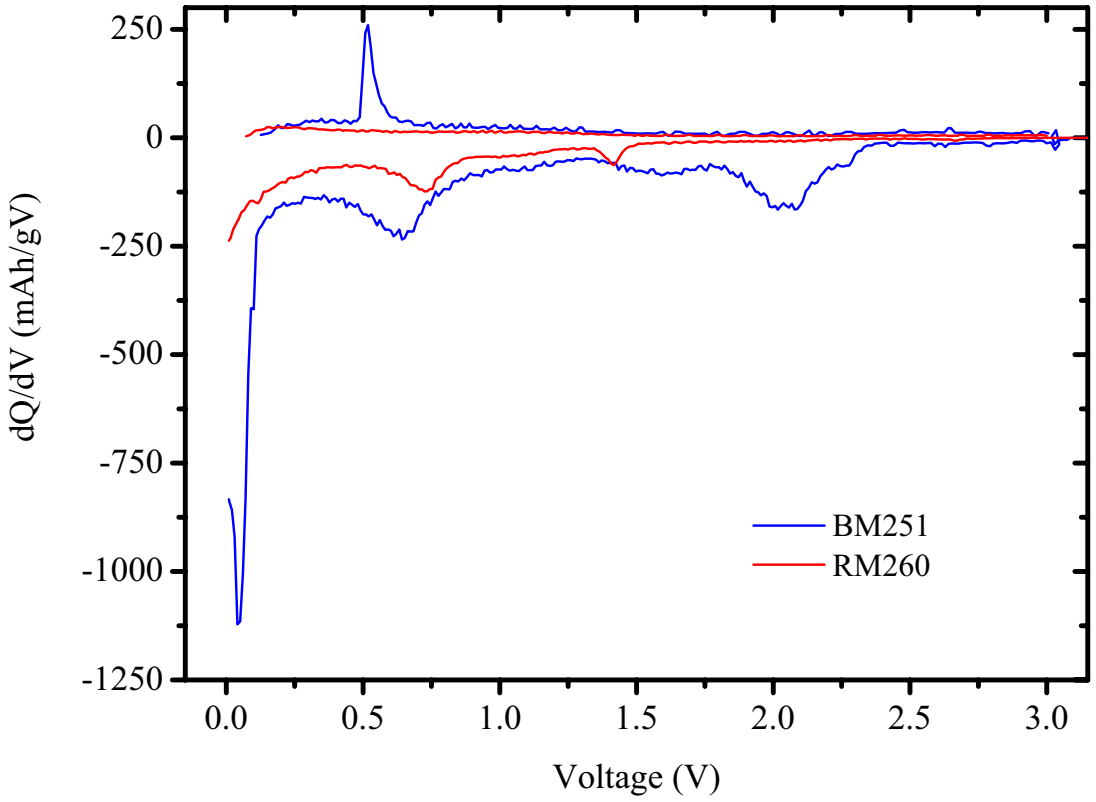

Figure 6-24: Differential capacity plot for the first cycle of BM251 and RM260 Al_5FeSi.

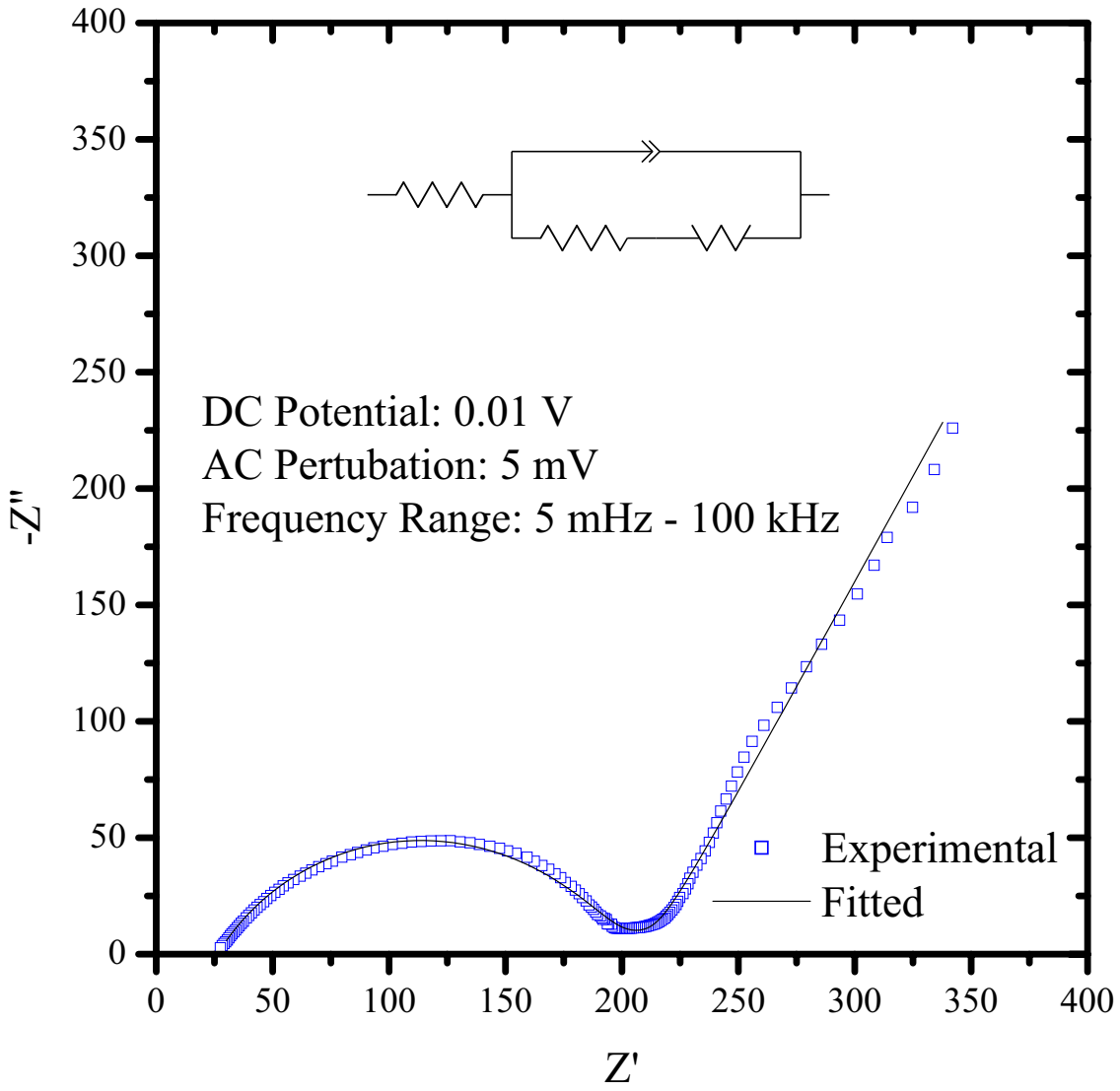

Figure 6-25: Nyquist plot of ac impedance spectroscopy of Al_5FeSi after the first discharge.

Extraction of lithium from the Al_5FeSi structure is difficult as demonstrated by the low charge capacities in comparison to those of the discharge. As a result the charge (Figure 6-23) and discharge capacities (Figure 6-22) declined and within ten cycles the discharge capacities were under 36 mAh/g and the charge capacities under 31 mAh/g. For both the charge and discharge the highest capacities were attributed to the BM135 material following the first cycle.

Differential capacity plots of the first charge and discharge of BM251 and RM260 (Figure 6-24) are different and notably a peak occurs at 0.52 V on the charge of BM251. Two peaks are evident in the discharge of both materials though at different potentials. Impedance spectroscopy was also carried out on RM260 following the first discharge to 0.01 V (Figure 6-25) and exhibited a depressed semicircle at low frequency and a high frequency tail.

6.3.2 Discussion

The intermetallic produced through the arc melting process led to the production of a material with a different structure and composition (Al_5FeSi) than was intended from the initial composition (Al_9FeSi_3). The importance of the microstructure has been highlighted with the variation of both the charge and discharge with milling time. The highest discharge capacity of 375 mAh/g (BM251) is well below the theoretical capacity for full reaction with lithium to form LiAl and $Li_{22}Si_5$ (1554 mAh/g). It is also well below the theoretical capacities for complete lithiation of aluminium to form LiAl (630 mAh/g) and silicon to from $Li_{22}Si$ (924 mAh/g). Suggesting that even on the first discharge a significant amount of active material is not alloying with lithium to reach completely lithiated compositions. So the lithiation is at least being retarded in these materials though microstructural modification may be able to improve the discharge capacities in line with the theoretical capacities and improve the cycle life of the material.

Differential capacity plots of BM251 and RM260 indicate different behaviour between the two materials. There are two distinct peaks in the discharge of both though at different potentials whilst only BM251 exhibits a single peak during the charge. The peak at 0.52 V during charge may correspond to the delithiation reaction $(LiAl \rightarrow Li + Al)$ though no peak for the proceeding lithiation reaction $(Li + Al \rightarrow LiAl)$ is evident around 0.2 V on the discharge.

The impedance spectra of the RM260 material was modelled with a simple circuit composed of two resistors, a constant phase element and a Warburg element as presented in Figure 6-25.

6.3.3 Conclusions

A ternary aluminium based intermetallic material has demonstrated electrochemical properties varying with milling time. The discharge capacities observed were well under the theoretical capacity of even the individual components suggesting the lithiation reaction is being retarded in these materials. The low charge capacities also suggest that the removal of lithium from the structure is also difficult and being retarded. Modification of the microstructure may be able to improve the capacities towards the theoretical and improve the cycle life of the material. Differential capacity

plots of first cycle of BM251 suggest that the delithiation of aluminium may be occurring though the proceeding lithiation reaction was not evident.

6.4 Conclusions

Although all three ternary aluminium based intermetallics demonstrated activity towards lithium the highest discharge capacities observed in each material are well under the theoretical capacities of the material for complete lithiation of the active materials to LiAl and $Li_{22}Si_5$. The highest discharge capacities observed in each material were under 40 % of the theoretical discharge capacities. The charge capacities of the materials were also particularly low suggesting that the lithiation and delithiation reactions are being retarded in these materials.

There is also some uncertainty over the reaction mechanism responsible for the observed capacities though differential capacity plots offered some evidence of the lithiation/delithiation reaction occurring in the $Al_{20}Fe_5Si_2$ and Al_9FeSi_3 material.

Chapter 7 FeSi

High purity iron and silicon were weighed out in the proportions corresponding to stoichiometric FeSi. The iron and silicon were then combined to form an alloy slug with the use of an arc melter. A portion of the resulting slug was then annealed at 1420°C for 1 hour in an argon atmosphere according to the thermal program indicated in Figure 7-1. Both the arc melted and annealed materials were then crushed separately a number of times until the resultant fines passed through a 150 µm sieve. The material that passed through the 150 µm sieve was then milled in a Pulverisette-5 planetary ball mill at a speed of 160 rpm in a steel-milling vessel. The milling vessel had an internal diameter of 80 mm and volume of approximately 200 cm^3. The theoretical discharge capacity of FeSi varies from 547 mAh/g for full reaction of silicon to form $Li_{12}Si_7$ to 1405 mAh/g for the formation of $Li_{22}Si_5$. The theoretical discharge capacities for these and the other lithium – silicon phases are listed in Table 7-1.

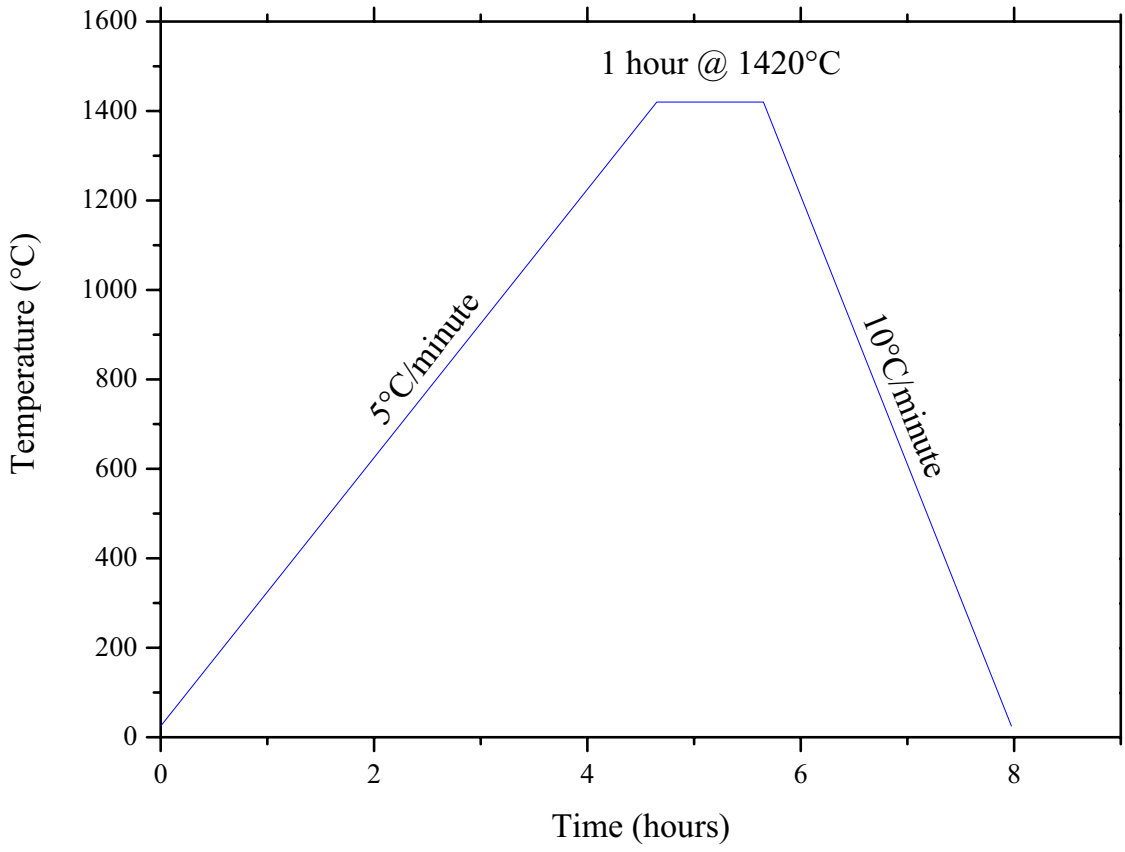

Figure 7-1: Annealing treatment for arc melted FeSi.

Table 7-1: Theoretical discharge capacities of FeSi for the formation of various Li – Si phases.

Phase	Theoretical Discharge Capacity (mAh/g)
$Li_{12}Si_7$	547
Li_7Si_3	745
$Li_{13}Si_4$	1038
$Li_{22}Si_5$	1405

7.1 Arc Melted

The arc melted material was milled with 5 mm diameter stainless steel balls utilising a ball to powder ratio of approximately 60:1 (60.06g balls: 1.035g powder). Ethanol was also added as a process control additive to the level of the top of the balls. Powder was removed at a number of intervals in small quantities up to a total milling time of 260 hours. Powder was removed at total milling times of 50, 120, 190 and the final milling time of 260 hours. Where milling continued after powder was removed ethanol was added to the milling jar if required to bring it back up to its initial level. The various powders and other results derived from their use will be referred to using a prefix of BM followed by the milling time of the powder in hours. Whilst the unmilled material that passed through the 150 μm sieve is referred to as BM0.

The fabrication of electrodes resulted in loadings of approximately 3 mg for BM0 and 1 mg for the remaining samples. The final composition of the electrodes corresponded to 85 wt. % powder, 10 wt. % conductivity additive and 5 wt. % PVDF.

7.1.1 Results

7.1.1.1 Structural and Microstructural Characterisation

The XRD pattern of the unmilled material (BM0 in Figure 7-2) corresponded to the cubic structure of FeSi. The peaks of the milled materials do however broaden and reduce in intensity suggesting an X-ray amorphous structure though the presence of some sharp peaks suggests crystalline material also remains.

Full width at half maxima (FWHM) were determined using the Traces program for the (210) and (211) peaks of BM0 and the crystalline size estimated using the Scherrer equation (3-6). A value of 0.9 for the K constant was used and instrumental

broadening was evaluated according to 3-8. From such an approach the crystallite size was estimated as 40 nm for the (210) peak and 44 nm for the (211) peak.

In order to examine the effect of milling on the particle size of the FeSi powders SEM was used to examine the particle size (Figure 7-3). The particle size decreased from a maximum of 120 μm for BM0 to less than 1 μm for all the ball-milled materials. BET analysis reported the specific surface area of the BM260 material as 105 m^2/g.

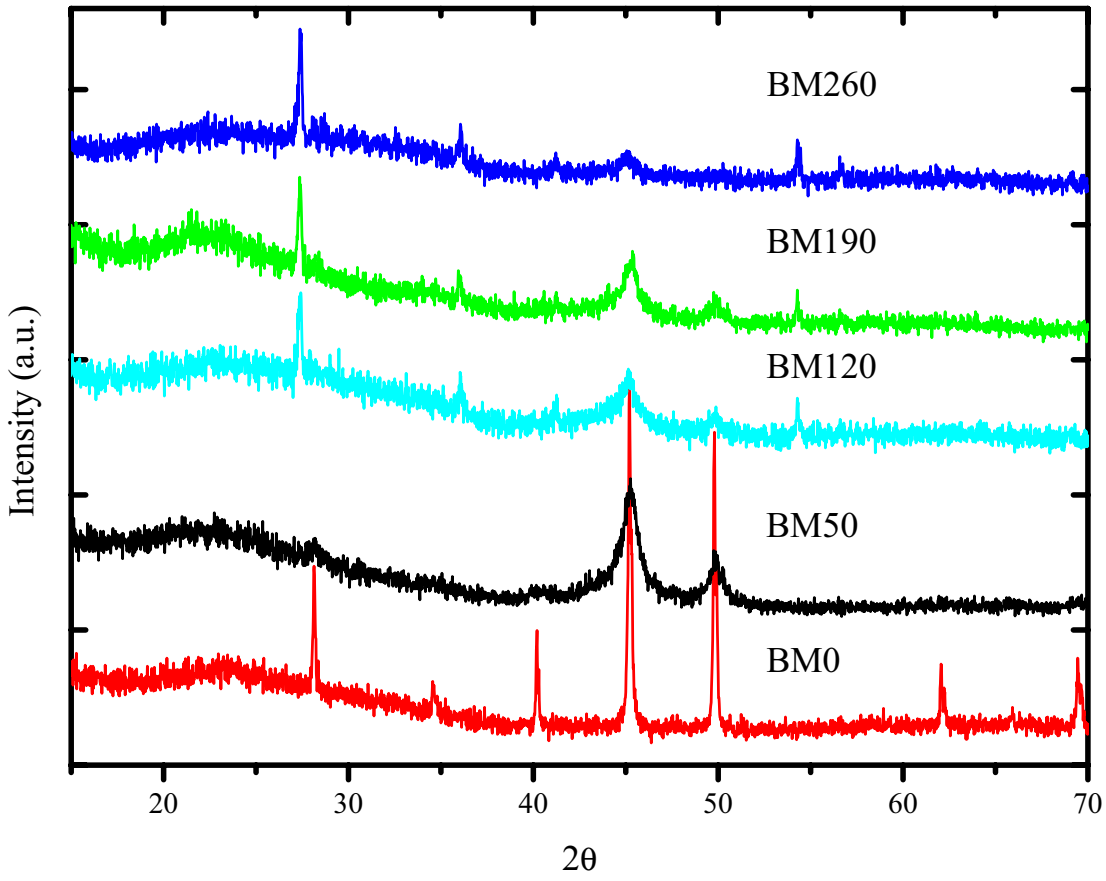

Figure 7-2: XRD patterns of arc melted and ball milled FeSi materials.

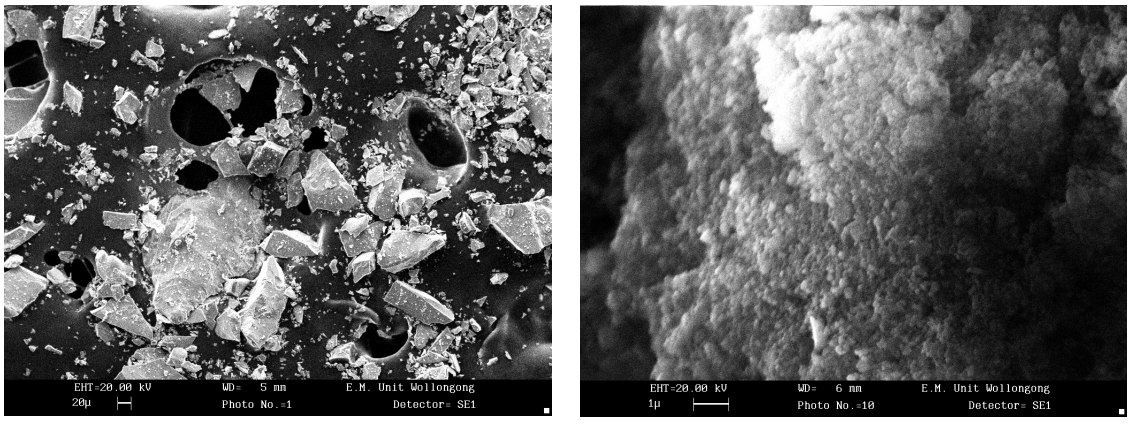

(a) (b)

Figure 7-3: Selected SEM micrographs of ball milled FeSi materials: (a) 150 μm, (b) 50 hours.

7.1.1.2 Electrochemical Characterisation

The electrochemical properties of FeSi were evaluated with the use of the prepared alloy electrodes as working electrodes and metallic lithium foils as the counter electrode. The electrochemical properties varied with milling time when examined with constant current charge/discharging (50 μA, 0.01 – 3.00 V). The first discharge capacity (Figure 7-4) increased continuously as a result of milling to a maximum of 983 mAh/g. The capacity of the BM190 material 926 mAh/g is only slightly lower though the discharge profiles for the materials did vary. The first charge capacities (Figure 7-5) also varied with milling time with the unmilled material having the lowest capacity and the BM260 the highest capacity (418 mAh/g). The first charge capacities and profiles of the BM50, BM120 and BM190 materials are very similar with capacities between 107 – 128 mAh/g.

The charge capacities (Figure 7-7) were much lower than the discharge capacities indicating the extraction of lithium from the structure is difficult though is improved as a result of the milling process. In comparison to the first discharge capacity those after ten cycles (Figure 7-6) are low with all materials having a capacity under 196 mAh/g with the best performance maintained by the BM260 material. The highest charge capacities were exhibited by the BM260 material and within ten cycles the capacities were all below 182 mAh/g.

Cyclic voltammetry of the BM260 material (Figure 7-8) indicates a large peak during the first discharge that is not evident in the subsequent cycles. The shape of the voltammogram for the first cycle is different to those of the subsequent cycles not just for the discharge but also for the charge.

7.1.2 Discussion

The broadening of XRD peaks suggest a reduction in crystallite size is occurring though some of the broadening will be attributed to strain as a result of the ball milling process. The crystallite size of the milled materials is thus likely to be under the 40 nm estimate for the unmilled material.

The highest discharge capacity observed of 983 mAh/g is below the theoretical capacity for complete formation of $Li_{22}Si_5$ (1405 mAh/g) though is close to that for the complete formation of $Li_{13}Si_4$ (1038 mAh/g). Most of the silicon is thus lithiated to a

high degree during the initial discharge. For the BM260 material just under half of this is retained in the structure in the subsequent initial charge.

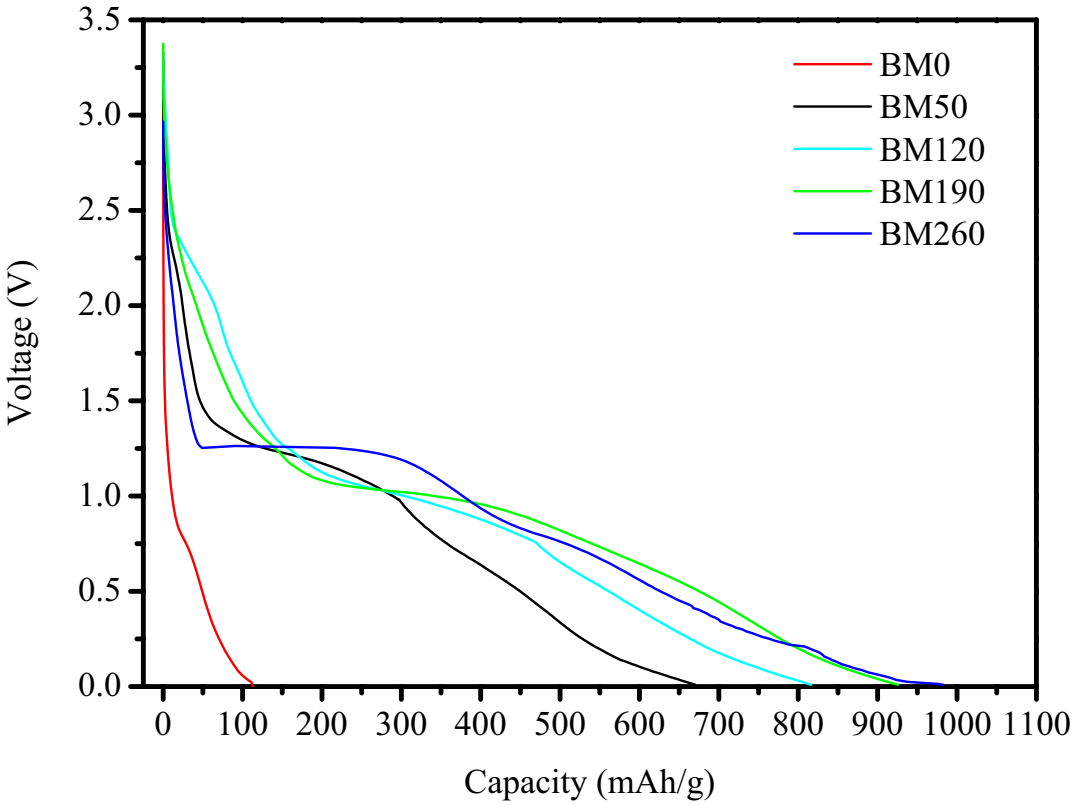

Figure 7-4: First discharge of various arc melted ball milled FeSi materials.

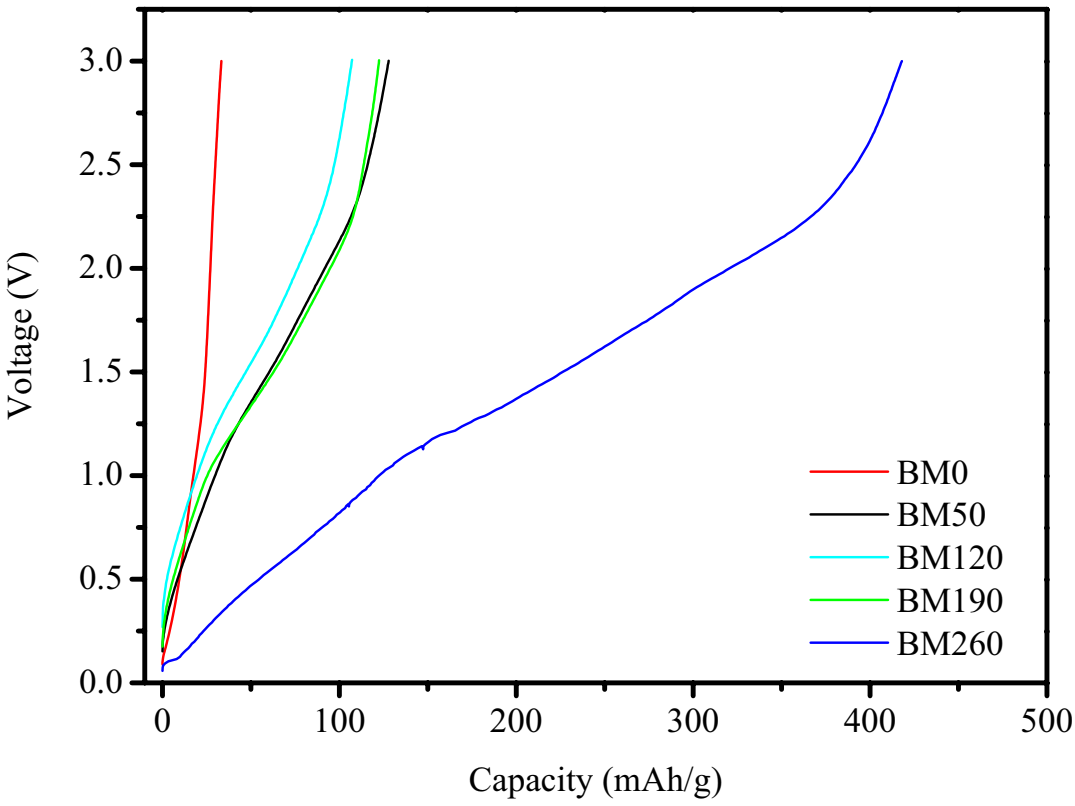

Figure 7-5: First charge of various arc melted ball milled FeSi materials.

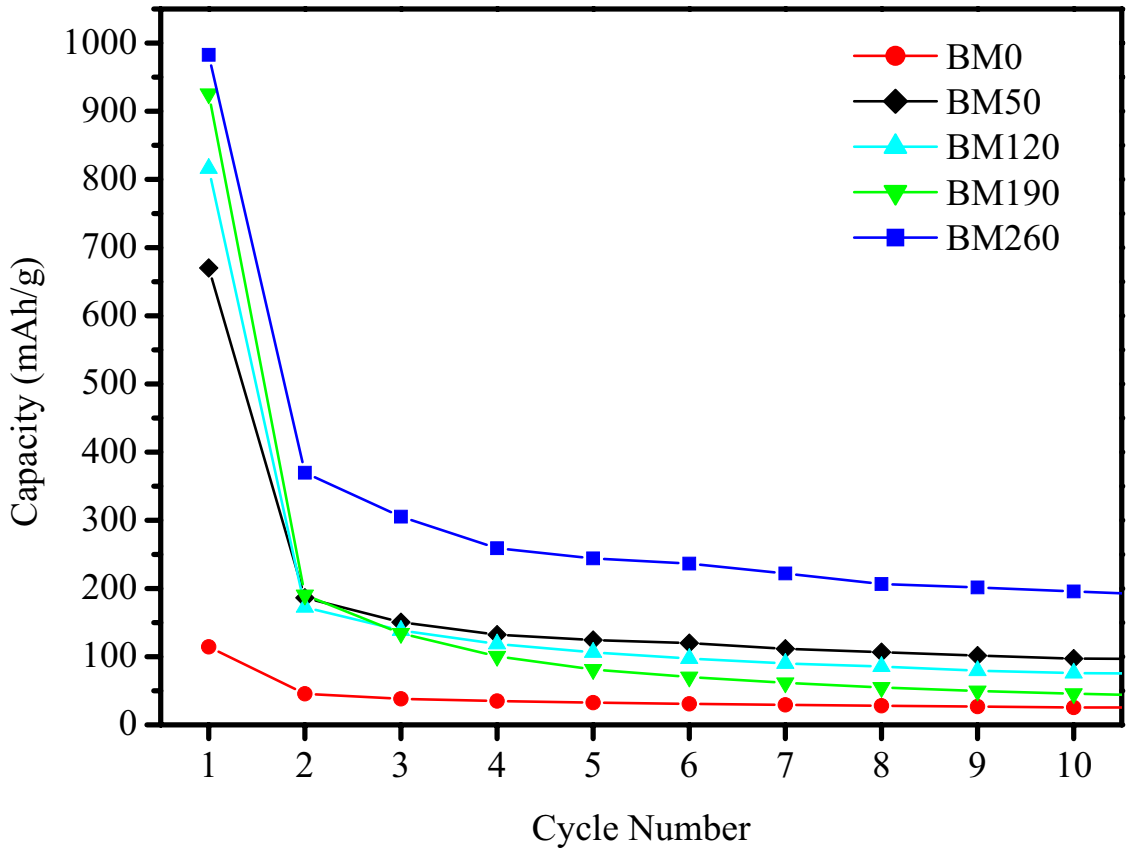

Figure 7-6: Variation of discharge capacity of arc melted FeSi with milling time.

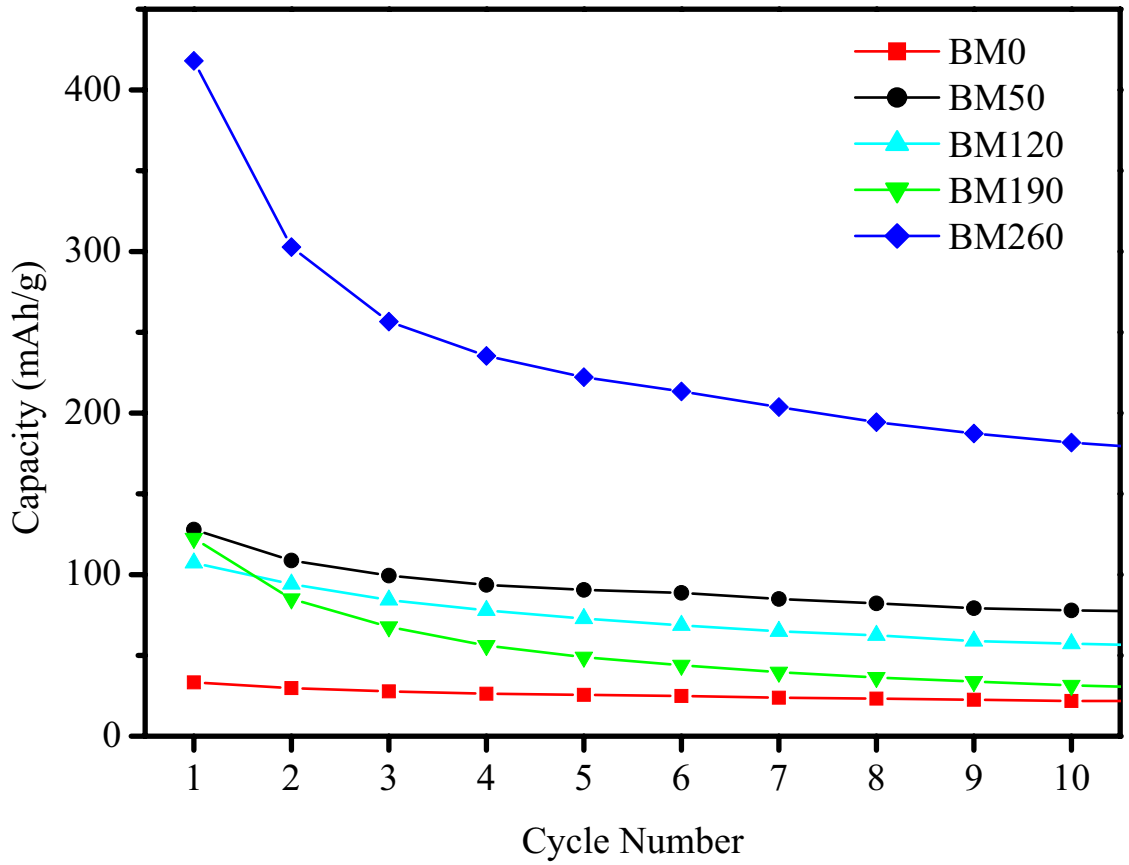

Figure 7-7: Variation of charge capacity of arc melted FeSi with milling time.

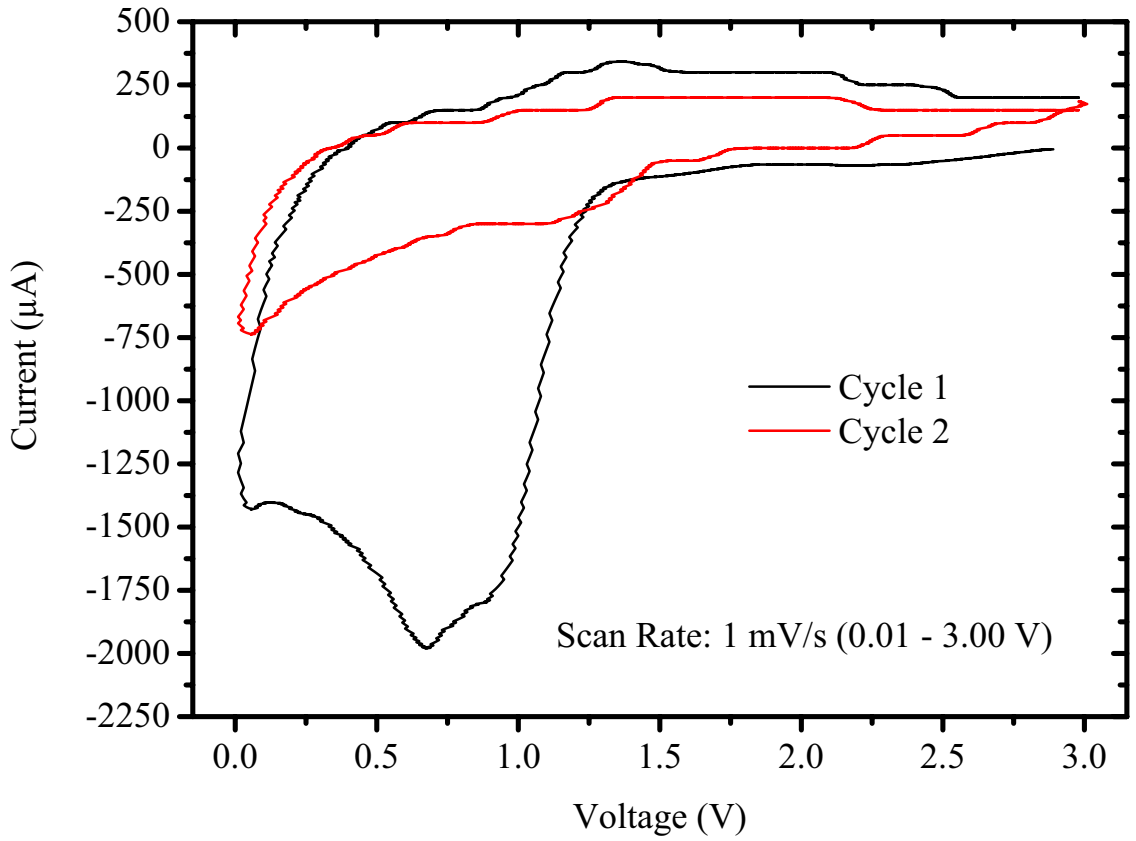

Figure 7-8: Cyclic voltammetry of arc melted FeSi BM260 electrode.

Of the other Fe – Si based materials reported in the literature the discharge profiles have the greatest resemblance to the graphite – $Fe_{20}Si_{80}$ materials of Lee et. al. [155]. The plateau voltages are however higher in this case at over 1.0 V compared to under 1.0 V observed by Lee *et. al.*. The charge profiles are however different from those reported by Lee where a slow rise to just over 0.5 V and a kick up to the 2.0 V that the materials were tested to.

7.1.3 Conclusions

The electrochemical properties of FeSi phase were examined with a number of ball milled materials. The charge and discharge capacities were increased as a result of ball milling. The charge capacities are much lower than the discharge capacities suggesting that removal of lithium from the structure remains difficult. Modification of the microstructure through further milling and/or annealing operations or a composite with carbon may be able to improve the electrochemical performance of the examined material. The discharge profiles of the ball milled materials were similar to those of the graphite – $Fe_{20}Si_{80}$ materials examined by Lee et. al. though the charge profiles were different.

7.2 Arc Melted + Annealed

The annealed material was milled with 5 mm diameter stainless steel balls utilising a ball to powder ratio of approximately 20:1 (65.56g balls: 3.423g powder). In this case the powder charge did not consist of the alloy alone but of alloy powder with a 10.0 weight percent addition of Vulcan XC-72. Milling was initially carried out for 260 hours without the use of a process control additive with small quantities of powder removed at total milling times of 50, 120, 190 and 260 hours. Ethanol was then added as a process control additive to the level of the top of the balls and milling continued for a further 260 hours. Small quantities of powder were also removed at a number of intervals during this extended milling period at total times of 50, 120, 190 and the final milling time of 260 hours. Where milling continued after powder was removed ethanol was added to the milling jar if required to bring it back up to its initial level.

Powders from the initial milling period of 260 hours and other results derived from their use will be referred to using a prefix of BM followed by the milling time of the powder in hours. Powders from the subsequent milling period of 260 hours and other results derived from their use will be referred to using a prefix of WM followed by the milling time of the powder in hours. Whilst the unmilled material that passed through the 150 μm sieve is referred to as BM0.

The fabrication of electrodes resulted in loadings of approximately 3 mg for BM0 and 1 mg for the remaining samples. The unmilled electrode contained only the carbon that was added during electrode fabrication whilst the milled electrodes also contained the carbon that was added at the start of the milling process. The final composition of the electrodes corresponded to 79 – 86 wt. % alloy powder, 16 – 9 wt. % conductivity additive (Vulcan XC-72) and 5 wt. % PVDF.

7.2.1 Results

7.2.1.1 Structural and Microstructural Characterisation

The XRD pattern of the unmilled material (BM0 in Figure 7-9) corresponded to the cubic structure of FeSi. The peaks of the milled materials broadened following 50 hours of milling though further broadening was not evident up to 260 hours. With the start of wet milling the peaks broadened further and subsequent diffraction patterns can be described as X-ray amorphous.

Full width at half maxima (FWHM) were determined using the Traces program for the (210) and (211) peak of BM0, BM50 and BM260 materials and the crystalline size estimated using the Scherrer equation (3-6). A value of 0.9 for the K constant was used and instrumental broadening was evaluated according to 3-8. From such an approach the crystallite size estimates varied from 44 nm for BM0 to 12 nm for BM260 (Table 7-2).

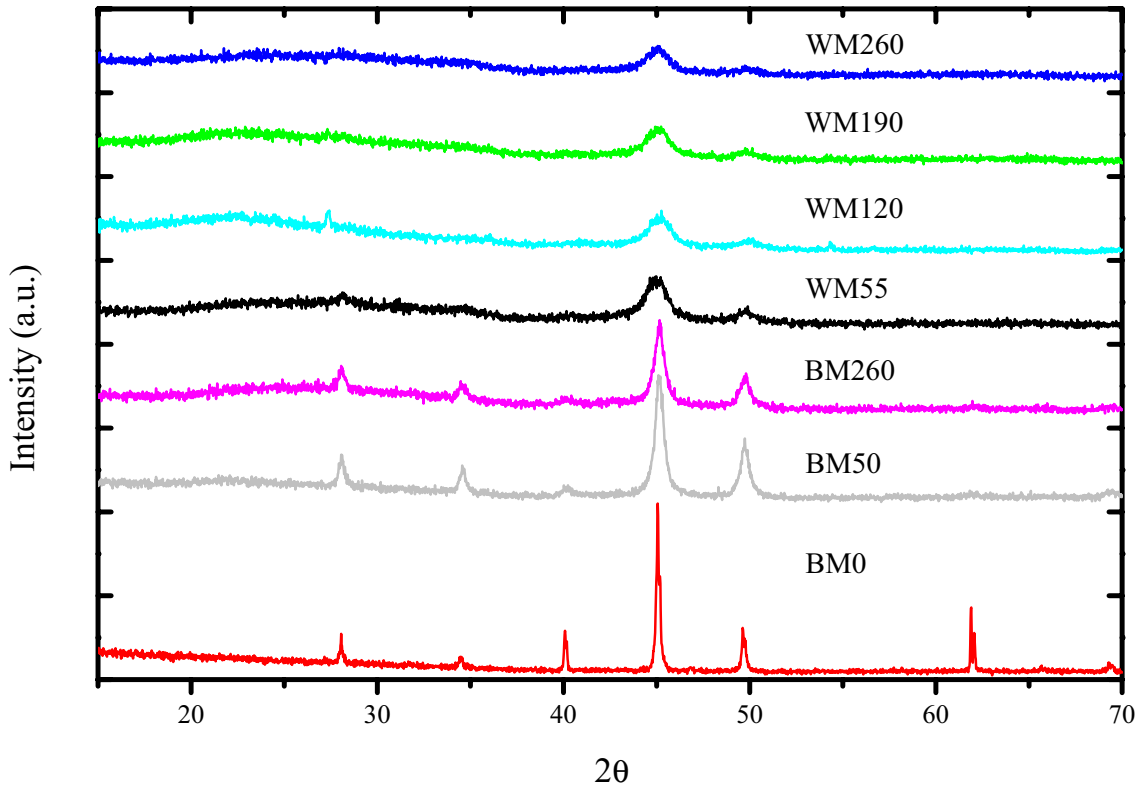

Figure 7-9: XRD patterns of annealed and ball milled FeSi materials.

In order to examine the effect of milling on the particle size of the FeSi powders SEM was used to examine the particle size (Figure 7-10). The particle size decreased from a maximum of 130 μm for BM0 to 1 μm and under for all the ball milled materials. BET analysis reported the specific surface area of the WM260 material as 65 m^2/g.

Table 7-2: Crystallite size estimates for annealed FeSi materials.

Material	Crystallite size (nm)	
	(210) Peak	(211) Peak
BM0	43	44
BM50	17	19
BM260	15	12

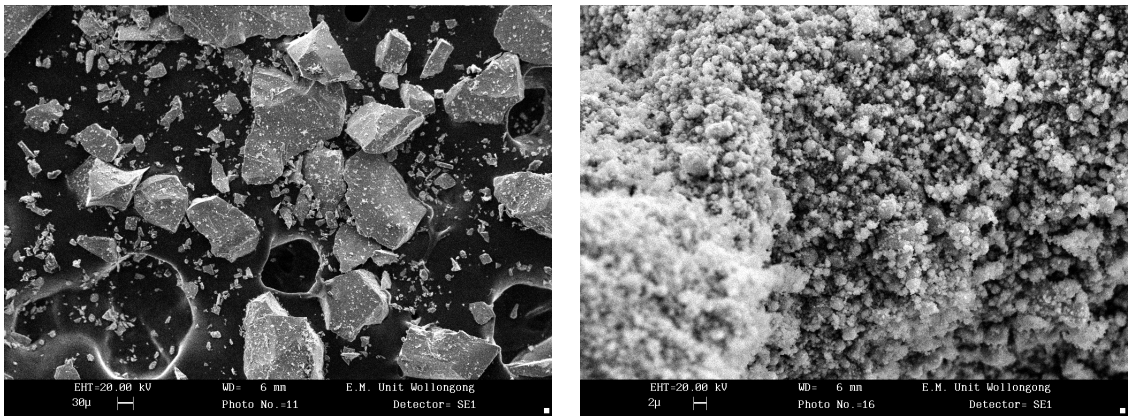

(a) (b)

Figure 7-10: Selected SEM micrographs of annealed and ball milled FeSi materials: (a) 150 µm, (b) BM260.

7.2.1.2 Electrochemical Characterisation

The electrochemical properties of FeSi were evaluated with the use of the prepared alloy electrodes as working electrodes and metallic lithium foils as the counter electrode. The electrochemical properties varied with milling time when examined with constant current charge/discharging (50 µA, 0.01 – 3.00 V). The first discharge capacity (Figure 7-11) increased as a result of ball milling with a maximum of 976 mAh/g for the WM190 material that was only just higher than WM120 at 934 mAh/g. Although the discharge capacities of the WM120 and WM190 materials are similar the discharge profiles of those and the other materials do differ.

The first charge capacities (Figure 7-12) increased up to 300 mAh/g for a milling time of 190 hours (WM190) before decreasing to 155 mAh/g for WM260. The charge profiles for all the milled materials are similar despite the variation in capacity (12 – 300 mAh/g) on the first cycle.

As the charge capacities are much lower than the discharge capacities the extraction of lithium from the structure is difficult but is improved as a result of the milling process. In comparison to the first discharge capacity those after ten cycles (Figure 7-13) are low with all materials having a capacity under 44 mAh/g with the best performance maintained by the WM190 material. The highest charge capacities (Figure 7-14) were also exhibited by the WM190 material and within ten cycles the capacities were all below 42 mAh/g.

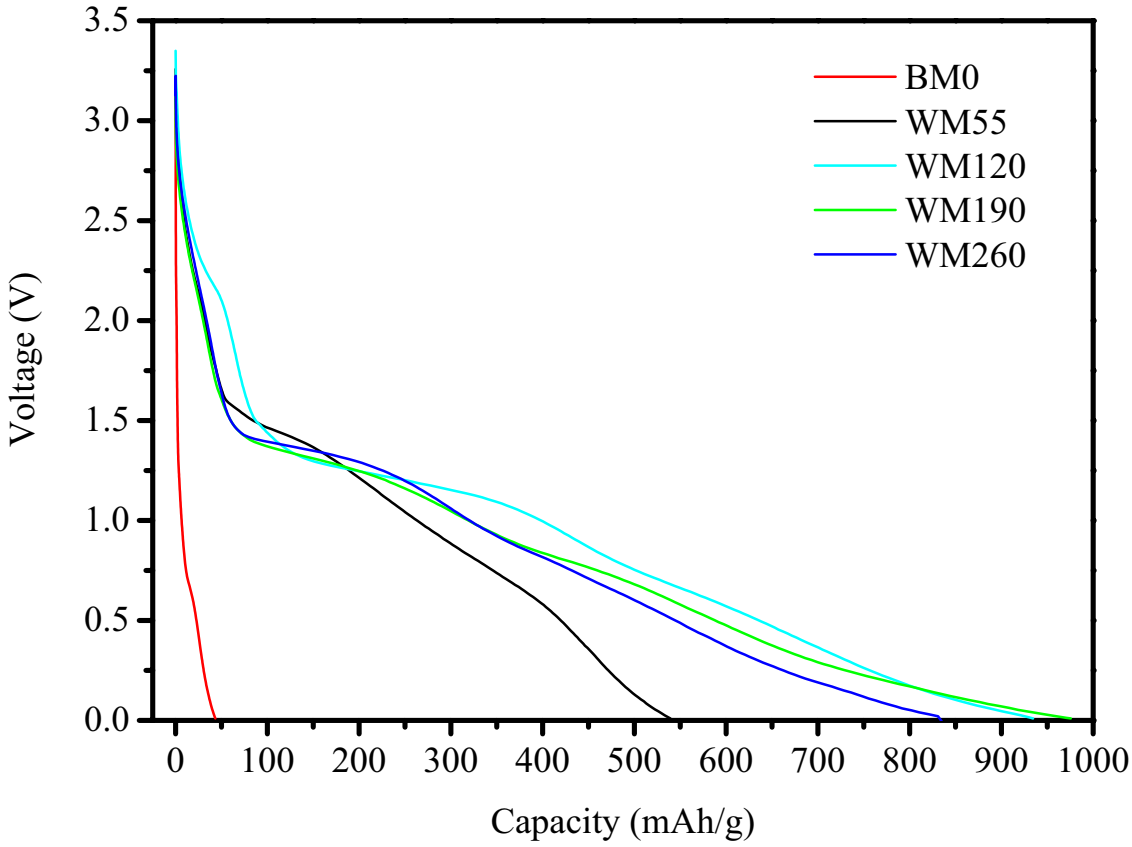

Figure 7-11: First discharge of various annealed ball milled FeSi materials.

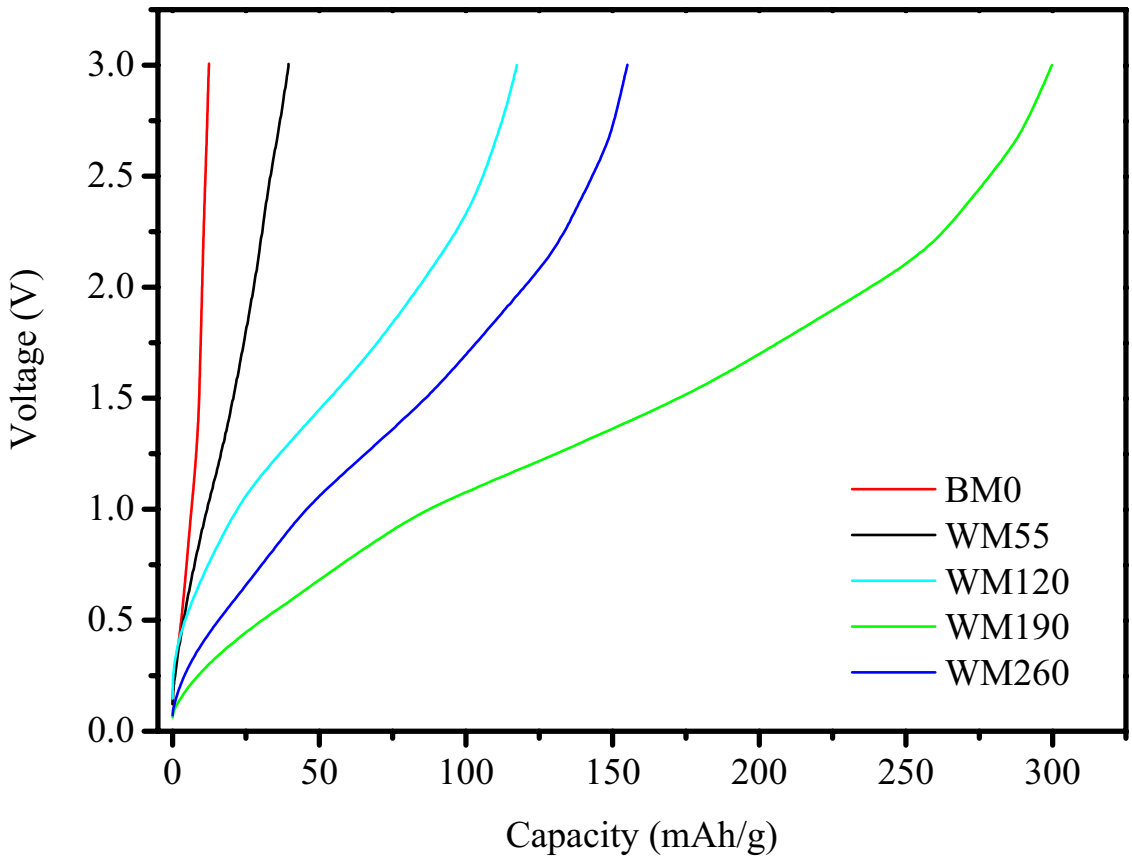

Figure 7-12: First charge of various annealed ball milled FeSi materials.

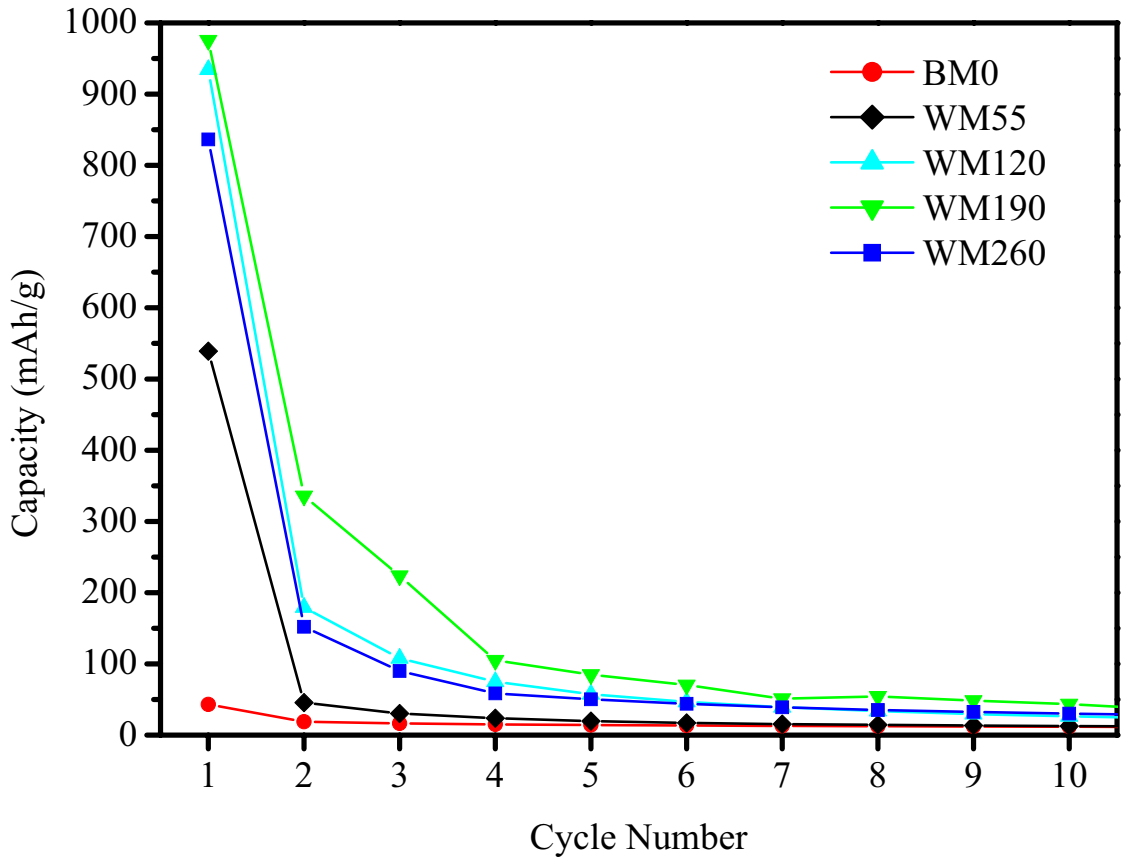

Figure 7-13: Variation of discharge capacity of annealed FeSi with milling time.

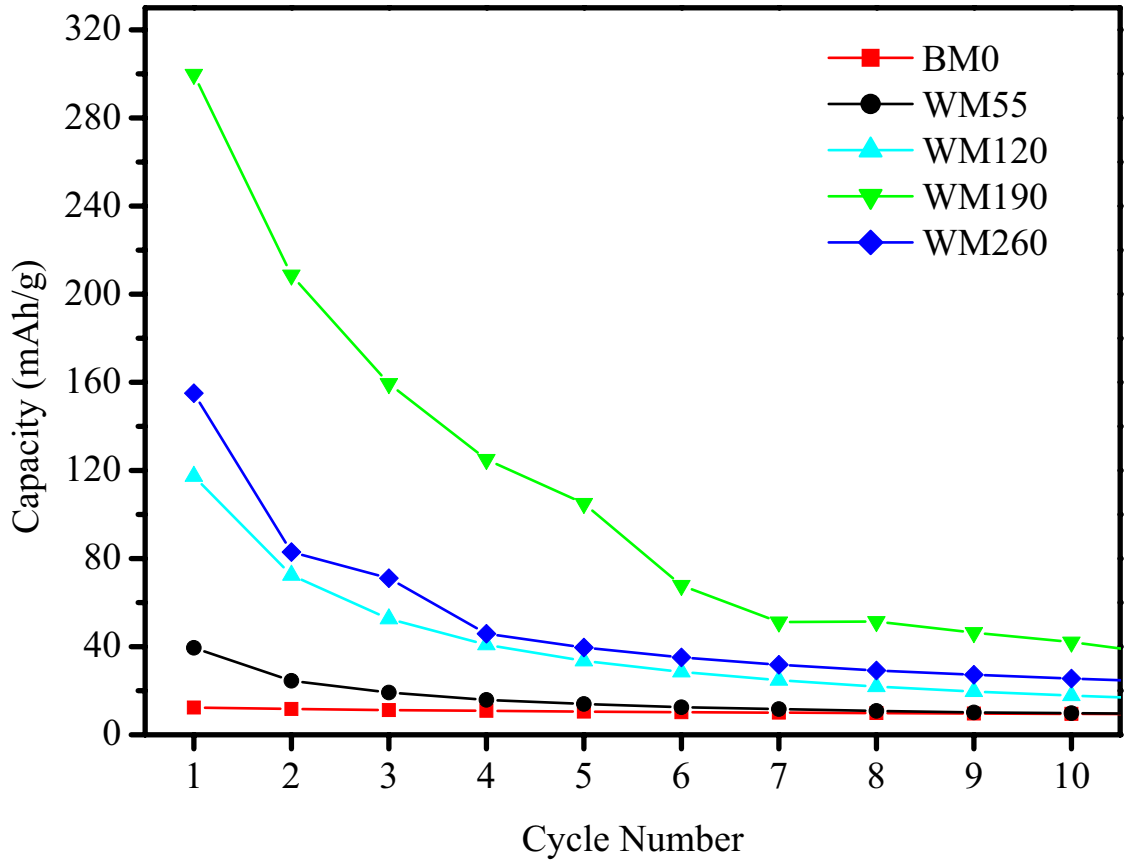

Figure 7-14: Variation of charge capacity of annealed FeSi with milling time.

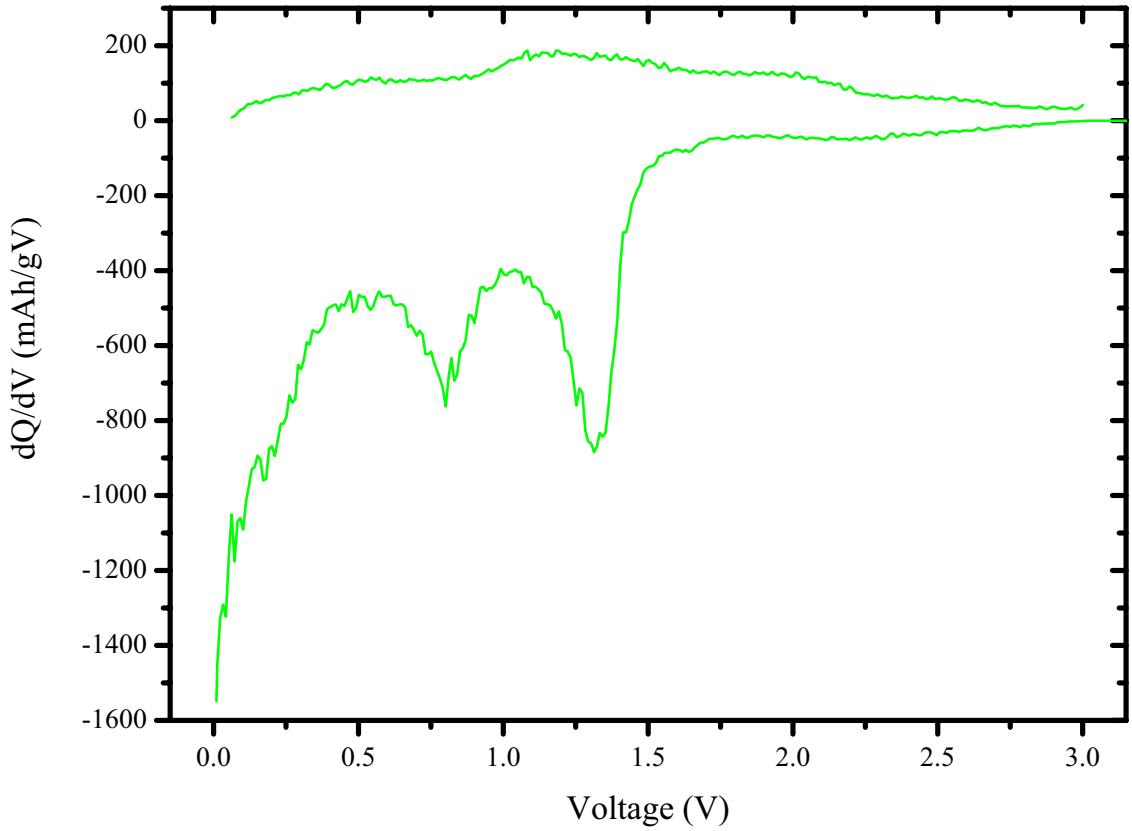

Figure 7-15: Differential capacity plot for the first cycle of annealed WM190 FeSi.

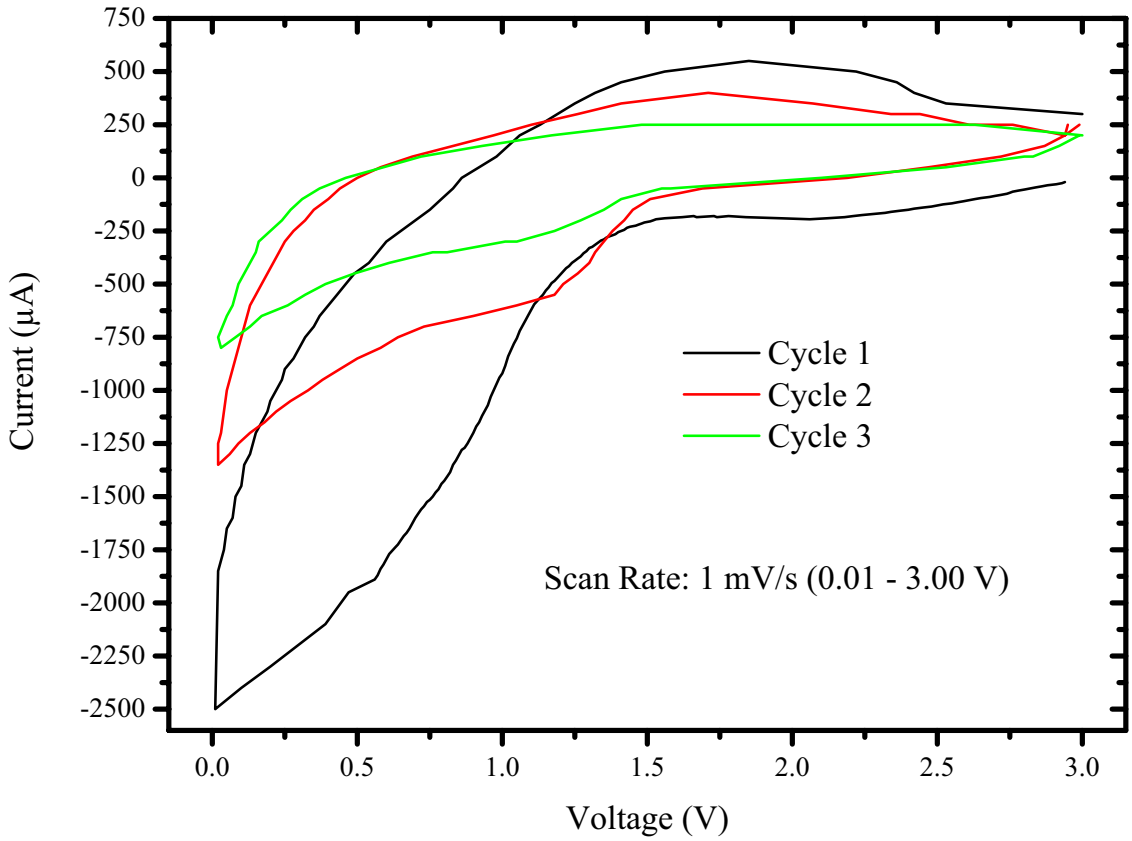

Figure 7-16: Cyclic voltammetry of annealed FeSi WM260 electrode.

Differential capacity plots of the first charge and discharge of WM190 (Figure 7-15) indicate two peaks during discharge at 0.80 V and 1.32 V whilst the charge is featureless. Cyclic voltammetry of the BM260 material (Figure 7-16) does not indicate any peaks as such during the first three cycles. The shape of the voltammogram for the first cycle is different to those of the subsequent cycles not just for the discharge but also for the charge.

7.2.2 Discussion

The broadening of XRD peaks suggest a reduction in crystallite size is occurring though some of the broadening will be attributed to strain as a result of the ball milling process. The crystallite size of the milled materials (WM) is thus likely to be under the 12 nm estimate for the BM260 material in comparison to the 43 nm estimate for the BM0 material.

The highest discharge capacity observed of 976 mAh/g is below the theoretical capacity for complete formation of $Li_{22}Si_5$ (1405 mAh/g) though is close to that for the complete formation of $Li_{13}Si_4$ (1038 mAh/g). Most of the silicon is thus lithiated to a high degree during the initial discharge. For the BM190 material over two thirds of the lithium is retained in the structure during the subsequent initial charge.

Of the other Fe – Si based materials reported in the literature the discharge profiles have the greatest resemblance to the graphite – $Fe_{20}Si_{80}$ materials of Lee et. al. [155]. The plateau voltages are however higher in this case at over 1.0 V compared to under 1.0 V observed by Lee *et. al.*. The charge profiles are different however from those reported by Lee where a slow rise to just over 0.5 V and a kick up to the 2.0 V that the materials were tested to was observed.

7.2.3 Conclusions

The electrochemical properties of FeSi phase were examined with a number of ball milled materials. The charge and discharge capacities were increased as a result of ball milling with the highest discharge capacity demonstrated by the WM190 material. The charge capacities are much lower than the discharge capacities suggesting that removal of lithium from the structure remains difficult. Modification of the microstructure through further milling and/or annealing operations or a higher carbon content in a composite with carbon may be able to improve the electrochemical performance of the examined material. The discharge profiles of the ball milled

materials were similar to those of the graphite – $Fe_{20}Si_{80}$ materials examined by Lee et. al. though the charge profiles were different.

7.3 Conclusions

The electrochemical properties of arc melted FeSi and annealed FeSi materials were examined with a variety of materials produced using ball milling. Although the highest discharge capacities observed in both the annealed and arc melted materials were similar (just under 1000 mAh/g) there were few other similarities. The first discharge capacity of the unmilled arc melted material (114 mAh/g) was over twice that of the unmilled annealed material (43 mAh/g). The crystallite size of the unmilled annealed material was estimated as 43 nm in comparison to 40 nm for the unmilled arc melted material for the (210) peak whilst both had an estimated crystallite size of 44 nm for the (211) peak. The crystallite size as estimated from the (210) peak are as expected, with that of the annealed material higher than that of the arc melted material.

The capacities of the annealed materials are also lower than those of the arc melted materials. The annealed materials were milled with carbon and despite being milled for a total time of over 500 hours the specific surface area of the WM260 material (65 m^2/g) was still lower than that of the arc melted BM260 material (105 m^2/g).

The discharge profiles of the arc melted and annealed materials were however similar to those of the graphite – $Fe_{20}Si_{80}$ materials of Lee et. al. [155] but the charge profiles were different. The highest discharge capacities of both the arc melted and annealed materials suggested that most of the silicon in the materials was lithiated to a high degree during the initial discharge. The charge capacities were however much lower than the initial discharge suggesting that significant amounts of lithium are retained in the structure during the charge as it is not easily extracted from the structure.

Chapter 8 $FeSi_2$

High purity iron and silicon were weighed out in the proportions corresponding to stoichiometric $FeSi_2$. The iron and silicon were then combined to form an alloy slug with the use of an arc melter. A portion of the resulting slug was then annealed at 1250°C for 1 hour in an argon atmosphere according to the thermal program indicated in Figure 8-1. Both the arc melted and annealed materials were then crushed separately a number of times until the resultant fines passed through a 150 µm sieve. The material that passed through the 150 µm sieve was then milled in a Pulverisette-5 planetary ball mill at a speed of 160 rpm in a steel-milling vessel. The milling vessel had an internal diameter of 85 mm and volume of approximately 140 cm^3. The theoretical discharge capacity of $FeSi_2$ varies from 820 mAh/g for full reaction of silicon to form $Li_{12}Si_7$ to 2106 mAh/g for the formation of $Li_{22}Si_5$. The theoretical discharge capacities for these and the other lithium – silicon phases are listed in Table 8-1.

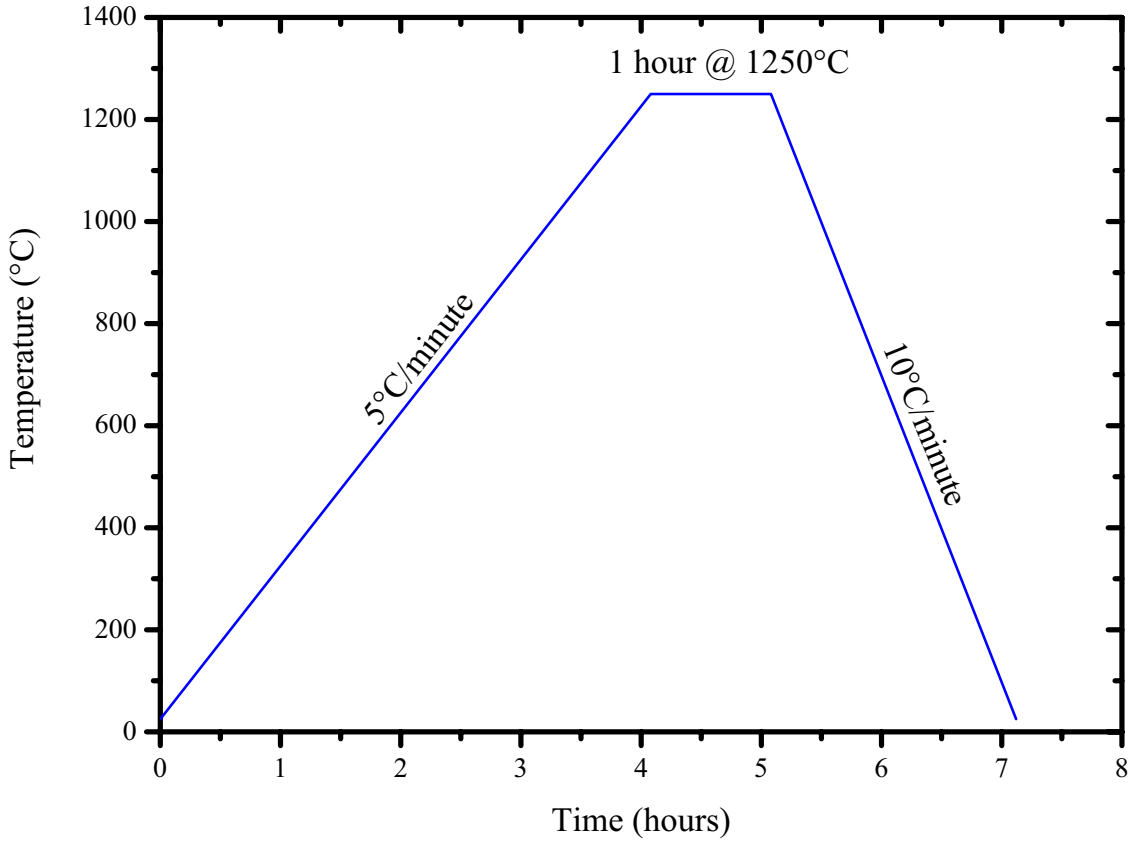

Figure 8-1: Annealing treatment for arc melted $FeSi_2$.

Table 8-1: Theoretical discharge capacities of $FeSi_2$ for the formation of various Li – Si phases.

Phase	Theoretical Discharge Capacity (mAh/g)
$Li_{12}Si_7$	820
Li_7Si_3	1117
$Li_{13}Si_4$	1555
$Li_{22}Si_5$	2106

8.1 Arc Melted

The arc melted material was milled with 5 mm diameter stainless steel balls utilising a ball to powder ratio of approximately 20:1 (60.08g balls: 3.030g powder). Ethanol was also added as a process control additive to the level of the top of the balls. Powder was removed at a number of intervals in small quantities up to a total milling time of 260 hours. Powder was removed at total milling times of 50, 120, 190 and the final milling time of 260 hours. Where milling continued after powder was removed ethanol was added to the milling jar if required to bring it back up to its initial level. The various powders and other results derived from their use will be referred to using a prefix of BM followed by the milling time of the powder in minutes. Whilst the unmilled material that passed through the 150 μm sieve is referred to as BM0.

The fabrication of electrodes resulted in loadings of approximately 3 mg for BM0 and 1 mg for the remaining samples. The final composition of the electrodes corresponded to 85 wt. % powder, 10 wt. % conductivity additive and 5 wt. % PVDF.

8.1.1 Results

8.1.1.1 Structural and Microstructural Characterisation

The XRD pattern of the unmilled material (BM0 in Figure 8-2) corresponded to tetragonal $FeSi_2$ and cubic FeSi. The peaks of the milled materials do broaden and reduce in intensity suggesting an X-ray amorphous structure though the presence of some sharp peaks suggests crystalline material also remains. The crystalline peaks are associated with both FeSi and $FeSi_2$.

Full width at half maxima (FWHM) were determined using the Traces program for a number of peaks for both FeSi and $FeSi_2$ in BM0 and the crystalline size estimated using the Scherrer equation (3-6). A value of 0.9 for the K constant was used and

instrumental broadening was evaluated according to 3-8. The estimated crystallite sizes for the various peaks and materials are presented in Table 8-2.

In order to examine the effect of milling on the particle size of the $FeSi_2$ powders SEM was used to examine the particle size (Figure 8-3). The particle size decreased from a maximum of 110 μm for BM0, 60 μm for BM50 and under 1 μm for the remaining materials. BET analysis reported the specific surface area of the BM260 material as 180 m^2/g.

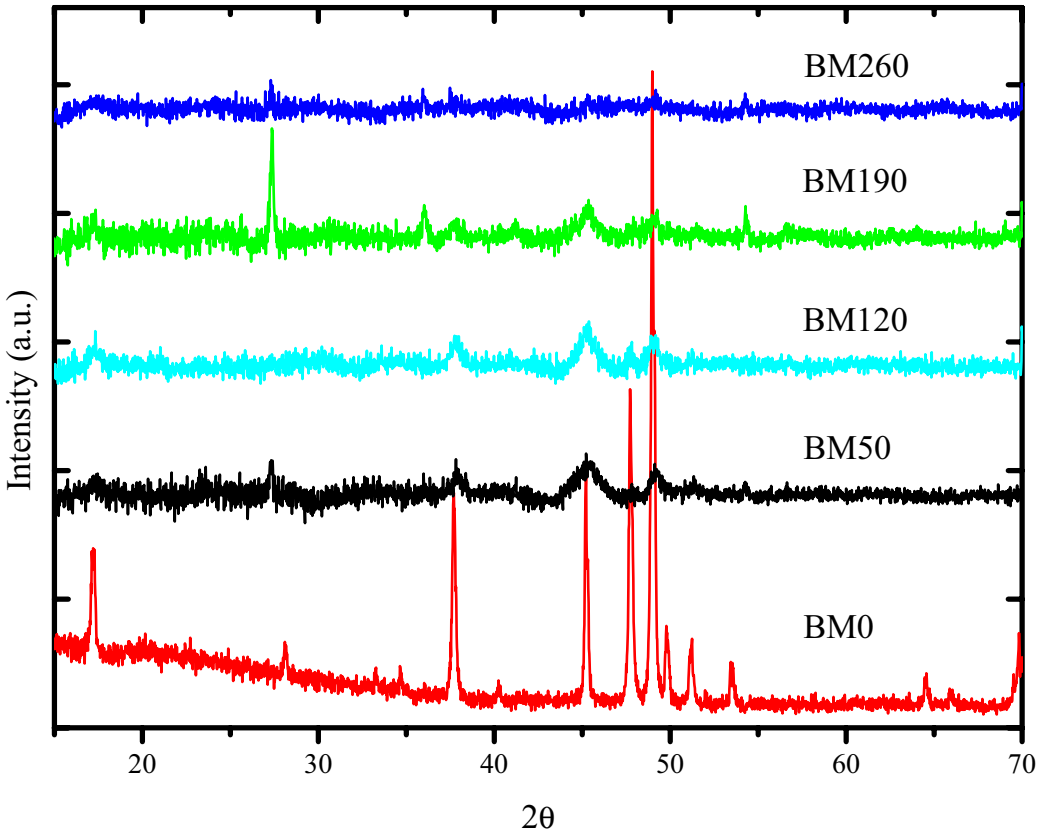

Figure 8-2: XRD patterns of arc melted and ball milled $FeSi_2$ materials.

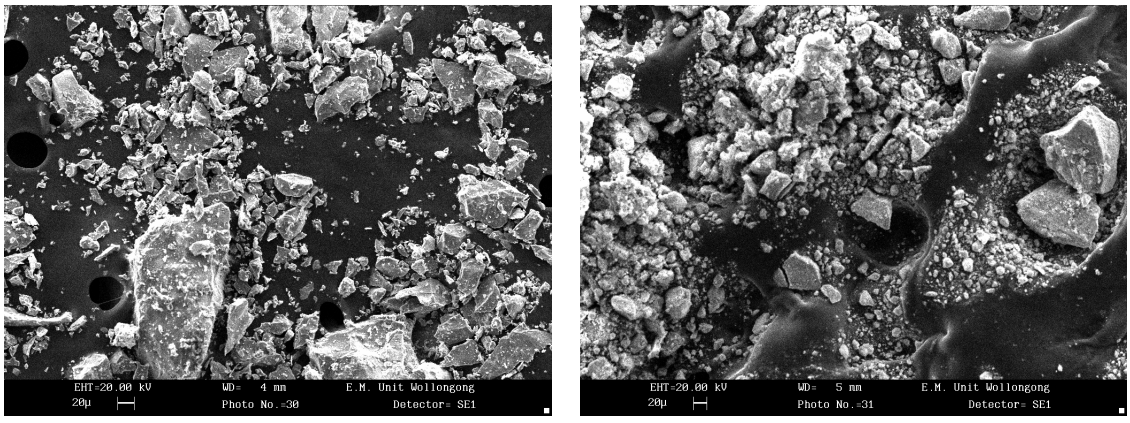

(a) (b)

Figure 8-3: Selected SEM micrographs of ball milled $FeSi_2$ materials: (a) 150 μm, (b) 50 hours.

Table 8-2: Estimated crystallite sizes for FeSi and $FeSi_2$ in arc melted $FeSi_2$ material.

Peak	Crystallite size (nm)	
	FeSi	$FeSi_2$
(210)	43	-
(211)	36	-
(101)	-	36
(102)	-	38
(110)	-	36

8.1.1.2 Electrochemical Characterisation

The electrochemical properties of $FeSi_2$ were evaluated with the use of the prepared alloy electrodes as working electrodes and metallic lithium foils as the counter electrode. The electrochemical properties varied with milling time when examined with constant current charge/discharging (50 μA, 0.01 – 3.00 V). The first discharge capacity (Figure 8-4) increased to a maximum of 618 mAh/g for the BM190 material before falling to 493 mAh/g for the BM260 material. The first charge capacities (Figure 8-5) in contrast reached a maximum of 117 mAh/g for the BM50 material and decreased on increasing milling time to 48 mAh/g for the BM260 which was however still greater than the capacity of the unmilled material (22 mAh/g).

The charge capacities were much lower than the discharge capacities indicating the extraction of lithium from the structure is difficult though somewhat improved as a result of the milling process. In comparison to the first discharge capacity those after ten cycles (Figure 8-6) are low with all materials having a capacity less than 82 mAh/g and the best performance maintained by the BM50 material after the first cycle. The highest charge capacities (Figure 8-7) were also exhibited by the BM50 from the first cycle and within ten cycles the capacities were all below 67 mAh/g.

Cyclic voltammetry of the BM260 material (Figure 8-8) indicates a large peak during the first discharge that is not evident in the subsequent cycle. The shape of the voltammogram for the first cycle is different to that of the subsequent cycles not just for the discharge but also for the charge.

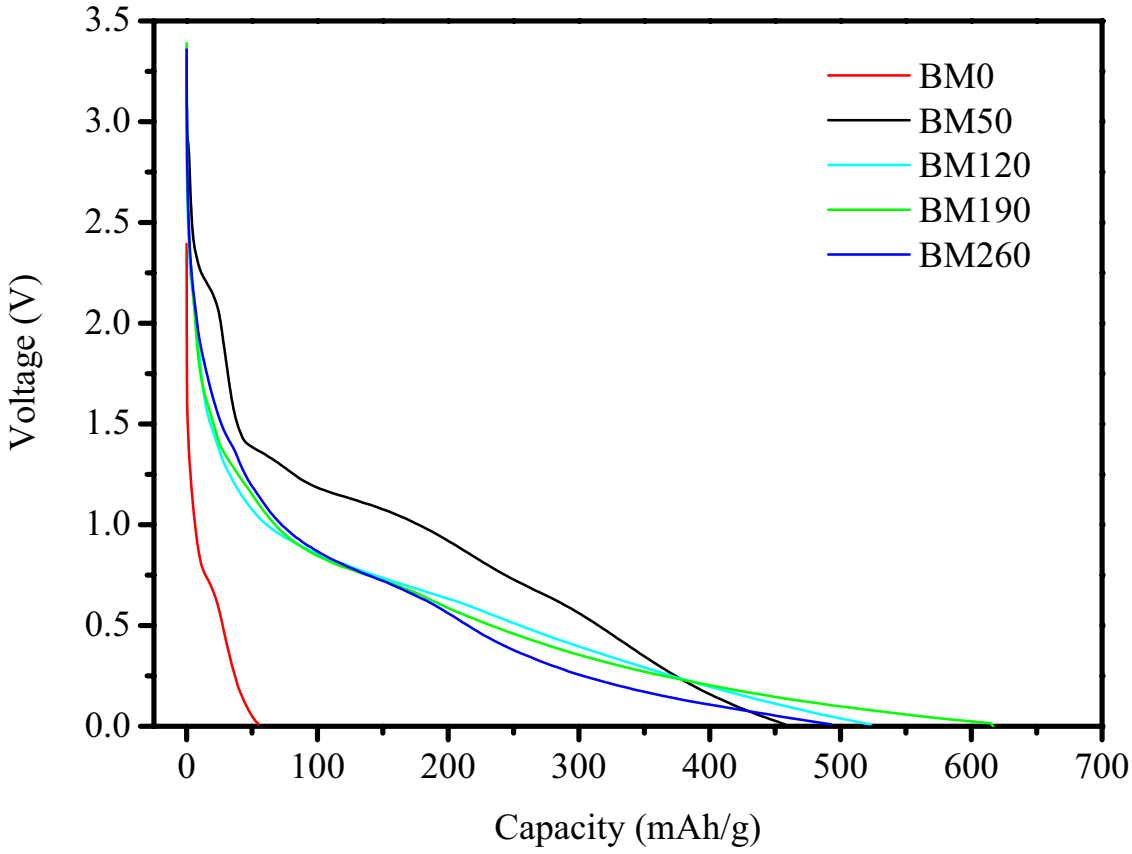

Figure 8-4: First discharge of various arc melted ball milled $FeSi_2$ materials.

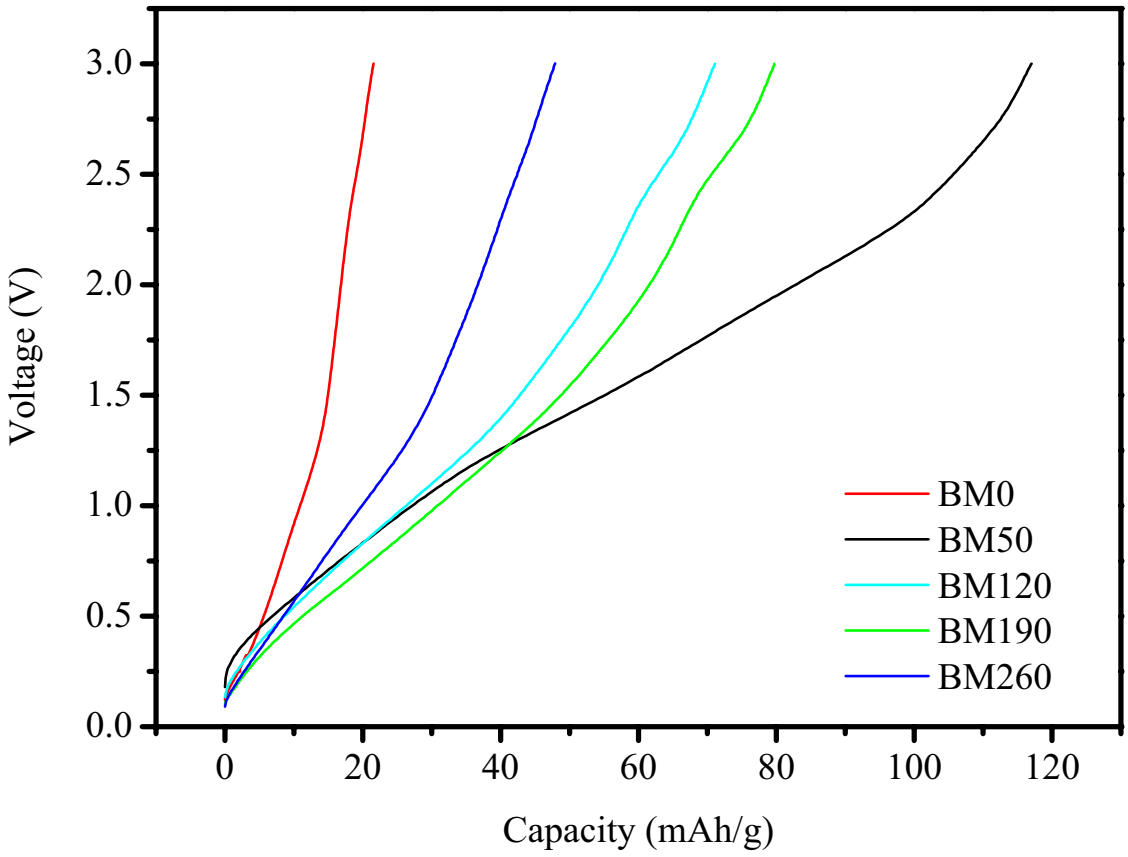

Figure 8-5: First charge of various arc melted ball milled $FeSi_2$ materials.

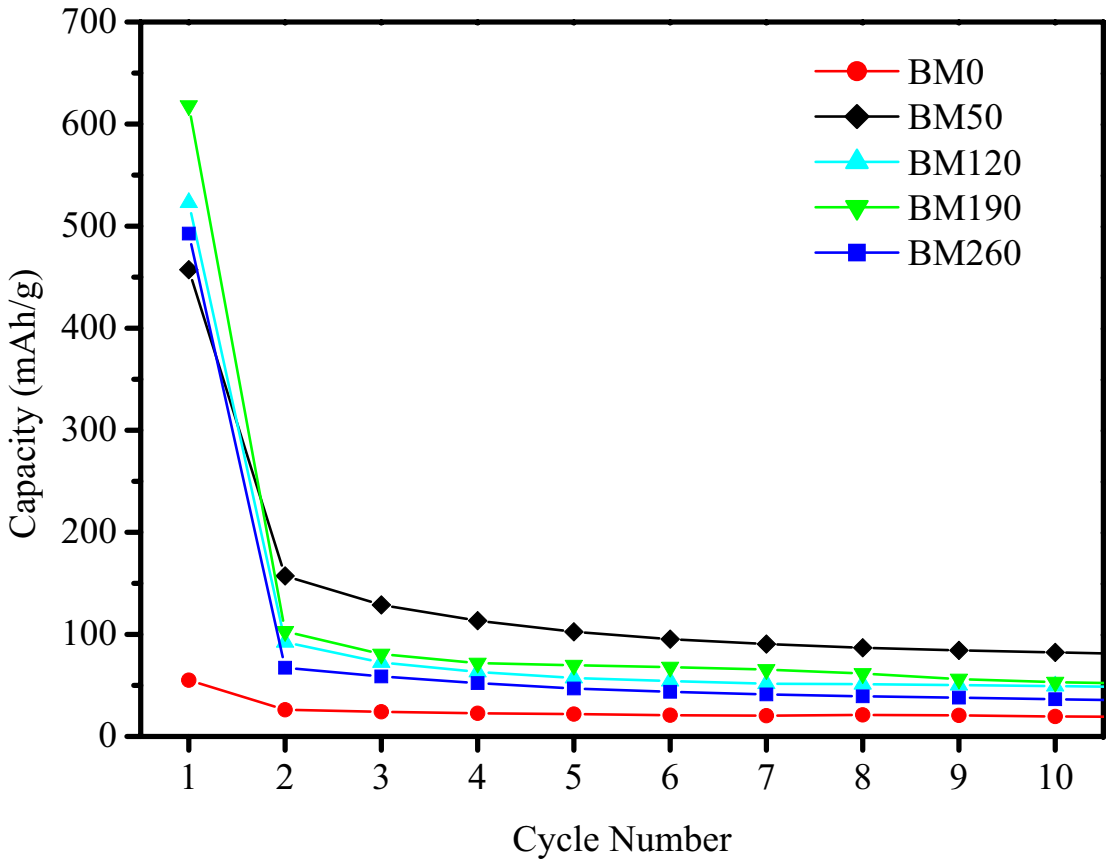

Figure 8-6: Variation of discharge capacity of arc melted $FeSi_2$ with milling time.

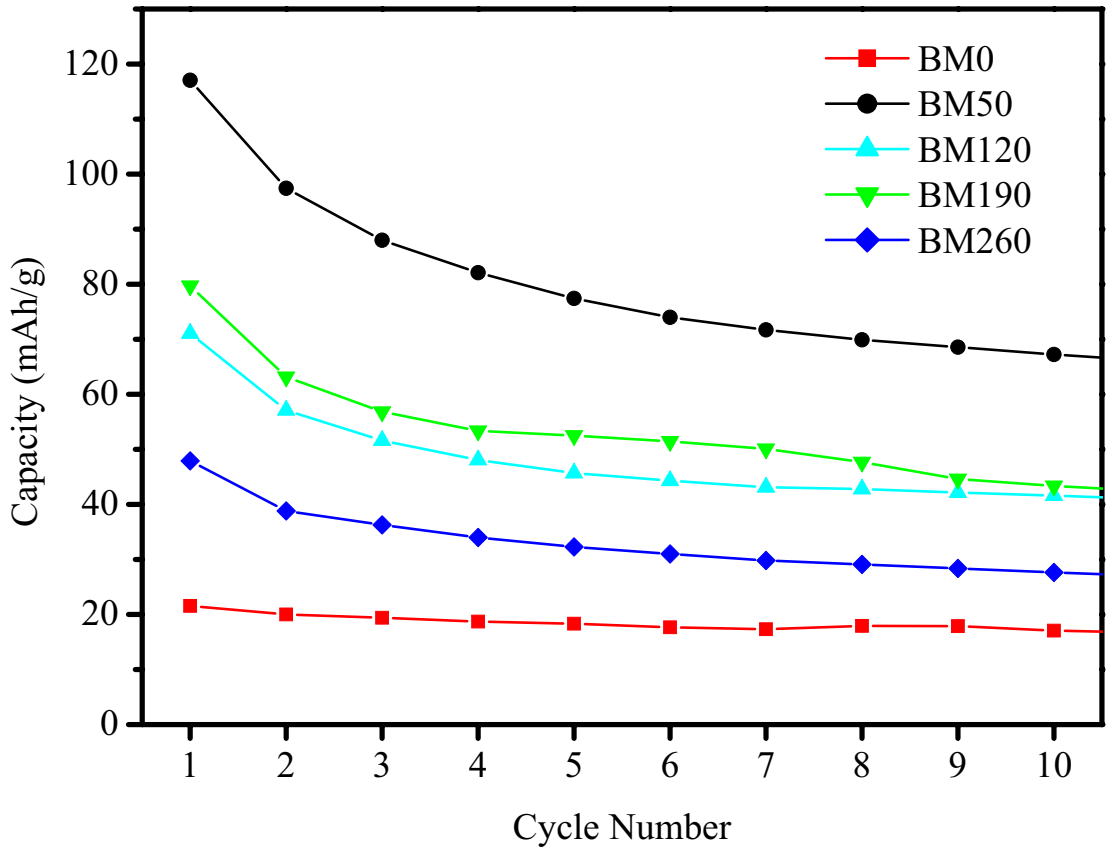

Figure 8-7: Variation of charge capacity of arc melted $FeSi_2$ with milling time.

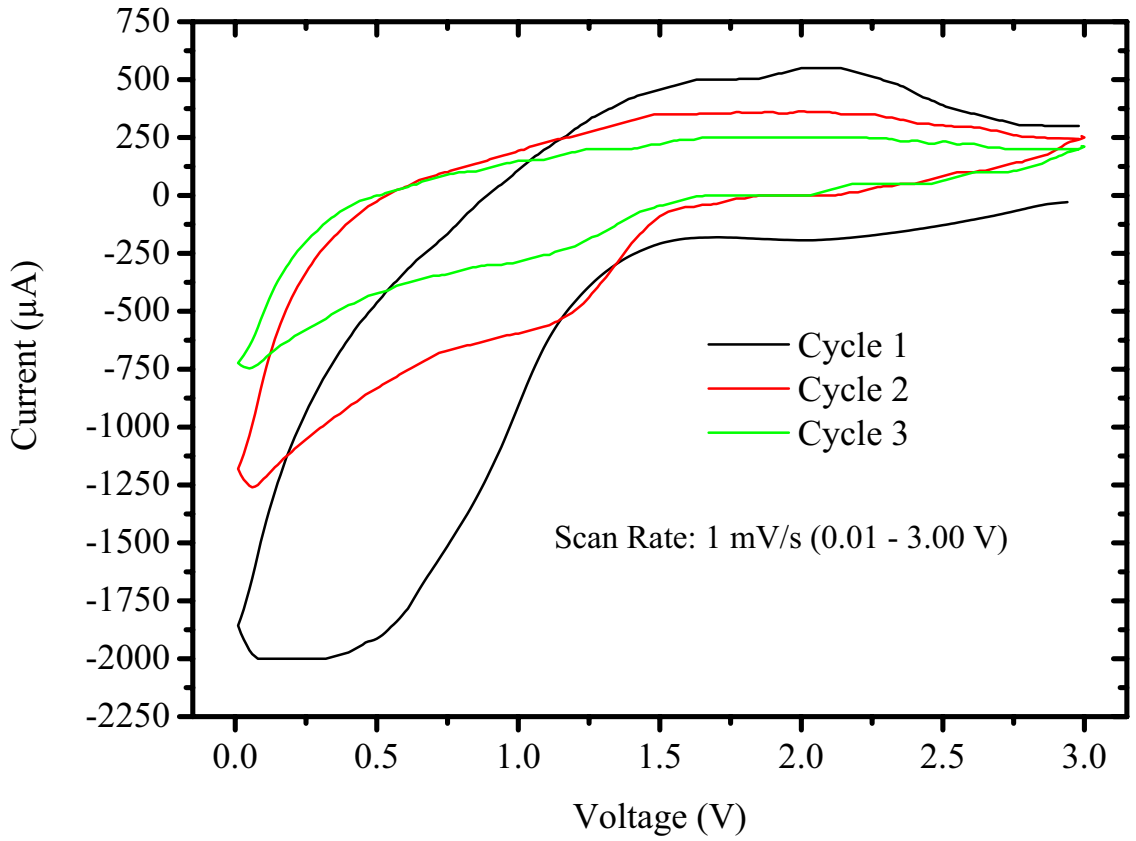

Figure 8-8: Cyclic voltammetry of arc melted $FeSi_2$ BM260 electrode.

8.1.2 Discussion

The broadening of XRD peaks suggest a reduction in crystallite size is occurring though some of the broadening will be attributed to strain as a result of the ball milling process. The crystallite size of the milled materials is thus likely to be under the 40 nm estimate for the FeSi and $FeSi_2$ phases in the unmilled material.

The highest discharge capacity observed of 618 mAh/g is below the theoretical capacity for complete formation of $Li_{22}Si_5$ (2106 mAh/g) and that for the first Li – Si phase ($Li_{12}Si_7$ 820 mAh/g). Most of the silicon is not lithiated to a high degree during the initial discharge limiting the capacity of the material. The initial charge capacities are also low suggesting that even with the low levels of lithium incorporated during the discharge removal of it during the subsequent charge is difficult. The first charge capacity of the BM190 material corresponds to less than 15 % of the first discharge.

Of the other Fe – Si based materials reported in the literature the discharge profiles have the greatest resemblance to the graphite – $Fe_{20}Si_{80}$ materials of Lee et. al. [155] though plateaus are not evident in these materials. The charge profiles are

different however from those reported by Lee where a slow rise to just over 0.5 V and a kick up to the 2.0 V that the materials were tested to was observed.

8.1.3 Conclusions

The electrochemical properties of a Fe – Si material with a composition of $FeSi_2$ though composed of a mixture of FeSi and $FeSi_2$ was examined with a number of ball-milled materials. The charge and discharge capacities were increased as a result of ball milling with the highest discharge capacity demonstrated by BM190 and following the first cycle the best performance was offered by the BM50 material. The charge capacities are much lower than the discharge capacities suggesting that removal of lithium from the structure remains difficult. Modification of the microstructure through further milling and/or annealing operations or a composite with carbon may be able to improve the electrochemical performance of the examined material. The discharge profiles of the ball milled materials were similar to those of the graphite – $Fe_{20}Si_{80}$ materials examined by Lee et. al. though the charge profiles were different.

8.2 Arc Melted + Annealed

The annealed material was milled with 5 mm diameter stainless steel balls utilising a ball to powder ratio of approximately 20:1 (60.01g balls: 2.978g powder). In this case the powder charge did not consist of the alloy alone but of alloy powder with a 10.1 weight percent addition of Vulcan XC-72. Milling was initially carried out for 260 hours without the use of a process control additive with small quantities of powder removed at total milling times of 50, 120, 190 and 260 hours. Ethanol was then added as a process control additive to the level of the top of the balls and milling continued for a further 260 hours. Small quantities of powder were also removed at a number of intervals during this extended milling period at total times of 50, 120, 190 and the final milling time of 260 hours. Where milling continued after powder was removed ethanol was added to the milling jar if required to bring it back up to its initial level.

Powders from the initial milling period of 260 hours and other results derived from their use will be referred to using a prefix of BM followed by the milling time of the powder in hours. Powders from the subsequent milling period of 260 hours and other results derived from their use will be referred to using a prefix of WM followed by the milling time of the powder in hours. Whilst the unmilled material that passed through the 150 μm sieve is referred to as BM0.

The fabrication of electrodes resulted in loadings of approximately 3 mg for BM0 and 1 mg for the remaining samples. The unmilled electrode contained only the carbon that was added during electrode fabrication whilst the milled electrodes also contained the carbon that was added at the start of the milling process. The final composition of the electrodes corresponded to 79 – 86 wt. % alloy powder, 16 – 9 wt. % conductivity additive (Vulcan XC-72) and 5 wt. % PVDF.

8.2.1 Results

8.2.1.1 Structural and Microstructural Characterisation

The XRD pattern of the unmilled material (BM0 in Figure 8-9) corresponded to tetragonal $FeSi_2$ with a couple of FeSi peaks just evident. The peaks of the milled materials do broaden and reduce in intensity suggesting an X-ray amorphous structure particularly after wet milling was commenced.

Full width at half maxima (FWHM) were determined using the Traces program for a number of peaks for $FeSi_2$ in BM0, BM50 and BM260 with the crystalline size estimated using the Scherrer equation (3-6). A value of 0.9 for the K constant was used and instrumental broadening was evaluated according to 3-8. The estimated crystallite sizes for the various peaks and materials are presented in Table 8-3.

In order to examine the effect of milling on the particle size of the $FeSi_2$ powders SEM was used to examine the particle size (Figure 8-10). The particle size decreased from a maximum of 100 μm for BM0 to 1 μm and under for all the ball milled materials. BET analysis reported the specific surface area of the WM260 material as 133 m^2/g.

Table 8-3: Estimated crystallite sizes for annealed $FeSi_2$ material.

Peak	**$FeSi_2$ Crystallite size (nm)**		
	BM0	BM50	BM120
(101)	36	16	17
(102)	41	18	19
(110)	31	20	19

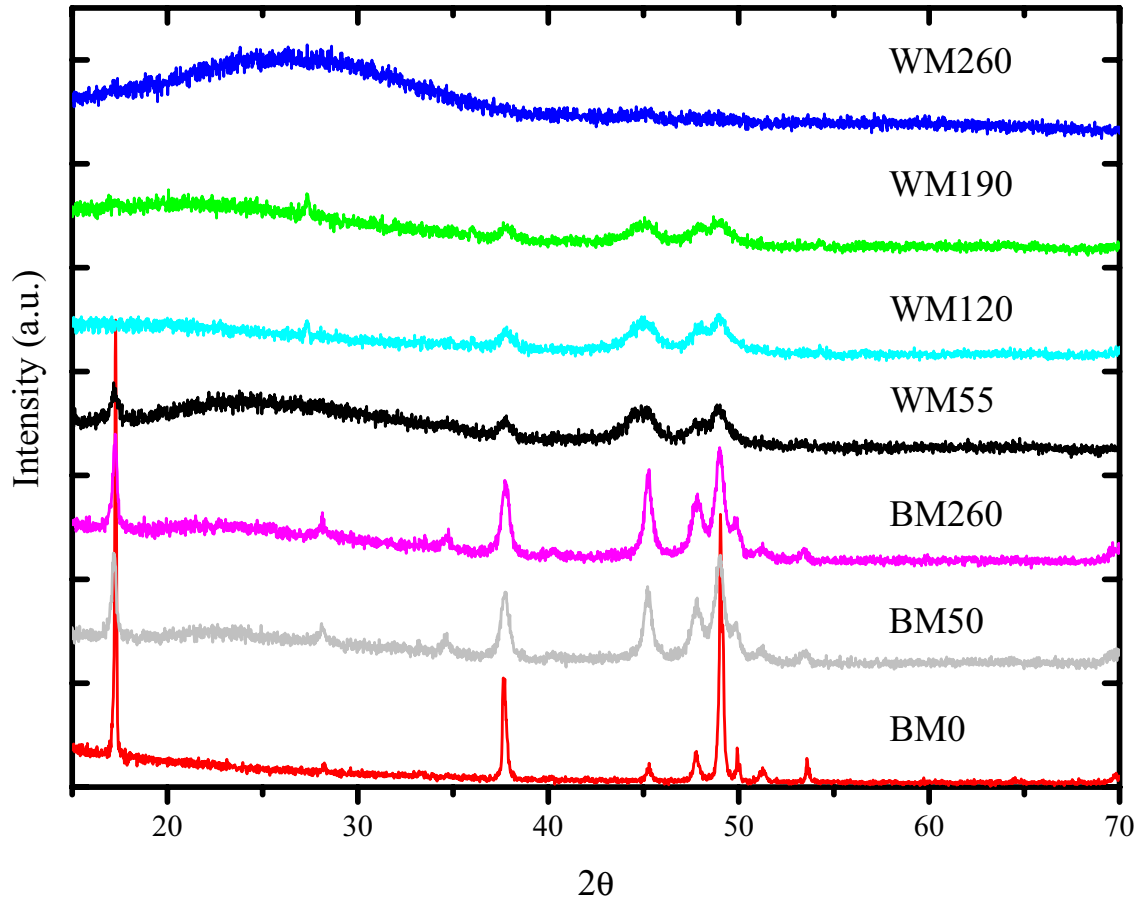

Figure 8-9: XRD patterns of annealed and ball milled $FeSi_2$ materials.

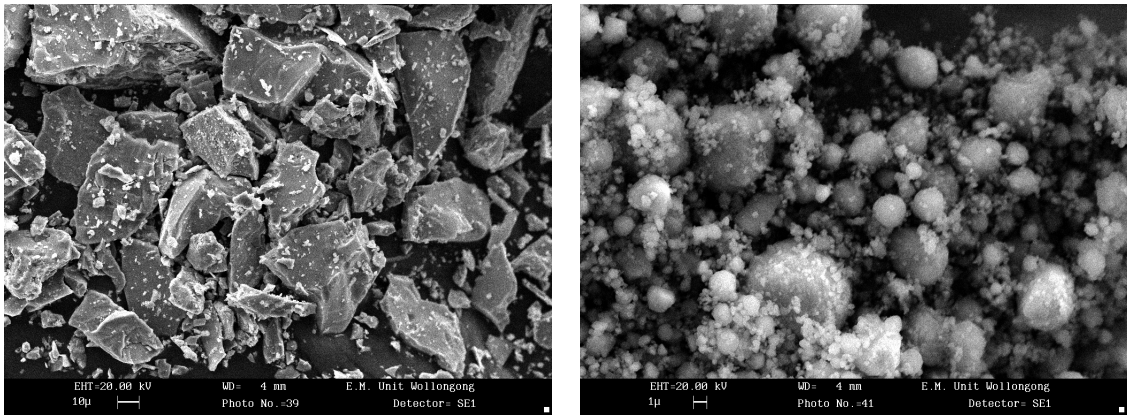

(a) (b)

Figure 8-10: Selected SEM micrographs of ball milled $FeSi_2$ materials: (a) 150µm (b) 260 hours.

8.2.1.2 Electrochemical Characterisation

The electrochemical properties of $FeSi_2$ were evaluated with the use of the prepared alloy electrodes as working electrodes and metallic lithium foils as the counter electrode. The electrochemical properties varied with milling time when examined through constant current charge/discharging (50 µA, 0.01 – 3.00 V). The first discharge

capacity (Figure 8-11) increased with milling time to a maximum of 892 mAh/g for the BM260 material though the capacity of BM190 was only just lower at 890 mAh/g. The discharge profiles however of the materials did vary.

The first charge capacities (Figure 8-12) in contrast reached a maximum of 221 mAh/g for the BM190 material with a small decrease to 210 mAh/g for the BM260 material. As for the discharge the charge profiles also varied though those for the BM120 and BM190 were very similar.

The charge capacities were much lower than the discharge capacities indicating the extraction of lithium from the structure is difficult though improved as a result of the milling process. In comparison to the first discharge capacity those after ten cycles (Figure 8-13) are low with all materials having a capacity less than 137 mAh/g and the best performance maintained by the BM120 material after the first cycle. The highest charge capacities (Figure 8-14) were also exhibited by the BM120 following the first cycle and within ten cycles the capacities were all below 112 mAh/g.

Cyclic voltammetry of the BM260 material (Figure 8-15) does not indicate any peaks as such during the first three cycles. The shape of the voltammogram for the first cycle is different to those of the subsequent cycles not just for the discharge but also for the charge.

8.2.2 Discussion

The broadening of XRD peaks suggest a reduction in crystallite size is occurring though some of the broadening will be attributed to strain as a result of the ball milling process. The crystallite size of the remilled materials is thus likely to be under the 19 nm estimate for the $FeSi_2$ phases in the BM120 material compared to 41 nm for the unmilled material.

The highest discharge capacity observed of 892 mAh/g is below the theoretical capacity for complete formation of $Li_{22}Si_5$ (2106 mAh/g) and between that of the two lithium – silicon phases ($Li_{12}Si_7$ and Li_7Si_3) with the lowest lithium content (820 – 1117 mAh/g). Most of the silicon is not lithiated to a high degree during the initial discharge limiting the capacity of the material. The initial charge capacities are also low suggesting that even with the low levels of lithium incorporated during the discharge removal of it during the subsequent charge is difficult. The first charge capacity of the BM190 material corresponds to less than 25 % of the first discharge.

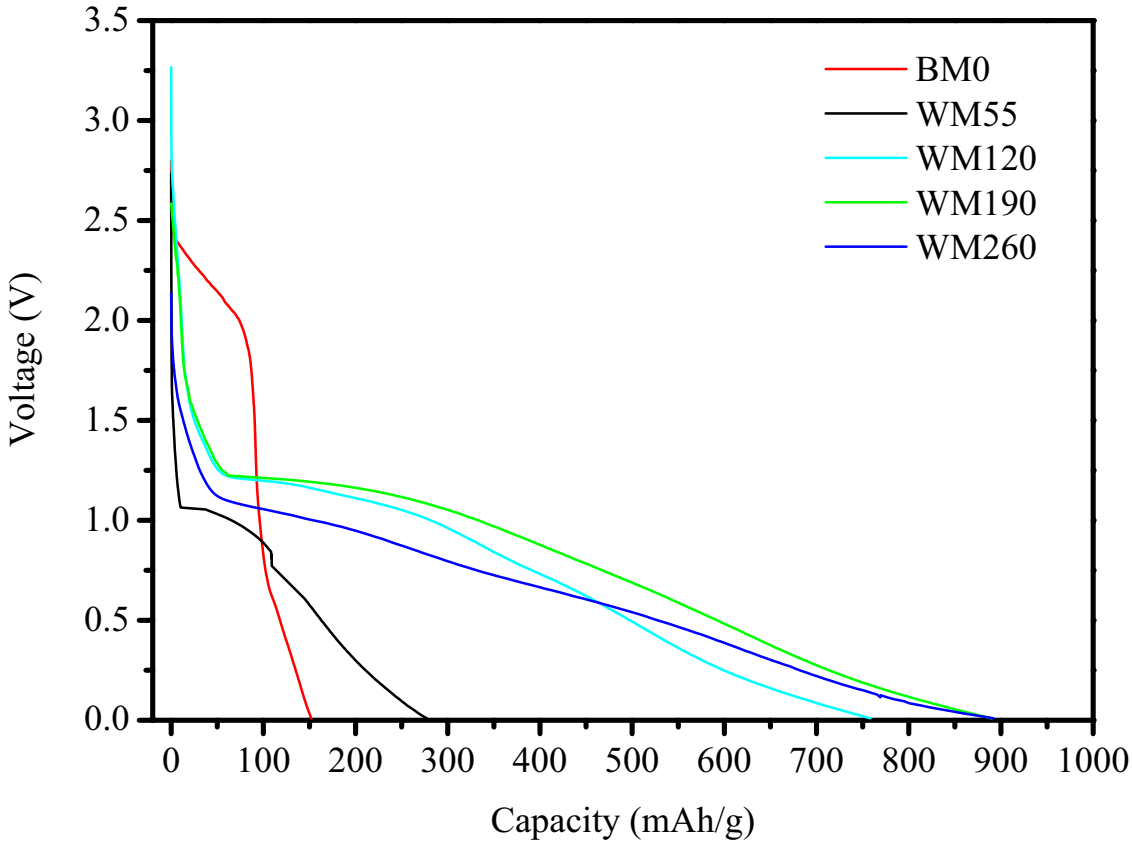

Figure 8-11: First discharge of various annealed ball milled $FeSi_2$ materials.

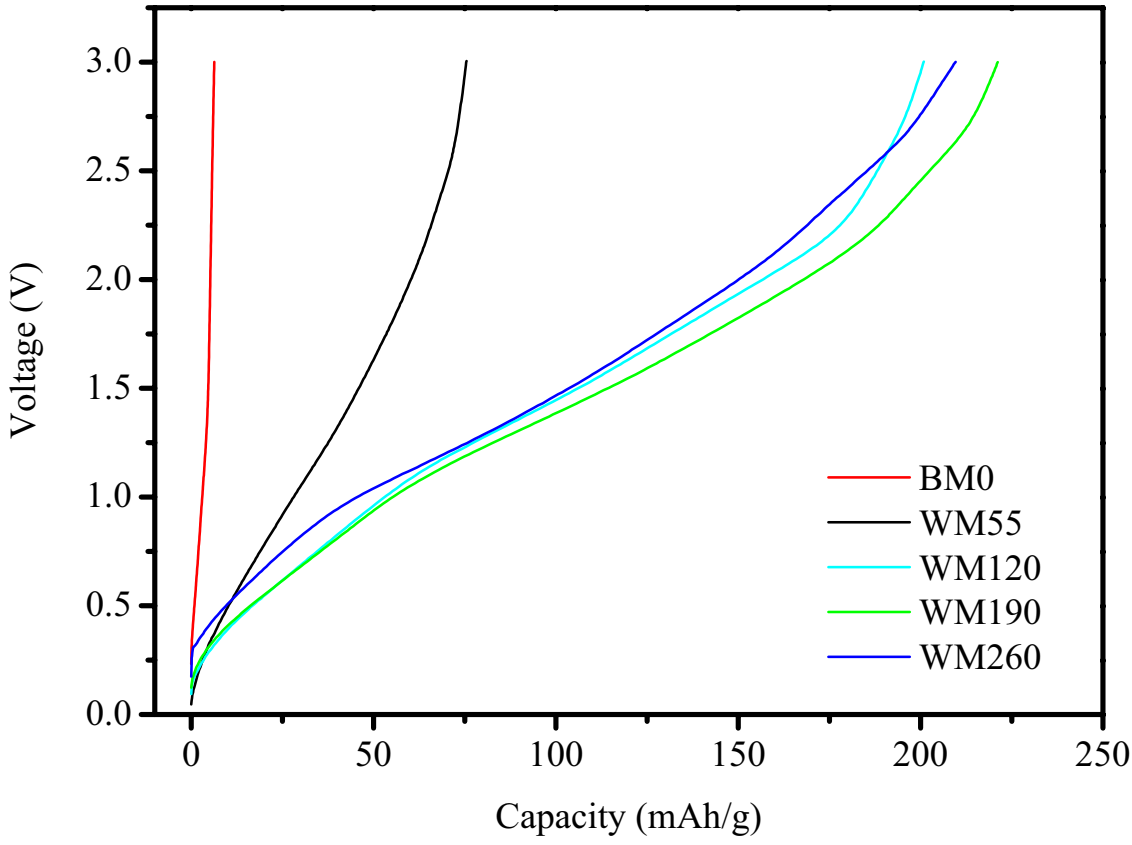

Figure 8-12: First charge of various annealed ball milled $FeSi_2$ materials.

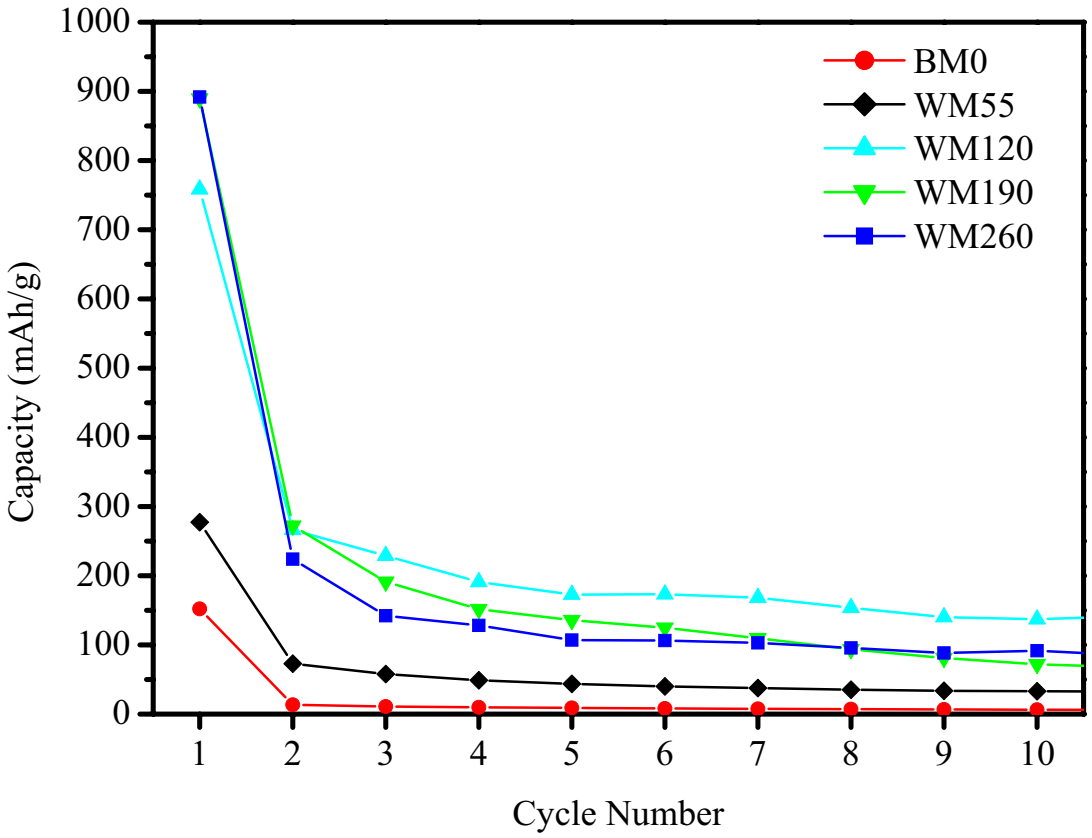

Figure 8-13: Variation of discharge capacity of annealed $FeSi_2$ with milling time.

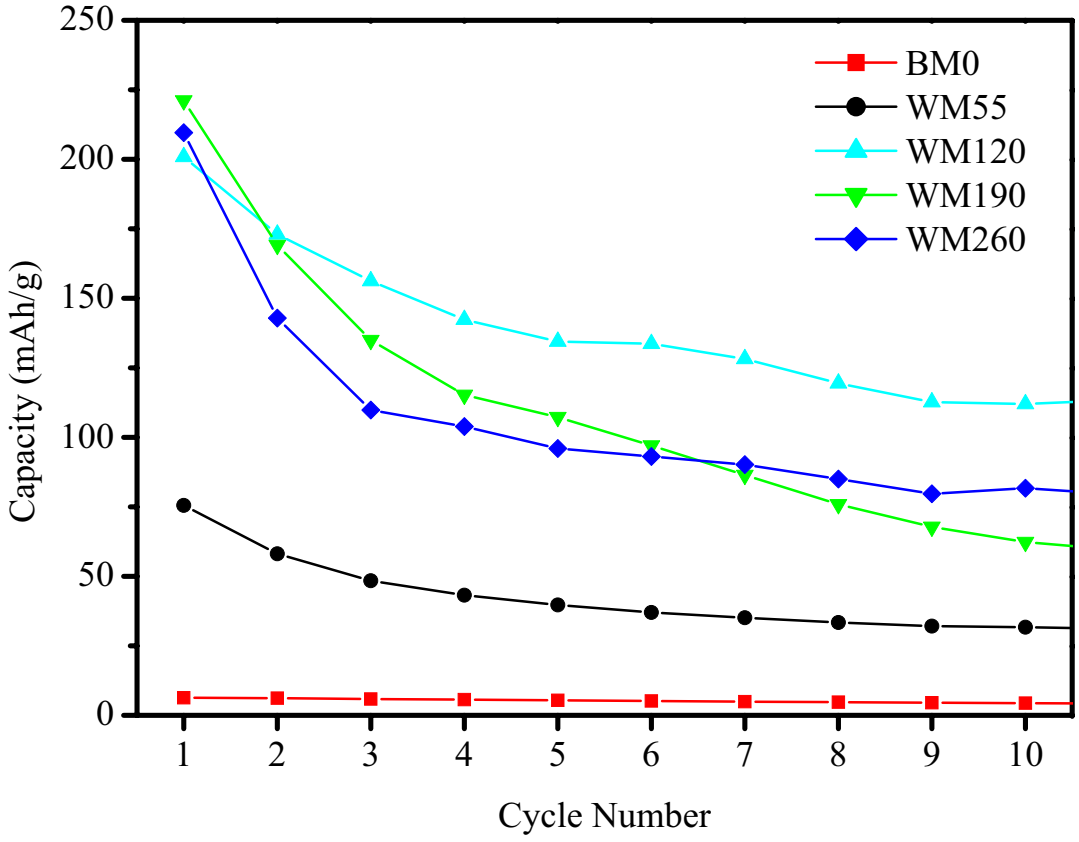

Figure 8-14: Variation of discharge capacity of annealed $FeSi_2$ with milling time.

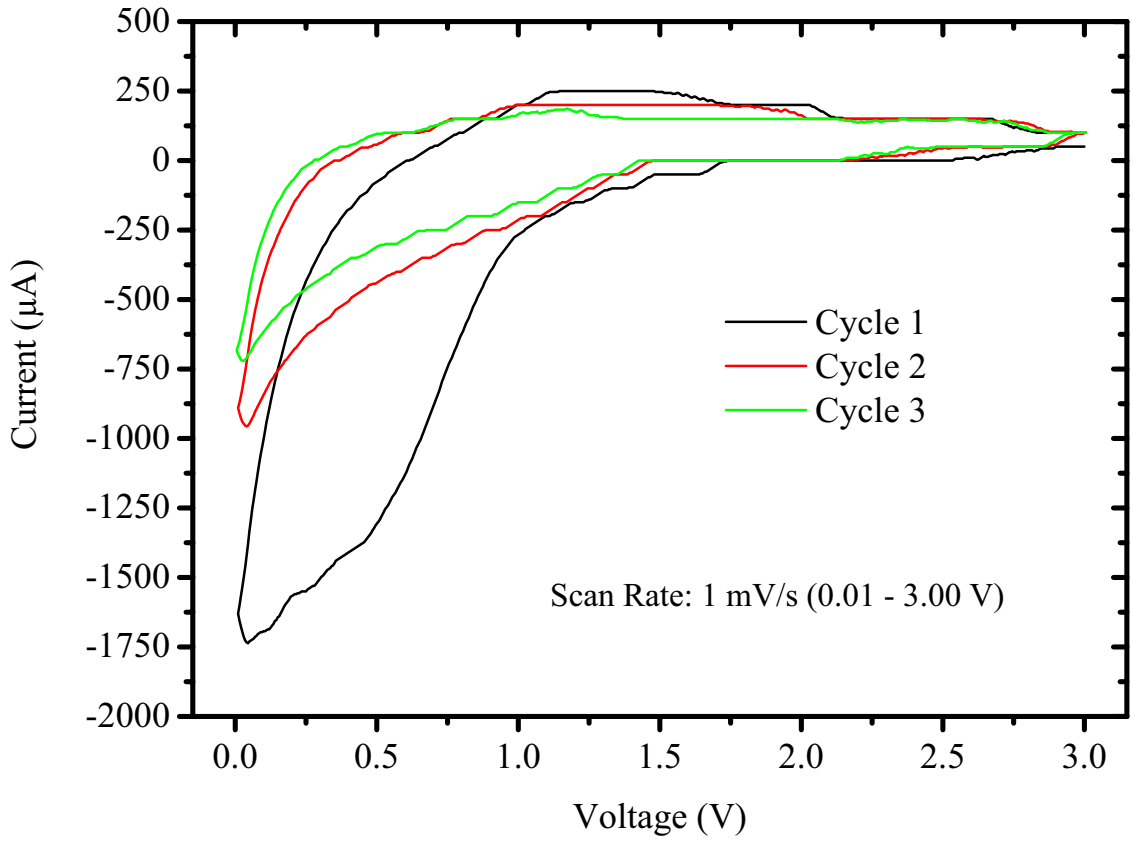

Figure 8-15: Cyclic voltammetry of annealed $FeSi_2$ BM260 electrode.

Of the other Fe – Si based materials reported in the literature the discharge profiles have the greatest resemblance to the graphite – $Fe_{20}Si_{80}$ materials of Lee *et. al.* [155]. The plateau voltages are however higher in this case at over 1.0 V compared to under 1.0 V observed by Lee *et. al.*. The charge profiles are different however from those reported by Lee where a slow rise to just over 0.5 V and a kick up to the 2.0 V that the materials were tested to was observed.

8.2.3 Conclusions

The electrochemical properties of a Fe – Si material with a composition of $FeSi_2$ though composed of a mixture of FeSi and $FeSi_2$ was examined with a number of ball-milled materials. The charge and discharge capacities were increased as a result of ball milling with the highest discharge capacity demonstrated by BM190 and following the first cycle the best performance was offered by the BM120 material. The charge capacities are much lower than the discharge capacities suggesting that removal of lithium from the structure remains difficult. Modification of the microstructure through further milling and/or annealing operations or a composite with carbon may be able to improve the electrochemical performance of the examined material. The discharge

profiles of the ball milled materials were similar to those of the graphite – $Fe_{20}Si_{80}$ materials examined by Lee et. al. though the charge profiles were different.

8.3 Conclusions

The electrochemical properties of arc melted $FeSi_2$ and annealed $FeSi_2$ materials were examined with a variety of materials produced using ball milling. The highest discharge capacities observed in the annealed (892 mAh/g) and arc melted (618 mAh/g) materials differed and so did other properties.

The first discharge capacity of the unmilled annealed material (152 mAh/g) was over twice that of the unmilled arc melted material (55 mAh/g). The crystallite size of $FeSi_2$ in the unmilled annealed material and unmilled arc melted material were both estimated as 40 nm. Given such estimates it seems that during the annealing process that the FeSi phase was consumed rather than significant growth of the $FeSi_2$ phase occurring.

The capacities of the annealed materials are higher than those of the arc melted materials. The annealed materials were milled with carbon and for a total time of over 500 hours with the specific surface area of the WM260 material (133 m^2/g) still lower than that of the arc melted BM260 material (180 m^2/g).

The discharge profiles of the arc melted and annealed materials were however similar to those of the graphite – $Fe_{20}Si_{80}$ materials of Lee et. al. [155] but the charge profiles were different. The highest discharge capacities of both the arc melted and annealed materials suggested that the silicon in the materials was not lithiated to a high degree during the initial discharge. The charge capacities were also much lower than the initial discharge suggesting that significant amounts of lithium are retained in the structure during the charge as it is not easily extracted from the structure.

Chapter 9 Bi-2212 based

A number of studies have investigated the electrochemical insertion of lithium into $Bi_2Sr_2CaCu_2O_{8+\delta}$ (Bi-2212) superconductors [234-238] using compressed powder pellets with no conductivity additive. A number of stoichiometries of the 2212 phase were examined in these investigations and a range of electrochemical properties reported. The amount of lithium inserted into the structure varied between the investigations up to a reported maximum of two moles per mole of Bi-2212 [235]. Bi-2212 was also suggested as an electrode material for reversible lithium cells [237]. The lithium diffusion coefficients for the two investigations where it was determined ranged from 10^{-7} cm^2 s^{-1} [237] to 10^{-13} cm^2 s^{-1} [234]. Two different reaction mechanisms were also proposed the first was the insertion of lithium between the bismuth – oxygen planes [236, 238] and the second was the substitution of lithium with copper [238]. Strobel *et. al.* [238] in fact proposed that the insertion reaction (9-1) was reversible up to a lithium content of 0.15 mole whilst the substitution reaction (9-2) occurred at higher lithium content. The presence of copper oxide was not however detected from the higher lithium contents.

Taking the maximum reported lithium content of two moles into account the theoretical capacity of $Bi_2Sr_2CaCu_2O_8$ would only be 60 mAh/g due to the large molecular weight of the Bi-2212 phase. Assuming the same maximum lithium content is realised for $Bi_2Sr_2Ca_{0.3}Y_{0.7}Cu_2O_8$ the theoretical capacity is just lower at 58 mAh/g.

$$Bi_2Sr_2CaCu_2O_{8+\delta} + xLi^+ + xe^- \rightarrow Li_xBi_2Sr_2CaCu_2O_{8+\delta} \quad \textbf{9-1}$$

$$Bi_2Sr_2CaCu_2O_{8+\delta} + xLi^+ + xe^- \rightarrow Bi_2Sr_2Ca(Cu_{2-x}Li_x)O_{8+\delta-x} + xCuO \quad \textbf{9-2}$$

9.1 $Bi_2Sr_2Ca_1Cu_2O_{8+\delta}$

Sintered material that had been hand ground in a mortar and pestle was milled in a Pulverisette-5 planetary ball mill at a speed of 160 rpm in a steel-milling vessel. The milling vessel had an internal diameter of 85 mm and volume of approximately 140 cm^3. The milling media were 5 mm diameter stainless steel balls utilised with a ball to powder ratio of approximately 20:1 (77.631 g balls: 3.874 g powder). The powder charge did not consist of the Bi-2212 material alone as it consisted of Bi-2212 powder with a 10.0 weight percent addition of Vulcan XC-72. Ethanol was also added as a

process control additive to the level of the top of the balls. Powder was removed at a number of intervals in small quantities up to a total milling time of 190 hours. Powder was removed at total milling times of 50, 120 and the final milling time of 190 hours. Where milling continued after powder was removed ethanol was added to the milling jar if required to bring it back up to its initial level. The various powders and other results derived from their use will be referred to using a prefix of BM followed by the milling time of the powder in hours with the unmilled material referred to as BM0.

The fabrication of electrodes resulted in loadings of approximately 1 mg for all the samples. The final composition of the electrodes corresponded to 75 wt. % powder, 20 wt. % conductivity additive and 5 wt. % PVDF.

9.1.1 Results

9.1.1.1 Structural and Microstructural Characterisation

XRD of the material following the first sintering operation indicated that the Bi-2212 phase had started to form though a number of other phases were also present (Figure 9-1). Following the second sintering operation Bi-2212 was the main phase (JCPDS card 41-317) though other phases were present in small quantities. On ball milling of the Bi-2212 material significant broadening of the peaks is not evident however the intensity of the peaks are reduced and diminish into the background (Figure 9-2).

In order to examine the effect of milling on the particle size of the Bi-2212 powders SEM was used to examine the particle size (Figure 9-3). Only the BM0 material had a particle size of greater than 1μm with a particle size of 2 μm. BET analysis reported the specific surface area of the BM190 material as 30 m^2/g.

9.1.1.2 Electrochemical Characterisation

The electrochemical properties of Bi-2212 were evaluated with the use of the prepared oxide electrodes as working electrodes and metallic lithium foils as the counter electrode. The electrochemical properties determined from constant current charge/discharging (50 μA, 0.70 – 3.00 V) of Bi-2212 electrodes varied with milling time. The first discharge capacity (Figure 9-4) was highest for the unmilled material (441 mAh/g) whilst the milled materials had the same capacity of 280 mAh/g though the discharge profiles did vary.

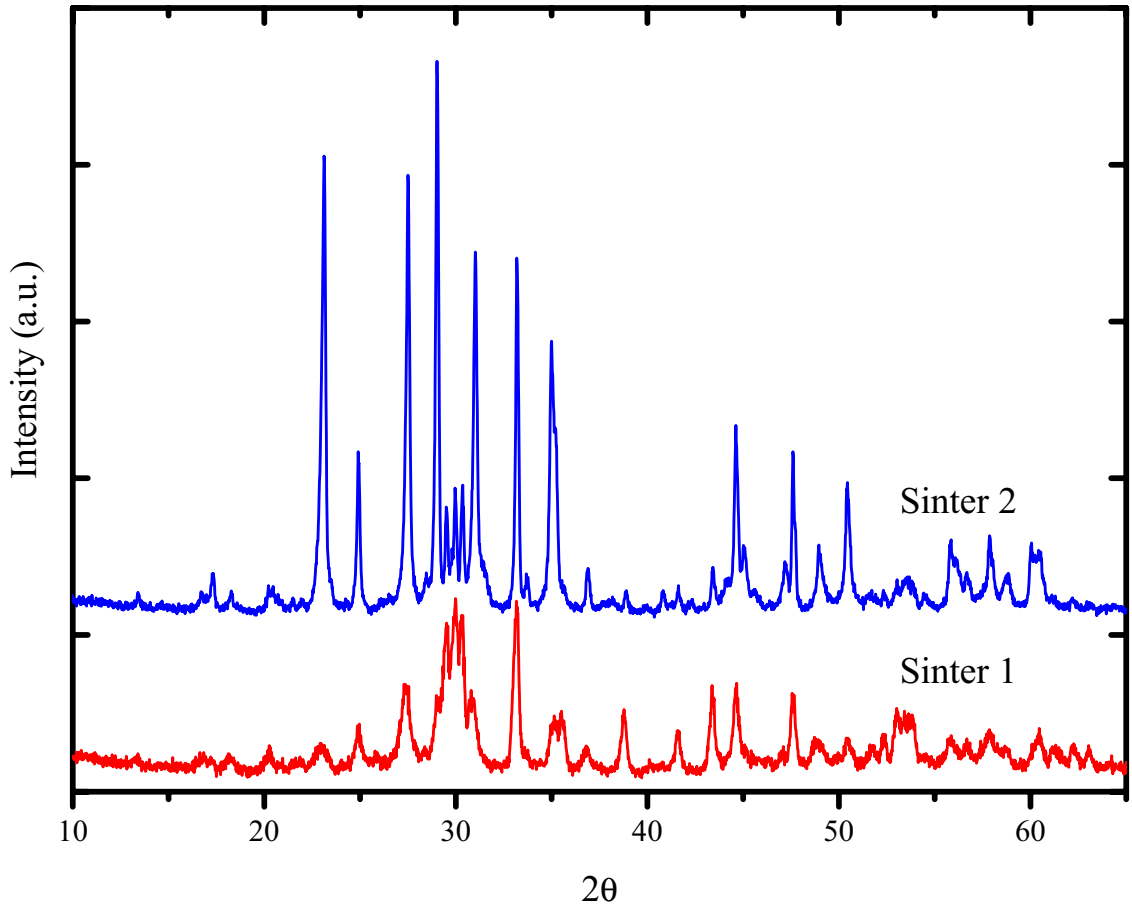

Figure 9-1: XRD patterns of $Bi_2Sr_2CaCu_2O_8$ materials after sintering operations.

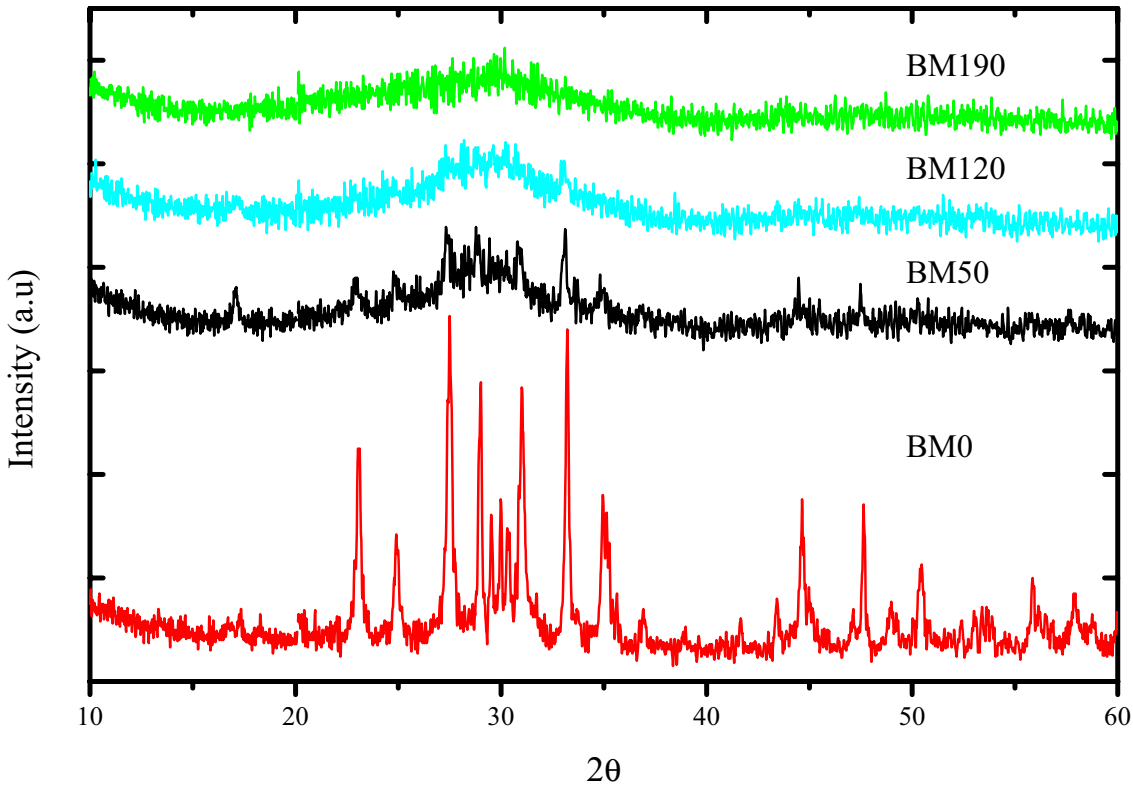

Figure 9-2: XRD patterns of ball milled $Bi_2Sr_2CaCu_2O_8$ materials.

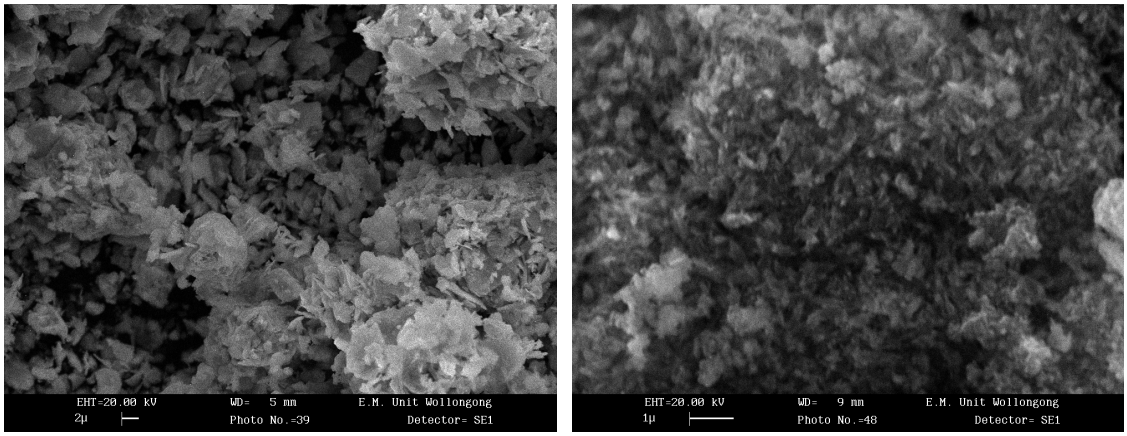

(a) (b)

Figure 9-3: SEM micrographs of selected $Bi_2Sr_2CaCu_2O_8$ ball milled powder samples: (a) unmilled, (b) 190 hours.

The first charge capacity (Figure 9-5) was also highest for the unmilled material (77 mAh/g) with the capacities of the milled materials between 64 and 71 mAh/g though the charge profiles varied. Following the second cycle however the charge capacities (Figure 9-7) were highest for the BM120 material but were under 42 mAh/g within 10 cycles. The discharge capacities (Figure 9-6) on the other hand were highest for the BM190 following the first discharge and were under 42 mAh/g within 10 cycles.

Extraction of lithium from the Bi-2212 structure is difficult as the charge capacities are much lower than the discharge capacities in the initial cycles. Although ball milling reduced the initial discharge capacity the capacity remained higher after the first cycle in the milled materials. The situation was similar with the charge capacity though the capacity of BM0 was higher than that of BM50 for the first four cycles. Differential capacity plots of the first charge and discharge of BM190 (Figure 9-8) showed a distinct peak at 1.75 V during discharge and a single broad peak at 2.7 V during the charge.

9.1.2 Discussion

The Bi-2212 material produced through spray drying and modified by ball milling with carbon demonstrated that the microstructure has an important influence on the electrochemical properties of the material. The discharge capacities observed were much higher than the theoretical capacity of 60 mAh/g based on the reaction of one mole of Bi-2212 with two moles of lithium. Differential capacity plots of BM190 indicate the occurrence of at least one reaction during the first charge and discharge.

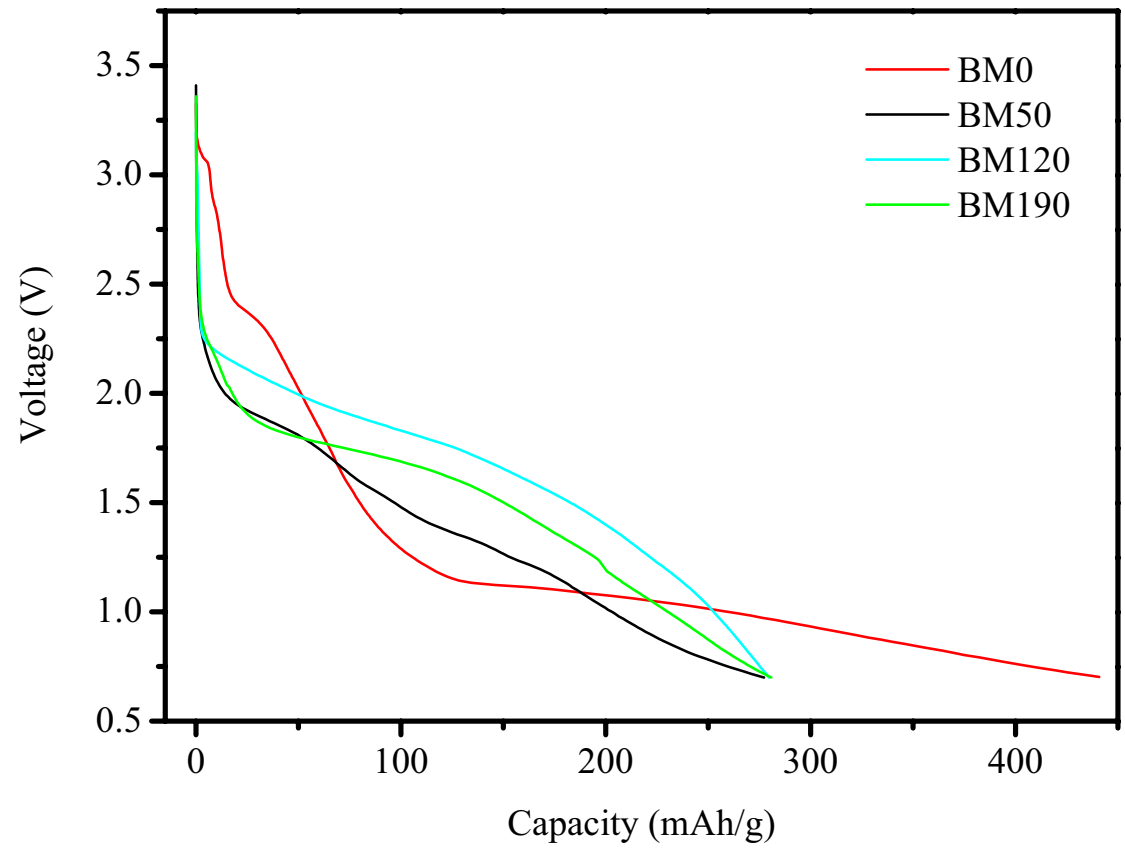

Figure 9-4: First discharge of various ball milled $Bi_2Sr_2CaCu_2O_8$ materials.

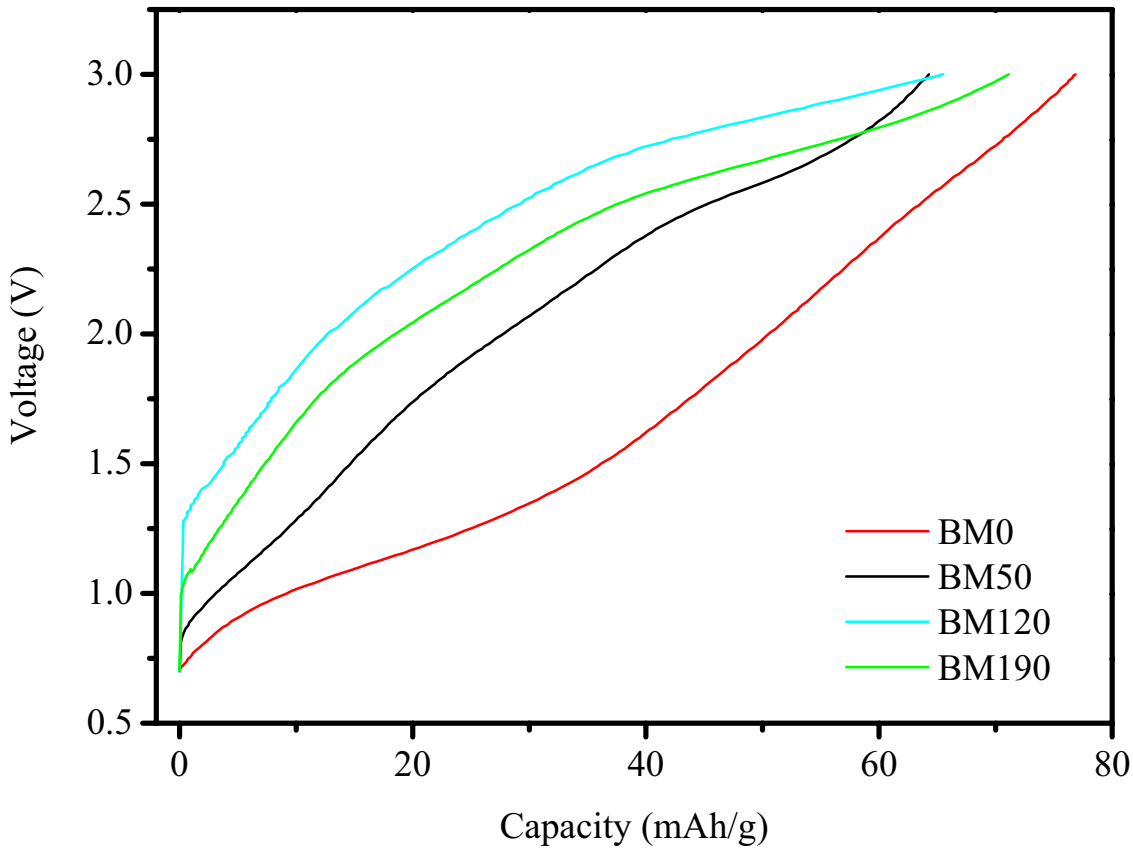

Figure 9-5: First charge of various ball milled $Bi_2Sr_2CaCu_2O_8$ materials.

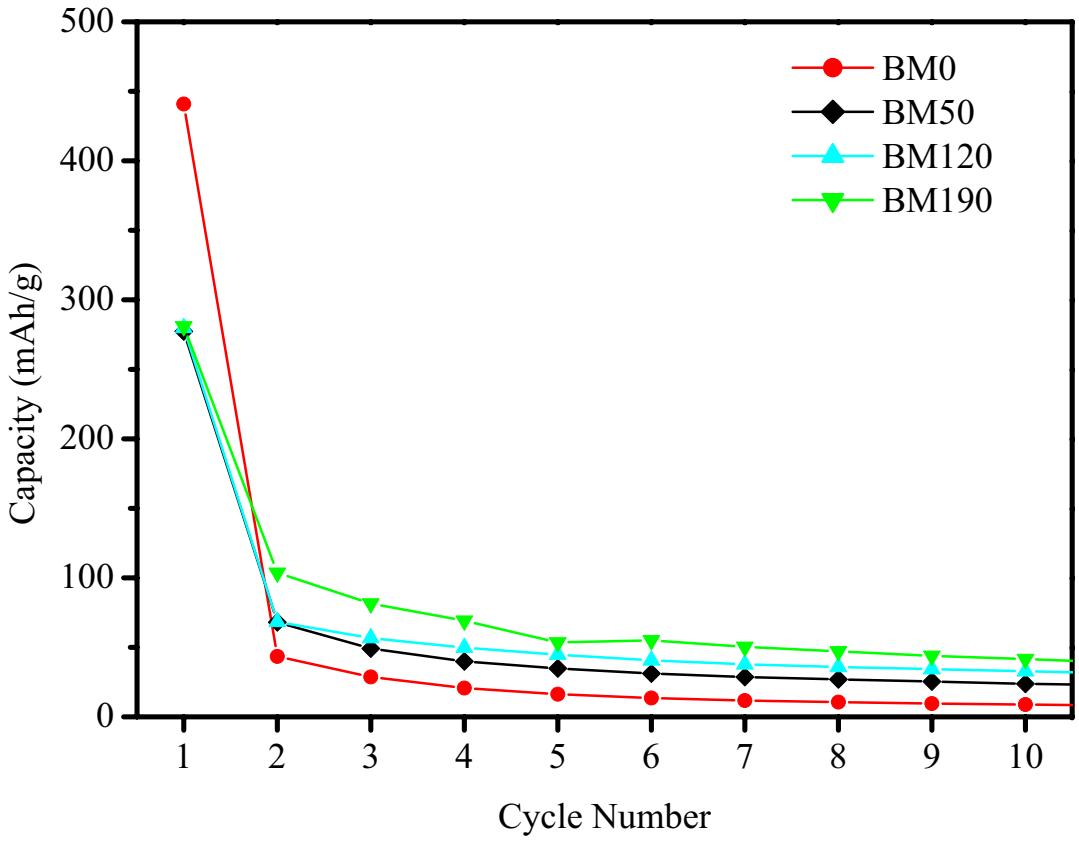

Figure 9-6: Variation of discharge capacity of $Bi_2Sr_2CaCu_2O_8$ with milling time.

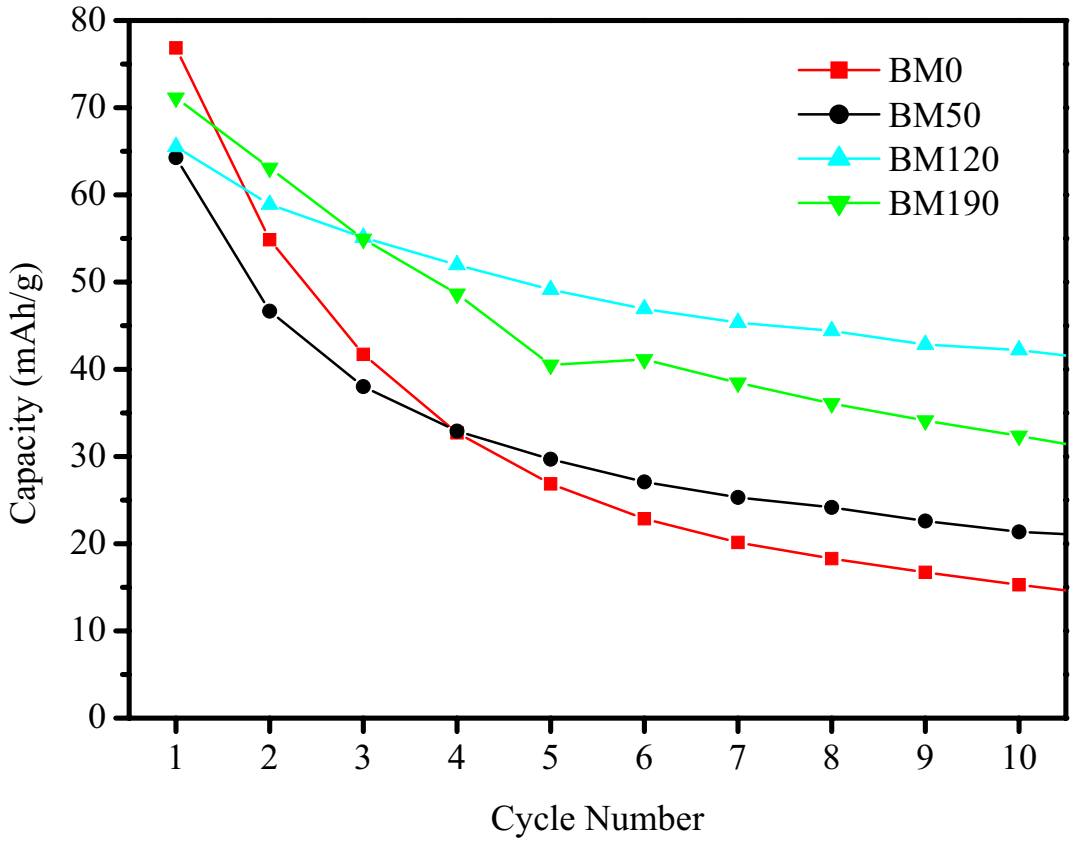

Figure 9-7: Variation of charge capacity of $Bi_2Sr_2CaCu_2O_8$ with milling time.

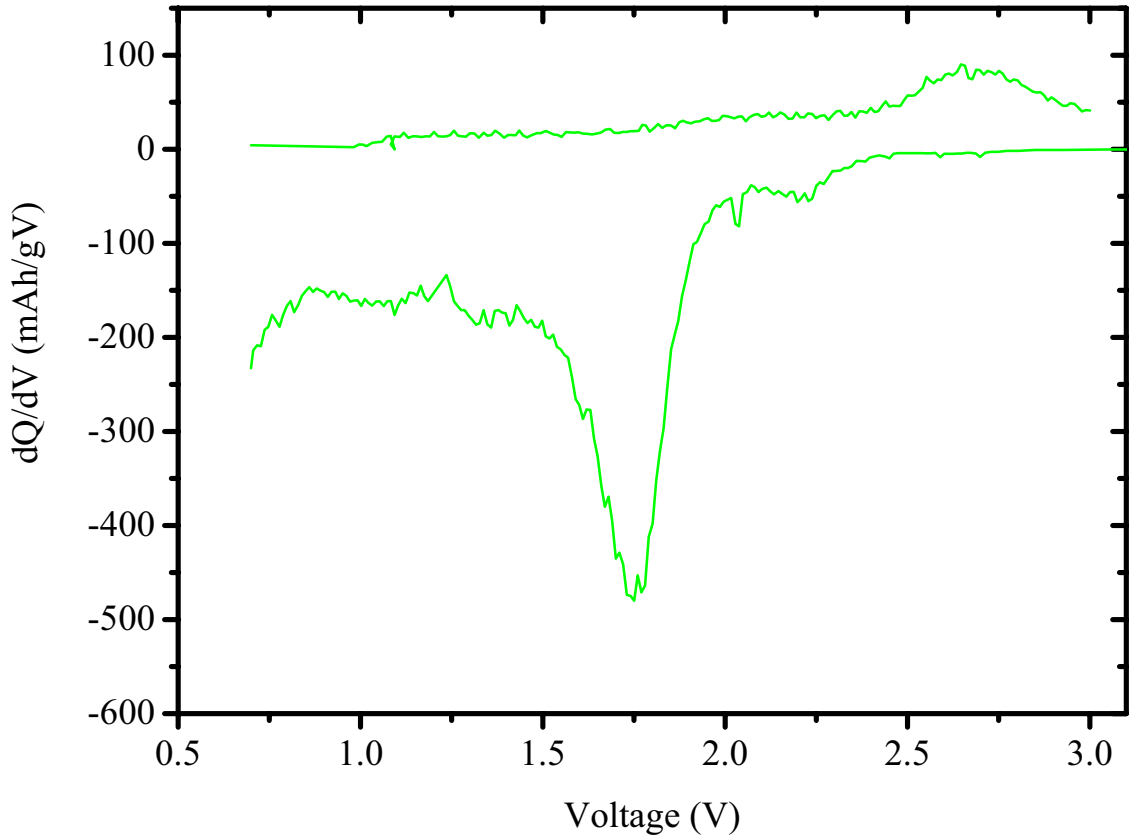

Figure 9-8: Differential capacity plot for the first cycle of BM190 $Bi_2Sr_2CaCu_2O_8$.

Given the discharge capacities observed were much higher than previously reported there is still uncertainty over the reaction mechanism with lithium and the degree to which it occurs. The use of pellets in previous investigations compared to the pasted film electrodes utilised here may provide some explanation to the differences observed.

9.1.3 Conclusions

The Bi-2212 materials produced have demonstrated like many other oxide materials an electrochemical interaction towards lithium. There is still uncertainty over the reaction mechanism whether it is an insertion of substitution reaction. In either case the degree to which it occurs was greater than had been previously reported. Previous reports had only mentioned the incorporation of two moles of lithium per mole of Bi-2212 equating to a capacity of only 60 mAh/g as a result of the high molecular weight of the Bi-2212 material.

9.2 $Bi_2Sr_2Ca_{0.3}Y_{0.7}Cu_2O_{8+\delta}$

Sintered material that had been hand ground in a mortar and pestle was milled in a Pulverisette-5 planetary ball mill at a speed of 160 rpm in a steel-milling vessel. The milling vessel had an internal diameter of 85 mm and volume of approximately 140 cm^3. The milling media were 5 mm diameter stainless steel balls utilised with a ball to powder ratio of approximately 20:1 (62.934 g balls: 3.144 g powder). The powder charge did not consist of the Bi-2212 material alone as it consisted of Bi-2212 powder with a 9.6 weight percent addition of Vulcan XC-72. Ethanol was also added as a process control additive to the level of the top of the balls. Powder was removed at a number of intervals in small quantities up to a total milling time of 190 hours. Powder was removed at total milling times of 50, 120 and the final milling time of 190 hours. Where milling continued after powder was removed ethanol was added to the milling jar if required to bring it back up to its initial level. The various powders and other results derived from their use will be referred to using a prefix of BM followed by the milling time of the powder in hours with the unmilled material referred to as BM0.

The fabrication of electrodes resulted in loadings of approximately 1 mg for all the samples. The final composition of the electrodes corresponded to 75 wt. % powder, 20 wt. % conductivity additive and 5 wt. % PVDF.

9.2.1 Results

9.2.1.1 Structural and Microstructural Characterisation

XRD of the material following the first sintering operation indicated that the Bi-2212 phase was already well formed though other minor phases were also present (Figure 9-9). Following the second sintering operation the Bi-2212 phase (JCPDS card 41-317) was also dominant with lower amounts of other phases. On ball milling the peaks did broaden though still remained evident above the background (Figure 9-10).

In order to examine the effect of milling on the particle size of the Bi-2212 powders SEM was used and the BM0 material had a particle size of 1 μm whilst the milled materials all had a particle size under 1 μm. BET analysis reported the specific surface area of the BM190 material as 63 m^2/g.

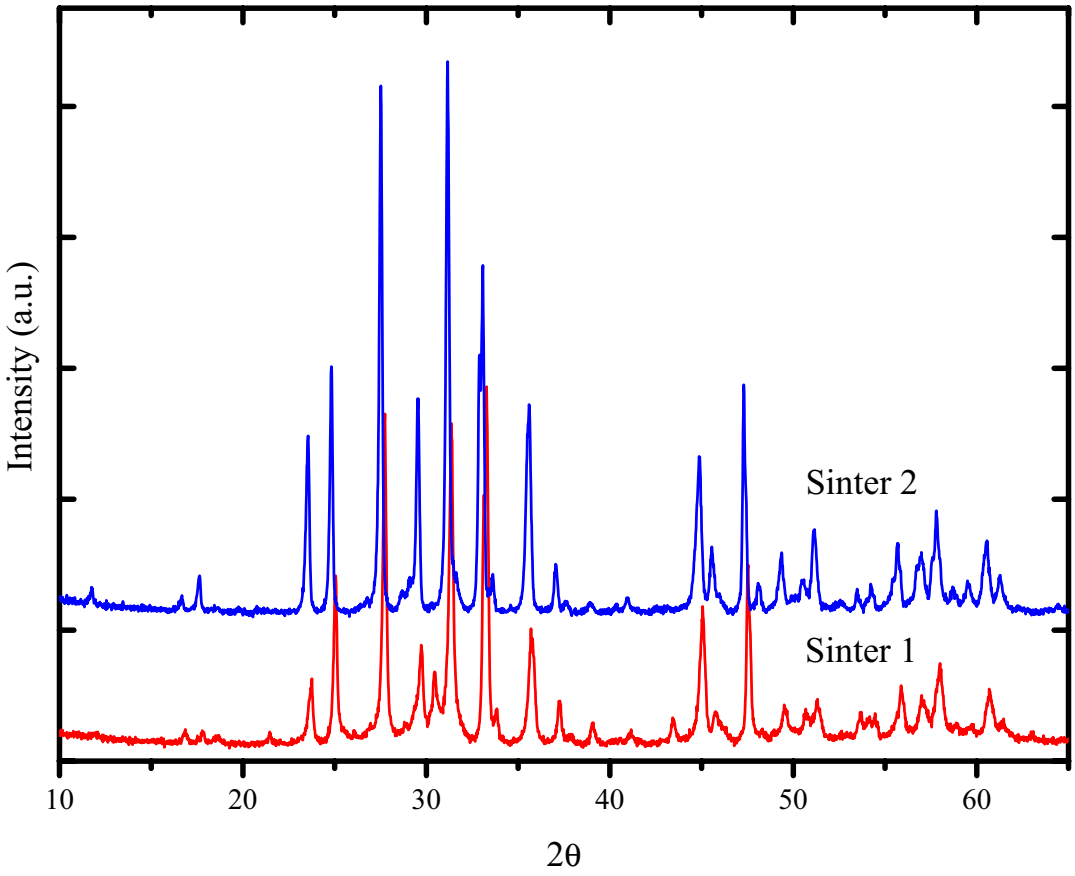

Figure 9-9: XRD patterns of $Bi_2Sr_2Ca_{0.3}Y_{0.7}Cu_2O_8$ materials after sintering.

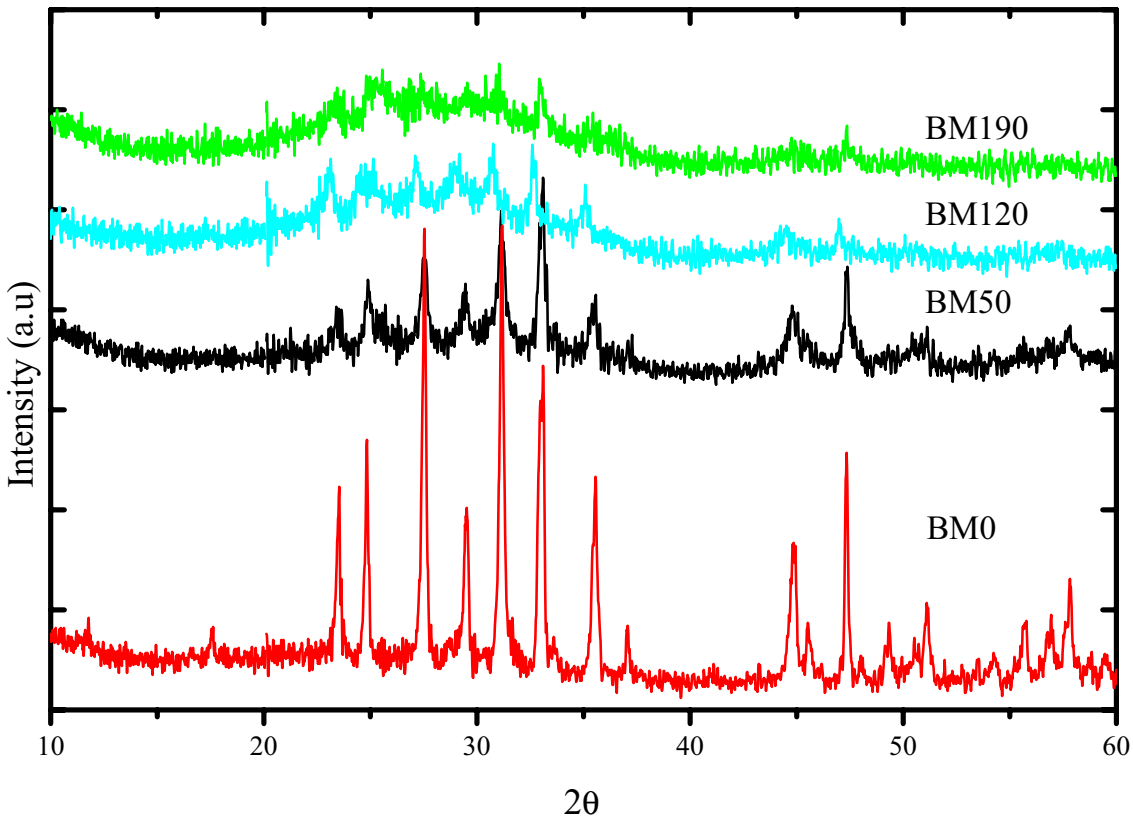

Figure 9-10: XRD patterns of ball milled $Bi_2Sr_2Ca_{0.3}Y_{0.7}Cu_2O_8$ materials.

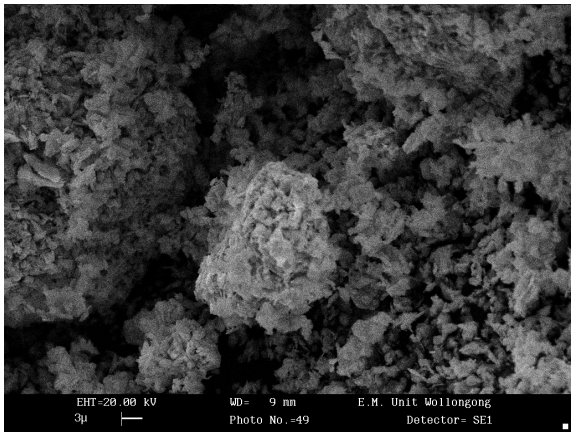

Figure 9-11: SEM micrograph of unmilled $Bi_2Sr_2Ca_{0.3}Y_{0.7}Cu_2O_8$.

9.2.1.2 Electrochemical Characterisation

The electrochemical properties of Bi-2212 were evaluated with the use of the prepared oxide electrodes as working electrodes and metallic lithium foils as the counter electrode. The electrochemical properties determined from constant current charge/discharging (50 µA, 0.70 – 3.00 V) of Bi-2212 electrodes varied with milling time. The first discharge capacity (Figure 9-12) was highest for the milled materials which all had a capacity of 300 – 310 mAh/g with varied discharge profiles whilst the unmilled material had a capacity of 267 mAh/g.

The first charge capacity (Figure 9-13) was also highest for the milled materials (80 – 87 mAh/g) though the charge profiles did vary whilst the capacities of the unmilled material was 53 mAh/g. Following the second cycle however the charge capacities (Figure 9-15) were highest for the BM120 material but were under 62 mAh/g within 10 cycles. The discharge capacities (Figure 9-14) were also highest for BM120 following the first discharge and were under 73 mAh/g within 10 cycles.

Extraction of lithium from the Bi-2212 structure is difficult as the charge capacities are much lower than the discharge capacities in the initial cycles. Ball milling has increased the first charge and discharge capacity as well as that on further cycling over that of the unmilled material.

Differential capacity plots of the first charge and discharge of BM190 (Figure 9-16) showed two distinct peaks at 0.85 and 1.65 V during discharge and a two broad peaks at 1.0 and 2.5 V during the charge.

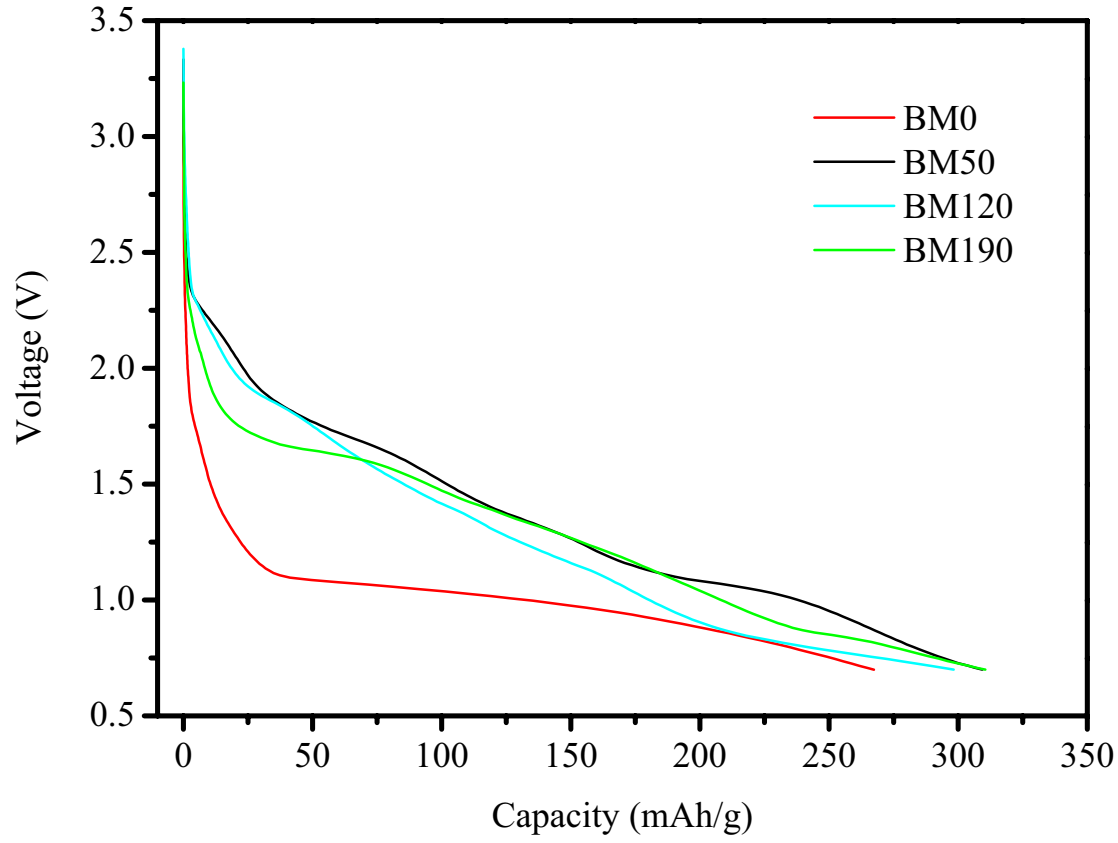

Figure 9-12: First discharge of various ball milled $Bi_2Sr_2Ca_{0.3}Y_{0.7}Cu_2O_8$ materials.

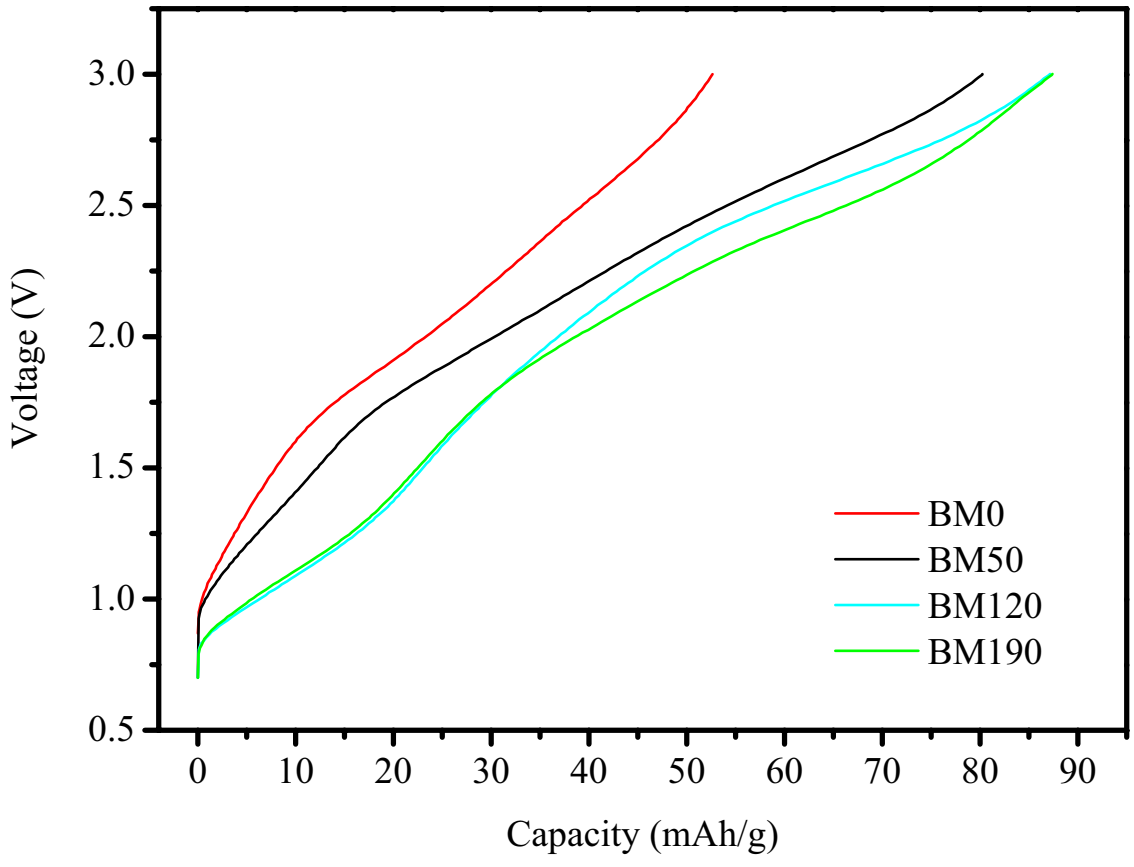

Figure 9-13: First charge of various ball milled $Bi_2Sr_2Ca_{0.3}Y_{0.7}Cu_2O_8$ materials.

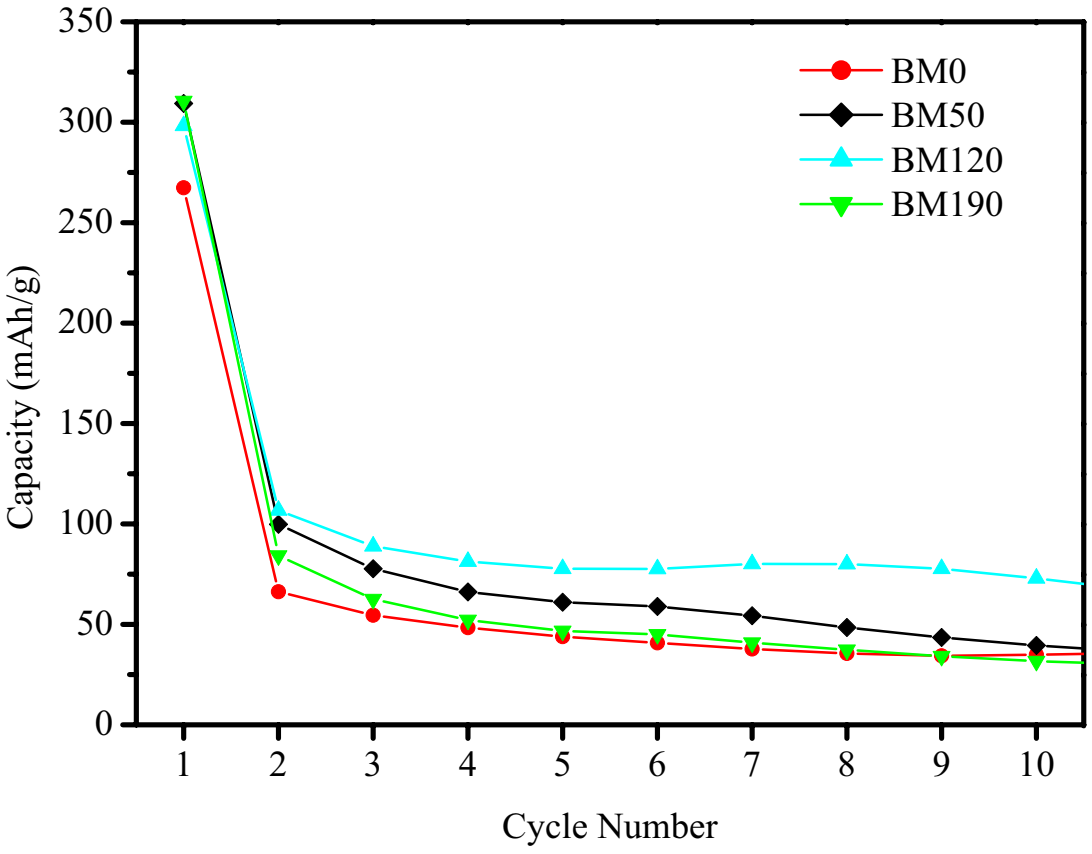

Figure 9-14: Variation of discharge capacity of $Bi_2Sr_2Ca_{0.3}Y_{0.7}Cu_2O_8$ with milling time.

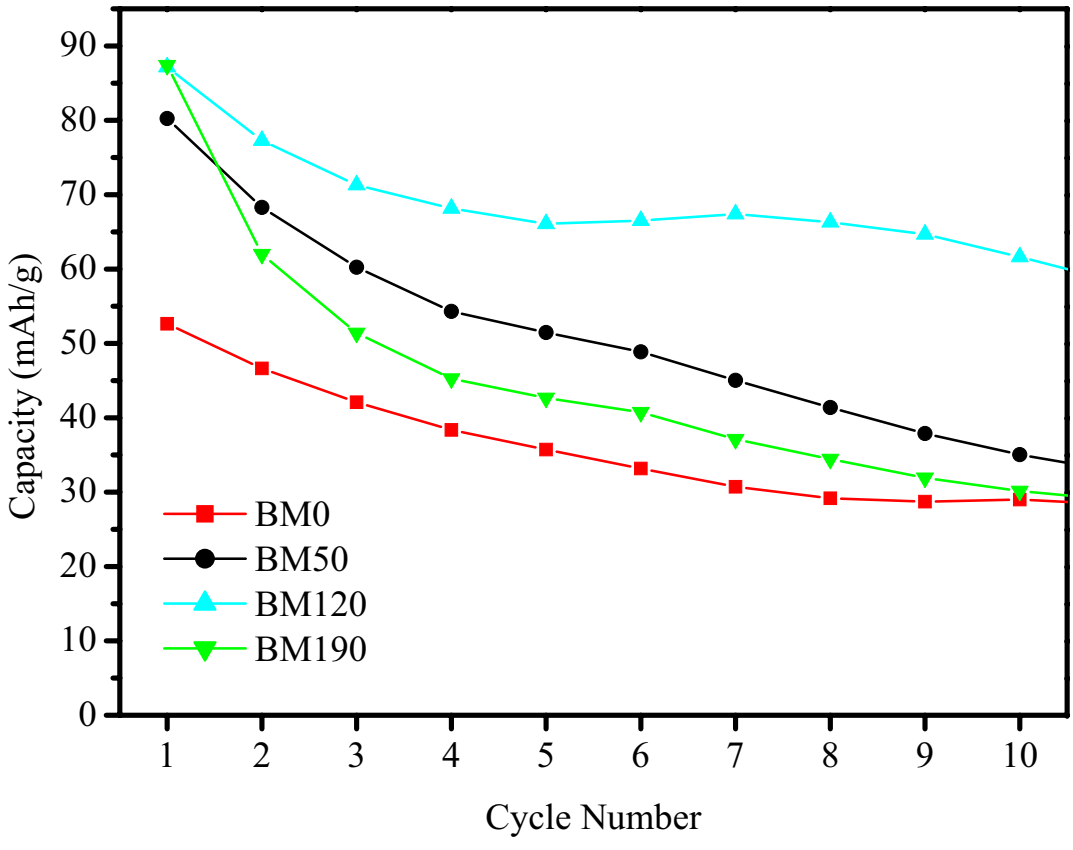

Figure 9-15: Variation of charge capacity of $Bi_2Sr_2Ca_{0.3}Y_{0.7}Cu_2O_8$ with milling time.

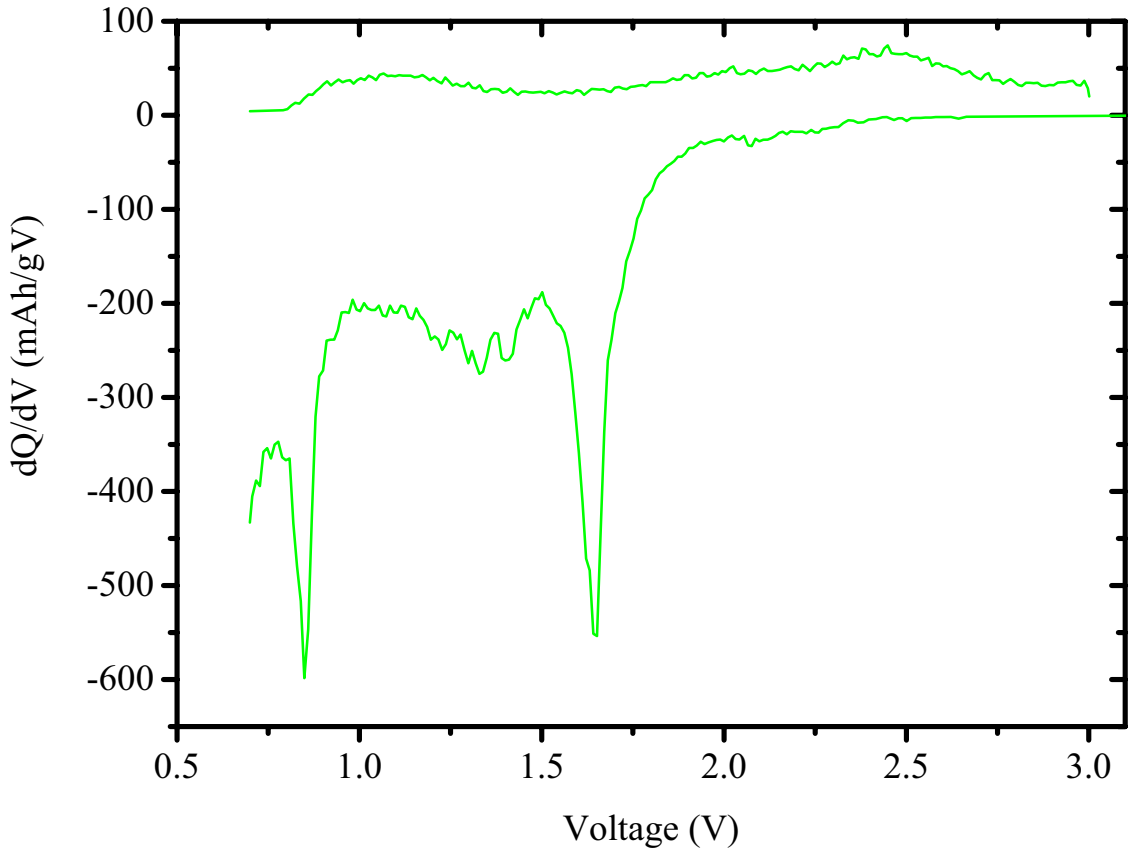

Figure 9-16: Differential capacity plot for the first cycle of BM190 $Bi_2Sr_2Ca_{0.3}Y_{0.7}Cu_2O_8$.

9.2.2 Discussion

The Bi-2212 material produced through spray drying and modified by ball milling with carbon demonstrated that the microstructure has an important influence on the electrochemical properties of the material. The discharge capacities observed were much higher than the theoretical capacity of 58 mAh/g based on the reaction of one mole of Bi-2212 with two moles of lithium. Differential capacity plots of BM190 indicate the occurrence of at least two reactions during the first charge and discharge.

Given the discharge capacities observed were much higher than previously reported there is still uncertainty over the reaction mechanism with lithium and the degree to which it occurs. The use of pellets in previous investigations compared to the pasted film electrodes utilised here may provide some explanation to the differences observed.

9.2.3 Conclusions

The Bi-2212 materials produced have demonstrated like many other oxide materials an electrochemical interaction towards lithium. There is still uncertainty over

the reaction mechanism whether it is an insertion of substitution reaction. In either case the degree to which it occurs was greater than had been previously reported. Previous reports had only mentioned the incorporation of two moles of lithium per mole of Bi-2212 equating to a capacity of only 58 mAh/g as a result of the high molecular weight of the Bi-2212 material.

9.3 Conclusions

Both the doped ($Bi_2Sr_2Ca_{0.3}Y_{0.7}Cu_2O_8$) and undoped ($Bi_2Sr_2CaCu_2O_8$) materials demonstrated much higher capacities than expected based on the previously reported maximum lithium uptake of two moles of lithium per mole of Bi-2212. The highest discharge capacity (441 mAh/g) was demonstrated by the unmilled and undoped material though the milled materials retained more of their capacity on cycling. The initial discharge capacities of the milled doped and undoped materials were all approximately 300 mAh/g. After cycling however the capacity of the doped BM190 material was higher than that of the other materials. The charge and discharge capacities of the undoped BM190 material after ten cycles as well as the specific surface area are approximately half those of the doped BM190 material. The electrochemical properties of the doped and undoped materials were similar despite the specific surface area of the doped material (63 m^2/g) being over two times that of the undoped material (30 m^2/g).

Chapter 10 Nanometre SiC

Thackeray has suggested that stable structures and in particular cubic structures may provide the key to achieving high electrode capacities and good cycle life [34]. A structure that is stable itself is less likely to be damaged on repeated lithium insertion and extraction. SiC is one material that possesses such properties with a stable covalently bonded zinc blende structure. A number of investigations have also examined the electrochemical performance of various carbon – silicon composite materials with some promising results reported [145, 146, 239, 240]. SiC itself has however been reported as inactive [146] though Huang et al [241] has examined SiC materials with a particle size of about 5 nm for hydrogen storage and reported absorption up to $H_{0.67}SiC$. Materials such as carbon nanotubes that have been examined as hydrogen storage materials have also demonstrated activity towards lithium in electrochemical testing.

Two different samples of nanometre scale SiC powders were obtained from commercial suppliers and their electrochemical properties compared. The SiC material with the smallest particle size is referred to as SiC-1 whilst the other as SiC-2.

10.1 Results

The fabrication of electrodes resulted in loadings of approximately 1 mg for both the SiC-1 and SiC-2 materials. The composition of the electrodes however varied dramatically. SiC-1 electrodes consisted of 50 wt. % SiC-1, 5 wt. % carbon and 45 wt. % PVDF. Attempts to produce electrodes with lower percentage of binder proved unsuccessful with the material not adhering to the copper substrate. Similar problems were encountered with the SiC-2 material and suitable electrodes consisted of 70 wt. % SiC-2, 5 wt. % carbon and 25 wt. % PVDF.

10.1.1 Structural and Microstructural Characterisation

XRD of SiC-1 showed only a single broad peak centred on 25 degrees two theta whilst SiC-2 had a less intense peak at the same location and two other peaks corresponding to cubic SiC (Figure 10-1). TEM observation of SiC-1 showed it was composed of particles under 20 nm (Figure 10-2) whilst SEM observation of SiC-2 showed particles of 50 – 60 nm (Figure 2-1). BET surface area measurements were also

made with the specific surface area of SiC-1 and SiC-2 determined as 169 m^2/g and 32 m^2/g respectively.

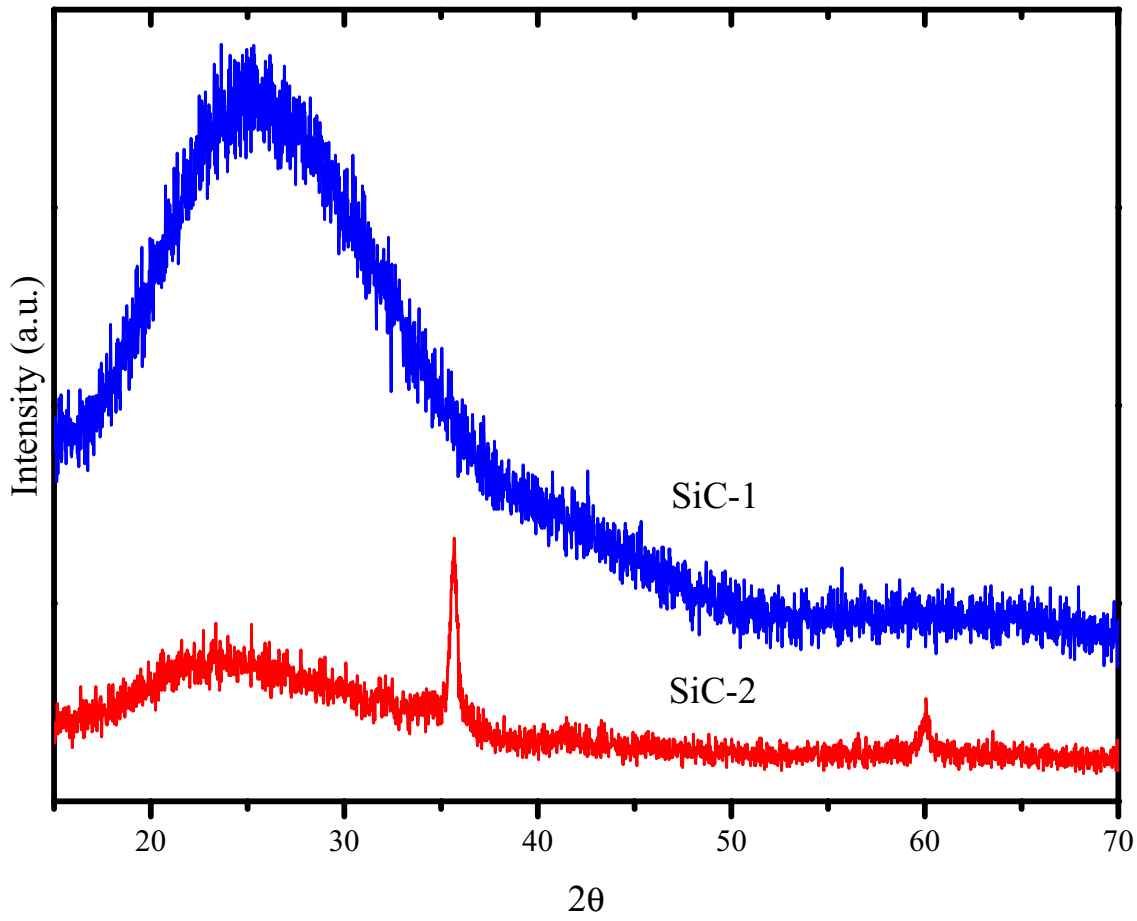

Figure 10-1: XRD of SiC-1 and SiC-2 commercial materials.

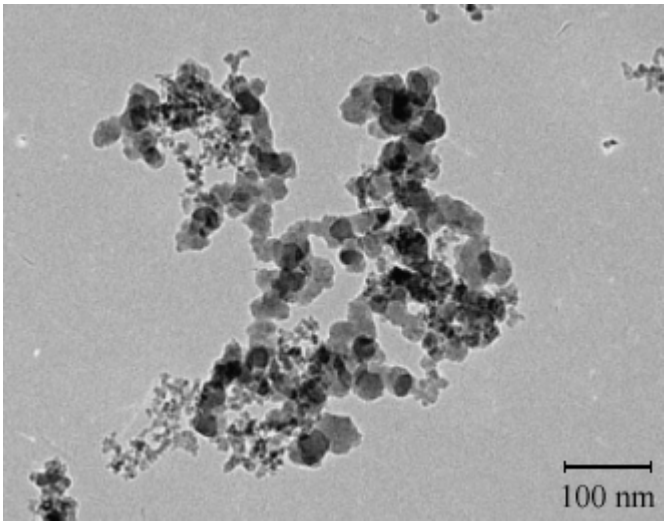

Figure 10-2: TEM image of SiC-1 material.

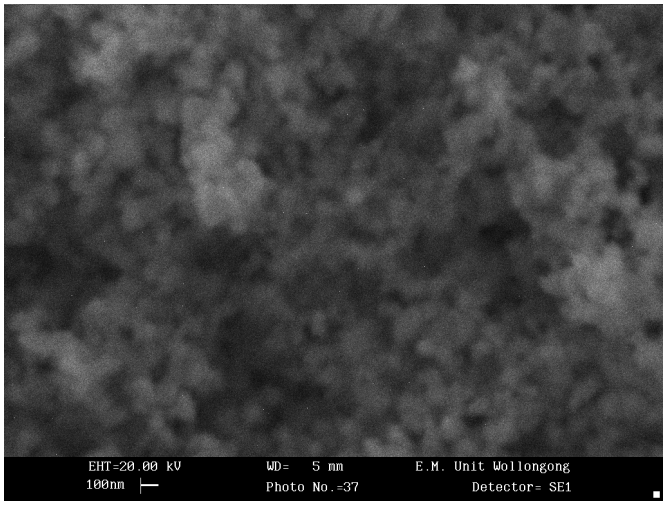

Figure 10-3: SEM image of SiC-2.

10.1.2 Electrochemical Characterisation

The electrochemical properties of the nanometre SiC materials were evaluated with the use of electrodes prepared from them as working electrodes and metallic lithium foils as the counter electrode. Constant current charge and discharging (50 μA, 0.01 – 3.00 V) was used to evaluate the electrochemical properties of the SiC materials. The SiC-1 material with its smaller particle size demonstrated higher first and subsequent discharge capacities than SiC-2 (Figure 10-4). The first discharge capacity of SiC-1 was 91.1 mAh/g compared to 44 mAh/g for SiC-2. SiC-1 maintained a discharge capacity of over 30 mAh/g for the 300 cycles for which it was tested whilst after 50 cycles SiC-2 maintained a capacity of only 12 mAh/g.

Differential capacity plots of the first cycle for SiC-1 and SiC-2 show similar characteristics (Figure 10-6). The features are however more distinct for the SiC-1 material. Cyclic voltammetry of SiC-1 also shows peaks corresponding to the same voltages as in the differential capacity plot (Figure 10-7).

10.2 Discussion

Small particle size nanometre SiC (SiC-1) is capable of delivering a small but steady discharge capacity of 30 mAh/g for over 300 cycles whilst that of the larger SiC-2 maintains only 12 mAh/g for the 50 cycles it was tested over. SiC has previously been classified as inactive towards lithium and this classification remains valid as the capacity is much less than the capacity that would otherwise be expected from either of its constituent elements.

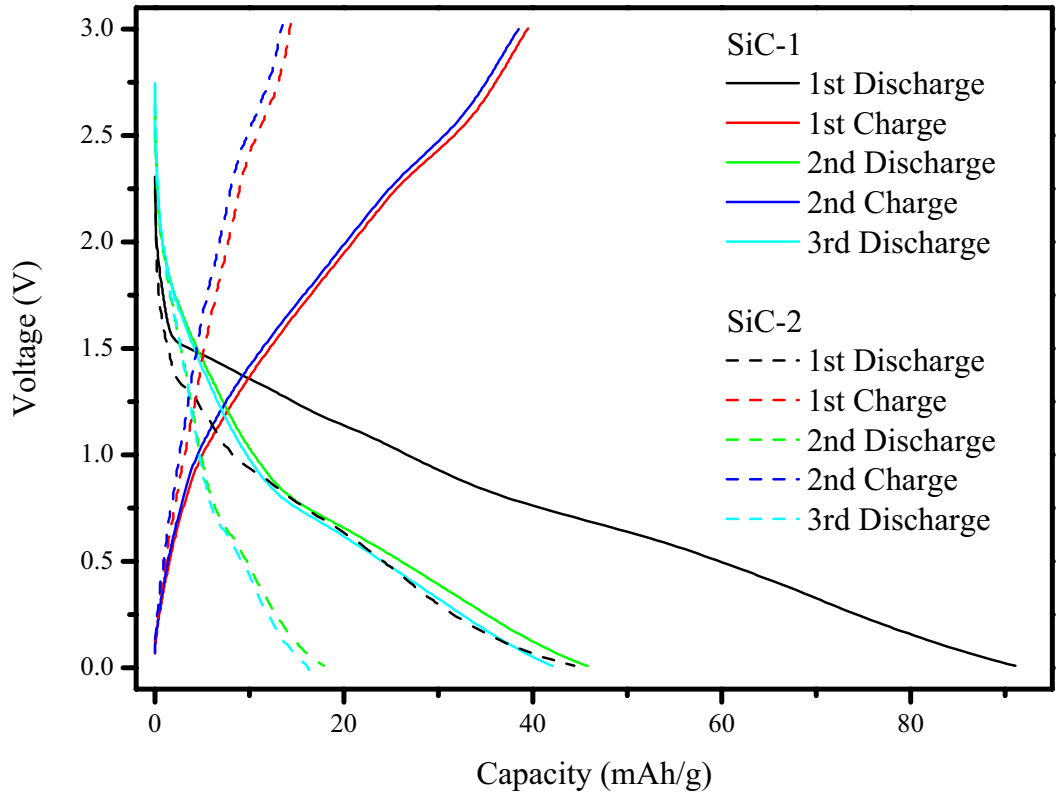

Figure 10-4: Discharge and charge capacities of SiC-1 and SiC-2 materials.

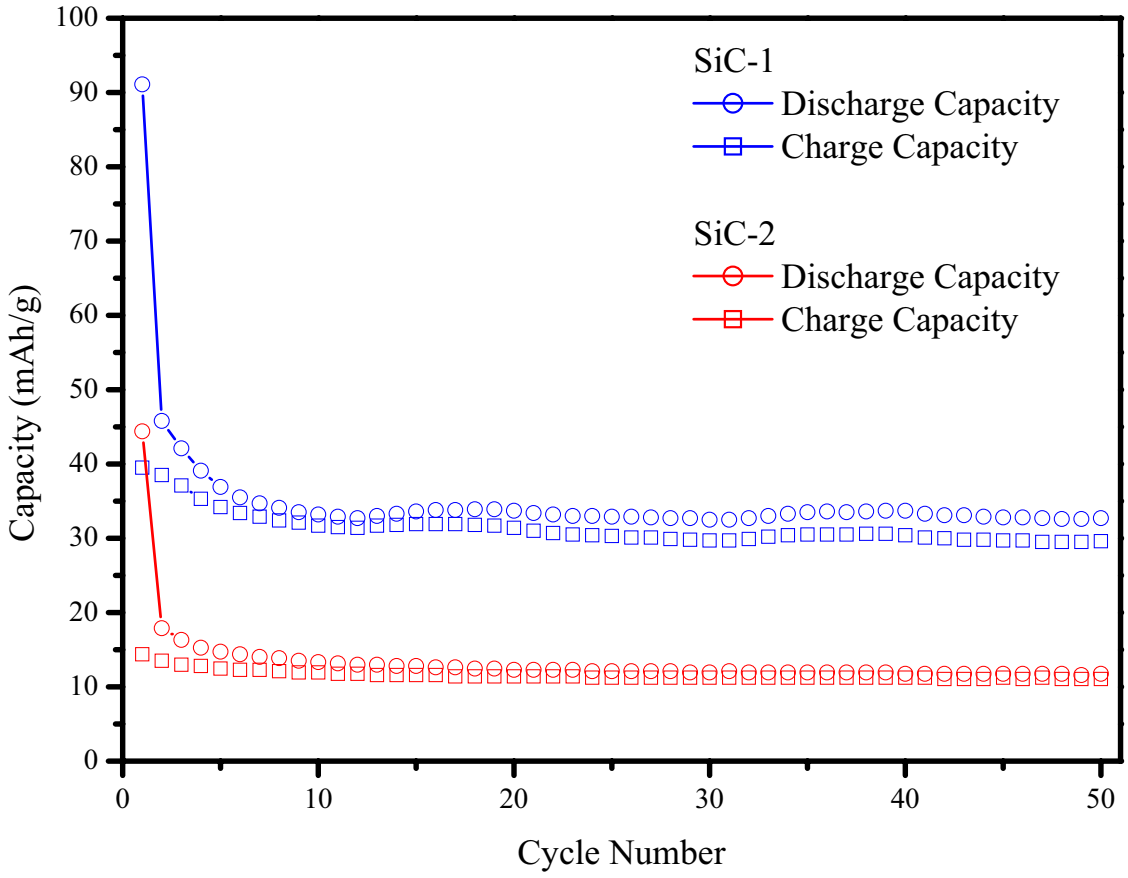

Figure 10-5: Cycle life of SiC-1 and SiC-2 materials.

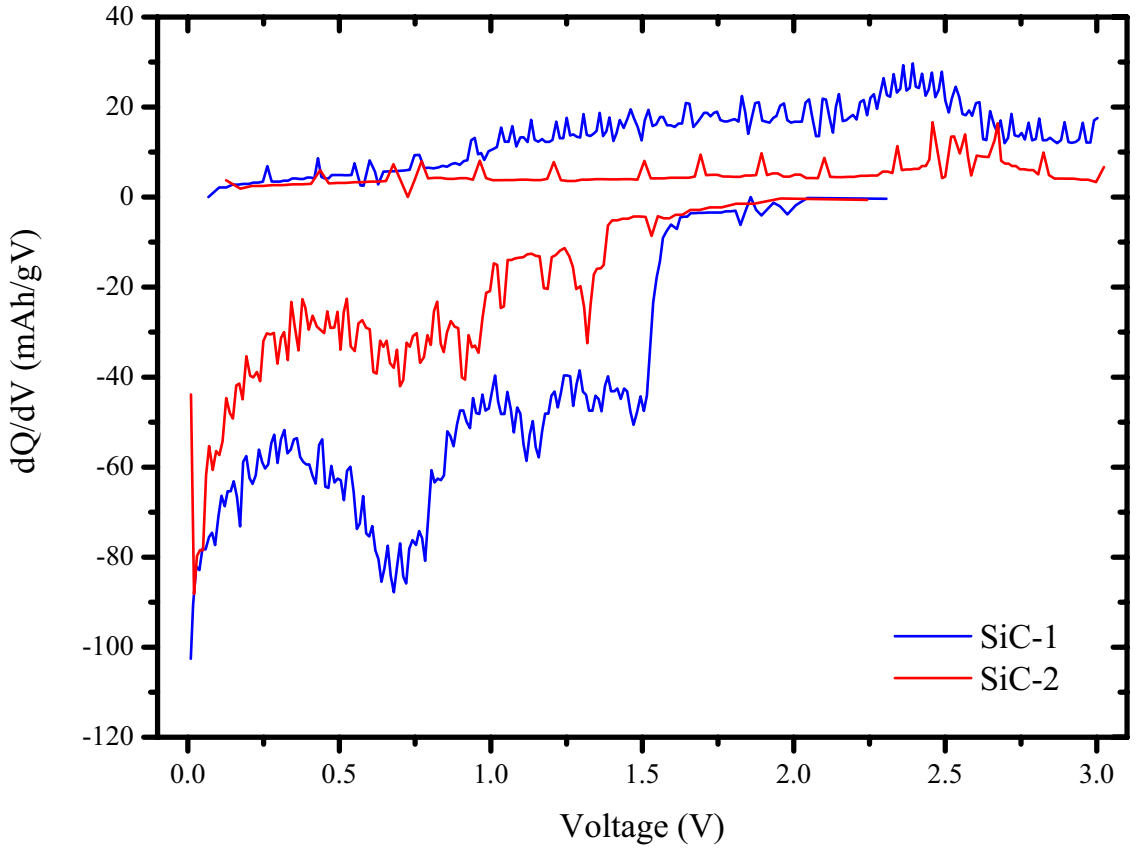

Figure 10-6: Differential capacity plots for the first cycle of SiC-1 and SiC-2.

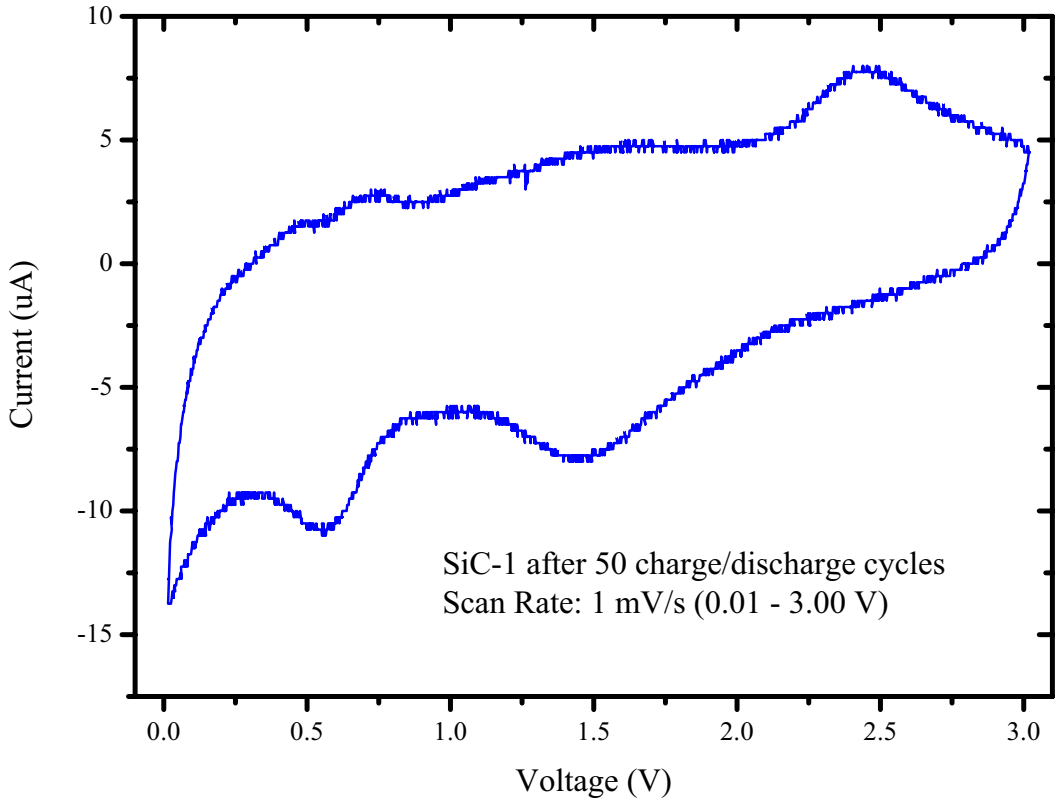

Figure 10-7: Cyclic voltammogram of SiC-1 following 50 charge/discharge cycles.

Having recognised the inactive classification of the material however the small capacity that was demonstrated may provide beneficial properties when utilised as an inactive material in an active/inactive composite. SiC additions albeit of much larger particle size (15 μm) and of 20 % by volume have already proved useful in improving the cycle life of aluminium [114].

Both differential capacity and cyclic voltammetry demonstrated that a number of reactions are occurring during the electrochemical cycling of nanometre SiC materials. In both differential capacity and cyclic voltammetry there is a single distinct peak during charge at 2.45 V with a smaller peak also evident at 0.76 V in cyclic voltammetry. Whilst during the discharge in cyclic voltammetry there are two peaks at 0.55 V and 1.45 V. The same features are also evident in the differential capacity plot of the discharge though at different voltages of 0.7 V and 1.3 V.

10.3 Conclusions

The electrochemical properties of nanometre SiC have been investigated and although the results still classify SiC as inactive its use as an inactive component in an active inactive composite may be beneficial. Much larger SiC particles have already been employed with favourable results achieved with the particles acting as a particulate reinforcement. Further investigation of nanometre SiC as an inactive material in composite materials is recommended with a loading of 30 wt. % as suggested by the observations based on particle packing and electrochemical performance of Sato et. al. [220].

Chapter 11 Discussion

The electrochemical properties of a variety of materials have been investigated as possible replacements for the carbon materials currently used in the anodes of commercial lithium ion batteries. Unfortunately as has been found for many of the materials that have already been explored the initial capacity is typically higher than that of existing materials but the capacity declines rapidly. For all the materials examined the importance of the microstructure to electrochemical performance has been highlighted.

11.1 Intermetallics

A wide range of intermetallic materials have been investigated including binary combinations of aluminium – iron and iron – silicon as well as ternary aluminium – iron – silicon materials. The phase detected from XRD analysis often varied from that of the original composition and the location of each has been presented in a ternary diagram (Figure 11-1). The production techniques themselves mean some variation in the composition is likely. During arc melting the element with the lowest melting point is most likely to be lost if any metal is vaporised. In the case of the binary aluminium – iron and ternary aluminium – iron – silicon materials this is aluminium. Whilst for the binary iron – silicon materials it is silicon. The ball milling process is also likely to influence the composition with elements such as iron and chromium picked up from the milling balls and jars.

11.1.1 Binary Al – Fe and Ternary Al – Fe – Si

The binary and ternary aluminium based intermetallics examined demonstrated activity towards lithium in contrast to the previous investigation of Dahn *et. al.* [107] that reported a number of materials as inactive (Al_2Cu, Al_6Mn, and Al_4Mn). The first discharge of the binary aluminium – iron materials were close to the theoretical capacities whilst those of the ternary aluminium – iron – silicon materials were much lower than their respective theoretical capacities. Selected properties of the binary and ternary materials from the maximum ball milling time are presented in Table 11-1. Considering only the properties of the materials of each composition for the maximum milling time the discharge capacities are seen to decrease with a number of variables. The discharge capacity decreased with an increase in the total weight percent of

aluminium and silicon in the material. The discharge capacity also decreased with an increase in the specific surface area of the materials. If the specific surface areas are converted to equivalent particle sizes through the use of empirical densities (Appendix D.2) as presented in Table 11-1 it can be seen that there is not a dramatic difference in particle size for either spherical (2.6 – 11.9 nm) or cylindrical particles (19.1 – 87.2 nm).

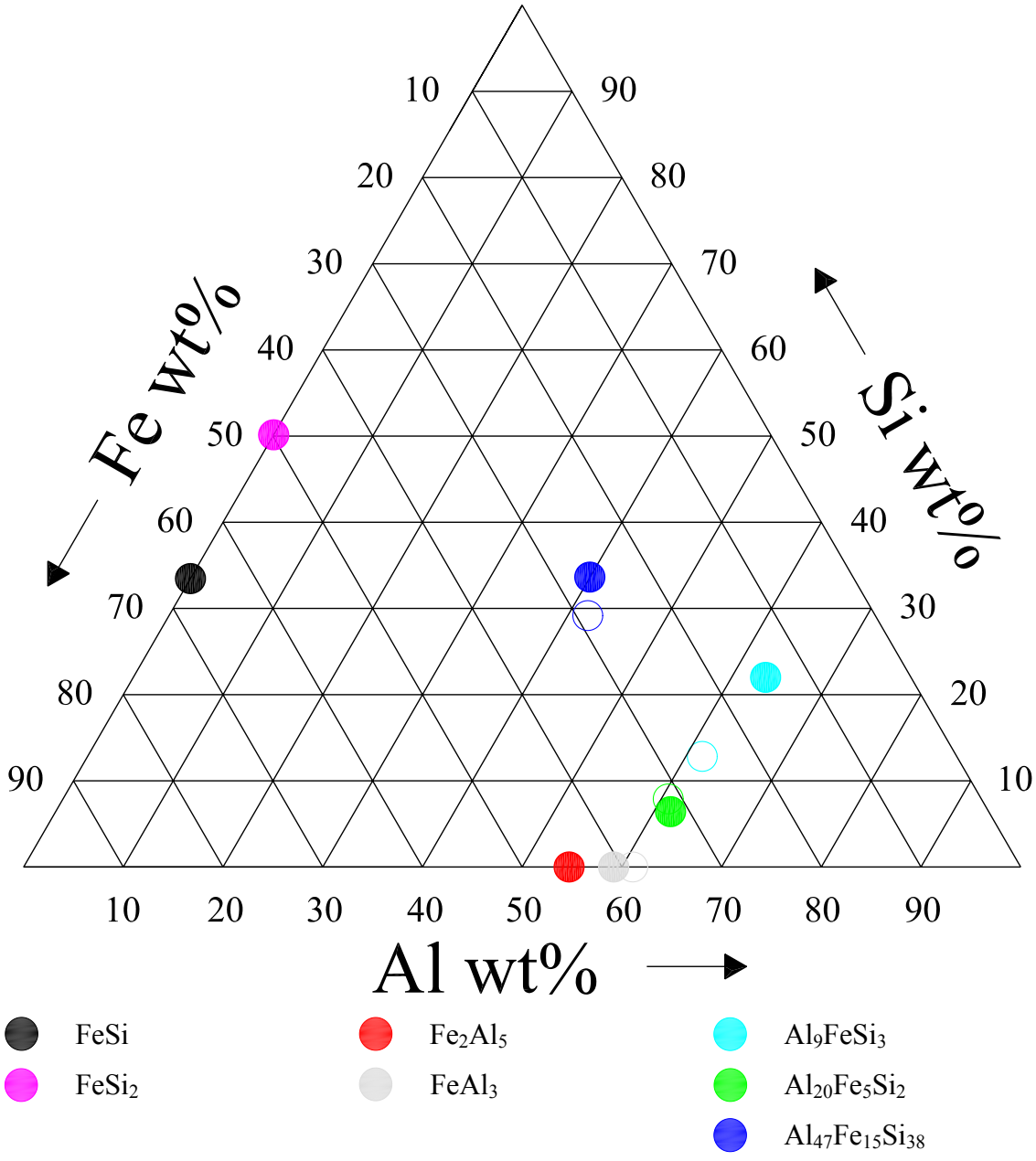

Open circles: Phase detected in XRD from the nominal composition of the same colour.

Figure 11-1: Ternary diagram demonstrating the nominal compositions examined and phases detected using XRD.

Table 11-1: Selected properties of aluminium based intermetallic materials.

Material	wt. % (Al + Si)	Specific surface area (m^2/g)	Equivalent Particle Size[a]		Capacity (mAh/g)	
			Sphere radius (nm)	Cylinder radius Height = $^r/_{10}$ (nm)	1st Discharge	1st Charge
$FeAl_3$ + C	53.3	55	11.9	87.2	827	200
$FeAl_3$	59.2	73	8.5	62.6	482	105
$Al_{20}Fe_5Si_2$	68.1	145	4.8	35.1	320	46
$Al_{47}Fe_{15}Si_{38}$	73.6	206	3.7	27.1	276	71
Al_9FeSi_3	85.4	341	2.6	19.1	114	28

[a] See Appendix D.3

The results suggest that the materials to target for further investigation to achieve a high discharge capacity should contain less than 70 wt. % active material/s and a specific surface area of under 145 m^2/g. The window of materials with under 60 wt. % active material/s and a specific surface area under 100 m^2/g may provide an even more appropriate range of materials for study.

There is still some uncertainty over the reaction mechanism responsible for the capacity observed, though differential capacity plots from some of the ternary materials suggested that AlLi may be formed during discharge and consumed during the subsequent charge. Why the first discharge capacities of the ternary materials are well under the theoretical capacities despite those of the binary materials being close to them is unknown.

11.1.2 Binary Fe – Si

The importance of the microstructure to the electrochemical properties has again been highlighted. Despite comparable first discharge capacities to other investigations of iron – silicon materials [135, 153, 155] the cycle life of the materials examined here were not as good. Of the other Fe – Si based materials reported in the literature the discharge profiles have the greatest resemblance to the graphite – $Fe_{20}Si_{80}$ materials of Lee et. al. [155] though the charge profiles were different. Cyclic voltammograms of the annealed and arc melted materials with the same composition (FeSi or $FeSi_2$) were different. The cyclic voltammograms of the annealed and arc melted materials with differing compositions (FeSi and $FeSi_2$) were however similar. Although the

compositions of the materials were different the processing of the materials were the same.

The arc melted FeSi material (BM260) demonstrated a higher capacity than annealed $FeSi_2$ (WM260) and better cycle life than annealed $FeSi_2$ (WM120). Selected properties of FeSi and $FeSi_2$ materials from the maximum ball milling time are presented in Table 11-2. Considering only the properties of the materials of each composition for the maximum milling time the discharge capacities and a number of other properties are seen to vary. The specific surface area of the two annealed and the two arc melted materials are quite different to each other. The specific surface areas of the annealed materials are lower than those of their respective arc melted materials despite being milled for a longer time. The carbon added for the milling of the annealed materials has acted as a process control agent and reduced the intensity of the milling.

The results suggest that the materials to target for further investigation to achieve a high discharge capacity should contain less than 60 wt. % active material/s and a specific surface area of under 180 m^2/g.

Table 11-2: Selected properties of Fe – Si based intermetallic materials.

Material	wt. % (Si)	Specific surface area (m^2/g)	Equivalent Particle Size[a]		Capacity (mAh/g)	
			Sphere radius (nm)	Cylinder radius Height = $^r/_{10}$ (nm)	1st Discharge	1st Charge
FeSi + C	30.1	65	8.1	59.6	836	155
FeSi	33.5	105	4.7	34.8	983	418
$FeSi_2$ + C	60.2	133	4.7	34.2	892	210
$FeSi_2$	66.9	180	3.3	24.0	493	48

[a] See Appendix D.3

11.2 Bi-2212

Both the doped ($Bi_2Sr_2Ca_{0.3}Y_{0.7}Cu_2O_8$) and undoped ($Bi_2Sr_2CaCu_2O_8$) materials demonstrated much higher capacities than expected based on the previously reported maximum lithium uptake of two moles of lithium per mole of Bi-2212. The Bi-2212 material produced through spray drying and modified by ball milling with carbon demonstrated that the microstructure has an important influence on the electrochemical properties of the material. The highest discharge capacity (441 mAh/g) was demonstrated by the unmilled and undoped material though the milled materials retained more of their capacity on cycling. The initial discharge capacities of the milled

doped and undoped materials were all approximately 300 mAh/g. After cycling however the capacity of the doped BM190 material was higher than that of the other materials. The charge and discharge capacities of the undoped BM190 material after ten cycles as well as the specific surface area are approximately half those of the doped BM190 material. Differential capacity plots of BM190 indicate the occurrence of at least one reaction occurring during the first charge and discharge. The electrochemical properties of the doped and undoped materials were similar despite the specific surface area of the doped material (63 m^2/g) being over two times that of the undoped material (30 m^2/g).

Given the discharge capacities observed were much higher than previously reported there is still uncertainty over the reaction mechanism with lithium and the degree to which it occurs. The use of pellets in previous investigations compared to the pasted film electrodes utilised here may provide some explanation to the differences observed.

11.3 Nanometre SiC

Small particle size nanometre SiC (SiC-1) is capable of delivering a small but steady discharge capacity of 30 mAh/g for over 300 cycles whilst that of the larger SiC-2 maintains only 12 mAh/g for the 50 cycles it was tested over. SiC has previously been classified as inactive towards lithium and this classification remains valid as the capacity is much less than the capacity that would otherwise be expected from either of its constituent elements. The specific surface area of the SiC-1 material of 169 m^2/g suggests good cycle life can be achieved with a material with such a surface area.

Chapter 12 Conclusions

A number of materials have been explored as anode materials for lithium ion batteries. The materials examined included;

- Fe_2Al_5
- $Al_{13}Fe_4$
- Al_3FeSi_2
- Al_8Fe_2Si
- Al_5FeSi
- FeSi
- $FeSi_2$
- $Bi_2Sr_2CaCu_2O_8$
- $Bi_2Sr_2Ca_{0.3}Y_{0.7}Cu_2O_8$
- Nanometre SiC

Each of the materials investigated has highlighted the fact that the microstructure has an important influence on the electrochemical properties of the material. For the materials that have been ball milled the highest discharge capacities and best cycle life were not always attributed to the final material of the milling process. The electrochemical performance of the examined materials was not sufficient to see them replace existing carbon materials. Given the high initial discharge capacity that many of the materials did exhibit however and the dramatic influence of the electrochemical properties further microstructural modification may be able to achieve this.

The activity of a number of binary and ternary based intermetallic materials towards lithium has been demonstrated, in contrast to previous investigations that reported aluminium based intermetallics as inactive despite the known activity of aluminium itself towards lithium. The low initial discharge capacities of the ternary aluminium intermetallics compared to the theoretical capacities is unusual given those of the binary aluminium materials were close to their theoretical capacities.

The iron – silicon materials despite demonstrating initial discharge capacities comparable to those of other iron silicon materials reported in the literature failed to replicate the cycle life of the same materials. The discharge profiles were however

similar to some of those reported in the literature for Fe – Si materials. The charge profiles in contrast were different.

The electrochemical performances of the two Bi-2212 materials were similar despite the specific surface area of the doped material (63 m^2/g) being twice that of the undoped material (30 m^2/g). Whilst the performance of the finer particle sized SiC (SiC-1) was different to that of the coarser SiC material (SiC-2).

Although a range of intermetallic compositions were examined and there were differences in the experimental methods used to examine them the results do suggest that for intermetallic materials compositions with under 60 weight percent of active material and a specific surface area less than 180 m^2/g should be examined.

Appendix A Effect of Variables on Specific Surface Area

A.1 Volume, Surface Areas and Ratios

A.1.1 Sphere (Radius = r)

For a sphere with a radius of r the volume (V) can be calculated using A-1. The surface area (A) of the same sphere can be calculated using A-2. The Area:Volume ratio $(A:V)$ can then be calculated through division of the surface area by the volume resulting in a simple relationship (A-3).

$$V = \frac{4\pi r^3}{3} \qquad \text{A-1}$$

$$A = 4\pi r^2 \qquad \text{A-2}$$

$$A:V = 4\pi r^2 \times \frac{3}{4\pi r^3}$$

$$A:V = \frac{3}{r} \qquad \text{A-3}$$

For a fixed particle volume (x) the corresponding radius (r) can be calculated by solving the volume equation (A-1) for r (A-4).

$$x = \frac{4\pi r^3}{3}$$

$$r = \sqrt[3]{\frac{3x}{4\pi}} \qquad \text{A-4}$$

For a fixed particle surface area (y) the corresponding radius (r) can be calculated by solving the surface area equation (A-2) for r (A-5).

$$y = 4\pi r^2$$

$$r = \sqrt{\frac{y}{4\pi}}$$

$$r = \frac{1}{2}\sqrt{\frac{y}{\pi}} \qquad \text{A-5}$$

A.1.2 Sphere (Radius = $\sqrt[3]{2}R$)

If instead of r the radius of the sphere is $\sqrt[3]{2}R$ then substituting for r, the volume can be calculated using A-6. The surface area through substitution would be given by A-7. The Area:Volume ratio can also be found through substitution and is given by A-8.

$$V = \frac{4\pi\left(\sqrt[3]{2}R\right)^3}{3}$$

$$V = \frac{8\pi R^3}{3} \quad \text{A-6}$$

$$A = 4\pi\left(\sqrt[3]{2}R\right)^2$$

$$A = 4\left(\sqrt[3]{2}\right)^2 \pi R^2 \quad \text{A-7}$$

$$A:V = \frac{3}{\sqrt[3]{2}R} \quad \text{A-8}$$

A.1.3 Cube (Side Length = a)

For a cube with a side length of a the volume (V) can be calculated using A-9. The surface area (A) of the cube will be given by A-10. The Area:Volume ratio $(A:V)$ can then be calculated through division of the surface area by the volume giving a simple relationship (A-11).

$$V = a^3 \quad \text{A-9}$$

$$A = 6a^2 \quad \text{A-10}$$

$$A:V = \frac{6a^2}{a^3}$$

$$A:V = \frac{6}{a} \quad \text{A-11}$$

For a fixed particle volume (x) the corresponding side length (a) can be calculated by solving the volume equation (A-9) for a (A-12).

$$x = a^3$$

$$a = \sqrt[3]{x} \quad \text{A-12}$$

For a fixed particle surface area (y) the corresponding side length (a) can be calculated by solving the surface area equation (A-10) for a (A-13).

$$y = 6a^2$$

$$a = \sqrt{\frac{y}{6}} \quad \text{A-13}$$

A.1.4 Square Prism (Side Length = a, Height = $2a$)

For a square prism where the height is equal to twice the length of the sides of the square base (a) the volume (V) can be calculated using A-14. The surface area (A) of this square prism can be calculated using A-15. The Area:Volume ratio $(A:V)$ can

then be calculated through division of the surface area (A) by the volume (V) giving a simple relationship (A-16).

$$V = 2a^3 \quad \textbf{A-14}$$

$$A = 10a^2 \quad \textbf{A-15}$$

$$A:V = \frac{10a^2}{2a^3}$$

$$A:V = \frac{5}{a} \quad \textbf{A-16}$$

For a fixed particle volume (x) the corresponding side length (a) can be calculated by solving the volume equation (A-14) for a (A-17).

$$x = 2a^3$$

$$a = \sqrt[3]{\frac{x}{2}} \quad \textbf{A-17}$$

For a fixed particle surface area (y) the corresponding side length (a) can be calculated by solving the surface area equation (A-15) for a (A-18).

$$y = 10a^2$$

$$a = \sqrt{\frac{y}{10}} \quad \textbf{A-18}$$

A.1.5 Cylinder (Radius = R = Height)

Consider a cylinder with a height equal to its radius (R). The volume (V) of the cylinder can be calculated using A-19. The surface area (A) can be calculated using A-20. The Area:Volume ratio $(A:V)$ can then be calculated through division of the surface area by the volume giving a simple relationship (A-21)

$$V = \pi R^3 \quad \textbf{A-19}$$

$$A = 4\pi R^2 \quad \textbf{A-20}$$

$$A:V = \frac{4\pi R^2}{\pi R^3}$$

$$A:V = \frac{4}{R} \quad \textbf{A-21}$$

For a fixed particle volume (x) the corresponding radius (R) can be calculated by solving the volume equation (A-19) for R (A-22).

$$x = \pi R^3$$

$$R = \sqrt[3]{\frac{x}{\pi}} \qquad \textbf{A-22}$$

For a fixed particle surface area (y) the corresponding radius (R) can be calculated by solving the surface area equation (A-20) for R (A-23).

$$y = 4\pi R^2$$
$$R = \frac{1}{2}\sqrt{\frac{y}{\pi}} \qquad \textbf{A-23}$$

A.1.6 Cylinder (Radius = R Height = $2R$)

Consider a cylinder with a radius of R and height of $2R$. The volume (V) of the cylinder can be calculated using A-24. The surface area (A) of the cylinder can be calculated using A-25. The Area:Volume ratio $(A:V)$ can then be calculated through division of the surface area by the volume giving a simple relationship (A-26).

$$V = 2\pi R^3 \qquad \textbf{A-24}$$

$$A = 6\pi R^2 \qquad \textbf{A-25}$$

$$A:V = \frac{6\pi R^2}{2\pi R^3}$$
$$A:V = \frac{3}{R} \qquad \textbf{A-26}$$

For a fixed particle volume (x) the corresponding radius (R) can be calculated by solving the volume equation (A-24) for R (A-27).

$$x = 2\pi R^3$$
$$R = \sqrt[3]{\frac{x}{2\pi}} \qquad \textbf{A-27}$$

For a fixed particle surface area (y) the corresponding radius (R) can be calculated by solving the surface area equation (A-25) for R (A-28).

$$y = 6\pi R^2$$
$$R = \sqrt{\frac{y}{6\pi}} \qquad \textbf{A-28}$$

A.1.7 Cylinder (Radius = R Height = $\frac{R}{10}$)

Consider a cylinder with a radius of R and height of $\frac{R}{10}$. The volume (V) of the cylinder can be calculated using A-29. The surface area (A) of the cylinder can be

calculated using A-30. The Area:Volume ratio $(A:V)$ can then be calculated through division of the surface area by the volume giving a simple relationship (A-31).

$$V = \frac{\pi R^3}{10} \quad \textbf{A-29}$$

$$A = \frac{11\pi R^2}{5} \quad \textbf{A-30}$$

$$A:V = \frac{11\pi R^2}{5} \times \frac{10}{\pi R^3}$$

$$A:V = \frac{22}{R} \quad \textbf{A-31}$$

For a fixed particle volume (x) the corresponding radius (R) can be calculated by solving the volume equation (A-29) for R (A-32).

$$x = \frac{\pi R^3}{10}$$

$$R = \sqrt[3]{\frac{10x}{\pi}} \quad \textbf{A-32}$$

For a fixed particle surface area (y) the corresponding radius (R) can be calculated by solving the surface area equation (A-30) for R (A-33).

$$y = \frac{11\pi R^2}{5}$$

$$R = \sqrt{\frac{5y}{11\pi}} \quad \textbf{A-33}$$

A.2 Dimension Based Comparison

Given a sphere with a radius of r how do the specific surface areas of other particle shapes compare on a dimension basis $(r = R = a = A)$ for a constant density. The specific surface area will be directly proportional to the Area:Volume ratio $(A:V)$. By dividing the Area:Volume ratio of other shapes by that of the sphere with radius r the relationship with its specific surface area can be examined.

A.2.1 Sphere (Radius $= \sqrt[3]{2}r$)

Given a sphere with radius r and a sphere with radius $\sqrt[3]{2}r$

$$\frac{A:V_{Sphere\ \ Radius=\sqrt[3]{2}r}}{A:V_{Sphere\ \ Radius=r}} = \frac{3}{\sqrt[3]{2}r} \times \frac{r}{3}$$

$$\frac{A:V_{Sphere\ \ Radius=\sqrt[3]{2}r}}{A:V_{Sphere\ \ Radius=r}} = \frac{1}{\sqrt[3]{2}} \approx 0.79 \quad \textbf{A-34}$$

Therefore a sphere with radius $\sqrt[3]{2}r$ would have a specific surface area of approximately 0.79 times that of a sphere with a radius of r.

A.2.2 Cube (Side Length = r)

Given a sphere with radius r and a cube with side length r.

$$\frac{A:V_{Cube\ \ Length=r}}{A:V_{Sphere\ \ Radius=r}} = \frac{6}{r}\times\frac{r}{3}$$

$$\frac{A:V_{Cube\ \ Length=r}}{A:V_{Sphere\ \ Radius=r}} = 2 \qquad \text{A-35}$$

Therefore a cube with a side length a would have a specific surface area of 2 times that of a sphere with a radius of r.

A.2.3 Square Prism (Side Length = r, Height = $2r$)

Given a sphere with radius r and a square prism with square side length r and height $2r$.

$$\frac{A:V_{Square\ Prism\ \ Length=r\ \ Height=2r}}{A:V_{Sphere\ \ Radius=r}} = \frac{5}{r}\times\frac{r}{3}$$

$$\frac{A:V_{Square\ Prism\ \ Length=r\ \ Height=2r}}{A:V_{Sphere\ \ Radius=r}} = \frac{5}{3}\approx 1.67 \qquad \text{A-36}$$

Therefore a square prism with a square side length r and height $2r$ would have a specific surface area approximately 1.67 times that of a sphere with a radius of r.

A.2.4 Cylinder (Radius = r = Height)

Given a sphere with radius r and a cylinder with radius r and height r.

$$\frac{A:V_{Cylinder\ \ Radius=Height=r}}{A:V_{Sphere\ \ Radius=r}} = \frac{4}{r}\times\frac{r}{3}$$

$$\frac{A:V_{Cylinder\ \ Radius=Height=r}}{A:V_{Sphere\ \ Radius=r}} = \frac{4}{3}\approx 1.33 \qquad \text{A-37}$$

Therefore a cylinder with a radius r and height r would have a specific surface area approximately 1.33 times that of a sphere with a radius of r.

A.2.5 Cylinder (Radius = r, Height = $2r$)

Given a sphere with radius r and a cylinder with radius r and height $2r$.

$$\frac{A:V_{Cylinder\ \ Radius=r\ \ Height=2r}}{A:V_{Sphere\ \ Radius=r}} = \frac{3}{r}\times\frac{r}{3}$$

$$\frac{A:V_{Cylinder\ \ Radius=r\ \ Height=2r}}{A:V_{Sphere\ \ Radius=r}} = 1 \qquad \text{A-38}$$

Therefore a cylinder with a radius r and height $2r$ would have the same specific surface area as a sphere with a radius of r.

A.2.6 Cylinder (Radius = r, Height = $\frac{r}{10}$)

Given a sphere with radius r and a cylinder with radius r and height $\frac{r}{10}$.

$$\frac{A:V_{Cylinder\ \ Radius=r\ \ Height=r/10}}{A:V_{Sphere\ \ Radius=r}} = \frac{22}{r}\times\frac{r}{3}$$

$$\frac{A:V_{Cylinder\ \ Radius=r\ \ Height=r/10}}{A:V_{Sphere\ \ Radius=r}} = \frac{22}{3} \approx 7.33 \qquad \text{A-39}$$

Therefore a cylinder with a radius r and height $\frac{r}{10}$ would have a specific surface area approximately 7.33 times that of a sphere with a radius of r.

A.3 Volume Based Comparisons

For a given particle volume x how do the specific surface areas of the other particle shapes compare to that of a sphere. As particles with the same density are being considered the effect is identical to considering particles of the same mass.

A.3.1 Sphere (Radius = r)

The Area:Volume $(A:V)$ ratio for a constant particle volume x for a sphere with radius r can be determined through substituting the value of r determined for a fixed volume x (A-4) into the existing $A:V$ relationship (A-3).

$$A:V = \frac{3}{r}$$

$$= \frac{3}{\left(\sqrt[3]{\frac{3x}{4\pi}}\right)}$$

$$A:V = \frac{3\sqrt[3]{4\pi}}{\sqrt[3]{3x}} \qquad \text{A-40}$$

A.3.2 Cube (Side Length = a)

For a particle volume x the Area:Volume $(A:V)$ ratio can be found by substituting the value of a for a constant particle volume (A-12) into the existing $A:V$ relationship (A-11). By dividing the $A:V$ of the cube (A-41) by that of the sphere (A-40) the relationship of the specific surface area of the cube to that of the sphere of the same volume can be examined.

$$A:V = \frac{6}{a}$$

$$A:V = \frac{6}{\sqrt[3]{x}} \qquad \text{A-41}$$

$$\frac{A:V_{Cube\ \ Length=a}}{A:V_{Sphere\ \ Radius=r}} = \frac{6}{\sqrt[3]{x}} \times \frac{\sqrt[3]{3x}}{3\sqrt[3]{4\pi}}$$

$$\frac{A:V_{Cube\ \ Length=a}}{A:V_{Sphere\ \ Radius=r}} = \frac{2\sqrt[3]{3}}{\sqrt[3]{4\pi}} \approx 1.24 \qquad \text{A-42}$$

Therefore a cube with a side length a would have a specific surface area of approximately 1.24 times that of a sphere with a radius of r with the same volume.

A.3.3 Square Prism (Side Length = a, Height = $2a$)

For a particle volume x the Area:Volume ratio $(A:V)$ can be found by substituting the value of a for a constant particle volume (A-17) into the existing $A:V$ relationship (A-16). By dividing the $A:V$ of the square prism (A-43) by that of the sphere (A-40) the relationship of the specific surface area of the square prism to that of the sphere of the same volume can be examined.

$$A:V = \frac{5}{a}$$

$$= \frac{5}{\sqrt[3]{\frac{x}{2}}}$$

$$A:V = \frac{5\sqrt[3]{2}}{\sqrt[3]{x}} \qquad \text{A-43}$$

$$\frac{A:V_{Square\ Prism\ \ Length=a\ \ Height=2a}}{A:V_{Sphere\ \ Radius=r}} = \frac{5\sqrt[3]{2}}{\sqrt[3]{x}} \times \frac{\sqrt[3]{3x}}{3\sqrt[3]{4\pi}}$$

$$\frac{A:V_{Square\ Prism\ \ Length=a\ \ Height=2a}}{A:V_{Sphere\ \ Radius=r}} = \frac{5\sqrt[3]{3}}{3\sqrt[3]{2\pi}} \approx 1.30 \qquad \text{A-44}$$

Therefore a square prism with a side length a and height $2a$ would have a specific surface area of approximately 1.30 times that of a sphere with a radius of r with the same volume.

A.3.4 Cylinder (Radius = R = Height)

For a particle volume x the Area:Volume ratio $(A:V)$ can be found by substituting the value of R for a constant particle volume (A-22) into the existing $A:V$ relationship (A-21). By dividing the $A:V$ of the cylinder (A-45) by that of the sphere (A-40) the relationship of the specific surface area of the cylinder to that of the sphere of the same volume can be examined.

$$A:V = \frac{4}{R}$$

$$= \frac{4}{\sqrt[3]{\frac{x}{\pi}}}$$

$$A:V = \frac{4\sqrt[3]{\pi}}{\sqrt[3]{x}} \qquad \text{A-45}$$

$$\frac{A:V_{Cylinder\ \ Radius=Height=R}}{A:V_{Sphere\ \ Radius=r}} = \frac{4\sqrt[3]{\pi}}{\sqrt[3]{x}} \times \frac{\sqrt[3]{3x}}{3\sqrt[3]{4\pi}}$$

$$\frac{A:V_{Cylinder\ \ Radius=Height=R}}{A:V_{Sphere\ \ Radius=r}} = \frac{4\sqrt[3]{3}}{3\sqrt[3]{4}} \approx 1.21 \qquad \text{A-46}$$

Therefore a cylinder with its height equal to its radius would have a specific surface area of approximately 1.21 times that of a sphere with the same volume.

A.3.5 Cylinder (Radius = R, Height = $2R$)

For a particle volume x the Area:Volume ratio $(A:V)$ can be found by substituting the value of R for a constant particle volume (A-27) into the existing $A:V$ relationship (A-26). By dividing the $A:V$ of the cylinder (A-47) the relationship of the specific surface area of the cylinder to that of the sphere of the same volume can be examined.

$$A:V = \frac{3}{R}$$

$$= \frac{3}{\sqrt[3]{\frac{x}{2\pi}}}$$

$$A:V = \frac{3\sqrt[3]{2\pi}}{\sqrt[3]{x}} \quad \text{A-47}$$

$$\frac{A:V_{Cylinder\ \ Radius=R\ \ Height=2R}}{A:V_{Sphere\ \ Radius=r}} = \frac{3\sqrt[3]{2\pi}}{\sqrt[3]{x}} \times \frac{\sqrt[3]{3x}}{3\sqrt[3]{4\pi}}$$

$$\frac{A:V_{Cylinder\ \ Radius=R\ \ Height=2R}}{A:V_{Sphere\ \ Radius=r}} = \frac{\sqrt[3]{3}}{\sqrt[3]{2}} \approx 1.14 \quad \text{A-48}$$

Therefore a cylinder with its height equal to twice its radius would have a specific surface area of approximately 1.14 times that of a sphere with the same volume.

A.3.6 Cylinder (Radius = R, Height = $\frac{R}{10}$)

For a particle volume x the Area:Volume ratio $(A:V)$ can be found by substituting the value of R for a constant particle volume (A-32) into the existing $A:V$ relationship (A-31). By dividing the $A:V$ of the cylinder (A-49) the relationship of the specific surface area of the cylinder to that of the sphere of the same volume can be examined.

$$A:V = \frac{22}{R}$$

$$= \frac{22}{\sqrt[3]{\frac{10x}{\pi}}}$$

$$A:V = \frac{22\sqrt[3]{\pi}}{\sqrt[3]{10x}} \quad \text{A-49}$$

$$\frac{A:V_{Cylinder\ \ Radius=R\ \ Height=R/10}}{A:V_{Sphere\ \ Radius=r}} = \frac{22\sqrt[3]{\pi}}{\sqrt[3]{10x}} \times \frac{\sqrt[3]{3x}}{3\sqrt[3]{4\pi}}$$

$$\frac{A:V_{Cylinder\ \ Radius=R\ \ Height=R/10}}{A:V_{Sphere\ \ Radius=r}} = \frac{22\sqrt[3]{3}}{3\sqrt[3]{40}} \approx 3.09 \quad \text{A-50}$$

Therefore a cylinder with its height equal to a tenth of its radius would have a specific surface area of approximately 3.09 times that of a sphere with the same volume.

A.4 Surface Area Based Comparisons

For a given particle surface area y how do the specific surface areas of other particles compare to that of a sphere.

A.4.1 Sphere (Radius = r)

The Area:Volume $(A:V)$ ratio for a constant particle surface area y for a sphere with radius r can be determined through substituting the value of r determined for a fixed surface area (A-5) into the existing $A:V$ relationship (A-3).

$$A:V = \frac{3}{r}$$

$$= \frac{3}{\left(\frac{1}{2}\sqrt{\frac{y}{\pi}}\right)}$$

$$A:V = \frac{6\sqrt{\pi}}{\sqrt{y}} \qquad \text{A-51}$$

A.4.2 Cube (Side Length = a)

For a particle surface area y the Area:Volume $(A:V)$ ratio can be found by substituting the value of a for a constant particle surface area (A-13) into the existing $A:V$ relationship (A-11). By dividing the $A:V$ of the cube (A-52) by that of the sphere (A-51) the relationship of the specific surface area of the cube to that of the sphere of the same surface area can be examined.

$$A:V = \frac{6}{a}$$

$$= \frac{6}{\sqrt{\frac{y}{6}}}$$

$$A:V = \frac{6\sqrt{6}}{\sqrt{y}} \qquad \text{A-52}$$

$$\frac{A:V_{Cube\ Length=a}}{A:V_{Sphere\ Radius=r}} = \frac{6\sqrt{6}}{\sqrt{y}} \times \frac{\sqrt{y}}{6\sqrt{\pi}}$$

$$\frac{A:V_{Cube\ Length=a}}{A:V_{Sphere\ Radius=r}} = \frac{\sqrt{6}}{\sqrt{\pi}} \approx 1.38 \qquad \text{A-53}$$

Therefore a cube would have a specific surface area of approximately 1.38 times that of a sphere when they have the same surface area.

A.4.3 Square Prism (Side Length = a, Height = $2a$)

For a particle surface area y the Area:Volume ratio $(A:V)$ can be found by substituting the value of a for a constant particle surface area (A-18) into the existing

$A:V$ relationship (A-16). By dividing the $A:V$ of the square prism (A-54) by that of the sphere (A-51) the relationship of the specific surface area of the square prism to that of the sphere of the same surface area can be examined.

$$A:V = \frac{5}{a}$$

$$= \frac{5}{\sqrt{\frac{y}{10}}}$$

$$A:V = \frac{5\sqrt{10}}{\sqrt{y}} \qquad \textbf{A-54}$$

$$\frac{A:V_{Square\ Prism\ \ Length=a\ \ Height=2a}}{A:V_{Sphere\ \ Radius=r}} = \frac{5\sqrt{10}}{\sqrt{y}} \times \frac{\sqrt{y}}{6\sqrt{\pi}}$$

$$\frac{A:V_{Square\ Prism\ \ Length=a\ \ Height=2a}}{A:V_{Sphere\ \ Radius=r}} = \frac{5\sqrt{10}}{6\sqrt{\pi}} \approx 1.49 \qquad \textbf{A-55}$$

Therefore a square prism with a height of twice its side length would have a specific surface area of approximately 1.49 times that of a sphere with the same surface area.

A.4.4 Cylinder (Radius = R = Height)

For a particle surface area y the Area:Volume ratio $(A:V)$ can be found by substituting the value of R for a constant particle surface area (A-23) into the existing $A:V$ relationship (A-21). By dividing the $A:V$ of the cylinder (A-56) by that of the sphere (A-51) the relationship of the specific surface area of the cylinder to that of the sphere of the same surface area can be examined.

$$A:V = \frac{4}{R}$$

$$= \frac{4}{\frac{1}{2}\sqrt{\frac{y}{\pi}}}$$

$$A:V = \frac{8\sqrt{\pi}}{\sqrt{y}} \qquad \textbf{A-56}$$

$$\frac{A:V_{Cylinder\ \ Radius=Height=R}}{A:V_{Sphere\ \ Radius=r}} = \frac{8\sqrt{\pi}}{\sqrt{y}} \times \frac{\sqrt{y}}{6\sqrt{\pi}}$$

$$\frac{A:V_{Cylinder\ \ Radius=Height=R}}{A:V_{Sphere\ \ Radius=r}} = \frac{4}{3} \approx 1.33 \qquad \textbf{A-57}$$

Therefore a cylinder with its height equal to its radius would have a specific surface area of approximately 1.33 times that of a sphere with the same surface area.

A.4.5 Cylinder (Radius = R, Height = $2R$)

For a particle surface area y the Area:Volume ratio $(A:V)$ can be found by substituting the value of R for a constant particle surface area (A-28) into the existing $A:V$ relationship (A-26). By dividing the $A:V$ of the cylinder (A-58) by that of the sphere (A-51) the relationship of the specific surface area of the cylinder to that of the sphere of the same surface area can be examined.

$$A:V = \frac{3}{R}$$

$$= \frac{3}{\sqrt{\frac{y}{6\pi}}}$$

$$A:V = \frac{3\sqrt{6\pi}}{\sqrt{y}} \qquad \textbf{A-58}$$

$$\frac{A:V_{Cylinder\ \ Radius=R\ \ Height=2R}}{A:V_{Sphere\ \ Radius=r}} = \frac{3\sqrt{6\pi}}{\sqrt{y}} \times \frac{\sqrt{y}}{6\sqrt{\pi}}$$

$$\frac{A:V_{Cylinder\ \ Radius=R\ \ Height=2R}}{A:V_{Sphere\ \ Radius=r}} = \frac{\sqrt{6}}{2} \approx 1.22 \qquad \textbf{A-59}$$

Therefore a cylinder with its height equal to twice its radius would have a specific surface area of approximately 1.22 times that of a sphere with the same surface area.

A.4.6 Cylinder (Radius = R, Height = $\frac{R}{10}$)

For a particle surface area y the Area:Volume ratio $(A:V)$ can be found by substituting the value of R for a constant surface area (A-33) into the existing $A:V$ relationship (A-31). By dividing the $A:V$ of the cylinder (A-60) by that of the sphere (A-51) the relationship of the specific surface area of the cylinder to that of the sphere of the same surface area can be examined.

$$A:V = \frac{22}{R}$$

$$= \frac{22}{\sqrt{\frac{5y}{11\pi}}}$$

$$A:V = \frac{22\sqrt{11\pi}}{\sqrt{5y}} \qquad \text{A-60}$$

$$\frac{A:V_{Cylinder\ \ Radius=R\ \ Height=R/10}}{A:V_{Sphere\ \ Radius=r}} = \frac{22\sqrt{11\pi}}{\sqrt{5y}} \times \frac{\sqrt{y}}{6\sqrt{\pi}}$$

$$\frac{A:V_{Cylinder\ \ Radius=R\ \ Height=R/10}}{A:V_{Sphere\ \ Radius=r}} = \frac{11\sqrt{11}}{3\sqrt{5}} \approx 5.44 \qquad \text{A-61}$$

Therefore a cylinder with its height equal to a tenth of its radius would have a specific surface area of approximately 5.44 times that of a sphere with the same surface area.

A.5 Summary of Results

Table A-1: Summary of particle volumes, surfaces areas, area:volume ratios and particle dimensions for fixed volumes and surface areas.

3D Shape	Volume (V)	Area (A)	Area:Volume $(A:V)$	Fixed Volume (x)	Fixed Area (y)
Sphere					
Radius $= r$	$\frac{4\pi r^3}{3}$	$4\pi r^2$	$\frac{3}{r}$	$r = \sqrt[3]{\frac{3x}{4\pi}}$	$r = \frac{1}{2}\sqrt{\frac{y}{\pi}}$
Radius $= \sqrt[3]{2}R$	$\frac{8\pi R^3}{3}$	$4\left(\sqrt[3]{2}\right)^2 \pi R^2$	$\frac{3}{\sqrt[3]{2}R}$	-	-
Cube					
Length $= a$	a^3	$6a^2$	$\frac{6}{a}$	$a = \sqrt[3]{x}$	$a = \sqrt{\frac{y}{6}}$
Square Prism					
Length $= a$ Height $= 2a$	$2a^3$	$10a^2$	$\frac{5}{a}$	$a = \sqrt[3]{\frac{x}{2}}$	$a = \sqrt{\frac{y}{10}}$
Cylinder					
Radius $= R$ Height $= R$	πR^3	$4\pi R^2$	$\frac{4}{R}$	$R = \sqrt[3]{\frac{x}{\pi}}$	$R = \frac{1}{2}\sqrt{\frac{y}{\pi}}$
Radius $= R$ Height $= 2R$	$2\pi R^3$	$6\pi R^2$	$\frac{3}{R}$	$R = \sqrt[3]{\frac{x}{2\pi}}$	$R = \sqrt{\frac{y}{6\pi}}$
Radius $= R$ Height $= \frac{R}{10}$	$\frac{\pi R^3}{10}$	$\frac{11\pi R^2}{5}$	$\frac{22}{R}$	$R = \sqrt[3]{\frac{10x}{\pi}}$	$R = \sqrt{\frac{5y}{11\pi}}$

Table A-2: Summary of area:volume ratios for comparisons made on the basis of dimension, volume and surface area.

3D Shape	Dimensional Basis		Volume Basis		Area Basis	
	$A:V$		$A:V$		$A:V$	
Sphere						
Radius = r	$\frac{3}{r}$	1	$\frac{3\sqrt[3]{4\pi}}{\sqrt[3]{3x}}$	1	$\frac{6\sqrt{\pi}}{\sqrt{y}}$	1
Radius = $\sqrt[3]{2}R$	$\frac{3}{\sqrt[3]{2}R}$	$\frac{1}{\sqrt[3]{2}} \approx 0.79$	-	-	-	
Cube						
Length = a	$\frac{6}{a}$	2	$\frac{6}{\sqrt[3]{x}}$	$\frac{2\sqrt[3]{3}}{\sqrt[3]{4\pi}} \approx 1.24$	$\frac{6\sqrt{6}}{\sqrt{y}}$	$\frac{\sqrt{6}}{\sqrt{\pi}} \approx 1.38$
Square Prism						
Length = a Height = $2a$	$\frac{5}{a}$	$\frac{5}{3} \approx 1.67$	$\frac{5\sqrt[3]{2}}{\sqrt[3]{x}}$	$\frac{5\sqrt[3]{3}}{3\sqrt[3]{2\pi}} \approx 1.30$	$\frac{5\sqrt{10}}{\sqrt{y}}$	$\frac{5\sqrt{10}}{6\sqrt{\pi}} \approx 1.49$
Cylinder						
Radius = R Height = R	$\frac{4}{R}$	$\frac{4}{3} \approx 1.33$	$\frac{4\sqrt[3]{\pi}}{\sqrt[3]{x}}$	$\frac{4\sqrt[3]{3}}{3\sqrt[3]{4}} \approx 1.21$	$\frac{8\sqrt{\pi}}{\sqrt{y}}$	$\frac{4}{3} \approx 1.33$
Radius = R Height = $2R$	$\frac{3}{R}$	1	$\frac{3\sqrt[3]{2\pi}}{\sqrt[3]{x}}$	$\frac{\sqrt[3]{3}}{\sqrt[3]{2}} \approx 1.14$	$\frac{3\sqrt{6\pi}}{\sqrt{y}}$	$\frac{\sqrt{6}}{2} \approx 1.22$
Radius = R Height = $\frac{R}{10}$	$\frac{3}{R}$	$\frac{22}{3} \approx 7.33$	$\frac{22\sqrt[3]{\pi}}{\sqrt[3]{10x}}$	$\frac{22\sqrt[3]{3}}{3\sqrt[3]{40}} \approx 3.09$	$\frac{22\sqrt{11\pi}}{\sqrt{5y}}$	$\frac{11\sqrt{11}}{3\sqrt{5}} \approx 5.44$

Appendix B BatteryTestDataProcessing Manual

The BatteryTestDataProcessing.xls spreadsheet performs a number of different functions to assist with the analysis of battery testing data. Most of the processing options within the spreadsheet automatically save one or more files. The files are saved in the same location as the original file with a filename based on the name of the file being opened for processing. When files are saved automatically if the file already exists it will be overwritten without any warning. As a result of the automatic saving of files, files should only be opened for processing from the hard disk.

There are many calculations performed within the spreadsheet. Double precision floating-point numbers are used to store the results of all calculations involving the data itself being processed. Double precision floating-point variables are capable of storing negative numbers from $-1.79769313486231\times10^{-308}$ to $-4.94065645841247\times10^{-324}$ and positive numbers $4.94065645841247\times10^{-324}$ to $1.79769313486232\times10^{308}$. This ensures that data sets containing large numbers - especially time values in seconds can be processed and that accuracy is maintained throughout calculations. Other variable types are also used where appropriate within the spreadsheet.

B.1 Security and using the spreadsheet

To enable users to verify that the spreadsheet they are using and the macros within came from Matthew Lindsay, the files have a digital signature attached to them. If the files are modified then this digital signature is removed. The macros themselves are also password protected to prevent modification of them and the functions they perform. On running the spreadsheet the first thing you are likely to see is a security warning box (Figure B-1). From this page you can verify that the spreadsheet has not been altered. The name Matthew Lindsay as shown in Figure B-1 does not guarantee the spreadsheet has not been modified because others could easily replicate this part of a digital signature. If the details of the certificate itself are examined and compared to known details of the certificate you can be fairly certain that the spreadsheet has not been modified. The details of the digital signature are accessible by clicking the "Details…" button in the "Security Warning" dialog box (Figure B-2).

Figure B-1: "Security Warning" dialog box.

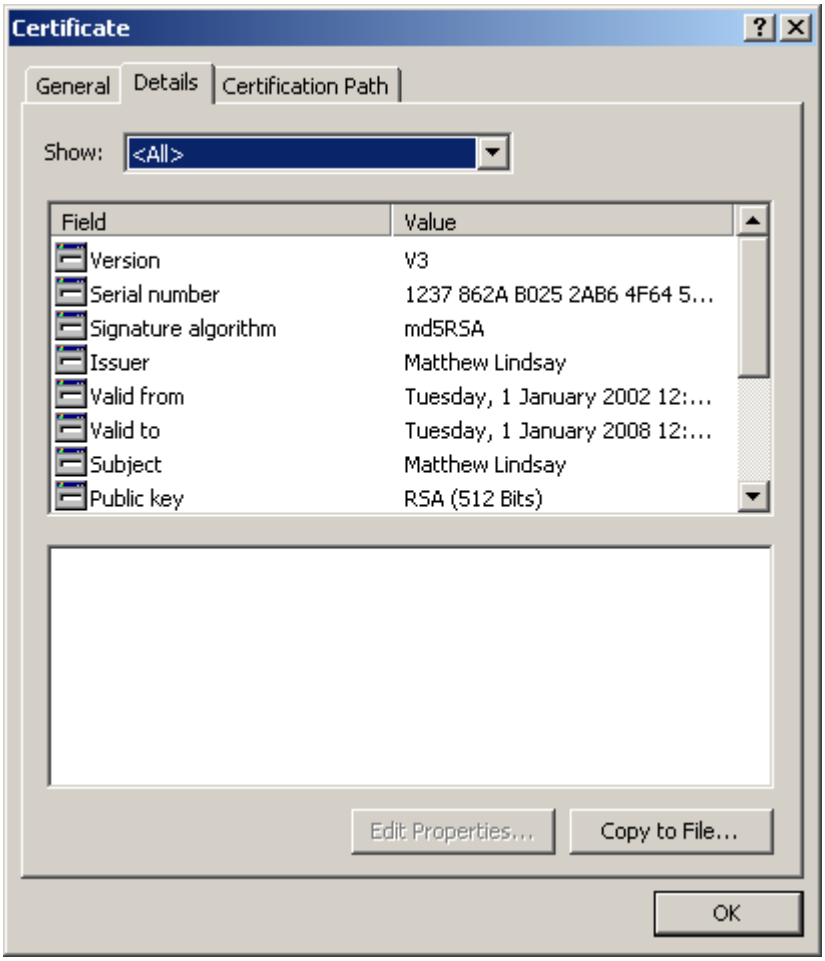

Figure B-2: Details of digital signature.

Having confirmed the spreadsheet has not been modified it is safe to "Enable Macros" on the "Security Warning" dialog box. If however this button is grayed out as it is in Figure B-3 there are two options to enable the macros:

- Tick the "Always trust macros from this source" check box in the "Security Warning" dialog box.
- Close the "Security Warning" dialog box and open the "Tools" menu in Excel, select the "Macro" menu item, and the "Security" item from that menu. The "Security" dialog box will then appear (Figure B-4). Change the security level to medium.

Figure B-3: "Security Warning" dialog box.

Having enabled the running of macros a "License Agreement" dialog box will appear (Figure B-5). The conditions of the agreement must be agreed to and clicking on "Accept" implies that you have read the conditions outlined in this agreement and agreed to them. This will also enable the spreadsheet to be used. If however you do not agree to the conditions and click "Reject" then the spreadsheet will be closed automatically.

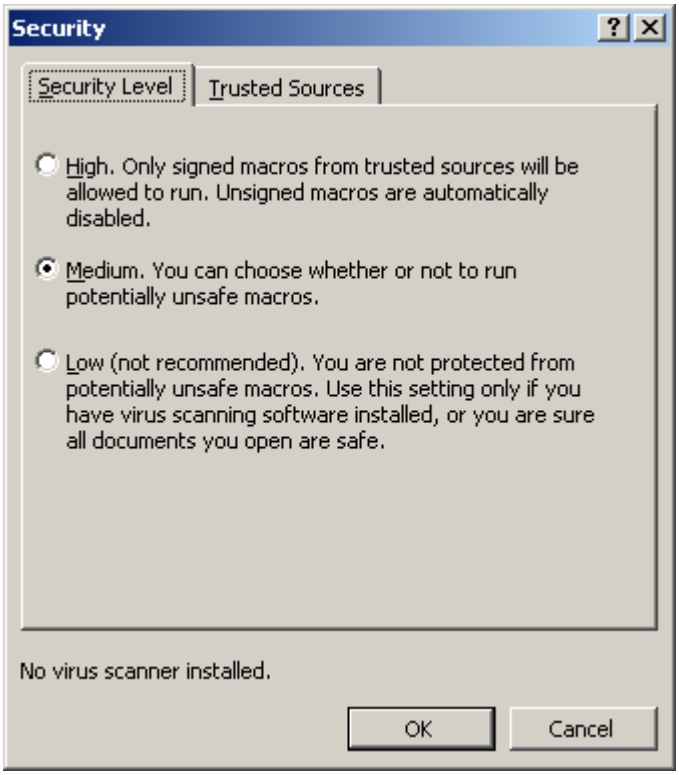

Figure B-4: "Security" settings dialog box.

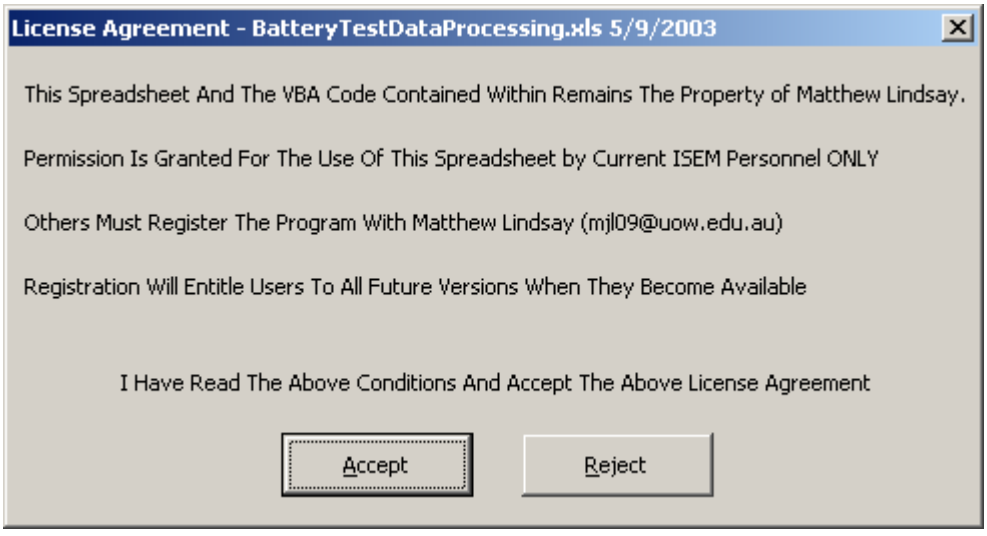

Figure B-5: License Agreement dialog box.

Following clicking on "Accept" the "Select Desired Processing Method" dialog box will appear. All the processing options in the spreadsheet are contained within the tabs of this dialog box (Figure B-6).

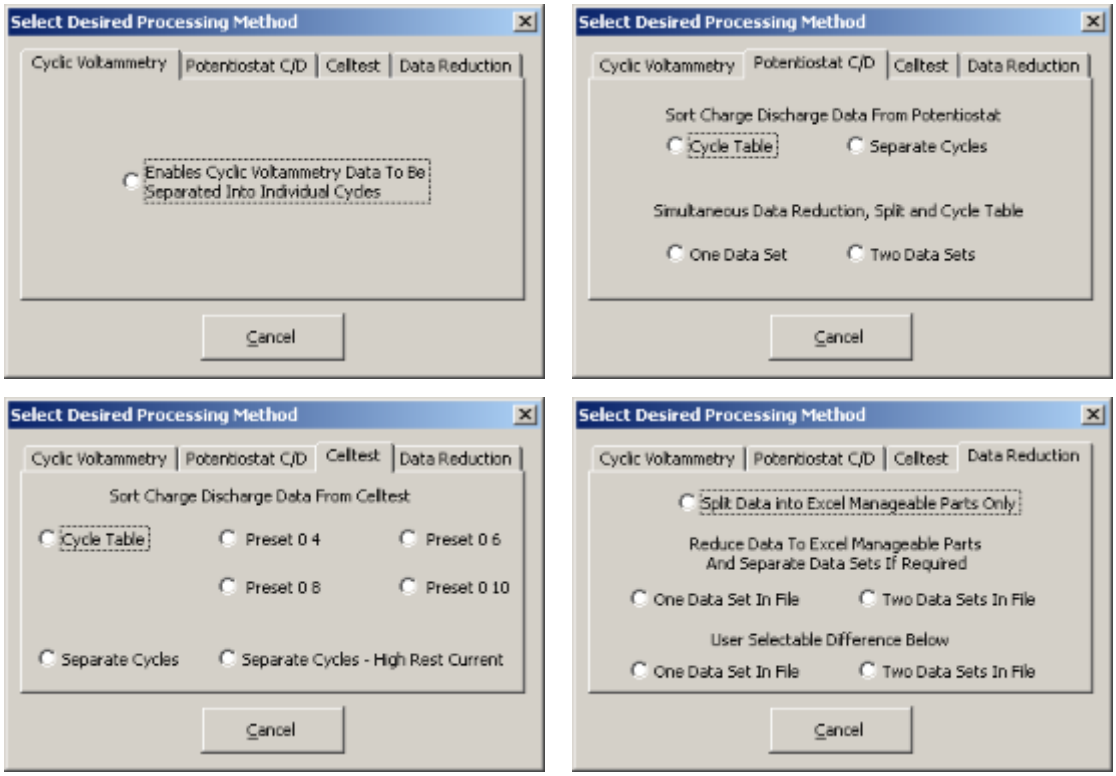

Figure B-6: "Select Desired Processing Method" dialog box and contents of the various tabs.

Further details on the processing procedures available can be found in the subsequent sections of this document. If the "Cancel" button is clicked a "Processing Aborted" dialog box will appear (Figure B-7). The same dialog box will appear if the "Cancel" Button on any of the dialog boxes is clicked.

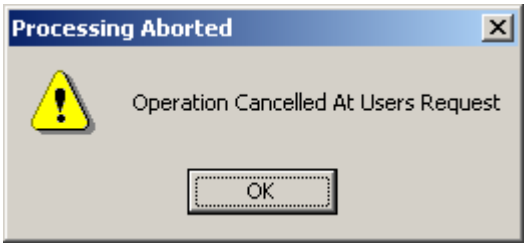

Figure B-7: "Processing Aborted" dialog box.

If an unexpected error occurs during processing (including whilst trying to open a file) then a different "Processing Aborted" dialog box will appear (Figure B-8). Another dialog box that can appear at the time of opening a file is the "Error Loading File - Processing Aborted" dialog box (Figure B-9). This appears when the file is not loaded entirely. Excel only has a certain number of rows available to load data into, if there are more rows of data in the file then Excel has to load them into this error occurs.

Currently Excel supports a maximum of 65536 rows, this is however limited by available memory and system resources. Any computer meeting the system requirements for Office 2000 should be capable of displaying this maximum number of rows. If this error does occur the "Data Reduction" features of the spreadsheet can be used to allow processing of the file.

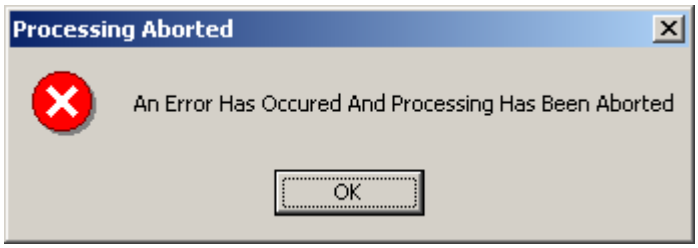

Figure B-8: "Processing Aborted" dialog box.

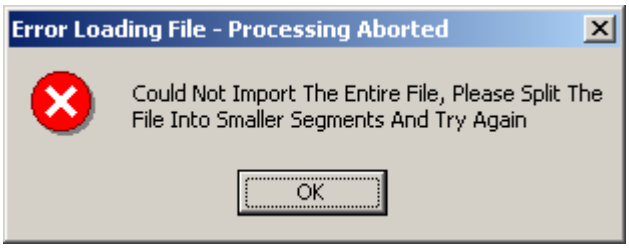

Figure B-9: "Error Loading File - Processing Aborted" dialog box.

A number of other dialog boxes will appear whilst using the spreadsheet to gather the required parameters to process the supplied data. If required parameters are missing or are entered incorrectly in these dialog boxes a warning dialog box will appear notifying of the invalid/missing entry.

B.2 Cyclic Voltammetry

B.2.1 Sorting Method

To sort cyclic voltammetry (CV) data a point **C** is used to divide the data into two segments (Figure B-10).

- Voltage region greater than or equal to **C** (Blue region in graph)
- Voltage region less than **C** (Red region in graph)

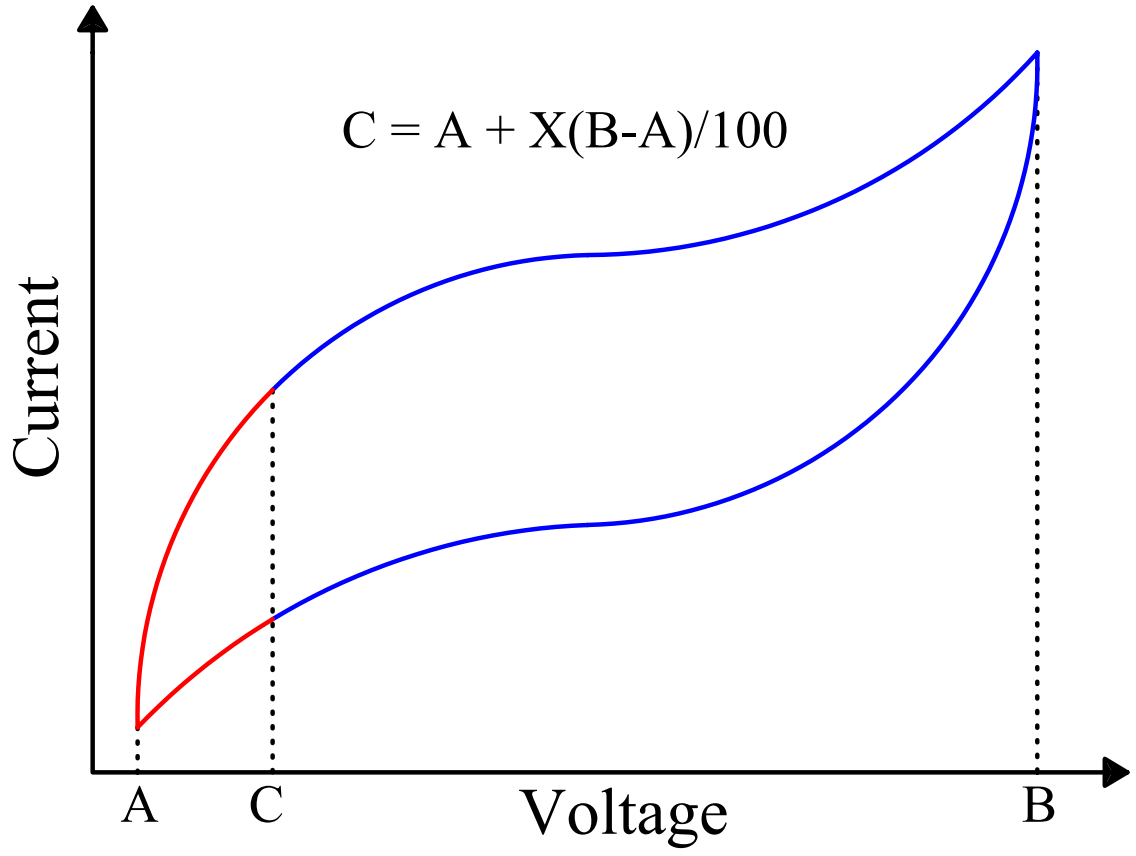

Figure B-10: Schematic of sorting method for CV data.

Following application of this principle CV data can then be sorted into approximate cycles by taking consecutive voltage regions of data. The value of **C** is chosen to have the desired affect on the sorted data. Ideally the value should be as close as possible to one of the cycling end points as this reduces the amount of data that actually belongs to either the previous or next cycle as the case may be. The choice of **C** for instance affects the order of the charge discharge process presented in the voltammogram. For instance either:

- Discharge and the subsequent charge
- Charge and the subsequent discharge

In processing the data the value of another variable **X** is altered to find the most appropriate value for **C** according to:

$$\mathbf{C} = \mathbf{A} + \mathbf{X}\,(\mathbf{B}-\mathbf{A})/100$$

where

X is such that $1 \leq \mathbf{X} \leq 99$

A is the minimum voltage in the data

B is the maximum voltage in the data

- For discharge and the subsequent charge - a high cutoff value is selected (See Figure B-11)
    - The cycle will contain a small part of the previous charge (near the upper cycle limit)
    - The cycle will be missing a small part of the actual charge (near the upper cycle limit)

- For charge and subsequent discharge - a low cutoff value is selected (see Figure B-12)
    - The cycle will contain a small part of the subsequent charge (near the lower cycle limit)
    - The cycle will be missing a small part of the actual charge (near the lower cycle limit)

B.2.1.1 High Cutoff

< Cutoff

- Given a hypothetical CV experiment where the first point in the data set is less than the cutoff value.
- The voltage-time relationship for the first few cycles of this experiment are shown in Figure B-11a demonstrating which cycle the data will belong to.
- The hypothetical voltammograms for the first and subsequent cycles are shown in Figure B-11b and Figure B-11e respectively.

> Cutoff

- Given a hypothetical CV experiment where the first point in the data set is greater than the cutoff value.
- The voltage-time relationship for the first few cycles of this experiment are shown in Figure B-11c demonstrating which cycle the data will belong to.
- The hypothetical voltammograms for the first and subsequent cycles are shown in Figure B-11d and Figure B-11e respectively.

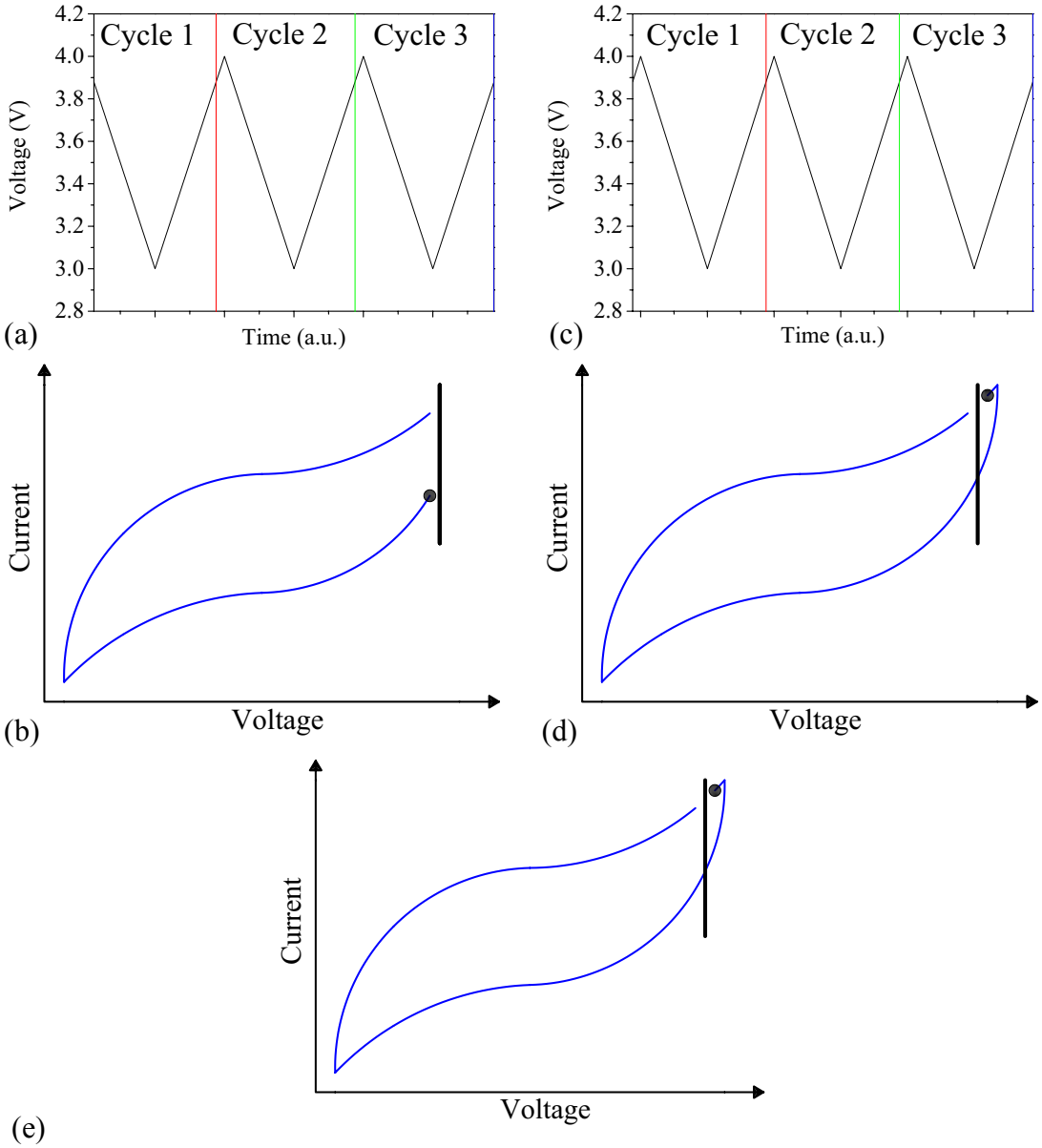

The solid black dot in these figures indicates the starting point of the voltammogram.

Figure B-11: Demonstration of sorted data for high cutoff value.

B.2.1.2 Low Cutoff

< Cutoff

- Given a hypothetical CV experiment where the first point in the data set is less than the cutoff value.
- The voltage-time relationship for the first few cycles of this experiment are shown in Figure B-12a demonstrating which cycle the data will belong to.
- The hypothetical voltammograms for the first and subsequent cycles are shown in Figure B-12b and Figure B-12e respectively.

> Cutoff

- Given a hypothetical CV experiment where the first point in the data set is greater than the cutoff value.
- The voltage-time relationship for the first few cycles of this experiment are shown in Figure B-12c demonstrating which cycle the data will belong to.
- The hypothetical voltammograms for the first and subsequent cycles are shown in Figure B-12d and Figure B-12e respectively.

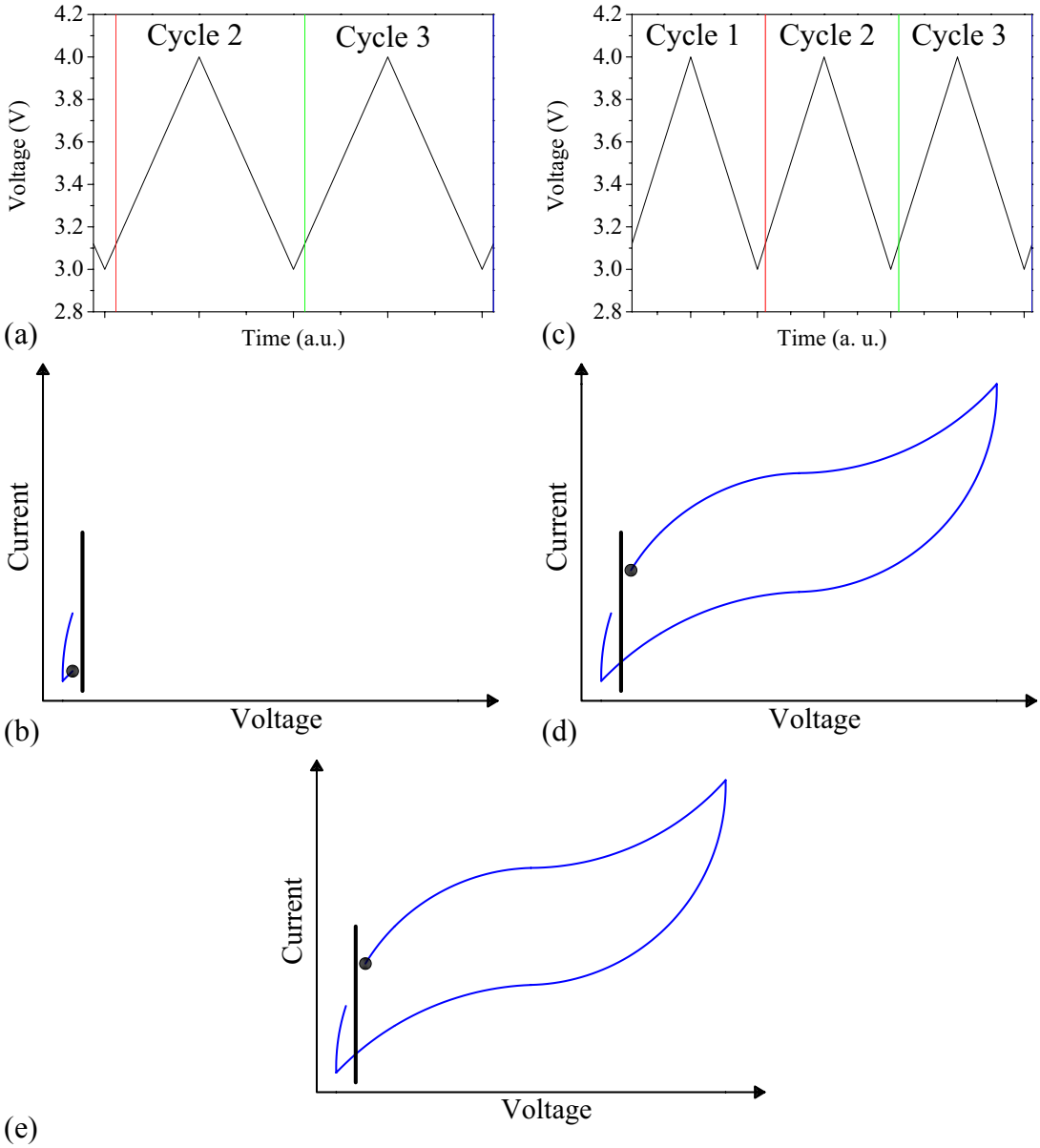

The solid black dot in these figures indicates the starting point of the voltammogram.

Figure B-12: Demonstration of sorted data for low cutoff value.

B.2.2 Processing CV Data

B.2.2.1 Format of Data File

The data file for CV data should consist of three Tab delimited columns containing time, voltage and current data respectively. These columns can have labels in the data file provided that the label of the first column is "time". In this case the labels will be ignored. Table B-1 provides two examples of input files and the demonstration file CV.txt is another example.

Table B-1: Examples of input file for CV data Sorter.

time	voltage	current				
0	2.2175	-10.25		0	2.2175	-10.25
1.75	2.15	-11.25		1.75	2.15	-11.25
4	2.2125	-10.25		4	2.2125	-10.25
6.5	2.21	-10.5	OR	6.5	2.21	-10.5
9.25	2.075	-11.75		9.25	2.075	-11.75
12	2.205	-10.75		12	2.205	-10.75
14.5	2.2025	-11		14.5	2.2025	-11
16.5	2.2	-11		14.5	2.2	-11
19.5	2.1975	-11.5		19.5	2.1975	-11.5

After selecting the CV processing option (Figure B-13) and loading the file a dialog box is presented to select the cycles to process (Figure B-14).

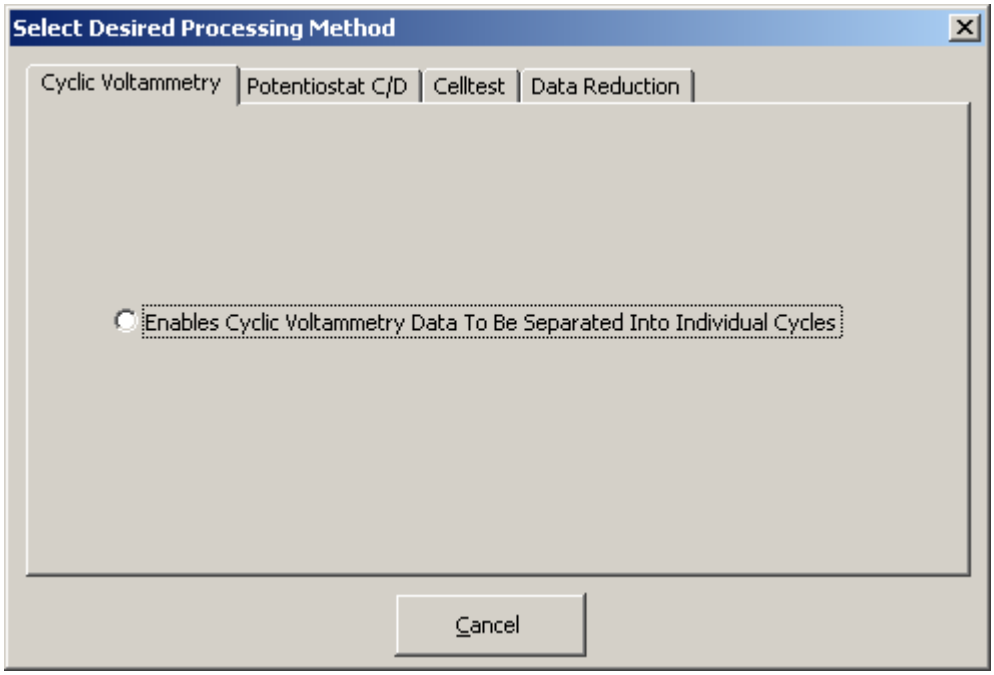

Figure B-13: "Cyclic Voltammetry" selection tab.

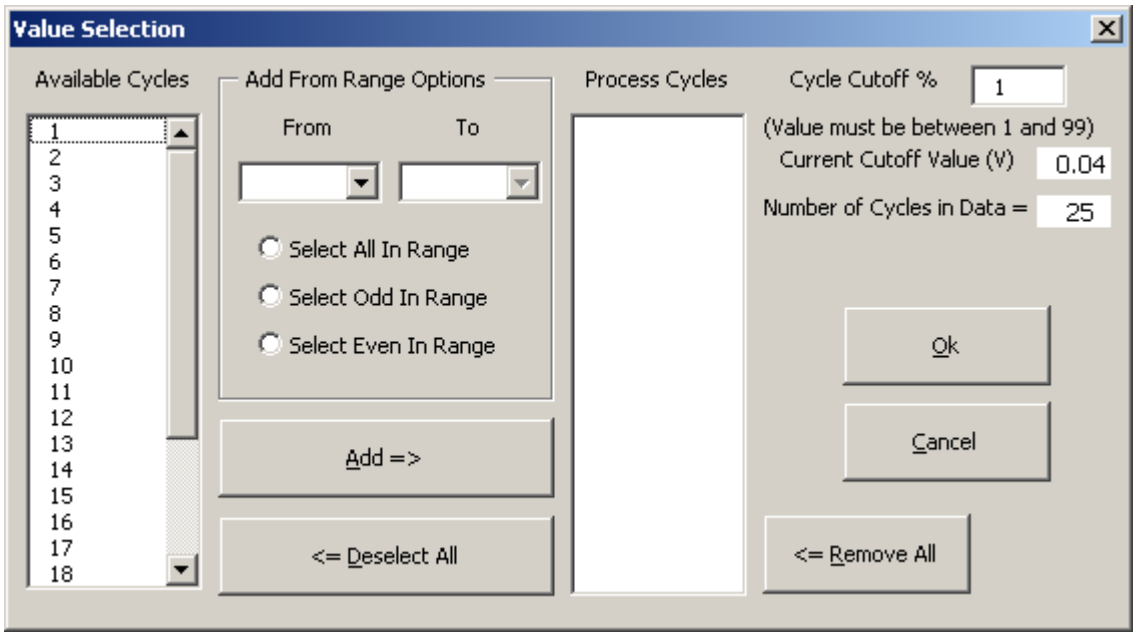

Figure B-14: Example of "Value Selection" dialog box.

The first item to change in the dialog box is the "Cycle Cutoff %". Its value should be changed a few times to find either the lowest or highest value depending on the sorting requirements.

When the "Cycle Cutoff %" value is changed:

- "Current Cutoff Value (V)" will change
- "Number of Cycles in Data" may change

It is the "Number of Cycles in Data" value that should be monitored to determine if an appropriate "Cycle Cutoff %" has been selected. By altering the "Cycle Cutoff %" value by a few percent the "Number of Cycles in Data" value should not change by more than 1 or 2, ideally it should not change at all. If the "Number of Cycles in Data" varies greatly with a change of a few percent of the "Cycle Cutoff %" then it should continue to be changed until a stable region can be found.

Once an appropriate cutoff value is found the cycles that you wish to extract the data for should be selected from the "Available Cycles" list.

This can be done two ways:

- Individual cycles can be selected by left clicking on the cycle number in the "Available Cycles" list

- Cycles can be added from a range using the “Add from Range Options”
    1. Select a number from the “From Range” drop down list.
    2. Select a number from the “To Range” drop down list.
    3. Click the desired option.
        - “Select All In Range”
        - “Select Odd In Range”
        - “Select Even In Range”

A cycle is selected if its value is highlighted. Selected items can be deselected individually by clicking on the relevant number in the “Available Cycles” list or all can be deselected by clicking the “<= Deselect All” button. All selected items are also removed from this list when they are added to the “Process Cycles” list.

With all the cycles desired to be sorted selected in the “Available Cycles” list they need to be added to the “Process Cycles” list by clicking the “Add =>” button. In this case items can be removed by double clicking the value in the “Process Cycles” list or all items can be removed by clicking the “<= Remove All” button.

With the dialog box complete (example Figure B-15) the “Ok” button can be clicked and the processing will start.

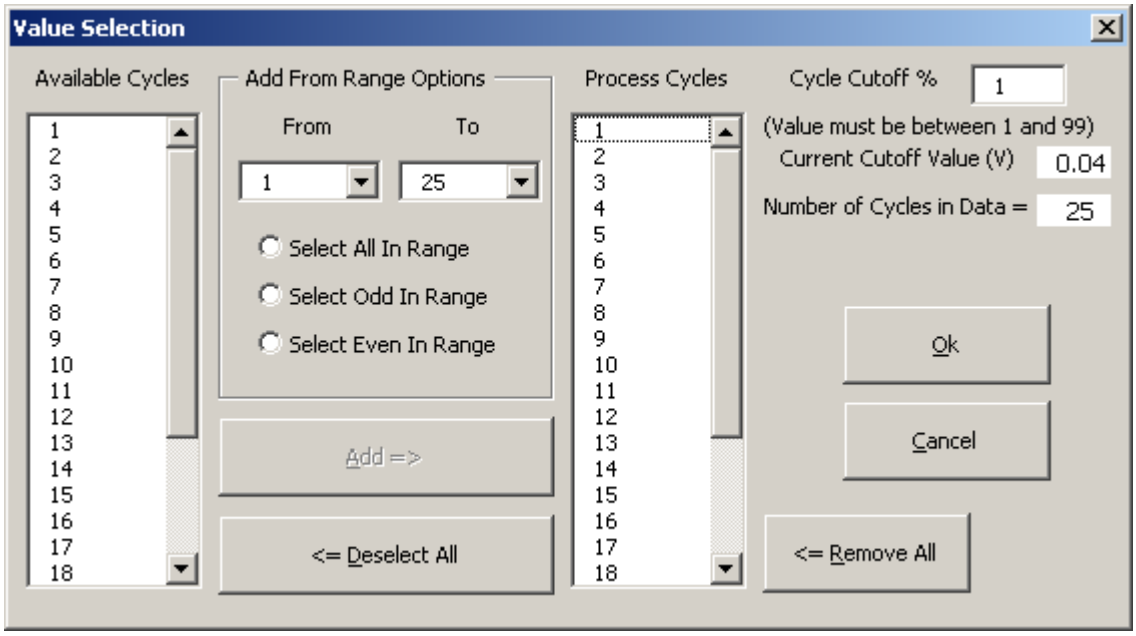

Figure B-15: Example of a completed “Value Selection” dialog box.

An indication of the processing being done at the time will be visible in the lower left of the Excel window. The first step is to process the rows with the current row being processed being indicated (Figure B-16). Once this is complete the selected cycles will be extracted with the details again indicated in the lower left of the Excel window (Figure B-17).

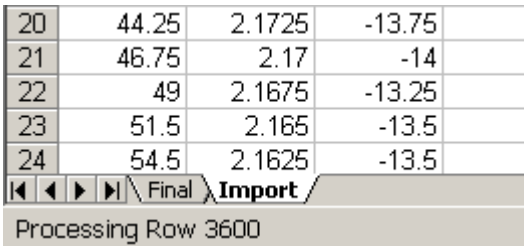

Figure B-16: Example of Excel row processing indication.

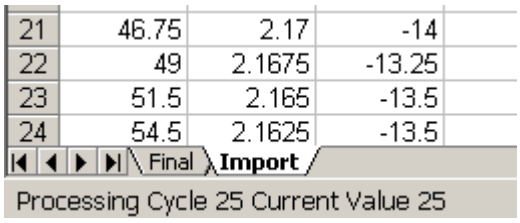

Figure B-17: Example of Excel processing cycle indication.

If 80 or less cycles are processed the file will be automatically saved with the same name and an added extension.

CV.txt => CV.txt_CV.txt

The spreadsheet will then be restarted so further data can be processed.

If 80 or more cycles are processed the spreadsheet stops running so that the data can be saved.

An example of the processed output is shown in Figure B-18, in which:

Column A contains time data

Column B contains voltage data

Column C contains current data

	A	B	C	D	E	F	
1	Cycle 1			Cycle 2			C
2	0	2.2175	-10.25	2238.75	0.05	-472.75	
3	1.75	2.215	-11.25	2241.25	0.0525	-471.25	
4	4	2.2125	-10.25	2243.75	0.055	-469.5	
5	6.5	2.21	-10.5	2246.25	0.0575	-468.5	
6	9.25	2.2075	-11.75	2248.5	0.06	-467.75	
7	12	2.205	-10.75	2251	0.0625	-466.5	
8	14.5	2.2025	-11	2251.25	0.06	-466	
9	16.5	2.2	-11	2251.5	0.0625	-466.25	
10	19.5	2.1975	-11.5	2253.5	0.065	-465.25	
11	21.75	2.195	-12.5	2256	0.0675	-464.75	

Figure B-18: Example of processed CV output.

B.3 Potentiostat C/D

B.3.1 Sorting Method

The first thing required before any other processing can be done is to identify the individual steps in the data. This is accomplished through comparing the values of the currents. There are two different comparisons being made at the same time.

- If the previous rows current is negative (< 0) and the current rows current is greater or equal to zero (≥ 0) then the current row represents a new step
- If the previous rows current is positive (> 0) and the current rows current is less than or equal to zero (≤ 0) then the current row represents a new step

This is easy to see in a schematic of a change in the current (Figure B-19). Using the 6 points that have been labelled in the diagram the results of the two comparisons can be seen (Table B-2). The capacity is calculated using the difference in time between the first point and last point in a cycle.

Table B-2: Features of points used in Figure B-19.

Point	Current	Cycle	Step Type
1	> 0	A	Charge
2	= 0	A	Charge
3	< 0	A+1	Discharge
4	< 0	A+1	Discharge
5	= 0	A+1	Discharge
6	> 0	A+2	Charge

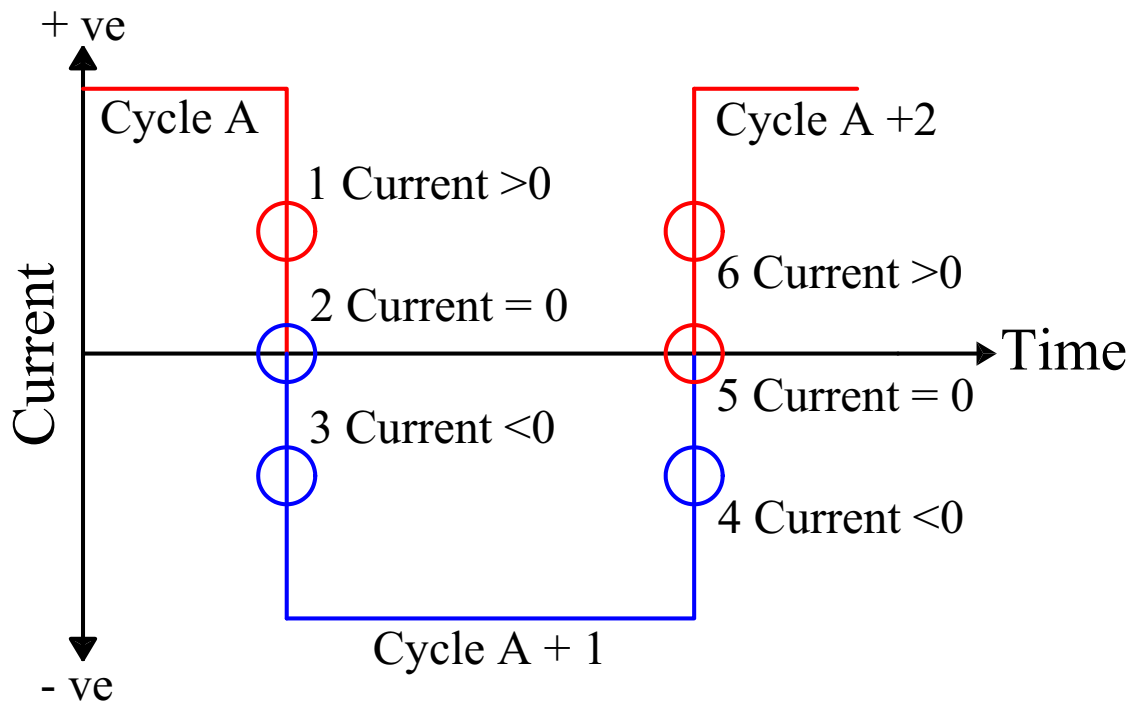

Figure B-19: Schematic of sorting method for potentiostat charge/discharge data.

B.3.2 Processing C/D Data

The purpose of the "Potentiostat C/D" (Figure B-20) functions is to retrieve capacity based data from a conforming data file. These functions include:

- "Cycle Table" - table of capacity values with respect to the cycle number for both charge and discharge.
- "Separate Cycles" - provide charge/discharge profiles data of desired cycles.
- "Simultaneous Data Reduction, Split and Cycle Table" - provides for the simultaneous data reduction, splitting if required and generation of Cycle Table.

B.3.2.1 Format of Data File

The data file for Potentiostat C/D "Cycle Table" and "Separate Cycles" consists of three tab delimited columns containing time, voltage and current data respectively with less than about 65530 rows of data. These columns can have labels in the data file provided that the label of the first column is "time". In this case the labels will be ignored.

Table B-3 provides two examples of input files and the demonstration file CapacitySorter.txt is another example. Although the example data shown in Table B-3 has not been reduced it is beneficial to do this with the "Data Reduction" features as

processing time is reduced. Reduced data is data in which two subsequent voltage readings are not the same.

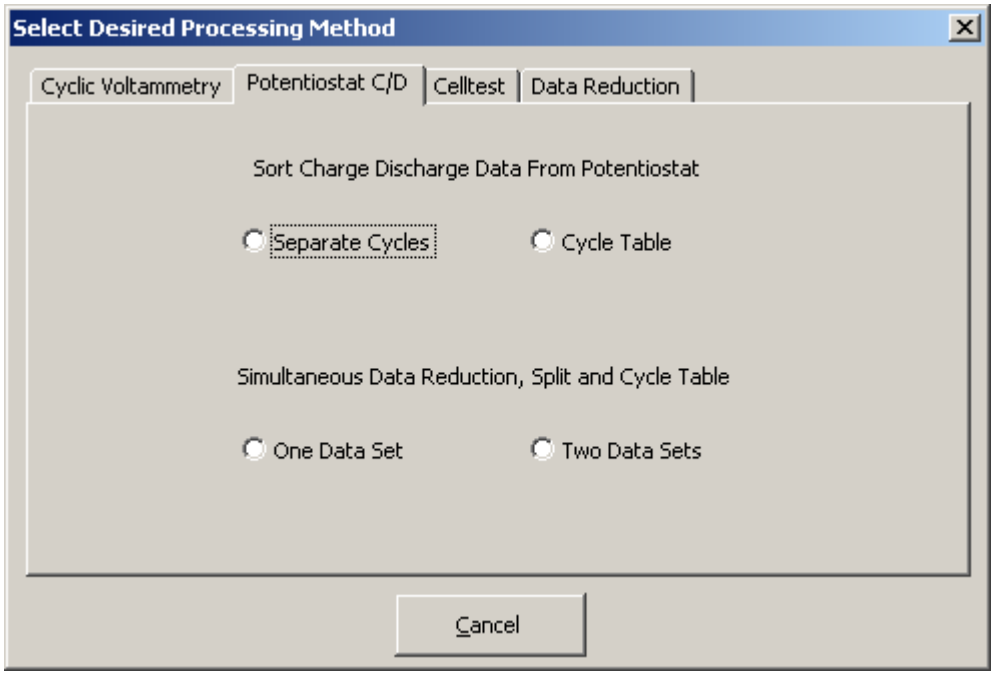

Figure B-20: "Potentiostat C/D" selection tab.

For the "One Data Set" and "Two Data Sets" options the requirements are the same as for the Data Reduction procedures. Regardless of which option is selected the first thing that needs to be done is to select the file to open. Following the file being opened a "Capacity Factor Entry" dialog box will appear (Figure B-21). On the form there are a number of options, including a conversion factor, mass and current entry. Through entry of all these factors the capacity can be calculated in mAh/g. Valid entries for each component of mass and current must be made for the analysis to continue. If invalid entries are detected a dialog box will appear to notify of the invalid data.

Table B-3: Examples of the format of data files for "Potentiostat C/D" data.

time	voltage	current				
0	3.514	-50		0	3.514	-50
1	3.514	-50		1	3.514	-50
2	3.513	-50		2	3.513	-50
3	3.512	-50		3	3.512	-50
4	3.511	-50		4	3.511	-50
5	3.511	-50	OR	5	3.511	-50
6	3.511	-50		6	3.511	-50
7	3.509	-50		7	3.509	-50
8	3.508	-50		8	3.508	-50
9	3.507	-50		9	3.507	-50
10	3.507	-50		10	3.507	-50

The conversion factor is used to convert the time in the data file to hours for the calculation of the capacity in mAh/g. Since the time in the data file is typically in seconds the appropriate conversion factor (in this case 3600) is the default value. So if no selection is used the default value is used automatically. Values for the electrode mass and current are also required for the capacity to be calculated. If however you want just the raw data sorted then the conversion factor should be set to 1, the current set to 1 mA and the mass set to 1g.

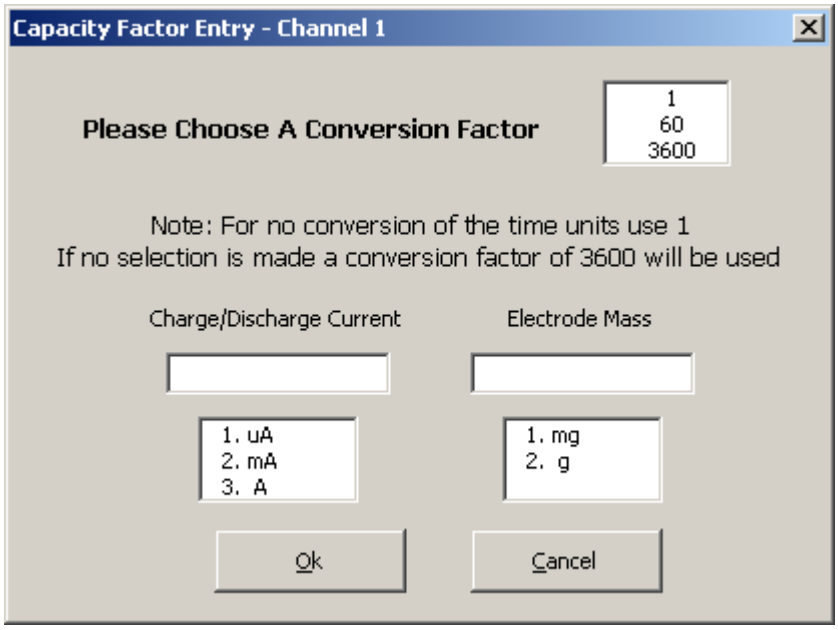

Figure B-21: "Capacity Factor Entry" dialog box.

With this dialog box completed the "Ok" button can be clicked. In the case of "Two Data sets" option being run a second "Capacity Factor Entry" dialog box will appear to collect the details for the second data set.

B.3.2.2 Cycle Table

With the required parameters having been gathered processing of the data begins. Once processing has been completed the processed file is automatically saved with the same name and an added extension.

CapacitySorter.txt => CapacitySorter.txtTableData.txt

The spreadsheet then restarts so further processing operations can be done.

During processing there will be an indication of the current processing being undertaken in the lower left of the Excel status bar (Figure B-22).

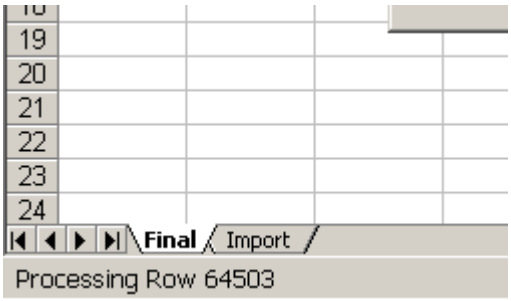

Figure B-22: Example of processing row indication in Excel status bar.

The processed data actually contains two representations of the same data (Figure B-23). Using this example there a number of items to point out. In the first row the electrode mass and the charge/discharge current are indicated.

	A	B	C	D	E	F	G	H	I	J	K	L
1	Current	0.05	mA	Mass	0.001	g						
2	1	1	1689.583	93.54167	2		1		1689.583	1		
3	3	2	199.7917	78.125	4	2	2	93.54167	199.7917	3		
4	5	3	166.6667	71.04167	6	4	3	78.125	166.6667	5		
5	7	4	139.7917	65.41667	8	6	4	71.04167	139.7917	7		
6	9	5	123.5417	61.04167	10	8	5	65.41667	123.5417	9		
7	11	6	111.875	58.54167	12	10	6	61.04167	111.875	11		
8	13	7	104.7917	56.25	14	12	7	58.54167	104.7917	13		
9	15	8	97.91667	54.16667	16	14	8	56.25	97.91667	15		
10	17	9	95.625	55.20833	18	16	9	54.16667	95.625	17		
11	19	10	95.83333	53.54167	20	18	10	55.20833	95.83333	19		
12	21	11	89.16667	52.08333	22	20	11	53.54167	89.16667	21		
13	23	12	84.79167	50.20833	24	22	12	52.08333	84.79167	23		
14	25	13	79.58333	48.54167	26	24	13	50.20833	79.58333	25		
15	27	14	75.625	47.5	28	26	14	48.54167	75.625	27		
16	29	15	72.70833	46.25	30	28	15	47.5	72.70833	29		
17	31	16	70.20833	44.79167	32	30	16	46.25	70.20833	31		
18	33	17	67.08333	814.7917	34	32	17	44.79167	67.08333	33		
19	35	18	101.875	402.9167	36	34	18	814.7917	101.875	35		
20	37	19	59.79167	17.08333	38	36	19	402.9167	59.79167	37		
21	39	20	29.58333	18.33333	40	38	20	17.08333	29.58333	39		
22	41	21	26.875	19.79167	42	40	21	18.33333	26.875	41		
23	43	22	26.04167	19.79167	44	42	22	19.79167	26.04167	43		
24	45	23	26.25	26.04167	46	44	23	19.79167	26.25	45		

CapacitySorter.txtTableData

Ready

Figure B-23: Example of processed data from "Cycle Table".

If the first step in your data was a charging procedure then the best set of data to examine is that in columns C and D.

- The number in column A represents the step number of the value in the same row in column C.
- The number in column E represents the step number of the value in the same row in column D.

- The number in column B represents the cycle number of that row.

If however the first step in your data was a discharge procedure then the best set of data to examine is that in columns H and I.

- The number in column F represents the step number of the value in the same row in column H.
- The number in column J represents the step number of the value in the same row in column I.
- The number in column G represents the cycle number of that row.

It is the step numbers that are used to actually get the full data of each cycle out using the "Separate Cycles" function contained within this spreadsheet.

B.3.2.3 Separate Cycles

With the file selected for processing and the "Capacity Factors Entry" dialog completed a small amount of preprocessing is necessary. During this time there will be an indication of the row being processed in the Excel status bar (Figure B-24)

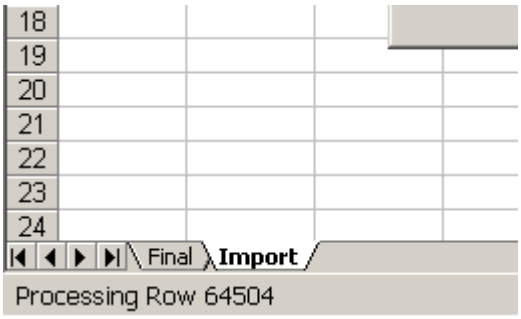

Figure B-24: Example of processing row indication in Excel status bar.

With the preprocessing completed a dialog box will appear to allow selection of the cycles to process Figure B-25.

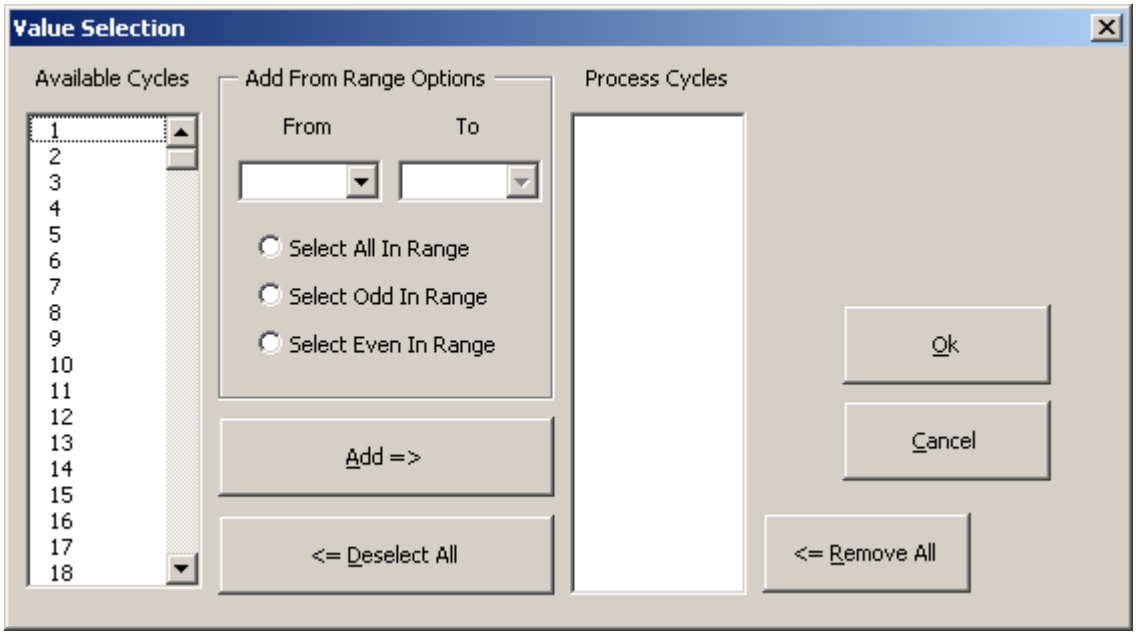

Figure B-25: "Value Selection" dialog box.

The cycles that you wish to extract the data for should be selected from the "Available Cycles" list.

This can be done two ways:

- Individual cycles can be selected by clicking on the cycle number in the "Available Cycles" list
- Cycles can be added from a range using the "Add from Range Options"
    1. Select a number from the "From Range" drop down list.
    2. Select a number from the "To Range" drop down list.
    3. Click the desired option.
        - "Select All In Range"
        - "Select Odd In Range"
        - "Select Even In Range"

A cycle is selected if its value is highlighted. Selected items can be deselected individually by clicking on the relevant number in the "Available Cycles" list or all can be deselected by clicking the "<= Deselect All" button. All selected items are also removed from this list when they are added to the "Process Cycles" list.

With all the cycles desired to be sorted selected in the "Available Cycles" list they need to be added to the "Process Cycles" list by clicking the "Add =>" button. In

this case items can be removed by double clicking the value in the "Process Cycles" list or all items can be removed by clicking the "<= Remove All" button.

With the dialog box complete (example Figure B-26) the "Ok" button can be clicked and the processing will start. Following completion of the dialog box the data for the selected cycles will be extracted, during this time an indication of the cycle data being processing will be visible in the Excel status bar (Figure B-27).

If 80 or less cycles are processed the file will be automatically saved with the same name and an added extension. Using the demonstration file CapacitySorter.txt as an example

CapacitySorter.txt => CapacitySorter.txt_CD.txt

A temporary file is also created during the processing of the data that again is saved with the same name and an added extension. In the case of the CapacitySorter.txt example file this temporary file would be called CapacitySorter.txt_Temp.txt and is usually deleted once processing is completed. Should the processing be aborted due to user request or error this file may still be present and can safely be deleted. The spreadsheet will also then reset itself so further data can be processed.

If 80 or more cycles are processed the spreadsheet stops running so that the data can be saved.

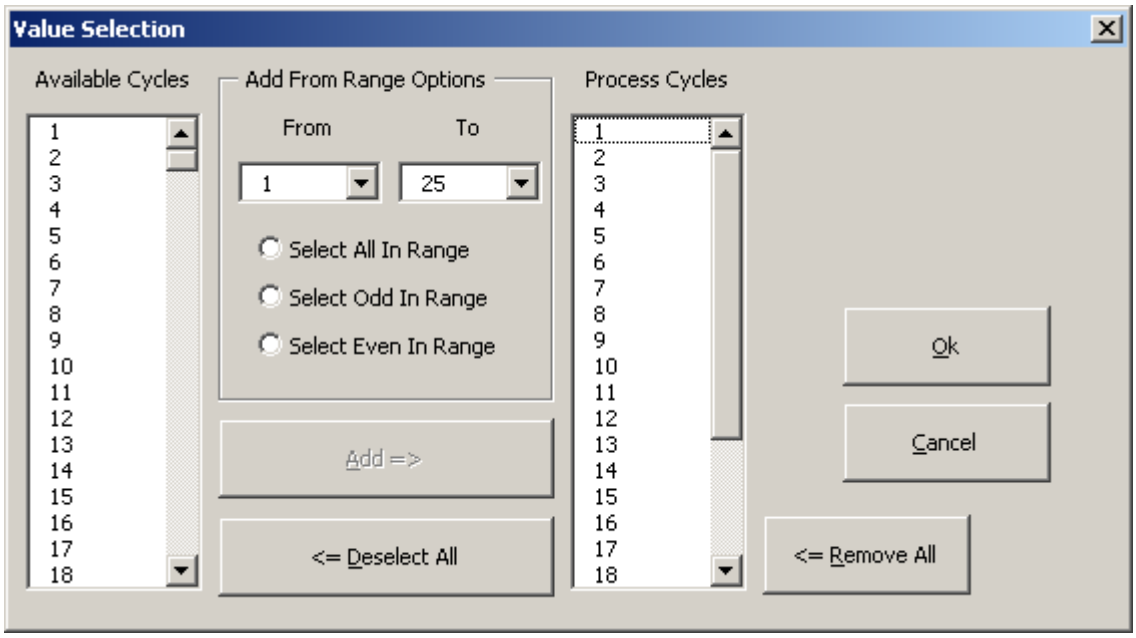

Figure B-26: Completed "Value Selection" dialog box.

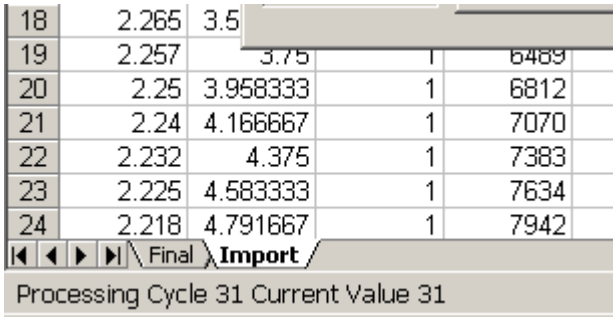

18	2.265	3.5		
19	2.257	3.75	1	6489
20	2.25	3.958333	1	6812
21	2.24	4.166667	1	7070
22	2.232	4.375	1	7383
23	2.225	4.583333	1	7634
24	2.218	4.791667	1	7942

Final | Import

Processing Cycle 31 Current Value 31

Figure B-27: Example of indication of cycle data extraction in Excel status bar.

The processed data (Figure B-28) contains a list of the current and electrode mass used to process the data in the first row. The second row contains the step numbers of the cycles that have been processed. The first column of each step number (eg column A and C) contains the voltage data for that step number, whilst the second column (eg column B and D) contains the capacity data in mAh/g.

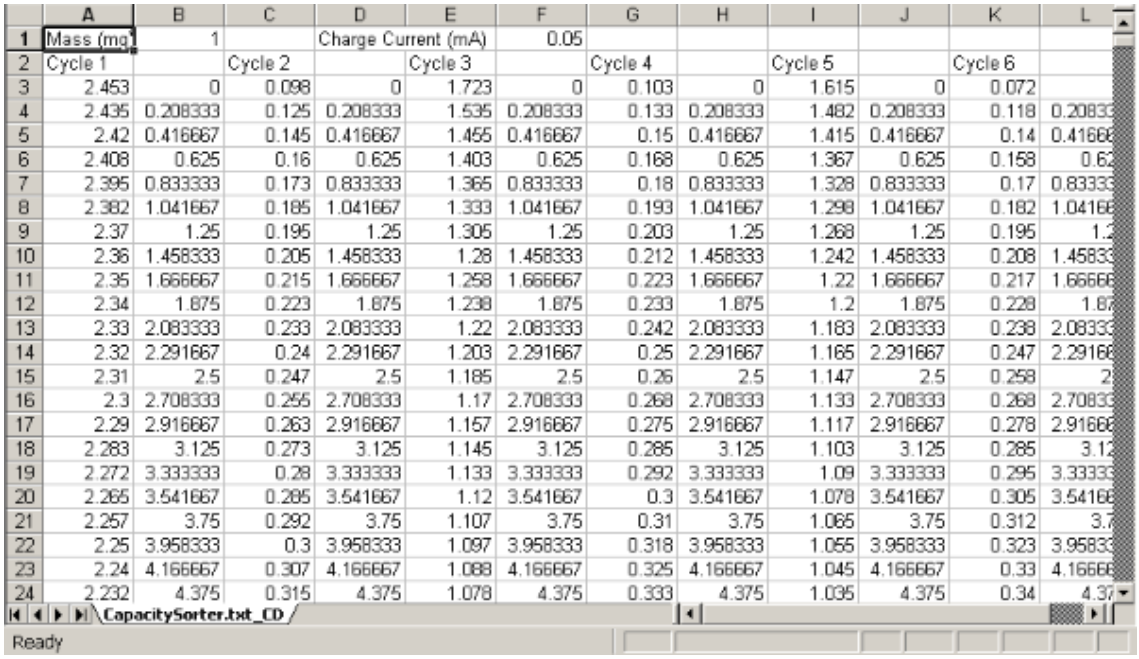

	A	B	C	D	E	F	G	H	I	J	K	L
1	Mass (mg)	1		Charge Current (mA)		0.05						
2	Cycle 1		Cycle 2		Cycle 3		Cycle 4		Cycle 5		Cycle 6	
3	2.453	0	0.098	0	1.723	0	0.103	0	1.615	0	0.072	
4	2.435	0.208333	0.125	0.208333	1.535	0.208333	0.133	0.208333	1.482	0.208333	0.118	0.20833
5	2.42	0.416667	0.145	0.416667	1.455	0.416667	0.15	0.416667	1.415	0.416667	0.14	0.41666
6	2.408	0.625	0.16	0.625	1.403	0.625	0.168	0.625	1.367	0.625	0.158	0.62
7	2.395	0.833333	0.173	0.833333	1.365	0.833333	0.18	0.833333	1.328	0.833333	0.17	0.83333
8	2.382	1.041667	0.185	1.041667	1.333	1.041667	0.193	1.041667	1.298	1.041667	0.182	1.04166
9	2.37	1.25	0.195	1.25	1.305	1.25	0.203	1.25	1.268	1.25	0.195	1.2
10	2.36	1.458333	0.205	1.458333	1.28	1.458333	0.212	1.458333	1.242	1.458333	0.208	1.45833
11	2.35	1.666667	0.215	1.666667	1.258	1.666667	0.223	1.666667	1.22	1.666667	0.217	1.66666
12	2.34	1.875	0.223	1.875	1.238	1.875	0.233	1.875	1.2	1.875	0.228	1.87
13	2.33	2.083333	0.233	2.083333	1.22	2.083333	0.242	2.083333	1.183	2.083333	0.238	2.08333
14	2.32	2.291667	0.24	2.291667	1.203	2.291667	0.25	2.291667	1.165	2.291667	0.247	2.29166
15	2.31	2.5	0.247	2.5	1.185	2.5	0.26	2.5	1.147	2.5	0.258	2
16	2.3	2.708333	0.255	2.708333	1.17	2.708333	0.268	2.708333	1.133	2.708333	0.268	2.70833
17	2.29	2.916667	0.263	2.916667	1.157	2.916667	0.275	2.916667	1.117	2.916667	0.278	2.91666
18	2.283	3.125	0.273	3.125	1.145	3.125	0.285	3.125	1.103	3.125	0.285	3.12
19	2.272	3.333333	0.28	3.333333	1.133	3.333333	0.292	3.333333	1.09	3.333333	0.295	3.33333
20	2.265	3.541667	0.285	3.541667	1.12	3.541667	0.3	3.541667	1.078	3.541667	0.305	3.54166
21	2.257	3.75	0.292	3.75	1.107	3.75	0.31	3.75	1.065	3.75	0.312	3.7
22	2.25	3.958333	0.3	3.958333	1.097	3.958333	0.318	3.958333	1.055	3.958333	0.323	3.95833
23	2.24	4.166667	0.307	4.166667	1.088	4.166667	0.325	4.166667	1.045	4.166667	0.33	4.16666
24	2.232	4.375	0.315	4.375	1.078	4.375	0.333	4.375	1.035	4.375	0.34	4.37

CapacitySorter.txt_CD

Ready

Figure B-28: Example of processed data output of "Separate Cycles".

B.3.2.4 Simultaneous Data Reduction, Split and Cycle Table

Provides the same functions as the "Reduce Data...If Required: One Data Set" and "Reduce Data...If Required: Two Data Sets In File" options in the "Data Reduction" section whilst also generating a "Cycle Table". Refer to these sections for further details

on the operations. A number of files are automatically saved with the same name and added extensions when processing files using these options.

When using the “Two Data Sets” option is does not matter if one of the data sets is CV data rather than charge/discharge data. The cycle table saved for this channel will however be meaningless.

Two example files have been provided.

B.3.2.4.1 “One Data Set”

Using the CapacitySplit_1.txt demonstration file the following processed files are automatically saved.

- CapacitySplit_1.txt_Part1_1.txt
- CapacitySplit_1.txtTableData1.txt

The Part1 file contains the reduced data set which is the same as would have been produced by running the “Reduce Data...If Required: One Data Set In File” option in the “Data Reduction” section. The TableData1 file contains the cycle table data that would have been produced by running the “Cycle Table” option.

B.3.2.4.2 “Two Data Sets”

Using the CapacitySplit_2.txt demonstration file the following processed files are automatically saved.

- CapacitySplit_2.txt _Part1_1.txt
- CapacitySplit_2.txt _Part2_1.txt
- CapacitySplit_2.txt _Part2_2.txt
- CapacitySplit_2.txtTableData1.txt
- CapacitySplit_2.txtTableData2.txt

The Part1 and Part2 files contains the reduced data set which is the same as would have been produced by running the “Reduce Data...If Required: Two Data Sets In File” option in the “Data Reduction” section. The TableData file contains the cycle table data that would have been produced by running the “Cycle Table” option on the data from each of the respective data sets. TableData1 belongs to the first data set and TableData2 to the second.

B.4 CellTest

B.4.1 Generating Data Files

In order to process battery test data from CellTest using the processing spreadsheet, it is first necessary to generate relevant data files using the CellTest software itself or if applicable the DataManager software. The basics of the procedure are the same for all versions of CellTest, though the names of menu items differ between the versions. The procedure when using DataManager is however different.

Two relevant data files can be created using CellTest and DataManager. The first is a data summary and is used to generate capacity tables. The second contains all the data and is used for retrieving charge/discharge profile data. In the case of CellTest both of these data files are text files whilst for DataManager the first is a text file and the second an Excel File.

CellTest Versions

Version 2.5 English

Chinese

Both versions will open files created by each other and file names have a *.cel extension. Version 4 of the software will not open these files, nor will version 2.5 open version 4 files.

Version 4 CD Version

Email Version

These versions will not open files created by each other and file names have a *.res extension. Version 2.5 will not open these files, nor will version 4 open version 2.5 files. The “Email Version” is the latest version of CellTest 4 and is the one currently in use. If your file can not be opened with the “Email Version” then it may have been recorded using the “CD Version” and that version is required to open the file.

DataManager

Files used by the DataManager software have a *.bts extension but *.res files can be opened by selecting to view all files when trying to open files. DataManager can’t however open *.cel files.

B.4.1.1 CellTest 2.5 - *.cel files

B.4.1.1.1 Opening Files and Manipulating Graphs

Open the *.cel file using CellTest. With the file open the raw data itself may not be visible, as indicated in Figure B-29. To make the raw data visible the frame divider located at the right hand side of the opened files windows must be dragged to the left (Figure B-30).

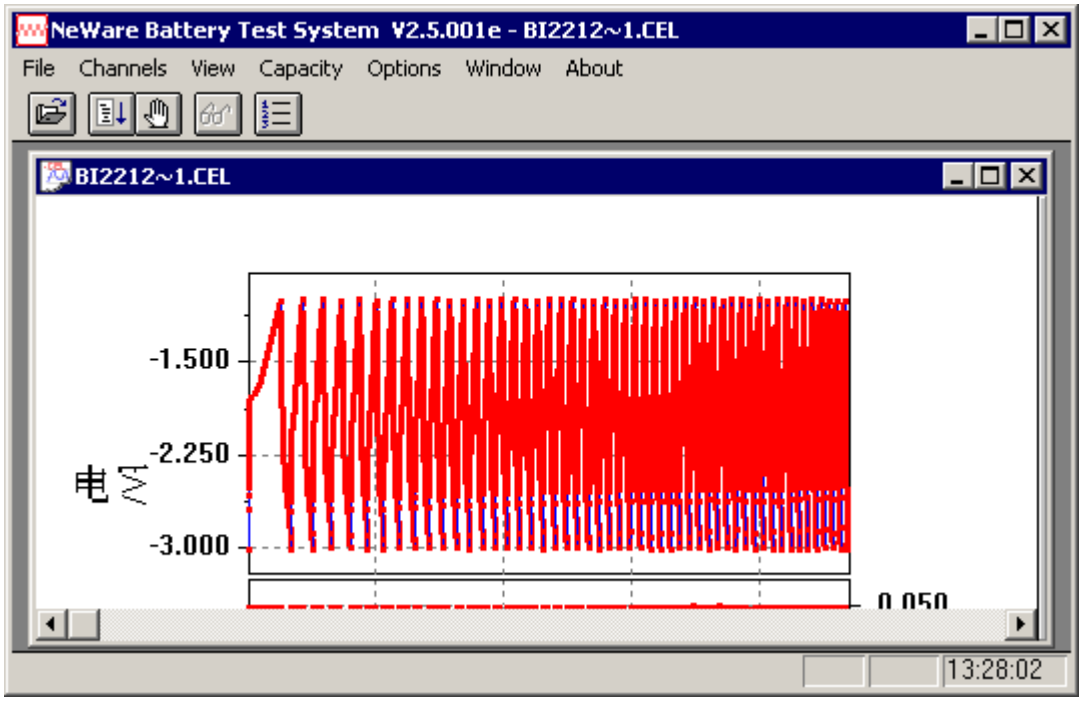

Figure B-29: An open *.cel file in CellTest 2.5.

Only data that has been graphed in the left frame will be shown in the right frame. This feature can be very useful in sorting out complex processes. A number of options are available to change the style of the graph and the data displayed in it. These are accessible by right clicking within the actual graphed region to display a new menu and left clicking on the “Graphics Set…” item located within that menu (Figure B-31).

As a result a new dialog box will appear as indicated in Figure B-32. The format of the graph can be changed using this dialog box. Most importantly the cycles displayed can be changed by altering the “From” and “To” “Cycle Loop” numbers.

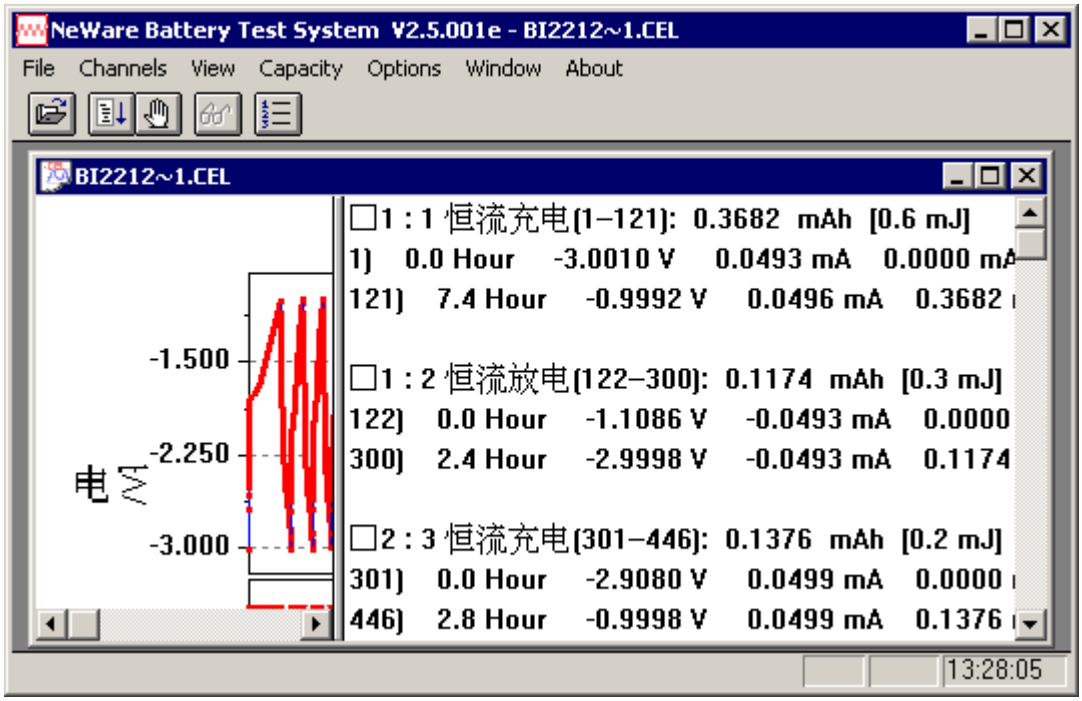

Figure B-30: An open *.cel file in CellTest 2.5 with frame repositioned to see raw data.

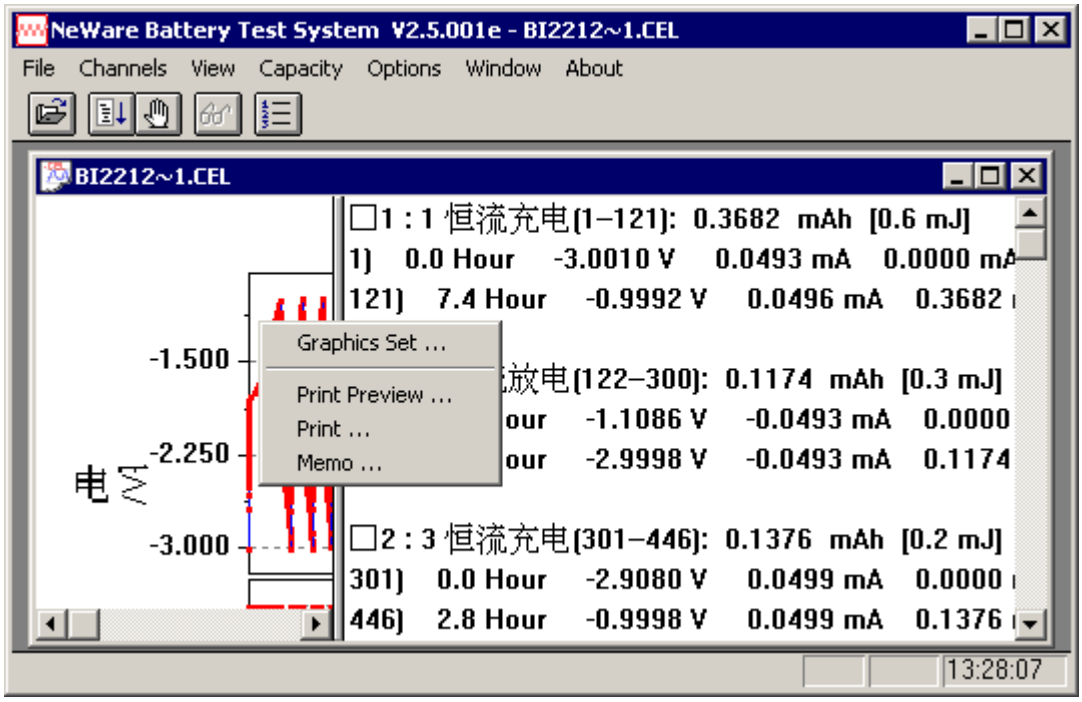

Figure B-31: Menu to alter graph settings.

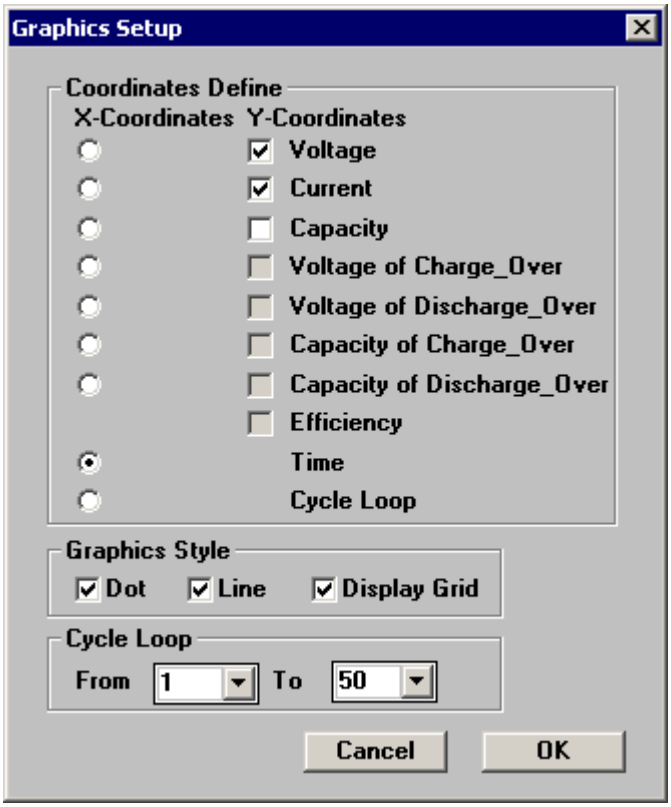

Figure B-32: "Graphics Setup" dialog box.

B.4.1.1.2 Saving Text Files

By right clicking in the data portion of the opened files window a new menu is revealed. This menu along with its default settings can be seen in Figure B-33.

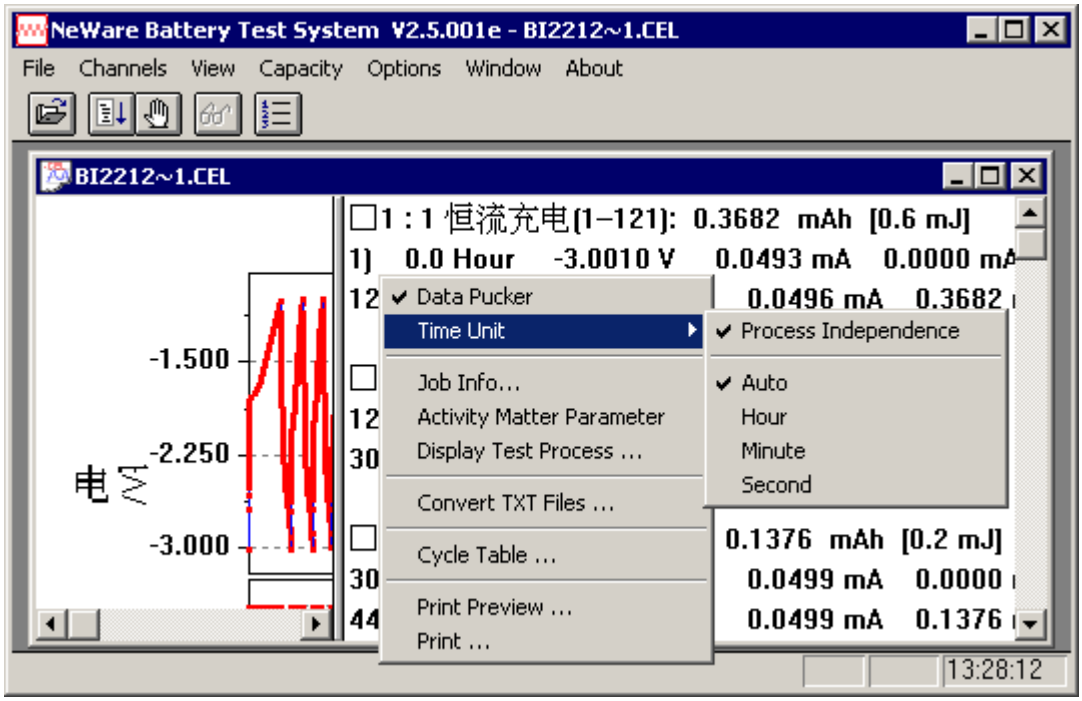

Figure B-33: Menu showing default properties.

Before generating the text file a number of options need to be set correctly and are demonstrated in Figure B-34 and Figure B-35. Figure B-34 demonstrates the correct settings for cycle table whilst Figure B-35 demonstrates the correct settings for separate cycles.

"Data Pucker"

To generate a text file for Cycle Table there should be a tick next to the item whilst for Separate Cycles it should be unticked. The ticked/unticked status can be changed by left clicking on the item.

"Time Unit"

The "Process Independence" and "Second" items must both be ticked. If either item is missing the tick they must be placed there by left clicking the appropriate menu item and if required opening the menu again with a right click.

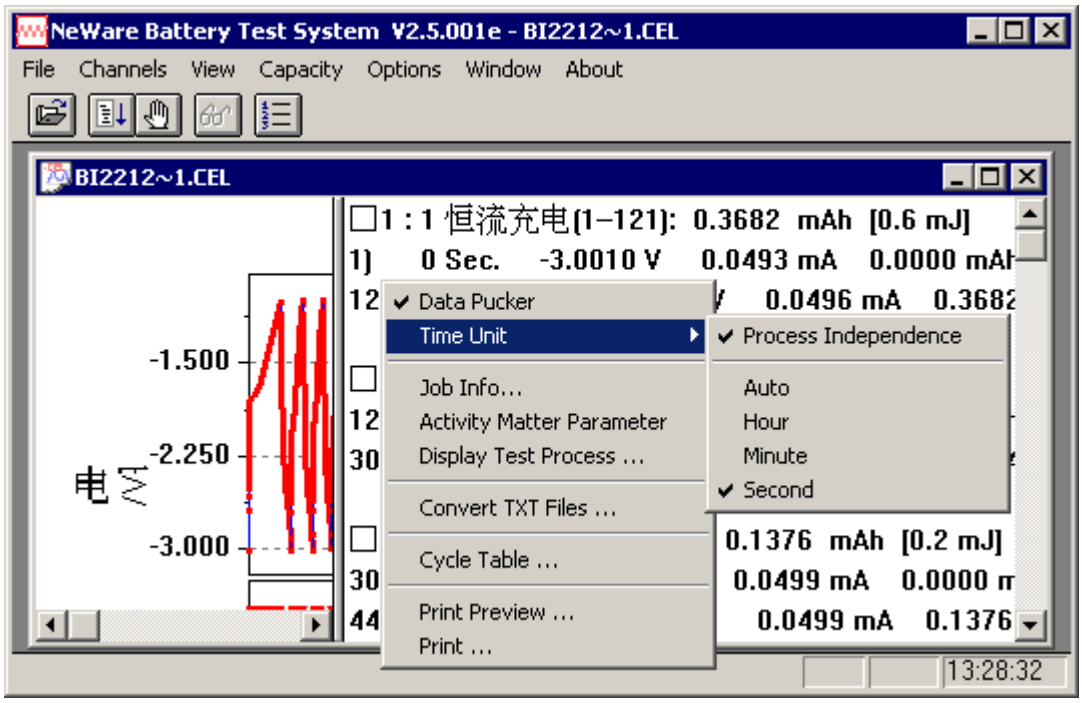

Figure B-34: Correct parameters for "Cycle Table" text file.

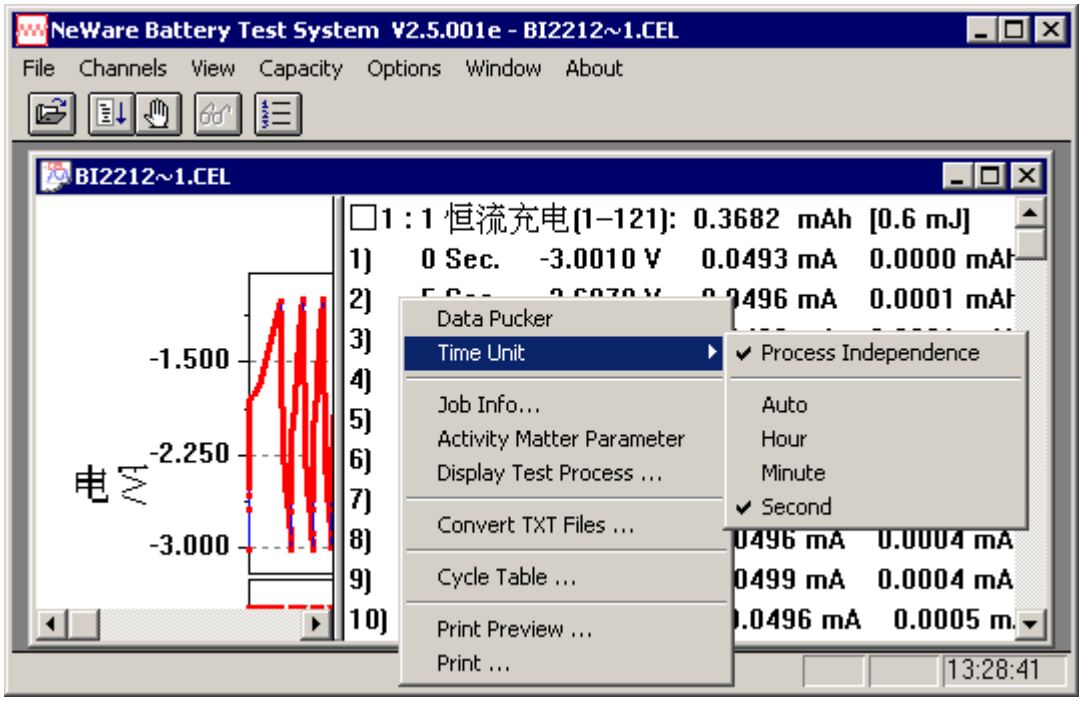

Figure B-35: Correct parameters for "Separate Cycles" text file.

With the appropriate items checked the item "Convert Txt files....." can be selected with a left click and another dialog box will appear (Figure B-36).

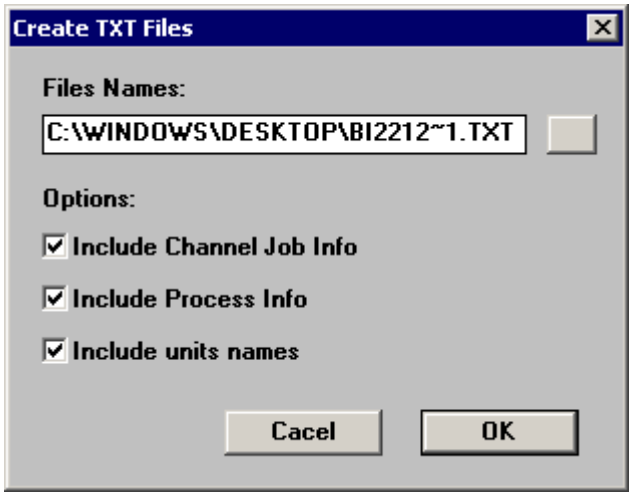

Figure B-36: "Create TXT Files" dialog box.

In this dialog box first select a name and location for the text file to be saved to, and then remove the ticks from all three boxes next to the items (Figure B-37). The file can then be saved by clicking on the "Ok" button.

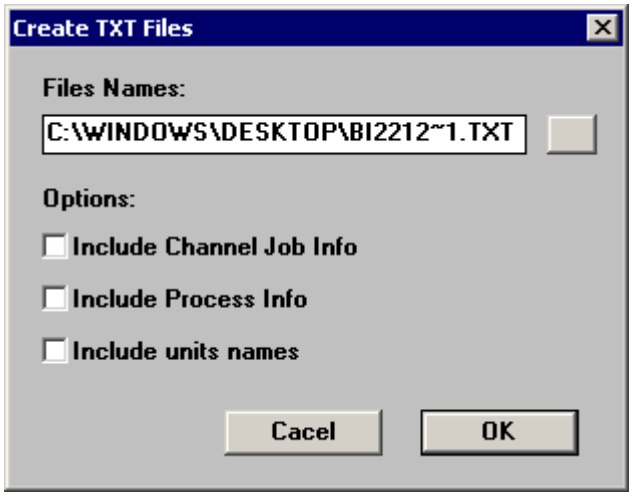

Figure B-37: "Create TXT Files" dialog box ready for file to be generated.

Whilst the file is open in CellTest you should check whether any errors occurred during the test process. If errors have occurred it may be necessary to edit the generated *.txt files to enable the spreadsheet to process them properly. In the data frame right click to bring up the menu and select the item "Display test process". A new dialog box will appear (Figure B-38) and in this example, no errors have occurred. The only items listed are for the start and the successful completion of the test process.

Figure B-38: "View Test Process" dialog box.

Another item that is worth checking is the "Job Info…" menu item, located on the menu that appears when right clicking in the data frame. The dialog box that appears

(Figure B-39) shows the testing process that was used. This information is useful for determining the appropriate parameters for compiling the cycle table.

Two parameters are needed in the spreadsheet to describe the test process to enable the Cycle Table to be generated. These are the "lead in" value and "data points" value. The lead in value reflects any steps in the test process that occur at the very start of the process and are not repeated. Examples of these may include a formation step or time delay till the start of the test process. The lead in value is double the number of steps defined in the test process for any such initial steps. If none of these steps are used the value is zero. In the example show in Figure B-39 there are no such steps and the value is zero. The data points value reflects double the number of steps that are looped in the test process. In the example shown in Figure B-39 there are two steps that are repeated. The first is a constant current discharge to 1.0V and the second is a constant current charge to 3.0V. It is only these two items that are looped and as a result the value of data points in this example is 4.

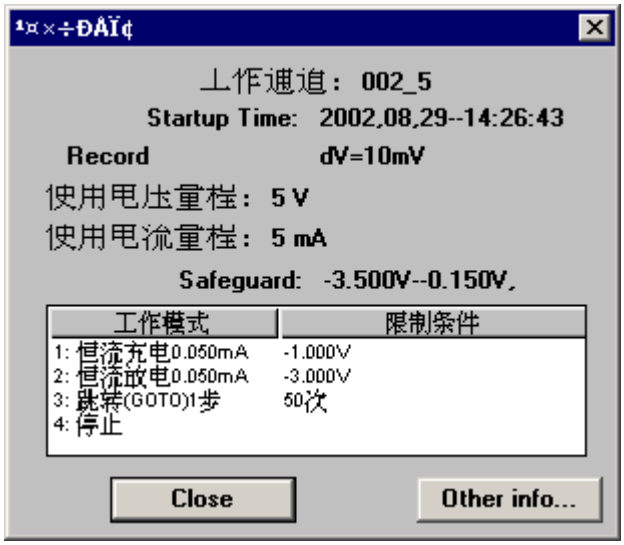

Figure B-39: "Job Info" dialog box.

B.4.1.2 CellTest 4 - *.res files

B.4.1.2.1 Opening Files and Manipulating Graphs

Open the *.res file using CellTest. With the file open the raw data itself may not be visible, as indicated in Figure B-40. To make the raw data visible the frame divider located at the right hand side of the opened files windows must be dragged to the left (Figure B-41).

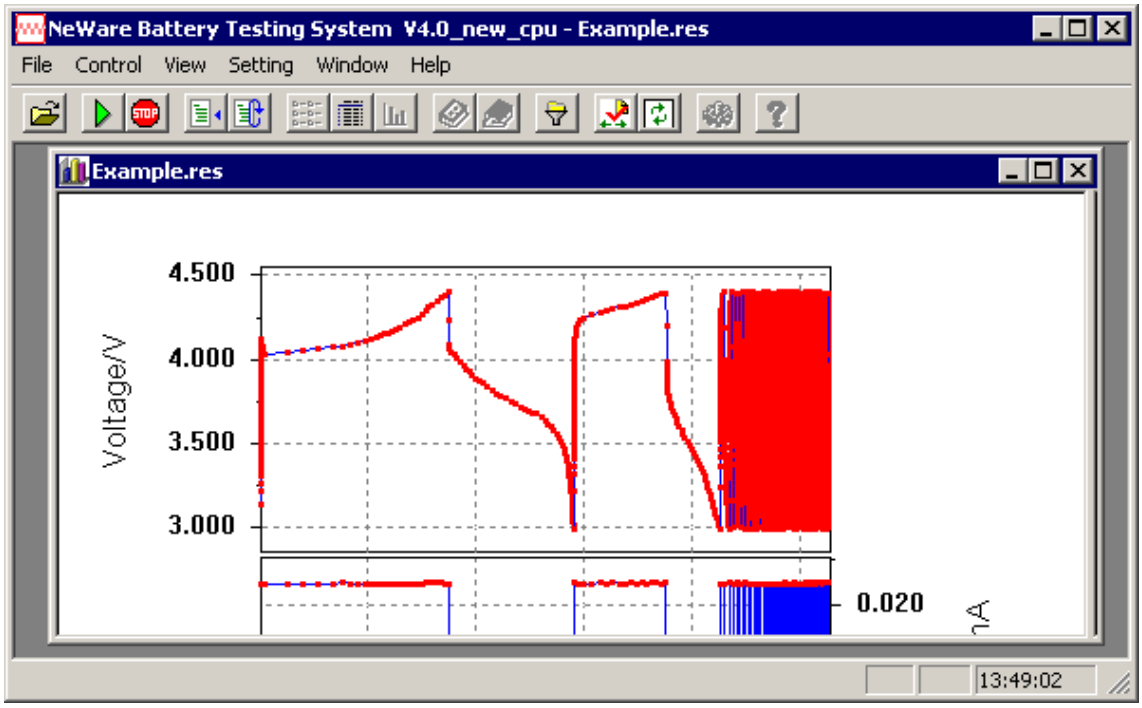

Figure B-40: An open *.res file in CellTest 4.

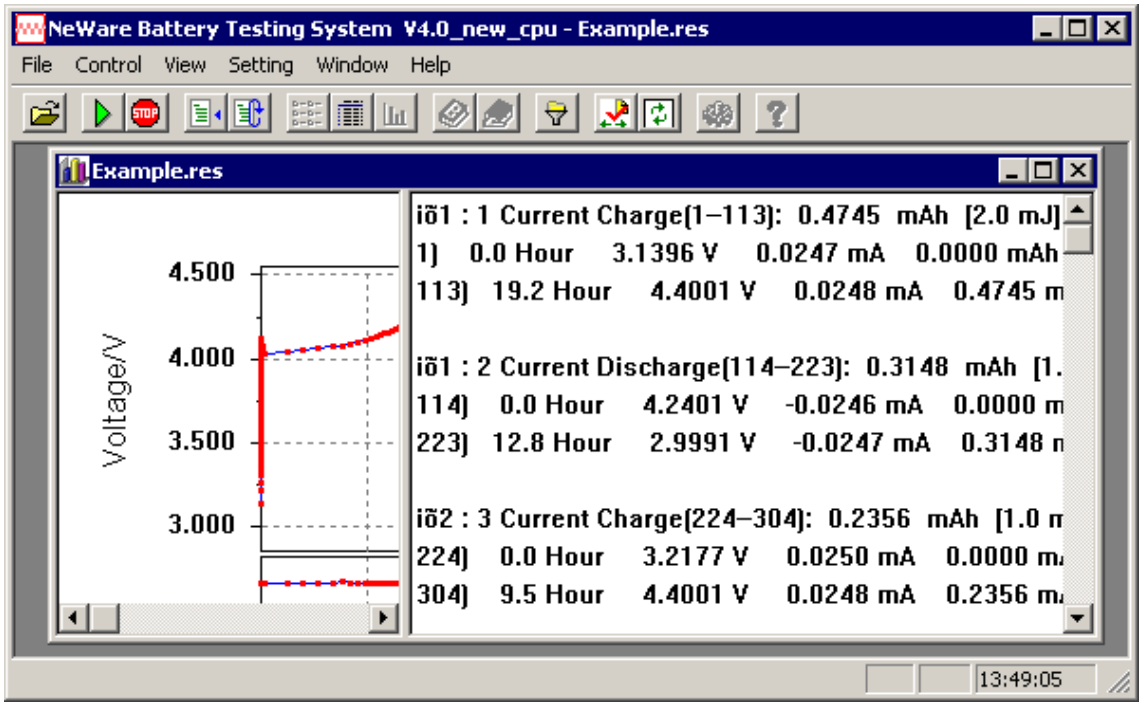

Figure B-41: An open *.res file in CellTest 4 with frame repositioned to see raw data.

Only data that has been graphed in the left frame will be shown in the right frame. This feature can be very useful in sorting out complex processes. A number of options are available to change the style of the graph and the data displayed in it. These are accessible by right clicking within the actual graphed region to display a new menu and left clicking on the "Graph Setting…" item located within that menu (Figure B-42).

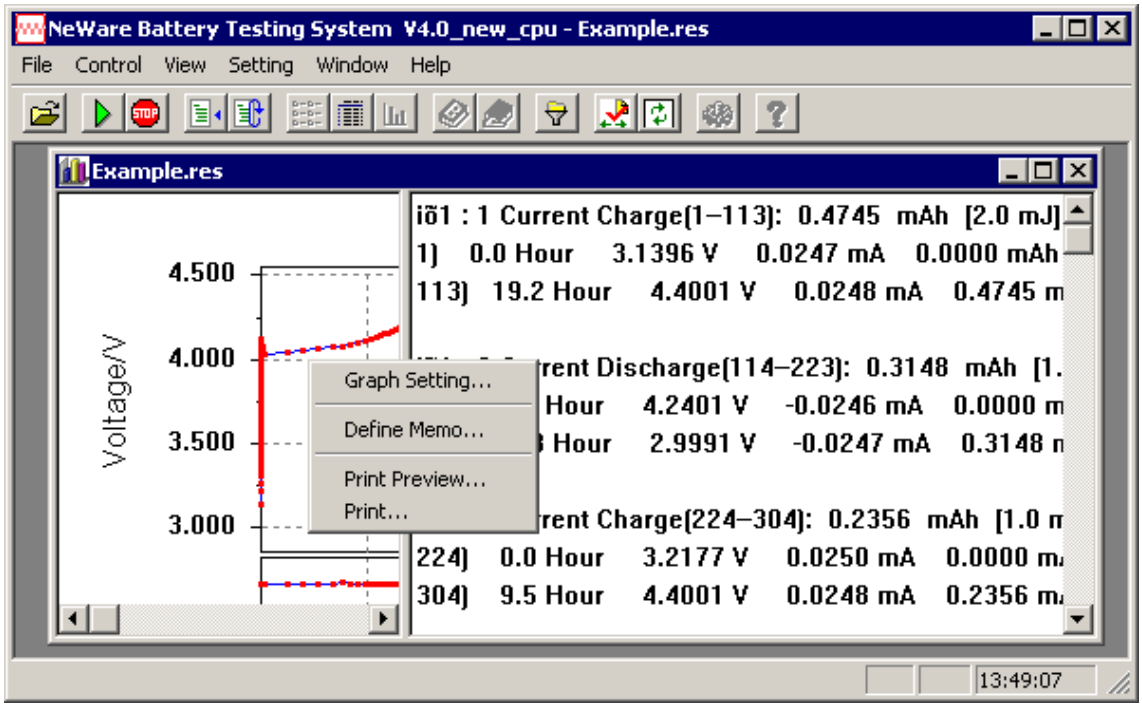

Figure B-42: Menu to alter graph settings.

As a result a new dialog box will appear as indicated in Figure B-43. The format of the graph can be changed using this dialog box. Most importantly the cycles displayed can be changed by altering the "From" and "To" "Display Cycle" numbers.

B.4.1.2.2 Saving Text Files

By right clicking in the data portion of the opened files window a new menu is revealed. This menu along with its default settings can be seen in Figure B-44. Before generating the text file a number of options need to be set correctly and are demonstrated in Figure B-45 and Figure B-46. Figure B-45 demonstrates the correct settings for cycle table whilst Figure B-46 demonstrates the correct settings for separate cycles.

"Data Fold"

To generate a text file for Cycle Table there should be a tick next to the item whilst for Separate Cycles should be unticked. The ticked/unticked status can be changed by left clicking on the item.

"Time Unit"

The "Step Independence" and "Second" items must both be ticked. If either item is missing the tick they must be placed there by left clicking the appropriate menu item and if required opening the menu again with a right click.

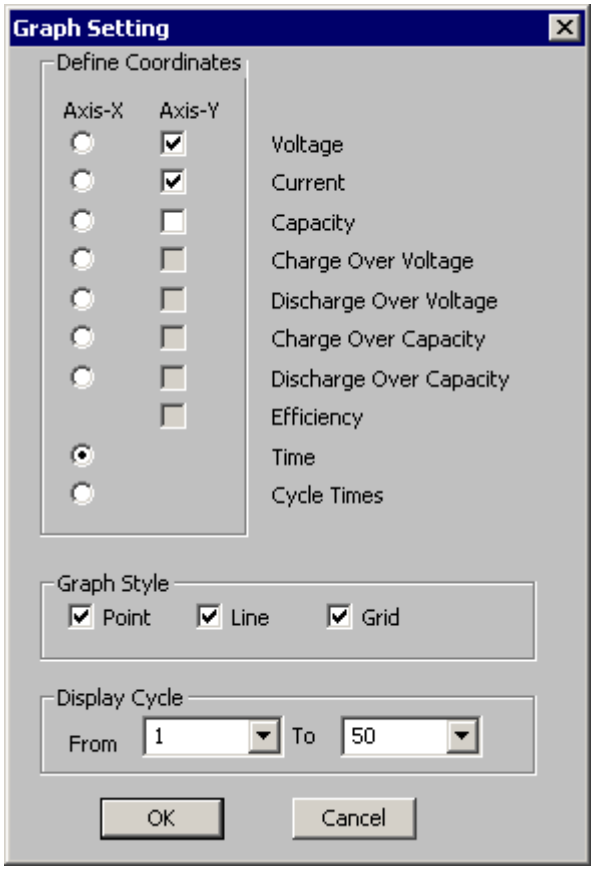

Figure B-43: "Graph Setting" dialog box.

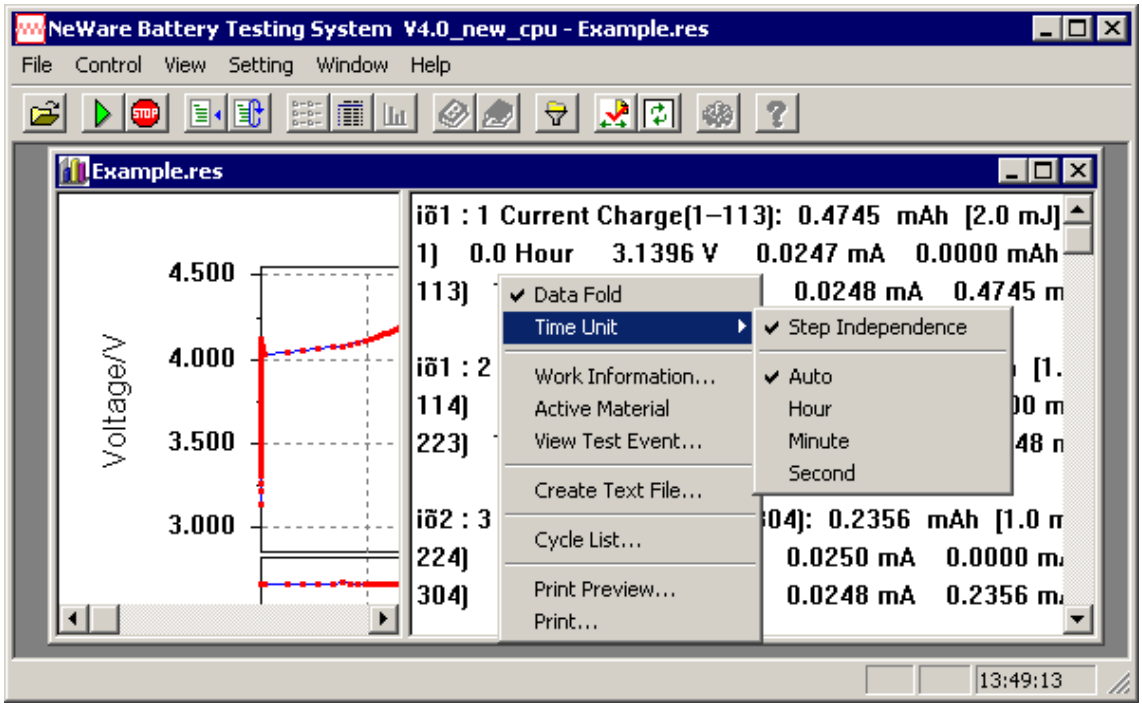

Figure B-44: Menu showing default properties.

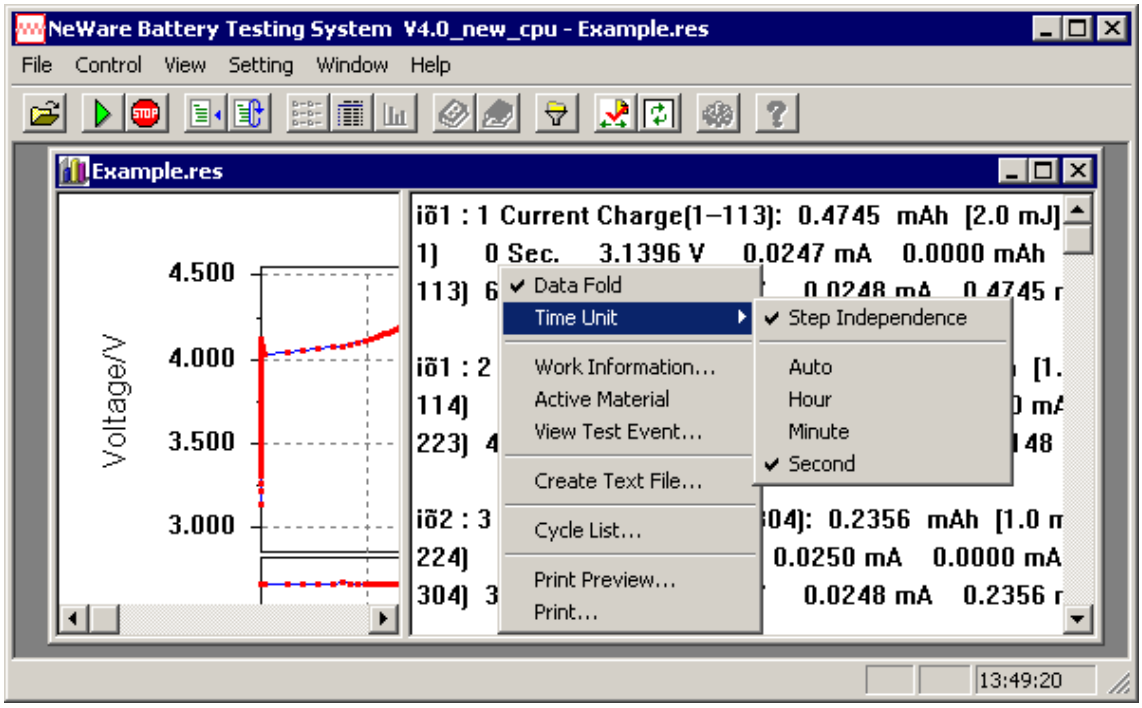

Figure B-45: Correct parameters for "Cycle Table" text file.

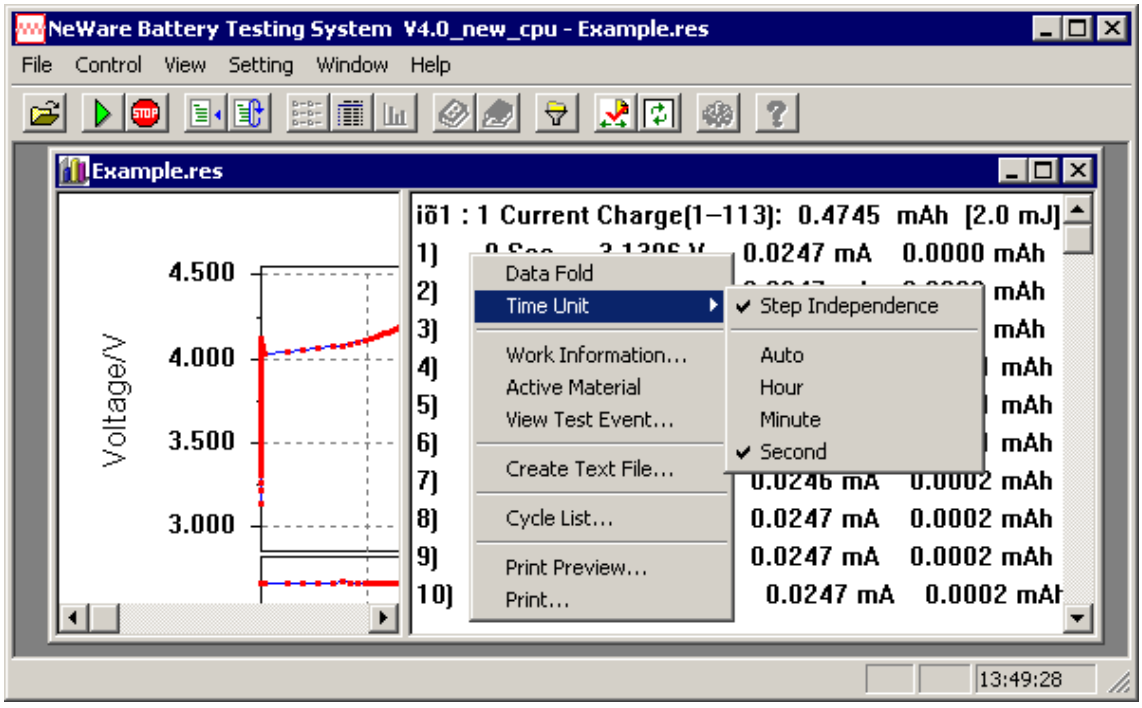

Figure B-46: Correct parameters for "Separate Cycles" text file.

With the appropriate items checked the item "Create Text File....." can be selected with a left click and another dialog box will appear (Figure B-47).

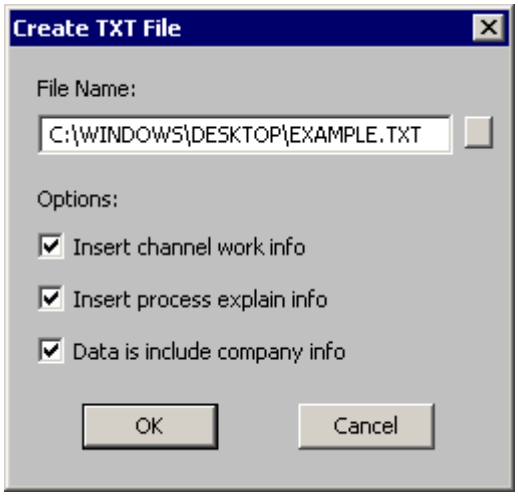

Figure B-47: "Create TXT File" dialog box.

In this dialog box first select a name and location for the text file to be saved to, and then remove the ticks from all three boxes next to the items (Figure B-48). The file can then be saved by clicking on the "Ok" button.

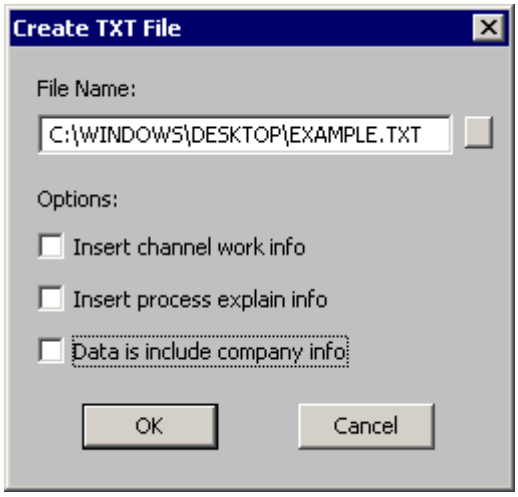

Figure B-48: "Create TXT File" dialog box ready for file to be generated.

Whilst the file is open in CellTest you should check whether any errors occurred during the test process. If errors have occurred it may be necessary to edit the generated *.txt files to enable the spreadsheet to process them properly. In the data frame right click to bring up the menu and select the item "View Test Event…". A new dialog box will appear (Figure B-49) and in this example, no errors have occurred. The only items listed are for the start and the stop at the successful completion of the test process.

Two parameters are needed in the spreadsheet to describe the test process to enable the Cycle Table to be generated. These are the "lead in" value and "data points" value. The lead in value reflects any steps in the test process that occur at the very start

of the process and are not repeated. Examples of these may include a formation step or time delay till the start of the test process. The lead in value is double the number of steps defined in the test process for any such initial steps. If none of these steps are used the value is zero. The data points value reflects double the number of steps that are looped in the test process. The best way to determine these values in CellTest 4 is to examine the step descriptions in a folded data set (Figure B-50). From the descriptions there are a constant current charge and discharge only. In this example the lead in would be zero and data points would be four.

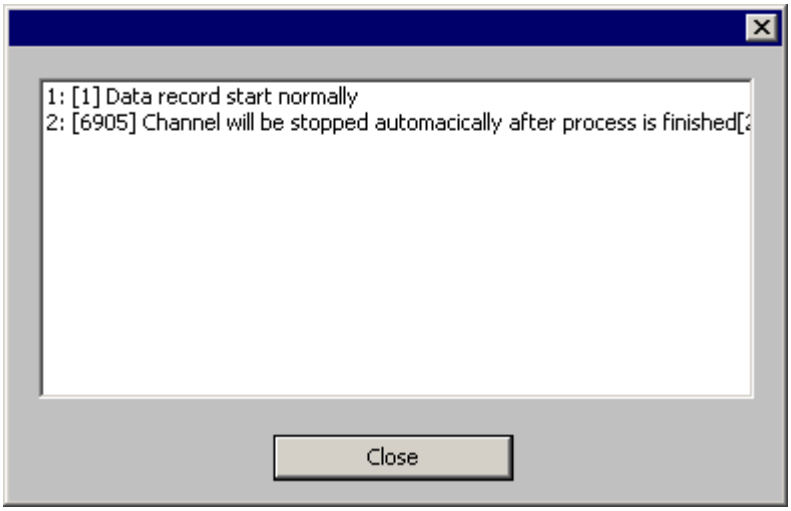

Figure B-49: "Display Test Process" dialog box.

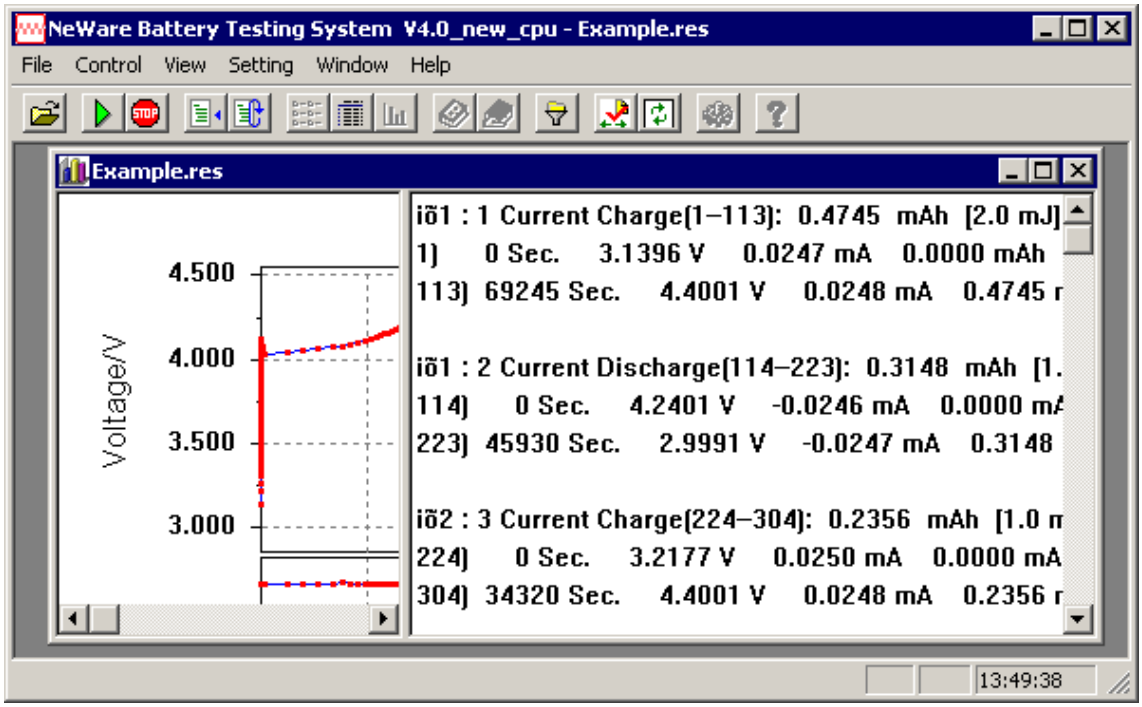

Figure B-50: Data folded for determining lead in and data points.

B.4.1.3 DataManager - *.bts files

B.4.1.3.1 Opening Files and Manipulating Graphs

Open the *.bts or *.res file using DataManager. With the file open the raw data itself may not be visible, as indicated in Figure B-51. To make the raw data visible the frame divider located at the right hand side of the opened files windows must be dragged to the left (Figure B-52). Alternatively select the “All Text” item in the “Window” menu. The graph and text can be viewed by selecting the “Picture” item in the “Window” menu. Selecting the “Compare” item in the “Window” menu allows quick graphs to be produced of multiple cycles in the same file and or different files to be produced. The graphs can be copied and pasted into word if required.

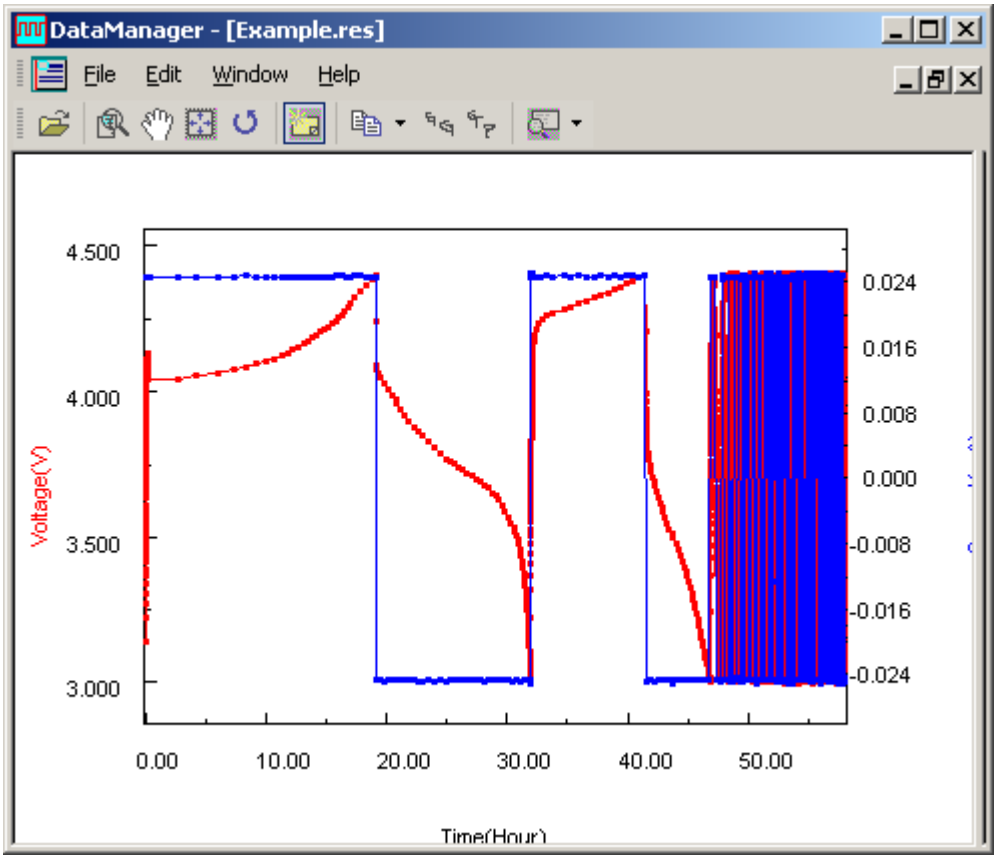

Figure B-51: An open file in DataManager.

All the data will continue to be shown in the right frame regardless of what is graphed in the left frame. However when saving the file for Separate Cycle purposes only the data for the cycles that are graphed will be exported. This feature can be very

useful in sorting out complex processes. A number of options are available to change the style of the graph and the data displayed in it. These are accessible by right clicking within the actual graphed region to display a new menu and left clicking on the "Graphics Setting…" item located within that menu (Figure B-53). The graph can also be copied by clicking on the "Copy" item located in this same menu.

As a result a new dialog box will appear as indicated in Figure B-54. The format of the graph can be changed using this dialog box. Most importantly the cycles displayed can be changed by altering the "From" and "To" "Cycle Loop" numbers.

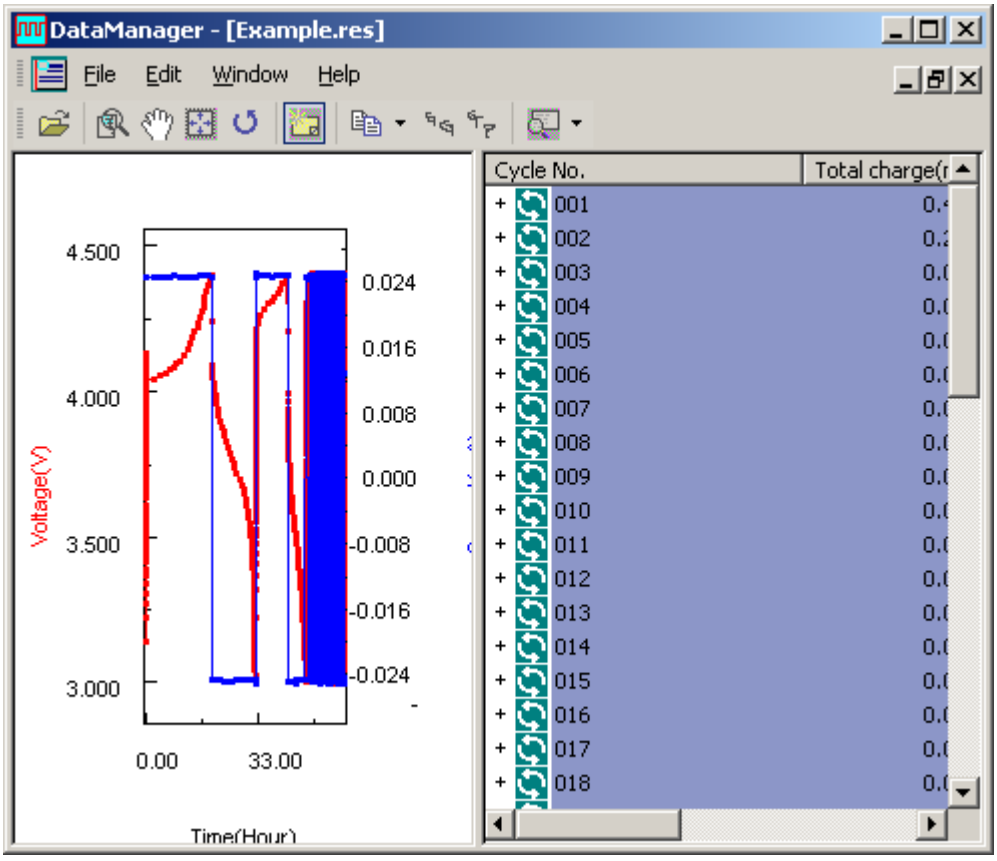

Figure B-52: An open file in DataManager with frame repositioned to see raw data.

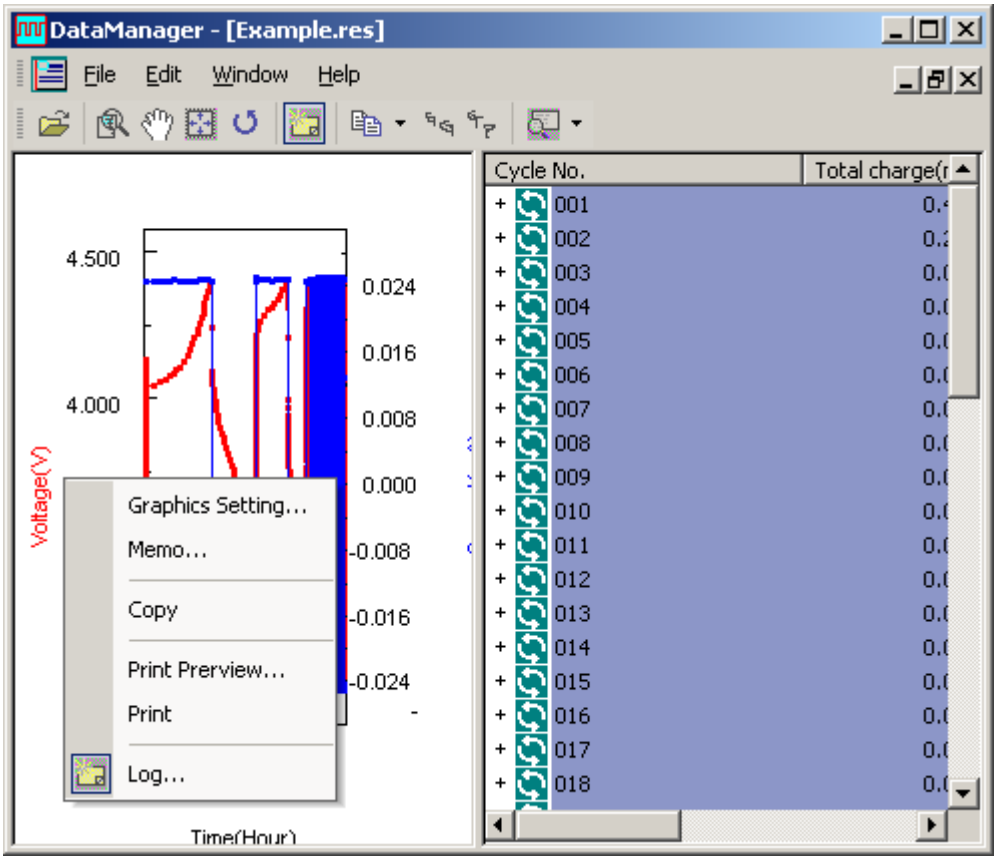

Figure B-53: Menu to alter graph settings.

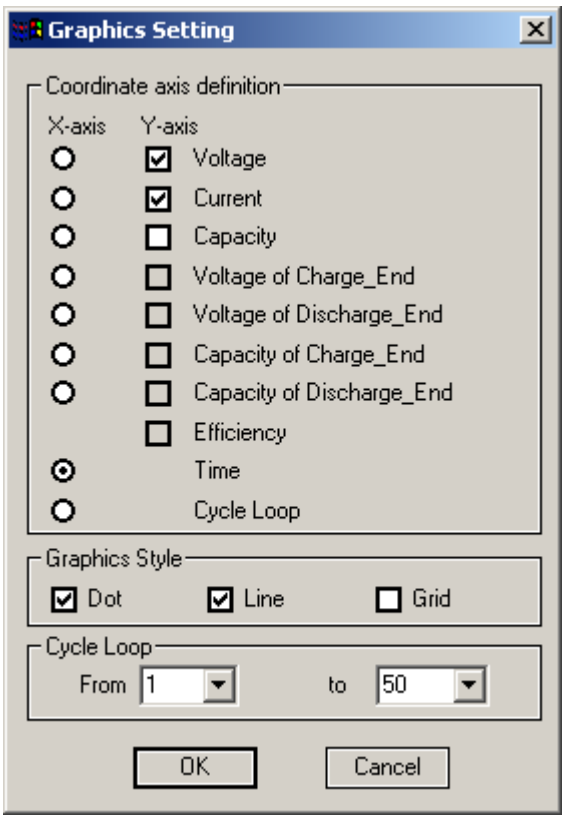

Figure B-54: "Graphics Setting" dialog box.

B.4.1.3.2 Saving Data Files

By right clicking in the data portion of the opened files window a new menu is revealed (Figure B-55).

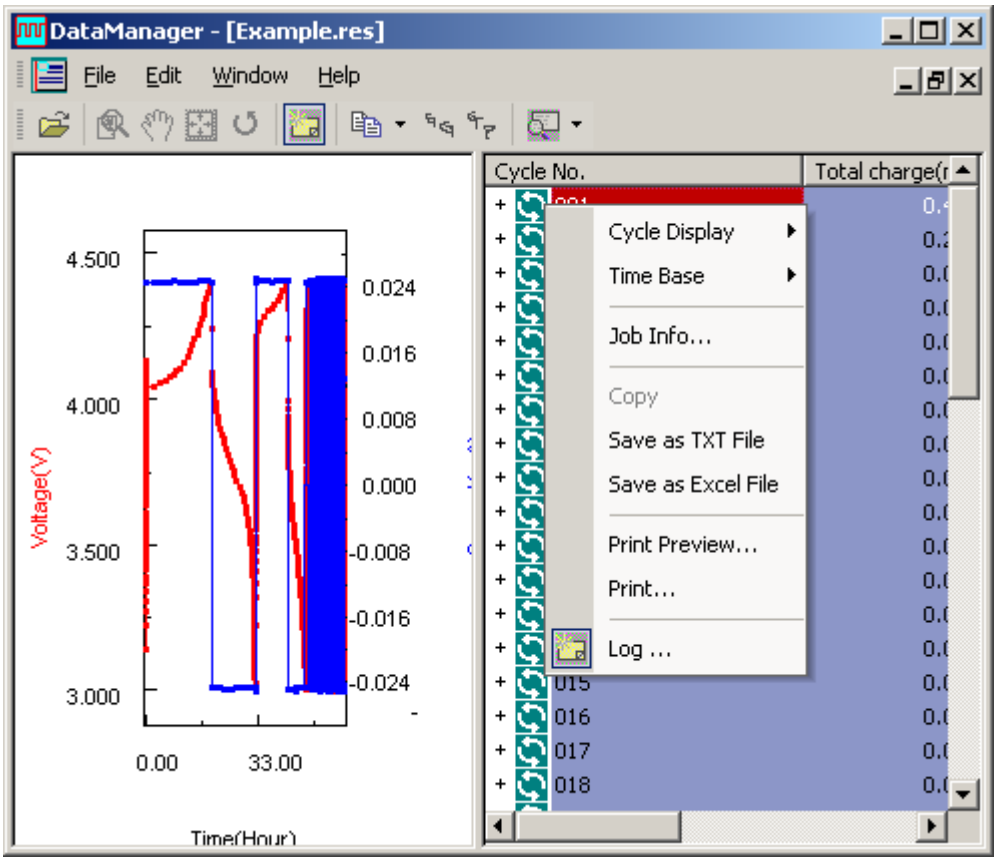

Figure B-55: Menu located in data window.

To create the text file for "Cycle Table" the "Save as TXT File" item is selected from the menu whilst to create the Excel file for "Separate Cycles" the "Save as Excel File" item is selected but a few settings must be confirmed first. These settings are located in the "Time Base" item located in the same menu. When this item is clicked the menu expands to reveal a number of options (Figure B-56). To create the correct data files there must be a tick next to "Step Independence" as indicated and the "Second" item must also be clicked. A tick will not however appear besides "Second" as a result.

With the appropriate parameters set the "Save as TXT File" and "Save as Excel File" items can be used to save the appropriate files. Following either selection a "Create file" dialog box will appear. If the "Save as TXT File" was selected none of the items in the "Create file" dialog box should have ticks next to them as indicated in Figure B-57. If however the "Save as Excel File" was selected then the "Record" item

in the “Create file” dialog box should be the only item with a tick next to it as indicated in Figure B-58.

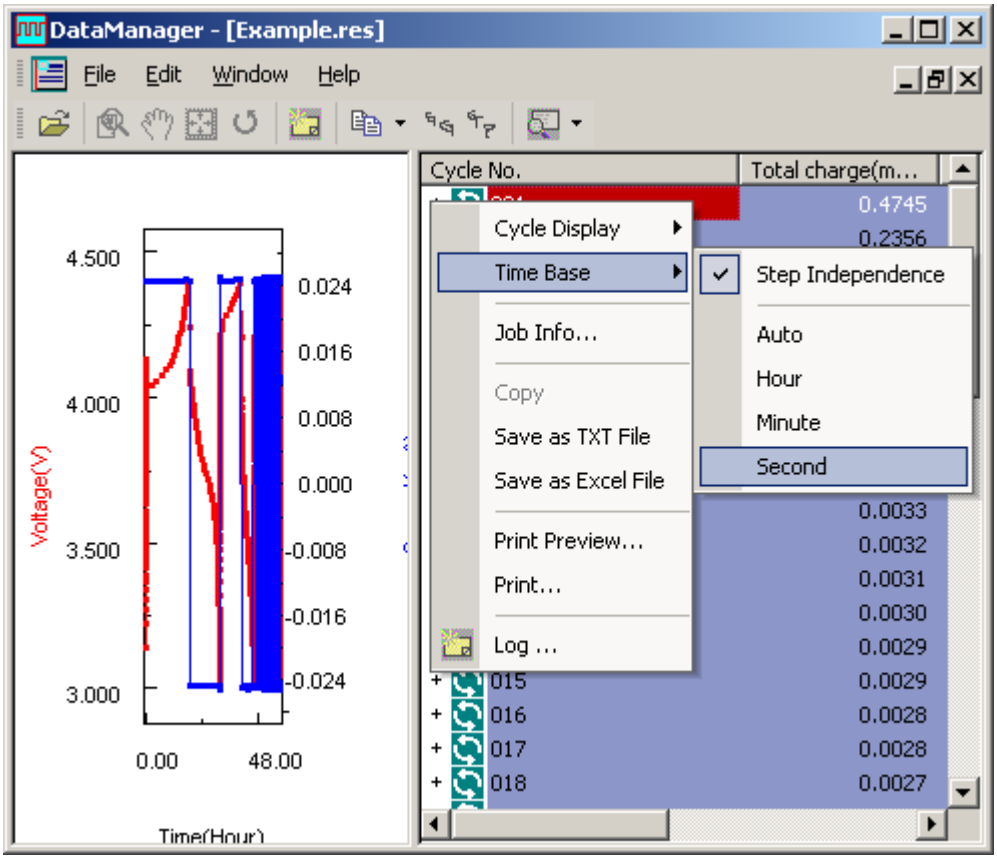

Figure B-56: Menu showing “Time Base” options.

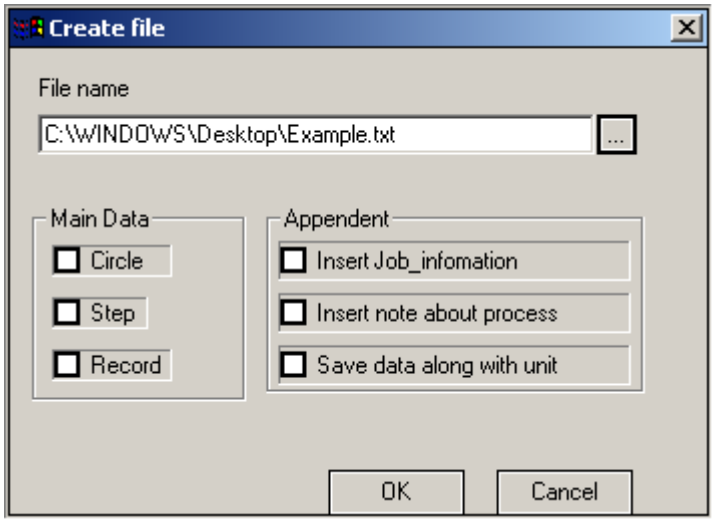

Figure B-57: “Create file” dialog box showing options required for “Save as TXT File”.

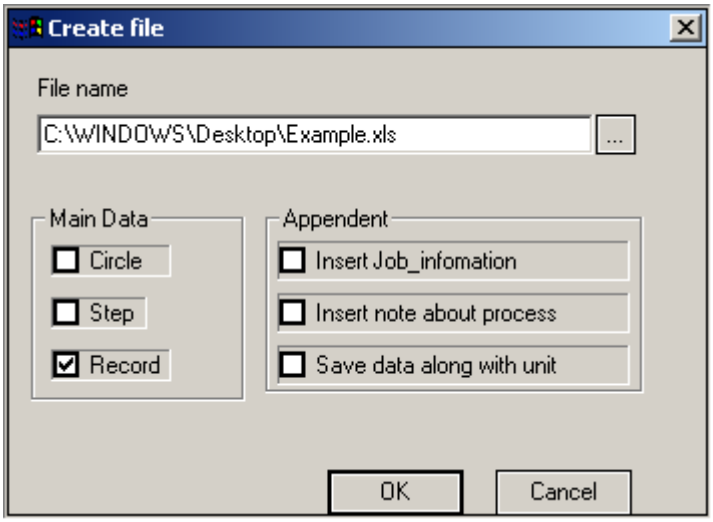

Figure B-58: "Create file" dialog box showing options required for "Save as Excel File".

In both cases the file can then be saved by clicking on the "Ok" button.

Whilst the file is open in DataManager you should check whether any errors occurred during the test process. If errors have occurred it may be necessary to edit the generated data files to enable the spreadsheet to process them properly. The test log can be viewed by right clicking in either the graph or data frame and selecting the "Log" item located in either menu. The log will typically then appear at the bottom of the window (Figure B-59) and in this example, no errors have occurred. The only items listed are for the start and the stop at the successful completion of the test process.

No additional parameters need to be identified in order to sort either data set. In the case of the text file generated for "Capacity Table" purposes the file already contains a table of capacity values in (mAh) so only the electrode mass needs to be entered during processing so the table can be presented as values in mAh/g.

B.4.2 Sorting Method

There are a number of different methods used in the sorting of battery testing data from the CellTest and Data Manager software. The creation of the data files for these methods has been covered in the previous section on generating data files using the CellTest and DataManager software. Additional details on the format of these data files and the sorting mechanisms will be examined in this section.

These are for:

- Cycle Table
  - CellTest
  - DataManager

- Separate Cycles
    - Rest at End of Cycle
    - Rest at Start of Cycle

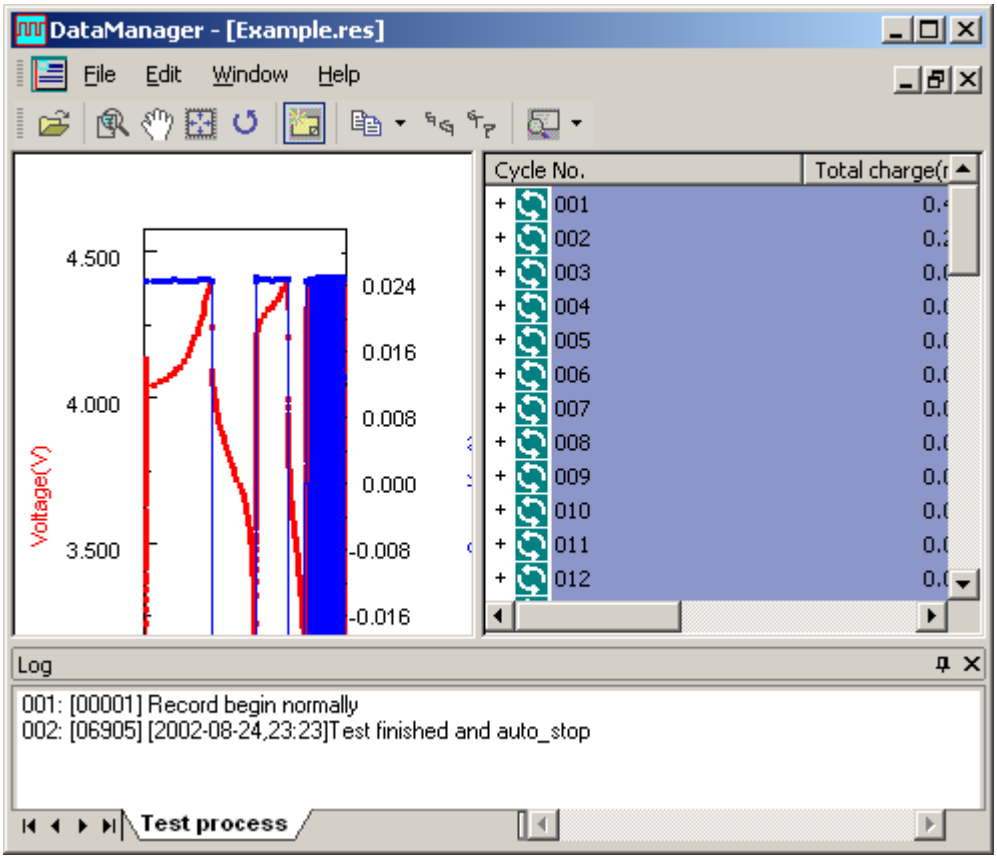

Figure B-59: Battery Test log.

B.4.2.1 Cycle Table

The data file format and sorting mechanisms for the “Cycle Table” methods vary depending on the origin of the data file.

- CellTest
- DataManager

B.4.2.1.1 CellTest

The method for the “Cycle Table” makes use of the file that has been saved for this purpose. The file consists of the following (Table B-4) and the example file Celltest_Table.txt is another example.

Table B-4: Example of part of a "Cycle Table" file.

1)	0	3.3305	0.0493	0
273)	32854	-0.0158	0.0505	0.4567
274)	0	0.0679	-0.0505	0
483)	1613	3.005	-0.0502	0.0225
484)	0	2.6835	0.0502	0
623)	1904	-0.0155	0.0502	0.0265
624)	0	0.0812	-0.0496	0
829)	1207	3.0118	-0.0499	0.0168
830)	0	2.7582	0.0502	0
965)	1483	-0.0155	0.0505	0.0207

The data in the various columns:

1. Sample or reading number
2. Time (seconds)
3. Voltage (V)
4. Current (mA)
5. Capacity (mAh)

This data format contains only the first and last point of each step in the testing process. For example

1) => 273)	Discharge
274) => 483)	Charge
484) => 623)	Discharge

In this case the charge and discharge steps are only one step long. However in some cases they are multiple steps. The sorting process simply divides the capacity column by the mass and rearranges the final column of values into a more readable format. Two values specify how this rearrangement occurs and these are called "Lead In" and "Data Points". See the relevant saving text files section for further details. This method allows a table of final capacity values to be generated quickly and also allows the capacities at any intermediary steps to be observed.

B.4.2.1.2 DataManager

The method for the "Cycle Table" makes use of the file that has been saved for this purpose. The file consists of the following (Table 3.2).

Table B-5: Example of part of a "Cycle Table" file.

1	0.4745	0.3148	66.4
2	0.2356	0.1321	56.1
3	0.0117	0.0116	99.3
4	0.0067	0.0069	103.3
5	0.0053	0.0053	100.6
6	0.0045	0.0045	100
7	0.0041	0.004	98.8
8	0.0038	0.0037	98
9	0.0035	0.0034	97.2
10	0.0033	0.0032	96.5

The data in the various columns:

1. Cycle Number
2. Charge Capacity (mAh)
3. Discharge Capacity (mAh)
4. Efficiency (%)

To generate a table of capacity values in mAh/g from this data the capacity values need to be divided by the mass.

B.4.2.2 Separate Cycles

The sorting method for all these functions is very similar. For data saved from CellTest a text file is utilised whilst for data saved from DataManager an Excel file is used. Part of an example text file is shown in Table B-6 with the demonstration file Celltest_SepCycles.txt being another example. The format of the Excel file is very similar but there are some differences. When either file type is initially opened the first five voltage readings are examined. If all five are negative the signs of the data in the voltage and current columns are reversed.

Table B-6: Example of text file used for "Separate Cycles".

1)	0	3.3305	0.0493	0
2)	5	3.218	0.0499	0.0001
3)	9	3.151	0.0502	0.0001
4)	13	3.0853	0.0499	0.0002
5)	16	3.0261	0.0493	0.0002
6)	19	2.9945	0.0499	0.0003
7)	23	2.9678	0.0499	0.0003
8)	27	2.9478	0.0502	0.0004
9)	31	2.9275	0.0502	0.0004
10)	35	2.9055	0.0502	0.0005

The data in the various columns:

1. Sample or reading number
2. Time (seconds)
3. Voltage (V)
4. Current (mA)
5. Capacity (mAh)

B.4.2.2.1 Rest At End of Cycle

Separate Cycles, Sep. Cycles - Low Rest Current

The separation of individual cycles using "Separate Cycles" and "Sep. Cycles - Low Rest Current" are based on the same algorithm. The difference in the two lies only in the value selected for the comparisons. This value for "Separate Cycles" is 0.01 and for "Sep. Cycles - Low Rest Current" is 0.005. The algorithm is the same if a file with an xls extension (Excel file) is loaded as the input file. The algorithm makes two comparisons and both must be true for a new cycle to occur.

- The current points Time = 0
- One of the following must be true:
    1. The previous points current $\geq$ - 0.01 and the current points current < 0
    2. The previous points current $\leq$ 0.01 and the current points current > 0

This is easy to see in a schematic of the processes involved (Figure B-60). Using the 10 points that have been labelled in the diagram the results of the checks can be seen (Table B-7).

Sep. Cycles - High Rest Current

The separation of individual cycles using "Separate Cycles - High Rest Current" is a result of two comparisons. The algorithm is the same if a file with an xls extension (Excel file) is loaded as the input file. Both statements must be true for a new cycle to occur.

- The current points Time = 0
- One of the following must be true:
    1. The previous points current > 0 and the current points current $\leq$ - 0.2
    2. The previous points current < 0 and the current points current $\geq$ 0.2
    3. The absolute value of the previous points current < 0.2 and the absolute value of the current points current $\geq$ 0.2

This is easy to see in a schematic of the processes involved (Figure B-61). Using the 10 points that have been labelled in the diagram the results of the checks can be seen (Table B-8).

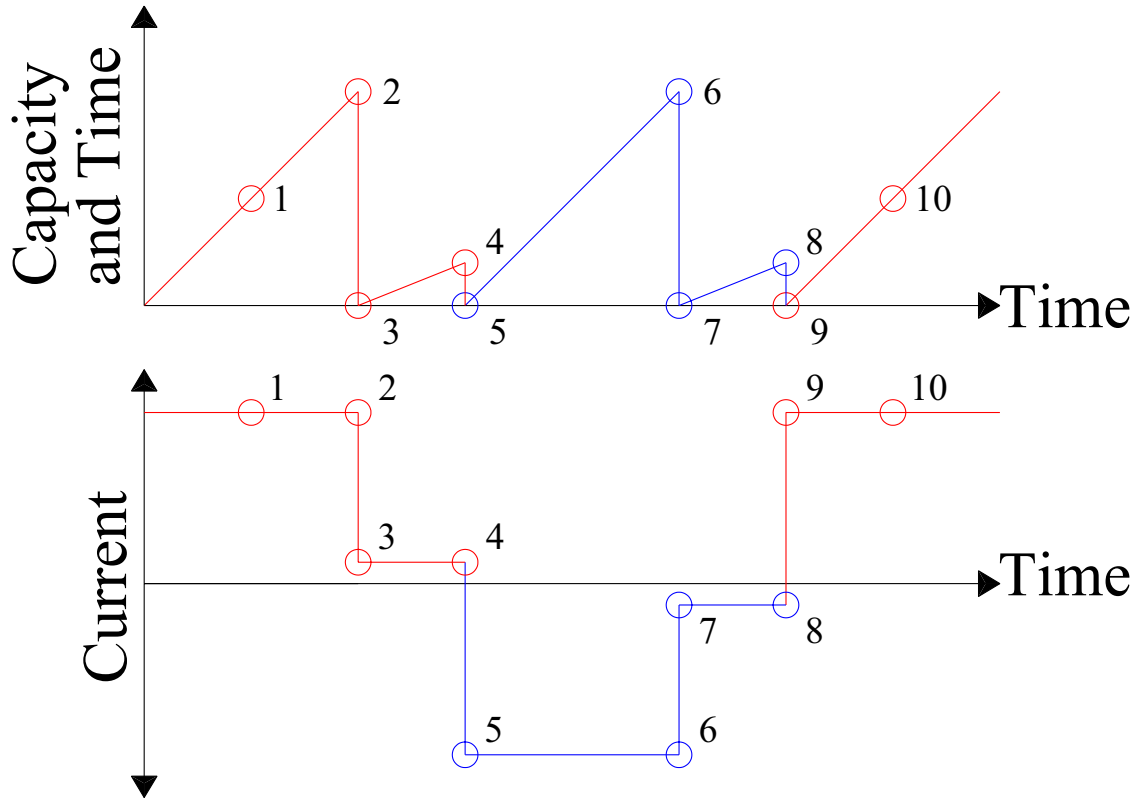

Figure B-60: Demonstration of sorting method used for "Separate Cycles".

Table B-7: Summary of sorting in Figure B-60

Point	Current	Time	Cycle	Step Type
1	> 0	> 0	A	Charge
2	> 0	> 0	A	Charge
3	≥ - 0.01	0	A	Wait
4	≥ - 0.01	> 0	A	Wait
5	< 0	0	A + 1	Discharge
6	< 0	> 0	A + 1	Discharge
7	< 0.01	0	A + 1	Wait
8	< 0.01	> 0	A + 1	Wait
9	> 0	0	A + 2	Charge
10	> 0	> 0	A + 2	Charge

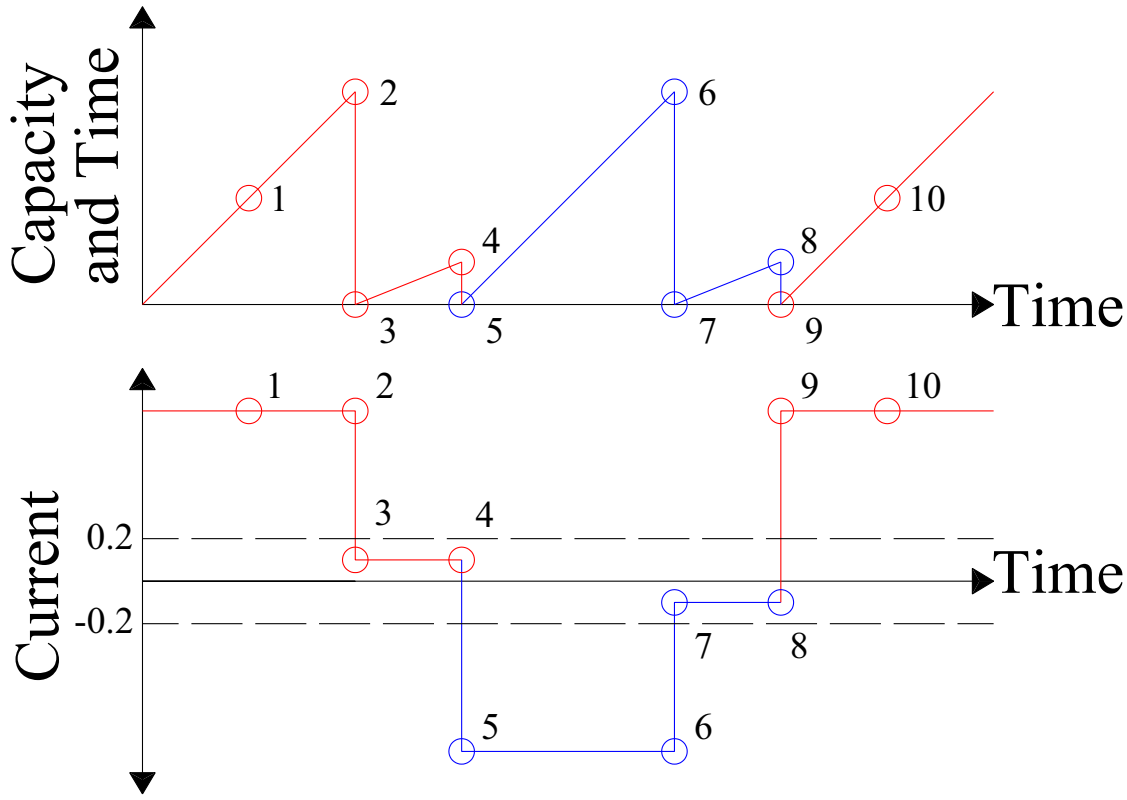

Figure B-61: Demonstration of sorting method used for "Separate Cycles – High Rest Current".

Table B-8: Summary of sorting in Figure B-61.

Point	Current	Time	Cycle	Step Type
1	> 0	> 0	A	Charge
2	> 0	> 0	A	Charge
3	| < 0.2 |	0	A	Wait
4	| < 0.2 |	> 0	A	Wait
5	≤ - 0.2	0	A + 1	Discharge
6	≤ - 0.2	> 0	A + 1	Discharge
7	| < 0.2 |	0	A + 1	Wait
8	| < 0.2 |	> 0	A + 1	Wait
9	> 0	0	A + 2	Charge
10	> 0	> 0	A + 2	Charge

B.4.2.2.2 Rest At Start of Cycle

The separation of individual cycles using "Separate Cycles" and "Sep. Cycles - High Rest Current" and "Sep. Cycles - Low Rest Current" are based on the same algorithm. The difference in the three lies only in the value selected for the comparisons. This value is 0.01 for "Separate Cycles", 0.2 for "Sep. Cycles - High Rest Current" and 0.005 for "Sep. Cycles - Low Rest Current. The algorithm is the same if a

file with an xls extension (Excel file) is loaded as the input file. The algorithm makes two comparisons and both must be true for a new cycle to occur.

- The current points Time = 0
- One of the following must be true:
    1. The previous points current > 0.01 and the current points current < 0.01
    2. The previous points current < 0.01 and the current points current > 0.01
    3. The previous points current < 0.01 and the absolute value of the current points current < 0.01

This is easy to see in a schematic of the processes involved (Figure B-62). Using the 10 points that have been labelled in the diagram the results of the checks can be seen (Table B-9).

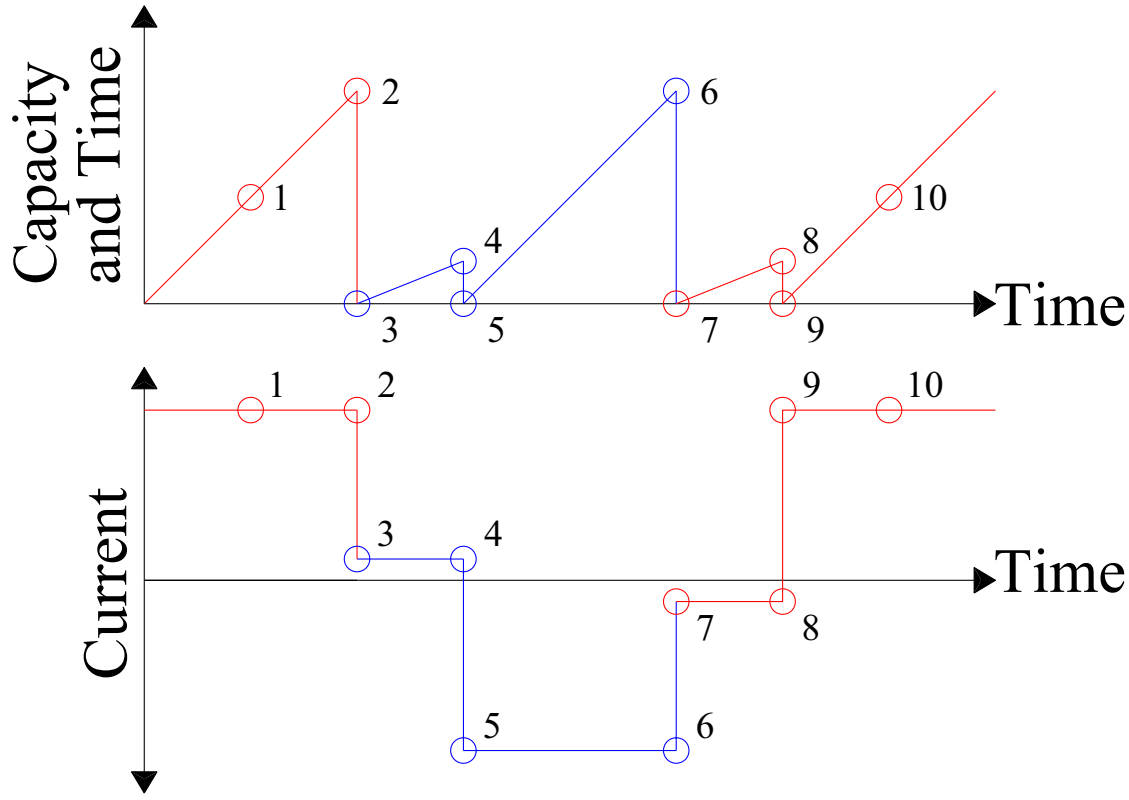

Figure B-62: Demonstration of sorting method used for "Separate Cycles".

Table B-9: Summary of sorting in Figure B-62.

Point	Current	Time	Cycle	Step Type
1	> 0.01	> 0	A	Charge
2	> 0.01	> 0	A	Charge
3	< 0.01	0	A + 1	Wait
4	< 0.01	> 0	A + 1	Wait
5	< 0.01	0	A + 1	Discharge
6	< 0.01	> 0	A + 1	Discharge
7	| < 0.01 |	0	A + 2	Wait
8	| < 0.01 |	> 0	A + 2	Wait
9	> 0.01	0	A + 2	Charge
10	> 0.01	> 0	A + 2	Charge

B.4.3 Processing CellTest Data

The purpose of the "Celltest" (Figure B-63) functions is to retrieve capacity based data from a conforming data file. These functions include:

- "Cycle Table" - table of capacity values with respect to the cycle number for both charge and discharge.
  - The presets perform "Cycle Table" functions but the "Lead In" and "Data Points" values are preset.

- "Separate Cycles" - provide charge/discharge profile data of desired cycles using a variety of algorithms.

Following selection of one of the options the file open dialog box will appear so that the file to process can be selected.

B.4.3.1 Cycle Table

A "Data Processing Parameters Selection" dialog box will appear next though the appearance will vary slightly depending on the "Cycle Table" option selected and the origin of the data file (CellTest or DataManager). If the text file was produced by Celltest and the "Cycle Table" option was selected the dialog box (Figure B-64) will contain three fields requiring data entry ("Lead In", "Data Points" and "Electrode Mass (mg)"). If one of the presets has been selected the dialog box (Figure B-65) will only require the "Electrode Mass (mg)" to be entered as the data for the other fields has

already been obtained through the use of the preset (Table B-10). If however the text file was produced by DataManager regardless of the Cycle Table option selected the dialog box (Figure B-65) will only require the entry of the "Electrode Mass (mg)". Identification of the origin of the file is carried out on the basis of the number of columns of data in the file. CellTest files are originally identified as having five columns whilst DataManager files are identified as having four columns.

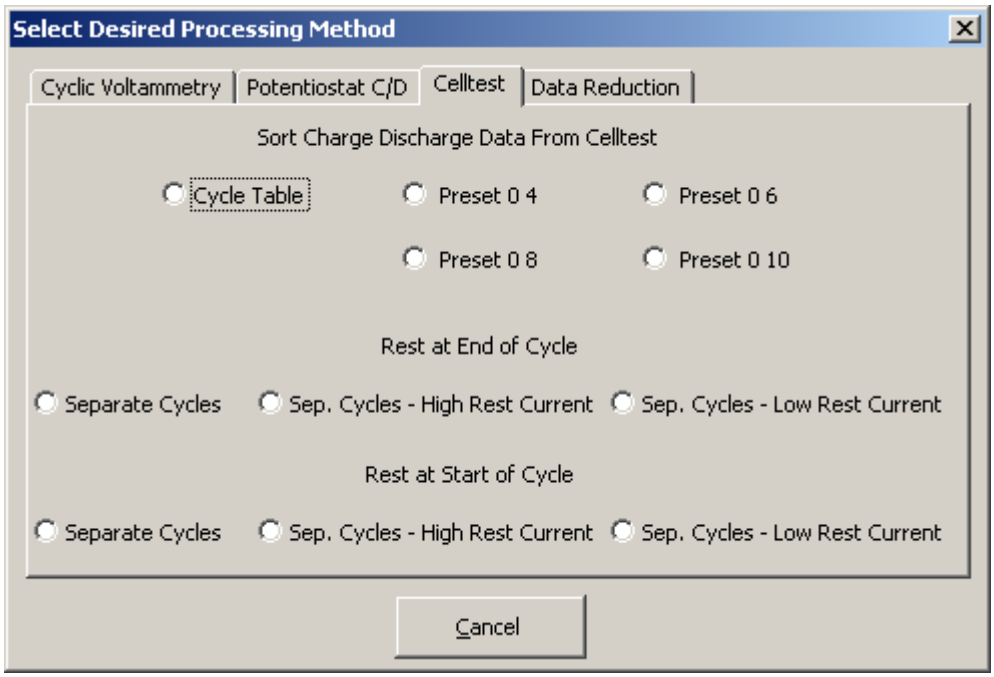

Figure B-63: CellTest selection dialog box.

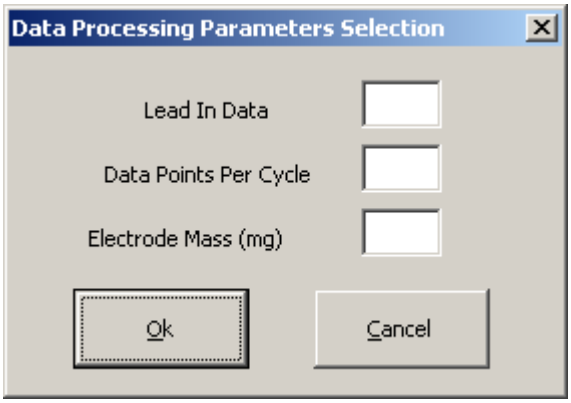

Figure B-64: "Data Processing Parameters Selection" for "Cycle Table" option.

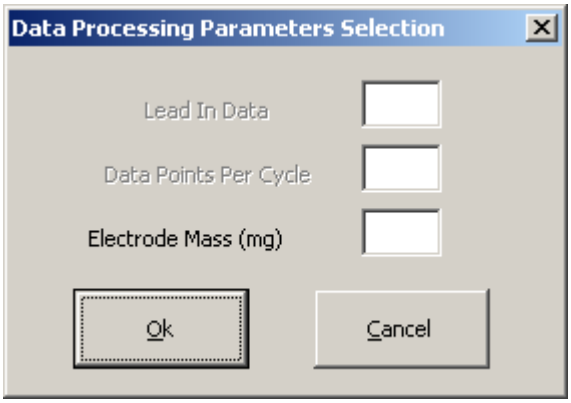

Figure B-65: "Data Processing Parameters Selection" for preset option.

Table B-10: Effect of presets on value of "Lead In" and "Data Points".

Preset	"Lead In"	"Data Points"
"Preset 0 4"	0	4
"Preset 0 6"	0	6
"Preset 0 8"	0	8
"Preset 0 10"	0	10

B.4.3.1.1 CellTest

The "Lead in Data" is the number of data points before the test procedure is in its normal pattern. For instance the first step in the test may be a wait period. Following this your standard test steps are carried out, consisting of a standard pattern of charge, discharge and wait periods for example. The lead in data is typically less than the data points per cycle. The data points per cycle is typically double the number of steps in the test profile (and is always an even number). For further details on "Lead In" and "Data Points" see the appropriate section on saving test files.

In a simple procedure such as a two step charge/discharge process such as the demonstration file (Celltest_Table.txt) and shown in the example of processed output (Figure B-66) the "Lead In" was 0 and "Data Points" was 4. With the correct values entered the sorted data appears in neat columns. If you are unsure of what parameters to enter start entering numbers and use 1000 as the mass. In this way the values can be compared to those in CellTest (by examining the capacity table within that software).

The position of the data you are interested in is going to vary depending on your test procedure. The presentation of the sorted data will however always remain the same. Column A will contain the number of data points that were specified as the lead in. In the example the lead in was zero, so there are no values in column A. The

numbers in the first row of column B and onwards represent the step numbers up to the maximum of the data points per cycle that was specified, in this case 4. The data in this sorted portion runs across the columns and then starts again at the next row.

In this example the step numbers 1 - 4 represent the following

1. First data point of constant current discharge
2. Last data point of constant current discharge
3. First data point of constant current charge
4. Last data point of constant current charge

The data of interest in this case appears in step number 2 and 4.

- Step 2 represents the final capacity of the discharge process
- Step 4 represents the final capacity of the charge process.

It is for the reason that this data needs to be examined that it is not automatically saved.

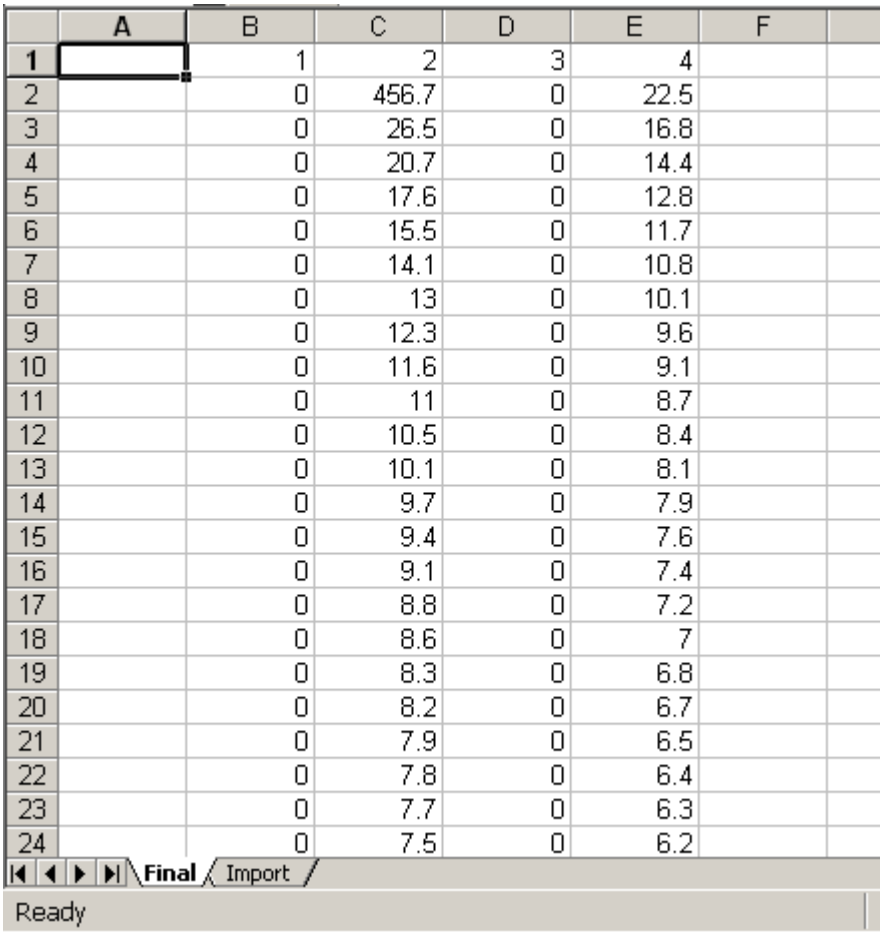

	A	B	C	D	E	F
1		1	2	3	4	
2		0	456.7	0	22.5	
3		0	26.5	0	16.8	
4		0	20.7	0	14.4	
5		0	17.6	0	12.8	
6		0	15.5	0	11.7	
7		0	14.1	0	10.8	
8		0	13	0	10.1	
9		0	12.3	0	9.6	
10		0	11.6	0	9.1	
11		0	11	0	8.7	
12		0	10.5	0	8.4	
13		0	10.1	0	8.1	
14		0	9.7	0	7.9	
15		0	9.4	0	7.6	
16		0	9.1	0	7.4	
17		0	8.8	0	7.2	
18		0	8.6	0	7	
19		0	8.3	0	6.8	
20		0	8.2	0	6.7	
21		0	7.9	0	6.5	
22		0	7.8	0	6.4	
23		0	7.7	0	6.3	
24		0	7.5	0	6.2	

Final | Import

Ready

Figure B-66: Example of processed output from "Cycle Table".

B.4.3.1.2 DataManager

Following completion of the "Data Processing Parameters Selection" dialog box the data will be processed and automatically saved with the same name and an added extension.

Example.txt => Example.txt_Table.txt

The spreadsheet is then reset so that further data can be processed. The processed output (Figure B-67) consists of a number of columns of data with labels. Column A contains a list of the Cycle numbers, Column B the Charge Capacities in mAh/g, Column C the Discharge Capacities in mAh/g, Column D Efficiency (%), whilst the electrode mass is listed in the first row of Column F in mg.

	A	B	C	D	E	F
1	Cycle Num	Charge Ca	Discharge	Efficiency	Electrode I	4.2
2	1	112.9762	74.95238	66.4		
3	2	56.09524	31.45238	56.1		
4	3	2.785714	2.761905	99.3		
5	4	1.595238	1.642857	103.3		
6	5	1.261905	1.261905	100.6		
7	6	1.071429	1.071429	100		
8	7	0.97619	0.952381	98.8		
9	8	0.904762	0.880952	98		
10	9	0.833333	0.809524	97.3		

Figure B-67: Example of processed output from "Cycle Table".

B.4.3.2 Separate Cycles

The processing procedure is the same for all the "Separate Cycles" methods. The sorting algorithm itself is the only difference between them (See Sorting Method - Separate Cycles). With the file selected for processing a dialog box will appear to allow selection of the cycles to process Figure B-68.

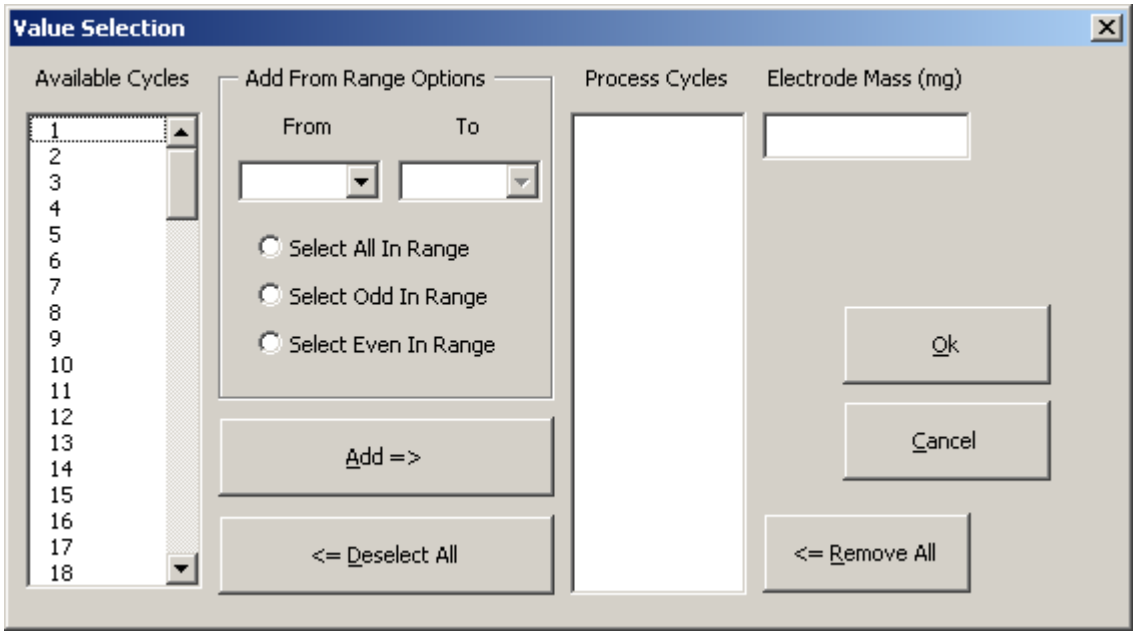

Figure B-68: Example of the "Value Selection" dialog box.

The cycles that you wish to extract the data for should be selected from the "Available Cycles" list.

This can be done two ways:

- Individual cycles can be selected by clicking on the cycle number in the "Available Cycles List"
- Cycles can be added from a range using the "Add from Range Options"
    1. Select a number from the "From Range" drop down list.
    2. Select a number from the "To Range" drop down list.
    3. Click the desired option.
        - "Select All In Range"
        - "Select Odd In Range"
        - "Select Even In Range"

A cycle is selected if its value is highlighted. Selected items can be deselected individually by clicking on the relevant number in the "Available Cycles" list or all can be deselected by clicking the "<= Deselect All" button. All selected items are also removed from this list when they are added to the "Process Cycles" list.

With all the cycles desired to be sorted selected in the "Available Cycles" list they need to be added to the "Process Cycles" list by clicking the "Add =>" button. In

this case items can be removed by double clicking the value in the "Process Cycles" list or all items can be removed by clicking the "<= Remove All" button.

The electrode mass is the only item required to be entered to complete the filling out of the dialog box Figure B-69. With the dialog box compete the "Ok" button can be clicked and the processing will start. During processing there will be an indication of the processing being undertaken in the left corner of the Excel status bar. Initially this will indicate row processing (Figure B-70) and then the processing of the selected cycles (Figure B-71).

If 80 or less cycles are processed the file will be automatically saved with the same name and an added extension. Using the demonstration file Celltest_SepCycles.txt as an example

Celltest_SepCycles.txt => Celltest_SepCycles.txt_CD.txt

The spreadsheet will then restart so further data can be processed. If 80 or more cycles are processed the spreadsheet stops running so that the data can be saved.

The processed data (Figure B-72) lists the electrode mass used to process the data in the first row. The second row contains the step numbers of the cycles that have been processed. The first column of each step number (eg column A and C) contains the voltage data for that step number, whilst the second column (eg column B and D) contains the capacity data in mAh/g.

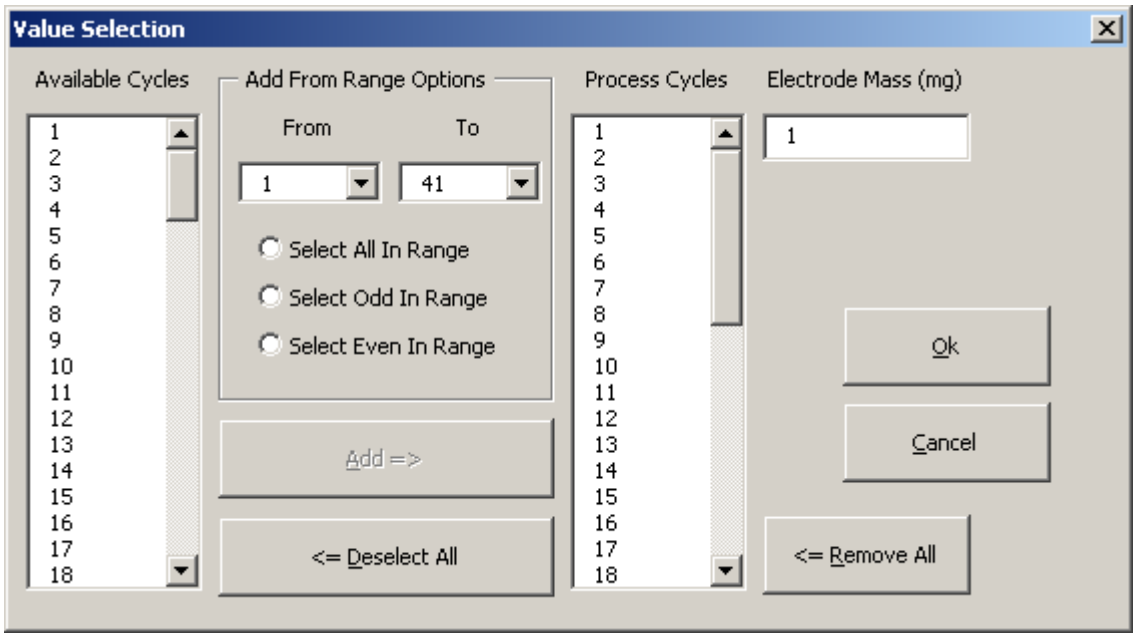

Figure B-69: Completed example of the "Value Selection" dialog box.

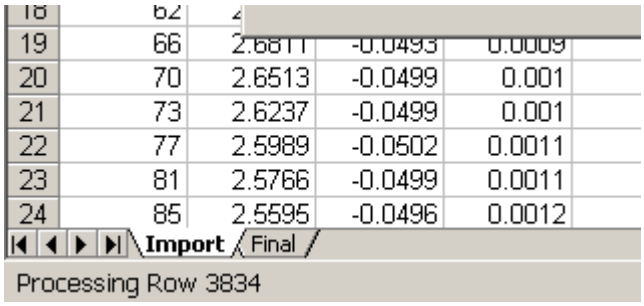

18	62	2		
19	66	2.6811	-0.0493	0.0009
20	70	2.6513	-0.0499	0.001
21	73	2.6237	-0.0499	0.001
22	77	2.5989	-0.0502	0.0011
23	81	2.5766	-0.0499	0.0011
24	85	2.5595	-0.0496	0.0012

Import | Final

Processing Row 3834

Figure B-70: Example of row processing indication in the Excel status bar.

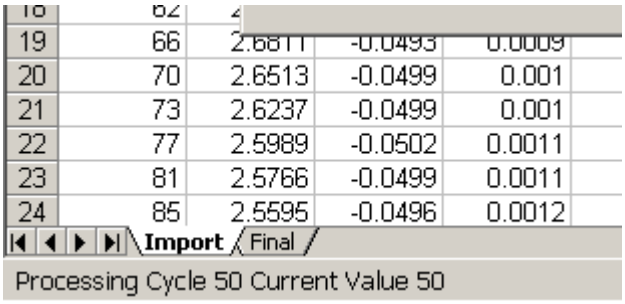

18	62	2		
19	66	2.6811	-0.0493	0.0009
20	70	2.6513	-0.0499	0.001
21	73	2.6237	-0.0499	0.001
22	77	2.5989	-0.0502	0.0011
23	81	2.5766	-0.0499	0.0011
24	85	2.5595	-0.0496	0.0012

Import | Final

Processing Cycle 50 Current Value 50

Figure B-71: Example of indication of selected cycles being processed.

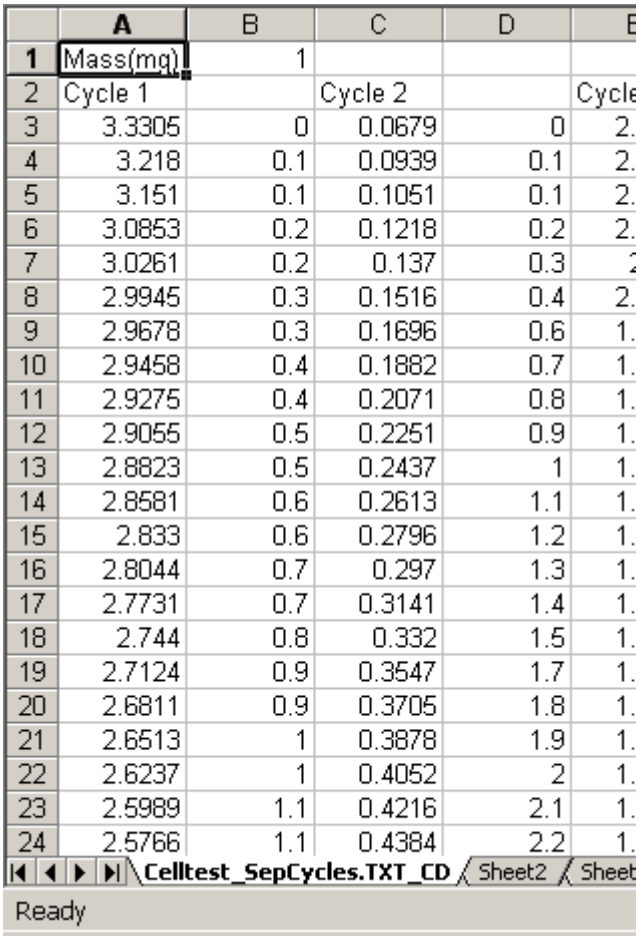

	A	B	C	D	E
1	Mass(mg)	1			
2	Cycle 1		Cycle 2		Cycle
3	3.3305	0	0.0679	0	2.
4	3.218	0.1	0.0939	0.1	2.
5	3.151	0.1	0.1051	0.1	2.
6	3.0853	0.2	0.1218	0.2	2.
7	3.0261	0.2	0.137	0.3	2
8	2.9945	0.3	0.1516	0.4	2.
9	2.9678	0.3	0.1696	0.6	1.
10	2.9458	0.4	0.1882	0.7	1.
11	2.9275	0.4	0.2071	0.8	1.
12	2.9055	0.5	0.2251	0.9	1.
13	2.8823	0.5	0.2437	1	1.
14	2.8581	0.6	0.2613	1.1	1.
15	2.833	0.6	0.2796	1.2	1.
16	2.8044	0.7	0.297	1.3	1.
17	2.7731	0.7	0.3141	1.4	1.
18	2.744	0.8	0.332	1.5	1.
19	2.7124	0.9	0.3547	1.7	1.
20	2.6811	0.9	0.3705	1.8	1.
21	2.6513	1	0.3878	1.9	1.
22	2.6237	1	0.4052	2	1.
23	2.5989	1.1	0.4216	2.1	1.
24	2.5766	1.1	0.4384	2.2	1.

Celltest_SepCycles.TXT_CD | Sheet2 | Sheet

Ready

Figure B-72: Example of processed output of "Separate Cycles".

B.5 Data Reduction

The purpose of the "Data Reduction" functions is to manipulate data to allow for further processing with Excel. This may be necessary because the file is too large to be opened directly by Excel or to increase the speed of further processing by reducing the size of the data set. The options carry out operations as required and directed by their selection and can include data reduction, split and separation.

The functions available on this selection tab are:

1. Split Data into Excel Manageable Parts Only
2. Reduce Data...If Required: One Data Set In File
3. Reduce Data...If Required: Two Data Sets In File
4. User Selectable Difference Below: One Data Set In File
5. User Selectable Difference Below: Two Data Sets In File

The Layout of these in the tab is illustrated in Figure B-73

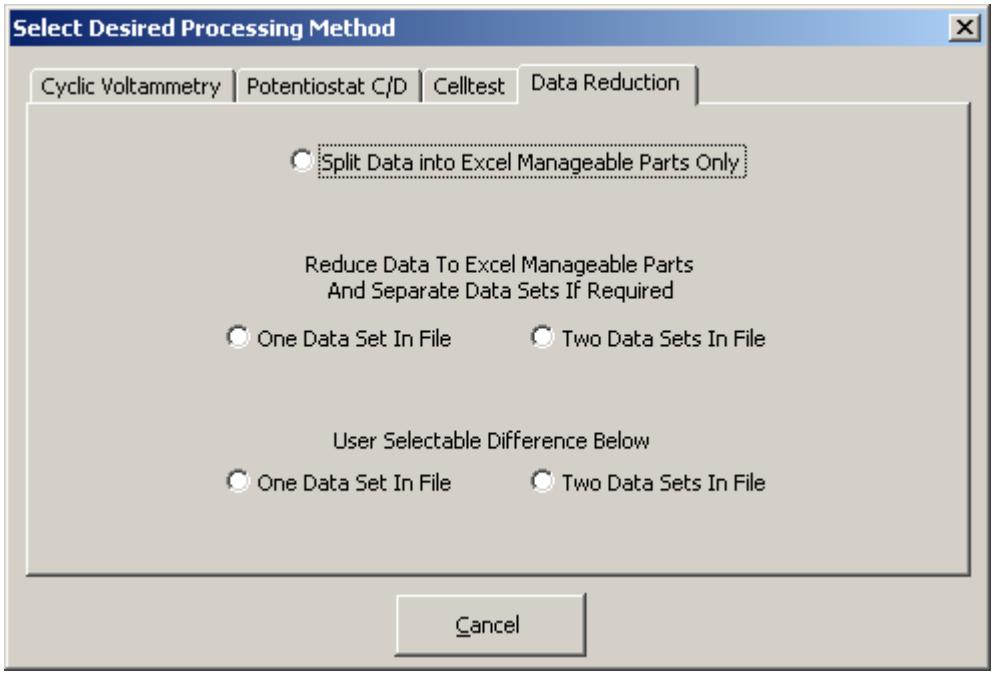

Figure B-73: "Data Reduction" selection tab.

For all the options concerning either "One Data Set In File" or "Two Data Sets In File" the file must conform to the following requirements:

- Contain Numeric Data Only
- Numbers should not contain commas
- Contain only the correct number of columns
  - Three for “One Data Set In File”
  - Five for “Two Data Sets In File”
- Each row of data is complete
- Use a valid Delimiter to separate the columns, which include:
  - Tab
  - ,
  - Space
  - , Tab
  - , Space

The two “One Data Set In File” options will perform the required operation on a data set consisting of 3 columns containing Time, Voltage and Current data in that order (Table B-11). CapacitySorter.txt and Split_1.txt are example files. Whist the two “Two Data Sets In File” options perform the required options on a data set consisting of 5 columns containing Time, Voltage1, Current1, Voltage2, Current2 data in that order (Table B-12). CapacitySorter2.txt and Split_2 are example files.

Table B-11: “One Data Set in File” file format.

Time	Voltage	Current
0	3.514	-50
1	3.514	-50
2	3.513	-50
3	3.512	-50
4	3.511	-50
5	3.511	-50
6	3.511	-50
7	3.509	-50
8	3.508	-50
9	3.507	-50
10	3.507	-50

Note: The column labels are for illustrative purposes only and must not appear in the file.

Table B-12: "Two Data Sets In File" file format.

Time	Voltage 1	Current 1	Voltage 2	Current 2
0	3.514	-50	1.576	-25
1	3.514	-50	1.575	-25
2	3.513	-50	1.574	-25
3	3.512	-50	1.574	-25
4	3.511	-50	1.574	-25
5	3.511	-50	1.573	-25
6	3.511	-50	1.572	-25
7	3.509	-50	1.570	-25
8	3.508	-50	1.569	-25
9	3.507	-50	1.565	-25
10	3.507	-50	1.564	-25

Note: The column labels are for illustrative purposes only and must not appear in the file.

B.5.1 Split Data into Excel Manageable Parts Only

Reads any data file line by line and automatically saves the file into parts that can be opened by Excel. Each part will contain 65500 rows or a part thereof in the case of the final file. Using the Split_1 demonstration file:

Split_1.txt => Split_1.txt_Part1_1.txt
Split_1.txt_Part1_2.txt
Split_1.txt_Part1_3.txt
…….
Split_1.txt_Part1_16.txt

B.5.2 Standard - Reduce Data … If Required

The data is read line by line to determine if the voltage has changed since the last reading was added to the processed file. If the voltage has changed the data is added to the processed file. If the voltage has not changed line by line processing continues until the voltage does change. Processing of the file continues in this way until the entire file has been processed. The processed file/files are automatically saved in the same location as the original file with an added extension.

B.5.2.1 One Data Set In File

The format of the file and a comparison to its processed output are given in Table B-13. Using the Split_1 demonstration file:

Split_1.txt => Split_1.txt_Part1_1.txt
Split_1.txt_Part1_2.txt

Table B-13: Data format and processed output example for "One Data Set in File".

Time	Voltage	Current		Time	Voltage	Current
0	3.514	-50		0	3.514	-50
1	3.514	-50		2	3.513	-50
2	3.513	-50		3	3.512	-50
3	3.512	-50		4	3.511	-50
4	3.511	-50	=>	7	3.509	-50
5	3.511	-50		8	3.508	-50
6	3.511	-50		9	3.507	-50
7	3.509	-50				
8	3.508	-50				
9	3.507	-50				
10	3.507	-50				

Note: Time, Voltage and Current column labels are not in file

B.5.2.2 Two Data Sets In File

The format of the file and a comparison to its processed output is given in Table B-14. Using the Split_2 demonstration file:

Split_2.txt => Split_2.txt_Part1_1.txt Split_2.txt_Part2_1.txt

The Part1 files are generated from the Time, Voltage1, Current1 data, whilst Part2 files are generated from the Time, Voltage2, Current2 data.

Table B-14: Data format and processed output example for "Two Data Sets in File".

Time	Voltage 1	Current 1	Voltage 2	Current 2
0	3.514	-50	1.576	-25
1	3.514	-50	1.575	-25
2	3.513	-50	1.574	-25
3	3.512	-50	1.574	-25
4	3.511	-50	1.574	-25
5	3.511	-50	1.573	-25
6	3.511	-50	1.572	-25
7	3.509	-50	1.570	-25
8	3.508	-50	1.569	-25
9	3.507	-50	1.565	-25
10	3.507	-50	1.564	-25

Time	Voltage 1	Current 1		Time	Voltage 2	Current 2
0	3.514	-50		0	1.576	-25
2	3.513	-50		1	1.575	-25
3	3.512	-50		2	1.574	-25
4	3.511	-50		5	1.573	-25
7	3.509	-50	AND	6	1.572	-25
8	3.508	-50		7	1.570	-25
9	3.507	-50		8	1.569	-25
				9	1.565	-25
				10	1.564	-25

Note: Time, Voltage1, Voltage2, Current1 and Current2 column labels are not in file.

B.5.3 Selectable - Reduce Data … If Required

The data is read line by line to determine if the voltage change since the last reading added to the processed file is greater than the specified difference. If the voltage has changed by the required amount the data is added to the processed file. If the voltage change is not sufficient line by line processing continues until the voltage change is great enough. Processing of the file continues in this way until the entire file has been processed. The processed file/files are automatically saved in the same location as the original file with an added extension.

After a file has been selected to process the user is prompted to select the voltage difference for the comparison (Figure B-74). If the value entered is not valid a dialog box will appear to warn of that fact (Figure B-75). For “Two Data Sets In File” the same voltage comparison is used for both data sets. If Zero is entered in the dialog box the behaviour is identical to that in the standard “Reduce Data to Excel Manageable Parts And Separate Data Sets If Required” section.

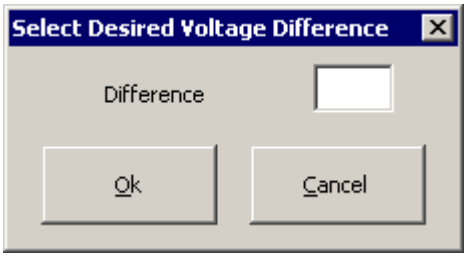

Figure B-74: “Select Desired Voltage Difference” dialog box.

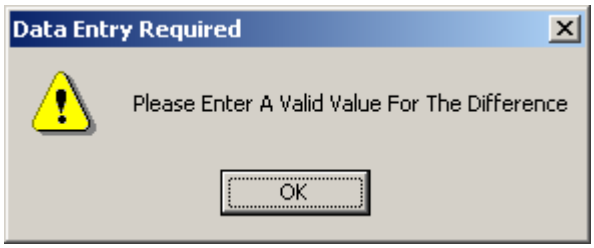

Figure B-75: Valid voltage difference required warning dialog box.

B.5.3.1 One Data Set In File

The format of the file and a comparison to its processed output is given in Table B-15. Using the Split_1 demonstration file:

Split_1.txt => Split_1.txt_Part1_1.txt
Split_1.txt_Part1_2.txt

Table B-15: "One Data Set" demonstration with difference of 0.001.

Time	Voltage	Current		Time	Voltage	Current
0	3.514	-50		0	3.514	-50
1	3.514	-50		3	3.512	-50
2	3.513	-50	=>	7	3.509	-50
3	3.512	-50		9	3.507	-50
4	3.511	-50				
5	3.511	-50				
6	3.511	-50				
7	3.509	-50				
8	3.508	-50				
9	3.507	-50				
10	3.507	-50				

Note: Time, Voltage and Current column labels are not in file.

B.5.3.2 Two Data Sets In File

The format of the file and a comparison to its processed output is given in Table B-16. Using the Split_2 demonstration file:

Split_2.txt => Split_2.txt_Part1_1.txt Split_2.txt_Part2_1.txt

The Part1 files are generated from the Time, Voltage1, Current1 data, whilst Part2 files are generated from the Time, Voltage2, Current2 data.

Table B-16: "Two Data Set" demonstration with difference of 0.001.

Time	Voltage 1	Current 1	Voltage 2	Current 2
0	3.514	-50	1.576	-25
1	3.514	-50	1.575	-25
2	3.513	-50	1.574	-25
3	3.512	-50	1.574	-25
4	3.511	-50	1.574	-25
5	3.511	-50	1.573	-25
6	3.511	-50	1.572	-25
7	3.509	-50	1.570	-25
8	3.508	-50	1.569	-25
9	3.507	-50	1.565	-25
10	3.507	-50	1.564	-25

Time	Voltage 1	Current 1		Time	Voltage 2	Current 2
0	3.514	-50		0	1.576	-25
3	3.512	-50		2	1.574	-25
7	3.509	-50	AND	6	1.572	-25
9	3.507	-50		7	1.570	-25
				8	1.569	-25
				9	1.565	-25

Note: Time, Voltage1, Voltage2, Current1 and Current2 column labels are not in file.

Appendix C Data Manipulation Manual

C.1 Introduction

The Data Manipulation spreadsheet is able to perform a number of manipulations on Separate cycle data generated from the BatteryTestDataProcessing spreadsheet. Each processing option within the spreadsheet automatically saves a single file. This file is saved in the same location as the original file with a filename based on the name of the file being opened for processing. When files are saved automatically if the file already exists it will be overwritten without any warning. As a result of the automatic saving of files, files should only be opened for processing from the hard disk.

C.1.1 Security and using the spreadsheet

To enable users to verify that the spreadsheet they are using and the macros within came from Matthew Lindsay, the files have a digital signature attached to them. If the files are modified then this digital signature is removed. The macros themselves are also password protected to prevent modification of them and the functions they perform.

Figure C-1: "Security Warning" dialog box.

On running the spreadsheet the first thing you are likely to see is a security warning box (Figure C-1). From this page you can verify that the spreadsheet has not been altered. The name Matthew Lindsay as shown in Figure C-1 does not guarantee the spreadsheet has not been modified because others could easily replicate this part of a digital signature. If the details of the certificate itself are examined and compared to known

details of the certificate you can be fairly certain that the spreadsheet has not been modified. The details of the digital signature are accessible by clicking the "Details…" button in the "Security Warning" dialog box (Figure C-2).

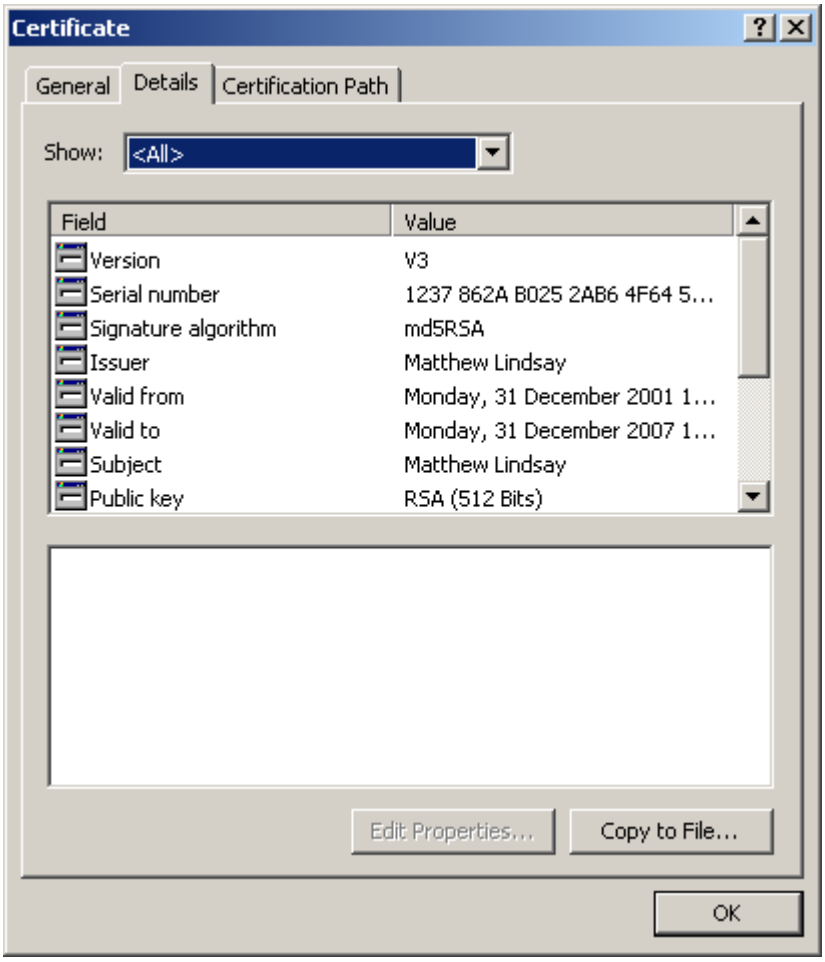

Figure C-2: Details of digital signature.

Having confirmed the spreadsheet has not been modified it is safe to "Enable Macros" on the "Security Warning" dialog box. If however this button is grayed out as it is in Figure C-3.

There are two options to enable the macros:

- Tick the "Always trust macros from this source" check box in the "Security Warning" dialog box.
- Close the "Security Warning" dialog box and open the "Tools" menu in Excel, select the "Macro" menu item, and the "Security" item from that menu. The "Security" dialog box will then appear (Figure C-4). Change the security level to medium.

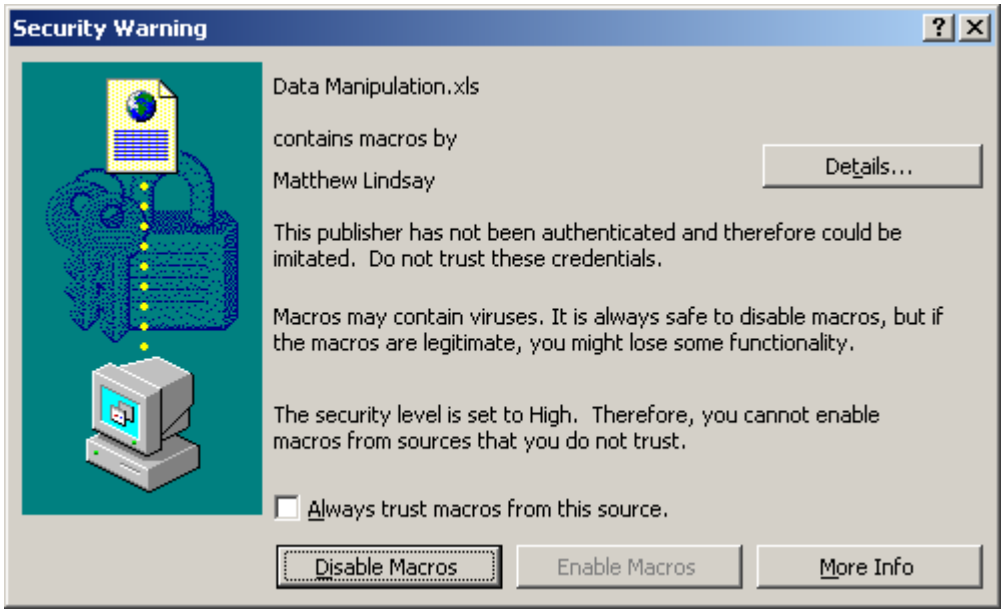

Figure C-3: "Security Warning" dialog box.

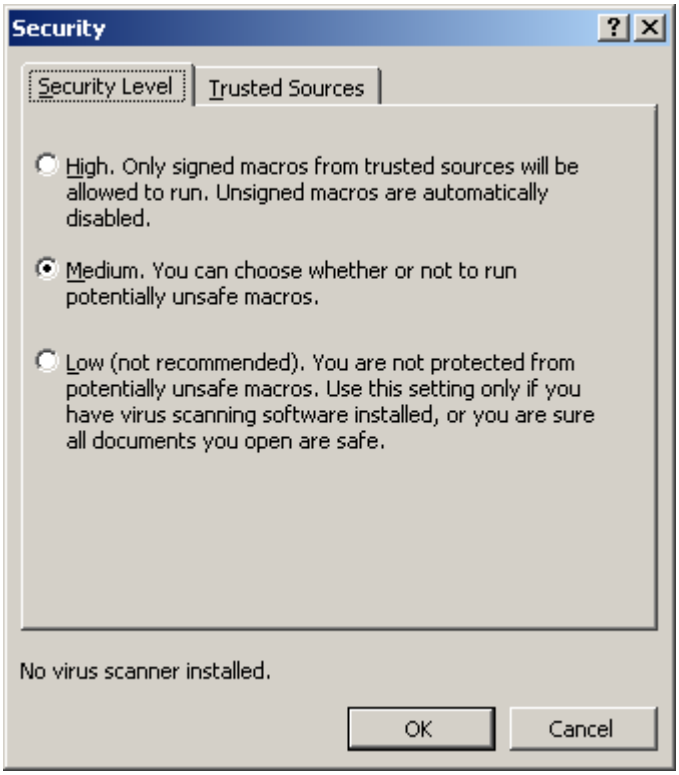

Figure C-4: "Security" settings dialog box.

Having enabled the running of macros a "License Agreement" dialog box will appear (Figure C-5). The conditions of the agreement must be agreed to and clicking on "Accept" implies that you have read the conditions outlined in this agreement and agreed to them. This will also enable the spreadsheet to be used. If however you do not

agree to the conditions and click "Reject" then the spreadsheet will be closed automatically.

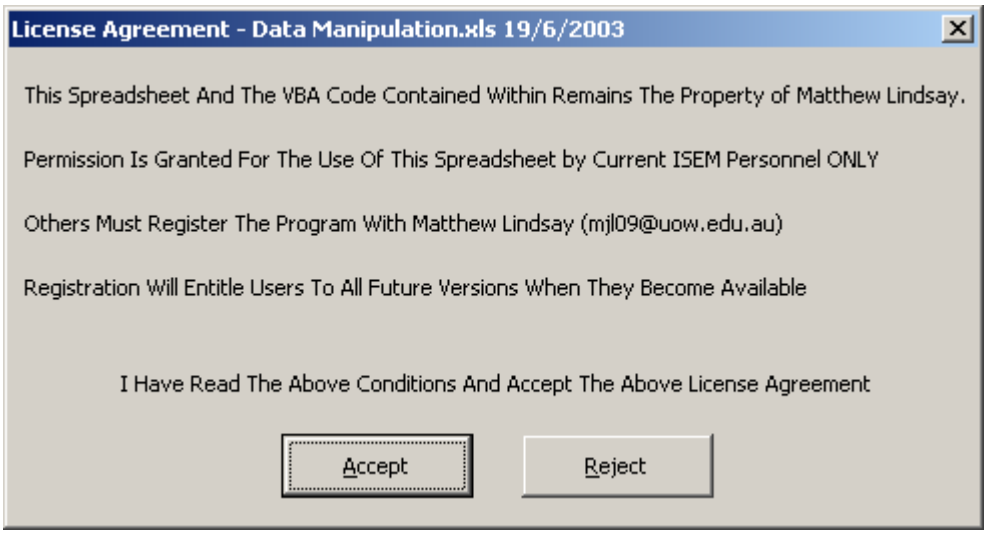

Figure C-5: License Agreement dialog box.

Following clicking on "Accept" a file open dialog box will appear to select the file to be processed. With a file selected and successfully opened a "Select Desired Processing Method" dialog box will appear. All the processing options in the spreadsheet are contained within this dialog box (Figure C-6).

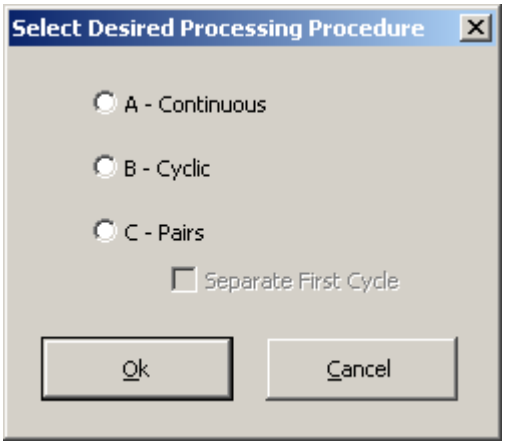

Figure C-6: "Select Desired Processing Method" dialog box.

Further details on the processing procedures available can be found in the subsequent section of this document.

If the "Cancel" button is clicked a "Processing Aborted" dialog box will appear (Figure C-7). The same dialog box will appear if the "Cancel" Button on any of the dialog boxes is clicked.

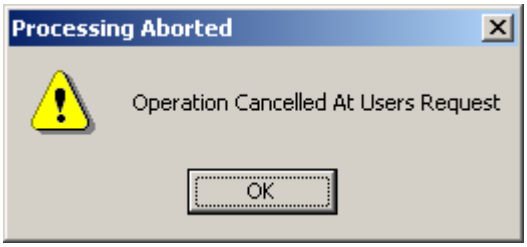

Figure C-7: "Processing Aborted" dialog box.

If an unexpected error occurs during processing (including whilst trying to open a file) then a different "Processing Aborted" dialog box will appear (Figure C-8). Another dialog box that can appear at the time of opening a file is the "Error Loading File - Processing Aborted" dialog box (Figure C-9). This appears when the file is not loaded entirely. Excel only has a certain number of rows available to load data into, if there are more rows of data in the file then Excel has to load them into this error occurs. Currently Excel supports a maximum of 65536 rows, this is however limited by available memory and system resources. Any computer meeting the system requirements for Office 2000 should be capable of displaying this maximum number of rows.

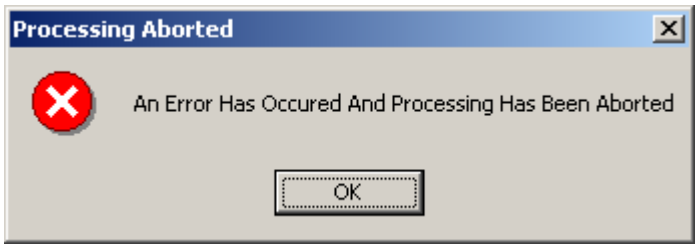

Figure C-8: "Processing Aborted" dialog box.

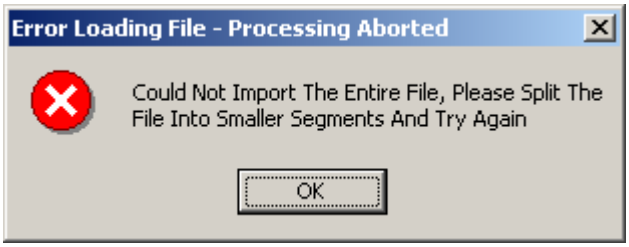

Figure C-9: "Error Loading File - Processing Aborted" dialog box.

C.2 Processing Options

Separate cycle data outputted from the BatteryTestDataProcessing spreadsheet can be manipulated by the Data Manipulation spreadsheet to produce data sets for four

different types of graphs. For this spreadsheet to be able to produce the required datasets directly rest periods (if they occur) should have been sorted so that they occur at the beginning of a cycle. For CellTest data this can be accomplished using the Separate Cycles – Rest at Start of Cycle functions in the BatteryTestDataProcessing spreadsheet.

The four manipulations are accomplished through the options available in the "Select Desired Processing Procedure" dialog box (Figure C-10).

The four manipulations are;

A – Continuous

B – Cyclic

C – Pairs

C – Pairs – Separate First Cycle

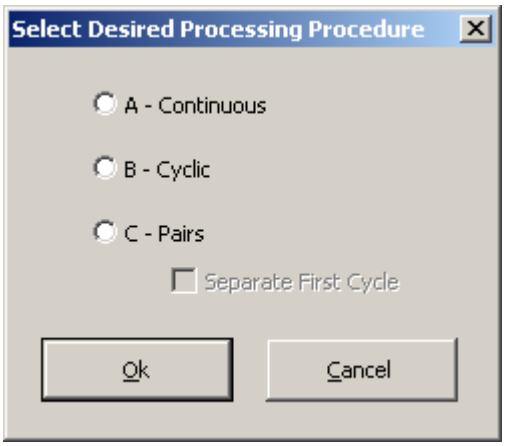

Figure C-10: "Select Desired Processing Method" Dialog Box.

The processed file is automatically saved in the same location as the opened file with an added extension. If the filename of the original file was filename.txt the output file would have an added extension which is dependent on the processing method selected (Table C-1).

Table C-1: Output file names for processing methods.

Processing Method	Input file	Output file
A – Continuous	filename.txt	filename.txt_A.txt
B – Cyclic	filename.txt	filename.txt_B.txt
C – Pairs	filename.txt	filename.txt_C.txt
C – Pairs – Separate First Cycle	filename.txt	filename.txt_C.txt

During processing an indication is given in the lower left corner of Excel (Figure C-11).

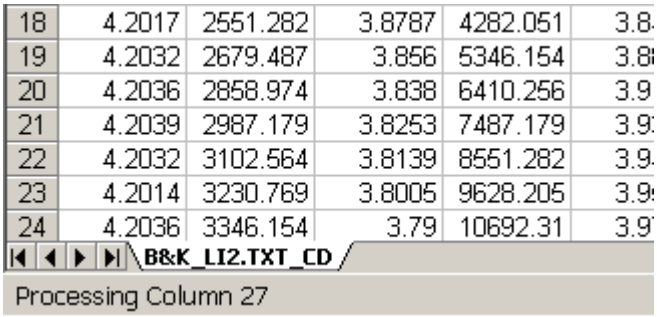

Figure C-11: Processing Indication in Excel.

The format of the data file produced will depend on the processing option selected. For the "A – Continuous" and "B – Cyclic" options the data will consist of two columns of data (Figure C-12). The first column contains voltage data whilst the second contains capacity data. The electrode mass is also recorded in the first row of the data file. For both "C – Pairs" options the data will consist of a number of sets of two columns (Figure C-13). The first column in each set contains voltage data whilst the second contains capacity data. The first row also contains a record of the electrode mass whilst the second row contains the labels of the cycle steps that have been combined to produce the new data.

The outcomes of the various methods are best seen in examples of graphs produced from the data sets produced using the spreadsheet (Figure C-14).

	A	B	C	D	E
1			Mass (mg)	7.8	
2	4.2817	0			
3	4.2817	38.46154			
4	4.2026	38.46154			
5	4.2036	346.1538			
6	4.2036	615.3846			
7	4.2017	846.1538			
8	4.2036	1051.282			
9	4.2036	1256.41			
10	4.2032	1435.897			
11	4.2017	1615.385			
12	4.2036	1782.051			
13	4.2017	1948.718			
14	4.2036	2102.564			
15	4.2036	2256.41			
16	4.2036	2397.436			
17	4.2017	2551.282			
18	4.2032	2679.487			
19	4.2036	2858.974			
20	4.2039	2987.179			
21	4.2032	3102.564			
22	4.2014	3230.769			
23	4.2036	3346.154			
24	4.2014	3461.538			

Figure C-12: Example of processed output for methods A and B.

	A	B	C	D	E
1			Mass (mg)	7.8	
2	Cycle 1 & Cycle 2		Cycle 3 & Cycle 4		Cycle 5
3	4.2817	0	2.9582	0	2.94
4	4.2817	38.46154	3.2022	0	3.18
5	4.2026	38.46154	3.2608	0	3.24
6	4.2036	346.1538	3.2983	0	3.28
7	4.2036	615.3846	3.3194	0	3.31
8	4.2017	846.1538	3.3414	0	3.32
9	4.2036	1051.282	3.3519	0	3.34
10	4.2036	1256.41	3.3634	0	3.34
11	4.2032	1435.897	3.3743	0	3.35
12	4.2017	1615.385	3.3814	0	3.36
13	4.2036	1782.051	3.3876	0	3.37
14	4.2017	1948.718	3.4942	0	3.47
15	4.2036	2102.564	3.6734	1064.103	3.64
16	4.2036	2256.41	3.7419	2141.026	3.71
17	4.2036	2397.436	3.8021	3205.128	3.77
18	4.2017	2551.282	3.8483	4282.051	3.81
19	4.2032	2679.487	3.8858	5346.154	3.85
20	4.2036	2858.974	3.9159	6410.256	3.88
21	4.2039	2987.179	3.9323	7487.179	3.90
22	4.2032	3102.564	3.9475	8551.282	3.92
23	4.2014	3230.769	3.9583	9615.385	3.93
24	4.2036	3346.154	3.9704	10730.77	3.94

Figure C-13: Example of processed output for method C.

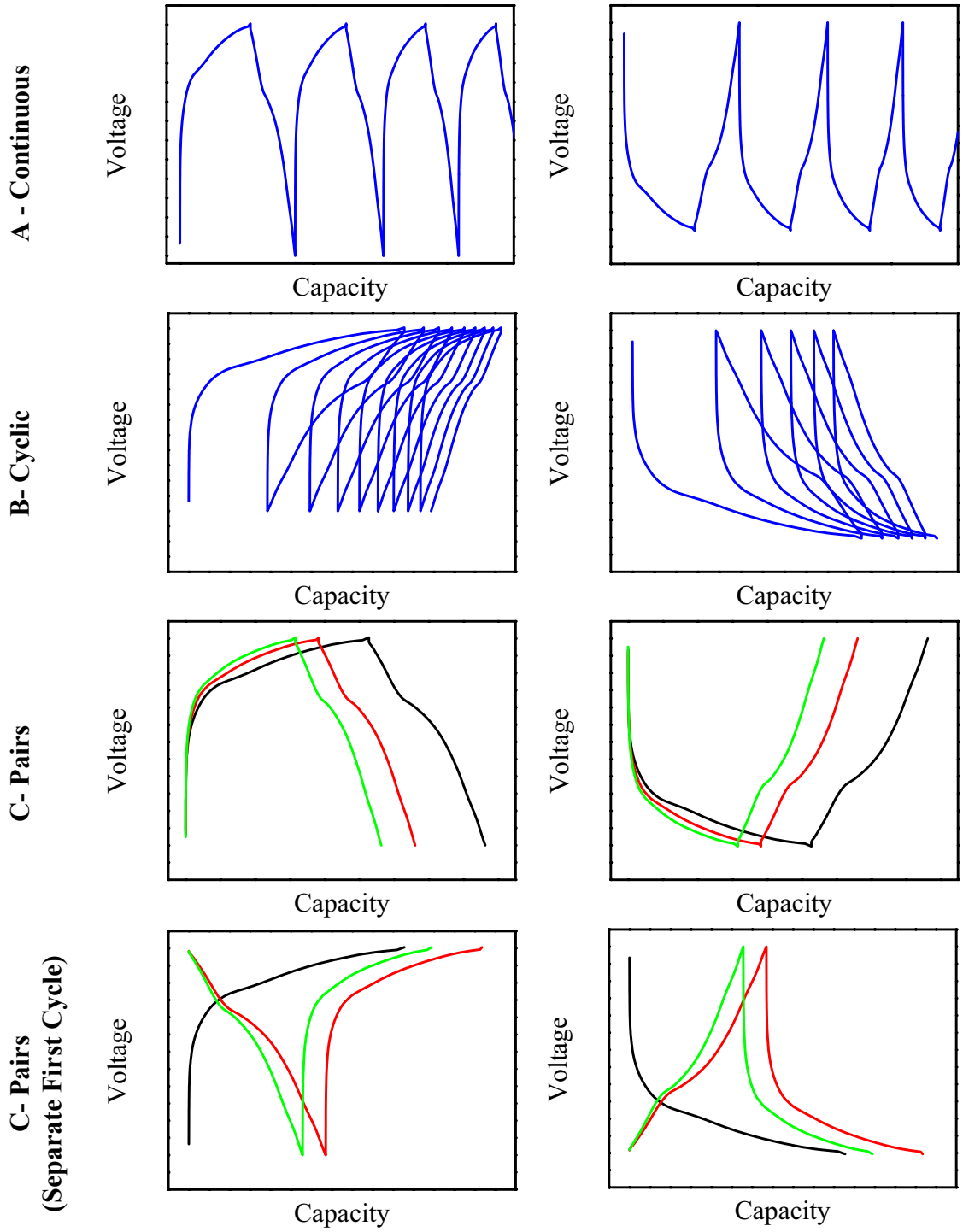

Figure C-14: Examples of graphs produced from processed output.

Appendix D BET Analysis

D.1 Multipoint BET Plots and Fitting Results

D.1.1 Binary Al-Fe and Ternary Al-Fe-Si

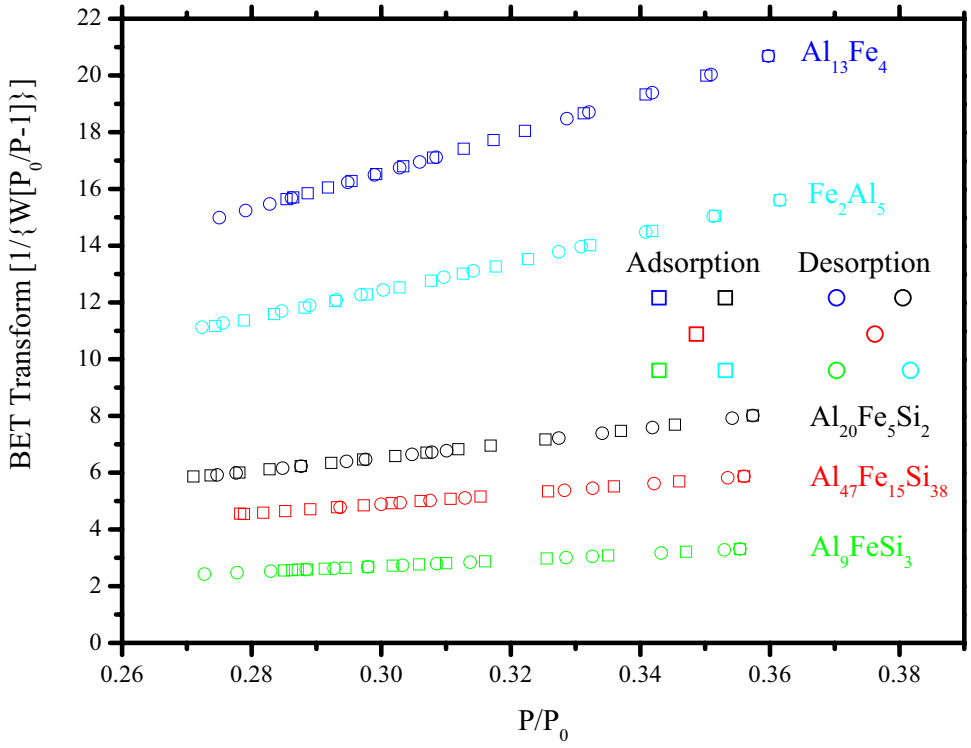

Figure D-1: BET plots of binary Al – Fe and ternary Al – Fe – Si materials.

Table D-1: BET analysis of binary Al – Fe and ternary Al – Fe – Si materials.

Material	Slope	Intercept	Correlation Coefficient	BET C	Specific Surface Area (m^2/g)
$Al_{13}Fe_4$	67.476007	-3.655001	0.999806	-17.461283	54.5669
Fe_2Al_5	50.727146	-2.808647	0.999651	-17.061059	72.6758
$Al_{20}Fe_5Si_2$	24.967740	-0.942773	0.999631	-25.483290	144.9541
$Al_{47}Fe_{15}Si_{38}$	17.120213	-0.234476	0.999780	-72.014878	206.2401
Al_9FeSi_3	10.703233	-0.502727	0.999625	-20.290333	341.4063

D.1.2 FeSi and $FeSi_2$

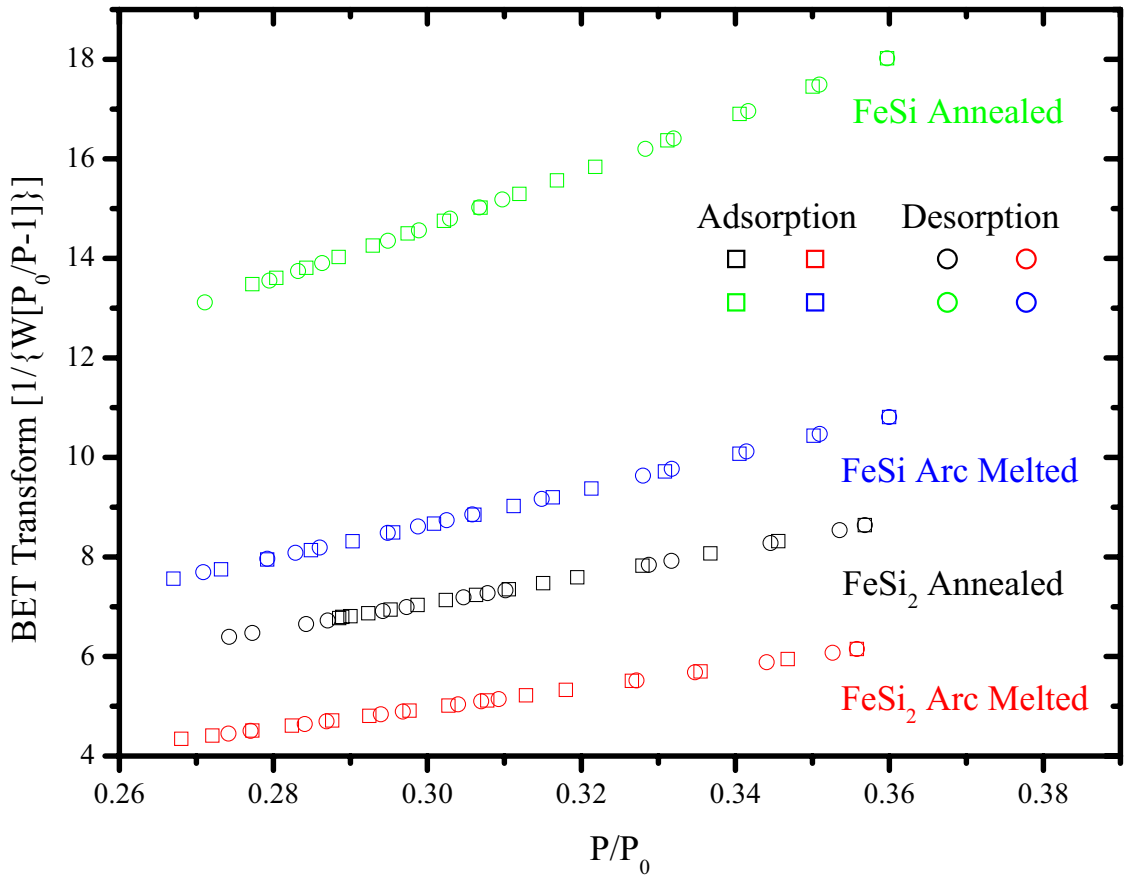

Figure D-2: BET plots of FeSi and $FeSi_2$ materials.

Table D-2: BET analysis of FeSi and $FeSi_2$ materials.

Material	Slope	Intercept	Correlation Coefficient	BET C	Specific Surface Area (m^2/g)
FeSi Arc Melted	34.878932	-1.802661	0.999546	-18.348576	105.2875
FeSi Annealed	55.256521	-1.912849	0.999735	-27.887020	65.2845
$FeSi_2$ Arc Melted	20.586734	-1.204026	0.999587	-16.098244	179.6713
$FeSi_2$ Annealed	27.207439	-1.088514	0.999820	-23.995026	133.3331

D.1.3 $Bi_2Sr_2CaCu_2O_{8+\delta}$ and $Bi_2Sr_2Ca_{0.3}Y_{0.7}Cu_2O_{8+\delta}$

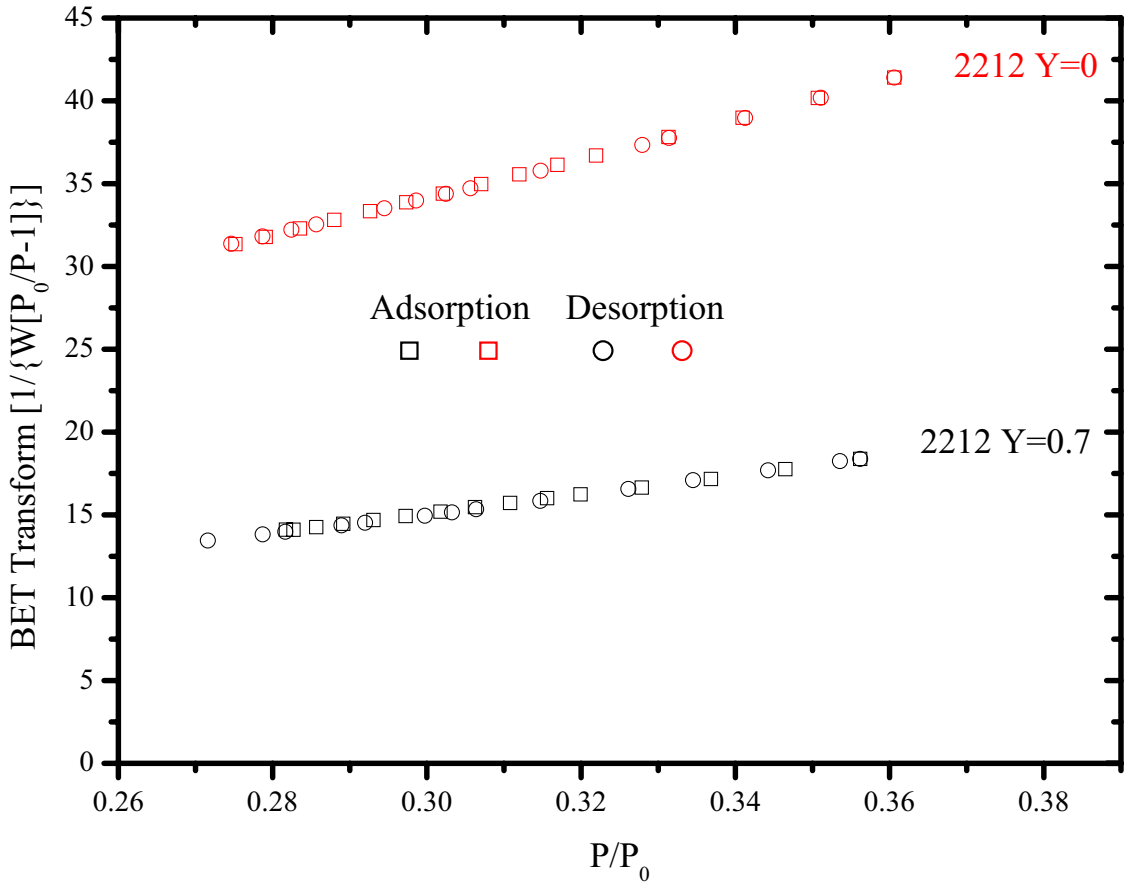

Figure D-3: BET plots of Bi-2212 materials.

Table D-3: BET analysis of Bi-2212 materials.

Material	Slope	Intercept	Correlation Coefficient	BET C	Specific Surface Area (m^2/g)
2212 y=0	117.241229	-0.979307	0.999872	-118.718550	29.9541
2212 y=0.7	57.354022	-2.107305	0.999761	-26.216764	63.0357

D.1.4 Nanometre SiC

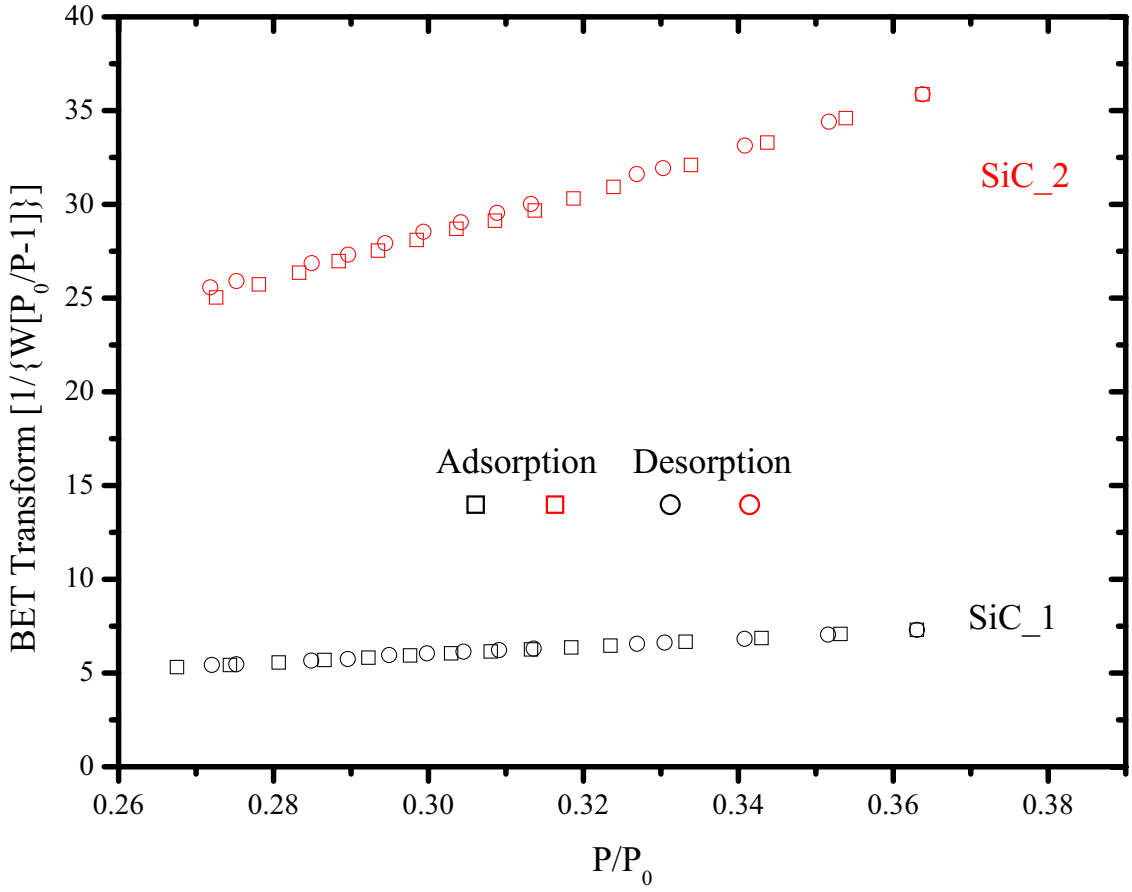

Figure D-4: BET plots of nanometre SiC materials.

Table D-4: BET analysis of nanometre SiC materials.

Material	Slope	Intercept	Correlation Coefficient	BET C	Specific Surface Area (m^2/g)
SiC_1	28.858882	-0.281145	0.999887	-73.192523	169.2371
SiC_2	116.793131	-6.805389	0.999543	-16.161859	31.6628

D.2 Empirical Densities

In some cases the densities of the materials produced are unavailable in the literature and as a result empirical densities have been calculated based on the weight percentage of the elements in the materials and their respective densities. In order to perform such calculations the densities and molecular weights of the elements are required (Table D-5).

Table D-5: Densities and molecular weights of selected elements.

Material	Density (g/cm^3) [242]	Molecular Weight (g) [3]
Al	2.698	26.98154
C	2.260	12.011
Fe	7.874	55.847
Si	2.329	28.0855

D.2.1 $FeAl_3$

$$MolecularWeight = 1\times 55.847 + 3\times 26.982$$

$$MolecularWeight = 136.793$$

$$Density\left(\frac{g}{cm^3}\right) = \frac{1\times 55.847}{136.793}\times 7.874 + 3\times\frac{26.982}{136.793}\times 2.698$$

$$Density\left(\frac{g}{cm^3}\right) = 4.811$$

D.2.2 $FeAl_3$ + Carbon Black

If instead the material also contained carbon black the density could be recalculated based on the weight proportions of the material.

$$Density\left(\frac{g}{cm^3}\right) = \frac{3.012}{3.303}\times 4.811 + \frac{0.291}{3.303}\times 2.260$$

$$Density\left(\frac{g}{cm^3}\right) = 4.586$$

D.2.3 $Al_{47}Fe_{15}Si_{38}$

$$MolecularWeight = 47\times 26.982 + 15\times 55.847 + 38\times 28.086$$

$$MolecularWeight = 3173.127$$

$$Density\left(\frac{g}{cm^3}\right) = \frac{47\times 26.982}{3173.127}\times 2.698 + \frac{15\times 55.847}{3173.127}\times 7.874 + \frac{38\times 28.086}{3173.127}\times 2.329$$

$$Density\left(\frac{g}{cm^3}\right) = 3.940$$

D.2.4 $Al_{20}Fe_{5}Si_{2}$

$$MolecularWeight = 20\times 26.982 + 5\times 55.847 + 2\times 28.086$$

$$MolecularWeight = 875.047$$

$$Density\left(\frac{g}{cm^3}\right) = \frac{20\times 26.982}{875.047}\times 2.698 + \frac{5\times 55.847}{875.047}\times 7.874 + \frac{2\times 28.086}{875.047}\times 2.329$$

$$Density\left(\frac{g}{cm^3}\right) = 4.326$$

D.2.5 $Al_{9}FeSi_{3}$

$$MolecularWeight = 9\times 26.982 + 1\times 55.847 + 3\times 28.086$$

$$MolecularWeight = 382.943$$

$$Density\left(\frac{g}{cm^3}\right) = \frac{9\times 26.982}{382.943}\times 2.698 + \frac{1\times 55.847}{382.943}\times 7.874 + \frac{3\times 28.086}{382.943}\times 2.329$$

$$Density\left(\frac{g}{cm^3}\right) = 3.372$$

D.2.6 FeSi

$$MolecularWeight = 1\times 55.847 + 1\times 28.086$$

$$MolecularWeight = 83.933$$

$$Density\left(\frac{g}{cm^3}\right) = \frac{1\times 55.847}{83.933}\times 7.874 + \frac{1\times 28.086}{83.933}\times 2.329$$

$$Density\left(\frac{g}{cm^3}\right) = \quad 6.019$$

D.2.7 FeSi + Carbon Black

$$Density\left(\frac{g}{cm^3}\right) = \quad \frac{3.112}{3.423}\times 6.019 + \frac{0.311}{3.423}\times 2.260$$

$$Density\left(\frac{g}{cm^3}\right) = \quad 5.677$$

D.2.8 $FeSi_2$

$$MolecularWeight = \quad 1\times 55.847 + 2\times 28.086$$

$$MolecularWeight = \quad 112.019$$

$$Density\left(\frac{g}{cm^3}\right) = \quad \frac{1\times 55.847}{83.933}\times 7.874 + \frac{2\times 28.086}{83.933}\times 2.329$$

$$Density\left(\frac{g}{cm^3}\right) = \quad 5.093$$

D.2.9 $FeSi_2$ + Carbon Black

$$Density\left(\frac{g}{cm^3}\right) = \quad \frac{2.704}{2.978}\times 6.019 + \frac{0.274}{2.978}\times 2.260$$

$$Density\left(\frac{g}{cm^3}\right) = \quad 4.832$$

D.2.10 SiC

$$MolecularWeight = \quad 1\times 28.086 + 1\times 12.011$$

$$MolecularWeight = \quad 40.097$$

$$Density\left(\frac{g}{cm^3}\right) = \quad \frac{1\times 28.086}{40.097}\times 2.329 + \frac{1\times 12.011}{40.097}\times 2.260$$

$$Density\left(\frac{g}{cm^3}\right) = \quad 2.308$$

D.2.11 Summary

Table D-6: Summary of empirical density calculation results.

Material	Empirical Density (g/cm^3)
$FeAl_3$	4.811
$FeAl_3$ + carbon black	4.586
$Al_{47}Fe_{15}Si_{38}$	3.940
$Al_{20}Fe_5Si_2$	4.326
Al_9FeSi_3	3.372
FeSi	6.019
FeSi + carbon black	5.677
$FeSi_2$	5.093
$FeSi_2$ + carbon black	4.832
SiC	2.308

D.3 Specific Surface Area and Particle Size

Given a measured specific surface area (S) from BET an equivalent particle size for the material can be calculated based on the material being completely homogenous and completely dense. That is that all the particles are identical and there are no voids within the solid particles. For a given powder an equivalent theoretical particle size can be calculated using the results derived in Appendix A (D-1). This can similarly calculated for a cylindrical particle with a radius of R and height of R/10 (D-2).

$$S = \frac{3}{r\rho}$$

$$r = \frac{3}{S\rho} \qquad \text{D-1}$$

$$S = \frac{22}{R\rho}$$

$$R = \frac{22}{S\rho} \qquad \text{D-2}$$

Using these results and the calculated empirical densities the equivalent particle sizes have been calculated for a number of materials (Table D-7).

Table D-7: Equivalent particle size results.

Material	Empirical Density (g/m^3)	Specific Surface Area (m^2/g)	Sphere (radius) (nm)	Cylinder (radius) (nm)
$FeAl_3$	4811000	73	8.5	62.6
$FeAl_3$ + carbon black	4586000	55	11.9	87.2
$Al_{47}Fe_{15}Si_{38}$	3940000	206	3.7	27.1
$Al_{20}Fe_5Si_2$	4326000	145	4.8	35.1
Al_9FeSi_3	3372000	341	2.6	19.1
FeSi	6019000	105	4.7	34.8
FeSi + carbon black	5677000	65	8.1	59.6
$FeSi_2$	5093000	180	3.3	24.0
$FeSi_2$ + carbon black	4832000	133	4.7	34.2
SiC_1	2308000	169	7.7	56.4
SiC_2	2308000	32	40.6	297.9

Appendix E Publications

- G.X. Wang, M.J. Lindsay, M. Ionescu, D.H. Bradhurst, S.X. Dou and H.K. Liu, *Physical and electrochemical characterisation of $LiNi_{0.8}Co_{0.2}O_2$ thin-film electrodes deposited by laser ablation*, Journal of Power Sources, 2001. **97-98**: p. 298-302.
- G.X. Wang, J.H. Ahn, M.J. Lindsay, L. Sun, D.H. Bradhurst, S.X. Dou and H.K. Liu, *Graphite-Tin composites as anode materials for lithium-ion batteries*, Journal of Power Sources, 2001. **97-98**: p. 211-215.
- G.X. Wang, Y. Chen, K. Konstantinov, M. Lindsay, H.K. Liu and S.X. Dou, *Investigation of cobalt oxides as anode materials for Li-ion batteries*, Journal of Power Sources, 2002. **109**: p. 142-147.
- H.K. Liu, B. Bright, C.Y. Wang, M. Lindsay and S. Zhong, *Effect of Zinc-Ion additive to the positive electrode of rechargeable nickel-metal hydride batteries*, Journal of New Materials For Electrochemical. Systems, 2002. **5**: p. 47-52.
- J.H. Ahn, Y.J. Kim, G.X. Wang, M. Lindsay, H.K. Liu and S.X. Dou, *Lithium Storage Properties of Ball Milled Ni-57 mass % Sn Alloy*, Materials Transactions, 2002. **43**(1): p. 63-66.
- G.X. Wang, J.H. Ahn, J. Yao, M. Lindsay, H.K. Liu and S.X. Dou, *Preparation and characterisation of carbon nanotubes for energy storage*, Journal of Power Sources, 2003. **119-121**: p. 16-23.
- M.J. Lindsay, G.X. Wang and H.K. Liu, *Al-based anode materials for Li-ion batteries*, Journal of Power Sources, 2003. **119-121:** p. 84-87.

References

1. *Collins Australian Pocket Dictionary of the English Language*. New ed, ed. W. A. Krebs and G. A. Wilkes. 1991, Sydney: Collins.
2. "Battery." E. Britannica. Encyclopædia Britannica Online. 08 May 2003, http://search.eb.com/eb/article?eu=108543.
3. T. L. Brown, J. H. Eugene Lemay, and B. E. Bursten, *Chemistry The Central Science*. Sixth ed. 1994, Englewood Cliffs: Prentice Hall, Inc.
4. W. D. Callister, Jr., *Materials Science and Engineering, An Introduction*. Third ed. 1994, New York: John Wiley & Sons, Inc.
5. "Amorphous and Nanocrystalline Materials." G. Herzer. Elsevier - Encyclopedia of Materials Science and Technology. 11 August 2003, http://www.elsevier.com/mrwclus/15/136/15/index.htt.
6. Z. S. Wronski, *Materials For Rechargeable Batteries And Clean Hydrogen Energy Sources.* International Materials Reviews, 2001. **46**(1): p. 1-49.
7. J.-S. Hong and J. R. Selman, *Relationship Between Calorimetric and Structural Characteristics of Lithium-Ion Cells.* Journal of The Electrochemical Society, 2000. **179**(9): p. 3183.
8. "When Was The Battery Invented?" I. Buchmann. Cadex Electronics Inc. 08 May 2003, http://www.buchmann.ca/Article3-Page1.asp.
9. *Encylopedia Of Physical Science And Technology*, ed. R. A. Meyers. Vol. 2. 1987: Academic Press. 388.
10. U. Koehler, F. J. Kruger, J. Kuempers, M. Maul, E. Niggemann, and H. H. Schoenfelder, *High Performance Nickel-Metal Hydride and Lithium-Ion Batteries*, in *Proceedings of the 32nd Intersociety Energy Conversion Engineering Conference*. 1997, IEEE. p. 93-98.
11. R. M. Dell, *Batteries fifty years of materials development.* Solid State Ionics, 2000. **134**(1-2): p. 139-158.
12. R. A. Powers. *Batteries for Low Power Electronics*. in *Proceedings of the IEEE*. 1995: IEEE.
13. A. C. Harkness, *High Rate Lithium Batteries For Military And Commerical Applications*, in *Proceedings of the Sixth Annual Battery Conference on Applications and Advances*. 1991, IEEE. p. 65-72.
14. R. Yazami and P. Touzain, *A reversible graphite-lithium negative electrode for electrochemical generators.* Journal of Power Sources, 1983. **9**(3): p. 365-371.
15. M. Winter, J. O. Besenhard, M. E. Spahr, and P. Novák, *Insertion Electrode Materials for Rechargeable Lithium Batteries.* Advanced Materials, 1998. **10**(10): p. 725-763.
16. Y. Idota, T. Kubota, A. Matsufuji, Y. Maekawa, and T. Miyasaka, *Tin-Based Amorphous Oxide: A High Capacity Lithium-Ion-Storage Material.* Science, 1997. **276**(5317): p. 1395-1399.
17. P. Lavela, M. Conrad, A. Mrotzek, B. Harbrecht, and J. L. Tirado, *Electrochemical lithium and sodium intercalation into the tantalum-rich layered chalcogenides Ta_2Se and Ta_2Te_3.* Journal of Alloys and Compounds, 1999. **282**(1-2): p. 93-100.
18. H. Kim and J. Choi, *The Insertion Mechanism of Lithium into Mg_2Si Anode Material for Li-Ion Batteries.* Journal of The Electrochemical Society, 1999. **146**(12): p. 4401-4405.

19. H. Li, X. Huang, and L. Chen, *Anodes based on oxide materials for lithium rechargeable batteries.* Solid State Ionics, 1999. **123**(3-4): p. 189-197.
20. O. Mao, R. A. Dunlap, and J. R. Dahn, *Mechanically Alloyed Sn-Fe(-C) Powders as Anode Materials for Li-Ion Batteries I. The Sn_2Fe-C System.* Journal of The Electrochemical Society, 1999. **146**(2): p. 405-413.
21. O. Mao and J. R. Dahn, *Mechanically Alloyed Sn-Fe(-C) Powders as Anode Materials for Li-Ion Batteries III. Sn_2Fe:$SnFe_3C$ Active/Inactive Composites.* Journal of The Electrochemical Society, 1999. **146**(2): p. 423-427.
22. R. Benedek and M. M. Thackeray, Journal of Power Sources, 2002. **110**: p. 406.
23. L. Y. Beaulieu and J. R. Dahn, Journal of The Electrochemical Society, 2000. **147**: p. 3237.
24. I. Kim, P. N.Kumta, and G. E. Blomgren, *Si/TiN Nanocomposites Novel Anode Materials for Li-Ion Batteries.* Electrochemical and Solid-State Letters, 2000. **3**(11): p. 493-496.
25. R. A. Huggins, *Alternative materials for negative electrodes in lithium systems.* Solid State Ionics, 2002. **152-153**: p. 61-68.
26. J. O. Besenhard, M. Hess, and P. Komenda, Solid State Ionics, 1990. **40-41**: p. 525.
27. J. O. Besenhard, J. Yang, and M. Winter, *Will advanced lithium-alloy anodes have a chance in lithium-ion batteries?* Journal of Power Sources, 1997. **68**(1): p. 87-90.
28. O. Crosnier, T. Brousse, X. Devaux, P. Fragnaud, and D. M. Schleich, *New anode systems for lithium ion cells.* Journal of Power Sources, 2001. **94**(2): p. 169-174.
29. J. Yang, M. Winter, and J. O. Besenhard, *Small particle size multiphase Li-alloy anodes for lithium-ion batteries.* Solid State Ionics, 1996. **90**(1-4): p. 281-287.
30. A. H. Whitehead, J. M. Elliott, and J. R. Owen, *Nanostructured tin for use as a negative electrode material in Li-ion batteries.* Journal of Power Sources, 1999. **81-82**(1-2): p. 33-38.
31. J. Wolfenstine, *Critical grain size for microcracking during lithium insertion.* Journal of Power Sources, 1999. **79**(1): p. 111-113.
32. J. Wolfenstine, D. Foster, J. Read, W. K. Behl, and W. Luecke, *Experimental confirmation of the model for microcracking during lithium charging in single-phase alloys.* Journal of Power Sources, 2000. **87**(1-2): p. 1-3.
33. L. Y. Beaulieu, K. W. Eberman, R. L. Turner, L. J. Krause, and J. R. Dahn, *Colossal Reversible Volume Changes in Lithium Alloys.* Electrochemical and Solid-State Letters, 2001. **4**(9): p. A137-A140.
34. M. M. Thackeray, *From gems to lithium battery electrodes: the significance of the diamond, ruby (sapphire), spinel and peridot structures.* Journal of Power Sources, 2001. **97-98**: p. 7-12.
35. R. Benedek and M. M. Thackeray, *Lithium reactions with intermetallic-compound electrodes.* Journal of Power Sources, 2002. **110**(2): p. 406-411.
36. W. A. v. Schalkwijk, *Lithium Rechargeable Batteries*, in *Proceedings of WESCON*. 1993, IEEE. p. 292.
37. M. Inaba and Z. Ogumi, *Up-to-Date Development of Lithium-Ion Batteries in Japan.* IEEE Electrical Insulation Magazine, 2001. **17**(6): p. 6-20.
38. W. Li, J. R. Dahn, and D. S. Wainwright, *Rechargeable Lithium batteries with aqueous electrolytes.* Science, 1994. **264**(5164): p. 1114-1118.
39. C. A. Vincent, *Lithium batteries: a 50-year perspective, 1959-2009.* Solid State Ionics, 2000. **134**(1-2): p. 160.

40. C. K. Huang, S. Surampudi, A. Attia, and G. Halpert, *Electrochemical Evaluation Of Alternate Anode Materials For Ambient Temperature Secondary Li Cells*, in *Proceedings of the 35th International Power Sources Symposium*. 1992, IEEE. p. 197-200.
41. T. Kasuh, A. Mabuchi, K. Tokumitsu, and H. Fujimoto, *Recent trends in carbon negative electrode materials.* Journal of Power Sources, 1997. **68**(1): p. 99-101.
42. D. Aurbach, H. Teller, M. Koltypin, and E. Levi, *On the behavior of different types of graphite anodes.* Journal of Power Sources, 2003. **119-121**: p. 2-7.
43. Z. Yang, Z. Li, H. Wu, and B. Simard, *Effects of doped copper on electrochemical performance of the raw carbon nanotubes anode.* Materials Letters, 2003. **57**(21): p. 3160-3166.
44. F. Leroux, K. Méténier, S. Gautier, E. Frackowiak, S. Bonnamy, and F. Béguin, *Electrochemical insertion of lithium in catalytic multi-walled carbon nanotubes.* Journal of Power Sources, 1999. **81-82**(1-2): p. 317-322.
45. A. S. Claye, J. E. Fischer, C. B. Huffman, A. G. Rinzler, and R. E. Smalley, *Solid-State Electrochemistry of the Li Single Wall Carbon Nanotube System.* Journal of The Electrochemical Society, 2000. **147**(8): p. 2845-2852.
46. A. Odani, A. Nimberger, B. Markovsky, E. Sominski, E. Levi, V. G. Kumar, M. Motiei, A. Gedanken, P. Dan, and D. Aurbach, *Development and testing of nanomaterials for rechargeable lithium batteries.* Journal of Power Sources, 2003. **119-121**: p. 517-521.
47. G. T. Wu, C. S. Wang, X. B. Zhang, H. S. Yang, Z. F. Qi, P. M. He, and W. Z. Li, *Structure and Lithium Insertion Properties of Carbon Nanotubes.* Journal of The Electrochemical Society, 1999. **146**(5): p. 1696-1701.
48. C. S. Wang, G. T. Wu, and W. Z. Li, *Lithium insertion in ball-milled graphite.* Journal of Power Sources, 1998. **76**(1): p. 1-10.
49. H. Wang, T. Ikeda, K. Fukada, and M. Yoshio, *Effect of milling on the electrochemical performance of natural graphite as an anode material for lithium-ion battery.* Journal of Power Sources, 1999. **83**(1-2): p. 141-147.
50. T. Takamura, K. Sumiya, J. Suzuki, C. Yamada, and K. Sekine, *Enhancement of Li doping/undoping reaction rate of carbonaceous materials by coating with an evaporated metal film.* Journal of Power Sources, 1999. **81-82**(1-2): p. 368-372.
51. B. Veeraraghavan, A. Durairajan, B. Haran, B. Popov, and R. Guidotti, *Study of Sn-Coated Graphite as Anode Material for Secondary Lithium-Ion Batteries.* Journal of The Electrochemical Society, 2002. **149**(6): p. A675-A681.
52. P. Yu, J. A. Ritter, R. E. White, and B. N. Popov, *Ni-Composite Microencapsulated Graphite as the Negative Electrode in Lithium-Ion Batteries II. Electrochemical Impedance and Self-Discharge Studies.* Journal of The Electrochemical Society, 2000. **147**(6): p. 2081-2085.
53. I. R. M. Kottegoda, Y. Kadoma, H. Ikuta, Y. Uchimoto, and M. Wakihara, *Enhancement of Rate Capability in Graphite Anode by Surface Modification with Zirconia.* Electrochemical and Solid-State Letters, 2002. **5**(12): p. A275-A278.
54. J. Y. Lee, R. Zhang, and Z. Liu, *Lithium Intercalation and Deintercalation Reactions in Synthetic Graphite Containing a High Dispersion of SnO.* Electrochemical and Solid-State Letters, 2000. **3**(4): p. 167-170.
55. W. X. Chen, J. Y. Lee, and Z. Liu, *Electrochemical lithiation and de-lithiation of carbon nanotube-Sn_2Sb nanocomposites.* Electrochemistry Communications, 2002. **4**(3): p. 260-265.

56. J. A. Carcone, *Performance of Lithium-Ion Battery Systems*, in *Proceedings of WESCON*. 1994, IEEE. p. 242.
57. P. Poizot, S. Laruelle, S. Grugeon, L. Dupont, and J.-M. Tarascon, *Nano-sized transition-metal oxides as negative-electrode materials for lithum-ion batteries.* Nature, 2000. **407**(6803): p. 496-499.
58. P. Poizot, S. Laruelle, S. Grugeon, L. Dupont, and J.-M. Tarascon, *Searching for new anode materials for the Li-ion technology: time to deviate from the usual path.* Journal of Power Sources, 2001. **97-98**: p. 235-239.
59. G. X. Wang, Y. Chen, K. Konstantinov, M. Lindsay, H. K. Liu, and S. X. Dou, *Investigation of cobalt oxides as anode materials for Li-ion batteries.* Journal of Power Sources, 2002. **109**(1): p. 142-147.
60. F. Badway, I. Plitz, S. Grugeon, S. Laruelle, M. Dollé, A. S. Gozdz, and J.-M. Tarascon, *Metal Oxides as Negative Electrode Materials in Li-Ion Cells.* Electrochemical and Solid-State Letters, 2002. **5**(6): p. A115-A118.
61. Z. Yuan, F. Huang, C. Feng, J. Sun, and Y. Zhou, *Synthesis and electrochemical performance of nanosized Co_3O_4.* Materials Chemistry and Physics, 2003. **79**(1): p. 1-4.
62. G. X. Wang, Y. Chen, K. Konstantinov, J. Yao, J.-h. Ahn, H. K. Liu, and S. X. Dou, *Nanosize cobalt oxides as anode materials for lithium-ion batteries.* Journal of Alloys and Compounds, 2002. **340**(1-2): p. L5-L10.
63. P. A. Connor and J. T. S. Irvine, *Combined X-ray study of lithium (tin) cobalt oxide matrix negative electrodes for Li-ion batteries.* Electrochimica Acta, 2002. **47**(18): p. 2885-2892.
64. S. Grugeon, S. Laruelle, R. Herrera-Urbina, L. Dupont, P. Poizot, and J.-M. Tarascon, *Particle Size Effects on the Electrochemical Performance of Copper Oxides toward Lithium.* Journal of The Electrochemical Society, 2001. **148**(4): p. A285-A292.
65. J. Sarradin, A. Guessous, and M. Ribes, *Synthesis and characterization of lithium intercalation electrodes based on iron oxide thin films.* Journal of Power Sources, 1996. **62**(2): p. 149-154.
66. D. Larcher, C. Masquelier, D. Bonnin, Y. Chabre, V. Masson, and J.-B. Leriche, *Effect of Particle Size on Lithium Intercalation into α-Fe_2O_3.* Journal of The Electrochemical Society, 2003. **150**(1): p. A133-A139.
67. Y. Wang and Q.-Z. Qin, *A Nanocrystalline NiO Thin-Film Electrode Prepared by Pulsed Laser Ablation for Li-Ion Batteries.* Journal of The Electrochemical Society, 2002. **149**(7): p. A873-A878.
68. J. Yang, Y. Takeda, N. Imanishi, C. Capiglia, J. Y. Xie, and O. Yamamoto, *SiO_x-based anodes for secondary lithium batteries.* Solid State Ionics, 2002. **152-153**(1): p. 125-129.
69. Y.-N. NuLi, Z.-W. Fu, Y.-Q. Chu, and Q.-Z. Qin, *Electrochemical and electrochromic characteristics of Ta_2O_5-ZnO composite films.* Solid State Ionics, 2003. **160**(1-2): p. 197-207.
70. Z.-W. Fu, F. Huang, Y.-Q. Chu, Y. Zhang, and Q.-Z. Qin, *Characterization of Amorphous Ta_2O_5 Film as a Novel Anode Material.* Journal of The Electrochemical Society, 2003. **150**(6): p. A776-782.
71. A. Kuhn, R. Amandi, and F. García-Alvarado, *Electrochemical lithium insertion in TiO_2 with the ramsdellite structure.* Journal of Power Sources, 2001. **92**(1-2): p. 221-227.

72. Y.-k. Zhou, L. Cao, F.-b. Zhang, B.-l. He, and H.-l. Li, *Lithium Insertion into TiO_2 Nanotube Prepared by the Hydrothermal Process.* Journal of The Electrochemical Society, 2003. **150**(9): p. A1246-A1249.
73. F. Belliard and J. T. S. Irvine, *Electrochemical performance of ball-milled ZnO-SnO_2 systems as anodes in lithium-ion battery.* Journal of Power Sources, 2001. **97-98**: p. 219-222.
74. Z.-W. Fu, F. Huang, Y. Zhang, Y. Chu, and Q.-Z. Qin, *The Electrochemical Reaction of Zinc Oxide Thin Films with Lithium.* Journal of The Electrochemical Society, 2003. **150**(6): p. A714-A720.
75. F. Belliard, P. A. Connor, and J. T. S. Irvine, *Novel tin oxide-based anodes for Li-ion batteries.* Solid State Ionics, 2000. **135**(1-4): p. 163-167.
76. J. Y. Lee, Y. Xiao, and Z. Liu, *Amorphous $Sn_2P_2O_7$, $Sn_2B_2O_5$ and Sn_2BPO_6 anodes for lithium ion batteries.* Solid State Ionics, 2000. **133**(1-2): p. 25-35.
77. I. A. Courtney, W. R. McKinnon, and J. R. Dahn, *On the Aggregation of Tin in SnO Composite Glasses Caused by the Reversible Reaction with Lithium.* Journal of The Electrochemical Society, 1999. **146**(1): p. 59-68.
78. S. C. Nam, C. H. Paik, W. I. Cho, B. W. Cho, H. S. Chun, and K. S. Yun, *Electrochemical characterization of various tin-based oxides as neative electrodes for rechargeable lithium batteries.* Journal of Power Sources, 1999. **84**(1): p. 24-31.
79. H. Morimoto, M. Nakai, M. Tatsumisago, and T. Minami, *Mechanochemical Synthesis and Anode Properties of SnO-Based Amorphous Materials.* Journal of The Electrochemical Society, 1999. **146**(11): p. 3970-3973.
80. N. Li, C. R. Martin, and B. Scrosati, *A High-Rate, High-Capacity, Nanostructured Tin Oxide Electrode.* Electrochemical and Solid-State Letters, 2000. **3**(7): p. 316-318.
81. N. Li, C. R. Martin, and B. Scrosati, *Nanomaterial-based Li-ion battery electrodes.* Journal of Power Sources, 2001. **97-98**: p. 240-243.
82. K. Wan, S. F. Y. Lim, Z. Gao, and K. S. Siow, *Tin-based oxide anode for lithium-ion batteries with low irreversible capacity.* Journal of Power Sources, 1998. **75**(1): p. 9-12.
83. D. L. Foster, J. Wolfenstine, J. R. Read, and W. K. Behl, *Nanocomposites of Sn and Li_2O Formed from the Chemical Reduction of SnO as Negative Electrode Material for Lithium-Ion Batteries.* Electrochemical and Solid-State Letters, 2000. **3**(5): p. 203-204.
84. G. R. Goward, F. Leroux, W. P. Power, G. Ouvrard, W. Dmowski, T. Egami, and L. F. Nazar, *On the Nature of Li Insertion in Tin Composite Oxide Glasses.* Electrochemical and Solid-State Letters, 1999. **2**(8): p. 367-370.
85. T. Brousse, S. M. Lee, L. Pasquereau, D. Defices, and D. M. Schleich, *Composite negative electrodes for lithium ion cells.* Solid State Ionics, 1998. **113-115**: p. 51-56.
86. J. Read, D. Foster, J. Wolfenstine, and W. Behl, *SnO_2-carbon composites for lithium-ion battery anodes.* Journal of Power Sources, 2001. **96**(2): p. 277-281.
87. H. Morimoto, M. Tatsumisago, and T. Minami, *Anode Properties of Amorphous 50SiO:50SnO Powders Synthesized by Mechanical Milling.* Electrochemical and Solid-State Letters, 2001. **4**(2): p. A16-A18.
88. M. Nishijima, T. Kagohashi, N. Imanishi, Y. Takeda, O. Yamamoto, and S. Kondo, *Synthesis and electrochemical studies of a new anode material, $Li_{3-x}Co_xN$.* Solid State Ionics, 1996. **83**(1-2): p. 107-111.

89. Y. Takeda, M. Nishijima, M. Yamahata, K. Takeda, N. Imanishi, and O. Yamamoto, *Lithium secondary batteries using a lithium cobalt nitride, $Li_{2.6}Co_{0.4}N$, as the anode.* Solid State Ionics, 2000. **130**(1-2): p. 61-69.
90. Y.-M. Kang, S.-C. Park, Y.-S. Kang, P. S. Lee, and J.-Y. Lee, *The improvement of the cycle life of $Li_{2.6}Co_{0.4}N$ as an anode of Li-ion secondary battery.* Solid State Ionics, 2003. **156**(3-4): p. 263-273.
91. Y. Takeda, J. Yang, and N. Imanishi, *Advanced composite anodes containing litihum cobalt nitride for secondary lithium battery.* Solid State Ionics, 2002. **152-153**(1): p. 35-41.
92. T. Shodai, Y. Sakurai, and T. Suzuki, *Reaction mechanisms of $Li_{2.6}Co_{0.4}N$ anode material.* Solid State Ionics, 1999. **122**(1-4): p. 85-93.
93. T. Shodai, S. Okada, S.-i. Tobishima, and J.-i. Yamaki, *Study of $Li_{3-x}M_xN$ (M: Co, Ni or Cu) system for use as anode material in lithium rechargeable cells.* Solid State Ionics, 1996. **86-88**(2): p. 785-789.
94. M. Nishijima, T. Kagohashi, Y. Takeda, N. Imanishi, and O. Yamamoto, *Electrochemical studies of a new anode material, $Li_{3-x}M_x$ (M=Co, Ni,Cu).* Journal of Power Sources, 1997. **68**(2): p. 510-514.
95. T. Shodai, S. Okada, S. Tobishima, and J. Yamaki, *Anode performance of a new layered nitride $Li_{3-x}Co_xN$ (x=0.2-0.6).* Journal of Power Sources, 1997. **68**(2): p. 515-518.
96. K. Wang, J. Yang, J. Xie, and S. Zhang, *Electrochemical studies of ternary and quadruple litihum metal nitrides synthesized by ballmilling.* Solid State Ionics, 2003. **160**(1-2): p. 69-73.
97. J. Yang, K. Wang, and J. Xie, *Ballmilling Synthesis and Electrochemical Characterization of Ternary Lithium Nitrides.* Journal of The Electrochemical Society, 2003. **150**(1): p. A140-A142.
98. H. Huang, E. M. Kelder, and J. Schoonman, *Lithium intercalation characteristics of B-C-N and C-B-Si-N carbon alloys.* Journal of Power Sources, 2001. **94**(1): p. 108-111.
99. M. Ishikawa, T. Nakamura, M. Morita, Y. Matsuda, S.-i. Tsujioka, and T. Kawashima, *Boron-carbon-nitrogen compounds as negative electrode matrices for rechargeable lithium battery systems.* Journal of Power Sources, 1995. **55**(1): p. 127-130.
100. N. Pereira, M. Balasubramanian, L. Dupont, J. McBreen, L. C. Klein, and G. G. Amatucci, *The Electrochemistry of Germanium Nitride with Lithium.* Journal of The Electrochemical Society, 2003. **150**(8): p. A1118-A1128.
101. N. Pereira, L. Dupont, J. M. Tarascon, L. C. Klein, and G. G. Amatucci, *Electrochemistry of Cu_3N with Lithium - A complex system with Parallel Processes.* Journal of The Electrochemical Society, 2003. **150**(9): p. A1273-A1280.
102. K. S. Park, Y. J. Park, M. K. Kim, J. T. Son, H. G. Kim, and S. J. Kim, *Characteristics of tin nitride thin film negative electrode for thin-film microbattery.* Journal of Power Sources, 2001. **103**(1): p. 67-71.
103. X. Wu, H. Li, L. Chen, and X. Huang, *Agglomeration and the surface passivating film of Ag nano-brush electrode in lithium batteries.* Solid State Ionics, 2002. **149**(304): p. 185.
104. L. Shi, H. Li, Z. Wang, X. Huang, and L. Chen, *Nano-SnSb alloy deposited on MCMB as an anode material for lithium ion batteries.* Journal of Materials Chemistry, 2001. **11**(5): p. 1502-1505.

105. X. B. Zhao, G. S. Cao, C. P. Lv, L. J. Zhang, S. H. Hu, T. J. Zhu, and B. C. Zhou, *Electrochemical properties of some Sb or Te based alloys for candidate anode materials of lithium-ion batteries.* Journal of Alloys and Compounds, 2001. **315**(1-2): p. 265-269.
106. J. O. Besenhard, M. Hess, and P. Komenda, *Dimensionally Stable Li-Alloy Electrodes For Secondary Batteries.* Solid State Ionics, 1990. **40-41**: p. 524-529.
107. D. Larcher, L. Y. Beaulieu, O. Mao, A. E. George, and J. R. Dahn, *Study of the Reaction of Lithium with Isostructural A_2B and Various Al_xB Alloys.* Journal of The Electrochemical Society, 2000. **147**(5): p. 1703-1708.
108. D. Rahner, S. Machill, H. Schlörb, K. Siury, M. Kloss, and W. Plieth, *Intercalation materials for lithium rechargeable batteries.* Journal of Solid State Electrochemistry, 1998. **2**(2): p. 79-84.
109. Y. Hamon, T. Brousse, F. Jousse, P. Topart, P. Buvat, and D. M. Schleich, *Aluminum negative electrode in lithium ion batteries.* Journal of Power Sources, 2001. **97-98**: p. 185-187.
110. J. Yang, Y. Takeda, N. Imanishi, T. Ichikawa, and O. Yamamoto, *Study of the cycling performance of finely dispersed lithium alloy composite electrodes under high Li-utilization.* Journal of Power Sources, 1999. **79**(2): p. 220-224.
111. S. Machill and D. Rahner, *Studies of Al-Al_3Ni eutectic mixtures as insertion anodes in rechargeable lithium batteries.* Journal of Power Sources, 1997. **68**(2): p. 506-509.
112. S. Machill and D. Rahner, *In situ electrochemical characterization of lithium-alloying materials for rechargeable anodes in lithium batteries.* Journal of Power Sources, 1995. **54**(2): p. 428-432.
113. C. Wang, A. J. Appleby, and F. E. Little, *Electrochemical study of nano-Sn, $Li_{4.4}Sn$ and $AlSi_{0.1}$ powders used as secondary lithium battery anodes.* Journal of Power Sources, 2001. **93**(1-2): p. 174-185.
114. G.-J. Jeong, Y. U. Kim, H.-J. Sohn, and T. Kang, *Particulate-reinforced Al-based composite material for anode in lithium secondary batteries.* Journal of Power Sources, 2001. **101**(2): p. 201-205.
115. J. Yin, M. Wada, S. Yoshida, K. Ishihara, S. Tanase, and T. Sakai, *New Ag-Sn Alloy Anode Materials for Lithium-Ion Batteries.* Journal of The Electrochemical Society, 2003. **150**(8): p. A1129-A1135.
116. L. Fang and B. V. R. Chowdari, *Sn-Ca anorphous alloy as anode for lithium ion battery.* Journal of Power Sources, 2001. **97-98**: p. 181-184.
117. H. Sakaguchi, H. Honda, Y. Akasaka, and T. Esaka, *Ce-Sn intermetallic compounds as new anode materials for rechargeable lithium batteries.* Journal of Power Sources, 2003. **119-121**: p. 50-55.
118. H. Kim, Y.-J. Kim, D. G. Kim, H.-J. Sohn, and T. Kang, *Mechanochemical synthesis and electrochemical characteristics of Mg_2Sn as an anode material for Li-ion batteries.* Solid State Ionics, 2001. **144**(1-2): p. 41-49.
119. G. A. Roberts, E. J. Cairns, and J. A. Reimer, *An Electrochemical and XRD Study of Lithium Insertion into Mechanically Alloyed Magnesium Stannide.* Journal of The Electrochemical Society, 2003. **150**(7): p. A912-A916.
120. L. Y. Beaulieu and J. R. Dahn, *The Reaction of Lithium with Sn-Mn-C Intermetallics Prepared by Mechanical Alloying.* Journal of The Electrochemical Society, 2000. **147**(9): p. 3237-3241.
121. L. Y. Beaulieu, K. C. Hewitt, R. L. Turner, A. Bonakdarpour, A. A. Abdo, L. Christensen, K. W. Eberman, L. J. Krause, and J. R. Dahn, *The Electrochemical*

Reaction of Li with Amorphous Si-Sn Alloys. Journal of The Electrochemical Society, 2003. **150**(2): p. A149-A156.

122. A. Ulus, Y. Rosenberg, L. Burstein, and E. Peled, *Tin-Alloy Graphite Composite Anode for Lithium-Ion Batteries.* Journal of The Electrochemical Society, 2002. **149**(5): p. A635-A643.
123. Y.-L. Kim, S.-J. Lee, H.-K. Baik, and S.-M. Lee, *Sn-Zr-Ag alloy thin-film anodes.* Journal of Power Sources, 2003. **119-121**: p. 106-109.
124. L. Y. Beaulieu, D. Larcher, R. A. Dunlap, and J. R. Dahn, *Reaction of Li with Grain-Boundary Atoms in Nanostructured Compounds.* Journal of The Electrochemical Society, 2000. **147**(9): p. 3206-3212.
125. K. D. Kepler, J. T. Vaughey, and M. M. Thackeray, *$Li_xCu_6Sn_5$ (0<x<13): An Intermetallic Insertion Electrode for Rechargeable Lithium Batteries.* Electrochemical and Solid-State Letters, 1999. **2**(7): p. 307-309.
126. D. Larcher, L. Y. Beaulieu, D. D. MacNeil, and J. R. Dahn, *In Situ X-Ray Study of the Electrochemical Reaction of Li with η'-Cu_6Sn_5.* Journal of The Electrochemical Society, 2000. **147**(5): p. 1658-1662.
127. M. M. Thackeray, C. S. Johnson, A. J. Kahaian, K. D. Kepler, J. T. Vaughey, Y. Shao-Horn, and S. A. Hackney, *Stabilization of insertion electrodes for lithium batteries.* Journal of Power Sources, 1999. **81-82**(1-2): p. 60-66.
128. K. D. Kepler, J. T. Vaughey, and M. M. Thackeray, *Copper-tin anodes for rechargeable lithium batteries: an example of the matrix effect in an intermetallic system.* Journal of Power Sources, 1999. **81-82**(1-2): p. 383-387.
129. G. X. Wang, L. Sun, D. H. Bradhurst, S. X. Dou, and H. K. Liu, *Lithium storage properties of nanocrystalline eta-Cu_6Sn_5 alloys prepared by ball-milling.* Journal of Alloys and Compounds, 2000. **299**(1-2): p. L12-L15.
130. Y. Xia, T. Sakai, T. Fujieda, M. Wada, and H. Yoshinaga, *Flake Cu-Sn Alloys as Negative Electrode Materials for Rechargeable Lithium Batteries.* Journal of The Electrochemical Society, 2001. **148**(5): p. A471-A481.
131. J. Wolfenstine, S. Campos, D. Foster, J. Read, and W. K. Behl, *Nano-scale Cu_6Sn_5 anodes.* Journal of Power Sources, 2002. **109**(1): p. 230-233.
132. N. Tamura, R. Ohshita, M. Fujimoto, M. Kamino, and S. Fujitani, *Advanced Structures in Electrodeposited Tin Base Negative Electrodes for Lithium Secondary Batteries.* Journal of The Electrochemical Society, 2003. **150**(6): p. A679-A683.
133. S. D. Beattie and J. R. Dahn, *Single Bath, Pulsed Electrodeposition of Copper-Tin Allot Negative Electrodes for Lithium-ion Batteries.* Journal of The Electrochemical Society, 2003. **150**(7): p. A894-A898.
134. J. H. Ahn, Y. J. Kim, G. X. Wang, M. J. Lindsay, H. K. Liu, and S. X. Dou, *Lithium Storage Properties of Ball Milled Ni-57 mass%Sn Alloy.* Materials Transactions, 2002. **43**(1): p. 63-66.
135. J. H. Ahn, G. X. Wang, S. X. Dou, and H. K. Liu, *Mechanically Milled Nanocrystalline Ni_3Sn_4 and $FeSi_2$ Alloys as an Anode Material for Li-ion Batteries.* Materials Science Forum, 2001. **360-362**: p. 595-602.
136. J. H. Ahn, G. X. Wang, J. Yao, H. K. Liu, and S. X. Dou, *Tin-based composite materials as anode materials for Li-ion batteries.* Journal of Power Sources, 2003. **119-121**: p. 45-49.
137. H.-Y. Lee, S.-W. Jang, S.-M. Lee, S.-J. Lee, and H.-K. Baik, *Lithium storage properties of nanocrystalline Ni_3Sn_4 alloys prepared by mechanical alloying.* Journal of Power Sources, 2002. **112**(1): p. 8-12.

138. G. M. Ehrlich, C. Durand, X. Chen, T. A. Hugener, F. Spiess, and S. L. Suib, *Metallic Negative Electrode Materials for Rechargeable Nonaqueous Batteries.* Journal of The Electrochemical Society, 2000. **147**(3): p. 886-891.
139. Y.-L. Kim, H.-Y. Lee, S.-W. Jang, S.-J. Lee, H.-K. Baik, Y.-S. Park, and S.-M. Lee, *Nanostructured Ni_3Sn_2 thin film as anodes for thin film rechargeable lithium batteries.* Solid State Ionics, 2003. **160**(3-4): p. 235-240.
140. H. Mukaibo, T. Sumi, T. Yokoshima, T. Momma, and T. Osaka, *Electrodeposited Sn-Ni Alloy Film as a High Capacity Anode Material for Lithium-Ion Secondary Batteries.* Electrochemical and Solid-State Letters, 2003. **6**(10): p. A218-A220.
141. O. Mao, R. L.Turner, I. A. Courtney, B. D. Fredericksen, M. I. Buckett, L. J. Krause, and J. R. Dahn, *Active/Inactive Nanocomposites as Anodes for Li-Ion Batteries.* Electrochemical and Solid-State Letters, 1999. **2**(1): p. 3-5.
142. O. Mao, R. A. Dunlap, and J. R. Dahn, *In situ ^{57}Fe and ^{119}Sn Mössbauer effect studies of the electrochemical reaction of lithium with mechanically alloyed SnFe.* Solid State Ionics, 1999. **118**(1-2): p. 99-109.
143. O. Mao and J. R. Dahn, *Mechanically Alloyed Sn-Fe(-C) Powders as Anode Materials for Li-Ion Batteries II. The Sn-Fe System.* Journal of The Electrochemical Society, 1999. **146**(2): p. 414-422.
144. H. Li, X. Huang, L. Chen, G. Zhou, Z. Zhang, D. Yu, Y. J. Mo, and N. Pei, *The crystal structural evolution of nano-Si anode caused by lithium insertion and extraction at room temperature.* Solid State Ionics, 2000. **135**(1-4): p. 181-191.
145. J. Niu and J. Y. Lee, *Improvement of Usable Capacity and Cyclability of Silicon-Based Anode Materials for Lithium Batteries.* Electrochemical and Solid-State Letters, 2002. **5**(6): p. A107-A110.
146. H. Li, X. Huang, L. Chen, Z. Wu, and Y. Liang, *A High Capacity Nano-Si Composite Anode Material for Lithium Rechargeable Batteries.* Electrochemical and Solid-State Letters, 1999. **2**(11): p. 547-549.
147. S. Bourderau, T. Brousse, and D. M. Schleich, *Amorphous silicon as a possible anode material for Li-ion batteries.* Journal of Power Sources, 1999. **81-82**(1-2): p. 233-236.
148. S.-J. Lee, J.-K. Lee, S.-H. Chung, H.-Y. Lee, S.-M. Lee, and H.-K. Baik, *Stress effect on cycle properties of the silicon thin-film anode.* Journal of Power Sources, 2001. **97-98**: p. 191-193.
149. J. Graetz, C. C. Ahn, R. Yazami, and B. Fultz, *Highly Reversible Lithium Storage in Nanostructured Silicon.* Electrochemical and Solid-State Letters, 2003. **6**(9): p. A194-A197.
150. J. P. Maranchi, A. F. Hepp, and P. N. Kumta, *High Capacity, Reversible Silicon Thin-Film Anodes for Lithium-Ion Batteries.* Electrochemical and Solid-State Letters, 2003. **6**(9): p. A198-A201.
151. S. Ohara, J. Suzuki, K. Sekine, and T. Takamura, *Li insertion/extraction reaction at a Si film evaporated on a Ni foil.* Journal of Power Sources, 2003. **119-121**: p. 591-596.
152. A. Netz, R. A. Huggins, and W. Weppner, *The formation and properties of amorphous silicon as negative electrode reactant in litihum systems.* Journal of Power Sources, 2003. **119-121**: p. 95-100.
153. G. X. Wang, L. Sun, D. H. Bradhurst, S. Zhong, S. X. Dou, and H. K. Liu, *Innovative nanosize lithium storage alloys with silica as active centre.* Journal of Power Sources, 2000. **88**(2): p. 278-281.

154. G. X. Wang, L. Sun, D. H. Bradhurst, S. Zhong, S. X. Dou, and H. K. Liu, *Nanocrystalline NiSi alloy as an anode material for Lithium-ion batteries.* Journal of Alloys and Compounds, 2000. **306**(1-2): p. 249-252.
155. H.-Y. Lee and S.-M. Lee, *Graphite-FeSi alloy composites as anode materials for rechargeable lithium batteries.* Journal of Power Sources, 2002. **112**(2): p. 649-654.
156. S.-W. Song, K. A. Striebel, X. Song, and E. J. Cairns, *Amorphous and nanocrystalline Mg_2Si thin-film electrodes.* Journal of Power Sources, 2003. **119-121**: p. 110-112.
157. S.-W. Song, K. A. Striebel, R. P. Reade, G. A. Roberts, and E. J. Cairns, *Electrochemical Studies of Nanocrystalline Mg_2Si Thin Film Electrodes Prepared by Pulsed Laser Deposition.* Journal of The Electrochemical Society, 2003. **150**(1): p. A121-A127.
158. G. A. Roberts, E. J. Cairns, and J. A. Reimer, *Magnesium silicide as a negative electrode material for lithium-ion batteries.* Journal of Power Sources, 2002. **110**(2): p. 424-429.
159. G. S. Cao, X. B. Zhao, T. Li, and C. P. Lu, *Zn_4Sb_3(-C_7) powders as a potnetial anode material for lithium ion batteries.* Journal of Power Sources, 2001. **94**(1): p. 102-107.
160. J.-M. Tarascon, M. Morcrette, L. Dupont, Y. Chabre, C. Payen, D. Larcher, and V. Pralong, *On the Electrochemical Reactivity Mechanism of $CoSb_3$ vs. Lithium.* Journal of The Electrochemical Society, 2003. **150**(6): p. A732-A741.
161. L. M. L. Fransson, J. T. Vaughey, K. Edström, and M. M. Thackeray, *Structural Transformations in Intermetallic Electrodes for Lithium batteries: An In Situ X-Ray Diffraction Study of Lithiated MnSb and Mn_2Sb.* Journal of The Electrochemical Society, 2003. **150**(1): p. A86-A91.
162. J. T. Vaughey, L. Fransson, H. A. Swinger, K. Edström, and M. M. Thackeray, *Alternative anode materials for lithium-ion batteries: a study of Ag_3Sb.* Journal of Power Sources, 2003. **119-121**: p. 64-68.
163. H. Honda, H. Sakaguchi, Y. Fukada, and T. Esaka, *Anode behaviours of aluminium antimony synthesized by mechanical alloying for lithium secondary battery.* Materials Research Bulletin, 2003. **38**(4): p. 647-656.
164. J. T. Vaughey, C. S. Johnson, A. J. Kropf, R. Benedek, M. M. Thackeray, H. Tostmann, T. Sarakonsri, S. Hackney, L. Fransson, K. Edström, and J. O. Thomas, *Structural and mechanistic features of intermetallic materials for lithium batteries.* Journal of Power Sources, 2001. **97-98**: p. 194-197.
165. H. Honda, H. Sakaguchi, I. Tanaka, and T. Esaka, *Anode behaviours of magnesium-antimony intermetallic compound for lithium secondary battery.* Journal of Power Sources, 2003. **123**(2): p. 216-221.
166. J. T. Vaughey, J. O'Hara, and M. M. Thackeray, *Intermetallic Insertion Electrodes with a Zinc Blende-Type Structure for Li Batteries: A study of Li_xInSb ($0 \leq x \leq 3$).* Electrochemical and Solid-State Letters, 2000. **3**(1): p. 13-16.
167. J. Yang, Y. Takeda, N. Imanishi, J. Y. Xie, and O. Yamamoto, *Intermetallic SnSbx compounds for lithium insertion hosts.* Solid State Ionics, 2000. **133**(3-4): p. 189-194.
168. J. Yang, Y. Takeda, N. Imanishi, and O. Yamamoto, *Ultrafine Sn and $SnSb_{0.14}$ Powders for Lithium Storage Matrices in Lithium-Ion Batteries.* Journal of The Electrochemical Society, 1999. **146**(11): p. 4009-4013.

169. J. Yang, M. Wachtler, M. Winter, and J. O. Besenhard, *Sub-Microcrystalline Sn and Sn-SnSb Powders as Lithium Storage Materials for Lithium-Ion Batteries.* Electrochemical and Solid-State Letters, 1999. **2**(4): p. 161-163.
170. J. Yang, Y. Takeda, Q. Li, N. Imanishi, and O. Yamamoto, *Lithium insertion into Sn- and $SnSb_x$-based composite electrodes in solid polymer electrolytes.* Journal of Power Sources, 2000. **90**(1): p. 64-69.
171. J. Yang, Y. Takeda, N. Imanishi, T. Ichikawa, and O. Yamamoto, *$SnSb_x$-based composite electrodes for lithium ion cells.* Solid State Ionics, 2000. **135**(1-4): p. 175-180.
172. H. Li, L. Shi, Q. Wang, L. Chen, and X. Huang, *Nano-alloy anode for lithium ion batteries.* Solid State Ionics, 2002. **148**(3-4): p. 247-258.
173. H. Li, L. Shi, W. Lu, X. Huang, and L. Chen, *Studies on Capacity Loss and Capacity Fading on Nanosized SnSb Alloy Anode for Li-Ion Batteries.* Journal of The Electrochemical Society, 2001. **148**(8): p. A915-A922.
174. J. Yang, Y. Takeda, C. Capiglia, X. D. Liu, N. Imanishi, and O. Yamamoto, *High-capacity composite anodes with SnSb and $Li_{2.6}Co_{0.4}N$ for solid polymer electrolyte cells.* Journal of Power Sources, 2003. **119-121**: p. 56-59.
175. K. C. Hewitt, L. Y. Beaulieu, and J. R. Dahn, *Electrochemistry of InSb as a Li Insertion Host.* Journal of The Electrochemical Society, 2001. **148**(5): p. A402-A410.
176. P. Lavela, J. Morales, L. Sánchez, and J. L. Tirado, *Novel layered chalcogenides as electrode materials for lithium-ion batteries.* Journal of Power Sources, 1997. **68**(2): p. 704-707.
177. Y. Piffard, F. Leroux, D. Guyomard, J.-L. Mansot, and M. Tournoux, *The amorphous oxides $MnV_2O_{6+\delta}$ ($0<\delta<1$) as high capacity negative electrode materials for lithium batteries.* Journal of Power Sources, 1997. **68**(2): p. 698-703.
178. D. Guyomard, C. Sigala, A. Le Gal La Selle, and Y. Piffard, *New amorphous oxides as high capacity negative electrodes for lithium batteries: the Li_xMVO_4 (M=Ni, Co, Cd, Zn; $1<x\leq 8$) series.* Journal of Power Sources, 1997. **68**(2): p. 692-697.
179. S. Laruelle, P. Poizot, E. Baudrin, V. Briois, M. Touboul, and J.-M. Tarascon, *X-ray absorption study of cobalt vanadates during cycling usable as negative electrode in lithium battery.* Journal of Power Sources, 2001. **97-98**: p. 251-253.
180. A. F. Fuentes, L. Treviño, A. Martínez-de la Cruz, and L. M. Torres-Martínez, *Electrochemical lithium insertion in some nickel, zinc and cadmium vanadates.* Journal of Power Sources, 1999. **81-82**(1-2): p. 264-267.
181. E. Andrukaitis, G. L. Torlone, and I. R. Hill, *Study of $Me_x(VO_3)_2$ vanadates, (Me = Co, Ni, Mn, $1<x<2$) for lithium rechargeable cells.* Journal of Power Sources, 1999. **81-82**(1-2): p. 651-655.
182. S. Denis, E. Baudrin, F. Orsini, G. Ouvrard, M. Touboul, and J.-M. Tarascon, *Synthesis and electrochemical properties of numerous classes of vanadates.* Journal of Power Sources, 1999. **81-82**(1-2): p. 79-84.
183. S.-S. Kim, H. Ikuta, and M. Wakihara, *Sythesis and characterization of MnV_2O_6 as a high capacity anode material for a lithium secondary battery.* Solid State Ionics, 2001. **139**(1-2): p. 57-65.
184. M. Kamata, G. Oriji, Y. Katamaya, T. Miura, and T. Kishi, *Lithium insertion behavior of ε-$Cu_{0.9}V_2O_5$.* Solid State Ionics, 2002. **146**(1-2): p. 95-100.
185. S. Okada, T. Tonuma, Y. Uebo, and J.-i. Yamaki, *Anode properties of calcite-type MBO_3 (M:V,Fe).* Journal of Power Sources, 2003. **119-121**: p. 621-625.

186. C. Gejke, L. Börjesson, and K. Edström, *Cycling performance and temperature stability of a tin-borate glass anode.* Electrochemistry Communications, 2003. **5**(1): p. 27-31.
187. J. L. C. Rowsell, J. Gaubicher, and L. F. Nazar, *A new class of materials for lithium-ion batteries: iron (III) borates.* Journal of Power Sources, 2001. **97-98**: p. 254-257.
188. T. Ohzuku, K. Tatsumi, N. Matoba, and K. Sawai, *Electrochemistry and Structural Chemistry of Li[CrTi]O4 (Fd3m) in Nonaqueous Lithium Cells.* Journal of The Electrochemical Society, 2000. **147**(10): p. 3592-3597.
189. B. Scrosati, S. Panero, P. Reale, D. Satolli, and Y. Aihara, *Investigation of new types of lithium-ion battery materials.* Journal of Power Sources, 2002. **105**(2): p. 161-168.
190. G. X. Wang, D. H. Bradhurst, S. X. Dou, and H. K. Liu, *Spinel $Li[Li_{1/3}Ti_{5/3}]O_4$ as an anode material for lithium ion batteries.* Journal of Power Sources, 1999. **83**(1-2): p. 156-161.
191. A. D. Robertson, L. Trevino, H. Tukamoto, and J. T. S. Irvine, *New inorganic spinel oxides for use as negative electrode materials in future lithium-ion batteries.* Journal of Power Sources, 1999. **81-82**(1-2): p. 352-357.
192. K. Zaghib, M. Simoneau, M. Armand, and M. Gauthier, *Electrochemical study of $Li_4Ti_5O_{12}$ as negative electrode for Li-ion polymer rechargeable batteries.* Journal of Power Sources, 1999. **81-82**(1-2): p. 300-305.
193. P. P. Prosini, R. Mancini, L. Petrucci, V. Contini, and P. Villano, *$Li_4Ti_5O_{12}$ as anode in all-solid-state, plastic, lithium-ion batteries for low-power applications.* Solid State Ionics, 2001. **144**(1-2): p. 185-192.
194. P. A. Connor and J. T. S. Irvine, *Novel tin oxide spinel-based anodes for Li-ion batteries.* Journal of Power Sources, 2001. **97-98**: p. 223-225.
195. R. Dedryvère, J. Oliver-Fourcade, and J. C. Jumas, *Lithium Insertion in Copper, Indium, Tin Thiospinels Characterized by ^{119}Sn Mössbauer Spectroscopy and Rietveld Analysis.* Chemistry of Materials, 2000. **12**(5): p. 1439-1445.
196. M. A. Cochez, J. C. Jumas, P. Lavela, J. Morales, J. Oliver-Fourcade, and J. L. Tirado, *New tin-containing spinel sulfide electrodes for ambient temperature rocking chair cells.* Journal of Power Sources, 1996. **62**(1): p. 101-105.
197. P. Krtil and D. Fattakhova, *Li Insertion into Li-Ti-O Spinels: Voltammetric and Electrochemical Impedance Spectroscopy Study.* Journal of The Electrochemical Society, 2001. **148**(9): p. A1045-A1050.
198. R. Dedryvère, S. Denis, P. E. Lippens, J. Oliver-Fourcade, and J. C. Jumas, *Phase separation and amorphisation in lithium inserted Cu-In-Sn sulfospinels: experimental and theoretical approach.* Journal of Power Sources, 2001. **97-98**: p. 204-207.
199. A. D. Robertson, H. Tukamoto, and J. T. S. Irvine, *$Li_{1+x}Fe_{1-3x}Ti_{1+2x}O_4(0.0\leq x\leq 0.33)$ Based Spinels: Possible Negative Electrode Materials for Future Li-Ion Batteries.* Journal of The Electrochemical Society, 1999. **146**(11): p. 3958-3962.
200. S.-K. Chang, H.-J. Kim, and S.-T. Hong, *A new lithium-copper-iron-oxide as a negative electrode material for lithium-ion batteries.* Journal of Power Sources, 2003. **119-121**: p. 69-75.
201. R. K. B. Gover, J. R. Tolchard, H. Tukamoto, T. Murai, and J. T. S. Irvine, *Investigation of Ramsdellite Titanates as Possible New Negative Electrode Materials for Li Batteries.* Journal of The Electrochemical Society, 1999. **146**(12): p. 4348-4353.

202. M. N. Obrovac, R. A. Dunlap, R. J. Sanderson, and J. R. Dahn, *The Electrochemical Displacement Reaction of Lithium with Metal Oxides.* Journal of The Electrochemical Society, 2001. **148**(6): p. A576-A588.
203. P. P. Prosini, M. Carewska, S. Loreti, C. Minarini, and S. Passerini, *Lithium iron oxide as alternative anode for li-ion batteries.* International Journal of Inorganic Materials, 2000. **2**(4): p. 365-370.
204. S.-S. Kim, S. Ogura, H. Ikuta, Y. Uchimoto, and M. Wakihara, *Reaction mechanisms of $MnMoO_4$ for high capacity anode material of Li secondary battery.* Solid State Ionics, 2002. **146**(3-4): p. 249-256.
205. M. Nagayama, T. Morita, H. Ikuta, M. Wakihara, M. Takano, and S. Kawasaki, *A new anode material $SnSO_4$ for lithium secondary battery.* Solid State Ionics, 1998. **106**(1-2): p. 33-38.
206. L. L. G. Tovar, P. A. Connor, F. Belliard, L. M. Torres-Martínez, and J. T. S. Irvine, *Investigation of lead tin fluorides as possible negative electrodes for Li-ion batteries.* Journal of Power Sources, 2001. **97-98**: p. 258-261.
207. Y. W. Xiao, J. Y. Lee, A. S. Yu, and Z. L. Liu, *Electrochemical Performance of Amorphous and Crystalline Sn2P2O7 Anodes in Secondary Lithium Batteries.* Journal of The Electrochemical Society, 1999. **146**(10): p. 3623-3629.
208. Z. Liu and J. Y. Lee, *Electrochemical performance of $Pb_3(PO_4)_2$ anodes in rechargeable lithium batteries.* Journal of Power Sources, 2001. **97-98**: p. 247-250.
209. T. Momma, N. Shiraishi, A. Yoshizawa, T. Osaka, A. Gedanken, J. Zhu, and L. Sominski, *SnS_2 anode for rechargeable lithium battery.* Journal of Power Sources, 2001. **97-98**: p. 198-200.
210. L. J. Zhang, X. B. Zhao, X. B. Jiang, C. P. Lv, and G. S. Cao, *Study on the insertion behaviors of Lithium-ions into $CoFe_3Sb_{12}$ based electrodes.* Journal of Power Sources, 2001. **94**(1): p. 92-96.
211. V. Pralong, D. C. S. Souza, K. T. Leung, and L. F. Nazar, *Reversible lithium uptake by CoP_3 at low potential: role of the anion.* Electrochemistry Communications, 2002. **4**(6): p. 516-520.
212. Y. Nishi, *Lithium ion secondary batteries; past 10 years and the future.* Journal of Power Sources, 2001. **100**(1-2): p. 101-106.
213. C. Suryanarayana, *Mechanical alloying and milling.* Progress In Materials Science, 2001. **146**(1-2): p. 1-184.
214. B. S. Murty and S. Ranganathan, *Novel materials synthesis by mechanical alloying/milling.* International Materials Reviews, 1998. **43**(3): p. 101-141.
215. *Metals Handbook*. Vol. 7: American Society For Metals.
216. N. Li, C. J. Patrissi, G. Che, and C. R. Martin, *Rate Capabilities of Nanostructured $LiMn_2O_4$ Electrodes in Aqueous Electrolyte.* Journal of The Electrochemical Society, 2000. **147**(6): p. 2044-2049.
217. C. R. Sides, N. Li, C. J. Patrissi, B. Scrosati, and C. R. Martin, *Nanoscale Materials for Lithium-Ion Batteries.* MRS Bulletin, 2002. **27**(8): p. 604-607.
218. N. Li and C. R. Martin, *A High-Rate, High-Capacity, Nanostructured Sn-Based Anode Prepared Using Sol-Gel Template Synthesis.* Journal of The Electrochemical Society, 2001. **148**(2): p. A164-A170.
219. Y. Shao-Horn, S. Osmialowski, and Q. C. Horn, *Nano-FeS_2 for Commercial Li/FeS_2 Primary Batteries.* Journal of The Electrochemical Society, 2002. **149**(11): p. A1499-A1502.

220. Y. Sato, T. Nakano, K. Kobayakawa, T. Kawai, and A. Yokoyama, *Particle-size effect of carbon powders on the discharge capacity of lithium ion batteries.* Journal of Power Sources, 1998. **75**(2): p. 271-277.
221. J. Shim and K. A. Strieble, *Effect of electrode density on cycle performance and irreversible capacity loss for natural graphite anodein lithium-ion batteries.* Journal of Power Sources, 2003. **119-121**: p. 934-937.
222. T. Takamura, M. Saito, A. Shimokawa, C. Nakahara, K. Sekine, S. Meano, and N. Kibayashi, *Charge/discharge efficiency improvement by the incorporation of conductive carbons in the carbon anode of Li-ion batteries.* Journal of Power Sources, 2000. **90**(1): p. 45-51.
223. R. Dominko, M. Gaberscek, J. Drofenik, M. Bele, S. Pejovnik, and J. Jamnik, *The role of carbon black distribution in cathodes for Li ion batteries.* Journal of Power Sources, 2003. **119-121**: p. 770-773.
224. K. S. Nanjundaswamy, H. D. Friend, C. O. Kelly, D. J. Standlee, and R. L. Higgins, *Electrode Fabrication for Li-Ion: Processing, Formulations and Defects During Coating*, in *Proceedings of the 32nd Intersociety Energy Conversion Engineering Conference*. 1997, IEEE. p. 42-45.
225. L. Fransson, T. Eriksson, K. Edström, T. Gustafsson, and J. O. Thomas, *Influence of carbon black and binder on Li-ion batteries.* Journal of Power Sources, 2001. **101**(1): p. 1-9.
226. *Smithells Metal Reference Book*. Seventh ed, ed. G. B. Brook: Butterworth Heinemann.
227. Z.-G. Yang and L. L. Shaw, *Synthesis of Nanocrystalline SiC at Ambient Temperature Through High Energy Reaction Milling.* Nanostructured Materials, 1996. **7**(8): p. 877.
228. E. W. Nuffield, *X-Ray Diffraction Methods*, New York: John Wiley & Sons, Inc.
229. S. Lowell and J. E. Shields, *Powder Surface Area and Porosity*. Second ed. 1984, London: Chapman And Hall.
230. *ASM Handbook - Alloy Phase Diagrams*, ed. H. Baker. 1992, Materials Park: ASM International.
231. A. V. Trifonova, A. A. Momchilov, B. L. Puresheva, and I. Abrahams, *Electrochemical lithium intercalation in lead-tin-aluminium solder.* Solid State Ionics, 2001. **143**(3-4): p. 319-328.
232. C. C. Koch, *Synthesis of Nanostructured Materials by Mechanical Milling: Problems and Opportunities.* Nanostructured Materials, 1997. **9**(1-8): p. 15.
233. G. V. Raynor and V. G. Rivlin, *Phase equilibria in iron ternary alloys*. 1988, London: Institute of Metals. 485.
234. M. Ohashi, W. Gloffke, and M. S. Whittingham, *Iodine and lithium intercalation into the high-T_c superconducting oxide $Bi_2Sr_2CaCu_2O_y$.* Solid State Ionics, 1992. **57**(3-4): p. 183-187.
235. N. A. Fleischer, J. Manassen, P. Coppens, P. Lee, and Y. Gao, *Electrochemical Insertion of Lithium into the $Bi_2Sr_2CaCu_2O_{8+y}$ high-T_c superconductor.* Physica C: Superconductivity, 1992. **190**(3): p. 367-378.
236. M. Fujiwara, M. Nakanishi, Y. Kusano, T. Fujii, J. Takada, Y. Takeda, and Y. Ikeda, *Electrochemical lithium intercalation into the Bi-2212 phase.* Physica C: Superconductivity, 1997. **279**(3-4): p. 219-224.
237. J. Molenda, I. Nowak, M. Paleczny, and J. Marzec, *Electrical and electrochemical properties of $Bi_2Sr_2CaCu_2O_{8+\delta}$ superconductor.* Solid State Ionics, 1999. **119**(1-4): p. 61-74.

238. P. Strobel, B. Bonnet, C. Mouget, and B. Souletie, *Optimization of hole density and Tc in $Bi_2(Sr,Ca)_3Cu_2O_{8+y}$ by lithium electrochemical reduction.* Physica C: Superconductivity, 1990. **172**(3-4): p. 193-198.
239. J. Yang, B. F. Wang, K. Wang, Y. Liu, J. Y. Xie, and Z. S. Wen, *Si/C Composites for High Capacity Lithium Storage Materials.* Electrochemical and Solid-State Letters, 2003. **6**(8): p. A154-A156.
240. S. B. Ng, J. Y. Lee, and Z. L. Liu, *Si-O network encapsulated graphite-silicon mixtures as negative electrodes for lithium-ion batteries.* Journal of Power Sources, 2001. **94**(1): p. 63-67.
241. J. Schoonman, *Nanoionics.* Solid State Ionics, 2003. **157**(1-4): p. 324.
242. P. M. B. Walker, ed. *Chambers Science and Technology Dictionary*. 1994, Chambers: Edinburgh. 992-993.